THE UNIVERSITY
of ADELAIDE

An investigation into the mechanics of sound propagation through turbulent non-isothermal exhaust jets in cross-flow

Orddom Yi Jie Leav

School of Mechanical Engineering
The University of Adelaide
South Australia 5005
Australia

Thesis submitted in fulfillment of the requirements for the degree of Ph. D. in Engineering on April 2020.

Ph. D. Thesis

April 2020

School of Mechanical Engineering
The University of Adelaide
South Australia 5005
Australia

Typeset by the author using LaTeX.
Printed in Australia.

Copyright © 2020 Orddom Yi Jie Leav, and The University of Adelaide, Australia.

All right reserved. No part of this report may be used or reproduced in any form or by any means, or stored in a database or retrieval system without prior written permission of the university except in the case of brief quotations embodied in critical articles and reviews.

Abstract

Open cycle gas turbines (OCGT) are increasingly being used for power generation as they are able to provide base loads in peaking or uncertain conditions and can respond quickly to power grid demands. However, it has been recorded in literature that OCGT (also known as single cycle gas turbines) have exhibited higher levels of low-frequency noise levels in communities near these plants than orthodoxy predicts. High levels of low-frequency noise within a community can cause the following effects: audible low frequency 'rumble', 'beating' sensations in the chest, nausea and acoustic excitation in structures with low resonant frequencies, such as glazing. It is hypothesised that the low-frequency noise affecting neighbouring communities is due to the sound emitted from the stack being refracted by hot turbulent exhaust gases and cross-winds. It is known that the shear layer, counter-rotating vortex pairs and horseshoe vortices that are generated from this type of flow scenario can affect the propagation of sound with effects such as refraction, diffraction and scattering.

This thesis investigates the effects of this fluid flow mechanism on the propagation of low-frequency sound from a plane-wave through a heated mean flow. The investigation is undertaken numerically with a commercial computational fluid dynamics (CFD) package using ANSYS FLUENT, and with an acoustic finite element model (FEM) using ANSYS Mechanical. Subsequent investigations were completed experimentally using a reduced scale exhaust rig within a wind tunnel at the University of Adelaide. The numerical and experimental results have shown that downwind of the exhaust stack the plume causes an increase in the sound pressure level (SPL) of up to 11 dB when compared to acoustic radiation from an exhaust stack in a homogeneous medium. Furthermore, the experimental and numerical results have shown qualitative similarities, that the sound propagation path is drastically altered by the non-isothermal, turbulent exhaust jet that is deflected by a cooler cross-flow. The results of the research have shown that the measured sound radiation from exhaust stacks in cross-flow is highly dependent on the following: acoustic frequency, distance from the exhaust stack, temperature

of the exhaust jet, thermal and velocity gradient in the plume, and the jet to cross-flow momentum flux ratio.

The change in the sound propagation path, which impacts the downwind SPL, can also be significantly altered by changing the outlet of the exhaust stack. A prototype exhaust nozzle was developed to reduce SPLs downwind. An investigation of a straight duct section with walls that are acoustically transparent, but relatively impervious to flow, has been completed both numerically and experimentally. The investigation has shown that the SPL downwind of the stack is reduced in the presence of the nozzle. Two other prototype nozzles of different geometries have also been designed and experimentally tested. The two additional prototype nozzle geometries have walls that are both acoustically transparent and impervious to flow but are implemented to change the fluid dynamics of the plume. All three nozzles show a reduction in the acoustic refraction downwind of the exhaust stack. It is expected that the results of the research will be used to develop new noise control measures for the electrical power generation industry.

Declarations

Originality

I certify that this work contains no material which has been accepted for the award of any other degree or diploma in my name in any university or other tertiary institution and, to the best of my knowledge and belief, contains no material previously published or written by another person, except where due reference has been made in the text. In addition, I certify that no part of this work will, in the future, be used in a submission in my name for any other degree or diploma in any university or other tertiary institution without the prior approval of the University of Adelaide and where applicable, any partner institution responsible for the joint award of this degree.

I acknowledge the support I have received for my research through the provision of an Australian Government Research Training Program Scholarship.

Orddom Yi Jie Leav

Permissions

I give consent to this copy of my thesis, when deposited in the University Library, being made available for loan and photocopying, subject to the provisions of the Copyright Act 1968.

I also give permission for the digital version of my thesis to be made available on the web, via the University's digital research repository, the Library catalogue, the Australasian Digital Theses Program (ADTP) and also through web search engines, unless permission has been granted by the University to restrict access for a period of time.

Orddom Yi Jie Leav

Acknowledgements and dedication

Firstly, I would like to thank my supervisors Professor Benjamin Cazzolato and Professor Carl Howard. You have both mentored and guided me both personally and professionally to be not only a better engineer but also a better person. Carl and Ben, you have both shown me that even though the PhD and research are essential, there is more to life than research. I will forever treasure the soft skills I have learnt that are essential to research that I would only have learnt under your guidance. Ben, thank you for supervising me for both my Honours projects and my PhD. I am grateful for the experience and would do it all in a heartbeat. Carl, it has been indeed an enjoyable experience working with you during the PhD and you have been a brilliant role model of professionalism, as both an engineer and a researcher.

I would also like to thank my colleagues and dear friends in the s324b office, for whom I had the pleasure of going through the PhD experience together. It has been a roller coaster of emotions, and I would not have had the emotional perseverance to complete the PhD dissertation without you all. Thank you to Dr Eshodarar Sureshkumar, Dr Francesco Larizza, Dr Shen Long, Dr Kae Ken Foo, Dr Dominic Davis, Dr Houzhi Wang, Dr Amy Lewis, Dr David Haydon, Dr Sam Sobey.

Professor Bentahar Mabrouk, thank you for facilitating a visit to the University of Technology of Compiègne and for spending time to educate me and review the mathematics for the linearised acoustic wave equation with and without the flow velocity potential.

I would like to thank Alison-Jane Hunter for her writing workshops and assisting me in developing my writing skills for scientific research. Furthermore, thank you, Alison-Jane for your professional services in proof reading and editing the thesis.

Next, I would like to thank my family: Phanh Nieng Leav, Alecia Chew Gak Leav, Monica Leav, Lachlan Oliver Leav, and Amelia Leav. As my family, you have helped build my character as a person and supported me through my journey. I have to thank, mum and dad, for being incredible role models that I have always looked up to, as a way of life. I would not be able to accomplish this body of work without the family in my life.

Finally, I would like to thank my partner Margaret (Xiaotong) Sun, for being by my side for the whole PhD experience. Thank you for being understanding and having the patience to deal with my diverse range of emotional stages during the PhD.

This thesis is dedicated to all the people that have shaped me to the person I am at the point of publishing this thesis.

Contents

Declarations i

Acknowledgements and dedication iii

Contents v

List of Figures viii

List of Tables xxxiv

Acronyms xxxvii

1 Introduction 1

1.1 Background and motivation 1
1.2 Aims and objectives 6
1.3 Thesis outline 7

2 Literature Review 9

2.1 Topics for review 9
2.2 Open cycle gas turbine noise source 9
2.3 Atmospheric sound propagation 12
2.4 Jets in cross-flow 23
2.5 Jet shear layer sound refraction 34
2.6 Research gaps 40
2.7 Assumptions and limitations 42

3 Time invariant numerical sound propagation through jets in cross-flow 45
3.1 Introduction . . . 45
3.2 Mathematical models, domain, and boundary conditions . . . 48
3.3 Results and discussion . . . 69
3.4 Discussion . . . 141
3.5 Conclusion . . . 152

4 Experimental measurements of sound propagation through jets in cross-flow 157
4.1 Outline . . . 157
4.2 Methodology and experimental apparatus . . . 160
4.3 Experimental flow and temperature results . . . 169
4.4 Acoustic results . . . 182
4.5 Discussion . . . 206
4.6 Summary of the findings . . . 210

5 Prototype exhaust stack noise mitigation 215
5.1 Introduction . . . 215
5.2 Previous work on exhaust nozzle design . . . 216
5.3 Acoustically transparent, impervious to flow nozzles . . . 216
5.4 Prototype nozzle designs . . . 218
5.5 Numerical validation of the acoustically transparent duct section . . . 222
5.6 Experimental tests on exhaust nozzles . . . 232
5.7 Discussion on noise mitigation and real life implementation . . . 243
5.8 Summary of noise mitigation . . . 248

6 Conclusions 251
6.1 Summary of the findings . . . 251
6.2 Future work . . . 264

References 271

A Reduced scale mathematical calculations 297

A.1 Numerical Calculations for a Real-Scale Exhaust Stack 298
A.2 AWT Non-Isothermal Experimental Testing 302
A.3 Numerical Simulations - Non-Isothermal Ground Level JICF 310

B Mathematical formulation for sound propagation with finite element model 317
B.1 Stationary acoustic wave equation 318
B.2 Non-stationary acoustic wave equation with mean fluid flow 325
B.3 Discretised acoustic wave equation for FEM 329

C Numerical validation 333
C.1 Sound Propagation through Ducts in 2-D 334
C.2 Sound Propagation through Ducts in 3-D 338
C.3 Sound Radiation from an Infinitely Thin Rectangular Baffled Piston in 2-D 347
C.4 Sound Radiation from a Circular Baffled Piston in Axisymmetry . . 350
C.5 Sound Propagation through the Thermal Gradients in a Plane Jet in 2-D 354
C.6 Sound Radiation from a Circular Unbaffled Piston in Axisymmetry . 359
C.7 Sound propagation from a point source in uniform flow in 2-D . . . 364
C.8 Sound propagation from a point source in sheared flow in 2-D . . . 376
C.9 Sound propagation from a point source in a heated, non-expanding jet in 2-D 391
C.10 Sound propagation from an infinitely baffled circular piston in 3-D . 402

D Anechoic Chamber Acoustic Results 409
D.1 Anechoic chamber testing with a free-standing compression driver . 410
D.2 Anechoic chamber testing with an exhaust stack 415

E Sound propagation through 2D jet in cross-flow 423

F Numerical sound propagation through elevated jet in cross-flow 435

G Experimental sound propagation through elevated jet in cross-flow 445

H Steady-state sound propagation through hot exhaust jets in cooler cross-flow: A computational study **457**

I Sound propagation through elevated, heated jets in cooler cross-flow: An experimental study **519**

List of Figures

1.1 Schematic of a typical industrial OCGT with an exhaust stack [55]. It should be noted that this figure also includes the typical extension for a combined cycle gas turbine, but the emphasis of the image is the system excluding the expansion joints and the stack damper. 2

1.2 Schematic of an exhaust stack with uniform circular cross-section (of external diameter, OD, internal diameter, D, height, H, and jet exit velocity, u_j) mounted perpendicular to a ground plane and immersed in a cross-flow (with boundary layer thickness, δ, stream-wise velocity profile, $u(y)$, and cross-flow free stream velocity, u_{cf}). Figure adapted from Adaramola et al. [1]: (a) top view and (b) side view. 3

1.3 Schematic of acoustic ray propagation with and without the presence of flow and temperature. 4

2.1 Schematic proposed by Björk [27] for two different noise mitigation strategies for sound radiation from hot exhaust jets in cross-flow, where (a) is a half-cylinder, and (b) is a conical lengthening of the stack. The angles in the figure are defined as: the conic angle α with a value of 20°, shadow angle β with a value of 40°, and the elevation angle τ with a value of 0°. The image was adapted from Björk [27]. 13

2.2 Schematic of the key features for atmospheric sound propagation models with a monopole source interacting with the atmospheric boundary layer. The sound propagation is for a near-ground source under high-wind conditions when the wind is blowing left to right [171]. 15
2.3 Schematic of the dominant fluid dynamic structures associated with a ground-level JICF [94]. 24
2.4 Schematic of the dominant fluid dynamic structures associated with an elevated JICF for a value of R that is in the jet dominated regime [1]. . . 31
2.5 Acoustic directivity from Atvars et al. [15] of an on-axis monopole sound source propagating through a non-isothermal jet with (a) varying acoustic frequencies (cps is equivalent to Hz), and (b) varying jet temperatures (T_1 = 70 °C, and T_2 = 282 °C). 36

3.1 Numerical schematic for sound propagation through four different systems; (a) sound propagation through the flush-mounted duct in a stationary field, (b) sound propagation through a ground-level, non-isothermal, heated JICF, (c) sound propagation through a stationary field with an elevated duct, and (d) sound propagation through an elevated, non-isothermal, heated JICF. 47
3.2 Simulation process for conducting the numerical simulations 49
3.3 Schematic and dimensions for the ground-level JICF simulations, where blue text represents the fluid dynamics boundary conditions and green text show the acoustic boundary conditions. PML refers to a Perfectly Matched Layer. 58
3.4 Mesh for CFD simulations 59
3.5 Schematic for the ground level JICF and the directivity definition from the duct outlet. The quantity a is the duct radius, θ is the directivity angle from the duct centreline, and r is the radius for the directivity arc from the centre of the duct outlet. 62
3.6 Mesh for the FEM acoustic simulations 63

3.7 Schematic and dimensions for the elevated level JICF simulations, where blue text represents the fluid dynamics boundary conditions and green text show the acoustic boundary conditions. PML refers to a Perfectly Matched Layer. 64
3.8 Schematic for the elevated stack and the directivity definition from the duct outlet. The quantity, a is the duct radius, θ is the directivity angle from the duct centreline, and r is the radius for the directivity arc from the centre of the duct outlet. 67
3.9 Non-isothermal elevated JICF, (a) mesh for CFD modelling and, (b) mesh for modelling sound propagation with FEM (b) 69
3.10 The CFD generated contour plots of (a) flow velocity, (b) temperature, and (c) the effective speed of sound along the Y-Z plane (of symmetry), where $T_j = 500\,°C$ and $R = 5$. The cross-flow is from left to right. 72
3.11 Velocity contour plot along the X-Y plane at six distances downwind from the centre of the duct ($z/D = [0, 0.5, 2, 4, 8, 32]$), where $T_j = 500\,°C$ and $R = 5$. 74
3.12 Temperature contour plots along the X-Y plane at six distances downwind from the centre of the duct ($z/D = [0, 0.5, 2, 4, 8, 32]$), where $T_j = 500\,°C$ and $R = 5$. 77
3.13 The mesh independence study with the centreline trajectory for a non-isothermal JICF where $R = 5$ and $T_j = 500\,°C$. 78
3.14 The plume centreline trajectory for JICF with $R = 5$ and 7.5, and T_j (27 °C, 250 °C, and 500 °C) 78
3.15 The elevated JICF CFD generated contour plots of (a) flow velocity, (b) temperature, and (c) , and (c) the effective speed of sound along the Y-Z plane (of symmetry), where $T_j = 500\,°C$ and $R = 5$. The cross-flow is from left to right. 80
3.16 Contour plots of (a) the sound pressure level and (b) the DI along the Y-Z plane (of symmetry) for sound propagation through the domain in the absence of flow, with $T_j = 27\,°C$, $\vec{v_0}(\vec{x}) = 0$, and $ka = 0.8$. 84

3.17 The DI along the Y-Z plane (of symmetry) for sound propagation through the domain in the absence of flow at two radii ($r = 16D$ and $32D$]), two Helmholtz numbers ($ka = 0.7$ and 0.8), $T_j = 27\,°\text{C}$, and $\vec{v_0}(\vec{x}) = 0$. The results are for a baffled circular piston (analytical and numerically solved in FEM) and circular duct of length $10D$ (solved in FEM). 85
3.18 Mesh convergence - the DI the Y-Z plane (of symmetry) for sound propagation through the domain, in the absence of flow, as a function of the FEM mesh node count, at $r = 32D$, $T_j = 27\,°\text{C}$, $\vec{v_0}(\vec{x}) = 0$, and $ka = 0.8$. 86
3.19 The 3-D DI contour plot over a spherical surface at a radius $r = 32D$ for sound propagation through an isothermal stationary field at an ambient temperature with $\vec{v_0}(\vec{x}) = 0$, and $ka = 0.8$. Values of DI less than $-12\,\text{dB}$ are saturated black. 88
3.20 The 3-D directivity radiation pattern at a radius $r = 32D$ for sound propagation through an isothermal stationary field at ambient temperature with $\vec{v_0}(\vec{x}) = 0$, and $ka = 0.8$. Values of DI less than $-12\,\text{dB}$ are saturated dark blue. 89
3.21 Contour plots of (a) the sound pressure level and (b) the DI along the Y-Z plane (of symmetry) for sound propagation through non-isothermal thermal gradients from a ground-level JICF with $R = 5$, $T_j = 500\,°\text{C}$, $\vec{v_0}(\vec{x}) = 0$, and $ka = 0.8$. The cross-flow is from left to right. Values of DI less than $-12\,\text{dB}$ are saturated black. 91
3.22 The DI at various distance from the duct outlet ($r = [2D, 4D, 8D, 16D, 32D]$) along the Y-Z plane (of symmetry) for sound propagation through thermal gradients from non-isothermal JICF at $R = 5$, $T_j = 500\,°\text{C}$, $\vec{v_0}(\vec{x}) = 0$, and $ka = 0.8$. 92
3.23 The DI at six different Helmholtz numbers ($ka = [0.3, 0.4, 0.5, 0.6, 0.7, 0.8]$) and at four different radii ($r = [2D, 8D, 16D, 32D]$) along the Y-Z plane (of symmetry) for sound propagation through non-isothermal JICF thermal gradients with $R = 5$, $T_j = 500\,°\text{C}$, and $\vec{v_0}(\vec{x}) = 0$. 94

3.24 Contour plots of (a) sound pressure level and (b) DI along the X-Z plane (ground-level) for sound propagation through the thermal gradients from non-isothermal JICF with $R = 5$, $T_j = 500\,°C$, $\vec{v_0}(\vec{x}) = 0$, and $ka = 0.8$. The cross-flow is from top to bottom. 95
3.25 The DI contour plot across a spherical surface at a radius $r = 32D$ for sound propagation through non-isothermal JICF with $R = 5$, $T_j = 500\,°C$, $\vec{v_0}(\vec{x}) = 0$, and $ka = 0.8$. Values of DI less than $-12\,dB$ are saturated black. 96
3.26 The 3-D directivity plot for DI at a radius $r = 32D$ for sound propagation through non-isothermal JICF with $R = 5$, $T_j = 500\,°C$, $\vec{v_0}(\vec{x}) = 0$, and $ka = 0.8$. Values of DI less than $-12\,dB$ are saturated dark blue. 98
3.27 The DI at a radius of $32D$ along the Y-Z plane (of symmetry) for sound propagation through the thermal gradients associated with non-isothermal JICF with varying R and T_j at $ka = 0.8$, and $\vec{v_0}(\vec{x}) = 0$. 99
3.28 Contour plots of (a) the sound pressure level and (b) the DI along the Y-Z plane (of symmetry) for sound propagation through the velocity gradients from a ground-level JICF with $R = 5$, $T_j = 27\,°C$, $\vec{v_0}(\vec{x}) \neq 0$, and $ka = 0.8$. The cross-flow is from left to right. 101
3.29 The DI at various distances from the duct outlet ($r = [2D, 4D, 8D, 16D, 32D]$) along the Y-Z plane (of symmetry) for sound propagation through isothermal velocity gradients from a JICF with $R = 5$, $T_j = 27\,°C$, $\vec{v_0}(\vec{x}) \neq 0$, and $ka = 0.8$. 102
3.30 The DI at six different Helmholtz numbers ($ka = [0.3, 0.4, 0.5, 0.6, 0.7, 0.8]$) and at four different radii ($r = [2D, 8D, 16D, 32D]$) along the Y-Z plane (of symmetry) for sound propagation through isothermal JICF with $R = 5$, $T_j = 27\,°C$, and $\vec{v_0}(\vec{x}) \neq 0$. 103
3.31 Contour plots of (a) sound pressure level and (b) DI along the X-Z plane (ground-level) for sound propagation through the velocity gradients from an isothermal JICF with $R = 5$, $T_j = 27\,°C$, $\vec{v_0}(\vec{x}) \neq 0$, and $ka = 0.8$. The cross-flow is from top to bottom. 104

3.32 The DI contour plot across a spherical surface at a radius of $r = 32D$ for sound propagation through isothermal velocity gradients from a JICF with $R = 5$, $T_j = 27\,°C$, $\vec{v_0}(\vec{x}) \neq 0$, and $ka = 0.8$. 105
3.33 The 3-D directivity radiation pattern for sound propagation through the isothermal velocity gradients from a JICF at a radius $r = 32D$ with $R = 5$, $T_j = 27\,°C$, $\vec{v_0}(\vec{x}) \neq 0$, and $ka = 0.8$. 107
3.34 Contour plots of (a) the sound pressure level and (b) the DI along the Y-Z plane (of symmetry) for sound propagation through non-isothermal velocity and thermal gradients from a JICF with $R = 5$, $T_j = 500\,°C$, $\vec{v_0}(\vec{x}) \neq 0$, and $ka = 0.8$. The cross-flow is from left to right. Values of DI less than $-12\,dB$ are saturated black. 109
3.35 The DI at various distances from the duct outlet ($r = [2D, 4D, 8D, 16D, 32D]$) along the Y-Z plane for sound propagation through non-isothermal steady-state convective and thermal gradients from a JICF with $R = 5$, $T_j = 500\,°C$, $\vec{v_0}(\vec{x}) \neq 0$, and $ka = 0.8$. 111
3.36 The DI at six different Helmholtz numbers ($ka = [0.3, 0.4, 0.5, 0.6, 0.7, 0.8]$) and at four different radii ($r = [2D, 8D, 16D, 32D]$) along the Y-Z plane (of symmetry) for sound propagation through a non-isothermal steady-state convective flow with thermal gradients from a JICF with $R = 5$, $T_j = 500\,°C$, and $\vec{v_0}(\vec{x}) \neq 0$. 112
3.37 Contour plots of (a) the sound pressure level and (b) the DI along the X-Z plane (ground-level) for sound propagation through non-isothermal velocity and thermal gradients from a JICF with $R = 5$, $T_j = 500\,°C$, $\vec{v_0}(\vec{x}) \neq 0$, and $ka = 0.8$. The cross-flow is from the top to the bottom in the Figure. 113
3.38 The DI contour plot across a spherical surface at $r = 32D$ for sound propagation through non-isothermal JICF with $R = 5$, $T_j = 500\,°C$, $\vec{v_0}(\vec{x}) \neq 0$, and $ka = 0.8$. The cross-flow is flowing parallel to the Z-axis, towards the negative direction. Values of DI less than $-12\,dB$ are saturated black. 114

3.39 The 3-D directivity radiation pattern for sound propagation through non-isothermal JICF at a radius $r = 32D$ with $R = 5$, $T_j = 500\,°C$, $\vec{v_0}(\vec{x}) \neq 0$, and $ka = 0.8$. The cross-flow is flowing parallel to the Z-axis, towards the negative direction. Values of DI less than $-12\,dB$ are saturated dark blue. 115
3.40 The DI at a radius of $32D$ along the Y-Z plane (of symmetry) for sound propagation through non-isothermal JICF with $R = [5, 7.5]$, $T_j = [27\,°C, 250\,°C, 500\,°C]$, $\vec{v_0}(\vec{x}) \neq 0$, and $ka = 0.8$. 117
3.41 Contour plots of (a) sound pressure level and (b) DI along the Y-Z plane (of symmetry) for sound propagation through non-isothermal velocity and thermal gradients from a JICF with $R = 7.5$, $T_j = 500\,°C$, $\vec{v_0}(\vec{x}) \neq 0$, and $ka = 0.8$. The cross-flow is from left to right in the figure. Values of DI less than $-12\,dB$ are saturated black. 118
3.42 Contour plots of (a) the sound pressure level and (b) the DI along the X-Z plane (ground-level) for sound propagation through non-isothermal velocity and thermal gradients from a JICF with $R = 7.5$, $T_j = 500\,°C$, $\vec{v_0}(\vec{x}) \neq 0$, and $ka = 0.8$. The cross-flow is from the top to the bottom in the Figure. 119
3.43 Schematic illustrating how the acoustic rays are bent downwards as the cross-flow velocity ratio, R, increases (i.e. the cross-flow velocity decreases). 120
3.44 Elevated JICF contour plots of the sound pressure level with (a) anechoic ground ($\alpha_s = 1$) and (b) hard reflective ground ($\alpha_s = 0$) along the Y-Z plane (of symmetry) for sound propagation in an isothermal stationary field, with $T_j = 27\,°C$, $\vec{v_0}(\vec{x}) = 0$, and $ka = 0.8$. Values less than $48\,dB$ of the maximum sound pressure level are saturated black. 122
3.45 The DI at various distances from the duct outlet ($r = [2D, 4D, 8D, 16D, 32D]$) along the Y-Z plane (of symmetry) for sound propagation through an elevated stack in an isothermal stationary field, with the absorptive boundary condition along the ground, where $\alpha_s = 1$, $T_j = 27\,°C$, $\vec{v_0}(\vec{x}) = 0$, and $ka = 0.8$. 124

3.46 The DI at various distances from the duct outlet ($r = [2D, 4D, 8D, 16D, 32D]$) along the Y-Z plane (of symmetry) for sound propagation through an elevated stack in an isothermal stationary field, with a hard reflective boundary condition along the ground, with $\alpha_s = 0$, $T_j = 27\,°\text{C}$, $\vec{v_0}(\vec{x}) = 0$, and $ka = 0.8$. 125
3.47 The DI at five different Helmholtz numbers ($ka = [0.4, 0.5, 0.6, 0.7, 0.8]$) and at four different radii ($r = [2D, 8D, 16D, 32D]$) along the Y-Z plane (of symmetry) for sound propagation through an elevated stack in an isothermal stationary field, with an absorptive boundary condition along the ground: $\alpha_s = 1$, $T_j = 27\,°\text{C}$, and $\vec{v_0}(\vec{x}) = 0$. 127
3.48 The DI at five different Helmholtz numbers ($ka = [0.4, 0.5, 0.6, 0.7, 0.8]$) and at four different radii ($r = [2D, 8D, 16D, 32D]$) along the Y-Z plane (of symmetry) for sound propagation through an elevated stack in an isothermal stationary field, with a hard reflective boundary condition along the ground, $\alpha_s = 0$, $T_j = 27\,°\text{C}$ and $\vec{v_0}(\vec{x}) = 0$. 129
3.49 The 3-D directivity radiation pattern for sound propagation through an isothermal stationary field at ambient temperature with a stack at a radius $r = 32D$ with $\alpha_s = 1$, $R = 0$, $T_j = 27\,°\text{C}$, $\vec{v_0}(\vec{x}) = 0$, and $ka = 0.8$. Values of DI less than $-12\,\text{dB}$ are saturated dark blue. 130
3.50 Elevated JICF contour plots of the sound pressure levels with (a) anechoic ground ($\alpha_s = 1$) and (b) hard reflective ground ($\alpha_s = 0$) along the Y-Z plane (of symmetry) for sound propagation through non-isothermal velocity and thermal gradients from a JICF with $R = 5$, $T_j = 500\,°\text{C}$, $\vec{v_0}(\vec{x}) \neq 0$, and $ka = 0.8$. The cross-flow is from left to right in the figure. Values less than 48 dB of the maximum SPL are saturated black. 132
3.51 The DI at various distances from the duct outlet ($r = [2D, 4D, 8D, 16D, 32D]$) along the Y-Z plane (of symmetry) for sound propagation through a non-isothermal steady-state convective flow with thermal gradients from an elevated JICF with an absorptive boundary condition along the ground: $\alpha_s = 1$, $R = 5$, $T_j = 500\,°\text{C}$, $\vec{v_0}(\vec{x}) \neq 0$, and $ka = 0.8$. 134

3.52 The DI at various distance from the duct outlet ($r = [2D, 4D, 8D, 16D, 32D]$) along the Y-Z plane (of symmetry) for sound propagation through a non-isothermal steady-state convective flow with thermal gradients from an elevated JICF with a hard reflective boundary condition along the ground, $\alpha_s = 0$, $R = 5$, $T_j = 500\,°C$, $\vec{v_0}(\vec{x}) \neq 0$, and $ka = 0.8$. 135
3.53 The DI at five different Helmholtz numbers ($ka = [0.4, 0.5, 0.6, 0.7, 0.8]$) and at four different radii ($r = [2D, 8D, 16D, 32D]$) along the Y-Z plane (of symmetry) for sound propagation through a non-isothermal steady-state convective flow with thermal gradients from an elevated JICF with an absorptive boundary condition along the ground: $\alpha_s = 1$, $R = 5$, $T_j = 500\,°C$, and $\vec{v_0}(\vec{x}) \neq 0$. 137
3.54 The DI at various distances from the duct outlet ($r = [2D, 4D, 8D, 16D, 32D]$) along the Y-Z plane (of symmetry) for sound propagation through a non-isothermal steady-state convective flow with thermal gradients from an elevated JICF with an absorptive boundary condition along the ground: $\alpha_s = 1$, $R = 5$, $T_j = 500\,°C$, and $\vec{v_0}(\vec{x}) \neq 0$. Five tones are band averaged over a one-third octave band of 3.15 kHz ($ka = 0.85$). 139
3.55 The 3-D directivity radiation pattern for sound propagation through a non-isothermal elevated JICF at a radius $r = 32D$ with $R = 5$, $T_j = 500\,°C$, $\vec{v_0}(\vec{x}) \neq 0$, and $ka = 0.8$. The cross-flow is flowing parallel to the Z-axis, towards the negative direction. Values of DI less than -12 dB are saturated dark blue. 140
3.56 The band-average one-third octave band 3-D directivity radiation pattern for sound propagation through a non-isothermal elevated JICF at a radius $r = 32D$ with $R = 5$, $T_j = 500\,°C$, $\vec{v_0}(\vec{x}) \neq 0$, and a centre frequency $ka = 0.85$ (3150 Hz). The cross-flow is flowing parallel to the Z-axis, towards the negative direction. Values of DI less than -12 dB are saturated dark blue. 142

3.57 The DI at a radius of $32D$ along the Y-Z plane (of symmetry) for sound propagation from a source with $ka = 0.8$ through four propagation conditions: Case 1 - an isothermal stationary field ($T_j = 27\,°C$, $R = 0$, $\vec{v_0}(\vec{x}) = 0$), Case 2 - a ground-level JICF at ambient temperature with no thermal gradients ($T_j = 27\,°C$, $R = 5$, $\vec{v_0}(\vec{x}) \neq 0$), Case 3 - the thermal gradients associated with a heated jet in ambient cross-flow with no convective effects modelled ($T_j = 500\,°C$, $R = 5$, $\vec{v_0}(\vec{x}) = 0$), and Case 4 - a ground-level JICF with the temperature and flow considered for modelling ($T_j = 500\,°C$, $R = 5$, $\vec{v_0}(\vec{x}) \neq 0$). 148

3.58 Visualising the 3-D directivity radiation pattern for four different propagation media: (a) isothermal stationary field with no JICF, (b) convective effects only with the JICF at ambient temperature, (c) temperature effects only with the heated jet and cooler cross-flow, and (d) combining the temperature and convective effects for a heated jet in cooler cross-flow. The 3-D directivity radiation was conducted along a hemisphere with a radius $r = 32D$, and at $ka = 0.8$. The cross-flow for (b), (c) and (d) is flowing parallel to the Z-axis, going from left to right. Values of DI less than $-12\,dB$ are saturated dark blue. 151

3.59 Comparison of the DI for an elevated JICF and a ground-level JICF at a radius of $32D$ along the Y-Z plane (of symmetry) for sound propagation from a source with $ka = 0.8$ and flow conditions $T_j = 500\,°C$, $R = 5$, and $\vec{v_0}(\vec{x}) \neq 0$). 153

4.1 Schematics of the experimental acoustic testing in the Anechoic Chamber of two different systems; (a) a free-standing compression driver, and (b) sound propagation from an exhaust stack. 158

4.2 Schematics of the experimental acoustic testing in the Thebarton Wind Tunnel of three systems; (a) sound propagation from an isothermal exhaust stack in the absence of flow, (b) sound propagation through a heated jet with no cross-flow, and (c) sound propagation through a non-isothermal heated JICF. 159

4.3 Illustration of the closed-loop four-sided University of Adelaide Wind Tunnel. The purpose-built small-scale exhaust rig was commissioned in the removable open section of the wind tunnel. 161
4.4 Illustration of the reduced-scale exhaust network experimental setup. . 162
4.5 Photo of the reduced-scale exhaust network experimental setup to be installed in the Thebarton Wind Tunnel, without the blower or inlet silencer. 162
4.6 Photo of the experimental set up at the University of Adelaide's Wind Tunnel showing the test set up with (a) both arrays, and (b) the $28D$ array only. 164
4.7 Schematic of the microphone arrays showing the microphone locations and corresponding reference numbers. 166
4.8 Photo of the exhaust rig including the Dantec 3-Axis traverse for flow and temperature measurements at the Thebarton Wind Tunnel. 168
4.9 Vertical velocity profiles at each velocity component, with (a) u, the span-wise velocity, (b) v, the vertical velocity, and (c) w, the cross-flow free-stream velocity. The vertical velocity profiles are at varying distances downwind and upwind ($z/D = [-8, -4, 1, 2, 4, 8, 16]$), and measured along a plane with $x = 0$ (along the duct centreline). The duct centreline is at $z/D = 0$, and the duct outlet height is at $y/D = 8$. The data points with more than 50% of the transient velocity data saturated by the Cobra Probe 209, due to the reverse flow, have been set to orange, and the other data points are blue. 172
4.10 Vertical TI profiles, with (a) I_{uu}, (b) I_{vv}, and (c) I_{ww}, and (d) I_{uvw}. The vertical TI profiles are at varying distances downwind and upwind ($z/D = [-8, -4, 1, 2, 4, 8, 16]$) of the exhaust stack, and measured along a plane with $x = 0$ (along the duct centreline). The duct centreline is at $z/D = 0$ and the duct outlet height is at $y/D = 8$. The data points with more than 50% of the transient velocity data saturated by the Cobra Probe, due to the reverse flow, have been set to orange, and the other data points are blue. 174

4.11 Span-wise velocity profiles at each velocity component, with (a) u, the span-wise velocity, (b) v, the vertical velocity, and (c) w, the cross-flow free-stream velocity. The span-wise velocity profiles are at three heights ($y/D = [17, 18, 21]$), at a single position downstream of the exhaust stack at $z/D = 8$. 177
4.12 Span-wise turbulence intensity profiles at each component, with (a) I_{uu}, (b) I_{vv}, and (c) I_{ww}. The span-wise turbulence intensity profiles are at three heights ($y/D = [17, 18, 21]$) and at single position downwind of the exhaust stack at $z/D = 8$. 179
4.13 Vertical temperature profiles at five distances downwind and upwind ($z/D = [-8, -4, 4, 8, 16]$), measured along the plane $x = 0$ (the duct centreline). 180
4.14 Experimental temperature contour plot from the non-isothermal JICF at two distances downwind from the exhaust stack (a) $z/D = 8$, and (b) $z/D = 16$, with $R = 5$, and $T_j = 500\,°C$. 181
4.15 The SPL measurement at two microphones at the top of the $14D$ and $28D$ array. The test was conducted in the Thebarton Wind Tunnel in an isothermal stationary field. The background measurements are taken with the plant equipment not operating, and the sound is propagating through the duct network. BG refers to the background noise levels. Relevant coherence is plotted in Figure 4.16. 185
4.16 The coherence, γ^2_{xy}, between the electro-acoustic signal into the compression driver and microphone SPL response for two microphones at the top of the $14D$ and $28D$ array. The test was taken in the Thebarton Wind Tunnel with an isothermal stationary field and the plant equipment not operating. Sound is propagating through the duct network. 186
4.17 The DI for sound propagation in an isothermal stationary field for band-averaged one-third octave bands with centre frequency $ka = [0.85, 1.08, 1.35, 1.70]$ ($f = [3.15\,kHz, 4\,kHz, 5\,kHz, 6.3\,kHz]$) at two radii ($14D$ and $28D$). The results are from tests conducted at the Thebarton Wind Tunnel. 188

4.18 The SPL response at two microphones (on the vertical and horizontal axis) on the $28D$ array for sound propagating through a non-isothermal jet with $T_j = 350\,°C$ and $M = 0.1$. BG refers to the background noise levels. Relevant coherence is plotted in Figure 4.19. 190
4.19 The coherence, γ^2_{xy} between the electro-acoustic signal into the compression driver and microphone SPL response for two microphones (on the vertical and horizontal planes) on the $28D$ array for sound propagating through a non-isothermal jet with $T_j = 350\,°C$ and $M = 0.1$. 191
4.20 The DI along the Y-Z plane (of symmetry) for sound propagation through a non-isothermal jet for band-averaged one-third octave bands with centre frequencies $ka = [0.85, 1.08, 1.35, 1.70]$ ($f = [3.15\,kHz, 4\,kHz, 5\,kHz, 6.3\,kHz]$) at $r = 28D$, $T_j = 350\,°C$, and $M = 0.1$. 193
4.21 The SPL response for the acoustic pressure at two microphone locations from sound radiating through a non-isothermal JICF with $R = 5$ and $T_j = 500\,°C$. BG refers to the background noise levels. Note that both microphones are horizontal (90°) downwind. Relevant coherence is plotted in Figure 4.22. 195
4.22 The coherence, γ^2_{xy} between the electro-acoustic signal into the compression driver and microphone SPL response from sound radiating through a non-isothermal JICF with $r = [14D, 28D]$, $R = 5$ and $T_j = 500\,°C$. Note that both microphones are horizontal (90°) downwind. 197
4.23 The band-averaged DI along the Y-Z plane (of symmetry) for sound propagation through a non-isothermal JICF for one-third octave bands with centre frequencies $ka = [0.85, 1.08, 1.35, 1.70]$ ($f = [3.15\,kHz, 4\,kHz, 5\,kHz, 6.3\,kHz]$) at two radii ($14D$ and $28D$) while $R = 5$ and $T_j = 500\,°C$. The cross-flow is from left to right. 199
4.24 The band-averaged DI along the Y-Z plane (of symmetry) for sound propagation through a non-isothermal JICF at 20 one-twelfth octave bands. The test conditions were $r = 28D$, $R = 5$ and $T_j = 500\,°C$. The cross-flow is from left to right. 201

4.25 The band-averaged DI along the Y-Z plane (of symmetry) as a function of jet temperature (T_j = [27 °C, 100 °C, 300 °C, 500 °C]) for sound propagation through a non-isothermal JICF. The test conditions were for ka = [0.85, 1.08, 1.35, 1.70] (f = [3.15 kHz, 4 kHz, 5 kHz, 6.3 kHz]), $r = 28D$ and $R = 5$. The cross-flow is from left to right. 203

4.26 The band-averaged DI along the Y-Z plane (of symmetry) for sound propagation through a non-isothermal JICF with R = [5, 7.5, 10, 12.5], while the one-third octave bands of interest are ka = [0.85, 1.08, 1.35, 1.70] (f = [3.15 kHz, 4 kHz, 5 kHz, 6.3 kHz]). The test conditions were $r = 28D$, $R = 5$ and T_j = 500 °C. The cross-flow is from left to right. 205

4.27 A comparison between the numerical and experimental results for the band-averaged DI along the Y-Z plane (of symmetry) for sound propagation through a non-isothermal JICF for two directivity radii, r = [14D, 28D], with $R = 5$. The one-third octave bands of interest, ka = 0.85 (f = 3.15 kHz), and T_j = 500 °C. The cross-flow is from left to right. The results are saturated at −12 dB. 208

5.1 Acoustic ray propagation for the sound propagation through non-isothermal elevated JICF (a) a hard-walled exhaust stack and (b) with the straight acoustically transparent nozzle. The acoustic rays are shown with grey lines. The exterior of the nozzle is symbolised by a black dashed line and filled in with red to show the constrained flow. 217

5.2 Schematics of the three prototype noise mitigation nozzles, where (a) Nozzle 1 is a straight section nozzle, (b) Nozzle 2 is a conical section nozzle with 5° expansion, and (c) Nozzle 3 is a venturi section nozzle. The nozzles are shown in grey and the exhaust ducts are shown in black. 218

5.3 A schematic of the straight section nozzle showing the non-dimensional geometry, where the red dash line represents the nozzle and the black line represents the exhaust duct. 219

5.4 A schematic of the conical expansion nozzle showing the non-dimensional geometry, where α is the inclination angle of the cone. The red dash line represents the nozzle and the black line represents the exhaust duct. . . 221

5.5 A schematic for the venturi nozzle to show the three different sections and the region for enhanced entrained cooler flow. The supports for the nozzle are omitted from the graphic to help with the visualisation of the cooler ambient flow. 222
5.6 Two views of the venturi nozzle (Nozzle 3) illustrating the non-dimensional geometry. Both nozzles in the figure are identical in scale and are used to show the geometry of each nozzle section. 223
5.7 Schematics to illustrating the case for sound propagation through the non-isothermal elevated JICF with two different rigid-walled duct lengths (a) $L = 10D$ and (b) $L = 6D$ along the Y-Z plane (of symmetry). Blue text represents the fluid dynamics boundary conditions and green text represents the acoustic boundary conditions. PML refers to a Perfectly Matched layer. 225
5.8 Contour plots for sound pressure levels for elevated JICF with a hard reflective ground surface at two rigid-walled duct lengths (a) $L = 10D$ and (b) $L = 6D$. The results are along the Y-Z plane (of symmetry) for sound propagation through the non-isothermal velocity and thermal gradients from a JICF with $\alpha_s = 0$, $R = 5$, $T_j = 500\,°\text{C}$, $\vec{v_0}(\vec{x}) \neq 0$, and $ka = 0.8$. The cross-flow is from left to right in the figure. Values 48 dB less than the maximum SPL are saturated black. 226
5.9 Contour plots of sound pressure levels for elevated JICF with an anechoic ground surface at two rigid-walled duct lengths (a) $L = 10D$ and (b) $L = 6D$. The results are along the Y-Z plane (of symmetry) for sound propagation through an elevated JICF with $\alpha_s = 1$, $R = 5$, $T_j = 500\,°\text{C}$, $\vec{v_0}(\vec{x}) \neq 0$, and $ka = 0.8$. The cross-flow is from left to right in the Figure. Values 48 dB less than the maximum SPL are saturated black. 228
5.10 The DI along the Y-Z plane (of symmetry) as a function of radial distance from the outlet, $r = [2D, 8D, 16D, 32D]$. For sound propagation through the non-isothermal JICF, with a rigid-walled duct length at $6D$ and $10D$, while $\alpha_s = 1$, $ka = 0.85$, $R = 5$ and $T_j = 500\,°\text{C}$. The cross-flow is from left to right. 230

5.11 The one-third octave band-average 3-D directivity radiation pattern for sound propagation through a non-isothermal elevated JICF at a radius $r = 32D$ with $R = 5$, $T_j = 500\,°\text{C}$, $\vec{v_0}(\vec{x}) \neq 0$, and centre frequency $ka = 0.85$ (3150 Hz). The cross-flow is flowing parallel to the Z-axis, towards the positive direction. Values of DI less than $-12\,\text{dB}$ are saturated dark blue. 231

5.12 The one-third octave band-average 3-D directivity radiation pattern for sound propagation through a non-isothermal elevated JICF for two rigid-walled duct lengths (a) $L = 10D$ and (b) $L = 6D$. Both configurations had a radius $r = 32D$ with $R = 5$, $T_j = 500\,°\text{C}$, $\vec{v_0}(\vec{x}) \neq 0$, and centre frequency $ka = 0.85$ (3150 Hz). The cross-flow is flowing parallel to the Z-axis, towards the negative direction. Values of DI less than $-12\,\text{dB}$ are saturated dark blue. 233

5.13 Photos of the experimental setup with three nozzles attached to the reduced-scale exhaust rig at the Thebarton Wind Tunnel, where: (a) is the straight section nozzle (Nozzle 1), (b) is the conical section nozzle (Nozzle 2), and (c) is the venturi section nozzle (Nozzle 3). 234

5.14 The band-averaged DI along the Y-Z plane (of symmetry) for sound propagation in the absence of a non-isothermal JICF, with and without the three nozzles. The test conditions were $ka = [0.85, 1.08, 1.35, 1.70]$, $r = 28D$, $R = 5$ and $T_j = 500\,°\text{C}$. 236

5.15 The band-averaged DI along the Y-Z plane (of symmetry) for sound propagation with the non-isothermal JICF, with and without the three nozzles. The test conditions were $ka = [0.85, 1.08, 1.35, 1.70]$, $r = 28D$, $R = 5$ and $T_j = 500\,°\text{C}$. The cross-flow is from left to right. 238

5.16 The band-averaged DI along the Y-Z plane (of symmetry) for sound propagation with the non-isothermal JICF, with and without the three nozzles. The test conditions were $ka = [0.85, 1.08, 1.35, 1.70]$, $r = 28D$, $R = 7.5$ and $T_j = 500\,°\text{C}$. The cross-flow is from left to right. 240

5.17 The band-averaged DI along the Y-Z plane (of symmetry) for sound propagation with the non-isothermal JICF, with and without the three nozzles. The test conditions were $ka = [0.85, 1.08, 1.35, 1.70]$, $r = 28D$, $R = 10$ and $T_j = 500\,°C$. The cross-flow is from left to right. 241
5.18 Comparing the numerical and experimental results for the band-averaged DI along the Y-Z plane (of symmetry) for sound propagation through a non-isothermal JICF for the case without a nozzle, and with a transparent section straight nozzle that is $4D$ long, with $R = 5$, $r = 28D$, the one-third octave bands of interest, $ka = 0.85$ ($f = 3.15\,kHz$), and $T_j = 500\,°C$. The cross-flow is from left to right. The results are saturated at $-12\,dB$. 245

6.1 Schematics of the numerical acoustic directivity results for three different cases; (a) sound propagation through an isothermal stationary field, (b) sound propagation through an isothermal ground-level JICF, and (c) sound propagation through a ground-level, heated jet with cooler cross-flow. The dash line is the acoustic radiation pattern. The cross-flow is from left to right. 253
6.2 Schematics of the numerical acoustic directivity results for two different cases; (a) sound propagation through an exhaust stack in an isothermal stationary field, and (b) sound propagation through an elevated, heated jet with cooler cross-flow. The dash line is the acoustic radiation pattern. The cross-flow is from left to right. The base plane is acoustically absorptive with $\alpha_s = 1$ 254
6.3 Schematics of the experimental acoustic directivity results for three different cases; (a) sound propagation through an isothermal stationary field, (b) sound propagation through a non-isothermal, heated jet, and (c) sound propagation through an elevated, heated jet with cooler cross-flow. The dash line is the acoustic radiation pattern. The cross-flow is from left to right. 257

6.4 Schematics of the experimental acoustic directivity results for varying parameters; (a) the distance from the duct outlet, r, (b) the jet temperature, T_j, and (c) the jet to cross-flow momentum flow ratio, R. The dash line is the acoustic radiation pattern. The cross-flow is from left to right. 262

C.1 SPL contour for 2-D plane wave propagation from left to right. The propagation medium is an isothermal stationary field at ambient temperature. 336

C.2 Acoustic pressure along the duct centreline for 2-D plane wave propagation. The propagation medium is an isothermal stationary field at ambient temperature. 336

C.3 SPL contour for 2-D plane wave propagation from top left to bottom right from ANSYS Mechanical. The propagation medium is an isothermal stationary field at ambient temperature. 339

C.4 Acoustic pressure along the duct centreline for 3-D plane wave propagation. The propagation medium is an isothermal stationary field at ambient temperature. 340

C.5 Acoustic pressure along the duct centreline for 3-D plane wave propagation. The propagation medium is a duct with uniform bulk flow, $u_{flow} = 50\,\mathrm{m\,s^{-1}}$. 341

C.6 Acoustic pressure along the duct centreline for 3-D plane wave propagation. The propagation medium is a heated duct, $T_j = 500\,°\mathrm{C}$, with no flow. 342

C.7 Acoustic pressure along the duct centreline for 3-D plane wave propagation. The propagation medium is a duct with a uniform flow profile where the flow velocity is, $u_{flow} = 50\,\mathrm{m\,s^{-1}}$ and the temperature of the duct is $T_j = 500\,°\mathrm{C}$. 343

C.8 Acoustic pressure along the duct centreline for 3-D plane wave propagation. The propagation medium is a duct with a non-uniform flow profile where the bulk velocity is, $u_{flow} = 55.11\,\mathrm{m\,s^{-1}}$. 344

C.9 Acoustic pressure along the duct centreline for 3-D plane wave propagation. The propagation medium is a duct with non uniform flow profile where the bulk velocity is, $u_{flow} = 55.11\,\mathrm{m\,s^{-1}}$ and the temperature of the duct is $T_j = 500\,°\mathrm{C}$. 345
C.10 Acoustic pressure along the duct centreline for 3-D plane wave propagation for four propagation conditions in the duct: an isothermal stationary field at ambient temperature, a uniform bulk flow at ambient temperature, a heated duct with no flow, and a heated duct with uniform bulk flow. 346
C.11 ANSYS Mechanical simulation for the SPL (dB re 20 µPa) for a baffled rectangular piston at 202 Hz 347
C.12 ANSYS Mechanical simulation for the SPL (dB re 20 µPa) for a baffled rectangular piston at 1622 Hz 348
C.13 ANSYS Mechanical simulation for the SPL (dB re 20 µPa) for a baffled rectangular piston at 3650 Hz 348
C.14 ANSYS Mechanical simulation for the SPL (dB re 20 µPa) for a baffled rectangular piston at 4866 Hz 349
C.15 Normalised acoustic impedance face for an infinitely baffled, infinitely thin rectangular piston 349
C.16 ANSYS Mechanical simulation for the SPL (dB re 20 µPa) for a 2-D baffled circular piston at 152 Hz 350
C.17 ANSYS Mechanical simulation for the SPL (dB re 20 µPa) for a 2-D baffled circular piston at 2292 Hz 351
C.18 ANSYS Mechanical simulation for the SPL (dB re 20 µPa) for a 2-D baffled circular piston at 3821 Hz 352
C.19 The analytical and ANSYS Mechanical simulation results for the normalised acoustic impedance at the piston face 353
C.20 Mean velocity magnitude contour plot from a non-isothermal plane rectangular jet 354
C.21 Mean pressure contour plot from a non-isothermal plane rectangular jet 355

C.22 Acoustic SPL (dB re 20 µPa) contour plot at 71Hz from a non-isothermal plane rectangular jet . . . 356
C.23 Acoustic SPL (dB re 20 µPa) contour plot at 571Hz from a non-isothermal plane rectangular jet . . . 357
C.24 Acoustic SPL (dB re 20 µPa) contour plot at 1428Hz from a non-isothermal plane rectangular jet . . . 358
C.25 SPL (dB re 20 µPa) contour plot with ANSYS Mechanical for a 2-D unbaffled circular piston at 274 Hz without the duct . . . 359
C.26 SPL (dB re 20 µPa) contour plot with ANSYS Mechanical for a 2-D unbaffled circular piston at 3018 Hz without the duct . . . 360
C.27 SPL (dB re 20 µPa) contour plot with ANSYS Mechanical for a 2-D unbaffled circular piston at 6036 Hz without the duct . . . 361
C.28 SPL (dB re 20 µPa) contour plot with ANSYS Mechanical for a 2-D unbaffled circular piston at 343 Hz with the duct . . . 362
C.29 SPL (dB re 20 µPa) contour plot with ANSYS Mechanical for a 2-D unbaffled circular piston at 3087 Hz with the duct . . . 362
C.30 SPL (dB re 20 µPa) contour plot with ANSYS Mechanical for a 2-D unbaffled circular piston at 6174 Hz with the duct . . . 363
C.31 The schematic for the case with a point source convected by a uniform mean flow, where the area in white is acoustic propagation domain, the area in green is the PML zone, the blue arrows represents the mean flow field throughout the acoustic domain, and the red cross at the origin represents the acoustic source. . . . 366
C.32 The numerical mesh for the acoustic FEM with (a) showing the the total mesh, and (b) the mesh near the acoustic source a non-uniform grid and high spatial resolution to resolve the acoustic source. . . . 366

C.33 The acoustic mesh generated by GMESH for solving the case with the point source convected by uniform, subsonic mean flow for solving using the UTC's FE solver and Galbrun's equation, where (a) is the total acoustic mesh, (b) is the mesh near the acoustic source at the origin, and (c) is the acoustic mesh at the interface between the acoustic propagating domain and the PML domain. The elements in blue represents the acoustic domain of interest and the elements in orange represents the domain with PML elements. 367

C.34 Acoustic pressure contour plots for a point source convected in uniform, subsonic flow with $M = 0.5$, and solved using a linearised acoustic wave equation with scalar potential flow formulation, with (a) showing the contour plot with a linear scale, (b) showing the contour plot with a logarithmic scale, and (c) showing the results from Bailly and Juve [18] as isocontour plots with the values ▬▬▬, 10^{-1}, 10^{-2}, 10^{-3}; ▬ ▬ ▬, 10^{-4}; and ■ ■ ■ ■, 10^{-5}. The flow in the figures is going from left to right. 369

C.35 The acoustic pressure along the line at $y = 0$ for a point source convected in uniform, subsonic flow with $M = 0.5$. The results compares two different acoustic FE methods, the linearised acoustic wave equation with mean flow using the scalar flow potential and the linearised Euler equation from Bailly and Juve [18]. The black cross represents the position of the acoustic source. 370

C.36 The acoustic pressure along the line at $y = 0$ for a point source convected in uniform, subsonic flow with $M = 0.5$. The acoustic results compare two different acoustic FE methods, the linearised acoustic wave equation with mean flow using the scalar flow potential and Galbrun's equation. The black cross represents the position of the acoustic source. The results presented are for three different frequencies, $f = [1/60, 1/30, 1/15]$, where f is normalised by c_0 and ρ_0. 372

C.37 The acoustic pressure along the line at $y = 0$ for a point source convected in uniform, subsonic flow with $M = 0.5$. The results from ANSYS Mechanical are compared to the results generated from Galbrun's equation with varying β from Equation (C.1). The black cross represents the position of the acoustic source. 373
C.38 The acoustic pressure along the line at $y = 0$ for a point source convected in uniform, subsonic flow at four different Mach numbers, $M = [0.1, 0.2, 0.3, 0.4]$. The acoustic results compare two different acoustic FE methods; the linearised acoustic wave equation with mean flow using the scalar flow potential and Galbrun's equation. The black cross represents the position of the acoustic source. 374
C.39 The schematic for the case with a point source convected by a finite thickness shear layer, where the area in white is acoustic propagation domain, the area in green is the PML zone, the blue arrows represents the mean velocity field throughout the acoustic domain, and the red cross at the origin represents the acoustic source. 378
C.40 The velocity profile for the mean flow with a finite thickness shear layer, based on Equation (C.4), with (a) showing the velocity profile as a function of y, and (b) showing a contour plot of velocity for the domain. 379
C.41 The acoustic mesh generated by GMESH for solving the case with the point source convected by a finite thickness sheared flow for solving using the UTC's FE solver and Galbrun's equation, where (a) is the total acoustic mesh, (b) is the mesh near the acoustic source at the origin, and (c) is the acoustic mesh at the interface between the acoustic propagating domain and the PML domain. The elements in blue represents the acoustic domain of interest and the elements in orange represents the domain with PML elements. 380

C.42 Acoustic pressure contour plots for a point source convected by a finite thickness shear flow defined by Equation (C.4), where (a) shows the results from ANSYS Mechanical generated using the linearised acoustic wave equation with mean flow using the scalar flow potential, (b) shows the time domain results from Feng et al. [59] with Galbrun's equation, and (c) shows the time domain results from Ewert and Schröder [57] with two different numerical methods: (left) the linearised Euler equations, and (right) a variant of the acoustic perturbation equation. . 381
C.43 The instantaneous acoustic pressure along the line at $y = 70$ for a point source convected by a finite thickness shear flow defined by Equation (C.4), comparing the results from the linearised acoustic wave equation with mean flow using the scalar flow potential, the linearised Euler equation from Ewert and Schröder [57], and Galbrun's equation from Feng et al. [59]. 382
C.44 The acoustic pressure along the line at $y = 70$ for a point source convected by a finite thickness shear flow defined by Equation (C.4), comparing the results from the linearised acoustic wave equation with mean flow using the scalar flow potential and Galbrun's equation. The results presented are for three different frequencies, $f = [1/(8\pi), 1/(4\pi), 1/(2\pi)]$. 385
C.45 The acoustic pressure along the line at $y = 70$ for a point source convected in a finite thickness shear layer flow defined by Equation (C.4) with four different Mach numbers, $M = [0.1, 0.2, 0.3, 0.4]$. The acoustic results compare two different acoustic FE methods, the linearised acoustic wave equation with mean flow using the scalar flow potential and Galbrun's equation. 386
C.46 A mesh independence study for the acoustic pressure along the line at $y = 70$ for a point source convected by a finite thickness shear flow defined by Equation (C.4), comparing the results from the linearised acoustic wave equation with mean flow using the scalar flow potential and Galbrun's equation. 388

C.47 The (a) velocity profile, (b) density profile, and (c) temperature profile for the 2-D heated, non-expanding, subsonic jet described by Agarwal and Morris [2]. 393
C.48 The schematic for the case with a point source convected by a heated, non-expanding, subsonic, jet where the area in white is acoustic propagation domain, the area in green is the PML zone, the blue arrows represents the mean velocity field throughout the acoustic domain, and the red cross at the origin represents the acoustic source. 394
C.49 The numerical mesh for the ANSYS acoustic FEM with (a) showing the the total mesh, and (b) the mesh near the acoustic source a non-uniform grid and high spatial resolution to resolve the acoustic source. 395
C.50 The acoustic mesh generated by GMESH for solving the case with the point source convected by a heated, non-expanding, subsonic jet for solving using the UTC's FE solver and Galbrun's equation, where (a) is the total acoustic mesh, (b) is the mesh near the acoustic source at the origin, and (c) is the acoustic mesh at the interface between the acoustic propagating domain and the PML domain. The elements in blue represents the acoustic domain of interest and the elements in orange represents the domain with PML elements. 396
C.51 Contour plots of acoustic pressure for a 2-D point source convected by a heated, non-expanding, subsonic jet with the results from (a) ANSYS Mechanical, and (b) Galbrun's equation. 397
C.52 The acoustic pressure along the line at $y = 15$ and 30 for a point source convected in a finite thickness shear layer flow defined by Equation (C.4) with two Mach numbers for the jet, $M = [0.1, 0.2]$. The acoustic results compare two acoustic FE methods, the linearised acoustic wave equation with mean flow using the scalar flow potential and Galbrun's equation. 398

C.53 A mesh independence study for the acoustic pressure along the line at $y = 15$ for a point source convected by 2-D heated, non-expanding, subsonic jet, comparing the results from the linearised acoustic wave equation with mean flow using the scalar flow potential and Galbrun's equation. 400
C.54 Schematic and dimensions for the infinitely baffled piston simulations, where the green text represents the acoustic boundary conditions. PML refers to a Perfectly Matched Layer. 403
C.55 Mesh for the FEM acoustic simulations. 404
C.56 Comparing the analytical and numerical solution for sound propagation from an infinitely baffled piston at four different Helmholtz numbers ($ka = [0.80, 0.96, 1.12, 1.28]$) along the Y-Z plane (of symmetry). The following parameters are used for the simulations $r = 16D$, and $\vec{v_0}(\vec{x}) = 0$.406
C.57 Comparing the analytical and numerical solution for sound propagation from an infinitely baffled piston at four different Helmholtz numbers ($ka = [0.80, 0.96, 1.12, 1.28]$) along the Y-Z plane (of symmetry). The following parameters are used for the simulations $r = 32D$, and $\vec{v_0}(\vec{x}) = 0$.407

D.1 Photo of the acoustic arrays in the University of Adelaide's Anechoic Chamber. The acoustic source is a free-standing compression driver suspended by a fishing line. 411
D.2 Photo of the acoustic arrays and the exhaust rig in the University of Adelaide's Anechoic Chamber. 412
D.3 The coherence, γ^2_{xy}, between the electro-acoustic signal into the compression driver and microphone SPL response for two different microphones at the top of the $14D$ and $28D$ array. The test was undertaken in the Anechoic Chamber with an isothermal stationary field. Sound is propagating from a free-standing compression driver. 413

D.4 The SPL and COP measurements for two different microphones at the top of the 14D and 28D array. The test was undertaken in the Anechoic Chamber with an isothermal stationary field. Sound is propagating from a free-standing compression driver. BG refers to background noise levels. Relevant coherence is plotted in Figure D.3. 414
D.5 The DI for sound propagation in an isothermal stationary field in the Anechoic Chamber for band-averaged one-third octave bands with centre frequencies $ka = [0.85, 1.08, 1.35, 1.70]$ ($f = [3.15\,\text{kHz}, 4\,\text{kHz}, 5\,\text{kHz}, 6.3\,\text{kHz}]$) at two different radii (14D and 28D). The results are from testing with a free-standing compression driver. 416
D.6 The coherence, γ^2_{xy}, between the electro-acoustic signal into the compression driver and microphone SPL response for two different microphones on the top of the 14D and 28D array. The test was undertaken in the Anechoic Chamber with an isothermal stationary field. Sound is propagating through the duct network. 417
D.7 The SPL and COP measurements at two different microphones at the top of the 14D and 28D array. The test was undertaken in the Anechoic Chamber with an isothermal stationary field. Sound is propagating through the duct network. BG refers to background noise levels. Relevant coherence is plotted in Figure D.6. 419
D.8 The DI along the Y-Z plane (of symmetry) for sound propagation in an isothermal stationary field for band-averaged one-third octave bands with centre frequency $ka = [0.85, 1.08, 1.35, 1.70]$ ($f = [3.15\,\text{kHz}, 4\,\text{kHz}, 5\,\text{kHz}, 6.3\,\text{kHz}]$) at two different radii (14D and 28D). The results are from testing in the Anechoic Chamber with sound propagation through the reduced-scale exhaust rig. 421

List of Tables

1.1 Relevant parameters for the Siemens SGT5-2000E gas turbine [150]. . . . 5

2.1 Experimental studies of subsonic, unforced, circular, ground-level JICF. The entries in the table are from the earliest to the most recent investigations. It should be noted that R is the jet to cross-flow momentum flux ratio, and Re is the Reynolds number for the jet. 25

2.2 Numerical studies of subsonic, unforced, circular, ground-level JICF. The entries in the table are from the earliest to the most recent investigations. It should be noted that R is the jet to cross-flow momentum flux ratio, and Re is the Reynolds number for the jet. 26

3.1 The difference in mean velocity (Δu_0) along the X-Y plane at six distances downstream (z/D) from the centre of the duct outlet. The cross-flow velocity is $u_{cf} = 6.8\,\mathrm{m/s}$. 75

3.2 The difference in mean temperature (ΔT_0), difference in mean speed of sound due to temperature variations (Δc_0), and ratio for the speed of sound (c_{temp}) along the X-Y plane at six distances downstream (z/D) from the centre of the duct outlet. The cross-flow temperature is $T_{cf} = 27\,^{\circ}\mathrm{C}$. 76

4.1 Physical parameters for the experimental tests. 163

5.1 The reduction in maximum DI for the acoustic lobe downwind of the exhaust stack where the three nozzles for the case with $R = 5$. The ka in the left column is the band-averaged one-third octave centre frequency. 242

5.2 The reduction in maximum DI for the acoustic lobe downwind of the exhaust stack where the three nozzles for the case with $R = 7.5$. The ka in the left column is the band-averaged one-third octave centre frequency. 242
5.3 The reduction in maximum DI for the acoustic lobe downwind of the exhaust stack where the three nozzles for the case with $R = 10$. The ka in the left column is the band-averaged one-third octave centre frequency. 243

A.1 Parameters for a typical exhaust stack for an OCGT 298
A.2 Parameters for experimental testing in AWT 302
A.3 Parameters for non-isothermal ground level JICF numerical simulations 310

B.1 Values for the reference state at environmental conditions for the formulation of the ideal gas law assumption from ANSYS [8, 9] 325

C.1 The numerical validation cases investigated using acoustic FE modelling in ANSYS Mechanical. 334
C.2 Parameters for isothermal stationary field in a duct 335
C.3 Parameters for isothermal stationary field in a duct 339
C.4 Parameters for the case with a point source submersed in a sheared flow. 365
C.5 Parameters for the case with a point source submersed in a sheared flow. 377
C.6 Solution time and numerical grid size for the simulation of sound propagation from a 2-D point source in a finite thickness shear layer. . . 387
C.7 Parameters for the case with a point source submersed in a 2-D heated, non-expanding, subsonic jet. 392
C.8 Solution time and numerical grid size for the simulation of sound propagation from a 2-D point source in a heated, non-expanding, subsonic jet. 401
C.9 Parameters for baffled piston. 402

Acronyms

2-D 2-Dimensional

3-D 3-Dimensional

AWT Adelaide Wind Tunnel

CAA Computational Aeroacoustics

CFD Computational Fluid Mechanics

CFL Courant-Friedrichs-Lewy

COP Coherent Output Power

CPU Central Processing Unit

CRVP Counter-Rotating Vortex Pairs

DI Directivity Index

DNS Direct Numerical Simulations

FDD Finite Difference, Time Domain

FE Finite Element

FEA Finite Element Analysis

FEM Finite Element Method

FFP Fast Field Programming

FFT Fast Fourier Transform

HPC High Performance Computing

ISO International Standards Organisation

JICF Jet in Cross-Flow

LEE Linearised Euler Equations

LES Large Eddy Simulations

MLBS Maximum Length Binary Sequence

OCGT Open Cycle Gas Turbines

PE Parabolic Equations

PSTD Pseudo Spectral Time Domain

PML Perfectly Matched Layers

RAM Random Accessible Memory

RANS Reynolds Averaged Navier-Stokes

SAS Scale Adaptive Simulations

SPL Sound Pressure Level

SRS Scale Resolving Scheme

SST Shear Stress Transport

UTC University of Technology of Compiègne

Chapter 1

Introduction

1.1 Background and motivation

Sound propagation through inhomogeneous media is a complex phenomenon that exists in many systems. An example of this is the radiation of duct noise, which is of particular interest in fields such as aircraft jet exhausts, large HVAC systems, or large exhaust stacks. An example of radiating duct noise through inhomogeneous media is the noise from the exhaust stack of a simple cycle gas turbine/open cycle gas turbine (OCGT), as shown in Figure 1.1. Simple cycle gas turbines are increasingly being used for power generation, as they are able to provide power in peaking or uncertain conditions and can respond quickly to power grid demands. However, there is considerable evidence showing that there are increased levels of low-frequency environmental noise in the far-field from OCGTs [27, 32, 33, 70, 109]. Typical low frequency noise for OCGT is within the range of 16 Hz to 63 Hz and has been reported in literature [32, 33, 70, 72, 100, 101, 109, 124, 125, 153]. Literature has shown that significant levels of low-frequency noise can lead to adverse effects, such as: perceived annoyance from 'throbbing' arising from high-intensity low frequency noise [31], a 'beating' sensation in the chest [30], nausea [31] and acoustic excitation of structures with low resonance frequencies, such as glass structures and wall panels [31].

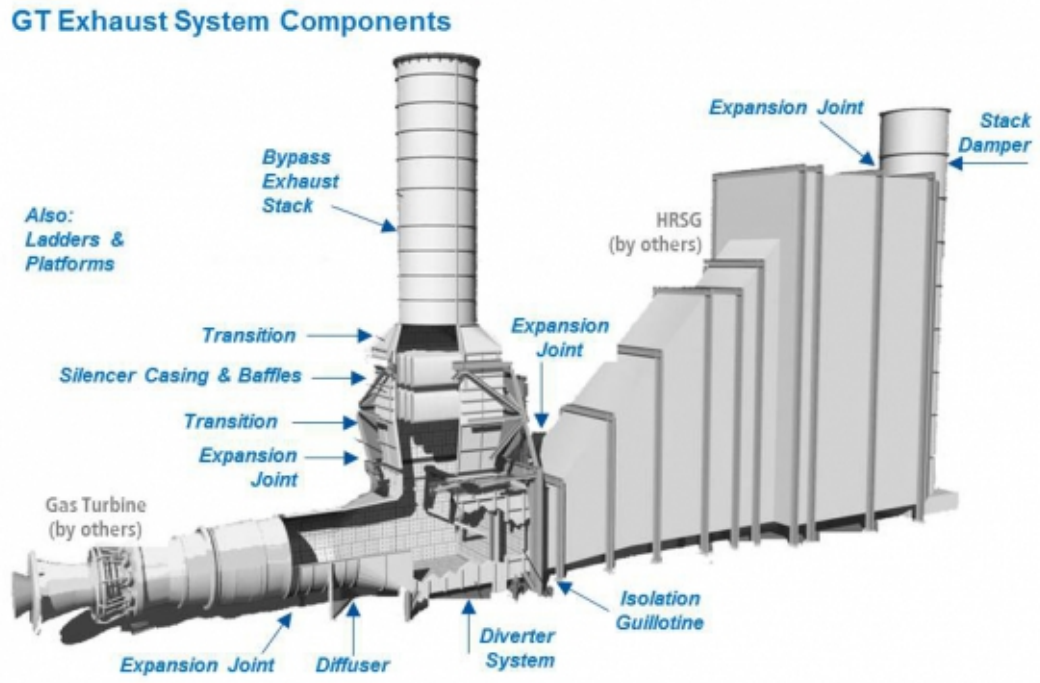

Figure 1.1: Schematic of a typical industrial OCGT with an exhaust stack [55]. It should be noted that this figure also includes the typical extension for a combined cycle gas turbine, but the emphasis of the image is the system excluding the expansion joints and the stack damper.

The fluid mechanics of an OCGT exhaust stack can be simulated as an elevated jet in cross-flow (JICF), as illustrated in Figure 1.2. The exhaust stack can be simulated as a cylindrical duct attached to a flat ground plane. At the base of the duct, there is a bulk turbulent fluid flow inlet that is heated above the ambient temperature and then coupled with a sound source, both of which travel through the duct. This bulk turbulent fluid flow, coupled with sound, then exhausts at the outlet of the duct, resulting in an open jet and sound source. The cross-flowing free stream subsequently interacts with the heated jet, sound, and the cylindrical duct to form complex flow structures and sound directivity patterns. The flow physics of this type of problem have been studied extensively, but the interaction of sound with the large flow structures and thermal distribution associated with heated jets in cooler cross-flow is a new area of research. More specifically, the following bulk fluid-acoustic interaction parameters associated with acoustically

driven elevated JICF have yet to be studied: the effects of the convective bulk fluid velocity, mean thermal distribution from heated exhaust jets, varying cross-flow free stream velocity, and varying sound sources on the sound propagation path radiating from the stack. Improved understanding of the interaction of sound with the flow physics will lead to future noise mitigation strategies that may benefit the energy industry and surrounding communities that use OCGT.

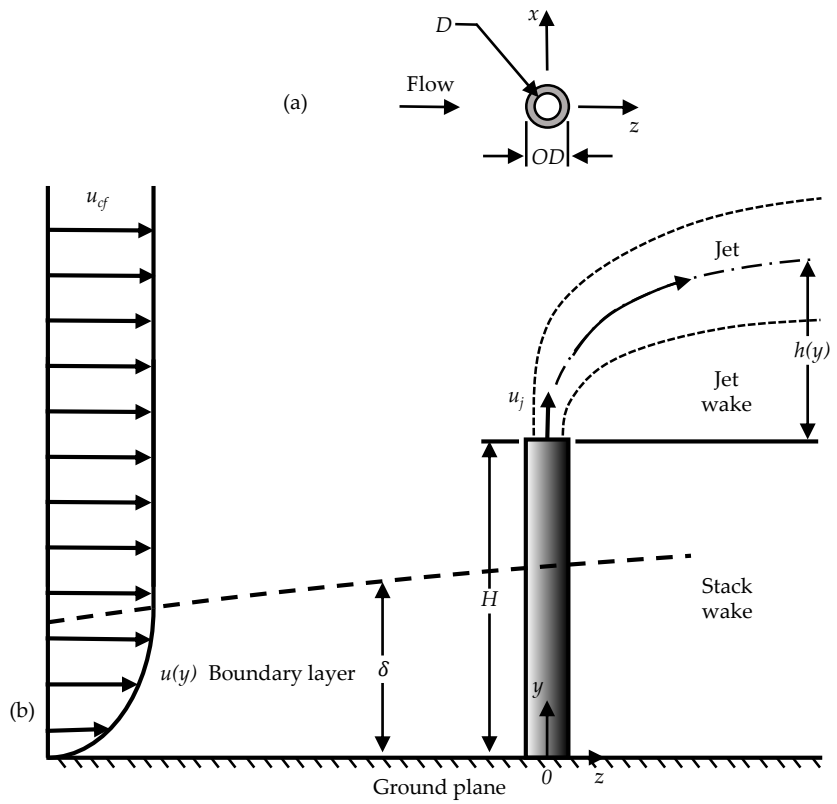

Figure 1.2: Schematic of an exhaust stack with uniform circular cross-section (of external diameter, OD, internal diameter, D, height, H, and jet exit velocity, u_j) mounted perpendicular to a ground plane and immersed in a cross-flow (with boundary layer thickness, δ, stream-wise velocity profile, $u(y)$, and cross-flow free stream velocity, u_{cf}). Figure adapted from Adaramola et al. [1]: (a) top view and (b) side view.

The measured noise levels at communities near OCGT exhaust stacks is greater than predicted. It is hypothesised that the higher than predicted SPLs are caused by the interaction between the sound emitted from the exhaust stack and the fluid

dynamics associated with the plume. As a first approximation, an OCGT exhaust stack can be modelled with a ground-level jet in cross-flow (JICF), which can be used to investigate the effect of the plume on sound propagation. Figure 1.3, shows with ray acoustics, the expected sound radiation with and without the plume. Figure 1.3a, shows the sound radiation from a monopole source in a homogeneous media, which is the common assumption used in various models, and represents a simplification of an acoustic source emanating from the duct outlet which has travelled up through the stack from the noise source, which in this case is the gas turbine. The presence of a plume in Figure 1.3b is hypothesised to increase the downwind sound levels as a result of sound refraction. The sound upwind would also change as a result of the sound interacting with the incoming cross-flow.

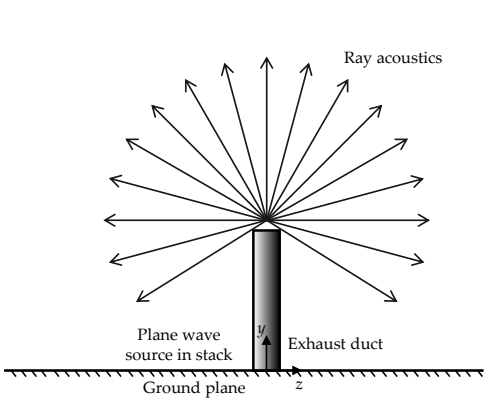

(a) Sound propagation in the absence of flow

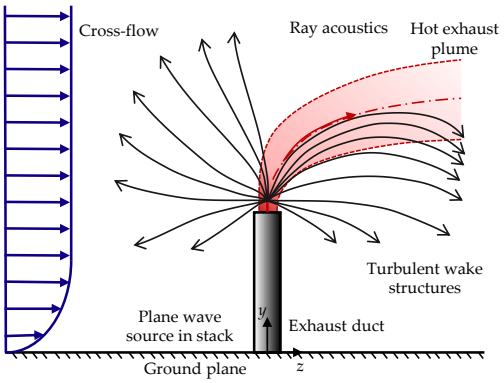

(b) Sound propagation with the presence of cross-flow and temperature gradients.

Figure 1.3: Schematic of acoustic ray propagation with and without the presence of flow and temperature.

There are a diverse range of gas turbines used for power generation, and for the hypothesis posed in this thesis, there are a wide range of meteorological conditions that can effect the fluid dynamics of the plume and sound propagation downwind, which are described in detail in Chapter 2. There are three large gas turbine original equipment manufacturers (OEMs); Siemens, General Electric, and Mitsubishi Heavy Industries. Siemens provide a wide range of industrial gas turbines for power generation, with simple cycle power outputs ranging from

4 MW to 593 MW and their data sheets are readily available [150]. Depending on the gas turbine offered by Siemens [150], these machines operate with exhaust flow temperatures ranging from 430 °C-680 °C. Similarly, depending on the gas turbine the exhaust mass flow can vary from 15.4 kg/s-1050 kg/s. A typical gas turbine for generation is the 160 MW Siemens V94.2 gas turbine and its newer superseded model Siemens SGT5-2000E gas turbine [126, 150]. Appendix A provides detailed calculations based on the Siemens SGT5-2000E gas turbine, and the important parameters for the analysis conducted in this thesis are included in Table 1.1. An important note is that the values calculated in Appendix A and presented in Table 1.1 are similar to real measurements for an exhaust stack attached to a Siemens V94.2 gas turbine at Uranquinty, New South Wales, Australia [127]. The environmental management report has stated the measured quantities for the exhaust stack are: volumetric flow rates of approximately 1200 $\mathrm{m\,s^{-3}}$, exhaust velocities of approximately 40 $\mathrm{m\,s^{-1}}$, and exhaust temperatures of 800 K [127].

Table 1.1: Relevant parameters for the Siemens SGT5-2000E gas turbine [150].

Description	Parameter	Value	Units
Duct diameter	D_j	6	m
Temperature in duct	T_j	809	K
Exhaust mass flow	$\dot{M}_j$	558	$\mathrm{kg\,s^{-1}}$
Exhaust velocity	u_j	45.2	$\mathrm{m\,s^{-1}}$
Mach number	M_j	0.08	-
Reynolds number	Re_j	3.17×10^6	-
Temperature in cross-flow	T_{cf}	300	K
Duct height	H_{duct}	60	m
Acoustic frequency range of interest	f	16-100	Hz
Helmholtz number	ka	0.53-3.19	-
Jet to cross-flow momentum flux ratio	R	3-20	-

The proposed research project is expected to have significance in applied acoustics, for the reduction of industrial noise, which will benefit the energy industry, since it aims to explore the fundamental mechanics of sound propagation emitted from exhaust stacks with cross-flow. From the literature review, it was found that OCGTs produce higher levels of low-frequency noise measured at

communities than are predicted by the current standards and conventional sound propagation models. Understanding the effects of the plume on sound propagation will help the energy industry control sound from OCGT exhaust stacks. This study represents the first investigation into sound propagation through a turbulent exhaust stack with cross-flow. It will be shown that the flow can redirect the low-frequency noise to neighbouring communities, and, as such, will potentially lead to the following: the introduction of a new area of research for aeroacoustics in the energy sector, amendments to the relevant industry standards, changes to relevant outdoor noise prediction models and future research into cost-effective solutions for noise mitigation for new and existing OCGT power stations.

1.2 Aims and objectives

The aim of the research is to investigate the mechanisms involved in the propagation of sound through heated, non-isothermal, low Mach number, vertically-oriented exhaust jets with a cooler horizontal cross-flow. It is hypothesised that the plume alters the propagation path of the sound, leading to asymmetric acoustic radiation in the plane parallel to the incoming cross-flow free stream velocities. The temperature and velocity gradients in the plume cause refraction of sound downwind of the exhaust stack, leading to an increase in the sound levels observed downwind, when compared with the idealised case of sound radiation in a homogeneous medium. It should be noted that this is not the first time the hypothesis has been speculated, and Björk [27] has also arrived at a similar hypothesis, but did not expand on the issue. Björk [27] briefly mentioned that the A-weighted sound levels at the receiver downwind from the exhaust stack can vary by up to $\pm 5\,\mathrm{dB}$ depending on the meteorological and plume conditions. Furthermore, Stephenson [153] also speculated that the increased levels of sound downwind is due to the directivity of the exhaust stack reported by Day and Bennett [48] and Day et al. [49] interacting with the cross-winds that favour conditions for increased levels of sound downwind. Stephenson [153] did not take into consideration the noise from the exhaust stack and the interaction with the plume, as discussed by Björk [27]

and is the primary focus of this research. Finally, the research results conclude with a preliminary study of nozzles for reducing the impact of the sound refraction.

1.3 Thesis outline

The thesis comprises of six chapters. Chapter 2 of the thesis is a literature review of relevant works. Chapter 3 of the thesis presents the numerical work undertaken during the research, examining the sound radiation through non-isothermal ground-level and elevated JICF. Chapter 4 presents results from an experimental campaign conducted on a non-isothermal elevated JICF. The experimental campaign investigates the effect of varying the cross-flow free-stream velocity, and subsequently, the jet to cross-flow momentum flux ratio, and the subsequent impact on the sound directivity. Chapter 5 of the thesis explores prototype designs for mitigating the increase in sound levels downwind of the exhaust stack, through various design iterations of nozzles. A summary of the findings from the research are presented in the final chapter, as well as future work to be conducted.

Supplementary material to support the research and findings in the thesis are presented in the appendices, where:

- Appendix A presents the numerical calculations for the research,
- Appendix B details the mathematical formulation for sound propagation with two different acoustic finite element method, and this was used in Chapter 3,
- Appendix C presents numerical validation to support the numerical method in Chapter 3,
- Appendix D details testing undertaken in the Anechoic chambers at the University of Adelaide to verify the experimental methods and results in Chapter 4, and
- the journal and conference publications arising from this thesis are presented in Appendices E, F, G, H, and I.

Chapter 2

Literature Review

2.1 Topics for review

Due to the diverse multidisciplinary problem of sound radiation through a heated, non-isothermal[1], low Mach number, exhaust jet in cross-flow, the literature review that follows will cover a wide range of topics. Firstly, a brief review on the noise sources in OCGT will be provided. The second review topic will be atmospheric sound propagation models. The third review topic will be on the fluid dynamics associated with JICF, both ground-level JICF and elevated JICF. The fourth review topic will be the sound refraction from fluid dynamic shear layers. A summary of the literature review will be provided at the end of the chapter, with a discussion of the gaps in the research that will be addressed in this thesis.

2.2 Open cycle gas turbine noise source

The dominant noise source in an OCGT is from the high-speed turbulent flow over the gas turbine diffusers and combustion process itself, however there are also other 'self-noise mechanisms' in the system, namely: flow interaction with bends; self-noise associated with flow separation from the silencer baffles; and self-noise associated with the flow separation from the bolts used to fix thermal tiles to the

[1]The term non-isothermal refers to a system with a heated jet injecting into a cooler cross-flow.

steel duct, also known as 'pin noise'. Bends are used in the exhaust stack to redirect the exhaust stack fluid, and sharp bends can lead to flow separation self-noise [25]. Bies et al. [25] have shown mitred joints can lead to unsteady flow and a reattachment flow that leads to the presence of dipoles sources. Contractions and expansions can also lead to impedance changes, as well as additional separation points for flow noise generation [25]. Baffles (also known as splitters) can be used to attenuate sound at certain frequencies, but flow over these baffles will not only degrade attenuation performance [25], it will also cause flow separation noise generation [118, 161]. Ver's [161] pioneering study into the relationship with sound power and flow speed over the baffles showed that the sound pressure level is proportional to 10 $\log_{10}(V^{5.5})$, where V is the flow velocity. Munjal [118] extended this theory and has derived equations for relating the self-noise sound levels, octave bands and flow velocities. Peters et al. [130] has shown that the presence of bolts in the exhaust flow generates 'pin noise', resulting in a significant increase in the generated sound power that is dependent on the flow speed. This does not take into consideration the dependency of 'cut-on' (the acoustic frequency limit for exciting higher order non-plane wave modes) in the duct [123]. For multiple elements of equal size, Mak [113] considers the centre frequency, coherence of the spoiler source, the distance between spoilers, and the ratio of the mean drag force, which are not considered by Peters et al. [130]. While the overall sound source within the exhaust stack is very complicated, it is not the focus of this research. The noise source in this research has been simplified, with the emphasis of the research on the various sound propagation mechanisms outside of the exhaust stack.

Furthermore, open jet noise is another potential noise source emitted from an exhaust stack. This form of noise generation has been studied by Lighthill [105, 106], who found that the jet sound power is directly proportional to the M^5, where M is the Mach number of the flow [105, 106]. In OCGT, the sound power from a jet is relatively small in comparison with the other noise mechanisms in the exhaust stack, in particular, the gas turbine and downstream diffusers, as the Mach number for the flow in the exhaust stack is relatively low at approximately 0.1. As a result, the sound power of the jet can be neglected for a preliminary study of

sound propagation from the exhaust stack. For a more accurate analysis, the flow generated noise in the shear layer could be included.

2.2.1 Near-field sound close to OCGT exhaust stack outlet

Sound pressure level (SPL) measurements have been conducted near the exhaust stack outlets of OCGTs by Björk [27], Hetzel and Putnam [72], and Kudernatsch [101]. Hetzel and Putnam [72] conducted additional SPL measurements for the exhaust stack outlets of combined cycle gas turbines. From the measured one-third octave band SPL spectra, with a centre frequency range of 8 Hz-63 Hz, Hetzel and Putnam [72] found that OCGTs have significantly higher SPLs than equivalent combined cycle gas turbines. Measurements of SPLs at the stack outlets of OCGTs from Björk [27] and Kudernatsch [101] showed similar trends; for low frequency noise is problematic, and that the current sound attenuation technology of baffles and liners provides limited noise reduction.

Björk [27] conducted sound directivity measurements near an OCGT exhaust stack outlet and suggested that sound refraction may result in higher sound levels in communities downwind of the exhaust stack. The sound directivity from the exhaust stack of OCGTs at approximately 30° off-axis, exhibits an acoustic lobe downwind [27]. In the OCGT investigated by Björk [27], in order to reduce the SPL at the community, and change the directivity, a heat recovery stage in the exhaust stack, new baffles, and a new duct liner were installed [27]. The modifications to the exhaust stack led to an attenuation of the SPL measured at the exhaust stack outlet, and caused the sound directivity to become more aligned with the centreline axis of the duct [27]. However, Björk [27] showed that there is a reduction in the acoustic attenuation performance of the new system over time, with the degradation of the baffles and liners from the build up of ash and particles on the surface. Björk [27] also hypothesised another issue; that the sound propagation path can be altered by certain meteorological conditions, with the sound interacting with the bent-over hot exhaust plume downwind of the stack. Björk [27] commented that the bent-over hot exhaust plume, along with the thermal gradients and varying wind conditions would cause the A-weighted sound levels downstream to vary

by up to ± 5 dB in the neighbourhood. The locations of the measurements are not explicitly described by Björk [27], but it can be implied with earlier discussion in the paper that the measurements were taken at 250 m or $86D$, where $D = 2.9$ m, is the exhaust duct diameter. However, Björk [27] could not verify this hypothesis and only measured the sound from a full-scale exhaust stack at approximately $1.5D$, and approximately $3D$ on a small-scale (1:20) model, where $D = 0.145$ m is the internal duct diameter of the reduced-scale model. Limitations of the previous work by Björk [27] are measurements were only undertaken in the near-field, where the onset of refraction was initiated, and no real cross-flow effects were observed.

Additionally, Björk [27] recommended solutions for reducing the sound downwind of the exhaust stack, or more accurately towards a community. The two solutions are shown in Figure 2.1, which were to (a) extend a section of the exhaust stack with half of the existing circumference, or (b), place a conical section at the duct outlet [27]. Both of Björk's [27] solutions aim to increase the acoustic 'shadow region' between the community and the exhaust stack, leading to a reduction in the sound levels observed in the community. The directivity measurements at $3D$ from the centre of the reduced-scale (1:20) exhaust stack outlet, using the half-cylinder extension shown in Figure 2.1, had a broader directivity pattern, when compared with the original stack [27]. However, the conical section, shown in Figure 2.1, produces sound directivity that is almost identical to the unmodified stack [27]. The change in the fluid dynamics caused by the addition of the two nozzle geometries was not investigated.

2.3 Atmospheric sound propagation

Atmospheric sound propagation modelling must consider the meteorological and terrain effects. It was found through early research by Arago [10] and Delaroche [50] that the presence of atmospheric wind alters sound propagation. This observation was later qualitatively explained by Stokes [154]. Experimental testing was then undertaken by Reynolds [136] to quantify the phenomenon of changing sound pressure levels according to wind velocity gradients. Reynolds [136] found exper-

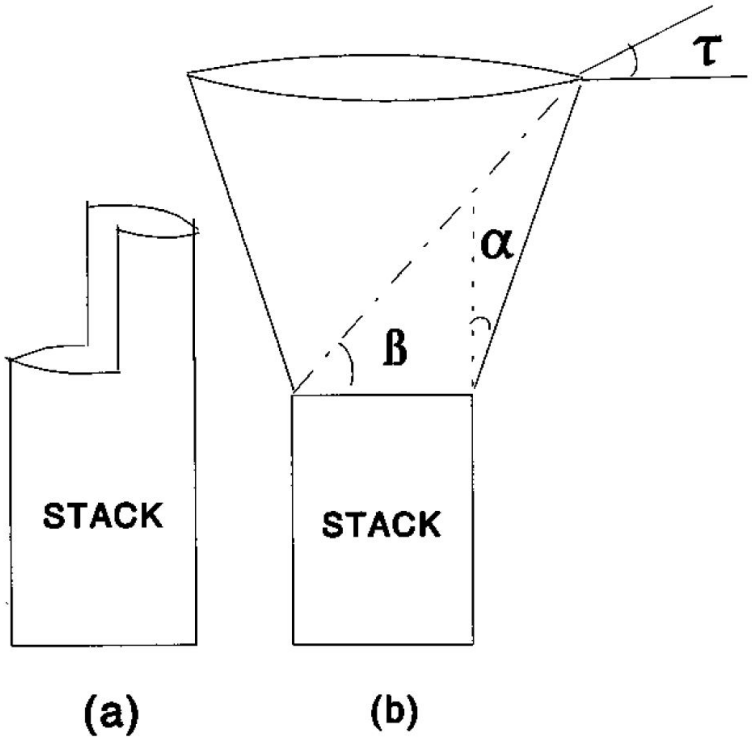

Figure 2.1: Schematic proposed by Björk [27] for two different noise mitigation strategies for sound radiation from hot exhaust jets in cross-flow, where (a) is a half-cylinder, and (b) is a conical lengthening of the stack. The angles in the figure are defined as: the conic angle α with a value of 20°, shadow angle β with a value of 40°, and the elevation angle τ with a value of 0°. The image was adapted from Björk [27].

imentally that the sound pressure levels downwind from a source will increase, whereas upwind there was a decrease in the sound pressure levels. Reynolds [137] also found experimentally that with a decrease in temperature with respect to the height above ground-level, the sound will bend upwards, and in the opposite case, the sound will bend downwards. Reynolds [137] attributed the latter conditions to be commonly associated with nighttime conditions, which he suggested meant that sound is heard more clearly during night conditions than day conditions. Rayleigh [135] then attempted to quantify this phenomenon with a mathematical approach, using the ray acoustics method. However, the formulation was incomplete, and there were errors in the formulation for the definition of vectors in terms of plane

waves [128]. Subsequently, corrections in the original formulation were made by Barton [19], who then successfully calculated the ray path from a source in the atmosphere by taking into account refraction. This research has progressed with alternative methods now available for quantifying atmospheric sound propagation, including numerous standards, analytical derivations, numerical calculations, and hybrid approaches (experimental and numerical approaches combined). The remainder of this review will discuss the various methods, as well as the limitations and gaps in this field of research.

2.3.1 Reviews of sound propagation

Typical outdoor sound predictions will commonly use far-field atmospheric sound propagation models, where the meteorological and terrain effects must be considered. Early research [10, 50] has shown that the presence of atmospheric wind will alter the propagation path of sound. Since then, multiple literature reviews [12, 54, 85, 128, 132] identified numerous methods for quantifying atmospheric sound propagation. The typical sound propagation model aims to analyse the propagation of a monopole acoustic source with varying molecular absorption, incoming velocity, turbulence, and temperature conditions, that resemble meteorological conditions, as depicted in Figure 2.2 [12, 13, 28, 54, 76, 129, 132, 134, 164–168, 170]. The change in the acoustic propagation parameters due to the variations of velocity and temperature in the atmosphere from meteorological conditions is governed by:

$$c_{eff} = c + v, \tag{2.1}$$

where c is the sound speed, and v is the bulk flow speed in the direction of sound propagation [128]. The speed of sound, c, can be calculated from the equation:

$$c = \sqrt{\gamma_d R_d T(1 + 0.511r)}, \tag{2.2}$$

where γ_d is the specific heat ratio for dry air, R_d is the gas constant for dry air, T is the absolute temperature, and r is the water vapour mixing ratio [128]. When analysing the far-field sound propagation from the effects listed, the dominant mechanism affecting the propagation of sound is refraction [12, 13, 28, 47, 54, 85, 99,

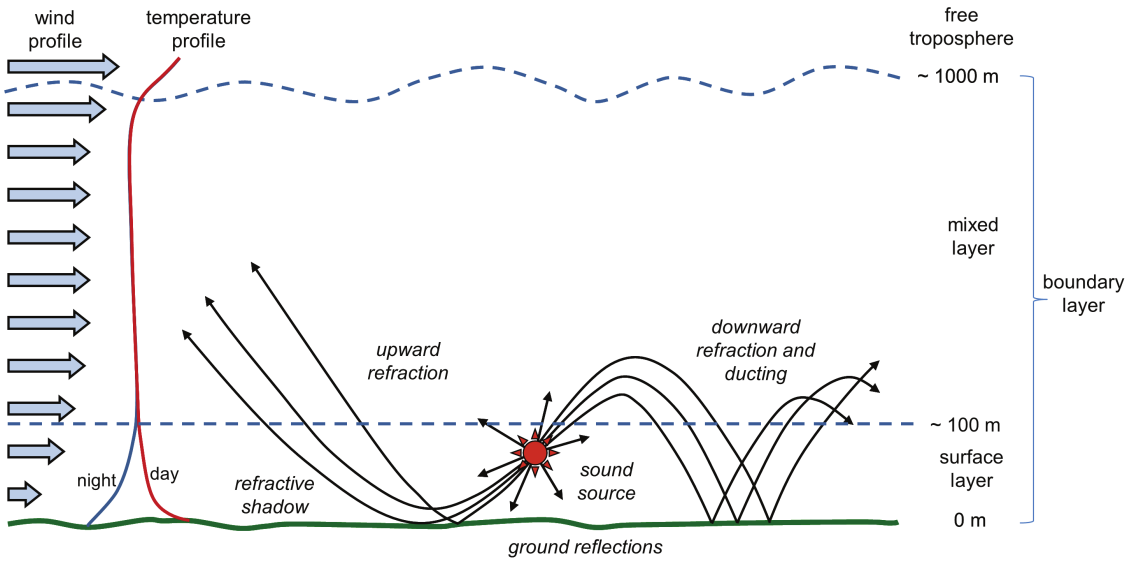

Figure 2.2: Schematic of the key features for atmospheric sound propagation models with a monopole source interacting with the atmospheric boundary layer. The sound propagation is for a near-ground source under high-wind conditions when the wind is blowing left to right [171].

102, 129, 132, 134, 163–168, 170]. These early models have been extended to include sound propagation through the atmosphere with the addition of uncertainties from atmospheric turbulence, which can cause further refraction, scattering and attenuation [68, 165, 167, 170]. While these sound propagation models account for the sound propagation in the far-field, they do not account for a local flow field, such as is the case with an exhaust stack. The exhaust plume will alter the propagation of sound, and the noise source may no longer resemble an elevated monopole.

The literature shows that certain meteorological conditions cause adverse situations downwind for increased sound, due to downward sound refraction [34, 47, 102, 163, 167–169, 171]. The most common case for downward acoustic refraction downwind is with stable stratification in the atmospheric surface layer, which is more commonly known having as clear night conditions with a temperature inversion [12, 34, 167–169, 171].

2.3.2 Analytical/numerical sound radiation models

Analytical atmospheric sound propagation models have been increasing in complexity, which has led to the application of numerical tools to compute these models. Traditionally, atmospheric sound propagation models began with geometric ray acoustic representation or ray theory, with an elevated monopole source radiating in a homogeneous space [19]. This point source is subjected to refractory effects from wind velocity gradients that vary linearly with height [103, 134], temperature gradients that vary linearly with height [134], and humidity. Barton [19] was the first to calculate the acoustic rays successfully. These analytical models have increased in complexity to include terrain with complex impedance characteristics, non-linear height dependent wind velocity profiles, non-linear height dependent temperature profiles, sophisticated atmospheric attenuation characteristics, and large static structures, which have led to researchers now using cost-effective numerical methods to compute these models [98, 128, 134, 166]. The ray tracing method has also been extended with commercial noise propagation software, such as Harmonoise and Nord2000 [25, 68]. Ray acoustic representation does have several shortcomings in calculating sound levels. In particular, the method does not account for caustics, diffraction or scattering [128]. The applications where this is important are small-scale turbulence causing scattering, intercepting ray paths from ground reflected waves and directly propagated waves, and 'shadow zones' from either upwind refraction or behind large structures where diffraction is prominent [128].

2.3.3 Standards

The internationally accepted standard for predicting outdoor noise levels is described in ISO 9613-2:1996 [88]. The standard uses various simplifications to reduce the complexity of the noise level predictions for both the source and path. For the source, the standards state a monopole point acoustic source can be used where possible, but for complicated sources simplifications can be made to model the source or sources into equivalent monopole sources and in particular, finite line

sources. Finite line sources are divided into either multiple monopole point sources or a single equivalent monopole point source [88]. Furthermore, a correction factor for directivity of the sound source can be applied, but there are no in-depth discussion for the directivity correction factor for particular applications, such industrial exhaust stacks. In estimating the sound pressure levels for the sound source approximation, the measuring methods described in ISO 10494:2018 [89] can be used. The sound source is propagated using analytical equations that take into consideration the attenuation due to the geometrical divergence, atmospheric absorption [86], ground, barriers, and miscellaneous effects [88]. The meteorological conditions in the analytical models are also adjusted by a correction factor in decibels, which is based on long term averages of the weather conditions that is favourable for sound propagation [88]. The correction factor can be determined by analysing the local meteorological statistics (based on meteorological conditions met by 50% or more of the time period of interest) or by information given by 'local authorities' [88, 170]. The consideration for varying meteorological conditions in the standards is simplistic and does not take into consideration the complex interaction of sound with complex turbulence scattering, time-dependant wind gradients with varying vertical profiles, temperature inversion in the atmosphere with varying vertical profiles, large variations in meteorological conditions in a given day, and are only recommended for estimating sound levels at distances of up to one kilometre from the source [170]. Detailed discussion of the complex interaction between sound and various meteorological conditions will be elaborated in the subsequent section. Hence, ISO 9613-2:1996 is adequate for providing an estimate of sound pressure levels in the community from a monopole source, but due to the assumptions and limitations, this method cannot be used for high fidelity sound level predictions [88].

As discussed previously, ISO 9613-2:1996 is a simplified method commonly used in industry to predict the sound levels in the far-field, and does not take into consideration the complex interaction of the sound with the hot jet exhausting from OCGTs with a cooler cross-flow [88, 170]. More detailed numerical models for atmospheric sound propagation have been investigated in the literature and

can be used to predict the sound levels in the far-field with greater accuracy. The subsequent section discusses these different numerical sound propagation models in the literature, and their technical applicability to the research in this thesis.

2.3.4 Numerical sound radiation models

Numerical models for calculating atmospheric sound propagation are becoming a more attractive approach for researchers with advances in computational capabilities. There are currently various sound propagation numerical methods that have been explored. The two main methods are ray theory and wave theory, which can be divided into the following techniques: numerical ray acoustics (previously discussed), the wave-based frequency domain method, the wave-based time domain method, and computational fluid dynamics (CFD) simulations using large eddy simulations (LES) [13, 128]. The two most common wave-based frequency domain methods are wavenumber integration, otherwise known as Fast Field Programming (FFP) [102, 157] and parabolic equations (PE) [13, 162, 163, 169]. Wave-based frequency domain methods are particularly attractive, as they provide frequency specific solutions and are not limited by high-frequency approximations, which is the case for ray theory [128]. The main disadvantages for wave-based frequency domain methods are that they were originally designed for propagating sound outwards and so do not handle reflections from buildings or terrain effectively. Furthermore, PE can only account for a finite width beam emanating from the acoustic source, whereas FFP is not limited by this issue [128]. However, FFP cannot account for atmospheric turbulence scattering, whereas the PE method can account for this [128]. This has led to PE being the more attractive wave-based frequency domain method and it is increasing in popularity. For wave-based time-domain numerical methods, the most commonly used is the Finite Difference Time Domain (FDTD) method. The FDTD method has several advantages over ray acoustics and the wave-based frequency domain, which include: sound refraction through complicated wind gradients and thermal gradients [28, 129], and scattering by turbulence [41], transient source mechanisms, dynamic atmospheric variation, scattering from complex terrains [128]. The Pseudo-Spectral Time Domain (PSTD) is

another time domain method that has been developed, which has been used for work with noise-barriers and ground interaction [76]. This method is efficient for homogeneous domains that can be partitioned into subdomains [128]. The main disadvantages of the wave-based time domain method is that it is computationally intensive with the available computational technology and is only capable of solving for audible frequencies in two-dimensional (2-D) analysis (three-dimensional, 3-D, simulations can be done using supercomputers and clusters). Another issue with the wave-based time domain method is the implementation of ground impedance conditions, which are complicated to program in the time-domain. Another time-based spatially discretised method for solving sound propagation numerically is to employ CFD simulations. Simulations with CFD numerically solve the Navier-Stokes equations for the bulk fluid dynamics, and the small perturbations are directly solved in the equation to account for acoustic fluctuations [167, 168]. CFD simulations have all the benefits of the wave-based methods but take into consideration the interaction effects between the sound and the flow itself [167, 168]. CFD simulations for sound propagation through inhomogeneous media exhibit the same main disadvantage as FTDT[167, 168], as described previously.

Different numerical sound radiation models have been used to estimate the sound levels in the far-field for sound propagation through the atmosphere from a simple monopole source, but more complicated acoustic sources and propagation conditions related to exhaust stacks from OCGT were not investigated. In the thesis, CFD simulations are used to estimate the flow and temperature field resulting from a heated jet from an exhaust stack in a cooler cross-flow. Whilst there are various suitable numerical sound propagation models available, finite element methods have been used in this research and are described in detail in Chapter 3. The finite element method for sound propagation incorporates the effects of flow and temperature from the heated jet from an exhaust stack in a cooler cross-flow for predicting the sound in the far-field.

2.3.5 Numerical sound radiation uncertainties

Research into the field of atmospheric sound propagation is currently more focused on modelling uncertainties in the atmosphere, in particular, atmospheric turbulence effects. To accommodate for the uncertainties in the atmosphere, stochastic models are used to describe these uncertainties, including the following: Monte-Carlo simulations, Latin hypercube samplings, and Latin hypercube samplings with importance sampling. These stochastic methods use atmospheric condition theory, such as Monin-Obukhov similarity theory (MOST) [98, 102, 166–168, 170] or sampling over a spatial domain to generate the atmospheric uncertainties. These stochastic models are used to account for fluctuating atmospheric conditions, different source spectra, turbulence, and complex ground surface impedances with numerical sound propagation using wave theory [76]. LES can also be used to solve numerically for the uncertainty parameters that are stochastically modelled in atmospheric sound propagation models, but modelling with LES is computationally intensive and shows poor agreement in the far-field [167, 168]. Therefore, there are various methods used to calculate the uncertainties in the atmosphere, with the Latin Hypercube sampling alongside importance sampling being the most appropriate method for modelling broadband sources numerically with any uncertainties being taken into consideration [128, 170].

Recent research into atmospheric sound propagation models concentrates on modelling uncertainties in the atmosphere, but the uncertainties increase the complexity in predicting the sound levels in the far-field. In modelling the sound propagation from the exhaust stack attached to an OCGT with cross-wind, there are uncertainties in both the incoming atmospheric cross-flow, and the turbulent structures downwind of the exhaust stack from the plume. This thesis will focus on the dominant time-averaged flow and temperature mechanisms from the hot exhaust jet in cross-flow and their effect on the sound propagation in the far-field. The temporal and spatial uncertainties in the atmosphere and the turbulent flow downwind of the exhaust stack are beyond the scope of this research.

2.3.6 Experimental field measurements of sound propagation

Experimental field measurements are essential for understanding atmospheric sound propagation. Various authors have conducted independent studies on this topic [102, 134, 169]. With regards to the topic of atmospheric sound propagation, the literature on experimental field measurements takes the following into consideration: the sound is from an elevated monopole source with varying heights, there are varying meteorological conditions, different impedance conditions for the ground, sound level measurement locations, and sound level measurement durations [102, 134, 169].

Rasmussen [134] undertook a limited experimental sound level measurement study, and concentrated on the validity of predicting sound propagation from a monopole source with varying frequencies, f = 100 Hz to 5 kHz, at four discrete locations (horizontal distance of 40 m and 80 m upwind and downwind of the monopole source, as well as two different heights of 0.5 m and 1.5 m) with a ray acoustic model. Rasmussen [134] identified the importance of measuring the atmospheric temperature and velocity profiles for accurate far-field sound predictions accurately, as the study only uses two points to generate a linear velocity and/or thermal gradient for sound propagation. Additionally, the impedance conditions for the ground surface of the numerical model differed slightly for grass, which the experiments were based on, leading to an uneven acoustic condition. Moreover, turbulence becomes an increasingly important parameter for either higher acoustic frequencies or at distances far from the source (500 m) [134].

L'Espérance et al. [102] have conducted experimental sound measurements, under varying atmospheric conditions with 13 pure tones at seven distances (4 m, 66 m, 88 m, 125 m, 175 m, 250 m, and 350 m) at a height of 1.8 m. Each of the multiple recordings lasted between 10 to 15 minutes. Furthermore, the experimental measurements were conducted with various meteorological conditions in Pennsylvania. The experimental results have shown the importance of the acoustic frequency and the meteorological conditions when predicting sound levels, but, more importantly, the effects of upward and downward refractions are more pronounced with the increase in acoustic frequency. Furthermore, the purpose of the

sound measurements was to compare real experimental measurements of sound propagation in the atmosphere with FFP sound level predictions. The comparison showed that there is a good agreement with the experimental sound measurements and the FFP sound level predictions downwind of the source, with a downwardly-refracting condition in the atmosphere. However, upwind of the source, the FFP method under predicts the sound due to the effects of turbulence not modelled with FFP.

Wilson et al. [169] conducted experimental field measurements in a nocturnal boundary layer. The sound measurements were conducted in conjunction with meteorological measurements for nocturnal boundary layers with the Cooperative Atmosphere-Surface Exchange Study-1999 (CASE-99) by Wilson et al. [169]. The study involved employing a hybrid scheme for predicting sound propagation using experimental data and numerical sound propagation methods [169]. The meteorological conditions were measured using multiple towers for the velocity and temperature. The sound was measured using both towers and multiple arrays. The sound radiation was from a loud speaker, and measurements were taken up to 1.3 km downwind. Interestingly, the measurements were taken at night (nocturnal boundary layer) with stable conditions in the atmospheric boundary layer and a temperature inversion. The paper also describes the comparison of numerical and experimental acoustic results, with the meteorological data measured from CASE-99 used as the medium for sound propagation with PE.

The survey of atmospheric sound propagation has shown that, in addition to standards, there are other analytical and numerical models available for predicting noise levels, but limitations exist with these methods. Firstly, simplified point sources are used in all the models within the literature, whereas realistic sound sources can exhibit complicated radiation patterns; for example, finite line sources or distinct sound directivity patterns. Sound interaction with turbulence has been modelled using statistical methods to account for the uncertainty, but stochastic models only account for atmospheric eddies, and fail to account for eddies created by the flow generated by moving bodies, forced flows (jets or JICF), and flow interactions with static structures or complicated terrains. Most wave-based time

domain methods cannot incorporate the effects of sound on the fluid flow, however LES can accommodate for these effects. High-resolution LES studies have not been conducted in great detail due to the high computational cost of such analysis. As computing capabilities advance, however, more accurate numerical sound prediction methods can be used. There remain limitations and gaps in the research for high fidelity outdoor sound propagation.

2.4 Jets in cross-flow

Jets in cross-flow (JICF), commonly called transverse jets, have been widely studied for their relevance in various industrial applications for the last 80 years. JICF are commonly seen in various industrial applications, including: cooling exhaust plumes, chimney plume dispersal, film cooling for turbine blades, and dilution holes in gas turbine combustors. The earliest work in JICF dates back to Bosanquet and Pearson's work in 1936 on chimney and exhaust stack plumes [29]. The majority of the research in this field primarily looks at a jet issuing from a wall-mounted flush outlet with cross-flow, otherwise known as a ground-level JICF. Experimental and numerical analyses of ground-level JICF have been conducted extensively, showing good agreement between the two methods for reproducing critical flow characteristics. There is, however, limited work on elevated JICF, which is more representative of a chimney or exhaust stack. Currently, research in elevated JICF is primarily experimental due to the significant computational resources required to capture the salient fluid dynamics accurately. The work conducted in this thesis examines both sound propagation from ground-level and elevated JICF, and the relevant literature is discussed in the following sections.

2.4.1 Ground-level jets in cross-flow

A schematic of a typical ground-level JICF is depicted in Figure 2.3. They have been extensively studied, with a summary of the literature provided in Tables 2.1 and 2.2 for research into subsonic, unforced, circular, ground-level JICF. The research into ground-level JICF has suggested that there are critical flow features and trends

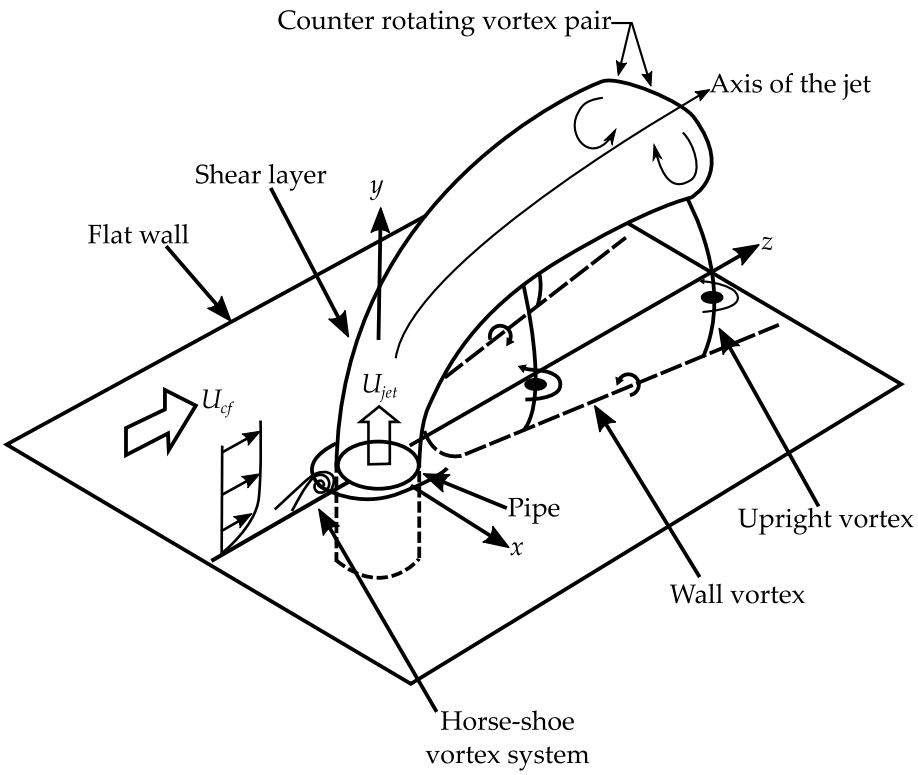

Figure 2.3: Schematic of the dominant fluid dynamic structures associated with a ground-level JICF [94].

[60, 94]. In these studies, four main coherent structures are seen: counter-rotating vortex pairs (CRVP), horse shoe vortices [94, 95], upright wake vortices, and jet shear layer vortices [60]. There are also other additional flow features which are commonly seen: 'hovering vortex' in the leading side of the jet outlet that develops into the shear layer vortices; nodes in the wake, wall vortices from the horse-shoe vortices that also develop into upright wake vortices [93, 94], and a deflected jet trajectory (dependent on the cross-flow momentum flux ratio, R) [92, 152]. The jet to cross-flow momentum flux ratio, R, is defined as:

$$R = \sqrt{\frac{\rho_j {u_j}^2}{\rho_{cf} {u_{cf}}^2}} \quad , \tag{2.3}$$

where the bulk jet exit velocity is u_j , the jet density is ρ_j, the free stream cross-flow velocity is u_{cf} and the free stream cross-flow density is ρ_{cf} [152].

Table 2.1: Experimental studies of subsonic, unforced, circular, ground-level JICF. The entries in the table are from the earliest to the most recent investigations. It should be noted that R is the jet to cross-flow momentum flux ratio, and Re is the Reynolds number for the jet.

Reference	Fluid	R	Re	Approach
Kamotani and Greber [92]	Air	3.87-7.75	2800-4200	Hot-wire anemometry, and thermo-couples
Fearn and Weston [58]	Air	3-10	2.6×10^3-3.6×10^5	Rake of seven yaw pitch probe
Crabb et al. [44]	Air	1.15-2.3	NA	Hot-wire anemometry, and LDA
Andreopoulos and Rodi [7]	Air	0.5, 1, and 2	440-6200	Three probe hot-wire anemometry
Andreopoulos [4]	Air	0.5	440-6200	Three probe hot-wire anemometry, and smoke visualisation
Sherif and Pletcher [148]	Water	1, 2, 4, and 7	16837-62377	Constant current anemometer and temperature bridge
Fric and Roshko [60]	Air	2-6	440-6200	Smoke streamline
Kelso and Smits [95]	Water	2, and 4	1200-4600	Hydrogen bubble wire visualisation
Kelso et al. [94]	Air and Water	2-6	440-6200	Dye injection, smoke visualisation, and flying hot-wire anemometry
Kelso et al. [93]	Air and Water	2-6	440-6200	Dye injection, smoke visualisation, and flying hot-wire anemometry
Smith and Mungal [152]	Air	5-25, and 200	1.66×10^4-4.15×10^4	Hot-wire anemometry, and PLIF
Lim et al. [107]	Water	4.6	1600	Dye injection
Cutler [46]	Water	$0.5 - 8$	2000-25000	Dye injection, hydrogen bubble wire visualisation, and PLIF
Su and Mungal [155]	Air	5.7	5000	PLIF and PIV
Rusch et al. [140]	Air	2.32	-	LDA and thermocouple

Table 2.2: Numerical studies of subsonic, unforced, circular, ground-level JICF. The entries in the table are from the earliest to the most recent investigations. It should be noted that R is the jet to cross-flow momentum flux ratio, and Re is the Reynolds number for the jet.

Reference	Fluid	R	Re	Approach
Jones and Wille [91]	Air	0.5	440-6200	LES
Yuan and Street [172]	Air and Water	2-6	440-6200	LES
He et al. [69]	Air	2.8, and 5.7	3300	RANS k-ϵ
Yuan et al. [173]	Air and Water	2-6	440-6200	LES
Chochua et al. [42]	Air	5.85, and 6.65	NA	RANS k-ϵ
Hoda and Acharya [74]	Air	0.5	4700	RANS k-ϵ
Cortelezzi and Karagozian [43]	Air	5.7	5000	Vortex method
Muppidi and Mahesh [121]	Water	$0.5 - 8$	2000-25000	DNS
Muppidi and Mahesh [119]	Air	5-25, and 200	$8.4 \times 10^3 - 4.15 \times 10^4$	DNS
Muppidi and Mahesh [120]	Water	4.6	1600	DNS
Rusch et al. [140]	Air	2.32	-	RANS (k-ϵ, k-ω, k-ω SST, and BSL RSM), DES, and SAS
Ziefle and Kleiser [176]	Water	3.3	6930	LES
Bagheri et al. [17]	Air	3	-	DNS
Muldoon and Acharya [116]	Air	3.87-7.75	2800-4200	DNS
Schlatter et al. [143]	Air	3	-	DNS
Galeazzo et al. [65]	Air	4	19200	RANS (k-ϵ, and k-ω SST), and LES
Galeazzo et al. [64]	Air	4.15	19200	URANS k-ω SST, RANS k-ω SST, and LES
Ruiz et al. [139]	Air	5.7	5000	LES
Esmaeili et al. [56]	Air	3.5-5.7	1070-5450	LES
Ling et al. [108]	Air	5.90	5000	RANS k-ϵ
Zhang and Yang [174]	Air	5.7	5000	LES

Jet in cross-flow simulations and experiments involve analysis of varying cross-flow momentum ratios, R, which is the ratio of the momentum of the fluid in the jet divided by the momentum of the fluid in the cross-flow field defined in Equation 2.3 [92, 152]. In the geometric near-field, at high cross-flow momentum flux ratios, flow is considered to be jet dominated with the flow exiting the outlet resembling an axisymmetric jet [92]. As the plume develops in the domain, the jet is deflected by the cross-flow momentum. The deflection in the jet then causes the plume to develop into a crescent-like structure [92]. In the far-field, the plume then transitions to a CRVP [92]. The CRVP becomes the dominant flow structure in the plume. For high values of jet to cross-flow momentum ratios, typically seen in exhaust stacks, the onset of the CRVP forms earlier in the plume than cases with a lower jet to cross-flow momentum ratio [92, 143]. Furthermore, using smoke visualisation, it has been seen that the majority of the gas exiting the jet is contained in the JICF plume [60, 94].

2.4.1.1 Numerical ground-level JICF

Numerical analyses of isothermal ground-level JICF have been conducted by various researchers with different turbulence models. Numerous case studies have used Reynolds Averaged Navier-Stokes (RANS) equations for predicting the ensemble averaged turbulence quantities in ground-level JICF [64, 65, 69, 74, 108]. Hoda and Acharya [74] found that unsteady-RANS models with isotropic eddy-viscosities are inaccurate for predicting the turbulent flow quantities, while using the anisotropic Reynolds Stress Transport Model yielded more accurate predictions for turbulent flow quantities. Studies by Galeazzo et al. [64, 65] have also found the same issue with inaccuracy when predicting turbulent flow quantities, but have compared Shear Stress Transport (SST) simulations with k-ϵ simulations, and found that SST gave good agreement with the mean velocity and pressure observed in experiments. Galeazzo et al. [65] recommended SST models over k-ϵ for turbulence modelling of ground-level JICF. Ling et al. [108] extended the idea of using an isotropic RANS model, k-ϵ, with machine learning to improve the fluid dynamic modelling of the anisotropic Reynold stress regions for ground-level JICF. Ling et al. [108] have

shown that with machine learning and training data from LES based simulation from Ruiz et al. [139], isotropic Reynolds Stress RANS simulations can improve the flow prediction in anisotripic Reynolds stress regions. The shortcomings with modelling ground-level JICF with isotropic RANS models can be further addressed using machine learning to improve the flow predictions without using computationally intensive models such as Scale Resolving Simulations (SRS), LES and Direct Numerical Simulations (DNS).

A number of other researchers have used SRS, in particular LES, for resolving turbulent structures seen in experimental studies such as CRVP, wake-vortices, shear layer vortices, and horse shoe vortices [56, 61, 64, 65, 91, 112, 139, 140, 172–176]. Galeazzo et al. [64, 65] found that LES leads to more accurate predictions for turbulent flow quantities with greater detail resolution of the fluid dynamic coherent structures in comparison with either RANS or unsteady-RANS. There are limitations in using LES for modelling JICF, with the back-flow near the outlet and resulting turbulent quantities not being resolved adequately with relatively coarse meshes. DNS studies have been undertaken for both laminar [17, 119, 143] and turbulent jets into cross-flow [116, 120, 121]. Similar to LES studies, DNS can accurately reproduce the critical flow structures [116, 120, 121]. Spectral analysis from DNS simulations results can also predict turbulent instabilities and provide spectral information on the formation of ring-like vortices [17, 143].

In summary, the prior research into the field of numerical simulations of ground-level JICF, suggests evidence that different turbulence models such as RANS, LES, and DNS simulations can accurately reproduce critical flow features. Hence, in this thesis CFD simulations can be used for numerically modelling ground-level JICF, with the research discussed in Chapter 3.

2.4.1.2 Heated ground-level JICF

Research on non-isothermal heated jets in cross-flow has been conducted by several authors [56, 92, 140, 147, 148]. Kamotani and Greber [92] undertook experimental analysis of the temperature distribution for ground-level JICF and the difference in trajectory between the velocity formulation and the temperature formulation. The

experiments by Sherif and Pletcher [148] were used to determine the temperature profile resulting from ground-level JICF with varying R. In varying R, the entrainment of the cooler cross-flow downstream is altered and there is a cut-off between the two different regimes. Incidentally, the definition for R used by Kamotani and Greber [92] (using the jet to cross-flow momentum flux ratio, $J = R^2$) differs from that used by Sherif and Pletcher [148] (which uses the velocity ratio, M_{vel}, and does not include the change in density between the heated jet and the cooler cross-flow). For heated jets, the CRVP in the far-field contains the hottest region in the plume [92, 148]. As fluid is entrained by the CRVP, the overall temperature of the plume decreases as it develops downstream and eventually the temperature of the plume's core slowly approaches the ambient temperature [92]. Previous experimental work has shown that the maximum vorticity in the plume is at the centre of the CRVP.

Investigation of non-isothermal ground-level JICF has been completed by Esmaeili et al. [56] and Rusch et al. [140] who examined the validity of using CFD for modelling the temperature downstream of the jet. Rusch et al. [140], compare experimental results with different CFD turbulence models (k-ϵ, k-ω, k-ω SST, BSL RSM, DES, and SAS) for modelling the temperature distribution of the plume downstream of the jet outlet. Steady-state or time-averaged simulations have shown that the plume is symmetrical along a vertical plane along the z-axis (i.e., $x = 0$) in Figure 2.3, with the smaller transient features (wake vortices and horseshoe vortices) not being visible in the domain. In the far-field, the dominant steady-state features of the CRVP are plane-symmetric. Rusch et al. [140] showed that for a steady-state ground-level JICF, the temperatures in the plume and the plume centerline trajectory are higher than expected. This is due to the fact that the smaller transient features, such as the horseshoe vortices and wake vortices that are entrained into the plume further, enhance mixing in the plume [140]. These transient features are not modelled in steady-state simulations. As expected with Rusch et al. [140], CFD simulations using various turbulence models show the CRVP, and that the hottest region is in the centre of the plume. However, a limitation of the work by Rusch et al. [140] is that the JICF is in a confined domain

to represent the heat transfer for flames in a tunnel and therefore is not applicable to the focus of the work in this thesis, where the jet is unconstrained. Esmaeili et al. [56] also showed that LES turbulence modelling can be used for non-isothermal ground-level JICF to reproduce, with good agreement, the key flow features. The key fluidic parameters reproduced by Esmaeili et al. [56] are: the CRVP, the jet penetration, the spreading rate of the plume downwind of the jet outlet, and the entrainment of the cooler cross-flow.

2.4.2 Elevated jets in cross-flow

A variation of the ground-level JICF is the elevated JICF, which is more representative of exhaust stacks, and has been researched by various authors [1, 5, 6, 51, 52, 78–84, 90, 141, 142, 155]. Figure 2.4 shows a schematic of an elevated JICF.

2.4.2.1 Fluid dynamic regimes for elevated JICF with varying R

Extensive research has been undertaken to investigate the dependency of the plume as R varies on changes to the stack-wake, jet trajectory and down-wash regions, which are features significantly different or unseen in ground source jets in cross-flow [1, 141, 142]. Adaramola et al. [1] have shown that as R varies there are three unique flow regimes in elevated JICF plumes: the down-wash region ($R < 0.7$), cross-flow dominated regime ($0.7 < R < 1.5$), and the jet dominant regime ($R > 1.5$). For low values of R ($R < 1.5$), the plume is cross-flow dependent, and with buoyant jets the down-wash region is prominent, the recirculation region is more dominant, and the jet trajectory is more horizontal [82]. For higher values of R ($R > 1.5$), the plume is jet dominant [1], with the key fluid dynamic structures seen in Figure 2.4. For the plume in the 'jet dominant' regime, there are three definitive vortical structures, with the CRVP in the plume, the tip vortex structures, with the von-Karman vortex sheets from the cross-flow interacting with the cylindrical stack [1]. Furthermore, the jet trajectory is more vertical. The experimental research in elevated JICF has led to a strong understanding of the common reproducible features that are unique to elevated JICF and similar to ground-level JICF.

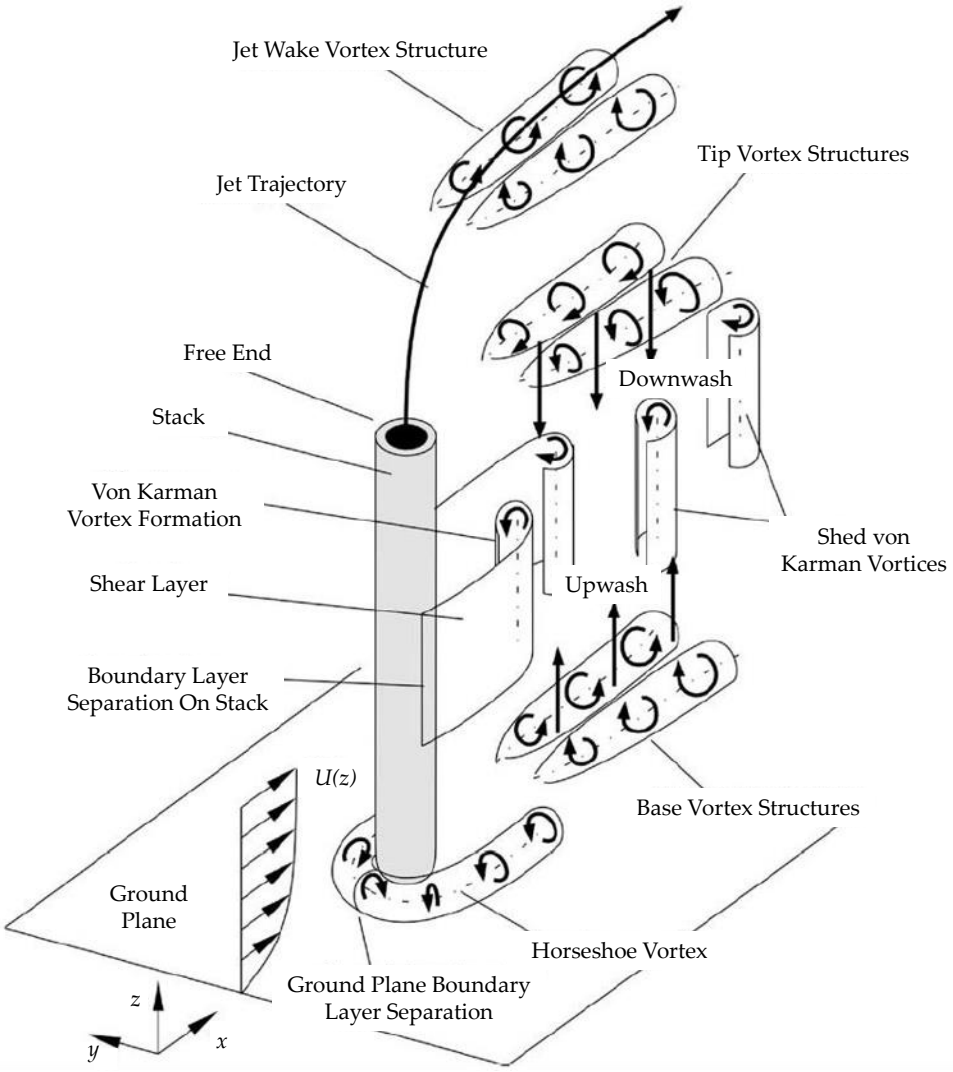

Figure 2.4: Schematic of the dominant fluid dynamic structures associated with an elevated JICF for a value of R that is in the jet dominated regime [1].

Additionally, various researchers have conducted geometric near-field flow measurements behind the exhaust stack and jet [1, 78, 80–82, 84, 141, 142]. All the researchers showed that for elevated JICF there is a region of reverse flow directly behind the stack and jet [5, 6, 78, 80–82, 84, 141, 142]. This region behind the stack has various recirculation zones in either the jet wake and/or the stack wake [5, 6, 78, 80–82, 84, 141, 142]. The region immediately behind the jet wake and stack wake also produces stagnant or 'dead-fluid'. As the cross-flow propagates towards the far-field region, there is no longer a region of reverse flow or recirculation in the jet wake and stack wake, with the flow travelling along the cross-flow free-stream [5, 6, 78, 80–82, 84, 141, 142]. Therefore, the flow in the geometric near-field behind the jet and stack show complex regions of reverse and stagnant flow.

2.4.2.2 Heated elevated JICF

Non-isothermal, heated elevated JICFs have been investigated experimentally with research conducted first by Andreopoulos [5, 6] and subsequently by Johnson et al. [90], showing similar trends with ground-level JICF. The research from Johnson et al. [90] investigated the development of the plume for heated JICF experimentally. Their paper shows that with stereoscopic PIV, non-isothermal heated JICF exhibit similar structural characteristics to isothermal JICF, in particular, the CRVP in both cases are structurally similar. The Reynolds number of the jet and R (their paper defines this as the blowing ratio) were kept consistent. The paper suggests that even though the jet is subjected to bulk heating, the structural composition of the turbulence in the plume downstream remains similar. More importantly, the hottest region in the plume is at the centre of the CRVP (the region of highest vorticity in the CRVP) and decreases outwards with the CRVP [5, 6, 90]. As the plume travels downstream, the temperature observed in the plume reduces as the plume entrains the cooler cross-flow, spatially spreads, and disperses in the cross-flow.

In the literature there are limited numbers of studies for non-isothermal elevated JICF, with some similarities to modelling real-scale exhaust stacks based on OCGT. Firstly, the non-isothermal elevated JICF in the literature investigate heated turbulent jets in a cooler cross-flow, but the flow conditions are not identical [5, 6,

90]. Although the non-dimensional parameters are different, there should be some key reproducible thermal features for non-isothermal elevated JICF and full-scale OCGT. Downstream of the exhaust stack, both systems should exhibit: a deflected jet on the leeward side of the exhaust stack, a CRVP in the geometric far-field for the plume, a thermal gradient in the plume with the hottest region at the centre of the CRVP, and a reduction in the overall temperature of the plume as it travels downstream.

2.4.2.3 Turbulence intensity and variations in elevated JICF

Andreopoulos [6] investigated the effects of the turbulence in the cross-flow boundary layer on the plume generated by elevated JICF. Andreopoulos [6] found that an increase in the external turbulence, in particular the large eddies, can lead to sudden direction changes and faster diffusion of the plume. The increase in external turbulence in the non-uniform cross-flow boundary layer also enhances the spreading rate, and reduces the normal velocity and thermal gradients in the plume, in comparison with a uniform cross-flow boundary layer [5, 6]. From the literature, it is evident that the turbulence from the cross-flow boundary layer, affects the fluid dynamics of the plume. Research into the effects of the cross-flow boundary layer displacement thickness on the plume or stack wake has yet to be undertaken. The cross-flow boundary layer effects on the fluid dynamics for this thesis will not be investigated in detail but will be measured and maintained for consistency in the research.

2.4.2.4 Similarities between elevated and ground-level JICF

Comparison between elevated JICF and ground-level JICF has shown that they have similar coherent fluid dynamic structures, as well as unique features [1, 5, 6, 51–53, 78–84, 90, 141, 142, 155]. The similar features are the deflected jet, horse shoe vortices, CRVP, shear layer vortices, and the node in the jet-wake [78, 79, 81, 82, 84, 141, 142, 155]. In the ground-level JICF, the wake vortices are generated from the ground-level and internal duct boundary layer, but for the elevated JICF, the jet-wake is from the internal duct boundary layer and the stack-

wake [142]. Andreopoulous' [5, 6] fundamental studies into jet-wake found a relationship between the jet-wake and the stack-wake. The study also found a strong dependency on the duct diameter, with the wake of the jet and the wake behind the exhaust stack. Later research showed that the wake and stack vortices are similar, with the wake vortices resembling von Karman vortex sheets with smaller magnitude vortices [51–53]. These vortices in the wake of an elevated JICF are also known as 'lock-in' vortices. Therefore, the stack diameter strongly alters the formation of the wake vortices, with the jet acting as an extension of the duct itself [52].

The literature has shown the similarities with flow features between ground-level and elevated JICF. The research in this thesis uses the results in the literature to investigate the interaction between the sound and the hot exhaust plume with cooler cross-flow for a ground-level JICF and an elevated JICF. The sound propagation through non-isothermal, heated ground-level JICF was investigated in Chapter 3 to establish the effect of the plume on the sound radiation. Subsequent analysis in Chapter 3 builds on the ground-level JICF results and the literature reviewed in this section to analyse the sound propagation through non-isothermal elevated JICF.

2.5 Jet shear layer sound refraction

Sound propagation through sheared flow is an area well researched by acousticians. Throughout the shear layer there are multiple types of sound propagation: refraction, scattering, diffraction, reflection and radiation. This literature review will discuss sound refraction through both velocity and temperature gradients in the shear layer and address three areas of analysis: experimental, numerical and analytical.

The effects of the local flow and temperature field on sound propagation from exhausts are critical for determining the resultant far-field acoustic radiation. The gas flow exiting an exhaust stack resembles a jet, and there have been various experimental studies into the propagation of sound through jets [14, 15, 66, 67,

110]. It has been shown by multiple authors [14, 15, 66, 67] that the velocity and temperature of the jet affects the sound directivity, as a result of local sound refraction. Figure 2.5 shows the acoustic directivity of a monopole sound source on-axis at $1.67D$ from a jet outlet that is submersed in a non-isothermal jet-flow, with varying frequencies and jet temperatures [15]. The acoustic directivity was measured at a radius of $100D$ from the jet nozzle outlet [15]. The resulting sound directivity for jets has shown that a 'cone', 'zone', or 'cusp' of silence is formed along the centreline of the jet, as a result of the sound being refracted away from the centreline. The increase in flow Mach number and temperature of the jet has been shown experimentally to enhance the depth of the 'cusp'. The subsequent refracted sound leads to the presence of strong lobes, which form off-axis. These effects are also reported by Schubert [145, 146], who revealed through ray tracing and solving the wave equation that many of the key features seen in the experimental directivity patterns can be reproduced numerically via simulation. These features include the 'cusp' of silence and the presence of the off-axis acoustic lobe. Mungur et al. [117] extended this work into a semi-numerical approach with the sound propagation through isothermal jets with varying Mach numbers (M_j = 0 to 0.9) and frequency parameters ($ka = \pi/3$ to 8π), where $k = \omega/c$ is the non-dimensional wavenumber, ω is the angular acoustic frequency, c is the speed of sound at the ambient temperature, and a is the nozzle radius. Schubert [145, 146] and Mungur et al. [117] showed that with an increase in jet Mach number and acoustic frequency, the effects of refraction are more apparent due to both the increase in velocity gradient and the reduction in the wavelength of sound. Unlike work completed experimentally [66, 67], the numerical studies [117, 145, 146] have alluded to the importance of spatial location for the directivity, by analysing the sound directivity in terms of varying distances from the source. With the development of the shear layer, the sound continues to refract, which leads to an increase in depth for the 'cone' of silence, as well an increase in the off-axis SPL.

The majority of the earlier literature on sound radiation from a jet analyses sound propagating from a source outside of the duct outlet, in the region of the jet. There have also been subsequent simulations investigating the sound radiation

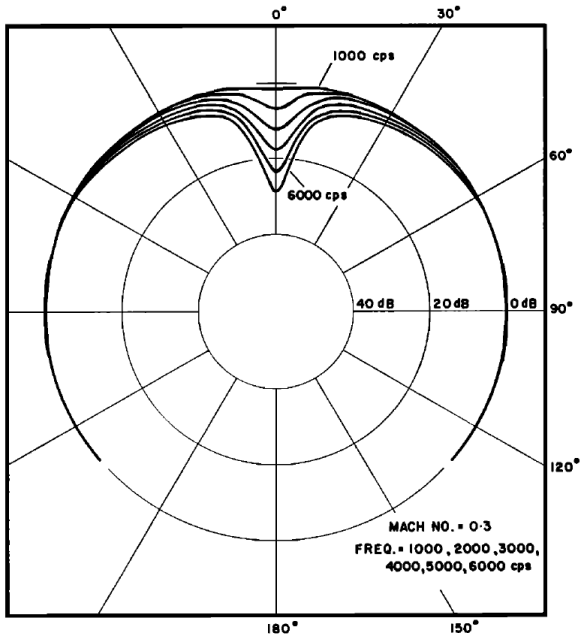

(a) Acoustic directivity with varying jet temperature [15].

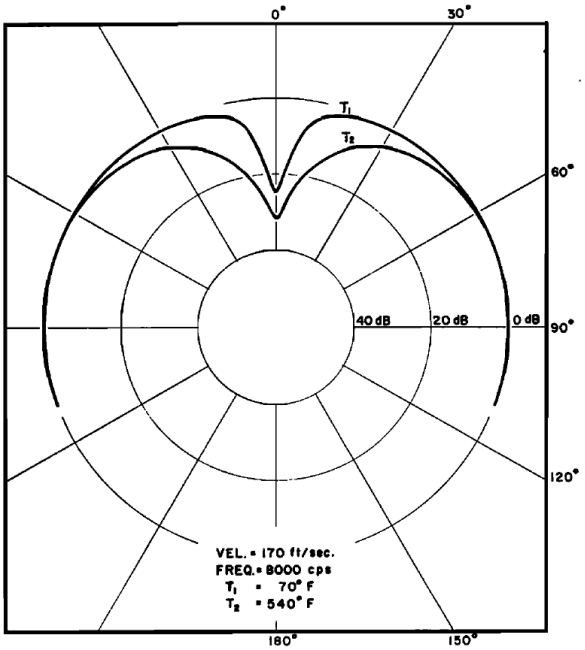

(b) Acoustic directivity with varying acoustic frequencies [15]

Figure 2.5: Acoustic directivity from Atvars et al. [15] of an on-axis monopole sound source propagating through a non-isothermal jet with (a) varying acoustic frequencies (cps is equivalent to Hz), and (b) varying jet temperatures (T_1 = 70 °C, and T_2 = 282 °C).

from off-axis sound sources [115, 158]. However, analysing sound propagation for open cycle gas turbines shows that the dominant sound source is from the turbine, and it is propagated and attenuated through the duct network before being radiated. There have been previous studies in the literature on sound propagation through straight ducts, with and without heated mean convective flows through a duct, with the outlet boundary condition being an unflanged duct [45, 73, 104, 151]. The majority of this previous work analyses the radiation efficiency of various duct modes with different flow and temperature conditions, by analysing the impedance and reflection coefficient at the duct outlet. The resulting directivity of sound radiation from the duct outlet through a heated jet is not of particular interest for a majority of the research in the earlier literature. Hence, the analysis of sound radiation into a domain from a source located in an unflanged duct is a field of research that has yet to receive significant attention.

From the literature reviewed above, the sound propagating through heated jets is complex, as is the resulting radiation pattern. The main focus of these previous studies on sound propagation through jets has been on Mach numbers that are much higher than those which are commonly seen in exhaust stacks (where $M = 0.1$). Furthermore, the jet temperatures in the prior research are much cooler than those commonly seen in exhaust stacks of OCGT which can approach 600 °C. In other words, the previous research on heated jets has been undertaken on cooler, faster flowing jets than the exhaust jets from OCGT exhausts. Furthermore, no previous research has considered the effect of cross-flow.

2.5.1 Isothermal shear layer sound refraction

Early research into the interaction of sound with a jet shear layer has shown that plane waves will refract in an infinitesimally thin shear layer [3]. Amiet's [3] pioneering work led to zero-thickness shear layer correction models for open jet wind tunnel measurements. The correction models do not take into consideration the 3-D shape, thickness and turbulence of the shear layer. However, Schlinker and Amiet [144] show good agreement with experimental models and the sheet vortex model, respectively. Candel et al. [38] have shown experimentally that sound

refraction occurs in a finite thickness shear layer. Further studies by various other researchers into the phenomenon of shear layer refraction in jets have shown that with modest Mach numbers ($M = 0.1$) large dips (in excess of 10 dB) in the sound directivity along the jet centreline were observed [14, 15, 67, 111, 133].

Early numerical studies into sound ray tracing and acoustic wave propagation through the shear layers in jets were conducted by Schubert [145, 146]. The numerical studies have found that ray tracing methods are sufficient to capture the refraction effects in the shear layer and show good agreement with the experimental results, with the exception of slight overprediction for on-axis sound level reduction [145]. This method does contain some flaws, as it does not capture the scattering and reflections. Acoustic wave propagation using the finite difference method by Schubert [146] is a method used for sound propagation through a non-isothermal shear layer in jet flow. It is one of the first studies showing that numerical finite difference schemes can be used to quantify sound refraction [146].

Mungur et al. [117] used the Navier-Stokes equation and spherical wave equations to calculate the acoustic radiation in a jet flow environment numerically. Their work showed good agreement with experimental data by Atvars et al. [14] and Maestrello et al. [111]. Casalino [40] also investigated placing sound sources in subsonic time-averaged jets and modelled acoustic propagation using the Finite Element Method (FEM) discretisation. Casalino [40] showed that using FEM discretisation for sound propagation enables sound to refract in time-averaged shear layers. The resulting sound field can be quantified numerically using subsonic time-averaged jets as the medium for sound propagation with an acoustic FEM.

Theoretical models have been developed to understand and approximate sound propagation through shear flow. One of the fundamental sheet vortex models used to quantify sound refraction when determining sound source corrections in far-field measurements is Amiet's model. Morfey and Joseph [115] have shown that off-axis sound sources will also refract in zero thickness shear layers. These zero thickness shear layer models have been extended with finite thickness shear layer models by Cargill [39], and Campos and Kobayashi [35]. These analytical models found in the literature can be used to provide approximate methods for

calculating the sound refraction due to the shear layer. The necessary fidelity of the model is driven by the accuracy of the required approximation.

2.5.2 Non-isothermal shear layer sound refraction

In this section, the phenomena of sound refraction in non-isothermal shear layers, in particular, the jet shear layer with thermal gradients is discussed. Experiments on sound propagation through heated jets with subsonic Mach numbers have been undertaken by various authors [14, 15, 67]. Original work by Atvars et al. [15] only compares jets experimentally at an ambient temperature using a heated jet at 371 °C. The research found that heating in a jet decreases the on-axis sound pressure levels (SPL) in the directivity plot [15]. In a later technical report, the author looked at three temperatures and established that the sound directivity is highly dependent on the jet temperature, with the on-axis attenuation proportional to the jet temperature. This was also supported by a later technical report by Grande [67]. Both researchers have attributed this to the refraction of sound in the thermal gradient of the shear layer.

A number of theoretical and numerical studies of sound refraction through non-isothermal shear layers have been published. Early research by Candel [37], using sheet models, found that sound refraction occurs across an infinitesimally thin temperature discontinuity. Later work by Schubert [145, 146] showed that ray tracing and acoustic wave propagation with finite difference methods can be used to predict the sound refraction in non-isothermal shear layers in a jet flow. Both numerical methods can predict the dependency between the thermal gradients in the jet flow with the on-axis reduction in sound level, due to the refraction effects in the shear layer [145, 146]. Bayliss and Maestrello [21] have extended the numerical studies of the interaction of a sound pulse with the shear layer of a heated axisymmetrical jet. This numerical study found that heating changed the stability property of the jet, as well as the thermal gradients, causing additional sound refraction effects in the far-field, which is in agreement with the literature [21, 145, 146]. Campos and Kobayashi [36] derived analytical models for sound refraction in non-isothermal boundary layers with finite thickness. Their analytical

model confirmed that a non-isothermal boundary layer causes changes in the temperature gradient and a subsequent change in the sound speed, which leads to additional refraction effects, when compared with isothermal boundary layers. However, their theoretical study neglects the anisotropic behaviour of the shear layer and the random nature of turbulence.

From the literature review thus far, there are two mechanisms for refraction: shear layer gradient and thermal gradient refraction. Since the exhaust stacks of OCGT are heated to temperatures typically between 500 °C to 600 °C, consequently the thermal effects on sound transmission are more dominant than the effects from the velocity gradient for Mach numbers in the order of $M_j = 0.1$. This is due to the dependence on the speed of sound with the square root of temperature [25], compared with the convective effects that are proportional to the Mach number. For example, the speed of sound at typical exhaust temperatures from OCGT are twice that of ambient temperatures, whereas the convective velocity due to a Mach number of $M_j = 0.1$ is only 10% greater than at ambient temperature. The primary concern for sound refraction for the research in this thesis will be the temperatures commonly seen in exhaust stacks from OCGT.

2.6 Research gaps

From the literature review, there are several evident gaps in the knowledge that are yet to be investigated and can be summarised as follows:

1. The sound radiating from exhaust stacks with similar non-dimensional acoustic and fluid dynamic parameters to real-scale OCGT have been investigated by Bies et al. [25] and Björk [27]. The former investigated the sound radiation from an exhaust stack in a homogeneous media. Björk [27], extended this by analysing the sound radiation with a jet present and hypothesised that the cross-flow would change the directivity of the sound downstream. However, tests on real OCGT and small scale experimental rigs only measured directivity downwind of the exhaust stack. Furthermore, the experimentally measured directivity arcs were at a radii of $2.5D$ for the real OCGT and $8D$ for

the reduced scale experiments. Hence, downwind and upwind measurements have not been conducted at distances greater than $8D$ for sound radiating from exhaust stacks with non-isothermal exhaust plumes.

2. Atmospheric sound propagation models typically only investigate sound propagation from a monopole sound source, how the sound propagation path is perturbed by the velocity and temperature gradients in the boundary layer, along with the impact of any turbulence. These models do not take into consideration the exhaust stack perturbing the flow and the sound radiating from the exhaust stack outlet as a complicated sound source. Furthermore, the changing effects of temperature and velocity gradients from the plume in terms of the sound radiation are not considered in the literature.

3. Previous research on sound propagation through isothermal and non-isothermal, axisymmetric jets has been completed, but the inclusion of cross-flow in acoustic measurements is a major gap in the research. Typically, the sound radiation for axisymmetric jets is quantified with sound directivity plots, with the results showing axisymmetric sound radiation. However, the cross-flow would introduce asymmetric thermal and velocity gradients, as discussed in the literature review, and consequently must result in asymmetric sound radiation. A gap in the existing research is the investigation of the effects of cross-flow on sound propagation through jets in cross-flow, and the resulting asymmetric sound radiation.

4. A design for reducing the sound radiation downstream from an exhaust stack was proposed by Björk [27], who recommended that half of the hard reflective duct should be extended on the problematic side to act like a barrier and hinder sound propagation. However, more in-depth research into the mechanisms involved with the propagation of sound downstream may suggest different design strategies for mitigating the sound radiating from the exhaust stack outlet. The change in sound observed downstream of the exhaust stack can be achieved by either changing the propagation path of sound, or altering the fluid dynamics of the plume.

This thesis continues with four remaining chapters that address the identified research gaps. Chapter 3 investigates the sound propagation through a heated ground-level JICF using simulations and forms the framework for the more complicated, elevated JICF. The research completed in Chapter 3 addresses Research Gaps 1, 2, and 3. To validate the numerical simulations, experiments on the exhaust JICF have been conducted in both an anechoic chamber and a large wind tunnel, with the outcomes reported in Chapter 4. The research in Chapter 4 also addresses Research Gaps 1, 2, and 3. The final original contribution of this research is the investigation into using 'nozzles' at the exhaust outlet to reduce the interaction of the sound with the plume, with the aim to reduce the downstream SPL. This forms the basis of Chapter 5. The research contributions from Chapter 5 aim to address Research Gap 4. The thesis is concluded in Chapter 6.

2.7 Assumptions and limitations

Before addressing the research gaps outlined in Section 2.6, assumptions and limitations of the research conducted in this thesis are explained in this section.

The analysis in this thesis concentrates on sound propagation from OCGTs. The particular gas turbine of interest is the Siemens V94.2 and its superseded model Siemens SGT5-2000E [126, 150]. The research can be extended to sound propagation from any hot exhaust stack with gentle cross-flow for different applications: large HVAC system, automotive exhaust, boilers, cement kilns, diesel generators, and other open cycle gas turbines with different power generation capacity. These other applications are not the focus of this research, but can be considered for future work. Furthermore, due to the difficulties with acoustic and flow measurements of a full-scale 160 MW OCGT exhaust stack, the research has been conducted on a reduced scale model (1:125) of the OCGT exhaust stack for both experimental and numerical analyses. The non-dimensional scaling of key fluid dynamic and acoustic parameters are presented in Appendix A.

It was identified in Section 2.3.1 that the propagation of sound is dependant on the meteorological conditions, and in context for the research conducted in

thesis this represents the cross-flow condition. The cross-flow condition for the numerical and experimental analyses in Chapters 3, 4, and 5 is assumed to be a constant velocity profile into the domain, which is not representative of real meteorological cross-flow conditions, but it makes it easier for comparison between different studies in this thesis. Additionally, it should be noted that the incoming cross-flow velocity profile resembles the velocity profile used in this thesis for flow over a flat plate, which will be explained in detail in Chapters 3 and 4.

It has been assumed that the acoustic source for sound propagation arises from the gas turbine combustion noise. Flow generated noise from elements within the exhaust stack, and flow generated noise from the jet exiting the exhaust stack will be neglected. This assumption can be made as the sound power from self-noise is relatively small. It is proportional to M^5, where M is approximately 0.1. The calculation supporting the choice of Mach number can be found in Appendix A.

As discussed in Section 1.1, the exhaust stack will be simplified to a cylindrical duct to reduce the complexity of the flow and acoustic fields. This is a common simplification for modelling the fluid mechanics for jet flow exiting exhaust stacks with gentle cross-flow, and has been discussed in Section 2.4.2.

This research focuses on the sound propagation in the intermediate acoustic far-field ($2D - 32D$), and will not investigate the near field acoustic effects (evanescent acoustics) near the exhaust stack outlet. Ideally, it would be preferable to investigate the sound propagation for domains larger than $32D$, but due to limitations in the available computational and experimental resources for this project, it is not feasible, and will be discussed in detail in Chapters 3, 4, and 5.

Chapter 3

Time invariant numerical sound propagation through jets in cross-flow

3.1 Introduction

The sound propagation from an acoustic source in inhomogeneous media with complex flow and temperature distribution is a phenomenon that exists in many systems. This chapter investigates sound propagation from a source through non-isothermal jets in cross-flow. The term non-isothermal jets in cross-flow refers to a system where there is a heated jet submersed in a cooler cross-flow, typically at ambient temperature, $T_j = 27\,°C$. The analysis involves initially using steady-state CFD simulations for calculating the flow and temperature fields associated with ground-level and elevated JICF. The flow and temperature fields are then mapped onto an acoustic FEM, which is used to simulate the sound propagation.

Using this numerical method the mechanism that alters the sound propagation from non-isothermal, low Mach number, exhaust jets in cooler cross-flow can be explained in detail. This chapter details the numerical techniques used in this thesis and the results for four different systems, as shown in Figure 3.1.[1] The first two systems shown in Figures 3.1a and 3.1b, are a ground-level JICF. The

[1]Even though the acoustic source is displayed in Figure 3.1 as a point source at the duct outlet, it represents a simplification of an acoustic source emanating from the duct outlet.

ground-level JICF was chosen by the author as a simplification of a real exhaust stack to analyse the effect of the heated plume on the sound propagation path. The ground-level JICF has been studied extensively and therefore provides a well-researched system for developing and validating the numerical method. The next two systems analysed are shown in Figures 3.1c and 3.1d, which are given with the stack protruding into the domain. The sound propagation through a non-isothermal elevated exhaust JICF is a more accurate representation of real exhaust stacks and builds upon the work used in the ground-level JICF. Furthermore, in this chapter the numerical cases investigated in Figure 3.1, are for a reduced scale (1 : 125) model of a 160 MW open cycle gas turbine exhaust stack. The justification for the non-dimensional scaling of the acoustic and fluid dynamics parameters are presented in Appendix A. It should also be noted that for the numerical investigation undertaken for the elevated exhaust JICF in Figures 3.1c and 3.1d, the boundary conditions and non-dimensional scaling of important parameters reflects the experimental work described in Chapter 4.

This study specifically investigates the interaction of a high temperature exhaust jet with a cooler cross-flow, and how it alters the propagation of sound. As previously mentioned, steady-state computational fluid dynamics (CFD) and numerical acoustic simulations, using the finite element method (FEM), are used for the analyses. The layout of the chapter is as follows. Section 3.2.1 describes the mathematical models that are utilised for the fluid flow simulations, which involve using CFD and acoustic propagation and the discretised acoustic wave equation with FEM. In Section 3.2.2, the domain and mesh used for the simulation are discussed. Section 3.3 describes the results from the CFD and acoustic FEA simulations. The main conclusions of this investigation are summarised in Section 3.5. Detailed validation of the method can be found in Howard and Cazzolato [77] and further work to support the numerical methodology can be found in Appendix C.

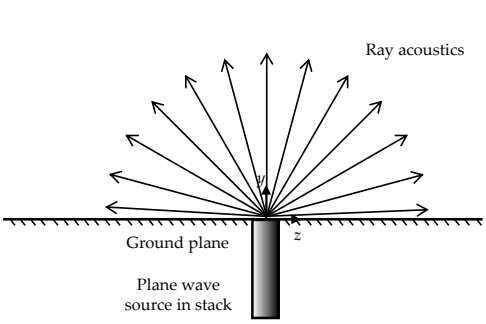

(a) Stationary field with flush-mounted duct

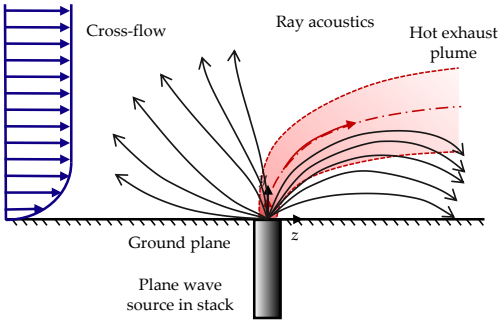

(b) Ground-level, non-isothermal JICF

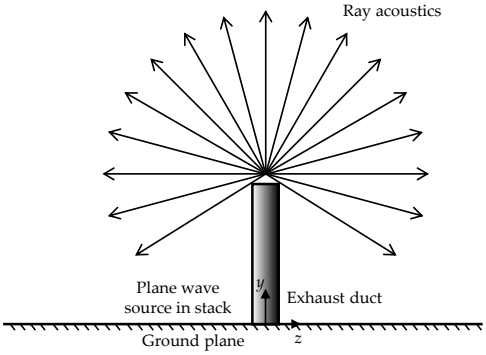

(c) Stationary field with elevated duct

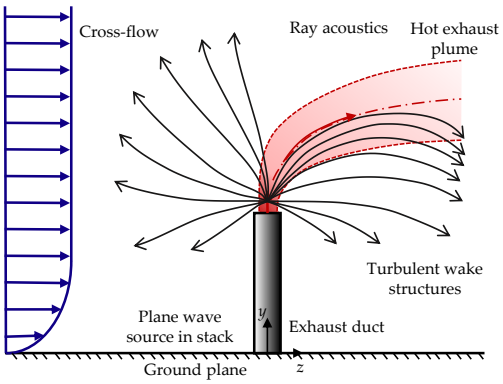

(d) Elevated, non-isothermal JICF

Figure 3.1: Numerical schematic for sound propagation through four different systems; (a) sound propagation through the flush-mounted duct in a stationary field, (b) sound propagation through a ground-level, non-isothermal, heated JICF, (c) sound propagation through a stationary field with an elevated duct, and (d) sound propagation through an elevated, non-isothermal, heated JICF.

3.2 Mathematical models, domain, and boundary conditions

The numerical research in this study is a hybrid computational aeroacoustic scheme that uses both steady-state CFD and the discretised acoustic wave equation, as shown in Figure 3.2. Initially, a CFD of the JICF was created using ANSYS FLUENT to generate the steady-state nodal fluid velocity and nodal temperature. The steady-state nodal temperature and fluid velocity are mapped using MATLAB onto the acoustic FEM. The acoustic FEM model in ANSYS Mechanical was used to predict the acoustic pressures. It should be noted that acoustic modelling with FEM using ANSYS Mechanical has been validated extensively in the reference, *Acoustic Analyses using MATLAB and ANSYS*, by Howard and Cazzolato [77]. This section of the thesis will discuss these mathematical models and the governing equations, followed by a discussion of the domain geometry, boundary conditions, and mesh.

3.2.1 Mathematical models and governing equations

The numerical acoustic simulations are conducted with a 3-dimensional (3-D) linearised acoustic wave equation method that is discretised and solved with FEM. The model was implemented and solved using ANSYS Mechanical [8, 9]. This section discusses the key governing equations that were used in the acoustic simulations, as well as a brief outline in discretisation of the model to be solved with FEM. A more detailed formulation of the governing equations that were used in the acoustic simulations is shown in Appendix B.

The formulation of the acoustic wave equation for the numerical work in this chapter is based on a number of assumptions. The fluid is compressible with relatively no large changes in the bulk pressure. The propagating medium is 'frozen' or stationary in time with small perturbations in acoustic pressure taken into consideration. It is also assumed that the fluid is irrotational. Additionally, it is assumed that there are no body forces and the gas is ideal, adiabatic and reversible. The flow is also assumed to be inviscid. Furthermore, the following derivation in

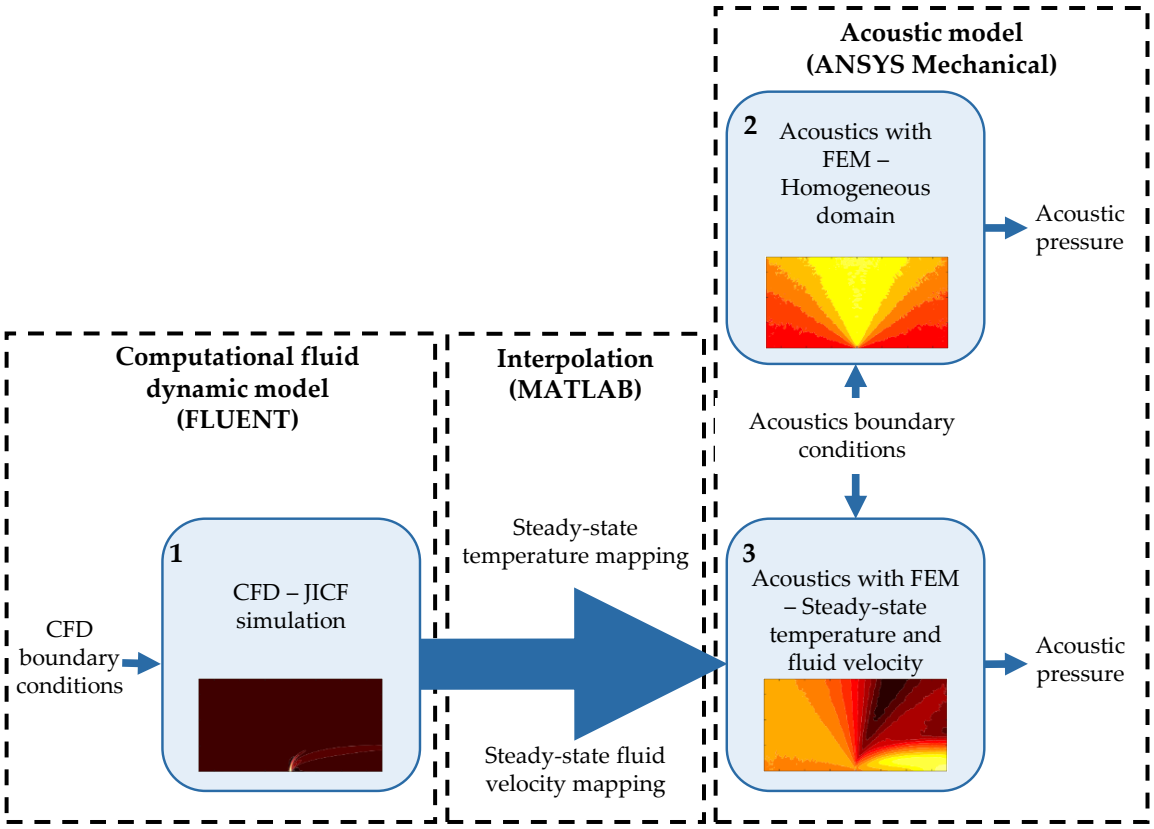

Figure 3.2: Simulation process for conducting the numerical simulations

this chapter is a first order approximation of the linearised acoustic wave equation with the second and higher order terms neglected.

Two different acoustic wave equations were used in this research for different propagation conditions: a stationary field with or without temperature variations spatially, and a non-homogeneous domain which accounts for the local temperature and local mean fluid velocity.

The following is a 3-D formulation in Cartesian coordinates, with four governing equations used for acoustic modelling; and they are the flow continuity equation, Navier-Stokes equations for fluid momentum, conservation of entropy, and equation of state, respectively given by:

$$D_t(\rho) + \nabla \cdot (\rho \vec{v}) = \rho Q, \tag{3.1}$$

$$\rho D_t(v) + \nabla p = \frac{\vec{F}}{\rho}, \tag{3.2}$$

$$D_t(s) = 0, \tag{3.3}$$

$$p = IP(\rho, s), \tag{3.4}$$

where ρ is the density, t is time, $\vec{v}$ is the velocity vector, Q is the mass source, p is the pressure, $\vec{F}$ is the body force, $D_t = \frac{\partial}{\partial t} + \vec{v} \cdot \nabla$ is the material derivative (also known as the substantial derivative or as Pierce [131] describes, the time derivative following the ambient flow[2]) and IP is the relation function. In Equations (3.1) and (3.2), ρ, p, and $\vec{v}$ are spatially dependant on position $\vec{x} = (x, y, z)$. Furthermore, the assumption of a 'frozen' or stationary propagating medium leads to the assumption that ρ is time invariant such that the time-averaged statistics are used. As discussed previously it is assumed that there are no body forces acting on the fluid ($\vec{F} = 0$), which implies that buoyancy is not considered.

Equations (3.1) to (3.4) can be further simplified, based on the assumptions outlined above and linearised to form the following states:

$$\rho = \rho_0(x, y, z) + \epsilon\rho'(x, y, z, t), \tag{3.5a}$$

$$p = p_0(x, y, z) + \epsilon p'(x, y, z, t), \tag{3.5b}$$

$$s = s_0(x, y, z) + \epsilon s'(x, y, z, t), \tag{3.5c}$$

$$\vec{v} = \vec{v_0}(x, y, z) + \epsilon\vec{v}'(x, y, z, t), \tag{3.5d}$$

$$Q \approx \epsilon Q(x, y, z, t), \tag{3.5e}$$

[2] An important note is that in different literature the material derivative is expressed in different forms with ANSYS Mechanical using $\frac{D_0}{dt}$ [8, 9], Bergmann [24] using $\frac{D}{Dt}$, Ostashev et al. [129] and Ross and Chivers [138] using $\frac{d}{dt}$, and Pierce [131] using D_t, which is the notation used in this thesis.

where the parameters with the subscript 0 represents the local steady-state or time averaged quantity, ϵ is the small perturbation in the quantity, and the $'$ notation represents the unsteady perturbation in that particular quantity. The word local refers to the time-averaged value at position $\vec{x}$. It should be noted that for the rest of the derivation all unsteady terms with fluctuating components will be replaced with subscript a, to represent the unsteady acoustic perturbation. The linearisation of Equations (3.1), (3.2), and (3.4) are derived in Appendix B, with the resulting stationary acoustic wave equation used by ANSYS Mechanical [8, 9] being an identical formulation to the work by Bergmann [24] and Ross and Chivers [138]. The time dependant stationary acoustic wave equation is

$$\nabla \cdot \left(\frac{1}{\rho_0(\vec{x})} \nabla p_a(\vec{x}, t) \right) - \frac{1}{\rho_0(\vec{x}) c_0^2(\vec{x})} \frac{\partial^2 p_a(\vec{x}, t)}{\partial t^2} = -\frac{\partial Q(\vec{x})}{\partial t}, \tag{3.6}$$

where $\rho_0(\vec{x})$ is the mean fluid density in $\mathrm{kg/m^3}$, $c_0(\vec{x})$ is the speed of sound in $\mathrm{m/s}$, $p_a(\vec{x})$ is the acoustic pressure in Pa, and $Q(\vec{x})$ is the mass source in $\mathrm{kg/m^3}$.

In order to solve for the harmonic normalised wave number, the following harmonically varying pressure formulation can be used:

$$p_a(\vec{x}, t) = \mathrm{Re}[p_a(\vec{x}) e^{j\omega t}], \tag{3.7}$$

where Re refers to the real component of the expression, $\omega = 2\pi f$ is the angular frequency of interest in $\mathrm{rad/s}$, and f is the linear frequency of interest in Hz.

When solving the acoustic wave equation in a stationary field, the Helmholtz equation may be used, and is given by:

$$\omega^2 \underbrace{\frac{p_a(\vec{x})}{\rho_0(\vec{x}) c_0^2(\vec{x})}}_{M_p} + \underbrace{\nabla \cdot \left(\frac{1}{\rho_0(\vec{x})} \nabla p_a(\vec{x}) \right)}_{K_p} = -j\omega \underbrace{Q(\vec{x})}_{f_p}, \tag{3.8}$$

where M_p is the term for the 'acoustic fluid mass' for acoustic pressure, K_p is the term for the 'acoustic stiffness' for acoustic pressure, and f_p is the 'acoustic fluid load' for the acoustic pressure. The homogeneous Helmholtz equation is suitable for modelling sound propagation through an ideal gas medium with uniform $\rho_0(\vec{x})$ and $c_0(\vec{x})$. It is also possible to account for temperature variations using the ideal

gas law, which can be used to relate the speed of sound, $c_0(\vec{x})$, and the density, $\rho_0(\vec{x})$, with temperature, T. The following equations were used to calculate $c_0(\vec{x})$ and $\rho_0(\vec{x})$ as a function of temperature, respectively:

$$c_0(\vec{x}) = \sqrt{\gamma R_{\text{gas}} T(\vec{x})}, \tag{3.9a}$$

$$\rho_0(\vec{x}) = \frac{P_{\text{state}}(\vec{x})}{R_{\text{gas}} T(\vec{x})}, \tag{3.9b}$$

where γ is the ratio for specific heats, R_{gas} is the universal gas constant $\mathrm{J/mol\,K}$, T is the absolute temperature in K at position $\vec{x}$, and P_{state} is the absolute pressure of the gas measured in fluid at a location $\vec{x}$. Therefore, the governing equation for numerical acoustic simulations with temperature variations in the domain are given by Equation (3.8), using Equations (3.9a) and (3.9b) in lieu of $\rho_0(\vec{x})$ and $c_0(\vec{x})$, respectively.

The non-stationary formulation for the acoustic wave equation used by ANSYS Mechanical [8, 9] was almost identical to the formulation by Pierce [131], with a slight difference in the final time variant equation that will be discussed later. Pierce [131] presents two different formulations for the linearised acoustic wave equation with mean flow using a scalar potential flow, which is dependent on the definition of the acoustic particle velocity, $\vec{v_a}(\vec{x})$, and acoustic pressure, $p_a(\vec{x})$, with

$$\vec{v_a}(\vec{x}) = -\frac{A}{\rho_0(\vec{x})} \nabla \phi(\vec{x}, t), \tag{3.10}$$

$$p_a(\vec{x}, t) = A D_t \phi(\vec{x}, t), \tag{3.11}$$

where A is a constant one can choose and it is related to $\rho_0(\vec{x})$ and $c_0(\vec{x})$. In the derivation by Pierce [131], the author proposes two values of A; $A = -1$ or $A = -\rho_0(\vec{x})$, where it leads to two different formulation of the linearised acoustic wave equation with mean flow using a scalar potential flow. Both formulations will be discussed later in this section. For the derivation used by ANSYS Mechanical, $A = -1$, and the acoustic velocity, $\vec{v_a}(\vec{x})$, and acoustic pressure, $p_a(\vec{x})$, are

$$\vec{v_a}(\vec{x}) = \frac{1}{\rho_0(\vec{x})} \nabla \phi(\vec{x}, t), \tag{3.12}$$

$$p_a(\vec{x}, t) = -D_t\phi(\vec{x}, t), \tag{3.13}$$

where $\phi(\vec{x}, t)$ is the velocity potential, and

$$D_t = \frac{\partial}{\partial t} + \vec{v_0}(\vec{x}) \cdot \nabla, \tag{3.14}$$

is the material derivative (or the time derivative following the ambient flow [131]), and $\vec{v_0}$ is the mean flow velocity. A detailed derivation for the time dependent non-stationary acoustic wave equation with mean flow is provided in Appendix B, with the equation given by:

$$\nabla \cdot \left(\frac{1}{\rho_0(\vec{x})} \nabla\phi(\vec{x}, t) \right) - D_t \left(\frac{1}{\rho_0(\vec{x}) c_0^2(\vec{x})} D_t\phi(\vec{x}, t) \right) = \frac{q(\vec{x})}{\rho_0(\vec{x})}, \tag{3.15}$$

where $q(\vec{x})$ is

$$q(\vec{x}) = Q(\vec{x}) - \frac{1}{c_0^2(\vec{x})} D_t(\rho_0(\vec{x})\phi(\vec{x}, t)). \tag{3.16}$$

Equation (3.15) is the time dependent acoustic wave equation taking into consideration the unsteady non-stationary mean fluid flow used by ANSYS Mechanical. It is important to note that Equation (3.15) is almost identical to the formulation derived by Pierce [131] shown as

$$\nabla \cdot \left(\frac{1}{\rho_0(\vec{x})} \nabla\phi(\vec{x}, t) \right) - \rho_0(\vec{x}) D_t \left(\frac{1}{\rho_0^2(\vec{x}) c_0^2(\vec{x})} D_t\phi(\vec{x}, t) \right) = 0. \tag{3.17}$$

Equations (3.15) and (3.17) are identical as a first order approximation, with the second terms in both equations differing slightly. The equation by Pierce [131] does not include a mass source, q, but can be easily included in the formulation. The second term on the left hand side in Equations (3.15) and (3.17) differ by ρ_0, which introduces a first order change of $O(L^{-1}) + O(T^{-1})$, where L is the length scale and T is the time scale. An important consideration and limitation for the acoustic wave equation in Equations (3.6), (3.15), and (3.17), it assumes that there is no vorticity in the pressure perturbation.

For the work presented in this section thus far, $A = -1$ for Equations (3.10) and (3.11), and with this chosen value for A, Equation (3.15) by ANSYS Mechanical and

Equation (3.17) by Pierce [131] are derived. Another formulation by Pierce [131] assumes $A = -\rho_0(\vec{x})$, and this is Pierce's preferred assumption of the constant, A. This leads to Pierce's [131] preferred form

$$\frac{1}{\rho_0(\vec{x})}\nabla\cdot(\rho_0(\vec{x})\nabla\phi(\vec{x},t)) - D_t\left(\frac{1}{c_0^2(\vec{x})}D_t\phi(\vec{x},t)\right) = 0. \tag{3.18}$$

Pierce [131] has stated that even though he presents two possible outcomes for the linearised acoustic wave equation with mean flow and using a scalar velocity potential shown in the article and expressed in Equations (3.17) and (3.18), there are other possible formulations based on the choice of the constant A. Pierce [131] has also noted that Equations (3.17) and (3.18) are equivalent to the first order approximation. However, the preferred form of Equation (3.18) is slightly more attractive, as the formulation is "exact" under the condition that the ambient medium has constant entropy per unit mass and when the flow is irrotational and steady.

For a harmonic solution of Equation (3.15) a harmonically varying velocity potential is introduced

$$\phi(\vec{x},t) = \mathrm{Re}[\phi(\vec{x}e^{j\omega t})], \tag{3.19}$$

whereby substituting Equation (3.19) into (3.15) gives the following harmonically formulated acoustic wave equation

$$\begin{aligned}\frac{\omega^2}{\rho_0(\vec{x})c_0^2(\vec{x})}\phi(\vec{x}) - j\omega\nabla\cdot\frac{\vec{v_0}(\vec{x})}{\rho_0(\vec{x})c_0^2(\vec{x})}\phi(\vec{x}) - j\omega\frac{\vec{v_0}(\vec{x})}{\rho_0(\vec{x})c_0(\vec{x})^2}\cdot\nabla\phi(\vec{x})\\ -\frac{\vec{v_0}(\vec{x})}{\rho_0(\vec{x})c_0^2(\vec{x})}\vec{v_0}(\vec{x})\nabla\phi(\vec{x}) + \nabla\cdot\frac{1}{\rho_0(\vec{x})}\nabla\phi(\vec{x}) = \frac{q(\vec{x})}{\rho_0(\vec{x})}.\end{aligned} \tag{3.20}$$

With further manipulation of Equation (3.20), the potential flow formulation of the acoustic wave equation with mean flow can be represented as

$$\begin{aligned}\omega^2\underbrace{\frac{\phi(\vec{x})}{\rho_0(\vec{x})c_0^2(\vec{x})}}_{M_\phi} - j\omega\underbrace{\left(\nabla\cdot\frac{\vec{v_0}(\vec{x})}{\rho_0(\vec{x})c_0^2(\vec{x})}\phi(\vec{x}) + \frac{\vec{v_0}(\vec{x})}{\rho_0(\vec{x})c_0^2(\vec{x})}\cdot\nabla\phi(\vec{x})\right)}_{C_\phi}\\ \underbrace{-\frac{\vec{v_0}(\vec{x})}{\rho_0(\vec{x})c_0^2(\vec{x})}\vec{v_0}(\vec{x})\nabla\phi(\vec{x}) + \nabla\cdot\frac{1}{\rho_0(\vec{x})}\nabla\phi(\vec{x})}_{K_\phi} = \underbrace{\frac{q(\vec{x})}{\rho_0(\vec{x})}}_{f_\phi},\end{aligned} \tag{3.21}$$

where M_ϕ is the term for the 'acoustic fluid mass' for the acoustic velocity potential, C_ϕ is the term for the 'acoustic fluid damping' for the acoustic velocity potential, K_ϕ is the term for the 'acoustic fluid stiffness' for the acoustic velocity potential, and f_ϕ is the term for the 'acoustic fluid load' for the acoustic velocity potential.

Equations (3.8) and (3.20) can be discretised using the Galerkin method for representation using FEM [20]. Detailed formulation for the discretisation of Equations (3.8) and (3.21) are provided in ANSYS [8] and Appendix B. In modelling the sound, the following uncoupled, non-symmetric formulation is used for both the Helmholtz equation without and with mean fluid flow, respectively:

$$(-\omega^2[M_p] + j\omega[C_p] + [K_p])\{p\} = f_p, \tag{3.22a}$$

$$(-\omega^2[M_\phi] + j\omega[C_\phi] + [K_\phi])\{\phi\} = f_\phi, \tag{3.22b}$$

where $[M_p]$ is the acoustic fluid mass matrix for acoustic pressures, $[C_p]$ is the acoustic damping matrix for acoustic pressures, $[K_p]$ is the acoustic stiffness matrix for acoustic pressures, f_p is the acoustic fluid load vector for acoustic pressures, $[M_\phi]$ is the acoustic fluid mass matrix for ϕ, $[C_\phi]$ is the acoustic damping matrix for ϕ, $[K_\phi]$ is the acoustic stiffness matrix for ϕ, f_ϕ is the acoustic fluid load vector for ϕ. It should be noted that for the case of inviscid flow, the $[C_p]$ is non-existent for the formulation that uses Helmholtz equation without mean fluid flow. Equations (3.22a) and (3.22b) are very similar in their implementation in ANSYS Mechanical. Equation (3.22a) is formulated using the single degree of freedom for pressure p and Equation (3.22b) is formulated using the single degree of freedom for the velocity potential ϕ. The acoustic pressure data from Equation (3.20) are derived using Equation (3.13). The matrix Equations (3.22a) and (3.22b), are solved directly with the 'Sparse' matrix solver in ANSYS as the matrices in Equations (3.22a) and (3.22b) have poor numerical conditioning. The matrix formulation for the solver treats the full domain as a matrix which is solved using the 'Shared Memory Parallel' mode. The 'Shared Memory Parallel' mode requires less Random Accessible Memory (RAM) to solve for Equations (3.22a) and (3.22b) using FEM with ANSYS Mechanical, compared with a model with the domain

partitioned. Hence, using FEM with ANSYS Mechanical and the 'Shared Memory Parallel' mode provides the ability to solve models that have a large number of nodes, a requirement for the accurate propagation of sound through non-isotropic media.

Modelling the steady-state fluid dynamics related to the non-isothermal ground-level and elevated JICF, was undertaken using ANSYS FLUENT. The CFD simulation utilised the compressible Reynolds Averaged Navier-Stokes (RANS) model Shear Stress Transport (SST) $\kappa - \omega$ [114]. This model was chosen on the recommendation off various researchers [64, 65, 74, 140], as it is the most appropriate RANS model for simulating the mixing characteristics in the plume downwind. Rusch et al. [140] has also shown that accurate predictions of the temperatures downwind of a JICF can be made when using RANS SST $\kappa - \omega$ formulation. The medium for the analysis was dry air. To model the temperatures in the plume adequately, the ideal gas law for density and Sutherland's law for dynamic viscosity were implemented to account for the temperature variations [156]. Furthermore, to capture the dynamics of the plume accurately, the buoyancy of the gas was also modelled. The CFD model uses a second order upwind spatial discretisation scheme for all its variables and the 'Coupled' scheme for the pressure-velocity coupling.

For modelling the steady-state fluid dynamics related to the non-isothermal ground-level and elevated JICF using ANSYS FLUENT, most of the modelling parameters are identical, except for the turbulence model. The two equation realisable $\kappa - \epsilon$ model was chosen to resolve the turbulence for the non-isothermal elevated JICF [149]. This model is computationally less expensive than other more complicated RANS models and transient scales when resolving turbulence models. However, there are limitations to the turbulence model: it assumes the eddy viscosity is isotropic; the turbulence can be modelled with two equations; the eddies in the models are not resolved with the average turbulence quantities being calculated in the shear layer; lack of prediction for flow separation at the jet inlet edge; and inaccurate prediction of the jet spreading and decay [149]. The boundary layer from the no-slip walls in the model were resolved using scalable wall functions.

For the CFD analysis in this thesis, only the critical steady-state features of the flow will need to be reproduced and the compressible steady RANS model is sufficient.

The simulations conducted in this thesis were solved using the University of Adelaide's Phoenix High Performance Computing cluster, but at two periods of time. For the work conducted with the ground-level JICF, the simulations were solved using a single node on the cluster, consisting of two Xeon E5-2698v3 Processors with 16 CPU (central processing units), each at a clock rate of 2.5 GHz. This configuration on the node leads to the availability of 32 CPUs per node, with each node possessing 128 GB RAM. However, the elevated JICF simulations were conducted at a later period of time and a single node of the cluster, which consisted of two Intel Xeon Gold 6148 Processors with 20 CPU each, and an individual clock rate of 2.40 GHz. This configuration on the node leads to the availability of 40 CPUs per node, with each node possessing 384 GB RAM. With the increase in RAM larger numerical models with a higher number of nodes can be used, and will be outlined in Section 3.2.2.2.

3.2.2 Domain and boundary conditions

This section of the thesis will discuss the domain and boundary conditions for the numerical simulations. The discussion will be separated into two parts: the domain and boundary conditions for ground-level JICF, and the domain and boundary conditions for the elevated JICF. Each section will begin explaining the geometry of the computational domain. After which, justification for the boundary conditions, numerical parameters, and the mesh are presented.

3.2.2.1 Domain and boundary conditions for ground-level jets in cross-flow

The geometry of the domain used in the case studies presented in this chapter is shown in Figure 3.3 and was consistent between the CFD and acoustic simulations. The domain had dimensions $48D \times 48D \times 80D$ ($L_x \times L_y \times L_z$), where $D = 0.0476$ m is the duct diameter. The dimension for D was chosen to be identical to the reduced scale (1:125) experimental exhaust duct diameter described in Chapter 4, with further calculations justifying the reduction in geometric scale detailed in

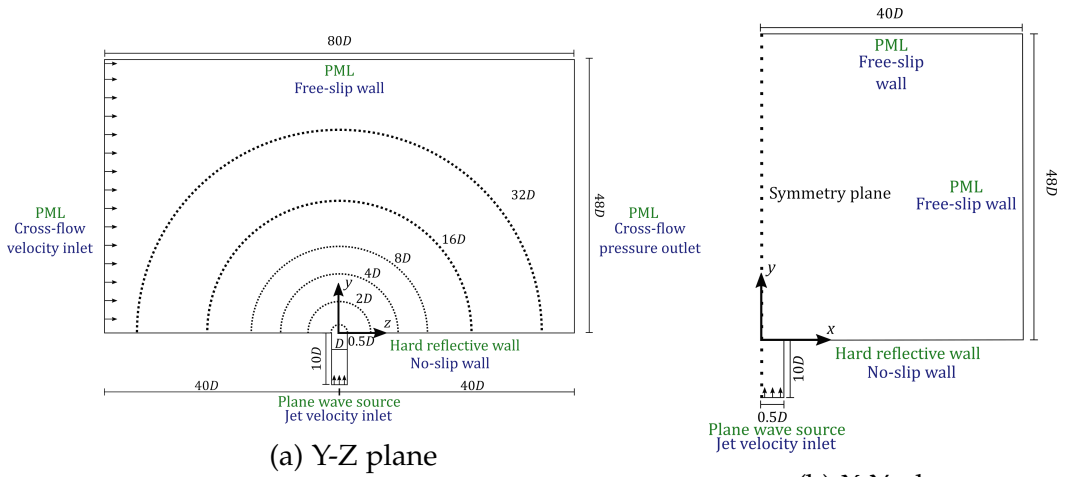

(a) Y-Z plane

(b) X-Y plane

Figure 3.3: Schematic and dimensions for the ground-level JICF simulations, where blue text represents the fluid dynamics boundary conditions and green text show the acoustic boundary conditions. PML refers to a Perfectly Matched Layer.

Appendix A. This domain is plane-symmetric about the centreline of the duct, with the domain extending $40D$ upwind and downwind of the duct centreline, in the direction of the cross-flow free stream. The length of the duct in these simulations is $10D$, and was chosen to allow the flow in the duct to develop and to account for the cross-flow effects on the duct outlet, as was shown to occur by Muppidi and Mahesh [119]. Furthermore, by including the duct itself in the computational acoustic simulations, the effects of diffraction at the edge of the duct outlet and the impedance change at the duct outlet are included.

The CFD mesh was generated using ANSYS and consisted of a fully structured mesh. The elements used are hexahedra 'brick' (first order, linear) elements with nodes residing on the vertices. The mesh contains approximately 9.1 million elements and can be seen in Figure 3.4. A mesh independence study was conducted in order to investigate mesh convergence, with the results presented in Section 3.3.1 showing that the current domain with 9.1 million elements is sufficient for solution convergence.

The non-dimensional scaling for the acoustic and fluid dynamics parameters used for the numerical simulations in this chapter are derived in Appendix A. The

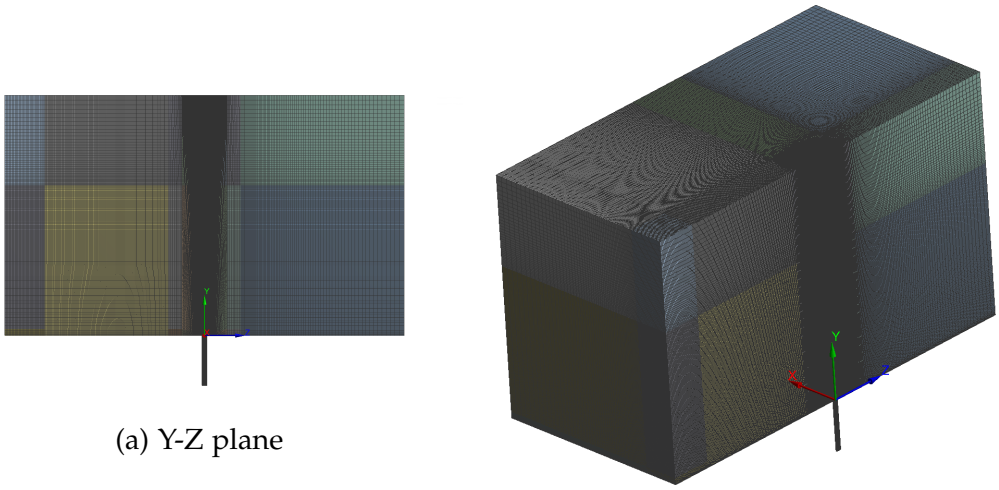

(a) Y-Z plane

(b) Isometric view

Figure 3.4: Mesh for CFD simulations

key fluid dynamics parameters for the numerical simulations will be summarised in this section. The jet velocity at the duct inlet, u_j, was Mach $M = 0.1$, and with a developed pipe flow velocity profile. The temperature at the duct inlet, T_j, and was either 27 °C (ambient), 250 °C or 500 °C. The cross-flow velocity, u_{cf}, and the quantitative values at the boundary were chosen to have varying cross-flow free-stream velocity. The velocities for u_{cf} were dependent on the effective velocity ratio, R, otherwise known as the square root of the jet to cross-flow momentum flux ratio, defined as

$$R = \sqrt{\frac{\rho_j u_j^2}{\rho_{cf} u_{cf}^2}} \quad , \tag{3.23}$$

where ρ_j is the jet density, and ρ_{cf} is the free stream cross-flow density [152]. In this particular study, R was chosen as 5 and 7.5, as they closely resemble the conditions in real exhaust stacks. The cross-flow temperature was set as ambient at 27 °C, with a uniform temperature profile. This was done to avoid the complexity of modelling real meteorological conditions, and to mimic the experimental conditions in Chapter 4. A 'non-slip' wall boundary condition was used along the internal duct wall and the 'ground' (wall adjacent to the duct outlet), which assists in the formation of the boundary layer. Along the internal duct wall, the mesh was

designed to resolve the wall boundary layer. However, Rusch et al. [140] suggested that the wall boundary layer along the 'ground' should not be resolved in the steady-state simulations for ideal convergence. It is known that resolving the boundary layer along the 'ground' level can lead to global instabilities being triggered, and therefore leads to 'poor' convergence statistics. The outlet of the domain was a pressure outlet boundary condition. A 'free-slip' boundary condition was used along the centreline symmetry-plane and the remaining walls in the CFD simulations.

The acoustic simulations used a harmonic velocity source, with a normal surface velocity of $u_a = 0.01\,\mathrm{m\,s^{-1}}$, at the base of the duct. The Helmholtz number for the acoustic source was defined as

$$ka = \frac{\pi f D}{c_j} \quad , \tag{3.24}$$

where f is the acoustic frequency of interest, and c_j is the speed of sound in the jet. With the calculations in A the problematic acoustic frequencies recorded in literature is approximately in the 16 Hz to 31.5 Hz one-third octave bands [32, 33, 70–72, 101, 109, 124, 125], and corresponds to values of ka ranging from 0.3 to 0.8. The ka range from 0.3 to 0.8 typically causes a hemispherical sound radiation pattern in the absence of the jet or cross-flow. A Helmholtz number of $ka = 0.8$ was the highest that could be simulated with the computational resources available. Ideally, a higher ka, closer to unity, would have been better, at which the wavelength of sound would be small enough to interact with the shear layer, but this was not possible due to the limitation of the available computational resources. A hard reflective, wall boundary condition was used along the internal duct wall, the 'ground' wall (the surface adjacent to the duct outlet), and the symmetry-plane. The remaining exterior of the domain contained Perfectly Matched Layer (PML) elements for simulating an infinite acoustic free-field. The PML was at least four elements thick, and was larger than one-quarter of the acoustic wavelength (λ) of interest for the simulation, which in this case is a layer that is $4D$ thick [77].

The results in the acoustic FEM are calculated using acoustic pressure and can be represented using sound pressure level (SPL) and directivity index (DI). The

SPL can be calculated from the root mean square of the acoustic pressure, p_{rms},

$$\text{SPL} = 20\log_{10}\left(\frac{p_{\text{rms}}(\vec{x})}{20\times 10^{-6}}\right). \tag{3.25}$$

Another way to represent the results is with the directivity index (DI), and is given by [25]:

$$\text{DI}(\theta) = \frac{I(\theta)}{I_{av}}, \tag{3.26}$$

where θ is the angular position in spherical coordinates, I is the acoustic intensity, and I_{av} is the average acoustic intensity over a hemispherical surface in the acoustic domain. The acoustic intensity for a plane wave, I, can be calculated using the following formulation from Bies et al. [25]

$$I(\vec{x}) = \frac{p^2_{\text{rms}}(\vec{x})}{\rho_0(\vec{x})c_0(\vec{x})}. \tag{3.27}$$

Bies et al. [25] discuss that Equation (3.27) can be used to to calculate the intensity in the far-field from a source, where the radius of curvature is ten times the acoustic wavelength. It should be noted that Equation (3.27) may break down in the near-field. A more detailed representation of the coordinate system for DI is shown in Figure 3.5. It should be noted that this definition for DI is used for the majority of the thesis, with a slight exception for the DI presented in Section 3.3.2.1 and explained in detail later.

In Equation (3.26) the average acoustic intensity, I_{av}, can be calculated using Equation (3.27) to form the spatial average

$$I_{av} = \frac{1}{N}\sum_{i=1}^{N}\frac{p^2_{\text{rms,i}}(\vec{x})}{\rho_{0,i}(\vec{x})c_{0,i}(\vec{x})}, \tag{3.28}$$

where N is the total number of nodes on a spherical surface, and i is the nodal number on the spherical surface. For calculating I_{av} at each radius from the stack outlet a, spatial average is taken with the expression in Equation (3.28), over a quarter-sphere, shown in the acoustic mesh in Figure 3.6. It should also be noted that for each surface over the quarter-sphere, the nodes are spaced evenly apart and the acoustic intensity at each node has equal weighting in calculating I_{av}.

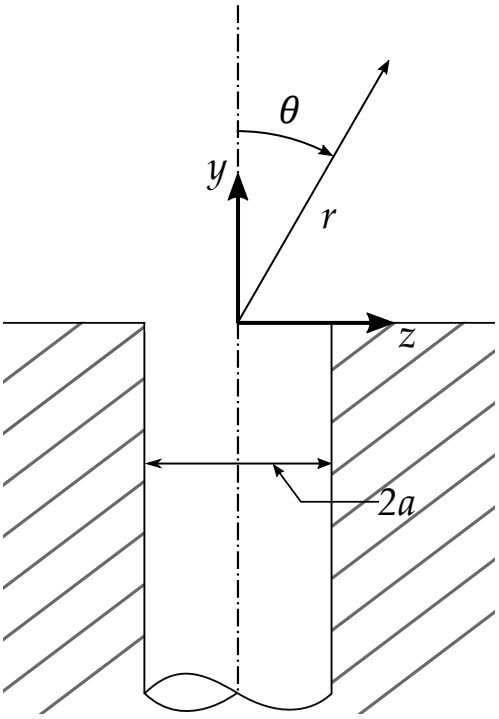

Figure 3.5: Schematic for the ground level JICF and the directivity definition from the duct outlet. The quantity a is the duct radius, θ is the directivity angle from the duct centreline, and r is the radius for the directivity arc from the centre of the duct outlet.

The mesh used for the acoustic simulations can be seen in Figure 3.6. The elements used in the acoustic simulation comprised a hybrid mesh with both structured hexahedra 'FLUID220' and unstructured tetrahedra 'FLUID221'. Both element types have mid-side nodes and are second-order (quadratic) elements. The nodal density of the acoustic simulation was derived using a rule of thumb of 11 nodes per λ at the highest frequency of interest [77], which resulted in a

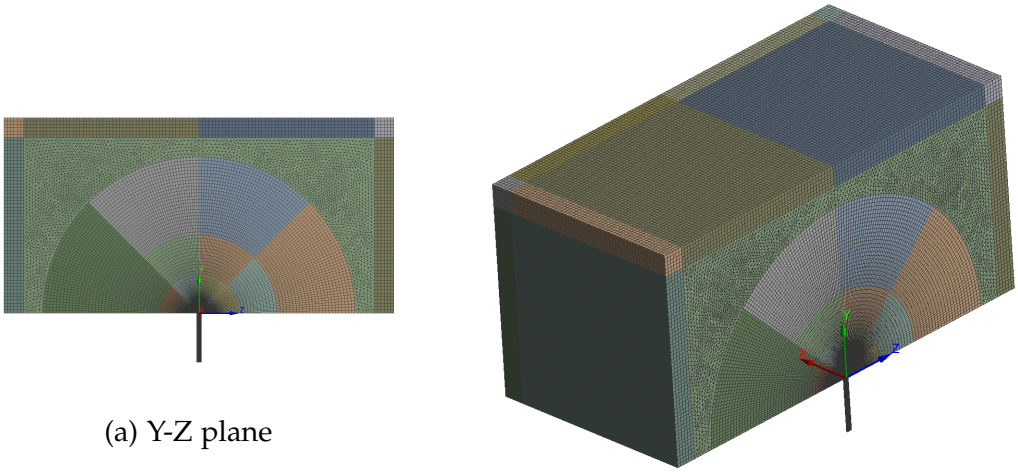

(a) Y-Z plane

(b) Isometric view

Figure 3.6: Mesh for the FEM acoustic simulations

node count of approximately 6 million nodes.[3] A mesh independence study was conducted and the results are presented in Section 3.3.2.1.

3.2.2.2 Domain and boundary conditions for elevated jets in cross-flow

The CFD and acoustic modelling of a real OCGT is a complex task, so consequently a simplified model of an elevated JICF has been employed for this study. A schematic of the computational domain with the dimensions and corresponding boundary conditions can be seen in Figure 3.7. The domain is similar to the ground-level JICF but is extended vertically to account for the stack, with dimensions $40D \times 58D \times 80D$ ($L_x \times L_y \times L_z$). This domain is plane-symmetric about the centreline of the duct, with the domain extending $40D$ upwind and downwind of the duct

[3]It should be noted at the time of completing the study for sound propagation through a ground-level JICF, the University of Adelaide's Phoenix High Performance Computing cluster consisted of the following computational resource: two Xeon E5-2698v3 Processors with 16 CPU (central processing units), each with a clock rate of 2.5 GHz and 128 GB RAM. The total number of CPU for each node was 32 CPU. Since then, the available computational resources for the University of Adelaide's Phoenix High Performance Computing cluster has improved and for a single node, the following computational resources are available: two Intel Xeon Gold 6148 Processor with 20 CPU, each with a clock rate of 2.4 GHz for the processor and 384 GB RAM for each node. With the increase in RAM from 128 GB to 384 GB the number of nodes for the acoustic FE model could increase, and this is discussed in the following section, which was completed at a later date.

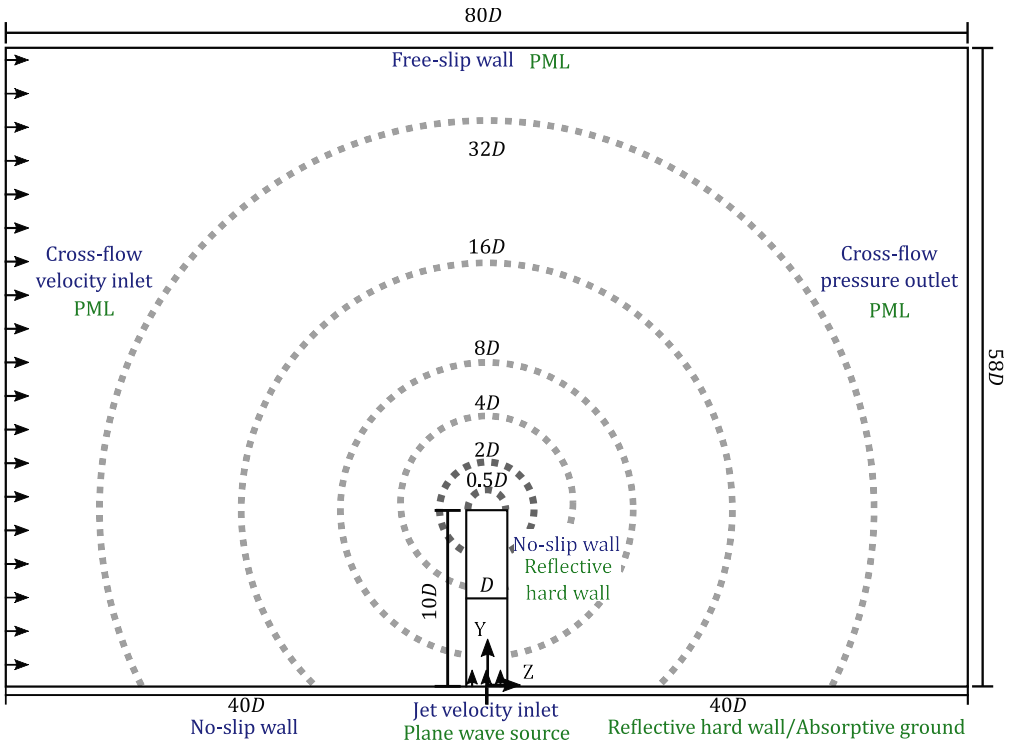

Figure 3.7: Schematic and dimensions for the elevated level JICF simulations, where blue text represents the fluid dynamics boundary conditions and green text show the acoustic boundary conditions. PML refers to a Perfectly Matched Layer.

centre, in the direction of the cross-flow free stream. The length of the duct in these simulations is $10D$. Only half of the domain is modelled in this particular simulation with a symmetry condition along the y-z plane. Not shown in Figure 3.7 is that the domain also spans $40D$ in the x-axis perpendicular to the symmetry plane of the jet (into the page). This truncation in the domain is possible due to previous literature indicating that the steady-state flow field is plane symmetric and preliminary acoustic simulations showing that the sound field is also plane symmetric [90].

The correct use of boundary conditions is essential in resolving both the CFD and computational acoustic solution accurately. The boundary conditions for the simulation can be seen in Figure 3.7. The following assumptions have been made for the inlet boundary conditions for the 3D CFD simulation. The inlet conditions

for the model are the turbulent, heated jet inlet at the base of the duct and the cross-flow on the windward side of the duct. For the jet inlet, a developed duct velocity profile with a bulk Reynolds Number, Re_j of 38900 was chosen. The fully developed duct velocity profile was achieved by first conducting simulations with a duct $40D$ long duct and the developed velocity profile at the duct outlet is interpolated onto the elevated JICF jet inlet. The R chosen for this study is 5. A constant mean velocity profile was applied to the inlet boundary. The resulting Mach number, M_j, for this simulation is approximately 0.1 and is typical of OCGT exhaust stacks. The jet inlet temperature was 773 K (500 °C), and the temperature at the cross-flow inlet was set to 300 K (27 °C). Similar to the reasoning described in Section 3.2.2.1, the cross-flow inlet temperature was set to a constant uniform profile to mimic the experimental condition in Chapter 4 and to reduce the complexity of modelling real meteorological conditions. The duct walls and the ground wall adjacent to the circular stack are no-slip walls.

In the far-field of the CFD model, two different outlet conditions are used. The outlet at the top of the domain in Figure 3.7 is a free-slip wall boundary condition. This was chosen to allow the shear stress along the wall to be set to zero. At the domain outlet, parallel to the cross-flow velocity inlet shown on the left in Figure 3.7, a pressure outlet condition is used.

In simulating the propagation of sound, two cases are considered here: with and without temperature and convective effects from an elevated JICF. The sound source was a planar harmonic source with a particle velocity amplitude of $0.5\,\mathrm{m\,s^{-1}}$. It is assumed in this study that the majority of the sound is generated from the sound source (turbine), and other flow generated noise mechanisms can be neglected. This can be justified by the fact, that the quadrupole terms from the shear layer noise are dependent on M_j^5, which is almost negligible for the Mach number in this study. A Helmholtz number, ka = 0.4 to 0.8, where k is the acoustic wavenumber based on the speed of sound, and a is the inner radius of the duct, was chosen as it is sufficiently high such that it is comparable to the simulated plume's shear layer and is well below the cut-on frequency of the duct. As described in Section 3.2.2.1, there was a limitation in the highest Helmholtz number of ka = 0.8 that could

be simulated with the computational resources available. A higher ka, closer to unity, would have been better to investigate smaller wavelength of sound and the complex interact with the shear layer, but this was not possible due to the limitation of the available resources.

It is important to point out that the definition for calculating DI for the elevated JICF and the numerical acoustic results presented in Section 3.3.3 is defined as:

$$\mathrm{DI}(\theta) = \frac{p^2_{\mathrm{rms}}(\theta)}{p^2_{av}}, \tag{3.29}$$

where θ is the angular position in spherical coordinates and defined by Figure 3.8, $p_a(\theta)$ is the acoustic pressure at θ, and p_{av} is the average acoustic pressure over the directivity arc in the radiating domain, which can be calculated using the spatial average over a each spherical surface to form

$$p^2_{av} = \frac{1}{N}\sum_{i=1}^{N} p^2_{\mathrm{rms,i}}(\vec{x}), \tag{3.30}$$

where N is the total number of nodes on the spherical surface, and i is the nodal number on the spherical surface. Similar to I_{av} in Equation (3.28), p_{av} is a spatial average over a spherical surface, shown Figures 3.7 and 3.9, where the radii is calculated from the centre of the duct outlet. It should also be noted that for each spherical surface in the domain, the acoustic results are interpolated in such a way that nodes are spaced evenly apart and the acoustic intensity at each node has equal weighting in calculating p_{av}. This definition for DI is different from the typical definition, shown with Equations (3.26) and (3.38) [25], and has been used because of the data available. This may be justified as the results are in the acoustic far-field of the source [25], and has been used by Björk [27] to quantify DI for acoustic radiation from exhaust stacks.

For the computational sound propagation simulation, along the boundaries of the domain, three different acoustic boundary conditions are used for two different cases. The far-field condition is uniform for all boundary conditions. PML elements are used for the far-field absorption of sound to simulate the free-field radiation condition. The number of PML elements used is dependent on the duct width, D,

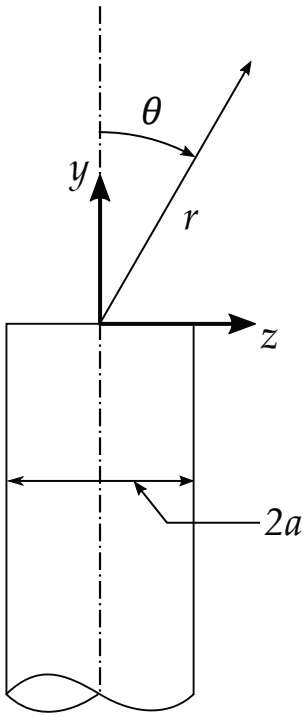

Figure 3.8: Schematic for the elevated stack and the directivity definition from the duct outlet. The quantity, a is the duct radius, θ is the directivity angle from the duct centreline, and r is the radius for the directivity arc from the centre of the duct outlet.

and the wavelength of the sound. Howard and Cazzolato [77] have recommended that the PML zone be at least one-quarter of the wavelength of the sound. Along the ground surface at the base of the exhaust stack, two different boundary conditions are used: a hard, reflective surface and an anechoic base. The different boundary conditions are used to model two different scenarios near OCGT exhaust stacks: hard reflective surroundings with hard structures and cement surroundings, and an absorptive surface with grass and other vegetation. From the geometry of the numerical model in Figure 3.7 it was not possible to place PML elements along the ground surface due to the vicinity of the exhaust stack, so an alternative boundary condition was used – a Robin radiation boundary condition [77]. The acoustic

boundary condition can be described mathematically with:

$$\frac{\partial p_a(\vec{x})}{n(\vec{x})} + \frac{j\omega\rho_0(\vec{x})p_a(\vec{x})}{\rho_0(\vec{x})c_0(\vec{x})} = 0, \tag{3.31}$$

where n is the normal vector. It should be noted that the Robin radiation boundary condition is not perfectly anechoic, with the boundary condition formulated for perfect absorption of incident sound normal to the surface. Even though the boundary condition is not perfectly anechoic, it is adequate for sound absorption along the ground surface, it significantly simplifies the sound radiation pattern observed from the exhaust stack, and will be discussed later in Section 3.3.3. For the figure captions in Section 3.3.3, the ground-level boundary condition implemented in the results are expressed with, α_s, the acoustic absorption coefficient for a surface, where $\alpha_s = 0$ represents a hard, reflective surface, and $\alpha_s = 1$ represents an anechoic ground surface using the Robin radiation boundary condition in Equation (3.31).

For the CFD simulation, the fluid dynamics were resolved using a mesh (shown in Figure 3.9a) with structured hexahedra elements. Refinements were made in regions necessary for adequately resolving the critical flow features. This mesh has $15,250,000$ elements and $15,480,000$ nodes. The non-dimensional wall distance, y^+, for this simulation is more than 13, which is acceptable for resolving the boundary layer with the scalable wall function. In the geometric far-field, where the flow characteristics are of less importance, the mesh has been generated using elements with a high aspect ratio. The element type used in ANSYS FLUENT only specifies nodes at the vertex of the element and these are known as 'brick' elements.

Mesh generation for modelling sound propagation with FEM has different requirements compared with the CFD simulation. The FEM mesh is shown in Figure 3.9b. In propagating acoustic waves, it is desirable to use a uniform mesh with minimal spatial changes in the element size, as different element sizes can cause numerical artefacts to form due to the minor impedance changes [77]. According to Howard and Cazzolato [77], at least six quadratic elements per wavelength are required for resolving the acoustic pressure wave accurately. Therefore, for the mesh shown in Figure 3.9, the ka achievable for this simulation is 0.6. The resulting acoustic element count is approximately $10,000,000$ and the node count

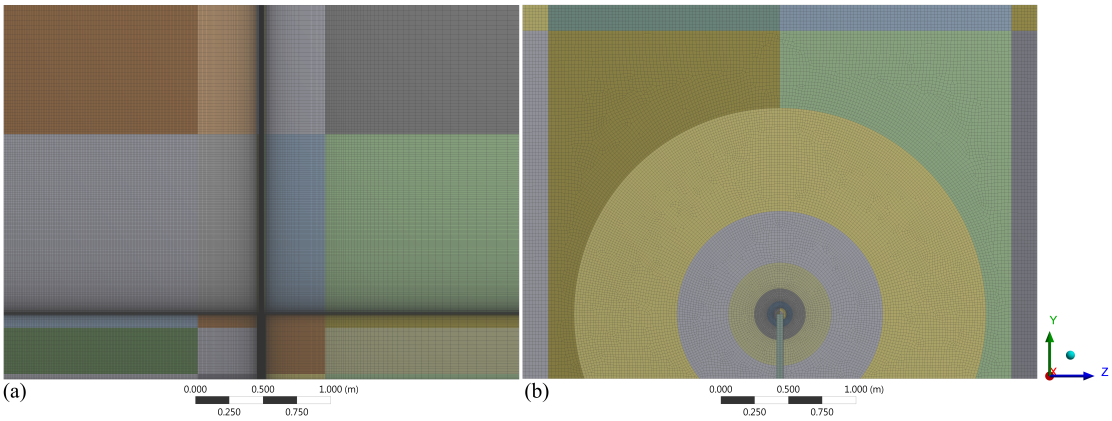

Figure 3.9: Non-isothermal elevated JICF, (a) mesh for CFD modelling and, (b) mesh for modelling sound propagation with FEM (b)

is approximately 15,000,000.[4] The mesh employs well-defined arcs for ease of data post processing sound directivity at the radii of interest, and structured hexahedra elements in the PML for the most effective attenuation of sound in the simulation [77]. Note that for the version of ANSYS Mechanical (18.2) used in this study the PML elements must be mapped onto the Cartesian coordinate system.

3.3 Results and discussion

This section discusses the results and key findings from the numerical study. First, the steady-state RANS CFD simulation results are discussed for both ground-level and elevated JICF. Following this, a discussion on the following numerical sound radiation cases for ground-level JICF is presented:

- sound radiation in the absence of a heated jet or cross-flow or otherwise known as an isothermal stationary field in the remainder of text,

[4] Again, the increase in node count for the acoustic FE simulation from the ground level JICF case, with 6,000,000 nodes, to the elevated JICF, with 15,000,000, is due to the improvements in computational resource for the University of Adelaide's Phoenix High Performance Computing cluster.

- sound radiation with the presence of the steady-state temperature associated with non-isothermal JICF,
- sound radiation with the presence of flow associated with a jet and cross-flow at ambient temperature,
- sound radiation with the combined temperature and fluid flow associated with a heated jet and cooler cross-flow, and
- a trajectory analysis varying R associated with a heated jet and cooler cross-flow for acoustic propagation.

After which the numerical sound radiation results for the elevated JICF are presented for the cases with sound radiation in the absence of the steady-state temperature and fluid flow, and sound radiation with the combined steady-state temperature and fluid flow associated with non-isothermal elevated JICF. Furthermore, for the elevated JICF, two different boundary conditions for the ground surface are considered: a hard, reflective surface ($\alpha_s = 0$) and an anechoic surface ($\alpha_s = 1$).

3.3.1 Non-isothermal jet in cross-flow fluid dynamics

The results for the CFD simulation of a non-isothermal (heated) ground-level JICF and elevated JICF will be discussed in this section. The time-averaged numerical results that are presented in this section include the following: the temperature, the velocity, and the plume centreline trajectory.

3.3.1.1 Ground-level jet in cross-flow fluid dynamics

The results for the CFD simulation of a non-isothermal ground-level JICF will be discussed in this section. The JICF fluid dynamics were explored for six different cases: three jet temperatures T_j (27 °C, 250 °C, and 500 °C) and two effective velocity ratios R (5 and 7.5). The results presented in this study are from steady-state simulations, and it will be shown that many of the important flow features seen in the literature are successfully reproduced. Figure 3.10a shows a contour plot

of the velocity magnitude along the Y-Z plane, and that the jet structure is dominant in the near-field close to the jet outlet adjacent to the ground wall. As the plume propagates, the cross-flow causes the jet to deflect and the plume is bent over. Figure 3.10a also shows that with the development of the plume, a velocity gradient formed by the shear layer develops as it propagates downwind. Similarly, Figure 3.10b shows a contour plot of the temperature along the Y-Z plane. There are similar features between the temperature distribution and the velocity magnitude contour plot in Figure 3.10a. Figure 3.10b, shows that the elevated temperature follows the deflected plume itself. The highest temperature is observed near the duct outlet, with the temperature of the plume reducing as it propagates. The decrease in plume temperature is a result of the spatial growth of the plume and the entrainment of the cooler cross-flow [92].

Combining the velocity and temperature results presented in Figures 3.10a and 3.10b, respectively, the effective speed of sound can be calculated and is shown in Figure 3.10c. The effective speed of sound is calculated using

$$c_{\text{eff}}(\vec{x}) = \sqrt{\gamma R_{\text{air}} T(\vec{x})} + v_0(\vec{x}), \tag{3.32}$$

where $\vec{x}$ is the node in Cartesian coordinates, γ is the ratio of specific heats, R_{air} is the specific gas constant for air, $T(\vec{x})$ is the temperature at the node from CFD, and $v_0(\vec{x})$ is the velocity magnitude at the node. The results in Figure 3.10c shows similar qualitative trends as Figures 3.10a and 3.10b, with the highest change in the speed of sound near the outlet of the duct, a plume that is deflected by the cross-winds, and spatial growth in the plume, which leads to a reduction in the maximum effective speed of sound observed downwind. It is important to consider that $v_0(\vec{x})$ is the velocity magnitude and does not take into consideration the flow direction with respect to the direction of the acoustic wave. Figure 3.10c is an estimation of the speed of sound that may alter the propagation path of sound, based on Equation (3.21).

Figures 3.11a to 3.11f present the fluid velocity at six locations; in the near-field of the jet, to the plume downwind in the far-field, and show the span-wise development of the plume. Figures 3.11a and 3.11b indicates that the deflected jet initiates downwind as a 'crescent' structure, which is the critical feature of the

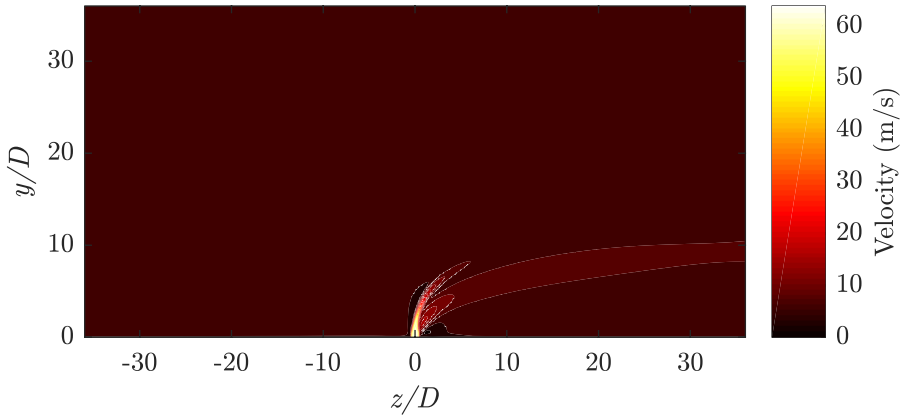

(a) Velocity magnitude

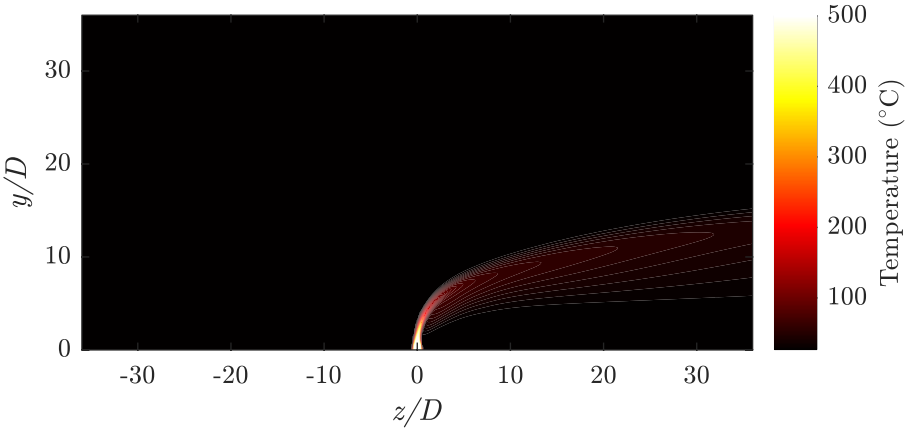

(b) Temperature

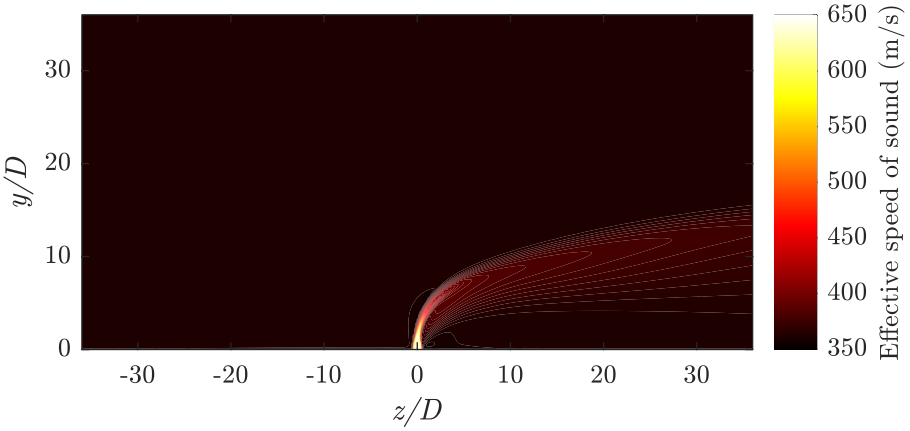

(c) Effective speed of sound

Figure 3.10: The CFD generated contour plots of (a) flow velocity, (b) temperature, and (c) the effective speed of sound along the Y-Z plane (of symmetry), where T_j = 500 °C and R = 5. The cross-flow is from left to right.

plume in the near-field. The plume's 'crescent' structure then transitions further to a counter-rotating vortex, which is shown in Figures 3.11c, 3.11d and 3.11e. The results in Figure 3.11f shows that the plume in the far-field has dissipated significantly, with the contour plot only showing the cross-flow velocity. For the cases studied in this research, it can be seen that the counter-rotating vortex structure is the dominant flow feature downwind between $2 < z/D < 8$, as seen in previous studies [4, 7, 60, 64, 65, 92–94, 119, 121, 140, 147, 148]. Furthermore, the results in Table 3.1 shows the maximum difference in flow velocity along an X-Y plane at various distances downwind from the exhaust stack, which can be calculated using

$$\Delta u_0 = u_{\max} - u_{cf}, \tag{3.33}$$

where Δu_0 is the difference in the flow velocity, $u_{\max}$ is the maximum velocity above the cross-flow velocity in the plume along the X-Y plane at a position downwind, and u_{cf} is the cross-flow velocity. The difference in the flow velocity and the effects on propagation can be quantified using the ratio of the speed of sound as

$$c_{\text{conv}} = \frac{c_{\max} + u_{\max}}{c_{\max}} = \frac{\sqrt{\gamma R_{\text{air}} T_{\max}} + u_{\max}}{\sqrt{\gamma R_{\text{air}} T_{\max}}}, \tag{3.34}$$

where $c_{\max}$ is the maximum speed of sound along the X-Y plane and dependant on temperature, and $T_{\max}$ is the maximum temperature along the X-Y plane. It should be noted that for quantifying the velocity gradient various definitions can be used as there are three velocity components and the speed of sound is determined by the temperature. Equations (3.33) and (3.34) use speed to define the velocity gradient and does not take into consideration the direction for flow. From the results of the numerical simulations conducted here, it can be observed that the increase in cross-flow ratio, R, also causes the formation of the counter-rotating vortex to occur earlier in the plume as it propagates downwind, with the lowest jet to cross-flow momentum flux ratio, $R = 5$, in the study leading to a 'crescent' plume being sustained furthest downwind in all the cases studied. This observation in the spatial formation of the counter-rotating vortex in the plume is consistent with the observations made by Kamotani and Greber [92].

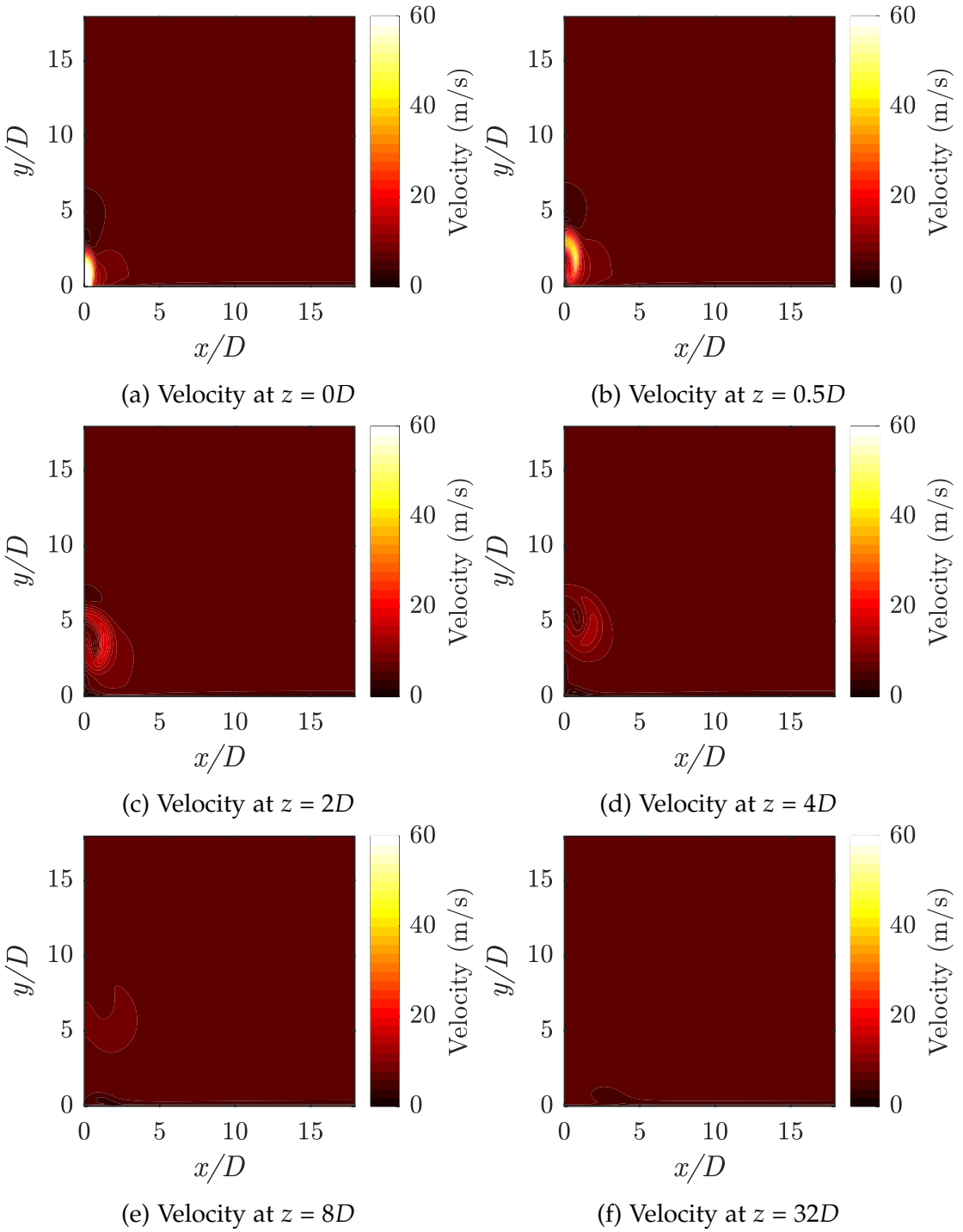

(a) Velocity at $z = 0D$

(b) Velocity at $z = 0.5D$

(c) Velocity at $z = 2D$

(d) Velocity at $z = 4D$

(e) Velocity at $z = 8D$

(f) Velocity at $z = 32D$

Figure 3.11: Velocity contour plot along the X-Y plane at six distances downwind from the centre of the duct ($z/D = [0, 0.5, 2, 4, 8, 32]$), where $T_j = 500\,°\text{C}$ and $R = 5$.

Table 3.1: The difference in mean velocity (Δu_0) along the X-Y plane at six distances downstream (z/D) from the centre of the duct outlet. The cross-flow velocity is $u_{cf} = 6.8\,\mathrm{m/s}$.

Downstream (z/d)	0	0.5	1	2	4	8	16	32
Δu_0 ($\mathrm{m\,s^{-1}}$)	57.2	39.2	22.6	12.6	6.5	3.0	1.20	0.9
c_{conv}	1.10	1.07	1.05	1.03	1.02	1.00	1.00	1.00

Figures 3.12b to 3.12f shows the contour plots of the nodal temperature along the X-Y planes at six distances downwind ($z/D = [0, 0.5, 2, 4, 8, 32]$) from the jet centreline. As previously observed by Kamotani and Greber [92], the centre of the 'crescent' and the counter-rotating vortex contain the hottest gases in the plume. This observation for the temperature of the plume was consistent with all the simulations presented in this study. Figure 3.12, also shows that as the plume propagates downwind there is a reduction in the temperature of the plume and a growth in the extent of the plume. The reduction in the plume temperature can quantified by

$$\Delta T_0 = T_{\max} - T_{cf}, \tag{3.35}$$

where ΔT_0 is the change in temperature along a X-Y plane downwind from the duct centreline, $T_{\max}$ is the maximum temperature along a X-Y plane downwind from the duct centreline, and $T_{cf} = 27\,^{\circ}\mathrm{C}$ is the cross-flow temperature along a X-Y plane downwind from the duct centreline. The results for Equation (3.35) at six distances downwind are expressed in Table 3.2. The change in temperature can also be expressed as a difference in the speed of sound using Equation (3.9a) and

$$\Delta c_0 = c_{\max} - c_{cf}, \tag{3.36}$$

where Δc_0 is the change in speed of sound along the X-Y plane downwind from the duct centreline, $c_{\max}$ is the maximum speed of sound along a X-Y plane downwind from the duct centreline, and c_{cf} is the cross-flow speed of sound. An alternative way to analyse the change in the speed of sound downstream of the duct outlet is to investigate the ratio of the speed of sound for max temperature at each X-Y plane and the minimum temperature at each X-Y plane to give the following relationship:

Table 3.2: The difference in mean temperature (ΔT_0), difference in mean speed of sound due to temperature variations (Δc_0), and ratio for the speed of sound (c_{temp}) along the X-Y plane at six distances downstream (z/D) from the centre of the duct outlet. The cross-flow temperature is $T_{cf} = 27\,°\text{C}$.

Downstream (z/D)	0	0.5	1	2	4	8	16	32
ΔT_0 (°C)	474.4	356.8	216.0	142.9	107.8	72.5	41.5	25.8
Δc_0 ($\text{m}\,\text{s}^{-1}$)	216.6	171.3	111.2	76.8	59.2	40.8	23.9	15.0
c_{temp}	1.61	1.48	1.31	1.22	1.17	1.11	1.07	1.04

$$c_{\text{temp}} = \frac{c_{\text{max}}}{c_{cf}}. \tag{3.37}$$

From Figure 3.12f and Table 3.2 it is evident that the plume at $z/D = 32$ the plume has dissipated drastically, with the temperature of the plume converging to the cross-flow temperature. Hence, from this observation the effects of temperature on the plume in the far-field ($z/D > 32$) are likely to be small. Overall, Figure 3.12 and Table 3.2 highlights the thermal gradients and the change in the speed of sound in the plume downwind of the exhaust stack.

A mesh grid independence study has been completed for flow associated with a non-isothermal JICF, where $R = 5$ and $T_j = 500\,°\text{C}$. Figure 3.13 shows the centreline trajectory as a function of the total grid mesh node count. The centreline trajectory for the plume was calculated using ANSYS Fluent by tracking a particle that originates from the duct inlet. For a converged solution the tracked particle travelled along the plane of symmetry in the domain, which implies the plume is plane-symmetric, which is to be expected for a steady-state simulation for a JICF. The results in Figure 3.13 show that there is minimal mesh grid dependence with the maximum variation in jet trajectory varying by 0.25% between the 9.1 million and 36.1 million node. The slight dependency with the mesh density is noted, but it is concluded that for the purpose of reproducing the necessary flow features, a mesh of 9.1 million nodes is appropriate.

The fluid dynamic structures generated using CFD simulations are very similar in all cases investigated, however the plume centreline trajectory changes with varying R. Figure 3.14 shows the centreline trajectory of the plume with different

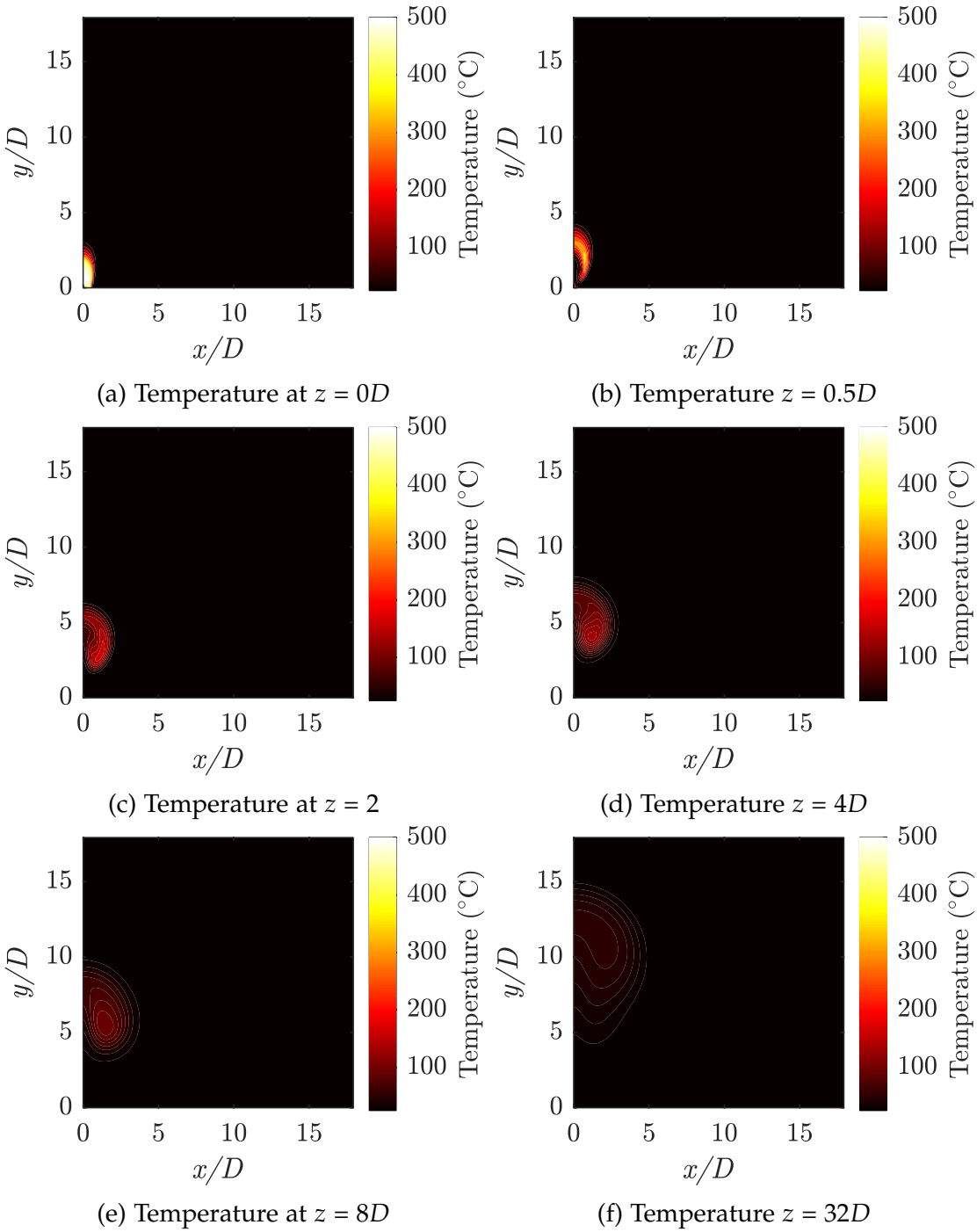

(a) Temperature at $z = 0D$

(b) Temperature $z = 0.5D$

(c) Temperature at $z = 2$

(d) Temperature $z = 4D$

(e) Temperature at $z = 8D$

(f) Temperature $z = 32D$

Figure 3.12: Temperature contour plots along the X-Y plane at six distances downwind from the centre of the duct ($z/D = [0, 0.5, 2, 4, 8, 32]$), where $T_j = 500\,°C$ and $R = 5$.

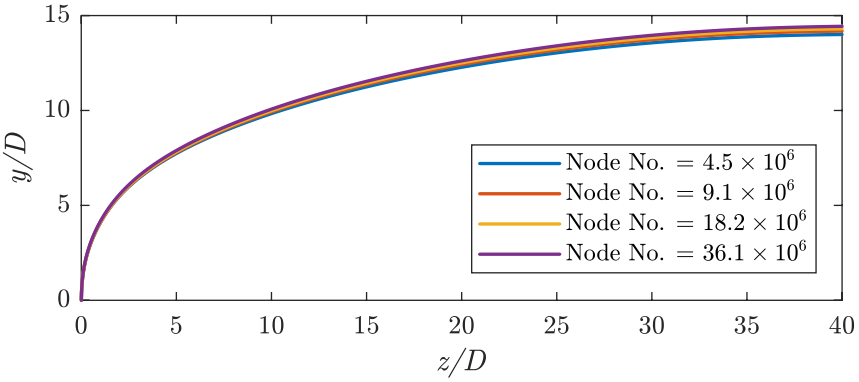

Figure 3.13: The mesh independence study with the centreline trajectory for a non-isothermal JICF where R = 5 and T_j = 500 °C.

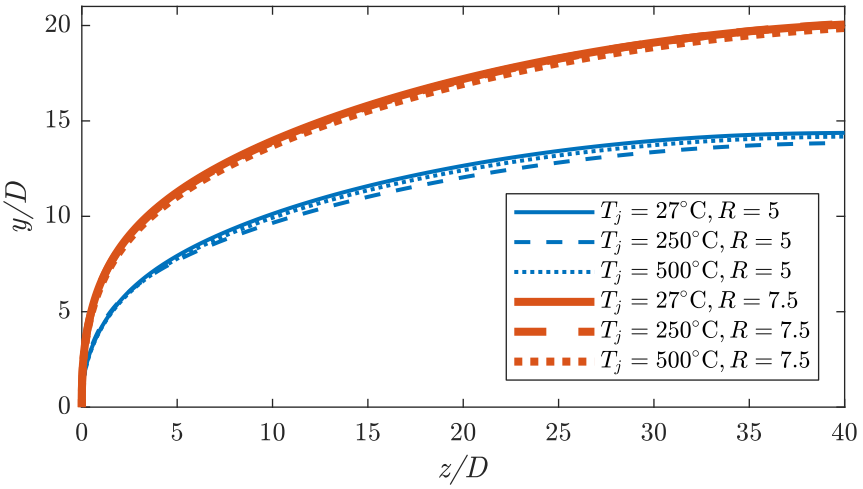

Figure 3.14: The plume centreline trajectory for JICF with R = 5 and 7.5, and T_j (27 °C, 250 °C, and 500 °C)

R. An increase in R causes an increase in the height of the plume above the ground-level. The change in plume trajectory is also due to the reduction in cross-flow momentum with the rise in R. Also shown in Figure 3.14 are centreline trajectories for the same R, but with varying jet temperatures, and these show that the centreline trajectories are effectively independent of the jet temperature.

Since the fluid dynamic results were computed using steady-state simulations and the turbulence was modelled using RANS, the transient turbulent scales were not modelled, as indicated in Section 3.2.1. Consequently, the transient features

of a JICF, such as vortical structures in the wake, were not modelled. Not taking into consideration the vortical structures in the wake, leads to a reduction in the entrainment of the cross-flow into the plume [119–121, 140]. The decrease in cross-flow entrainment may lead to a slight over-estimation of the plume temperature.

3.3.1.2 Elevated jet in cross-flow fluid dynamics

The results for the steady-state CFD simulation of a non-isothermal elevated JICF are discussed in this section. The fluid dynamic results for steady-state velocity and temperature presented in this section are for an elevated JICF with parameters: $R = 5$, $T_j = 500\,°C$, and $M_j = 0.1$. The steady-state temperature and velocity results from CFD are displayed as contour plots and show the important features necessary for sound propagation through the inhomogeneous media.

It can be seen in Figure 3.15a that the fluid issued from the duct outlet initiates as a jet in the geometric near-field. As the jet fluid propagates downwind, the jet begins to deflect due to the presence of the cross-flow momentum. The deflected plume transitions from a conical jet to a counter rotating vortex. The counter rotating vortex further develops and forms as the dominant vortical structure in the plume downwind. During the formation of the counter rotating vortex, fluid is entrained from both the cooler cross-flow and the wake behind the stack in the simulation. A shear layer is also formed on the leeward side of the stack, which is due to the stack acting as a bluff body.

Figure 3.15b shows the temperature contour plot for the elevated JICF in the Y-Z plane. It can be seen that at the geometric near-field close to the duct outlet the temperature profile resembles a jet, with the hottest region residing in the jet potential core. As the jet propagates downwind, the plume is deflected by the cooler momentum of the cross-flow stream and enhanced mixing occurs. This mixing causes the lower temperatures seen in the thermal gradients as the plume develops downwind. As the plume propagates downwind and develops into a counter rotating vortex, enhanced mixing with the cooler cross-flow occurs, which reduces the temperature in the plume. The hottest region in the plume is the centre of the counter rotating vortex. This development of the plume has led to the

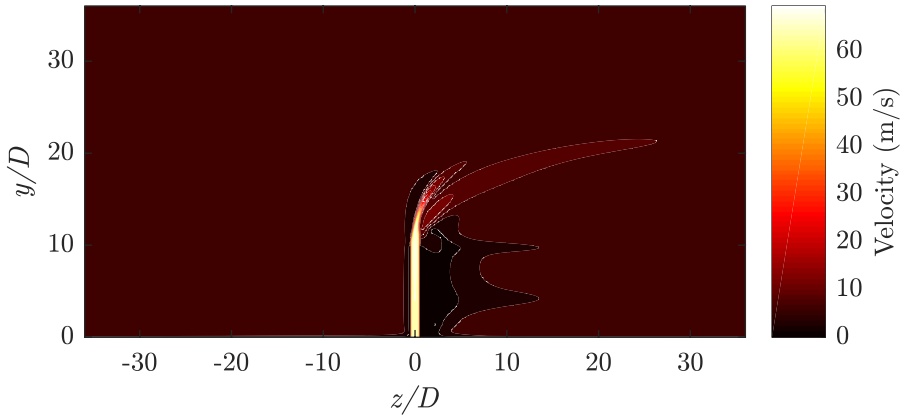

(a) Velocity magnitude

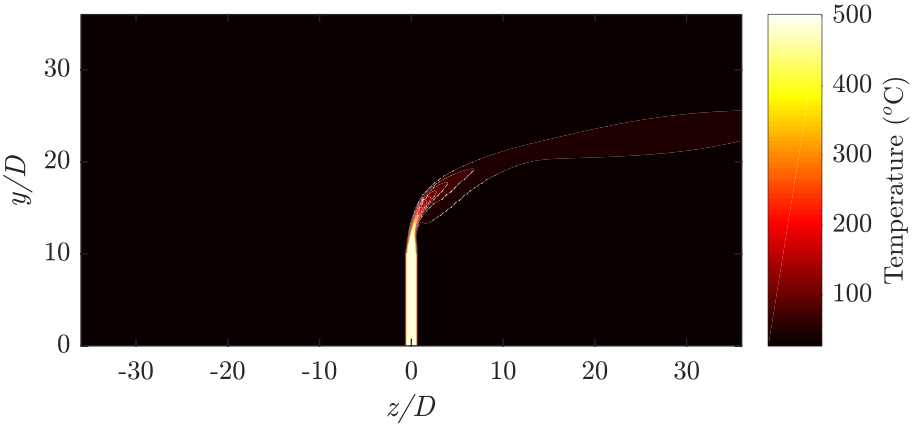

(b) Temperature

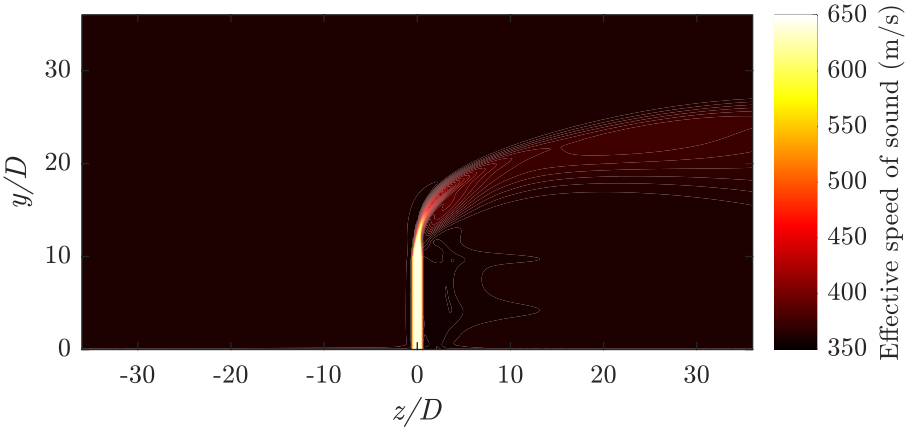

(c) Effective speed of sound

Figure 3.15: The elevated JICF CFD generated contour plots of (a) flow velocity, (b) temperature, and (c) , and (c) the effective speed of sound along the Y-Z plane (of symmetry), where T_j = 500 °C and R = 5. The cross-flow is from left to right.

formation of significant thermal gradients where refraction of sound can occur. The effect of the thermal gradient on sound refraction is investigated in the following section.

The results in Figure 3.15c shows the effective speed of sound calculated using Equation (3.32) for the elevated JICF along the the Y-Z plane. The results show similar qualitative features to Figures 3.15a and 3.15b, with:

- the highest magnitude in the speed of sound in the duct and in the geometric near-field of duct outlet,
- reductions in the speed of sound near the leading edge of the duct outlet,
- in the wake of the exhaust stack the lowest values in the effective speed of sound are observed,
- as the plume spatially expands downwind the effective speed of sound also follows a similar trend, and
- as the plume propagates downwind of the exhaust stack the effective speed of sound continues to reduce in magnitude.

It is important to remind the reader that $v_0(\vec{x})$ in Equation (3.32) is the velocity magnitude and does not take into consideration the flow direction with respect to the direction of the acoustic wave. Similar reasoning with portraying the plot in Figure 3.10c, Figure 3.15c is an estimation of the speed of sound that may change the propagation path of sound, based on Equation (3.21).

3.3.2 Ground-level jet in cross-flow sound propagation

This section presents results from acoustic simulations where four different conditions were imposed. As shown in Figure 3.2, first a CFD simulation is conducted to evaluate the nodal temperatures and steady-state bulk fluid velocities, due to selected conditions. The results from the CFD simulations are then applied to the nodes in the acoustic FE model. Note, this is a one-way coupling, so there is no

backwards influence of the sound field on the fluid motion or temperature. The conditions in the acoustic FE model that were simulated include:

- isothermal stationary field at ambient temperature[5],
- the nodal temperatures from a CFD simulation of a non-isothermal JICF were applied to the FE model[6],
- nodal steady-state bulk fluid velocities from a CFD simulation of an isothermal JICF were applied to the FE model[7], and
- nodal steady-state temperatures and bulk fluid velocities from a CFD simulation of a non-isothermal JICF were applied to the FE model.

For these cases three jet temperatures, T_j (27 °C, 250 °C, and 500 °C), two jet to cross-flow momentum flux ratios, R (5 and 7.5), and six Helmholtz numbers ($0.2 \leq ka \leq 0.8$) were considered.

3.3.2.1 Sound propagation through an isothermal stationary field

The results presented in this section are the acoustic results for sound propagation through an isothermal stationary field at ambient temperature. The Helmholtz numbers of interest are $0.3 \leq ka \leq 0.8$. Two acoustic sources were used; (i) a harmonic velocity source at the outlet which is equivalent to a baffled piston and facilitates comparison against analytical modes [25], (ii) a harmonic velocity source at the opposite end of the duct, which represents what happens in practice. The inclusion of a duct with a sound source at the base of the duct changes the acoustic

[5]The captions in the figures of this chapter uses the notation $\vec{v}_0(\vec{x}) = 0$ to indicate the domain is in the absence of mean flow and the model is solved with Equation (3.8). Furthermore, the term isothermal refers to the jet and cross-flow temperature being identical at $T_j = 27\,°C$, which is the ambient temperature.

[6]Similarly to the previous footnote, $\vec{v}_0(\vec{x}) = 0$ refers to the domain in the absence of mean flow and the model is solved with Equation (3.8). However, the term non-isothermal refers to the jet temperature, T_j, and cross-flow temperature at two different temperatures, where $T_{cf} = 27\,°C$, and is constant for all cases. However, T_j will vary and the figure caption will specify the jet temperature.

[7]Again, for simplification in the caption the notation $\vec{v}_0(\vec{x}) \neq 0$ refers to the domain with varying mean flow and the model is solved with Equation (3.21).

directivity slightly and is discussed in this section. A grid independence study was also conducted, which demonstrated that the results change as the mesh is altered.

Figure 3.16 presents the sound radiation along the Y-Z plane (of symmetry). Figure 3.16a shows the contour plots of the SPL along the Y-Z plane, at $ka = 0.8$ in the absence of the jet plume, where it can be seen that the sound radiation pattern is axisymmetric and spreading (nearly) hemispherically. Figure 3.16b shows the contour plot of the directivity index (DI) along the Y-Z plane of symmetry, where there is an increase in the DI on-axis ($-1.5\,\text{dB} \leq \text{DI} \leq 1.5\,\text{dB}$) showing approximately spherical sound radiation. The small irregularities in the contour plot and DI are due to artefacts as the sound propagates through the mesh, with a finer mesh decreasing the irregularities.

In Figure 3.17 are plotted as polar line graphs and compared with the analytical solution for the DI of a baffled piston in an infinite plane. Figure 3.17 shows the DI polar plots at two different radii ($r = 16D$ and $32D$) and two Helmholtz numbers ($ka = 0.7$ and 0.8). The definition for DI in Figure 3.17 is slightly different from Equation (3.26), as the DI for the analytical baffled piston solution is defined here as

$$\text{DI}(\theta) = \frac{I(\theta)}{I_{\text{max}}}, \tag{3.38}$$

where $I(\theta)$ is calculated using Equation (3.27) with the coordinate system defined by Figure 3.5, and I_{max} is the maximum acoustic intensity defined by Equation (3.27) along a spherical surface in the computational domain, with the same radii as the directivity arc of interest [25, 97].[8] The reader should note that the accepted definition of directivity index has the divisor as the average intensity over the measurement surface [25]. All the polar plots in Figure 3.17 show similar key features, where the sound is radiated hemispherically and is axisymmetric. Figure 3.17 shows a good agreement with the DI polar plot results for the analytical and numerical sound radiation from a baffled piston. The reader should refer to Section C.10 for additional validation of the numerical results against the analytical results for an infinitely baffled piston in 3-D. The validation shows good agreement

[8]The reader should note that Equation (3.38) is only used in this section to compare the numerical acoustic results with a known analytical solution.

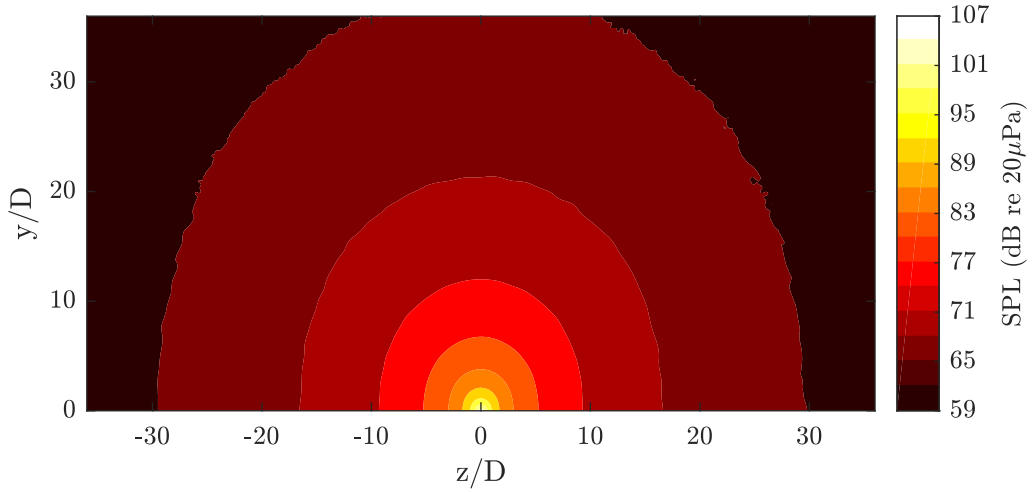

(a) SPL

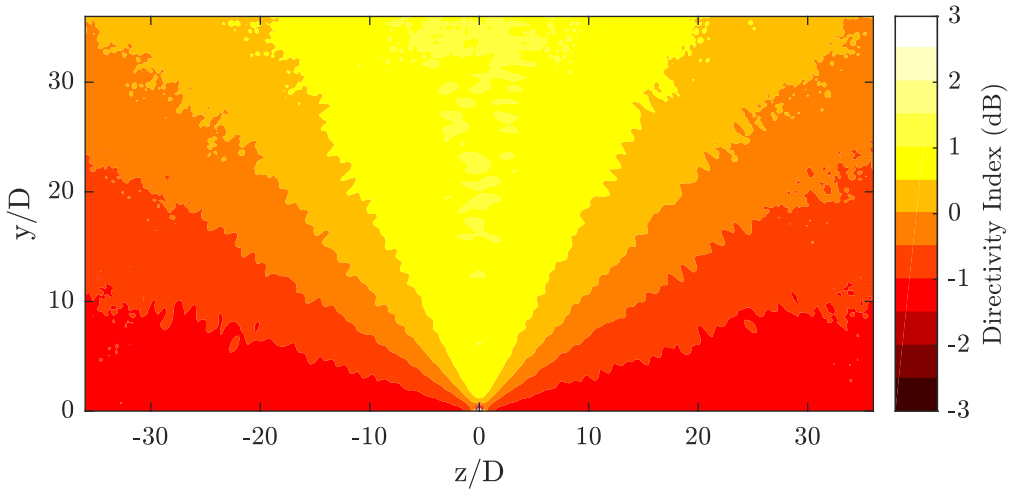

(b) Directivity index

Figure 3.16: Contour plots of (a) the sound pressure level and (b) the DI along the Y-Z plane (of symmetry) for sound propagation through the domain in the absence of flow, with $T_j = 27\,°\text{C}$, $\vec{v}_0(\vec{x}) = 0$, and $ka = 0.8$.

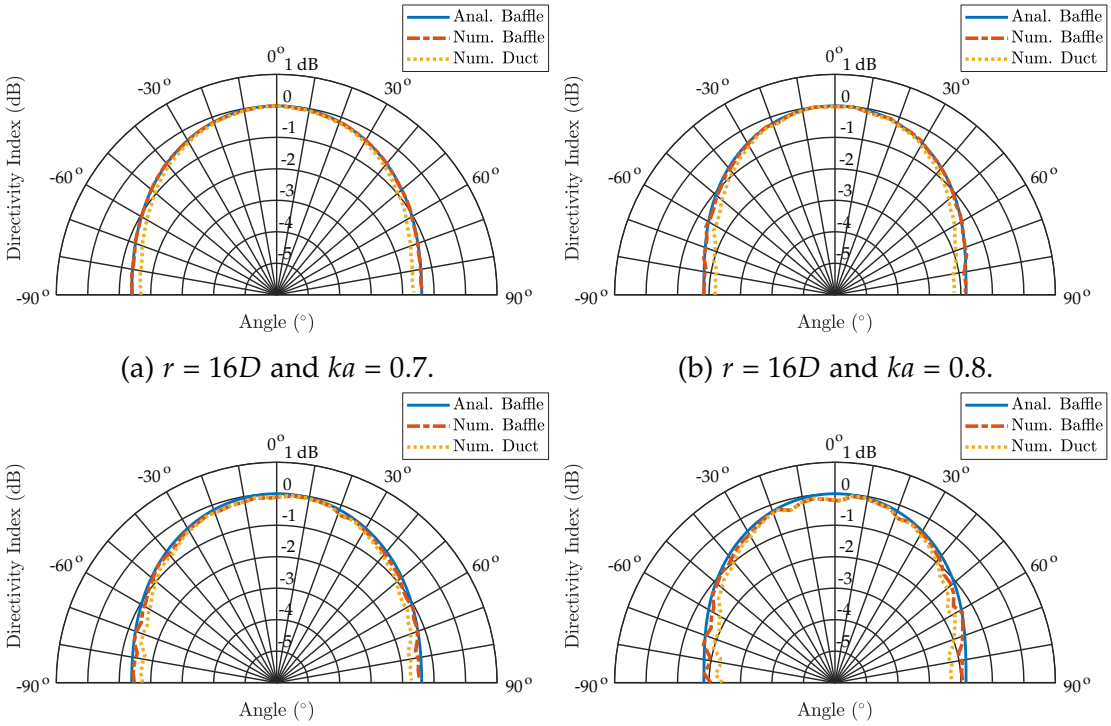

(a) $r = 16D$ and $ka = 0.7$.

(b) $r = 16D$ and $ka = 0.8$.

(c) $r = 32D$ and $ka = 0.7$.

(d) $r = 32D$ and $ka = 0.8$.

Figure 3.17: The DI along the Y-Z plane (of symmetry) for sound propagation through the domain in the absence of flow at two radii ($r = 16D$ and $32D$]), two Helmholtz numbers ($ka = 0.7$ and 0.8), $T_j = 27\,°\text{C}$, and $\vec{v}_0(\vec{x}) = 0$. The results are for a baffled circular piston (analytical and numerically solved in FEM) and circular duct of length $10D$ (solved in FEM).

for the directivity results in the far-field ($r = [16, 32D]$) with the numerical method and analytical results at four different frequencies. However, in Figure 3.17, the inclusion of the duct produces DI polar results with a more directed acoustic lobe on-axis.

Grid independence for a directivity polar plot along the Y-Z plane is used to show both a converged solution and the model's limitation with the total number of mesh nodes. Figure 3.18 shows the DI polar plot as a function of the total number of mesh nodes. The acoustic results in Figure 3.18vary depending on the mesh density, with the largest case (12 million nodes) showing that the solution has converged. However, due to the limitations with the computational

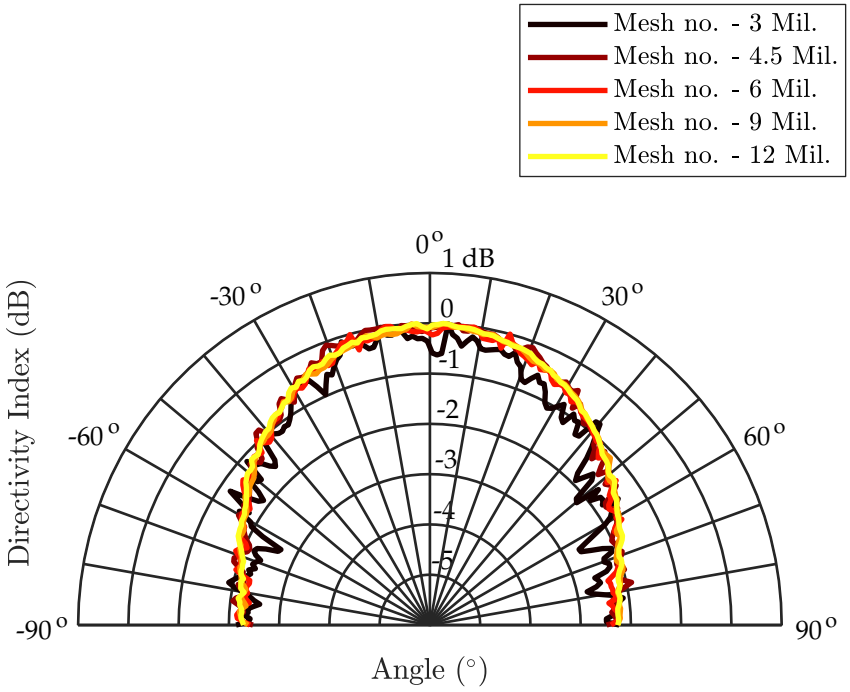

Figure 3.18: Mesh convergence - the DI the Y-Z plane (of symmetry) for sound propagation through the domain, in the absence of flow, as a function of the FEM mesh node count, at $r = 32D$, $T_j = 27\,°\text{C}$, $\vec{v_0}(\vec{x}) = 0$, and $ka = 0.8$.

hardware and numerical code, there is an upper limit to the number of nodes in the acoustic model. In conducting the acoustic FEM simulations, if an uncoupled, non-symmetric formulation is used for the solver maximum node count for the mesh is 6 million nodes, but if an uncoupled, symmetric formulation is used for the solver the maximum node count for the mesh is 12 million nodes. The acoustic results presented in the remainder of this study will use an uncoupled, non-symmetric formulation with a node count of 6 million nodes.

The data presented above in the form of line plots and planar contour plots has also been visualised in 3-D to show different key acoustic features in one of two ways:

- **3-D DI contour plot over a spherical surface**: This plot represents the DI at a fixed radius ($32D$), where the colour represents the DI given by Equa-

tion (3.26). The spherical surface for the contour plot was a quarter of a sphere.

- **3-D directivity radiation pattern**: This plot represents the radiation pattern at a radius of $32D$ for a point source, where the radius and colour are proportional to the normalised DI given by Equation (3.26). The radius for generating the surface uses the following limits for DI, $-12\,\text{dB}$ to $12\,\text{dB}$, and scales the plot with a radius of 0 to 24, respectively for the limit. Additionally, the results have been mirrored along the Y-Z plane of symmetry to show the 3-D directivity radiation pattern for a hemisphere.

In order to avoid confusion, the 3-D DI contour plot over a spherical surface is plotted using MATLAB's 'hot' colour map and the 3-D directivity radiation pattern is plotted using MATLAB's 'jet' colour map. Additionally, the 3-D directivity radiation pattern MATLAB's jet colour map shows distinctively the upper and lower limits in DI magnitude for the 3-D directivity radiation pattern. The following discussion in this section will be on the 3-D contour plots of the DI.

Figure 3.25 presents the results for the 3-D DI contour plot along a spherical surface. This 3-D view of the DI shows an additional acoustic feature that was not visible in the previous line plots or planar contour plots, which is the 3-D representation for axisymmetric sound about the duct centreline. Moreover, the acoustic spreading is not spherical, with the DI slightly concentrated on-axis.

Another 3-D contour plot of the acoustic results is shown in Figure 3.20, with the 3-D directivity radiation pattern. The alternative representation for the DI shows the consistent acoustic features presented previously in this section, which are:

- the sound is radiating axisymmetrically about the duct centreline,
- the sound is not radiating spherically with the monopole assumption and the DI radiating with equal magnitude in all directions, and
- the sound is slightly concentrated on-axis with a lobe forming.

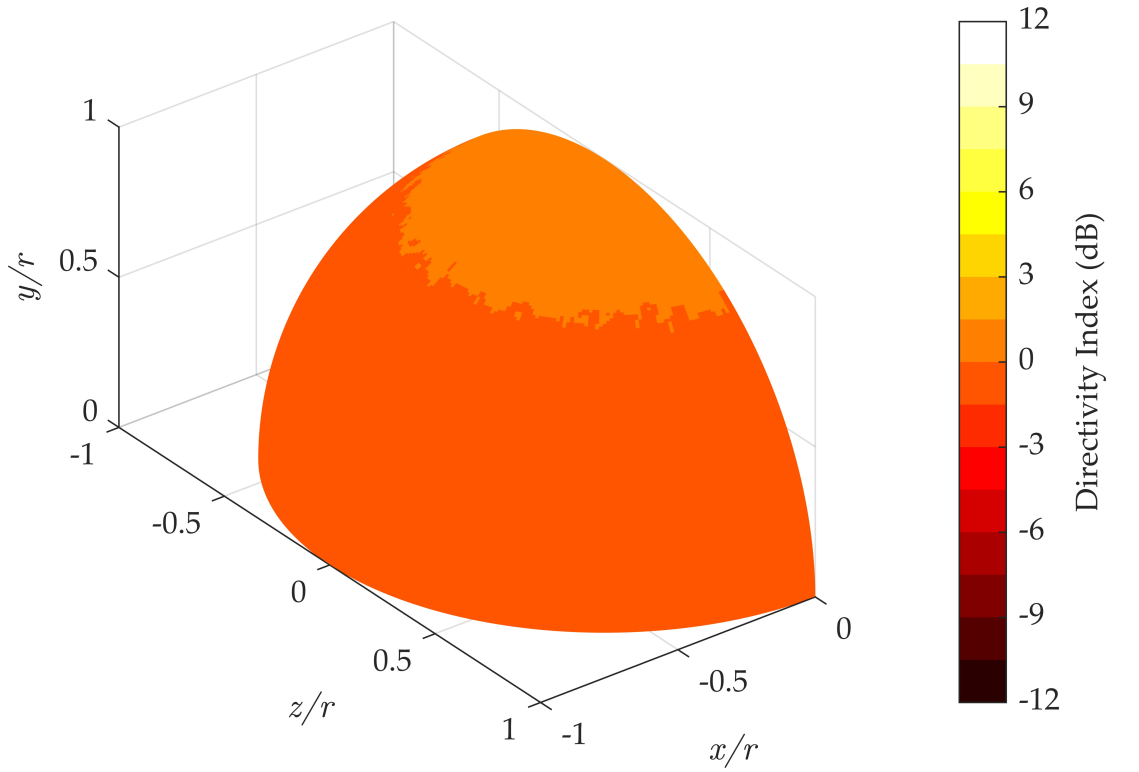

Figure 3.19: The 3-D DI contour plot over a spherical surface at a radius $r = 32D$ for sound propagation through an isothermal stationary field at an ambient temperature with $\vec{v_0}(\vec{x}) = 0$, and $ka = 0.8$. Values of DI less than -12 dB are saturated black.

3.3.2.2 Thermal effects on sound propagation

In this section, the effect of thermal gradients on the change in sound directivity are explained. It will be shown that the inclusion of the temperature associated with non-isothermal JICF in the sound radiation model drastically alters the sound propagation when compared with the results for the isothermal stationary field ($\vec{v_0}(\vec{x}) = 0$) at ambient temperature ($T_j = 27\,°C$) in Section 3.3.2.1. It should be noted that the temperature distribution was generated using CFD and the results were presented in Section 3.3.1.1.[9] The cases that will be discussed are: $R = [5, 7.5]$, $T_j = [250\,°C, 500\,°C]$, and $ka = [0.3, 0.4, 0.5, 0.6, 0.7, 0.8]$.

[9]The reader can refer to Figures 3.10b and 3.12, to view the temperature distribution related to the acoustic results presented in this section. The effects of mean velocity are not accounted for in these plots ($\vec{v_0}(\vec{x}) = 0$).

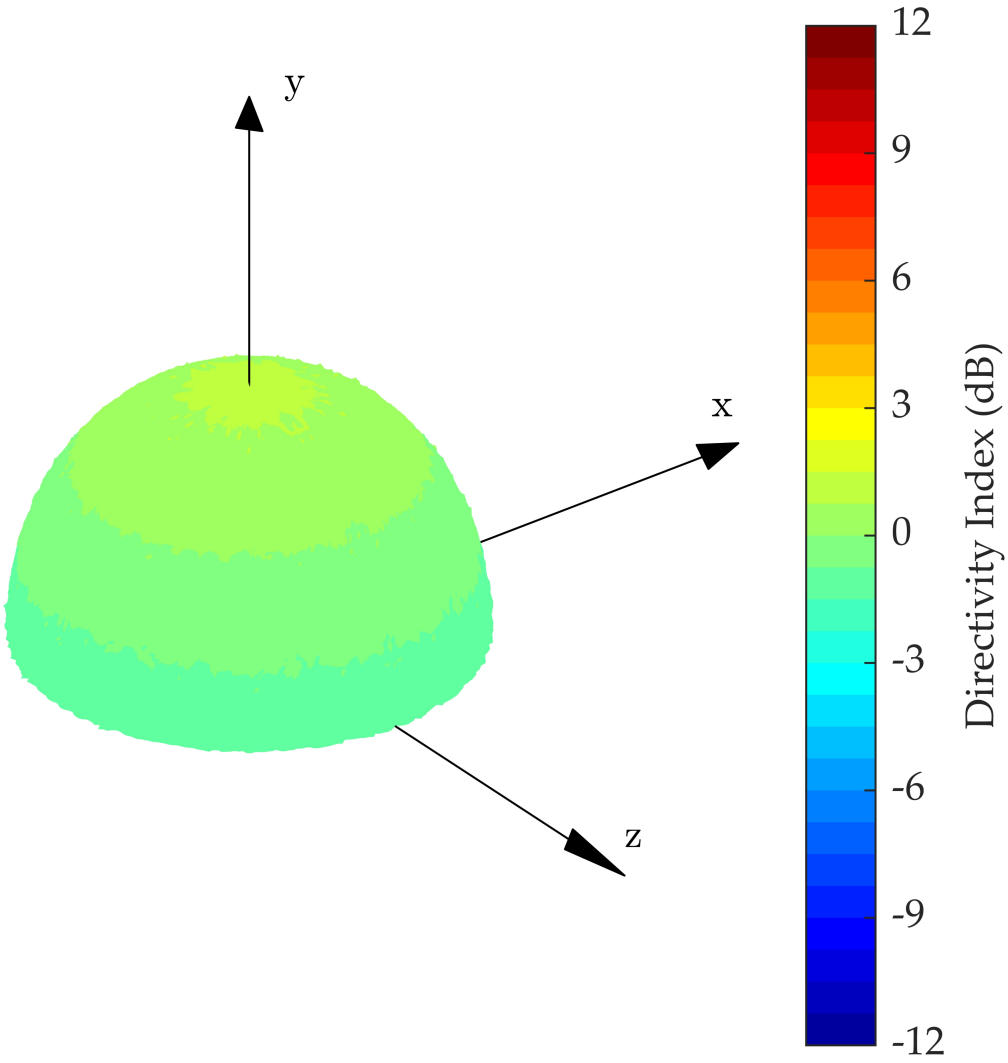

Figure 3.20: The 3-D directivity radiation pattern at a radius $r = 32D$ for sound propagation through an isothermal stationary field at ambient temperature with $\vec{v}_0(\vec{x}) = 0$, and $ka = 0.8$. Values of DI less than -12 dB are saturated dark blue.

Figure 3.21 shows the contour plots of SPL and DI [10] along the Y-Z plane (of symmetry). Figure 3.21a shows a contour plot of SPL and shows that in the near-field of the outlet, the acoustic propagation is approximately spherical, as the sound has not propagated a sufficient distance to interact with the thermal gradients in the plume. In the near-field, the acoustic wavelengths are large relative to the spatial extent of the thermal gradients, and refraction effects are minimal. As the sound progresses through the domain, the spherical spreading behaviour ceases. The downwind thermal-acoustic interaction leads to a prominent concentration of sound, otherwise known as a 'lobe' of sound. This acoustic lobe is due to acoustic refraction from the plume and the increase in acoustic energy is due to a redirection of the acoustical energy that would have existed in the pressure null seen near the duct centreline axis. Upwind of the duct outlet, the results in Figure 3.21a show that in the absence of the plume the sound spreads more uniformly in an approximately spherical pattern.

Figure 3.21b, shows the contour plot of DI along the Y-Z plane, calculated using Equation (3.26). In the near-field of the duct outlet, Figure 3.21b shows consistent acoustic propagation results with Figure 3.21a and the sound spreads approximately spherically with a DI of approximately 0 dB. Figure 3.21b clearly shows the concentration of sound downwind that was seen in Figure 3.21a, however it shows the SPL being increased up to approximately 10 dB. At an angle of about 10° from the duct centreline, there is a distinct pressure null in Figure 3.21b. This pressure null is different from the work seen previously with axisymmetric jets, as the null is now asymmetric, biasing towards downwind. Upwind of the duct outlet, the spherical acoustic spreading in Figure 3.21a is also evident in Figure 3.21b, with a region of DI ranging from 0 dB to 3 dB.

The DI results presented in Figure 3.21b are plotted in Figure 3.22 as a polar plot at five radii, and clearly show the change in sound propagation with distance. Initially, in the near-field ($2D - 4D$), the sound has not yet propagated a sufficient distance for refraction to occur, with the sound propagating approximately spherically. In Figure 3.22, at a radius of $2D$, a slight increase in sound level at

[10] The acoustic results for DI for the remainder of this section will use Equation (3.26) as the definition for DI, which can lead to values greater than 0 dB.

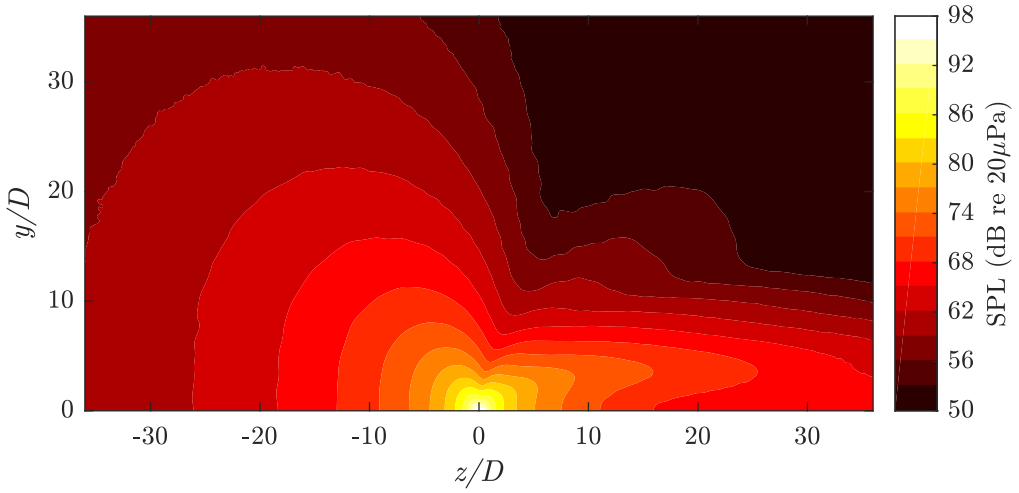

(a) SPL

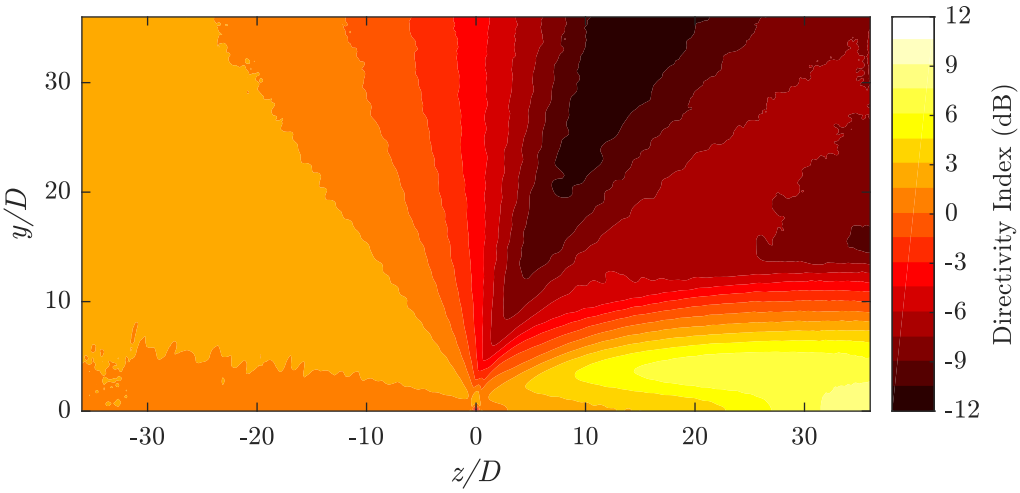

(b) Directivity index

Figure 3.21: Contour plots of (a) the sound pressure level and (b) the DI along the Y-Z plane (of symmetry) for sound propagation through non-isothermal thermal gradients from a ground-level JICF with $R = 5$, $T_j = 500\,°\text{C}$, $\vec{v}_0(\vec{x}) = 0$, and $ka = 0.8$. The cross-flow is from left to right. Values of DI less than $-12\,\text{dB}$ are saturated black.

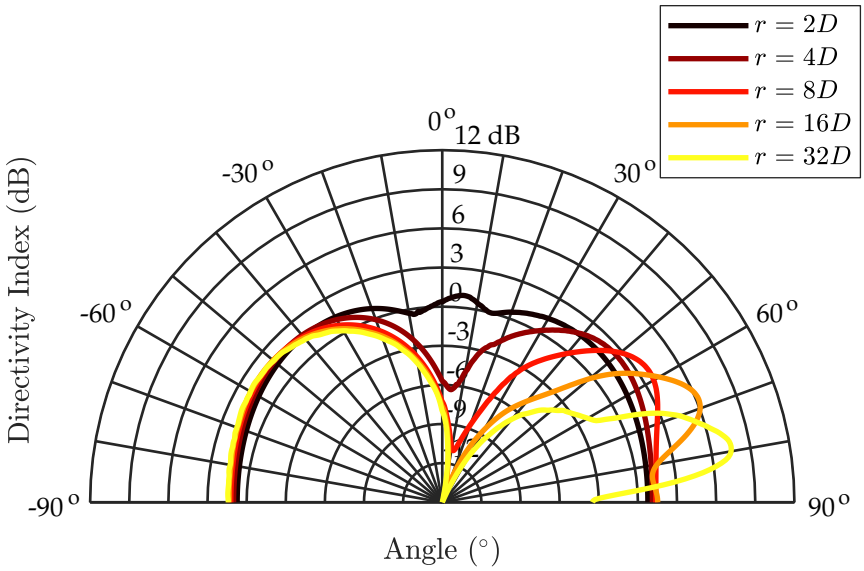

Figure 3.22: The DI at various distance from the duct outlet ($r = [2D, 4D, 8D, 16D, 32D]$) along the Y-Z plane (of symmetry) for sound propagation through thermal gradients from non-isothermal JICF at $R = 5$, $T_j = 500\,°C$, $\vec{v_0}(\vec{x}) = 0$, and $ka = 0.8$.

approximately 5° can be seen. The increase in DI is a result of the sound refraction due to the thermal gradient at $2D$. Figure 3.22 shows that with the increase in polar radius from the stack, the propagating sound continues to refract to give a unique sound propagation path. Figure 3.22 shows three features, namely:

- downwind, at angles from 30° to 90° a lobe is formed,
- on the axis of the duct at 20° an acoustic 'cusp' or 'null' is formed, and
- upwind of the duct, at angles from $-40°$ to $-90°$, spherical spreading occurs.

The change in the propagation path of sound is a result of the acoustic energy being redistributed by the plume. From the DI polar plots, it is evident that even at a radius of $32D$ the sound is still being affected by the plume. In future work, a larger model would be desirable to investigate this phenomenon further and determine if convergence of DI is achieved in the far-field.

The sensitivity of the DI to frequency is illustrated in Figure 3.23, which shows the DI polar plot for values of ka between 0.3 to 0.8. In Figure 3.23a it can be

seen that at $2D$ the onset of refraction is wavelength dependent, with the plume causing a slight increase in DI at 55° that is ka dependent. The effects of refraction at these radial distances cause the acoustical energy that was previously at 5° to be refracted either downwind or upwind, resulting in a slight increase in DI off-axis. Figure 3.23b shows the DI polar plot at $r = 8D$, where the sound directivity becomes more asymmetric with increasing ka. At approximately 55°, it can be seen that a lobe forms with increasing values of ka, which is a result of acoustic refraction causing a redistribution of acoustic energy, and the creation of a null at approximately 10° to 20°. Figures 3.23c and 3.23d present the DI polar plot for varying values of ka for two radii, $16D$ and $32D$, respectively. It can be seen, that as the distance from the stack outlet increases, the lobes move closer to the horizontal. The lobe forms at 60° in Figure 3.23c, and 80° in Figure 3.23d. Hence, downwind of the duct, spherical spreading of the sound does not occur but becomes increasingly concentrated in the lobe.

Sound level predictions at ground-level are important in quantifying the noise levels received at communities. Figure 3.24a shows the SPL contours along the X-Z plane (i.e. ground-level) for a jet temperature of $T_j = 500\,°C$, $R = 5$, $ka = 0.8$, where the cross-flow is occurring from the top to bottom in the Figures. Figure 3.24b shows the corresponding DI, which is useful for identifying regions where the sound levels have increased as a result of refraction. Figure 3.24a shows that for $(z/D > 0)$, the SPL upwind spreads approximately spherically, which is also supported by the constant contours of DI in Figure 3.24b. Figure 3.24a shows that there is a concentration of sound along the Y-Z plane (of symmetry) of the domain downwind of the duct $(z/D < 0)$. In Figure 3.24b, the peak in DI occurs at the bottom-left edge of the domain. Along the span-wise $(x/D > 0)$ direction in Figure 3.24b there is a reduction in the DI, with the reduction in sound along the span-wise explained by referring to the temperature gradients in Figures 3.12e and 3.12f, and quantified in Table 3.2. Figure 3.12e shows that the dominant fluidic structure that affects the temperature downwind is the counter-rotating vortex. This counter-rotating vortex is present in Figure 3.12f, but has dissipated drastically and it is difficult to discern the thermal gradients in the plume. Table 3.2 shows that

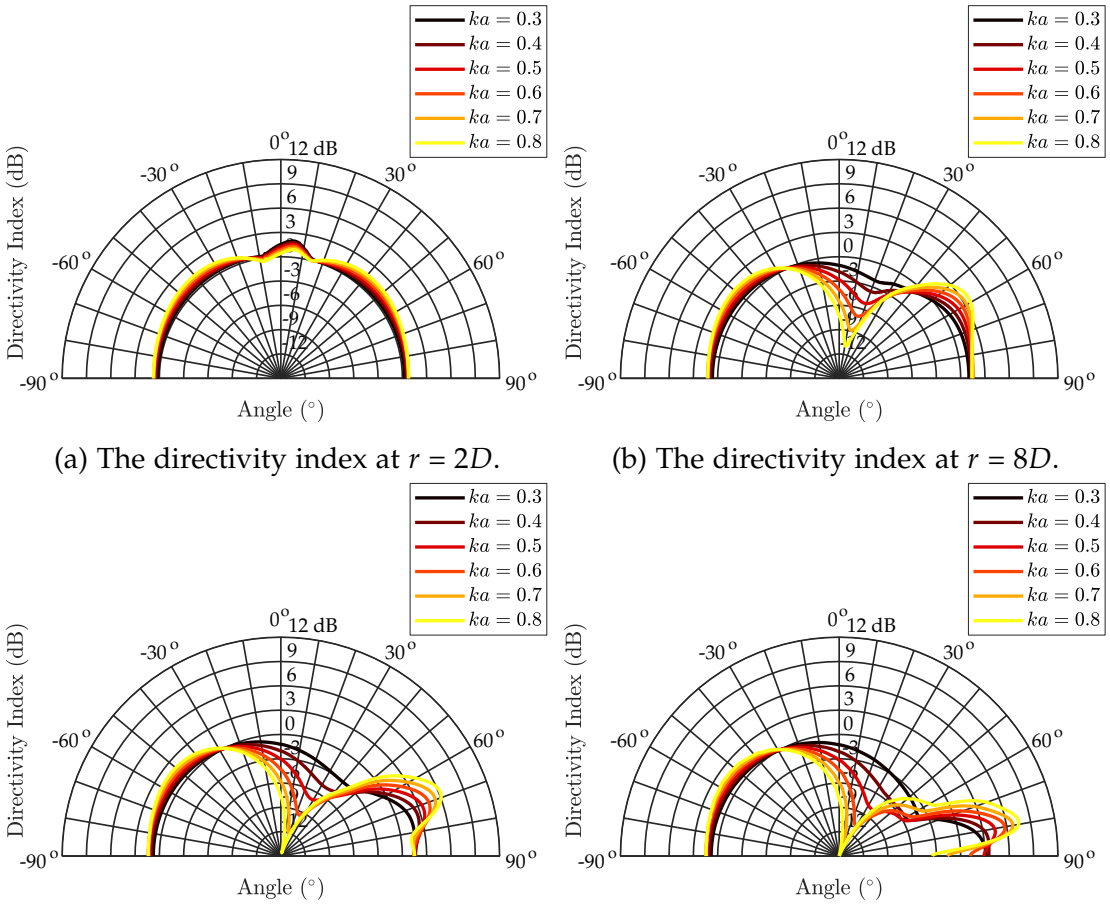

(a) The directivity index at $r = 2D$.

(b) The directivity index at $r = 8D$.

(c) The directivity index at $r = 16D$.

(d) The directivity index at $r = 32D$.

Figure 3.23: The DI at six different Helmholtz numbers ($ka = [0.3, 0.4, 0.5, 0.6, 0.7, 0.8]$) and at four different radii ($r = [2D, 8D, 16D, 32D]$) along the Y-Z plane (of symmetry) for sound propagation through non-isothermal JICF thermal gradients with $R = 5$, $T_j = 500\,°\text{C}$, and $\vec{v_0}(\vec{x}) = 0$.

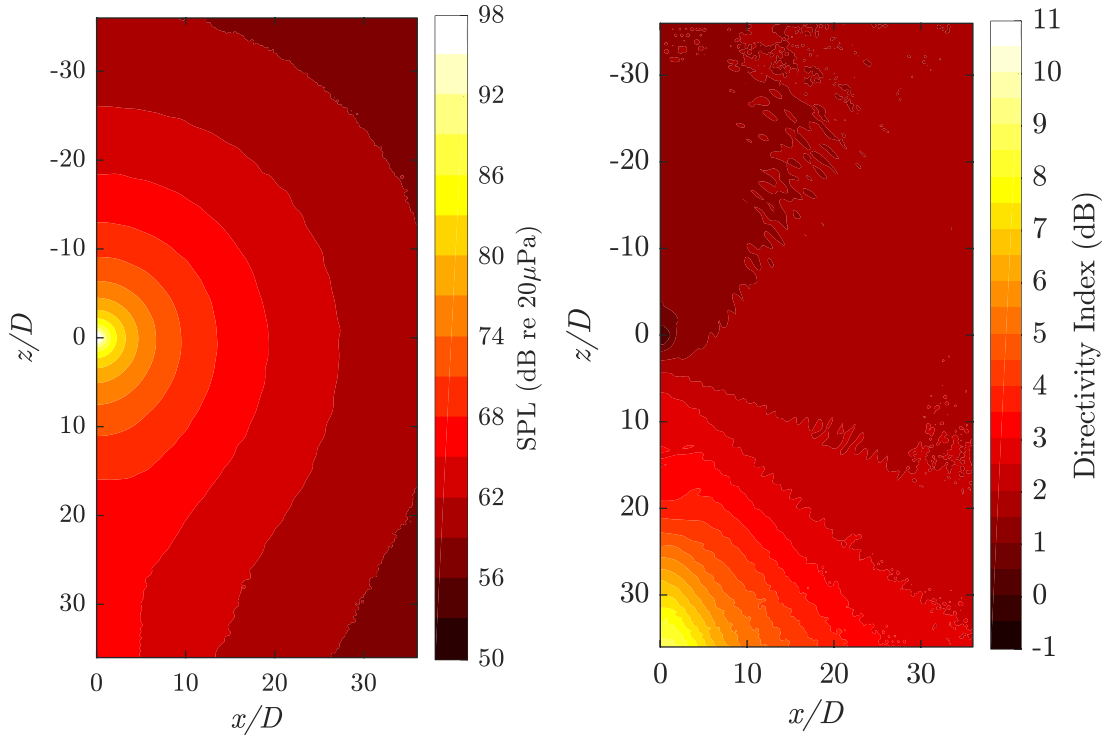

(a) SPL (b) Directivity index

Figure 3.24: Contour plots of (a) sound pressure level and (b) DI along the X-Z plane (ground-level) for sound propagation through the thermal gradients from non-isothermal JICF with $R = 5$, $T_j = 500\,°\text{C}$, $\vec{v}_0(\vec{x}) = 0$, and $ka = 0.8$. The cross-flow is from top to bottom.

the difference in temperature in the plume compared to the ambient temperature is $\Delta T_0 \approx 25\,°\text{C}$. The thermal gradients in the plume's counter-rotating vortex causes acoustic refraction, which leads to an increase in SPL at ground-level and along the Y-Z plane (of symmetry). The increase in SPL along the Y-Z plane at ground-level is attributed to the superposition of refracted sound that would typically exist from the interaction of the two counter-rotating vortices that is reproduced with the symmetry boundary condition along the Y-Z plane.

Figure 3.25 presents the results with a 3-D DI contour plot over a spherical surface. This 3-D view of the DI shows the complex non-axisymmetric sound radiation that was not visible in the 2-D planar DI contour plots, such as Figures 3.21b and 3.24b. Figure 3.25 shows a region of increased sound downwind with a distinct

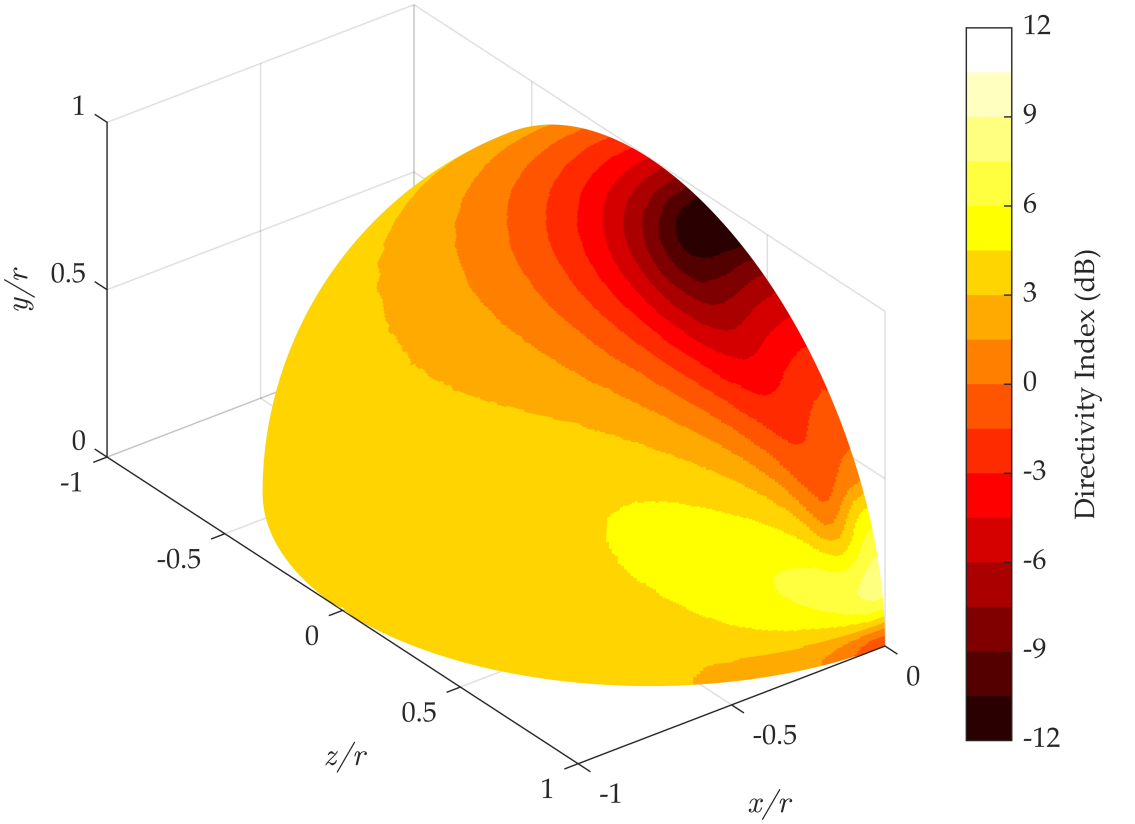

Figure 3.25: The DI contour plot across a spherical surface at a radius $r = 32D$ for sound propagation through non-isothermal JICF with $R = 5$, $T_j = 500\,°\text{C}$, $\vec{v}_0(\vec{x}) = 0$, and $ka = 0.8$. Values of DI less than $-12\,\text{dB}$ are saturated black.

maxima. The downwind DI maxima are along the symmetry-plane of the domain, which is due to the superposition of refracted acoustic energy on either side of counter-rotating vortex pairs. Figure 3.25, shows that there is a pressure null region at the top of the sphere, which has a 'crescent' like shape. The shape of the pressure null is strongly governed by the deflected jet with a 'crescent' shape plume and a deflected shear layer, as seen in Figure 3.12b. The deflected shear layer has caused a pressure null to form with approximately the same shape. Along the developing plume, the sound close to the centre of the counter-rotating vortex exhibits an acoustic cusp where sound is refracted from this region.

Another graphical 3-D representation for the acoustic results, similar to Figure 3.25, is a 3-D directivity radiation pattern, as shown in Figure 3.26. The 3-D

directivity radiation pattern results shows the redistribution of acoustic energy and reinforces the results in this section, with the non-axisymmetric sound radiation. Downwind of the jet outlet it can be observed that the refraction of sound has led to the formation of an acoustic lobe. Although, the 2-D planar contour plots and the line plots do not fully capture the width of the acoustic lobe downwind of the exhaust stack, Figure 3.25 shows the acoustic lobe has a finite width. A cusp has formed along the centreline axis of the jet outlet. Furthermore, upwind of the jet outlet, the 3-D directivity radiation pattern shows the DI is approximately uniform with both a spherical surface and a uniform colour band. All the features listed are consistent with all the results in this section for sound propagation through the thermal gradients from a non-isothermal ground-level JICF.

The results show that the propagation of sound is dependent on the temperature of the jet. Figure 3.27 shows the DI polar plot with two different jet temperatures (T_j = 250 °C and 500 °C) and two different cross-flow ratios, R = 5 and R = 7.5. The reduction in T_j from 500 °C to 250 °C has reproduced three features:

- downwind of the duct outlet from 30° to 90° an acoustic lobe is formed,
- on the axis of the duct, at 20°, an acoustic 'cusp' is formed, and
- upwind of the duct outlet, from $-40°$ to $-90°$, spherical spreading occurs.

However, the acoustic lobe downwind of the duct outlet has a DI that is reduced by up to 3 dB, with the decrease in T_j from 500 °C to 250 °C. Near the duct axis, at 30°, the acoustic 'cusp' is dependent on T_j, with the depth of the acoustic 'cusp' in the DI increasing with T_j. Figure 3.27 also shows the effects of changing the cross-flow ratio R, from R = 5 to 7.5, in other words, reducing the cross-flow velocity. Downwind of the duct outlet the acoustic lobe has shifted with the increase in R, from R = 5 to 7.5, with the position of the acoustic lobe moved from 20° to 80°. In Figure 3.27 the DI magnitude for the acoustic lobe downwind and the acoustic 'cusp' for R = 7.5 is dependent on T_j.

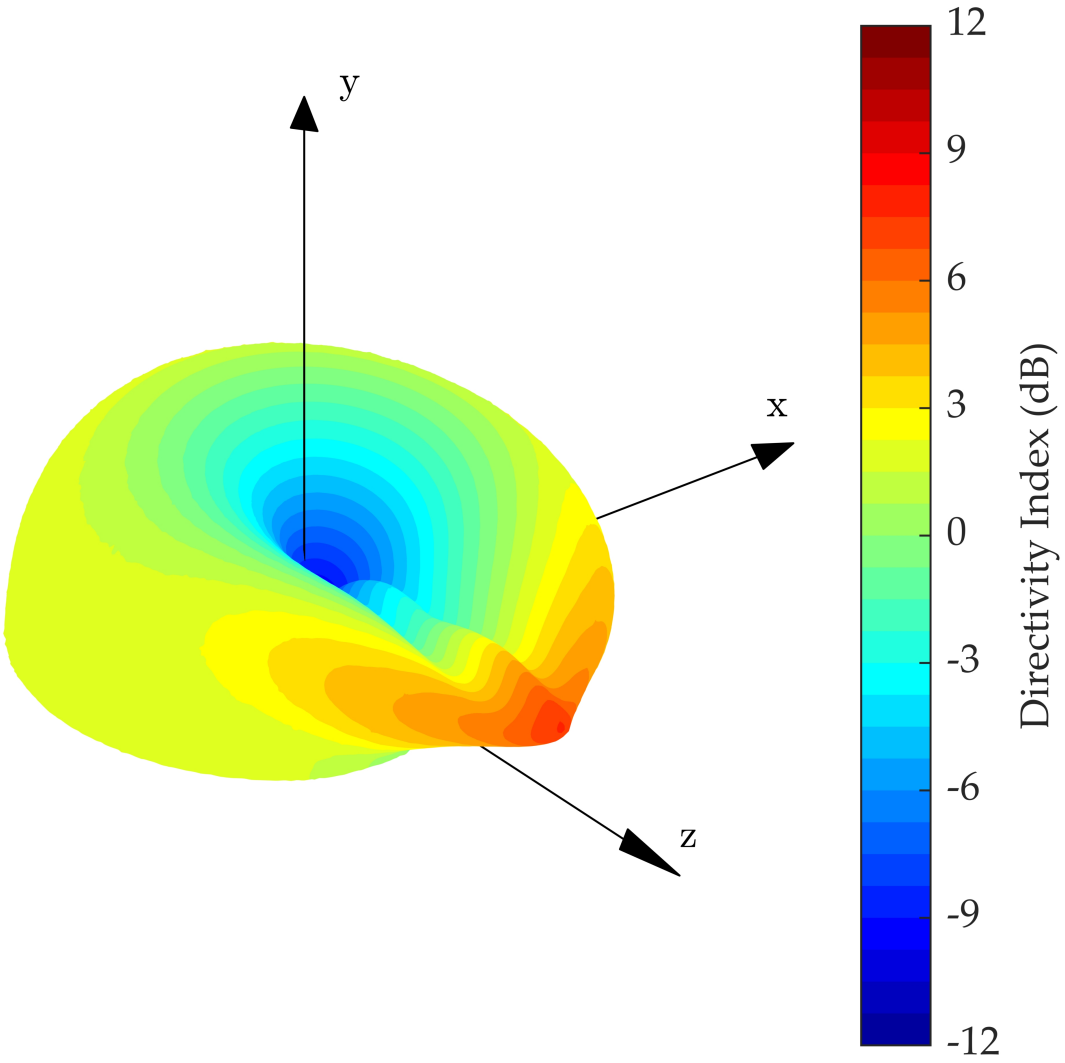

Figure 3.26: The 3-D directivity plot for DI at a radius $r = 32D$ for sound propagation through non-isothermal JICF with $R = 5$, $T_j = 500\,°\text{C}$, $\vec{v}_0(\vec{x}) = 0$, and $ka = 0.8$. Values of DI less than $-12\,\text{dB}$ are saturated dark blue.

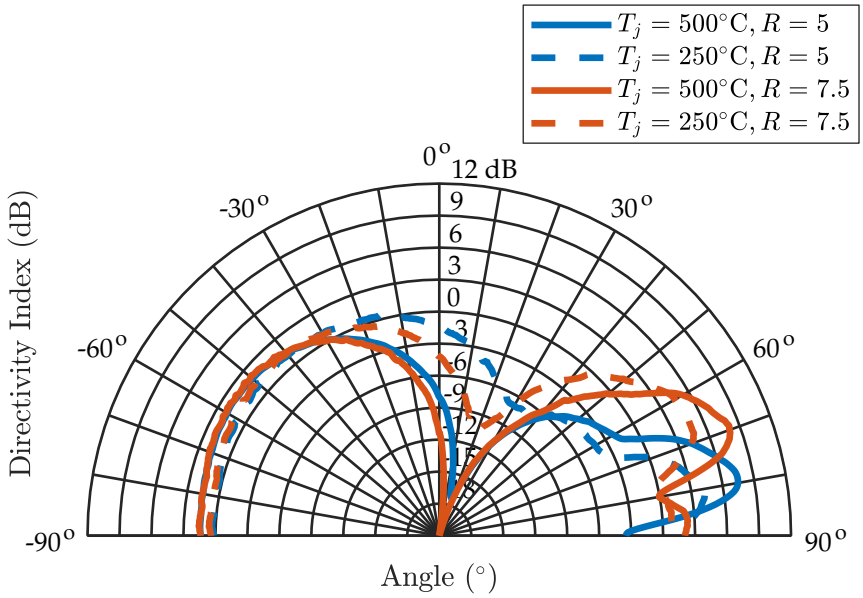

Figure 3.27: The DI at a radius of $32D$ along the Y-Z plane (of symmetry) for sound propagation through the thermal gradients associated with non-isothermal JICF with varying R and T_j at $ka = 0.8$, and $\vec{v_0}(\vec{x}) = 0$.

3.3.2.3 Steady-state convective effects on sound propagation

In this section, the convective effects of the flow on sound propagation are explained. The ground-level JICF the jet temperature is considered ambient (isothermal) at $T_j = 27\,°C$ and the jet to cross-flow momentum flux ratio is $R = 5$. The convective effects or mean flow used as the acoustic medium for sound propagation are from the CFD results discussed in Section 3.3.1.1.

Figure 3.28 shows contour plots of the SPL and DI for sound propagation along the Y-Z plane (of symmetry) through the steady-state fluid flow associated with the JICF. Figure 3.28a shows that upwind of the plume ($z/D > 0$), sound is refracted upwards due to the velocity gradient within the boundary layer of the cross-flow. The upwards sound refraction seen in Figure 3.28 is not observed in Figure 3.21. Figure 3.28b shows asymmetric acoustic spreading, with a 'cusp' forming 10° from the duct outlet, as a result of the fluid-acoustic interaction with the velocity gradients in the shear layer. Figures 3.21b and 3.28b show similar results, with an increase in sound levels downwind of the duct, as the propagation

of sound into the far-field interacts with the plume's velocity gradients. When comparing Figures 3.21 and 3.28, it can be seen that the difference in DI amplitude downwind is significant and it is due to the difference in the change in effective speed of sound, c_{eff} caused by the convective cross-flow. For the temperature and cross-flow conditions considered in this chapter, a change in gas temperature from $T_j = 27\,°\text{C}$ to $T_j = 500\,°\text{C}$ causes a greater change in the effective speed of sound ($\Delta c_{\text{eff}} \approx 200\,\text{m}\,\text{s}^{-1}$) compared with the effect of convection on the effective speed of sound ($\Delta c_{\text{eff}} \approx 30\,\text{m}\,\text{s}^{-1}$).

Figure 3.29 shows the DI as a function of angle at six distances from the duct outlet ($r = [2D, 4D, 8D, 16D, 32D]$) along the Y-Z plane (of symmetry) for sound propagation through the steady-state convective effects from an isothermal JICF. In Figure 3.29, upwind ($-90° \leq \theta \leq 0°$) of the duct outlet, the DI is essentially spherical and is independent of distance from the duct outlet, r. Furthermore, upwind of the duct outlet from $-85°$ to $-90°$, there is a reduction in sound with increasing distance from the duct outlet r, of up to 3 dB at $r = 32D$. Whereas downwind ($0° \leq \theta \leq 90°$) of the duct outlet, the sound becomes directed towards the ground at increasing distances from the duct. Figure 3.29 also shows that the position of the acoustic cusp is dependent on the distance from the duct outlet r, with the position shifting from 0° at $r = 2D$ to 30° at $r = 32D$. When the jet is heated, these observations become more pronounced.

The steady-state convective effects from the non-isothermal JICF on sound propagation is strongly dependent on the Helmholtz number, ka. Figure 3.30, shows DI at six values of Helmholtz numbers ($ka = [0.3, 0.4, 0.5, 0.6, 0.7, 0.8]$) and at four different radii ($r = [2D, 8D, 16D, 32D]$). The results in Figure 3.30a suggest that in the near-field ($r = 2D$) the sound directivity closely resembles the acoustic directivity pattern of a jet with axisymmetric acoustic spreading and a 'cusp' on-axis. The jet-like directivity pattern is to be expected, as Figure 3.10a shows a jet dominated plume in the near-field region ($r = 2D$). Figures 3.30a, and 3.30b all show a similar feature: a dip in the sound pressure level at approximately 5° to 10° from the duct outlet, and an increase in SPL downwind of the duct outlet. Figures 3.30c, and 3.30d show the most significant change in sound radiation pattern for all the

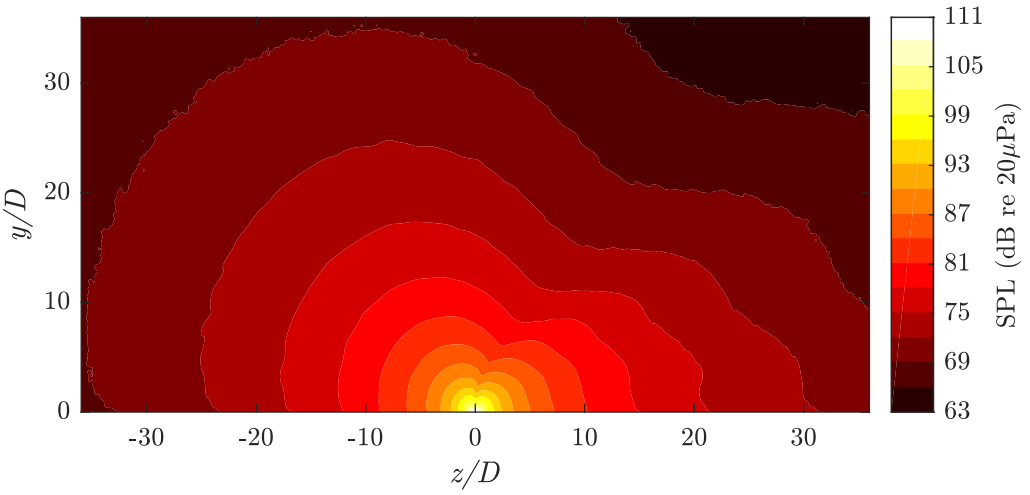

(a) SPL

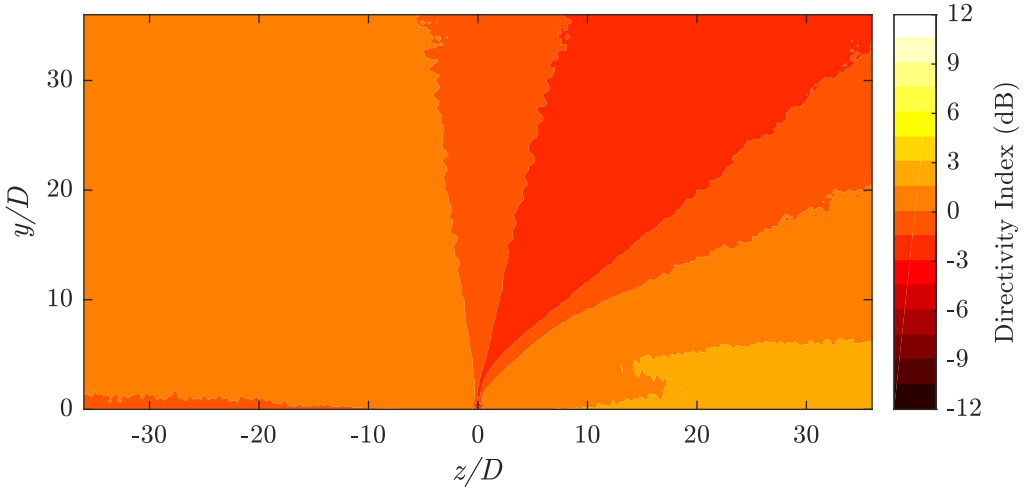

(b) Directivity index

Figure 3.28: Contour plots of (a) the sound pressure level and (b) the DI along the Y-Z plane (of symmetry) for sound propagation through the velocity gradients from a ground-level JICF with $R = 5$, $T_j = 27\,°\text{C}$, $\vec{v}_0(\vec{x}) \neq 0$, and $ka = 0.8$. The cross-flow is from left to right.

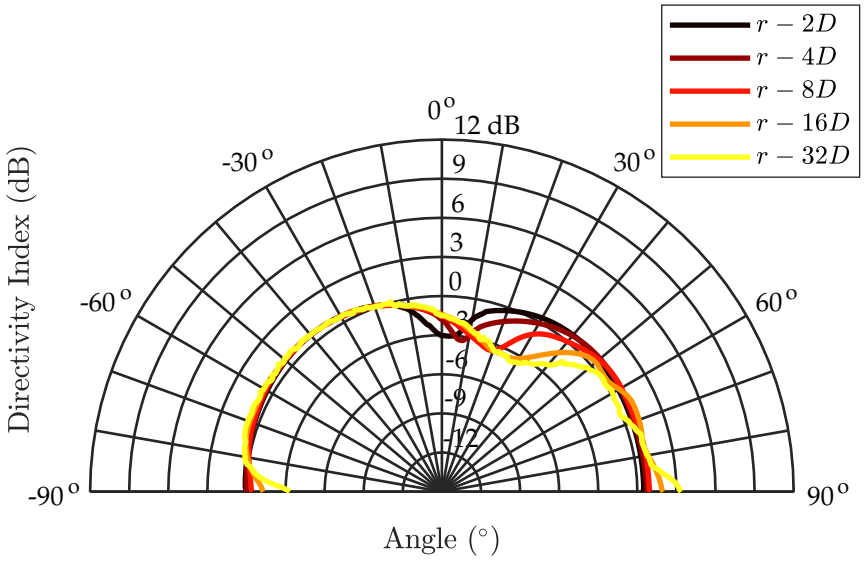

Figure 3.29: The DI at various distances from the duct outlet ($r = [2D, 4D, 8D, 16D, 32D]$) along the Y-Z plane (of symmetry) for sound propagation through isothermal velocity gradients from a JICF with $R = 5$, $T_j = 27\,°C$, $\vec{v_0}(\vec{x}) \neq 0$, and $ka = 0.8$.

values of ka examined in this study. Figures 3.30c, and 3.30d show the largest dips in DI at approximately 20° to 30° from the duct outlet, respectively, and the largest increase in SPL downwind of the duct outlet.

Figure 3.31 shows contour plots of the SPL and DI along ground-level, with the presence of the steady-state convective effects associated with an isothermal JICF. Figure 3.31a shows that the acoustic spreading upwind and downwind is slightly elliptical, with a slight sound increase in the SPL downwind from acoustic refraction, and a slight reduction in SPL upwind of the duct outlet, which is a result of upwards acoustic refraction. The elliptical acoustic spreading results are supported in Figure 3.31b with a negative DI observed upwind and a positive DI downwind. In comparing Figures 3.24b and 3.31b, there is a difference in the position of maximum downwind DI. As discussed in Section, 3.3.2.2, the position of the maximum DI downwind is at the edge of the domain near the centreline, which is different for Figure 3.31b. The maximum DI in Figure 3.31b is at the edge of the domain, which is downwind from where the counter-rotating

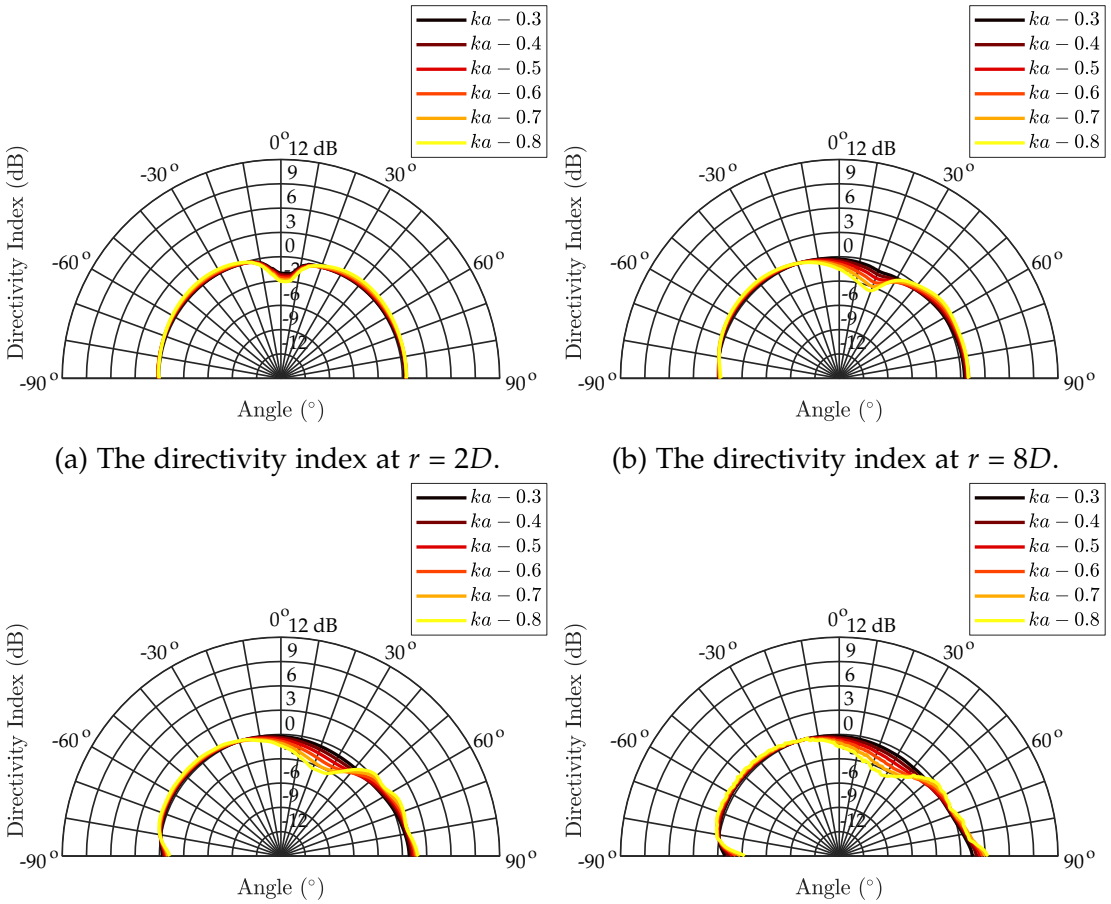

(a) The directivity index at $r = 2D$.

(b) The directivity index at $r = 8D$.

(c) The directivity index at $r = 16D$.

(d) The directivity index at $r = 32D$.

Figure 3.30: The DI at six different Helmholtz numbers ($ka = [0.3, 0.4, 0.5, 0.6, 0.7, 0.8]$) and at four different radii ($r = [2D, 8D, 16D, 32D]$) along the Y-Z plane (of symmetry) for sound propagation through isothermal JICF with $R = 5$, $T_j = 27\,°\text{C}$, and $\vec{v}_0(\vec{x}) \neq 0$.

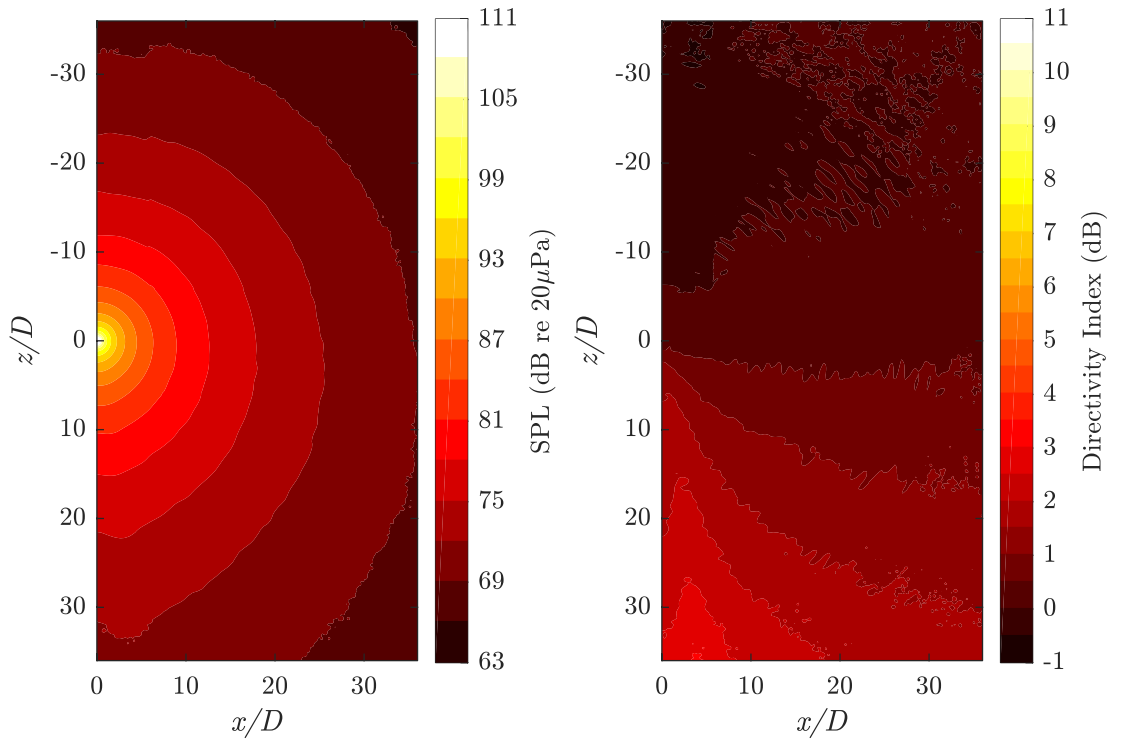

(a) SPL (b) Directivity index

Figure 3.31: Contour plots of (a) sound pressure level and (b) DI along the X-Z plane (ground-level) for sound propagation through the velocity gradients from an isothermal JICF with $R = 5$, $T_j = 27\,^{\circ}\text{C}$, $\vec{v}_0(\vec{x}) \neq 0$, and $ka = 0.8$. The cross-flow is from top to bottom.

vortex would typically reside. In Figures 3.24b and 3.31b, the maximum DI spatial location downwind of the duct outlet can be explained with Figures 3.11e and 3.12e. The velocity gradients from the presence of the counter-rotating vortex and the formation of the vortical structures downwind cause sound to be refracted away from the centreline. The position of sound concentration downwind is positioned directly below the counter-rotating vortex. There is also a significant difference in the magnitude of increased DI downwind of the duct outlet seen in Figures 3.24b and 3.31b, which is mainly due to the difference in the c_{eff} between the thermal gradient and velocity gradients, respectively.

Figure 3.32 shows a contour plot of the DI along a quarter sphere surface at a radius of $32D$. There are some key acoustic features observed in the contour plot

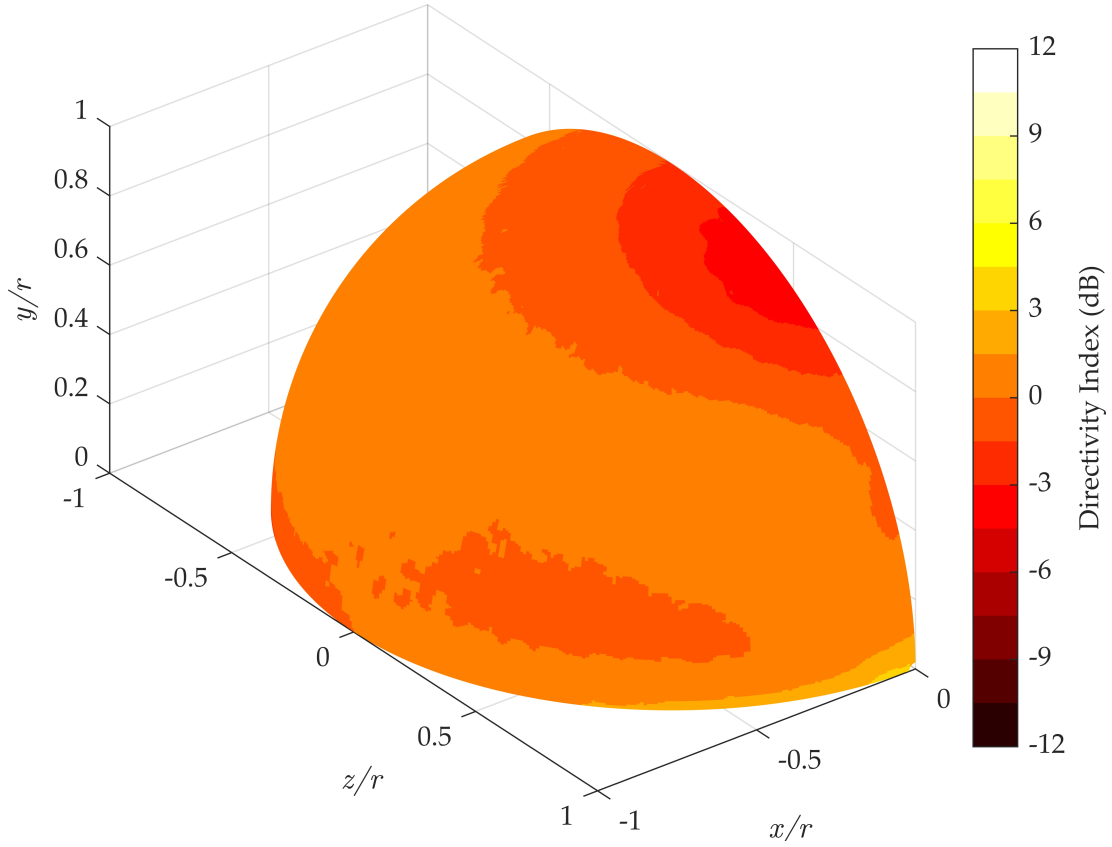

Figure 3.32: The DI contour plot across a spherical surface at a radius of $r = 32D$ for sound propagation through isothermal velocity gradients from a JICF with $R = 5$, $T_j = 27\,°C$, $\vec{v}_0(\vec{x}) \neq 0$, and $ka = 0.8$.

along the spherical surface that are not visible with acoustic contour plots over a plane, which include the following: asymmetric acoustic spreading, region for downwind increase in SPL at the ground-level; an approximately elliptical pressure cusp; and a region of upwind sound reduction. In Figure 3.32, the increase in SPL downwind of the duct exists along the edge of the sphere, at ground-level. The region where SPL has increased in Figure 3.32 is a very narrow band, however it spans a wider ground-level region when compared with Figure 3.25. Another unique feature in Figure 3.32 is the shape of the acoustic cusp, which is an ellipse, whereas the acoustic cusp in Figure 3.25 resembles more of a 'crescent' shape.

The 3-D directivity plot for the case with sound propagation through an isothermal velocity gradient from a JICF has shown both consistent and/or unique

acoustic features seen in other graphical representations of the results. Figure 3.33 shows the 3-D directivity plot at a radius of $r = 32D$, and at $ka = 0.8$. Figure 3.33 shows the following key features seen previously in this section:

- formation of the acoustic lobe downwind of the duct along the ground surface,
- an acoustic cusp on-axis of the duct,
- upwind of the duct there is the presence of upwards sound refraction, and
- above the region of upwards sound refraction upwind of the duct, the sound is approximately spherical.

However, comparing the case with the non-isothermal gradient and the case with the steady-state convective results, shown in Figures 3.26 and 3.33, shows a clear difference in the sound radiation, but in particular the non-axisymmetric sound radiation. However, comparing Figures 3.26 and 3.33 shows the temperature gradients drastically increases the maximum DI, when comparing both 3-D directivity radiation patterns. In summary, Figure 3.26 shows key acoustic features previously observed in this section and an important detail for 3-D directivity plots for acoustic cases that spread approximately spherically.

3.3.2.4 Combining steady-state convective and thermal effects on sound propagation

The acoustic results presented in this section represent steady-state temperature and velocity effects associated with a non-isothermal ground-level JICF. The cases investigated are $R = 5$, $T_j = 500\,°C$, for various ka ([0.3, 0.4, 0.5, 0.6, 0.7, 0.8]) and radial distances (r = [$2D$, $4D$, $8D$, $16D$, $32D$]) from the exhaust stack. The results in this section are presented with the following graphical representation to investigate the complex sound radiation:

- YZ planar contour plots for SPL and DI,

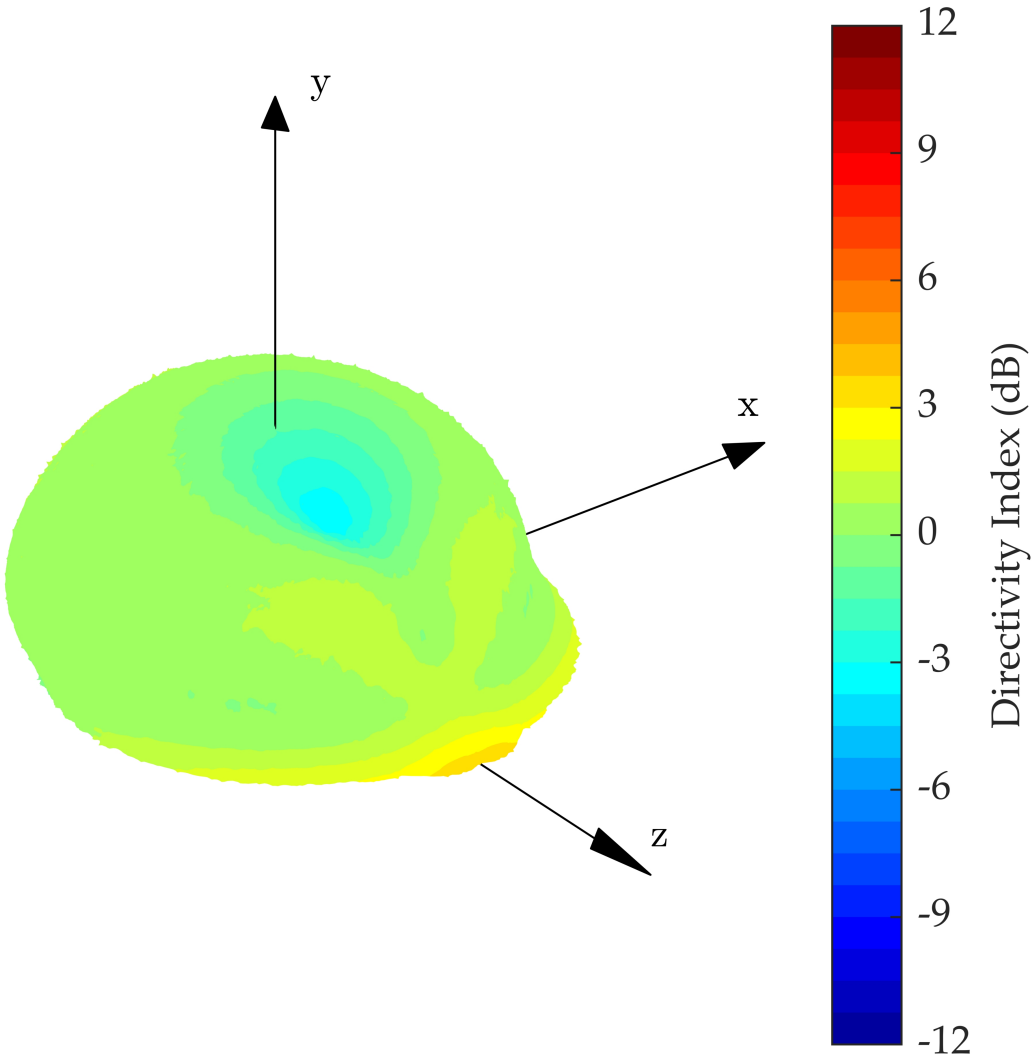

Figure 3.33: The 3-D directivity radiation pattern for sound propagation through the isothermal velocity gradients from a JICF at a radius $r = 32D$ with $R = 5$, $T_j = 27\,°C$, $\vec{v}_0(\vec{x}) \neq 0$, and $ka = 0.8$.

- line directivity polar plots for varying wavenumber (ka = [0.3, 0.4, 0.5, 0.6, 0.7, 0.8]) at four different radii (r = [2D, 8D, 16D, 32D]) in the YZ plane,
- XZ planar contour plots for SPL and DI,
- 3-D DI contour plot over a spherical surface, and
- 3-D directivity radiation pattern.

The key findings for the sound propagation through the medium with both the steady-state temperature and velocity effects associated with non-isothermal ground-level JICF are summarised in this section.

The superposition of the convective and thermal effects on the sound propagation leads to a distinctive sound radiation pattern along the Y-Z plane (of symmetry). Figures 3.34a and 3.34b show contour plots of the SPL and DI along the Y-Z plane (of symmetry), respectively. The results in Figure 3.34a indicate that in the near-field surrounding the duct outlet, the sound spreads spherically, as observed in previous cases found in Sections 3.3.2.2 and 3.3.2.3. As the sound propagates and the plume develops a lobe in the sound field forms (Figure 3.34a). The thermal gradients in the plume are the dominant cause of the increase in SPL downwind of the duct, but the elevated 'beam' of sound observed in Figure 3.21a has now refracted further towards the ground due to the presence of the moving gas flow, as seen in Figure 3.34a. Near the duct centreline axis, a 'cusp' that forms as a result of the shear layer of the deflected plume. In Figure 3.34b, the superposition of the steady-state convective and thermal effects changes both the magnitude and spatial extent of the cusp observed in Figures 3.21b and 3.28b.

Figure 3.35 shows the DI results as a polar plot along the Y-Z plane (of symmetry) at five different radii from the duct outlet (r = [2D, 4D, 8D, 16D, 32D]) and at a ka = 0.8. As discussed previously, at a distance of r = 2D from the duct outlet, the sound has travelled an insufficient distance for fluid-acoustic interaction and a jet dominated plume leads to an approximately axisymmetric sound directivity pattern, which is approximately hemispherical with the exception of a slight 'cusp'

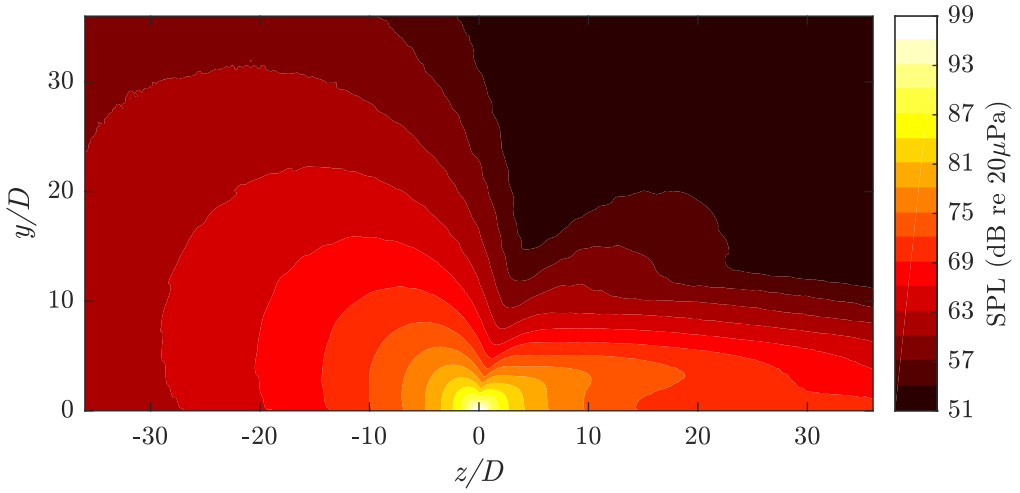

(a) SPL

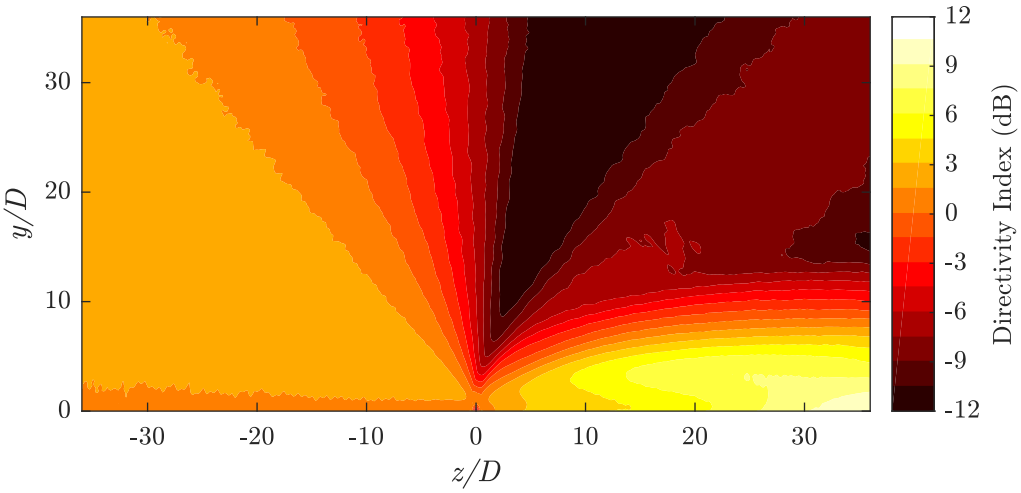

(b) Directivity index

Figure 3.34: Contour plots of (a) the sound pressure level and (b) the DI along the Y-Z plane (of symmetry) for sound propagation through non-isothermal velocity and thermal gradients from a JICF with $R = 5$, $T_j = 500\,°\mathrm{C}$, $\vec{v}_0(\vec{x}) \neq 0$, and $ka = 0.8$. The cross-flow is from left to right. Values of DI less than $-12\,\mathrm{dB}$ are saturated black.

forming. Figure 3.35 shows at $r = 4D$, that the sound has propagated a sufficient distance to interact with the plume and with the acoustic directivity becoming axisymmetric, with a more pronounced 'cusp' at approximately 10°. As the radial distance from the stack outlet the depth of the cusp grows and this acoustic energy is redirected towards the horizontal and predominantly downstream. The directivity at $r = 32D$ show the largest increase in DI of up to 9 dB. Whereas, for the case of only cross-flow (convective effects) there was an increase of 3 dB, and for a high temperature jet there was an increase of 7.5 dB. The increase in DI downwind observed in Figure 3.35 is a result of the plume refracting sound downwards. As previously stated, the effective speed of sound, which governs sound propagation, is mainly influenced by the gas temperature, rather than the steady-state fluid flow, however the superposition of the two terms has led to a significant increase in downwind SPL. Upwind of the duct outlet ($\theta < 0°$) the DI polar plots are approximately elliptical and are observed in Figures 3.22, 3.29, and 3.35. In Figures 3.29, and 3.35, the incoming velocity gradient in the boundary layer causes upwards acoustic refraction upwind of the duct outlet, which reduces the SPL at ground-level.

The sound propagation is also dependent on the Helmholtz number, ka. Figure 3.36 shows the DI results with a polar plot at six Helmholtz numbers ($ka = [0.3, 0.4, 0.5, 0.6, 0.7, 0.8]$) and at four different radial distances ($r = [2D, 4D, 8D, 16D, 32D]$) along the Y-Z plane (of symmetry). In Figure 3.36a, the radiation pattern is approximately spherical, where the sound has not propagated a sufficient distance for it to interact with the plume. The directivity plots in Figures 3.36b, 3.36c, and 3.36d all exhibit the following similar features that are ka dependent: the increase in downwind SPLs, a sound pressure level 'cusp', and upwind elliptical spreading with upwards acoustic refraction at ground-level. The increase in downwind SPL is Helmholtz number dependent, where a ka of 0.8 results in the greatest increase in SPL observed in Figures 3.36b, 3.36c, and 3.36d. The depth of the cusp in the directivity plots at $8D, 16D$ and $32D$ is influenced by ka, with $ka = 0.8$ producing the deepest cusp.

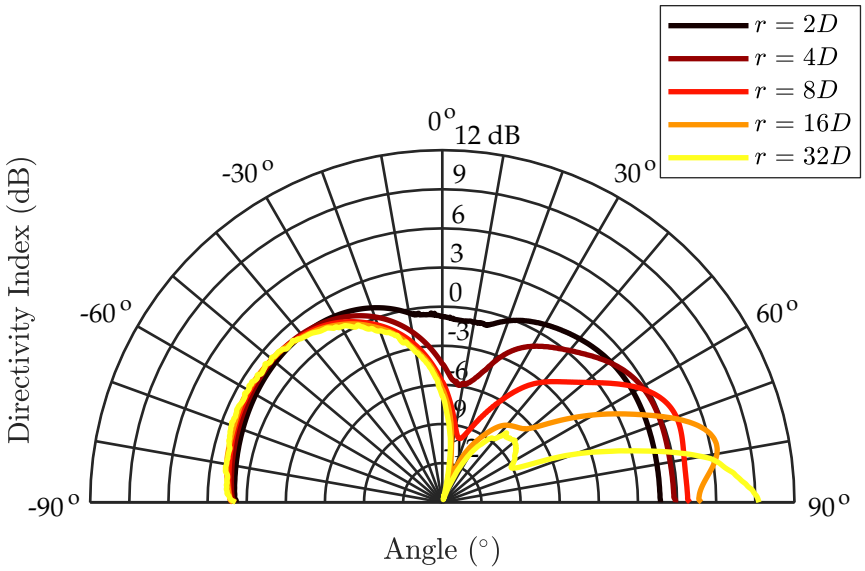

Figure 3.35: The DI at various distances from the duct outlet ($r = [2D, 4D, 8D, 16D, 32D]$) along the Y-Z plane for sound propagation through non-isothermal steady-state convective and thermal gradients from a JICF with $R = 5$, $T_j = 500\,°\text{C}$, $\vec{v_0}(\vec{x}) \neq 0$, and $ka = 0.8$.

Figure 3.37 contains contour plots of the SPL and DI along the ground-level (X-Z plane). Figure 3.37a shows an increase in the downwind SPL similar to Figure 3.24a, and is clearly dominated by the refraction, where the greatest increase in sound level observed is downwind of the exhaust stack, at the bottom left corner of Figure 3.37. This finding is supported by Figure 3.31a, with the sound propagation resembling elliptical spreading, rather than a concentration of sound along the plane of symmetry. In comparing the magnitudes in the DI contour plots for Figures 3.24b, 3.31b, and 3.37b, it can be concluded that the addition of the steady-state convective hot jet in the simulation produced an additional 2 dB in the downwind DI, resulting in a total increase of 11 dB at the limits of the simulation. This is a significant result and means that an observer on the ground, downwind of an exhaust stack, would experience significantly louder sound levels.

Figure 3.38 is the DI contour plot across a spherical surface at a radial distance of $r = 32D$ and is used to illustrate the combined effects of the steady-state convective and thermal gradients from non-isothermal JICF. Figure 3.38 shows that the SPL has

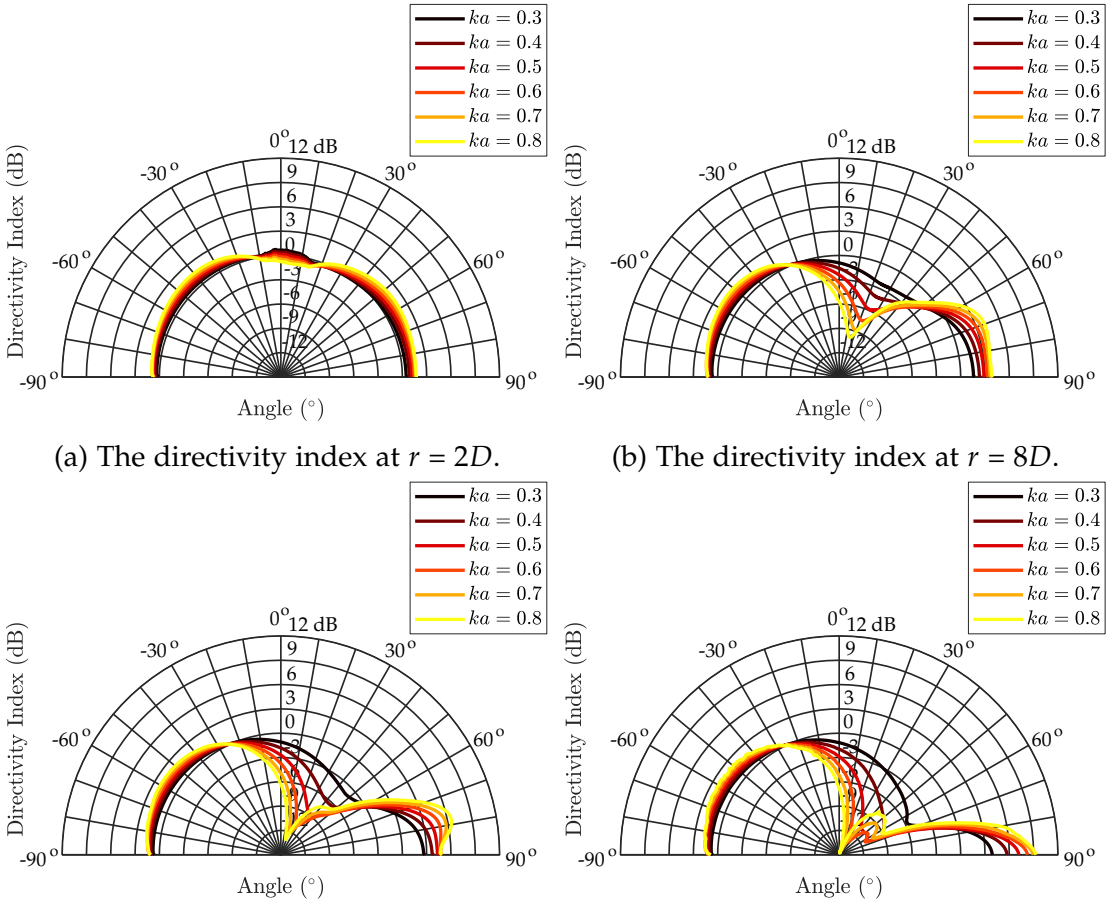

(a) The directivity index at $r = 2D$.

(b) The directivity index at $r = 8D$.

(c) The directivity index at $r = 16D$.

(d) The directivity index at $r = 32D$.

Figure 3.36: The DI at six different Helmholtz numbers ($ka = [0.3, 0.4, 0.5, 0.6, 0.7, 0.8]$) and at four different radii ($r = [2D, 8D, 16D, 32D]$) along the Y-Z plane (of symmetry) for sound propagation through a non-isothermal steady-state convective flow with thermal gradients from a JICF with $R = 5$, $T_j = 500\,°\text{C}$, and $\vec{v_0}(\vec{x}) \neq 0$.

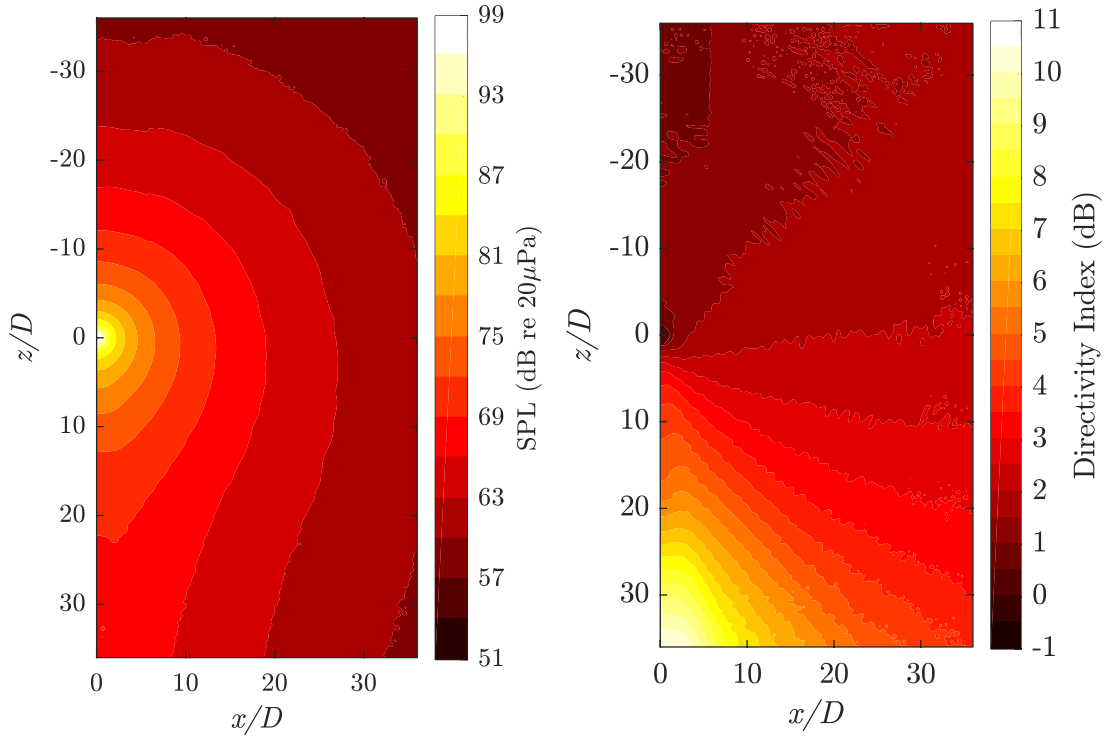

(a) SPL (b) Directivity index

Figure 3.37: Contour plots of (a) the sound pressure level and (b) the DI along the X-Z plane (ground-level) for sound propagation through non-isothermal velocity and thermal gradients from a JICF with $R = 5$, $T_j = 500\,°C$, $\vec{v}_0(\vec{x}) \neq 0$, and $ka = 0.8$. The cross-flow is from the top to the bottom in the Figure.

increased at ground-level downwind of the duct, and the region where the greatest increase in directivity occurs is along the Y-Z plane (of symmetry). The increase in sound along the Y-Z plane (of symmetry) is due to the thermal and velocity gradients associated with the counter-rotating vortex pairs in the plume refracting sound downwards.Even though a single counter-rotating vortex is modelled in Figures 3.11 and 3.12, with the symmetry condition it is expected that there is a counter-rotating vortex pair, as seen in the literature with Figure 2.3. With the counter-rotating vortex pairs there is an increase of sound along the Y-Z plane (of symmetry), where the acoustic energy from the accompanying counter-rotating vortex would contribute. It can be seen in Figure 3.38 that the sound pressure cusp

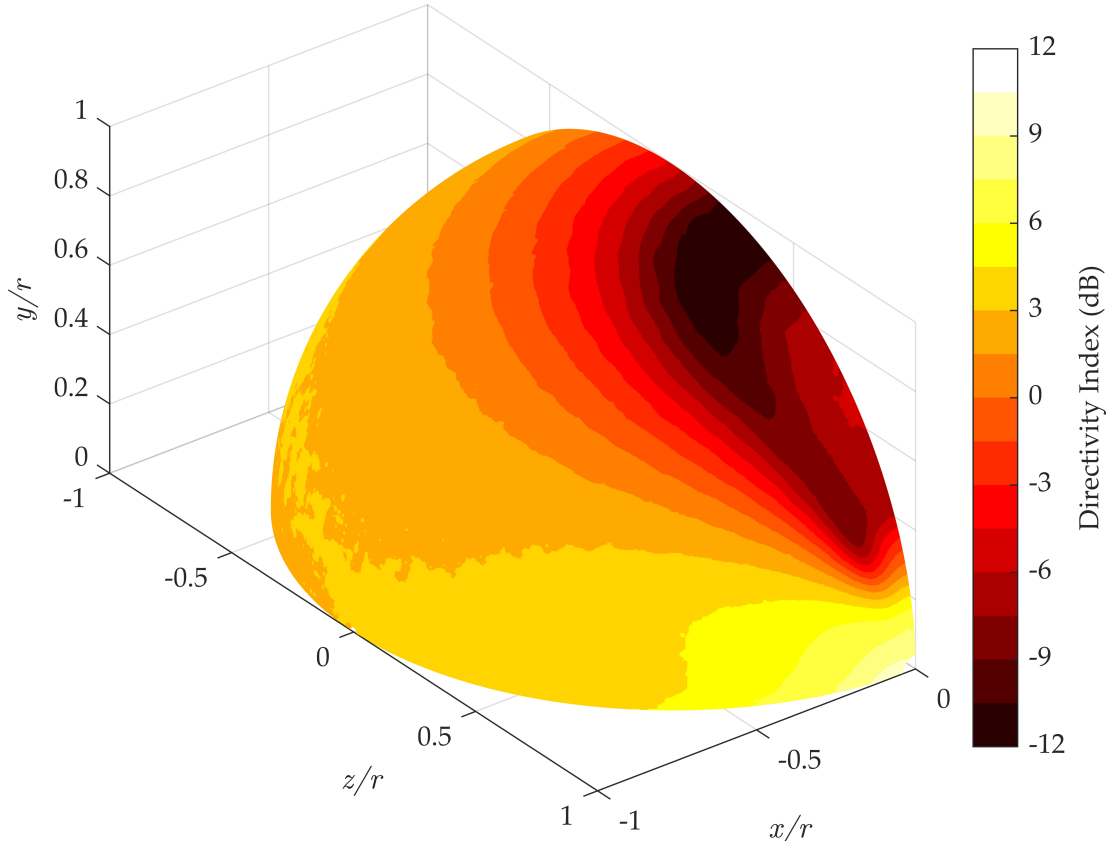

Figure 3.38: The DI contour plot across a spherical surface at $r = 32D$ for sound propagation through non-isothermal JICF with $R = 5$, $T_j = 500\,°\text{C}$, $\vec{v_0}(\vec{x}) \neq 0$, and $ka = 0.8$. The cross-flow is flowing parallel to the Z-axis, towards the negative direction. Values of DI less than $-12\,\text{dB}$ are saturated black.

is in the shape of a crescent that resembles the deflected jet and is caused by the velocity and thermal gradients within the shear layer of the jet.

To complement the contour plot over a sphere in Figure 3.38, the acoustic results are presented with a 3-D directivity radiation pattern to summarise the acoustic features for the case with sound propagation through a non-isothermal JICF. Figure 3.38 shows the 3-D directivity radiation pattern. The key acoustic features seen in Figure 3.38 include:

- downwind of the duct an acoustic lobe has formed along the ground surface,
- an acoustic cusp has formed on-axis of the duct, and

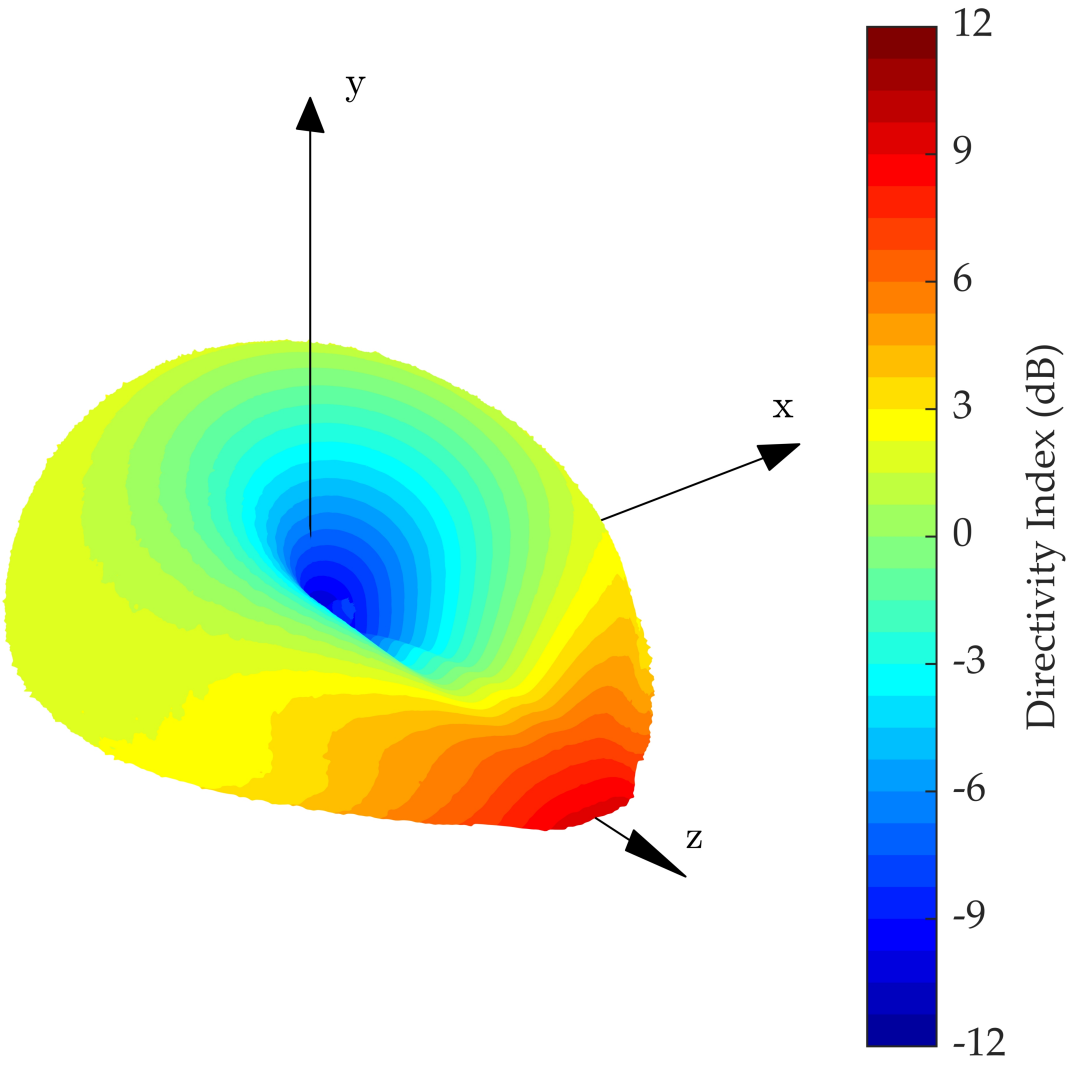

Figure 3.39: The 3-D directivity radiation pattern for sound propagation through non-isothermal JICF at a radius $r = 32D$ with $R = 5$, $T_j = 500\,°C$, $\vec{v_0}(\vec{x}) \neq 0$, and $ka = 0.8$. The cross-flow is flowing parallel to the Z-axis, towards the negative direction. Values of DI less than $-12\,dB$ are saturated dark blue.

- upwind of the duct there is approximately spherical acoustic spreading.

All these acoustic features, also seen in Figure 3.38, are consistent with the results presented in this section.

3.3.2.5 Jet trajectories on sound propagation

The fluid dynamics of the plume itself are sensitive to the incoming cross-flow conditions, which subsequently change the sound propagation. This section investigates the sensitivity of the sound propagation to cross-flow ratio (R = 5 and 7.5) and jet temperature (T_j = 27 °C, 250 °C, and 500 °C). The variation in cross-flow ratio is achieved by altering the cross-flow free stream velocity, whilst keeping the jet velocity and temperature constant. An increase in the cross-flow ratios cause the plume trajectory to increase in height and therefore alters the sound radiation pattern.

The trajectory of the plume is affected by the cross-flow velocity. Figure 3.40 shows the effects of increasing the plume height by increasing R (i.e. reducing the cross-flow velocity) at a distance of $32D$ from the duct outlet. The downwind lobe patterns are clearly visible for T_j = 250 °C and 500 °C, and are elevated ($\theta < 90°$) with increasing values of R. For the case of R = 5, it can be seen that there is a significant increase in sound level downwind of the duct outlet, along the ground-level, but when R increases to 7.5, the acoustic lobe is elevated above ground-level at approximately 70°. It is clear that R has an impact on the angle of the acoustic lobe downwind. The angle of the 'cusp' is around 20° in Figure 3.40, and is also dependent on R. For the two values of R investigated in Figure 3.40, there is a strong relationship between R and the depth of the 'cusp' in the DI polar plot. The increase in jet temperature, T_j, and hence higher thermal gradients, leads to an increase in sound refraction and a deepening in the 'cusp' in Figure 3.40.

Figures 3.41a and 3.41b show the SPL and DI contour along the Y-Z plane (of symmetry), respectively, for a cross-flow ratio of R = 7.5. Figure 3.41a shows that for R = 7.5, a strong lobe in the SPL forms downwind above ground-level. The DI contour results in Figure 3.41b indicate that there is an increase in the downwind SPL occurring above ground-level. It is evident that the refraction of sound downwind continues to the extent of the domain. If the domain in Figure 3.41b were extended, it is expected that the continual refraction of sound would lead to the downwind sound eventually striking ground-level. It can be seen in Figure 3.14 from the CFD study of the jet that when R = 7.5 there is a higher

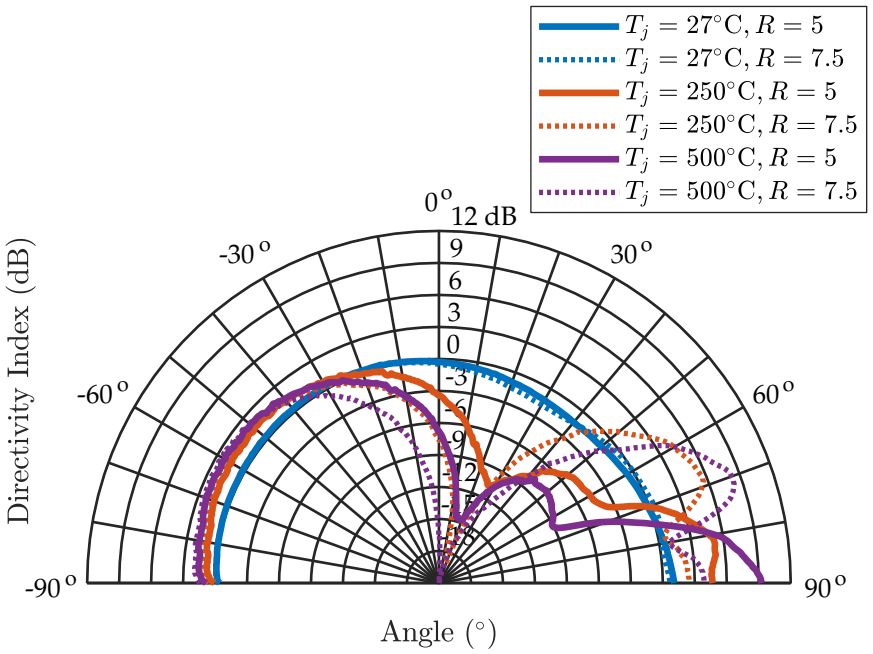

Figure 3.40: The DI at a radius of $32D$ along the Y-Z plane (of symmetry) for sound propagation through non-isothermal JICF with R = [5, 7.5], T_j = [27 °C, 250 °C, 500 °C], $\vec{v_0}(\vec{x}) \neq 0$, and ka = 0.8.

trajectory of the plume, which has prevented the onset of the sound downwind from striking the ground in this domain. Hence, for the cases analysed in this research, it has been shown that the distance from the duct outlet to the region where the SPL has increased significantly at ground-level is influenced by the cross-flow ratio R. This finding will need to be further explained with a larger simulation domain and greater ranges of cross-flow ratios but these are beyond the availability of the super-computing resources for this project.

Figures 3.42a and 3.42b show contour plots of SPL and DI, respectively. The results show that with the higher cross-flow ratio, R = 7.5, in Figure 3.42a, the increase in SPL downwind of the duct outlet along the ground is significantly less than is the case for R = 5 (shown in Figure 3.37a). The difference in ground-level SPL is up to 6 dB, when comparing the DI results from Figures 3.37b and 3.42b. Hence, for the current domain, the increase in cross-flow ratio, R, causes the

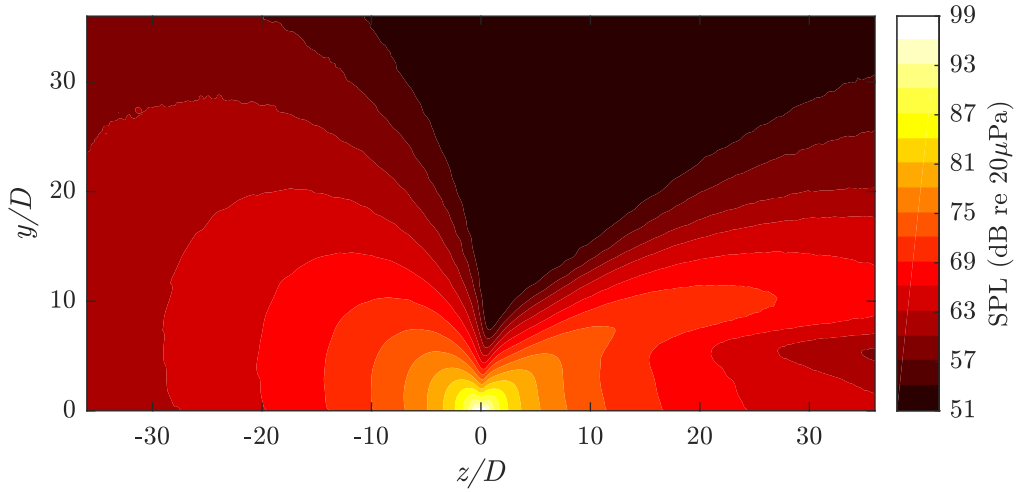

(a) SPL

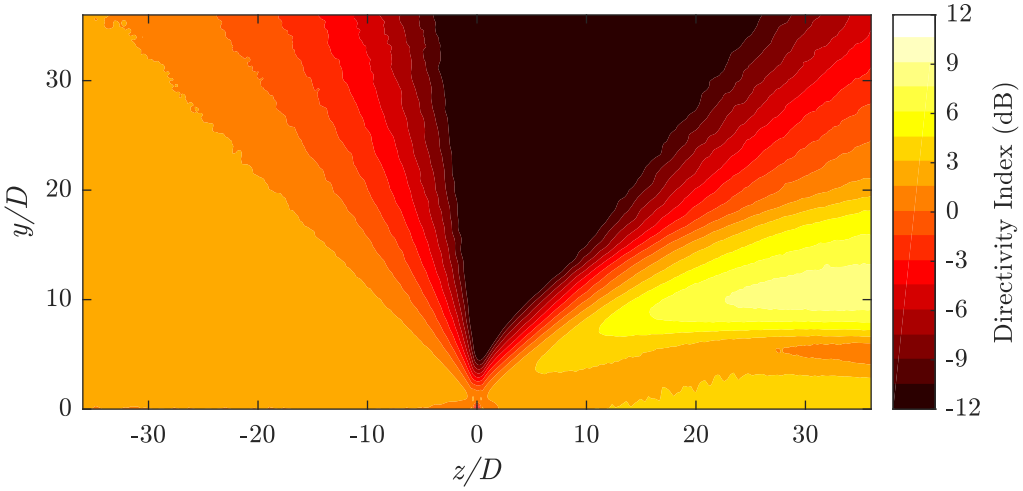

(b) Directivity index

Figure 3.41: Contour plots of (a) sound pressure level and (b) DI along the Y-Z plane (of symmetry) for sound propagation through non-isothermal velocity and thermal gradients from a JICF with $R = 7.5$, $T_j = 500\,°\mathrm{C}$, $\vec{v}_0(\vec{x}) \neq 0$, and $ka = 0.8$. The cross-flow is from left to right in the figure. Values of DI less than $-12\,\mathrm{dB}$ are saturated black.

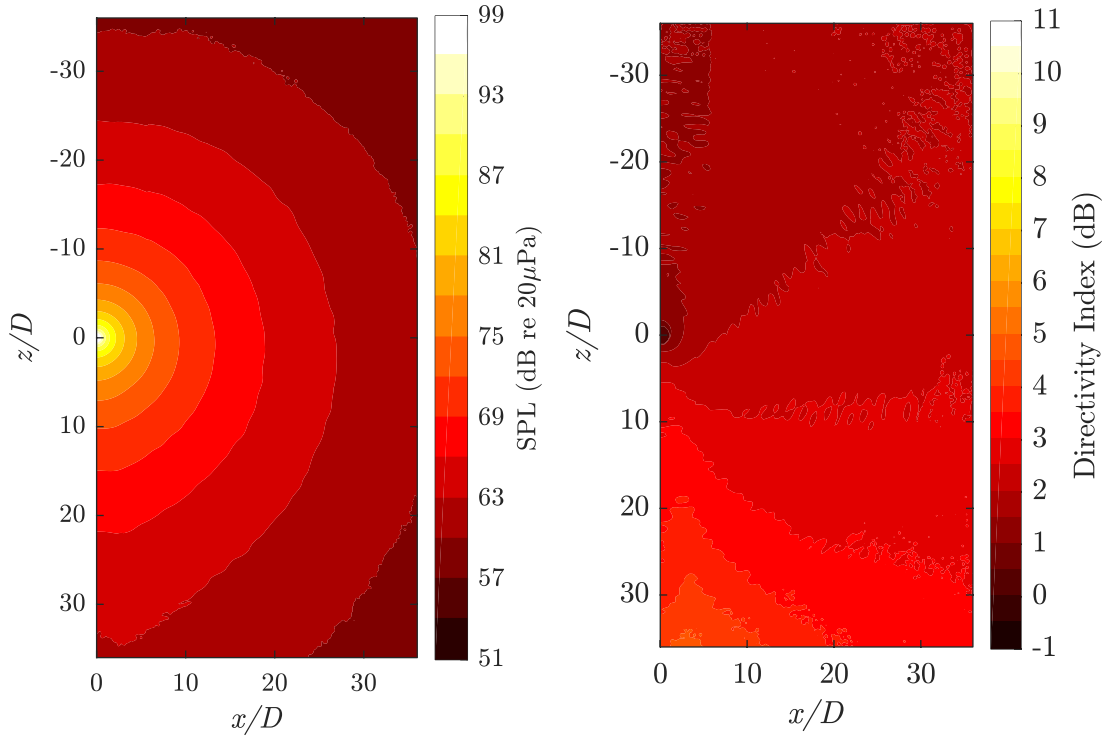

(a) SPL (b) Directivity index

Figure 3.42: Contour plots of (a) the sound pressure level and (b) the DI along the X-Z plane (ground-level) for sound propagation through non-isothermal velocity and thermal gradients from a JICF with $R = 7.5$, $T_j = 500\,°C$, $\vec{v}_0(\vec{x}) \neq 0$, and $ka = 0.8$. The cross-flow is from the top to the bottom in the Figure.

acoustic lobe to be at a higher position, and therefore the SPL on the ground is lower than when compared with a case with a lower cross-flow ratio.

Figure 3.43 illustrates that as the cross-flow ratio, R increases, the trajectory of the plume of hot gas is deflected upwards. The sound that is radiated from the duct exit is refracted by the hot plume and bends the 'rays' of sound towards the ground, causing them to strike the ground. This effect would be problematic for a community, as they would experience an increase in SPLs, compared with the ideal case, if the sound from the exhaust stack had radiated in a spherical pattern. As the cross-flow ratio R increases, it causes the location of the sound ray that strikes the ground to move further downwind from the duct outlet.

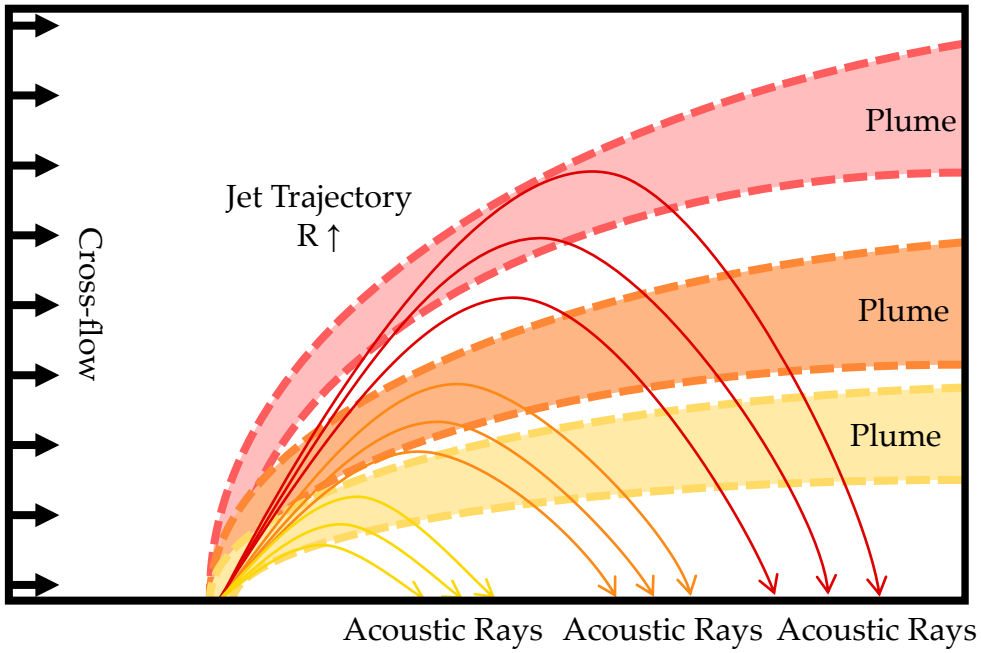

Figure 3.43: Schematic illustrating how the acoustic rays are bent downwards as the cross-flow velocity ratio, R, increases (i.e. the cross-flow velocity decreases).

For real exhaust stacks, the incoming cross-flow conditions and meteorological conditions are variable and more complex, and hence result in unsteady cross-flow ratios. Furthermore, in the area surrounding a real exhaust stack, the ground topology is rough, which causes an unsteady cross-flow. As shown in Section 3.3.1, counter rotating vortex pairs are formed, which refract sound downwards. The combined effects of the dynamic shape of the vortex, the variable incoming cross-flow and meteorological conditions, would cause movement of the downwards travelling ray of sound. A person on the ground would likely experience variations in the SPL over time, which is very annoying.

3.3.3 Elevated jet in cross-flow sound propagation

The numerical results of sound propagation from an elevated JICF are presented in this section. The results will be presented in two parts. The first part is the sound radiation in the absence of the steady-state temperature or fluid flow associated

with the JICF. The subsequent discussion will be the sound radiation through a non-isothermal JICF with steady-state temperature and fluid flow.

3.3.3.1 Sound propagation through an isothermal stationary field

In this section, the numerical sound radiation through the exhaust stack in the absence of the flow associated with the non-isothermal elevated JICF is presented in this section. The effects of varying ground-level boundary conditions ($\alpha_s = 0$ and $\alpha_s = 1$), the sound directivity dependency with distance ($r = [2D, 4D, 8D, 16D, 32D]$), and the sound directivity dependence with frequency $ka = [0.4, 0.5, 0.6, 0.7, 0.8]$ are examined. The acoustic results in this section are presented using 2-D planar contour plots, line polar plots, and 3-D directivity radiation patterns.

Figure 3.44 shows the SPL contour plot for sound radiation along the Y-Z plane of symmetry through an isothermal stationary field at ambient temperature (27 °C). The acoustic frequency for the analysis is $ka = 0.8$. Figure 3.44a shows the SPL with an absorptive boundary condition along the ground surface, whereas Figure 3.44b is a reflective boundary condition. The sound radiation along the along the duct centreline is plane symmetric and there is an acoustic lobe forming on-axis. Figure 3.44a shows that as the sound radiates there is a reduction in sound off-axis, but in particular below the horizontal plane of the duct outlet. The sound radiation in Figure 3.44a does not resemble an axisymmetric monopole source.

Figure 3.44b shows the SPL contour plot along the Y-Z plane of symmetry for sound propagation through an isothermal stationary field, but the boundary condition along the ground-level is a hard reflective surface. The SPL contour plot shows complex sound radiation from the diffraction patterns produced by hard reflective surfaces. Figure 3.44b shows the diffraction pattern is plane symmetric along the duct centreline axis. In comparing Figures 3.44a and 3.44b, the hard reflective surface does not produce an acoustic lobe on-axis; instead, an acoustic null is formed. Additionally, the diffraction pattern in Figure 3.44b shows that the acoustic peaks and cusps are also dependent on the acoustic wavelength. Hence, the sound radiation from an elevated duct with a hard reflective ground-level boundary condition will produce a complex diffraction pattern.

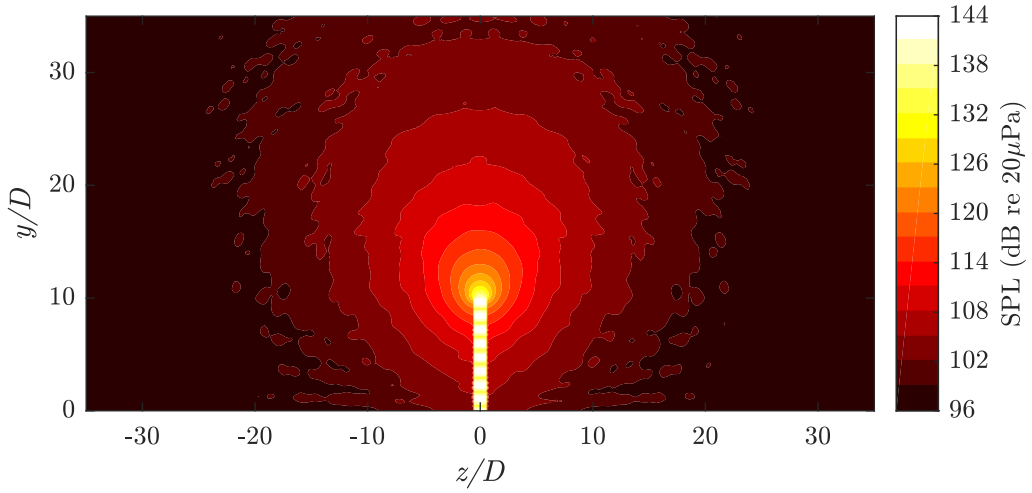

(a) Anechoic ground (α_s = 1)

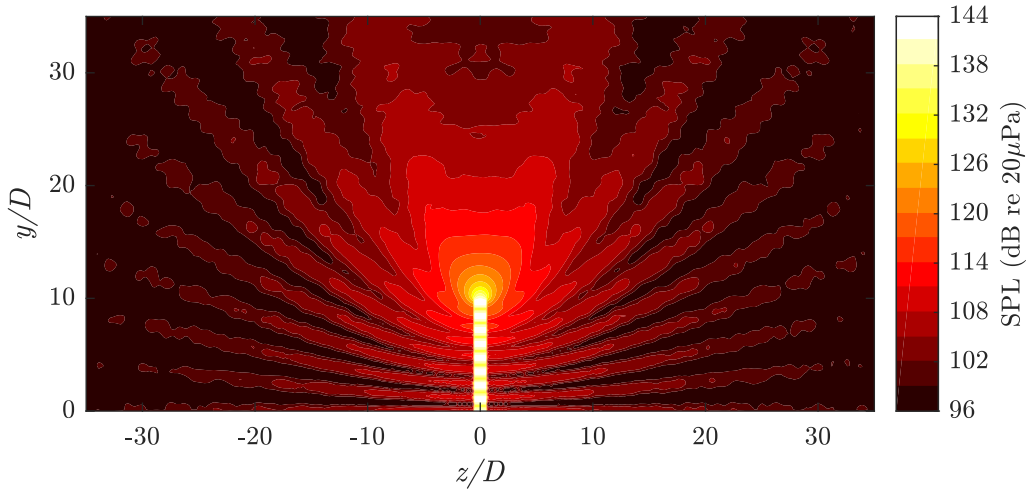

(b) Hard reflective ground (α_s = 0)

Figure 3.44: Elevated JICF contour plots of the sound pressure level with (a) anechoic ground (α_s = 1) and (b) hard reflective ground (α_s = 0) along the Y-Z plane (of symmetry) for sound propagation in an isothermal stationary field, with T_j = 27 °C, $\vec{v_0}(\vec{x})$ = 0, and ka = 0.8. Values less than 48 dB of the maximum sound pressure level are saturated black.

The acoustic results may also be presented as a directivity plot [11]. In Figure 3.45, the acoustic directivity is presented, along with the results, along the Y-Z plane of symmetry through an isothermal stationary field at ambient temperature (27 °C), but with varying radial distance, r, a single frequency, $ka = 0.8$, for the absorptive boundary condition along the ground surface. The acoustic directivity from the outlet of the elevated stack is commonly assumed to be spherical, but this is not the case in Figure 3.45. In Figure 3.45, the acoustic directivity shows an acoustic lobe forming on-axis at 0°, with the DI being approximately 3.5 dB in magnitude. From the sound directivity plots, there is a reduction in sound off-axis, and in particular there is a drastic reduction in sound for angles below the horizontal ($\theta \leq -90°$ and $\theta \geq 90°$).

Furthermore, Figure 3.45 also shows that the sound directivity for $r \leq 8D$ produces smooth directivity results, where as the sound directivity for $r \geq 16D$ shows 'ripples' in the results. The smoother directivity plots for $r \leq 8D$ are due to the fact that at smaller radial distances the number of FEM nodes per acoustic wavelength is much greater than 6, and the sound is yet to propagate far enough to be subjected to the diffraction patterns from the hard reflective duct and refraction from the mesh. In Figure 3.45, for $r \geq 16D$, it is clear that the diffraction pattern has changed the sound radiation, and the reduction of FEM nodes per wavelength has also lead to the reduced accuracy of the numerical results. The effects of reducing the FEM nodes per wavelengths was also observed in Figure 3.18 and discussed in Section 3.3.2.1.

Figure 3.46 shows the sound directivity from the exhaust stack in the absence of the elevated JICF along the Y-Z plane of symmetry with varying radial distances and a hard reflective wall along the ground surface. Comparing Figures 3.45 and 3.46, it is clear that the directivity plots show a drastic difference with different boundary conditions along the ground surface. Figure 3.46 shows the complex diffraction pattern, as a result of a hard reflective ground surface and it is difficult to discern any trends from the results. However, Figure 3.46 shows that the dominant mechanism for sound radiation at $r \geq 8D$ comprises the complex

[11] As a reminder to the reader, when calculating DI for sound radiation from the exhaust stack protruding into the domain, Equation (3.29) was used.

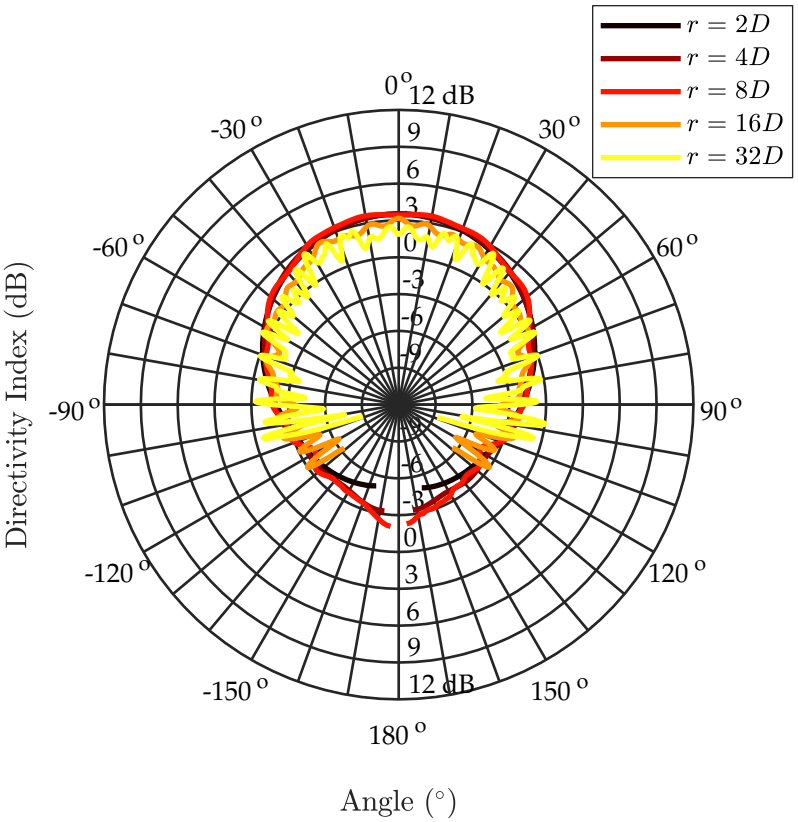

Figure 3.45: The DI at various distances from the duct outlet ($r = [2D, 4D, 8D, 16D, 32D]$) along the Y-Z plane (of symmetry) for sound propagation through an elevated stack in an isothermal stationary field, with the absorptive boundary condition along the ground, where $\alpha_s = 1$, $T_j = 27\,°\text{C}$, $\vec{v_0}(\vec{x}) = 0$, and $ka = 0.8$.

diffraction and reflections from the duct and the hard reflective wall, respectively. Additionally, Figures 3.45 and 3.46, show that on-axis the sound radiation with the absorptive boundary condition produces an acoustic lobe, whereas with the reflective boundary condition the sound directivity shows an on-axis 'null'. Therefore, the hard reflective boundary condition along the ground surface produces a complex directivity pattern, which may cause difficulties in identifying trends in the directivity plots.

The sound directivity of the stack in an isothermal stationary field with an absorptive boundary condition along the ground surface, which is dependent on

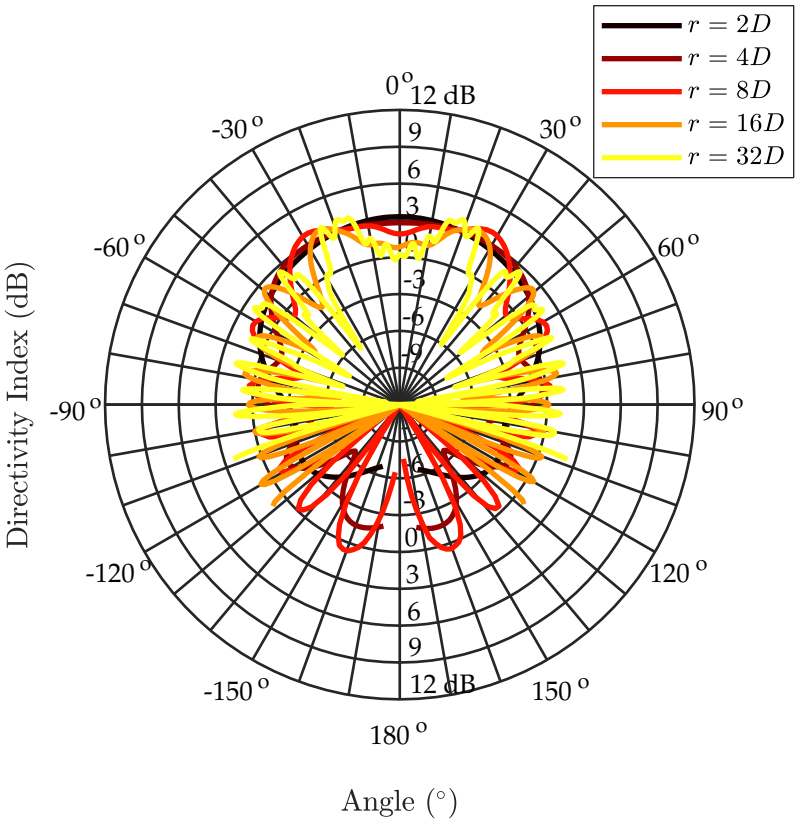

Figure 3.46: The DI at various distances from the duct outlet ($r = [2D, 4D, 8D, 16D, 32D]$) along the Y-Z plane (of symmetry) for sound propagation through an elevated stack in an isothermal stationary field, with a hard reflective boundary condition along the ground, with $\alpha_s = 0$, $T_j = 27\,°\text{C}$, $\vec{v_0}(\vec{x}) = 0$, and $ka = 0.8$.

the acoustic frequency. Figure 3.47 shows the acoustic directivity at four different radii ($r = [2D, 8D, 16D, 32D]$) and each plot contains five different acoustic frequencies ($ka = [0.4, 0.5, 0.6, 0.7, 0.8]$). Figures 3.47a and 3.47b show that the sound directivity at smaller radii ($r \leq 8D$) shows a strong lobe forming on-axis, with the increase in ka. As expected, the increase in ka leads to more directional sound, with the increase in acoustic lobe magnitude on-axis for $r \leq 8D$ and a reduction in off-axis sound. The sound directivity for $r = 16D$ (Figure 3.47c) shows complex sound radiation below the horizontal axis ($\theta \leq -90°$ and $\theta \geq 90°$) with a clear sound diffraction pattern. For Figure 3.47c the sound diffraction pattern or the

'ripples' in the directivity plot is wavelength dependent. Furthermore, as expected with the increase in ka, the sound radiation is more directional on-axis at $r = 16D$. At $r = 32D$ (Figure 3.47d), it can be seen that the increase in ka also leads to the formation of the lobe on-axis, with the increase in DI on axis and the reduction off-axis DI, and is similar to $16D$ (Figure 3.47c). The results for $r = 32D$ and for varying ka lead to the conclusion that either diffraction effects from the duct or the reduction in elements per wavelength are responsible for the 'ripples' in the directivity plots.

For the sake of completeness, the directivity was re-analysed for a hard reflective ground condition and is presented in Figure 3.48. All directivity plots (for each of the four radii) show that the sound radiation is axisymmetric about the duct centreline (0° axis). Figure 3.48a shows that at $r = 2D$, the sound directivity is almost an ideal monopole source in the near-field with a slight discrepancy in this assumption below the horizontal axis ($\theta < -90°$ and $\theta > 90°$), where it can be seen that there is a reduction in DI. Figure 3.48b shows that the directivity at $r = 8D$ is subjected to a complex sound radiation pattern, as a result of diffraction and reflection from the hard reflective walls. The dominant diffraction pattern in the directivity plot is evident from $\theta < -50°$ and $\theta > 50°$. The diffraction pattern is also ka dependent at $r = 8D$ with the angular width of each lobe reducing with increasing ka. Furthermore, on-axis a relatively 'flat' lobe forms, which differs from Figure 3.48a, where a directional lobe forms on-axis. Figures 3.48b and 3.48c, and 3.48d all show similar trends in the directivity plots. Firstly, all three directivity plots with $r \geq 8D$ show that on-axis a directional lobe does not form, and with the increase in r a 'null' actually forms on-axis. Additionally, for $r \geq 8D$ there are complex diffraction patterns that form, with the increase in radii leading to the change in the position of the lobes in the diffraction pattern from $\theta < -50°$ and $\theta > 50°$ to $\theta < -35°$ and $\theta > 35°$. At $r = 32D$ there are also two dominant off-axis lobes forming near on-axis at $\pm 10°$. It should also be noted that at $r = 32D$, the directivity plots are also not smooth for $ka > 0.6$, which is likely to be a result of the following: the FEM element density at this distance is insufficient in resolving the acoustic wave accurately, and/or the scattering from the exhaust duct at the higher

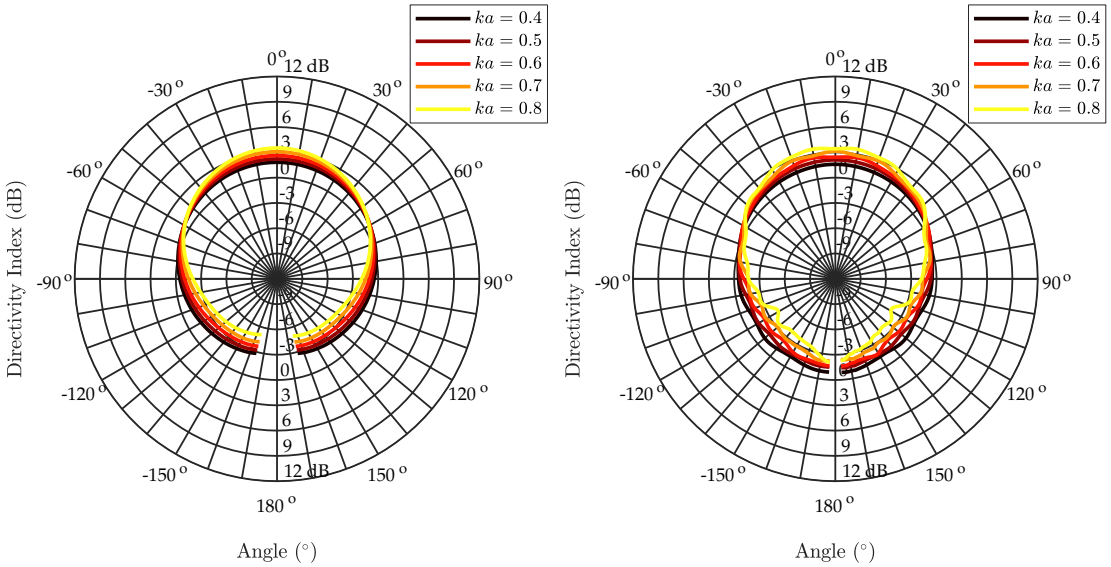

(a) The directivity index at $r = 2D$.

(b) The directivity index at $r = 8D$.

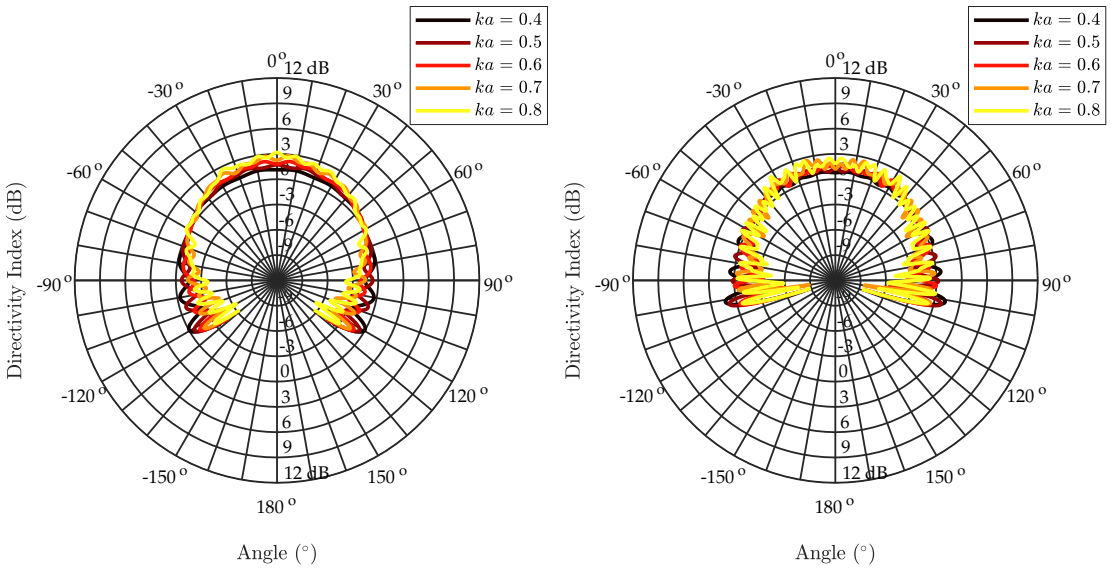

(c) The directivity index at $r = 16D$.

(d) The directivity index at $r = 32D$.

Figure 3.47: The DI at five different Helmholtz numbers ($ka = [0.4, 0.5, 0.6, 0.7, 0.8]$) and at four different radii ($r = [2D, 8D, 16D, 32D]$) along the Y-Z plane (of symmetry) for sound propagation through an elevated stack in an isothermal stationary field, with an absorptive boundary condition along the ground: $\alpha_s = 1$, $T_j = 27\,°\text{C}$, and $\vec{v_0}(\vec{x}) = 0$.

frequencies propagating through as ripples in the directivity plot. Future work will need to be completed with an increase in mesh element density to determine if the ripples are a physical or a numerical artefact but this was not possible with the computing resources available for this project.

The acoustic radiation pattern can be visualised using a 3-D directivity radiation pattern to show additional acoustic features. Figure 3.49 shows the 3-D directivity radiation pattern for sound exiting the stack in an isothermal stationary field with an anechoic ground surface. The results show consistent acoustic trends with the line plots in this section.

Therefore, the sound radiation is axisymmetric about the duct centreline. The radiation is not a monopole, and as expected. There is a concentration of sound on-axis of the duct. It should be noted that the ripples in the results are also consistent with the previous line plots, and, again, further numerical simulations with increased mesh density will need to be conducted.

3.3.3.2 Combining steady-state convective and thermal effects on sound propagation through elevated jets in cross-flow

This section focuses on the sound radiation from a non-isothermal elevated JICF and investigates the effects of distance from the exhaust stack on sound propagation, different ground-level boundary conditions, and the effects of acoustic frequency on the sound radiation. The cases that will be investigated are: a hard reflective ground surface, an absorptive ground surface, $R = 5$, $T_j = 500\,°\text{C}$, $r = [2D, 4D, 8D, 16D, 32D]$, and $ka = [0.4, 0.5, 0.6, 0.7, 0.8]$. Additionally, band-averaged one-third octave results are presented in this section and the need for the broadband results will also be discussed.

Figure 3.50, shows the SPL contour plots for sound radiation along the Y-Z plane of symmetry with two different ground-level boundary conditions; absorptive and hard reflective. Figure 3.50a shows the SPL contour plot with the absorptive boundary condition. It can be observed from Figure 3.50a that in the presence of cross-flow, the sound radiation is no longer axisymmetric along the centreline of the duct. Figure 3.50a shows that there are three key acoustic features for the

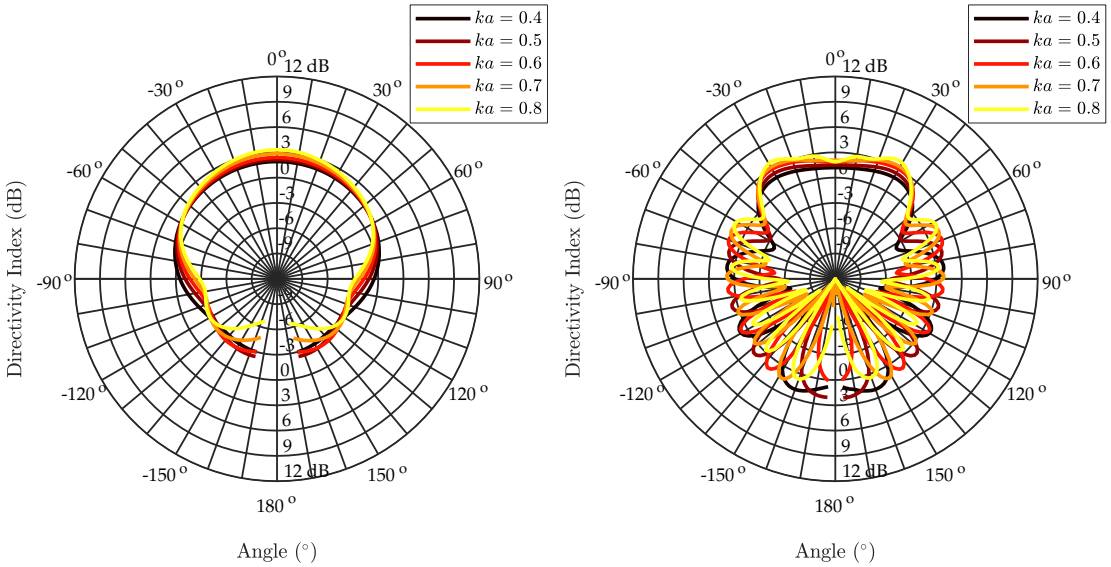

(a) The directivity index at $r = 2D$.

(b) The directivity index at $r = 8D$.

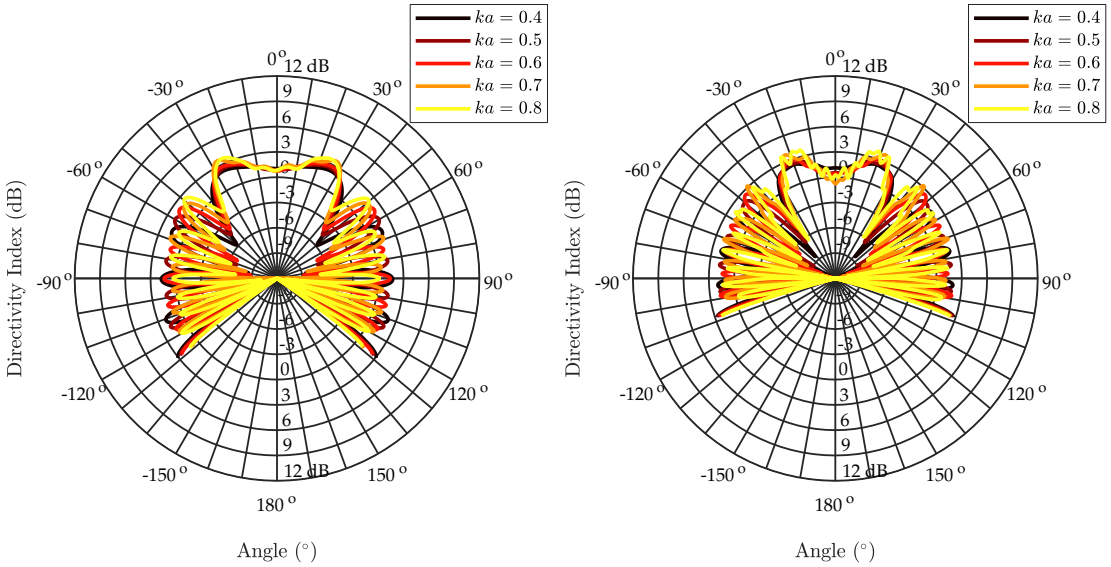

(c) The directivity index at $r = 16D$.

(d) The directivity index at $r = 32D$.

Figure 3.48: The DI at five different Helmholtz numbers ($ka = [0.4, 0.5, 0.6, 0.7, 0.8]$) and at four different radii ($r = [2D, 8D, 16D, 32D]$) along the Y-Z plane (of symmetry) for sound propagation through an elevated stack in an isothermal stationary field, with a hard reflective boundary condition along the ground, $\alpha_s = 0$, $T_j = 27\,°\text{C}$ and $\vec{v_0}(\vec{x}) = 0$.

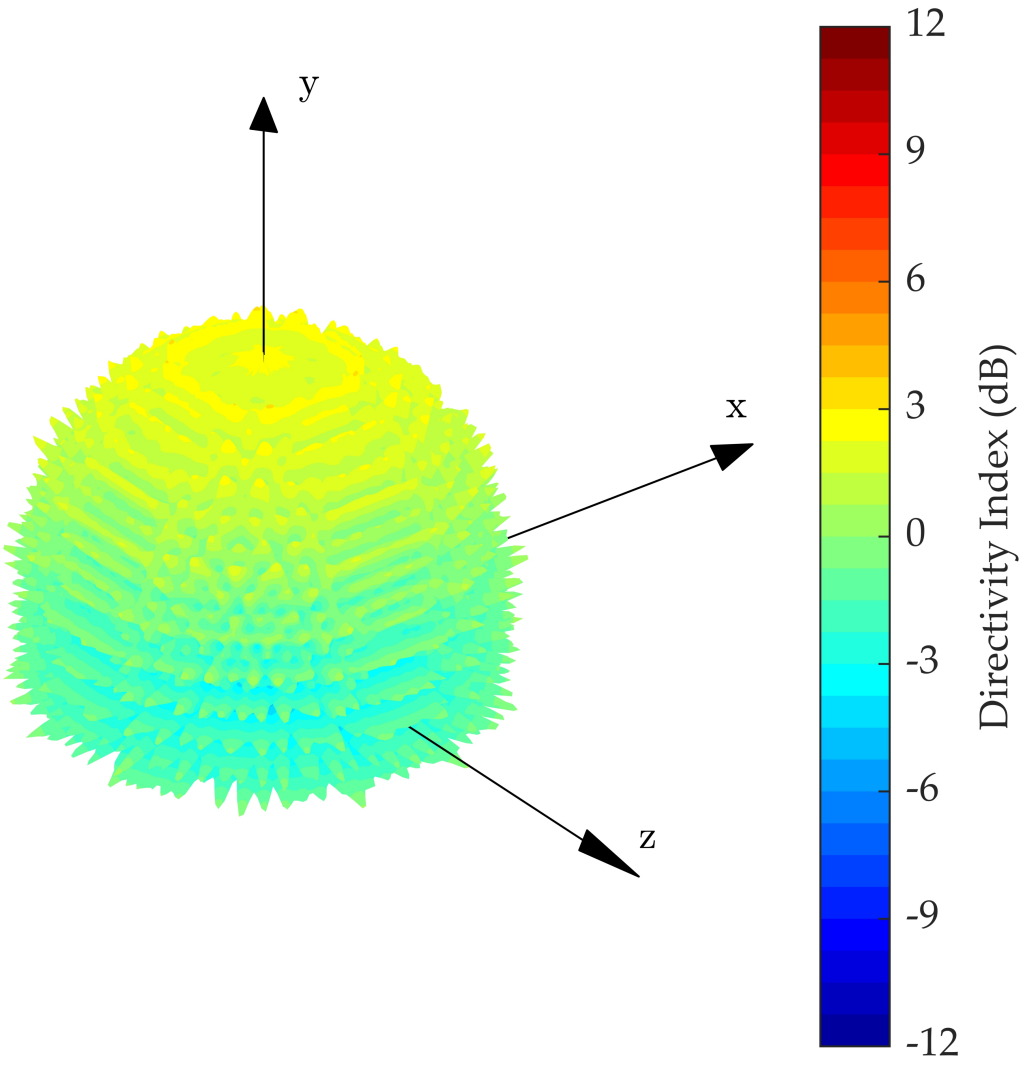

Figure 3.49: The 3-D directivity radiation pattern for sound propagation through an isothermal stationary field at ambient temperature with a stack at a radius $r = 32D$ with $\alpha_s = 1$, $R = 0$, $T_j = 27\,°\mathrm{C}$, $\vec{v_0}(\vec{x}) = 0$, and $ka = 0.8$. Values of DI less than $-12\,\mathrm{dB}$ are saturated dark blue.

SPL contour plots, which are: an acoustic lobe downwind of the exhaust stack, an acoustic cusp near the duct centreline, and a broad acoustic lobe forming upwind of the duct outlet. Downwind of the duct outlet, the interaction of the sound with the steady-state velocity and thermal gradients from the plume (shown in Figures 3.15a and 3.15b), leads to the formation of an acoustic lobe. As the sound propagates downwind from the exhaust stack outlet, it can be seen that the sound lobe becomes more 'narrow' and the trajectory is slowly being refracted downwards. Interestingly, the acoustic lobe downwind in Figure 3.50a resides above the duct outlet with height, $10D$. It should be noted that Figure 3.50a only shows the sound radiation up to $36D$ in the cross-flow free stream direction, but if the domain could be extended, the acoustic lobe downwind will continue to refract and would lead to a more concentrated and narrow lobe, eventually refracting to strike the ground. Near the duct centreline, it can be seen that there is the formation of a cusp. Upwind of the duct axis, the sound radiation pattern is elliptical, and due to the absence of the thermal and velocity gradients from the plume, the sound is not concentrated as a lobe.

Figure 3.50b presents the same system as Figure 3.50a, but for reflective ground. Figures 3.50a and 3.50b show that the ground-level boundary condition alters the sound radiation drastically. In Figure 3.50b there is a complex diffraction pattern in the SPL contour plot, which is similar to the SPL diffraction pattern of the isothermal system in Figure 3.44b. However, Figure 3.50b shows that with the presence of the thermal velocity gradients associated with the elevated JICF there is downwind refraction occurring, with an acoustic lobe forming above the horizontal plane of the exhaust duct outlet. Figures 3.44b and 3.50b also show that the horizontal plane below the duct outlet exhibits the same acoustic diffraction pattern. Furthermore, upwind of the duct outlet, both Figures 3.44b and 3.50b show almost identical diffraction patterns. The acoustic reflection pattern is dominant upwind of the duct outlet for Figure 3.50b and the off-axis lobe seen in Figure 3.50a is almost unobservable. The acoustic cusp seen in Figure 3.50a is also present in Figure 3.50b. Hence, whilst the hard wall boundary condition along the ground surface does change the sound radiation through non-isothermal elevated

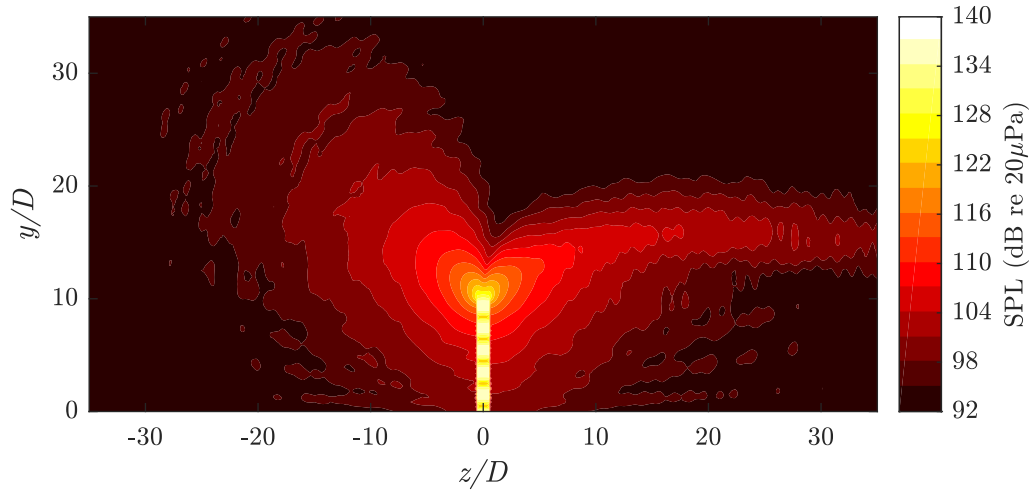

(a) Anechoic ground ($\alpha_s = 1$)

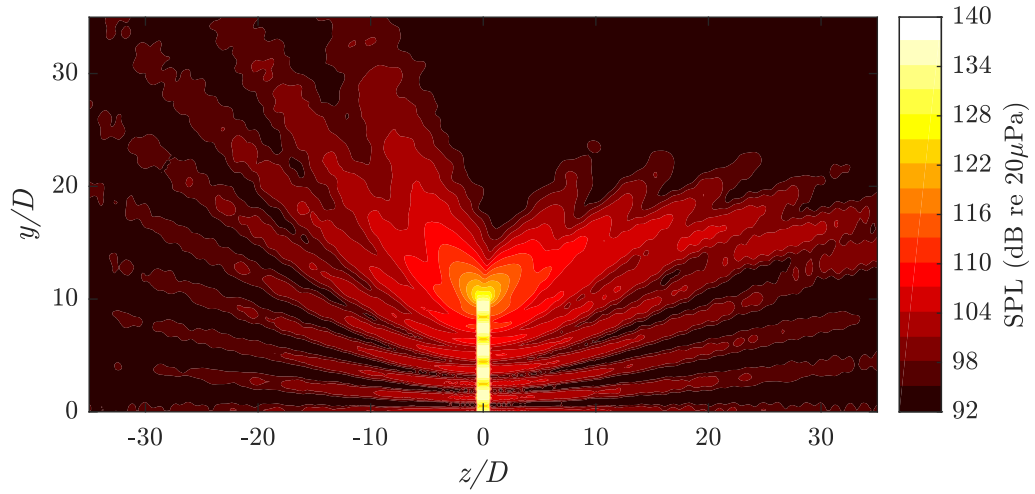

(b) Hard reflective ground ($\alpha_s = 0$)

Figure 3.50: Elevated JICF contour plots of the sound pressure levels with (a) anechoic ground ($\alpha_s = 1$) and (b) hard reflective ground ($\alpha_s = 0$) along the Y-Z plane (of symmetry) for sound propagation through non-isothermal velocity and thermal gradients from a JICF with $R = 5$, $T_j = 500\,°\text{C}$, $\vec{v}_0(\vec{x}) \neq 0$, and $ka = 0.8$. The cross-flow is from left to right in the figure. Values less than 48 dB of the maximum SPL are saturated black.

JICF, some key acoustic features in the SPL contour plots are consistent across Figures 3.44b, 3.50a, and 3.50b.

The results in Figure 3.51 show the mean normalised acoustic directivity at different radii, with the presence of the non-isothermal elevated JICF thermal gradients and velocity gradients at a $ka = 0.8$. The Figure shows that the acoustic directivity results are radii dependent. The acoustic directivity at $r = 2D$ shows that the sound is approximately axisymmetric, with a cusp forming along the duct centreline and acoustic lobes forming off-axis. This is similar to the acoustic directivity produced for sound propagation through non-isothermal jets, as seen previously in Atvars et al. [14, 15] and is reproduced in Figures 2.5a and 2.5b. The results at $r = 2D$ are to be expected, as the plume in this region is 'jet-dominant' in the near-field before interaction with the cross-flow. In Figure 3.51, the acoustic directivity for $r > 2D$ shows that the sound radiation is asymmetric. Figure 3.51 shows that at approximately 35° to 80°, there is an acoustic lobe forming downwind which is dependent on the radial distance. As the radius, r, increases, the acoustic directivity plots show an increase in the magnitude of the acoustic lobe from 3.5 dB at $r = 8D$ to 9 dB at $r = 32D$, and a change in the acoustic lobe position from 60° to 80°. Additionally, the width of the acoustic lobe downwind is also radial position dependent with the increase in r leading to a narrower lobe, with the lobe width reducing from 60° at $r = 8D$ to 15° at $r = 32D$. The change in the acoustic lobe behaviour downwind, while radial distance is caused by the sound interacting with the thermal and velocity gradients in the spatially growing plume, leading to enhanced acoustic refraction. This same behaviour is observed in Figure 3.50a. Figure 3.51 shows that upwind of the duct outlet the sound radiation is elliptical, with the sound radiation pattern almost being almost identical for $r > 2D$.

The hard reflective boundary condition along the ground surface throughout this chapter for the elevated JICF has shown a complex sound radiation pattern, and for Figure 3.52 the directivity results show a similar trend. Comparing Figures 3.51 and 3.52 the results show similar trends, with three key distinct features: the downwind acoustic lobe, upwind elliptical spreading and the acoustic cusp. However, Figures 3.51 and 3.52 also show that the hard reflective ground surface

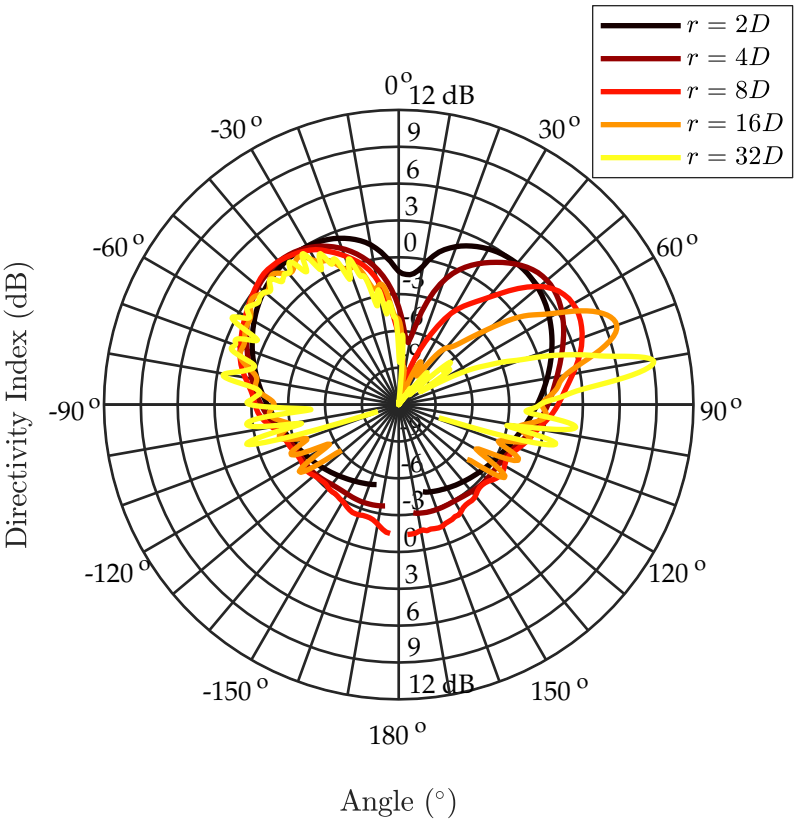

Figure 3.51: The DI at various distances from the duct outlet ($r = [2D, 4D, 8D, 16D, 32D]$) along the Y-Z plane (of symmetry) for sound propagation through a non-isothermal steady-state convective flow with thermal gradients from an elevated JICF with an absorptive boundary condition along the ground: $\alpha_s = 1$, $R = 5$, $T_j = 500\,°C$, $\vec{v_0}(\vec{x}) \neq 0$, and $ka = 0.8$.

makes it more difficult to observe key features. The directivity plot in Figure 3.52 shows that with an increase in r, the depth of the 'null' at approximately 0° increases, which is similar to the results in Figure 3.51. Figures 3.51 and 3.52 show a similar trend downwind, with the increase in r from $2D$ to $32D$ leading to an increase in the angular position of the acoustic lobe downwind from 45° to 80°, respectively. Figure 3.52 shows that upwind of the stack, the dominant mechanism in the acoustic radiation plot is a reflection from the hard reflective surfaces and not an elliptical lobe, as seen in Figure 3.52. Hence, Figures 3.51 and 3.52 show that, despite the ground-level boundary conditions, there are similar trends resulting

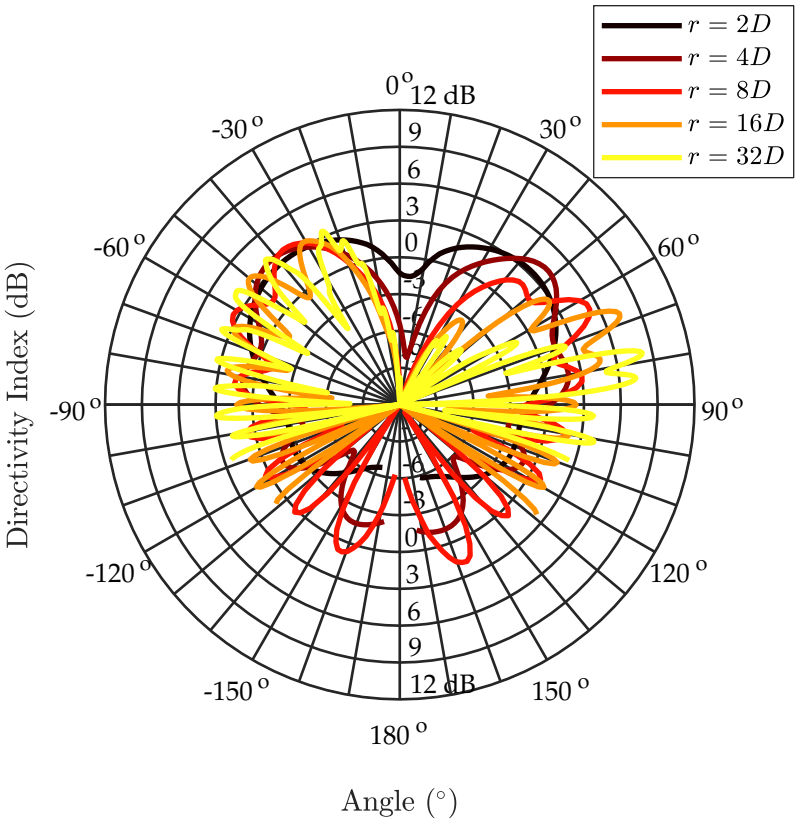

Figure 3.52: The DI at various distance from the duct outlet ($r = [2D, 4D, 8D, 16D, 32D]$) along the Y-Z plane (of symmetry) for sound propagation through a non-isothermal steady-state convective flow with thermal gradients from an elevated JICF with a hard reflective boundary condition along the ground, $\alpha_s = 0$, $R = 5$, $T_j = 500\,°C$, $\vec{v_0}(\vec{x}) \neq 0$, and $ka = 0.8$.

from the sound propagating through the thermal and velocity gradients associated with a non-isothermal elevated JICF.

Figure 3.53 shows the acoustic directivity results for sound propagation through non-isothermal elevated JICF, with thermal and velocity gradients, with varying acoustic frequencies ($ka = 0.4$-0.8) and at four different radii ($r = [2D, 8D, 16D, 32D]$). It is evident in Figure 3.53 that the sound directivity plots are frequency dependent. Figure 3.53a shows that for $r = 2D$ the sound directivity is almost independent of the acoustic frequency, as insufficient distance

has propagated for the sound to interact with the velocity and thermal gradients from the plume.

Figures 3.53b, 3.53c, and 3.53d show the sound directivity for $r \geq 8D$ is acoustic frequency dependent, with three key acoustic features being drastically affected: the downwind acoustic lobe, upwind elliptical spreading and the depth of the acoustic cusp. The directivity plots show that an increase in the acoustic frequency leads to the following:

- an increase in the DI magnitude of the acoustic lobe observed downwind of the duct,
- a slight increase in the angular position of the acoustic lobe downwind,
- an increase in the depth of the acoustic cusp seen on-axis of the duct, and
- upwind of the duct the acoustic radiation remains relatively unchanged.

Figure 3.53 shows that the highest ka, $ka = 0.8$, and $r = 32D$ has the greatest asymmetry in the directivity plot. Future numerical studies, with greater computational capabilities, should investigate the sound directivity for $ka > 0.8$ to observe if the trends listed are consistent with higher ka. Additionally, a larger computational domain should be explored to investigate the effects of distance on the directivity plots with the increase in ka.

The previous directivity plots were for results at discrete frequencies and consequently exhibited ripples due to several factors including diffraction from the stack, reflection from the ground and uneven propagation due to the mesh itself. These effects can be reduced by averaging the results over several discrete frequencies. To illustrate this, the acoustic results can be further processed by averaging the SPL over five discrete frequencies to produce a band-averaged one-third octave result using either of the following formulations:

$$\mathrm{DI}(\theta) = 10\log_{10}\left(\frac{1}{n}\sum_{i=1}^{n}\frac{p^2_{\mathrm{rms,i}}(\theta)}{p^2_{av,i}}\right), \tag{3.39}$$

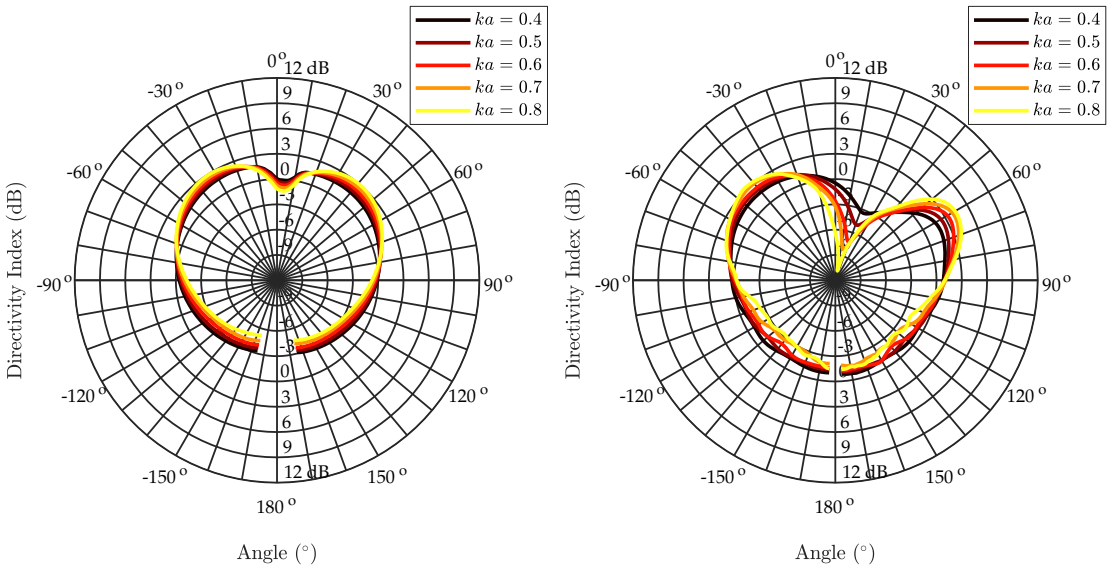

(a) The directivity index at $r = 2D$.

(b) The directivity index at $r = 8D$.

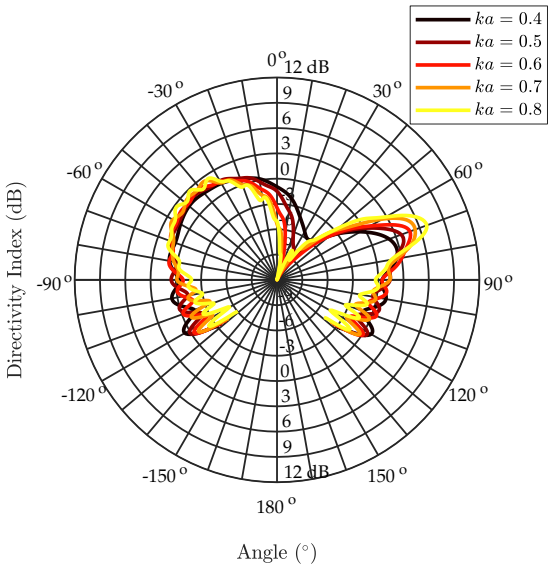

(c) The directivity index at $r = 16D$.

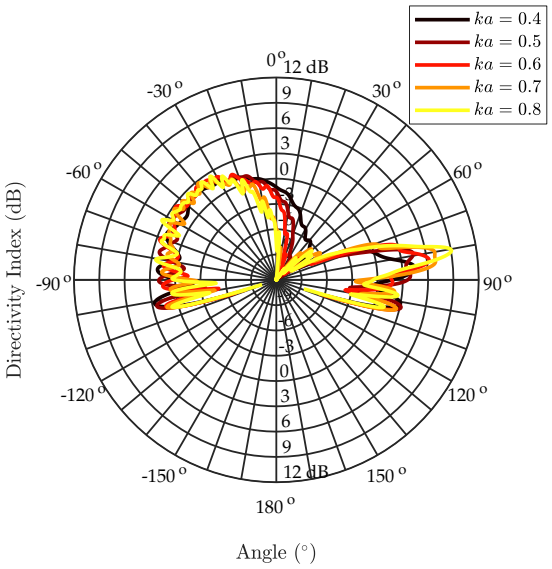

(d) The directivity index at $r = 32D$.

Figure 3.53: The DI at five different Helmholtz numbers ($ka = [0.4, 0.5, 0.6, 0.7, 0.8]$) and at four different radii ($r = [2D, 8D, 16D, 32D]$) along the Y-Z plane (of symmetry) for sound propagation through a non-isothermal steady-state convective flow with thermal gradients from an elevated JICF with an absorptive boundary condition along the ground: $\alpha_s = 1$, $R = 5$, $T_j = 500\,°\text{C}$, and $\vec{v}_0(\vec{x}) \neq 0$.

$$\mathrm{DI}(\theta) = 10\log_{10}\left(\frac{\sum_{i=1}^{n} p^2_{\mathrm{rms,i}}(\theta)}{\sum_{i=1}^{n} p^2_{av,i}}\right), \tag{3.40}$$

where n is the number of discrete frequencies for the average, $p_{a,i}$ is the acoustic pressure at a point for a discrete frequency, and $p^2_{av,i}$ is the average squared acoustic pressure along the directivity arc for a discrete frequency. Equation (3.39) was chosen as the preferred method for the band-averaged one-third octave band acoustic results, as the results for each frequency is weighted evenly, and neglect any discrepancy with the $p^2_{av,i}$ along each arc. The difference in $p^2_{av,i}$ for each frequency could be from the following: multi-modal responses for sound propagation through a duct with ka near one, different radiated acoustic powers from the impedance response at the duct outlet, and different acoustic powers into the model from using a harmonic acoustic velocity source with uniform amplitude along the duct inlet. Figure 3.54 shows the 3.15 kHz one-third octave band (ka = 0.85) averaged acoustic directivity for sound propagation through a non-isothermal elevated JICF, with an absorptive boundary condition for the ground surface. The results in Figure 3.54 and 3.51 show a large degree of similarity for the acoustic directivity plots, even though the results are for a tone in Figure 3.51 and band averaged for Figure 3.54. Ideally, all tonal results presented earlier in the chapter would have been represented as band-averaged one-third octave band results, but this was computationally prohibitive and does not change the outcomes or conclusion presented.

Previous plots in this section are 2-D planar contour plots and line plots, but the results can be visualised using a 3-D directivity radiation pattern to show additional acoustic features. Figure 3.55 shows the 3-D directivity radiation pattern for the sound radiation through the velocity and thermal gradients from a non-isothermal elevated JICF with an anechoic ground surface, at ka = 0.8. The 3-D acoustic visualisation has reproduced key acoustic features seen previously in this section and can be summarised as the following:

- the sound radiation is complex and non-axisymmetric,

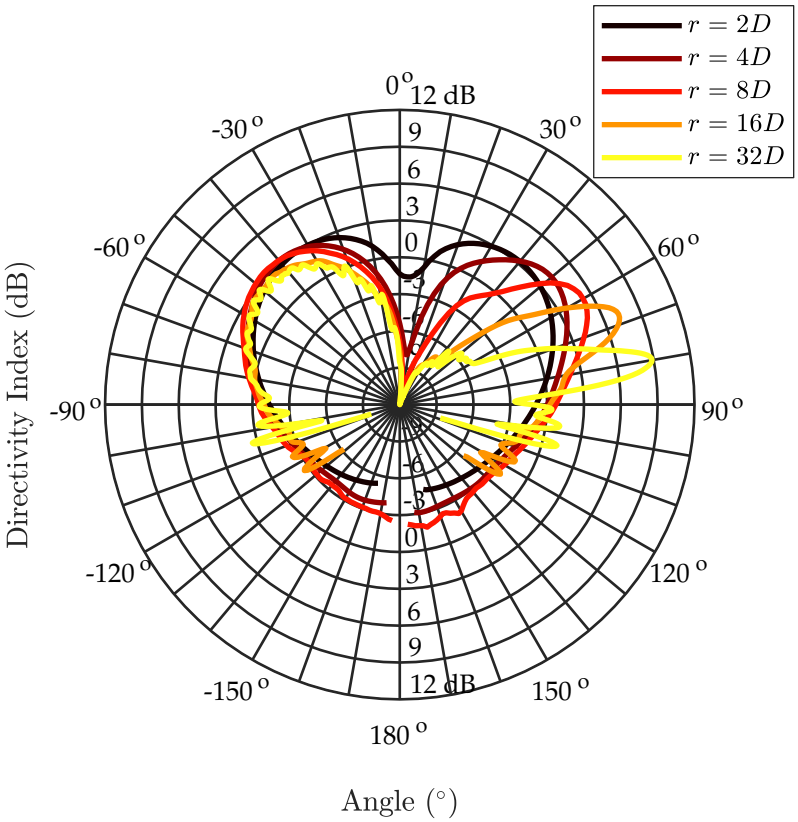

Figure 3.54: The DI at various distances from the duct outlet ($r = [2D, 4D, 8D, 16D, 32D]$) along the Y-Z plane (of symmetry) for sound propagation through a non-isothermal steady-state convective flow with thermal gradients from an elevated JICF with an absorptive boundary condition along the ground: $\alpha_s = 1$, $R = 5$, $T_j = 500\,°\text{C}$, and $\vec{v_0}(\vec{x}) \neq 0$. Five tones are band averaged over a one-third octave band of 3.15 kHz ($ka = 0.85$).

- an acoustic lobe is formed downwind of the exhaust stack from the refraction of sound through the shear layer,
- the acoustic lobe observed downwind of the exhaust stack is elevated off the ground surface,
- an acoustic cusp has formed near the central axis of the duct, and
- upwind of the exhaust stack the sound is approximately uniform.

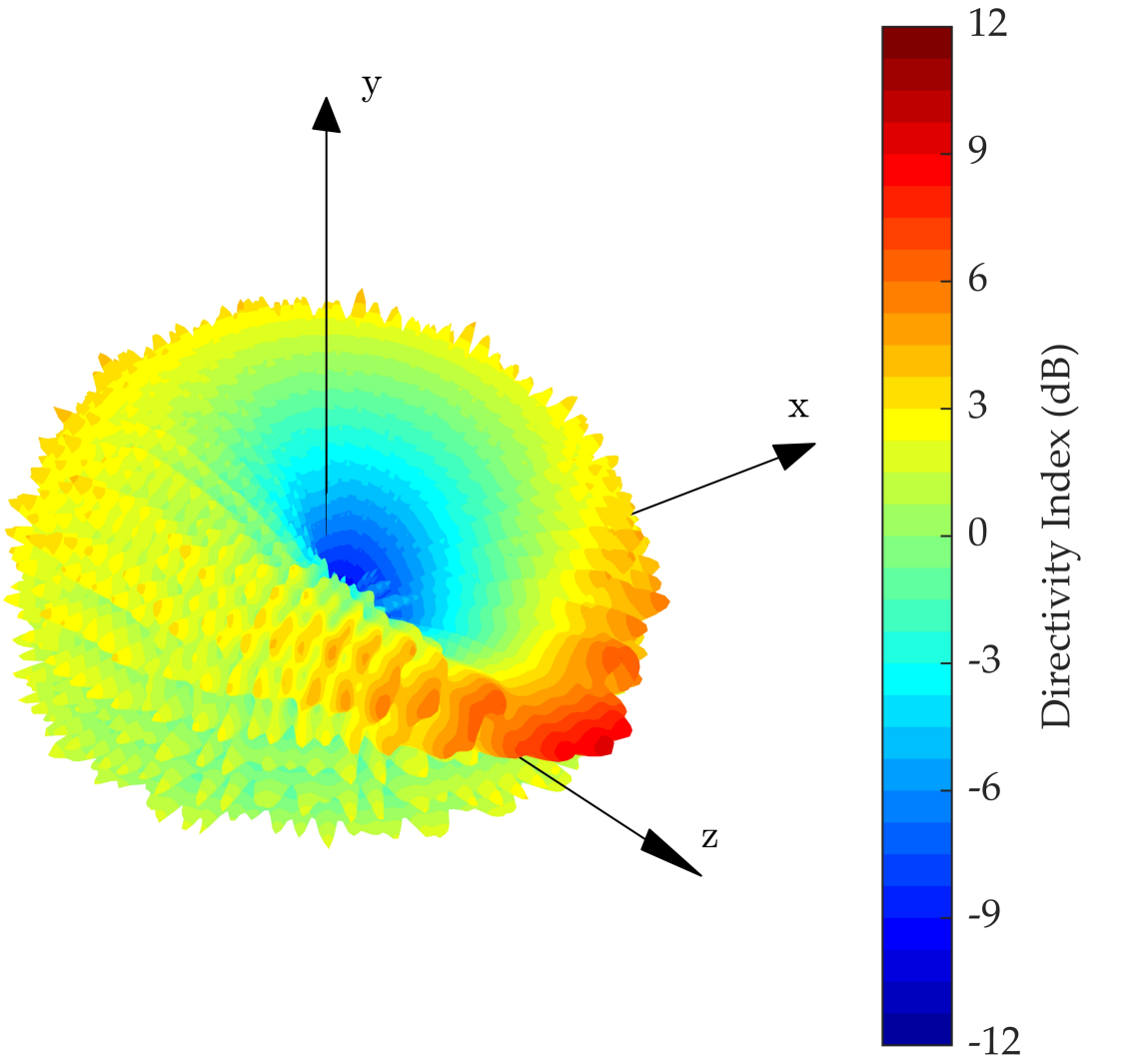

Figure 3.55: The 3-D directivity radiation pattern for sound propagation through a non-isothermal elevated JICF at a radius $r = 32D$ with $R = 5$, $T_j = 500\,°\text{C}$, $\vec{v_0}(\vec{x}) \neq 0$, and $ka = 0.8$. The cross-flow is flowing parallel to the Z-axis, towards the negative direction. Values of DI less than $-12\,\text{dB}$ are saturated dark blue.

However, Figure 3.55 shows that the acoustic lobe downwind of the exhaust stack has a finite width. It should be noted that the ripples previously seen in the line plots and 2-D planar contour plots, also exist in the 3-D directivity radiation pattern. Even though the ripples exist due to numerical artefacts in the numerical mesh, the key acoustic features are visible in the 3-D directivity radiation pattern.

In order to reduce the ripples due to the numerical artefacts from sound propagation through the numerical mesh, the acoustic results can be averaged over a one-third octave band. The following equation for DI was used to average numerous discrete frequencies over a one-third octave band:

$$\mathrm{DI}(\theta,\phi) = 10\log_{10}\left(\frac{1}{n}\sum_{i=1}^{n}\frac{p^2_{\mathrm{rms}}(\theta,\phi)}{p^2_{\mathrm{sphere},i}}\right), \tag{3.41}$$

where n is the number of discrete frequencies for the average, $p_{a,i}$ is the acoustic pressure at a point, and $p^2_{\mathrm{sphere},i}$ is the average squared acoustic pressure along the spherical surface. The number of discrete acoustic frequencies for the band-average one-third octave results was $n = 5$, where each frequency was spaced linearly. Figure 3.56 shows the band-averaged one-third octave 3-D directivity radiation pattern for sound radiation through the thermal and velocity gradients from a non-isothermal elevated JICF. When comparing Figures 3.55 and 3.56, both plots show the reproduction of key acoustic features. However, comparing Figures 3.55 and 3.56, the latter shows a smoother 3-D directivity radiation pattern with the reduction in the ripples being a result of averaging the results over a one-third octave band. Therefore, the acoustic results can be presented using a 3-D directivity radiation pattern, with the results band-averaged over a one-third octave band to reduce the numerical artefacts but retain key acoustic features from the sound interacting with the non-isothermal elevated JICF.

3.4 Discussion

This section presents an in-depth discussion of the numerical study, with a focus on the validity of the results and important outcomes from the study of the propagation of sound from hot exhaust stacks with a cooler cross-flow. The first discussion involves the assumptions and limitations for the numerical method, but in particular using the linearised acoustic wave equation with scalar potential flow to model the sound with convective mean flow. The discussion is then followed by a summary of the acoustic results for the ground-level JICF, with the implications of the plume on the sound radiation on directivity.

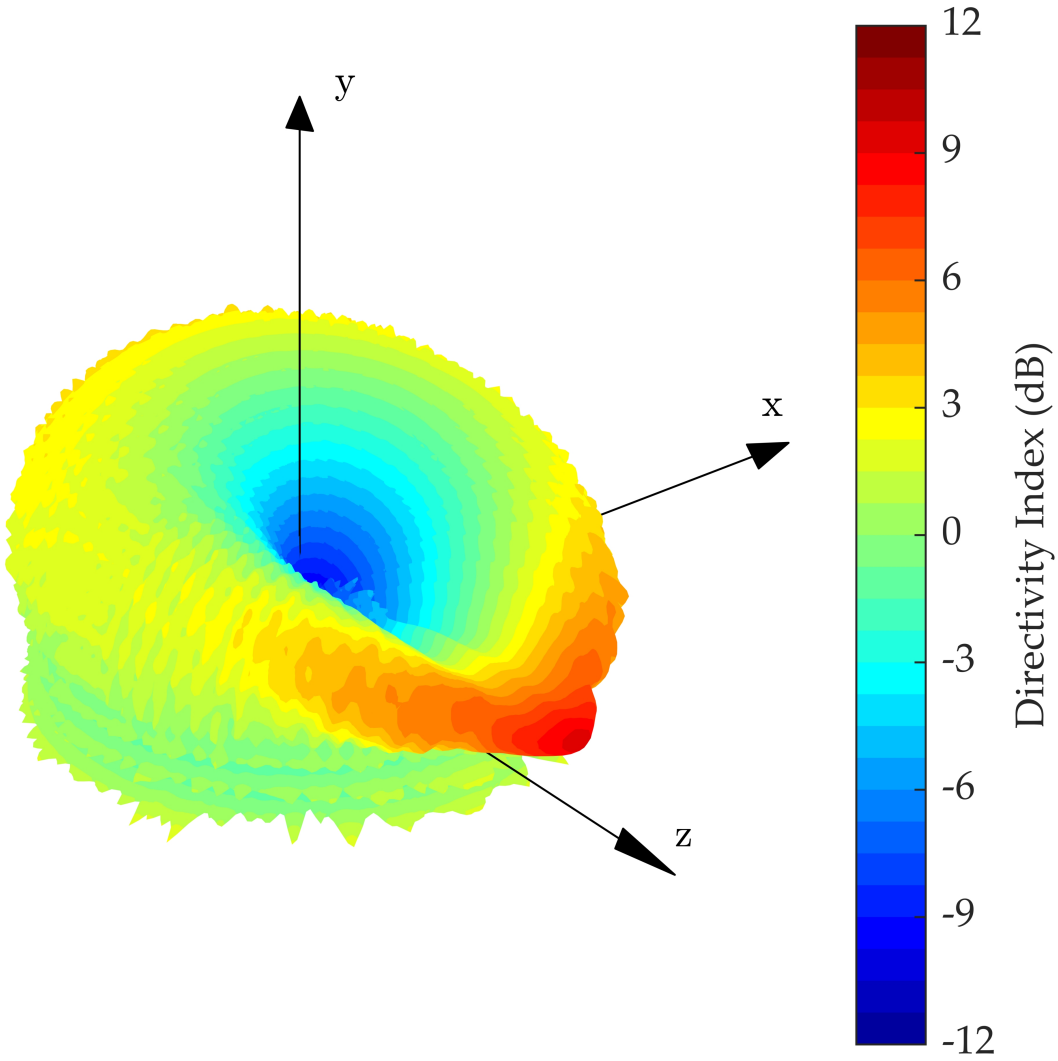

Figure 3.56: The band-average one-third octave band 3-D directivity radiation pattern for sound propagation through a non-isothermal elevated JICF at a radius $r = 32D$ with $R = 5$, $T_j = 500\,°\mathrm{C}$, $\vec{v_0}(\vec{x}) \neq 0$, and a centre frequency $ka = 0.85$ (3150 Hz). The cross-flow is flowing parallel to the Z-axis, towards the negative direction. Values of DI less than $-12\,\mathrm{dB}$ are saturated dark blue.

3.4.1 Validity of the linearised wave equation with scalar potential flow

The results in this section were generated using both CFD and acoustic FE modelling, with two different methods: the linearised acoustic wave equation without mean flow ($\vec{v_0}(\vec{x}) = 0$), and the linearised acoustic wave equation with mean flow using a scalar potential flow ($\vec{v_0}(\vec{x}) \neq 0$), which predicate on various assumptions and limitations. For the scenarios without mean flow the standard Helmholtz equation or linearised acoustic wave equation with mean flow using a scalar potential flow was used to model the sound propagation. For the scenario with non-uniform mean flow ($\vec{v_0}(\vec{x}) \neq 0$), the linearised acoustic wave equation with scalar potential flow was used, with the assumptions and limitations outlined in Section 3.2.1. A limitation of the model is that it assumes there are no perturbations in the density and speed of sound, where it is assumed that these quantities do not vary with time or are 'frozen'. Furthermore, it is assumed that the mean flow is irrotational and the acoustic field does not account for the rotational component of the acoustic velocity. This assumption may lead to speculations on the accuracy of the model for modelling the sound radiation, but it should be noted that the velocity gradients in the plume, summarised in Table 3.1 and shown in Figures 3.10a and 3.11, are in the subsonic regime with a Mach number of $M = 0.1$. Various case studies were investigated in Appendix C to analyse the validity of using the linearised acoustic wave equation with mean flow using a scalar potential flow, which has shown promising outcomes. A summary of the results in Appendix C will be outlined in the following.

There are five cases in Appendix C that were used to investigate the linearised wave equation with mean flow using a scalar potential flow. These have been validated analytically and/or with other numerical cases or code in the literature. Firstly, Sections C.1 and C.2 shows numerically that in a duct, both the linearised acoustic wave equation with pressure (Helmholtz equation) and the linearised acoustic wave equation with mean flow using a scalar potential flow can accurately quantify the SPLs in the ducts and the correct wavelength.

The results are further supported with Section C.7 which presents an investigation of the sound radiation from a 2-D point source submersed in a uniform, subsonic mean flow, and is based on a case study presented by Bailly and Juve [18]. The linearised acoustic wave equation with mean flow using the scalar potential flow in ANSYS Mechanical was verified against the analytical and numerical results from the linearised Euler equation, from Bailly and Juve [18]. Additional numerical work was conducted with the University of Technology of Compiègne's FE solver using Galbrun's equations [16, 62, 63, 159, 160] and shows good agreement with the linearised acoustic wave equation with mean flow using a scalar potential flow in ANSYS Mechanical, under different acoustic frequencies and flow conditions.

Expanding on the numerical validation, Section C.8 shows the sound propagation from a 2-D point source in a finite thickness shear layer, which is based on the work by Ewert and Schröder [57] and Feng et al. [59]. Again, the linearised acoustic wave equation with mean flow using a scalar potential flow in ANSYS Mechanical shows good agreement with the results in literature [57, 59] and with the University of Technology of Compiègne's FE solver using Galbrun's equations.

Finally, Section C.9 presents the numerical work for the sound radiation from a 2-D point source in a heated, non-expanding jet, which is a slight modification to the work conducted by Agarwal and Morris [2] and National Aeronautics and Space Administration [122]. This was a particularly difficult case to validate with ANSYS Mechanical, as it was shown by National Aeronautics and Space Administration [122] that for particular flow conditions it is difficult model the acoustic pressure with different numerical methods. Hence, the results presented in Section C.9 are for modified flow conditions and compare the results between the linearised acoustic wave equation with mean flow using a scalar potential flow in ANSYS Mechanical and the University of Technology of Compiègne's FE solver using Galbrun's equations. The results show good agreement between the two numerical methods.

At this stage, the acoustic FE model, and the methods used in this chapter have limitations and assumptions with the approach, and higher fidelity models could have been used, but are not necessary to capture salient features of this study. It

should be noted that higher fidelity acoustic FE models such as the linearised Euler equations [18, 57], Galbrun's equations [159, 160], and linearised Navier-Stokes [26, 75, 96] could be used to model the problem, but there are drawbacks to these methods. The number of degrees of freedom at a node in 3-D for the linearised Euler equation is five [18, 57], the linearised Navier-Stokes equation is five [26, 75, 96], and for Galbrun's equation it is four [159, 160], whereas, the linearised acoustic wave equation uses a scalar formulation with only a single degree of freedom, which is pressure for the case without flow [8, 9, 11, 24, 138], and scalar potential flow for the case with flow [131].[12] By only solving a single degree of freedom for an acoustic FE model, it reduces the computational resources and computational runtime needed to solve a system, when compared to a higher fidelity model with multiple degrees of freedom. Hence, 3-D models with a larger number of nodes can be computed with scalar formulations for the acoustic FE method, with the limited computational resources and computational runtime. The cases investigated in this thesis were at the limits of the computational resources available, and using higher fidelity models would have meant that the number of nodes would have been drastically increased. The justification for using a scalar formulation for the acoustic FE model was also presented in the work by Astley and Eversman [11], where they discussed the benefits of a single degree of freedom system for solving models with a large number of nodes, with limited computational resources. It has been shown in Section C.9 that on the same computer, a problem with 1 million nodes can take up to one hour to solve with Galbrun's equation and for the linearised acoustic wave equation with scalar potential flow it takes only 4 minutes to solve with ANSYS Mechanical. The difference in time taken to solve the problem may be exaggerated by the fact the in-house solver by the University of Technology of Compiègne was not coded to be the most time efficient solver, but it emphasises that the increase in degree of freedoms solved will also increase both computational resources and computational runtime necessary. It is important to note that the size of the matrices increases in size based on the square of the number of degrees of freedom. There is sufficient evidence to suggest that the acoustic FE method

[12] Detail formulation for the linearised acoustic wave equations with scalar pressure and potential flow are provided in Appendix B.

using scalar pressure and potential flow is adequate, but not perfectly ideal to quantitatively capture the acoustic pressure, with the previous discussion in this section outlining the accuracy and limitations of the approach. Hence, at the cost of minor differences in numerical accuracy, a less computationally demanding and time efficient acoustic FE model can be utilised as a tool to investigate and understand the acoustic interaction with hot-exhaust jets with cooler cross-flow in the far-field ($r = 32D$).

3.4.2 Ground-level jet in cross-flow factors dictating sound propagation

As discussed in Section 3.3.2, there are a plethora of factors that affects the sound propagation, whether they are spatial factors, acoustic factors or factors related to the fluid dynamics associated with the jet in cross-flow. This section attempts to discuss the critical factors that govern the sound propagation downwind for ground-level JICF when compared to the case for sound propagation through an isothermal stationary field at ambient temperature.

Figure 3.57 shows the directivity with four different propagation conditions at $r = 32D$ and with $ka = 0.8$. These four conditions are:

1. an isothermal stationary field ($T_j = 27\,°\text{C}$, $R = 0$, $\vec{v_0}(\vec{x}) = 0$), previously discussed in Subsection 3.3.2.1,
2. a steady-state temperature field associated with non-isothermal JICF ($T_j = 27\,°\text{C}$, $R = 5$, $\vec{v_0}(\vec{x}) \neq 0$), previously discussed in Subsection 3.3.2.2,
3. a steady-state convective flow associated with isothermal JICF ($T_j = 500\,°\text{C}$, $R = 5$, $\vec{v_0}(\vec{x}) = 0$), previously discussed in Subsection 3.3.2.3, and
4. a combined steady-state temperature and convective fluid flow associated with non-isothermal JICF ($T_j = 500\,°\text{C}$, $R = 5$, $\vec{v_0}(\vec{x}) \neq 0$), discussed above in this subsection.

For the remainder of the discussion in this section, each case will be given a number to simplify the discussion, with the cases in the previous list given a number from

1-4. An important outcome of the result is the increase in sound downwind of the exhaust stack, with Figure 3.57. For Case 1, the results show an axisymmetric result about the 0° axis, with a lobe forming on-axis and a slight reduction in sound level off-axis ($\theta = -90°$ or $\theta = 90°$). Case 2 shows the slight asymmetry in the sound radiation when compared to Case 1. Cases 3 and 4 shows the most drastic change in sound directivity, and exhibit similar three key similar features:

- downwind, at angles greater than 30° to 90° a lobe is formed,
- on the axis of the duct at approximately 10° to 20° an acoustic 'cusp' or 'null' is formed, and
- upwind of the duct, at angles from $-30°$ to $-90°$, spherical spreading occurs.

It is important to note that Cases 3 and 4 shows the importance of the temperature distribution from the heated jet in cooler cross-flow. This is supported by the results in Section 3.3.1.1, whereby Tables 3.1 and 3.2 emphasise the quantitative velocity and temperature gradients downwind. For Tables 3.1 and 3.2, the ratios c_{temp} and c_{conv} are expressed for the plume at different positions downwind, and can be used as a tool to understand the refraction of sound downwind, where $c_{\text{temp}} > c_{\text{conv}}$ for every X-Y plane investigated downwind. This implies the thermal gradients have a greater effect on the propagation of sound downwind than the convective effects, and this is supported by the results in Figure 3.57. Figure 3.57 shows the inclusion of the convective effects in Case 4, where it can be seen that the lobe downwind in Case 3 at $\theta = 80°$ has shifted towards the ground in Case 4 to $\theta = 90°$. Furthermore, comparing the acoustic lobe downwind in Cases 3 and 4 shows a slight increase in the amplitude of the acoustic lobe by up to approximately 1.5 dB.

To emphasise the effects of the steady velocity and thermal gradients from non-isothermal ground-level JICF, 3-D directivity radiation plots are compared for four different conditions. The four different sound propagation conditions identical to the results in Figure 3.57. The corresponding 3-D directivity radiation patterns are shown in Figure 3.58, but at a different viewing angle from previous 3-D directivity radiation patterns, with a perspective along the Y-Z plane of symmetry.

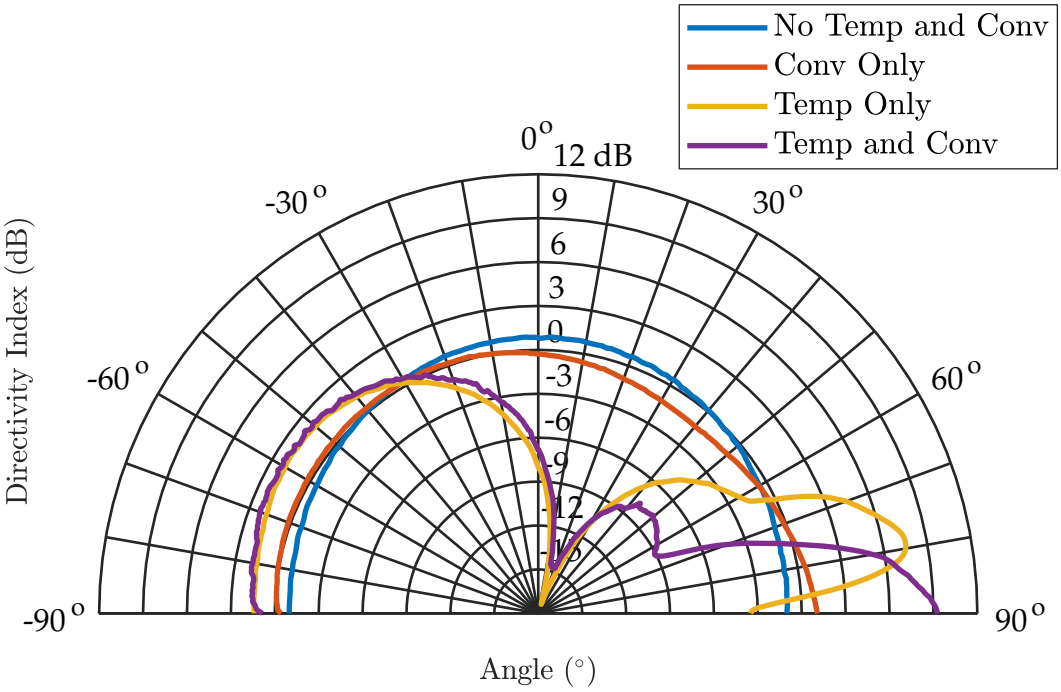

Figure 3.57: The DI at a radius of $32D$ along the Y-Z plane (of symmetry) for sound propagation from a source with $ka = 0.8$ through four propagation conditions: Case 1 - an isothermal stationary field ($T_j = 27\,°C$, $R = 0$, $\vec{v_0}(\vec{x}) = 0$), Case 2 - a ground-level JICF at ambient temperature with no thermal gradients ($T_j = 27\,°C$, $R = 5$, $\vec{v_0}(\vec{x}) \neq 0$), Case 3 - the thermal gradients associated with a heated jet in ambient cross-flow with no convective effects modelled ($T_j = 500\,°C$, $R = 5$, $\vec{v_0}(\vec{x}) = 0$), and Case 4 - a ground-level JICF with the temperature and flow considered for modelling ($T_j = 500\,°C$, $R = 5$, $\vec{v_0}(\vec{x}) \neq 0$).

The acoustic results for the chapter can be shown with Figure 3.58 and summarised with the following:

- Figure 3.58a shows in the absence of the thermal and velocity gradients imposed from the CFD simulation. The acoustic radiation is axisymmetric, with a slight concentration of acoustic energy along the duct centreline as would be expected from previously published works.
- Figure 3.58b shows the acoustic radiation is no longer axisymmetric, with the presence of the steady-state velocity from the ground-level JICF, the sound observed downwind of the exhaust stack has been refracted downwards, with

an increase in sound observed at ground-level. Upwind of the exhaust stack, the steady-state velocity from the incoming boundary layer shows upwards refraction in Figure 3.58b.

- Figure 3.58c represents the effects of thermal gradients on the sound propagation. The sound radiation is now clearly asymmetric. A very distinct lobe has formed just above the horizontal downstream of the duct. The peak in this lobe grows with radial distance and is yet to converge.
- Figure 3.58d shows the combination with the thermal and convective effects and exhibit the greatest increase in DI downstream of the duct outlet. The convective effect shown in Figure 3.58b have caused the elevated acoustic lobe in Figure 3.58c to refract further downwards to be positioned at ground-level, as seen in Figure 3.58d.

It should be noted that due to the way the results are visualised and the viewing perspective in Figure 3.58, the acoustic cusp previously observed in this chapter was not observable. Hence, the four different mediums for sound propagation discussed above produced different acoustic features. The inclusion of both the convective and thermal gradients from non-isothermal ground-level JICF has shown the most drastic acoustic radiation plot, when compared directly in Figure 3.58d, with the 'tongue' from the thermal effects observed in Figure 3.58c pushed onto ground-level by the convective effects (Figure 3.58b).

3.4.3 Ground-level and elevated jet in cross-flow comparison

The inclusion of the stack, which leads to an elevated JICF, changes the sound directivity, when compared to the ground-level JICF. Figure 3.59 shows the sound directivity at $r = 32D$ with the sound propagation from a heated jet in cross-flow, for both an elevated stack and a stack at ground-level. Investigating the sound directivity with the outlet at ground-level is an attempt to understand the sound radiation through the plume, without the interaction of the exhaust stack. However, it is shown in Figure 3.59 that downwind of the exhaust stack the outlet relative

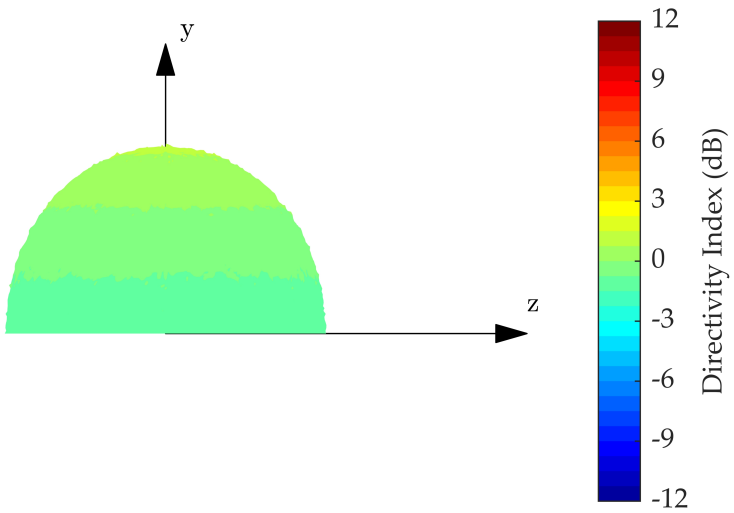

(a) Isothermal stationary field ($\vec{v_0}(\vec{x}) = 0$, $T_j = 27\,°\mathrm{C}$, $R = 0$)

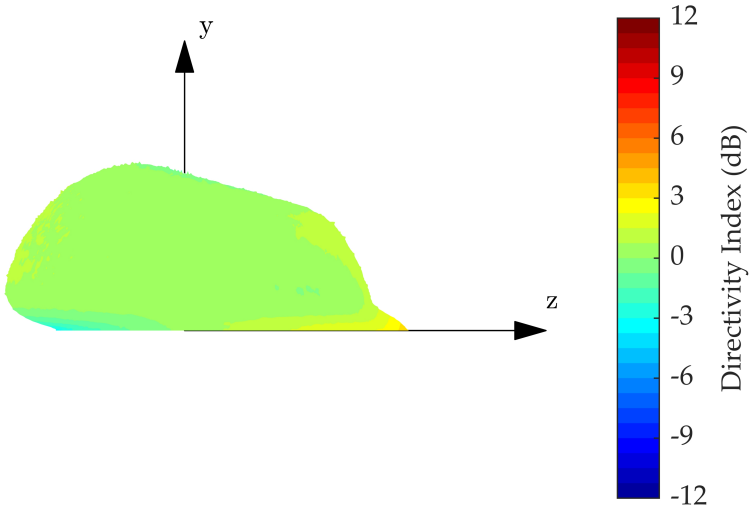

(b) Convective effects only ($\vec{v_0}(\vec{x}) \neq 0$, $T_j = 27\,°\mathrm{C}$, $R = 5$)

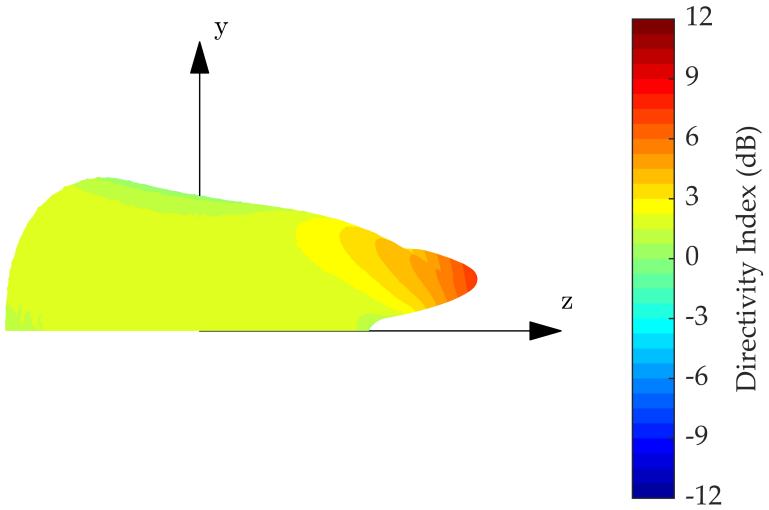

(c) Thermal effects only ($\vec{v_0}(\vec{x}) = 0$, $T_j = 500\,°C$, $R = 5$)

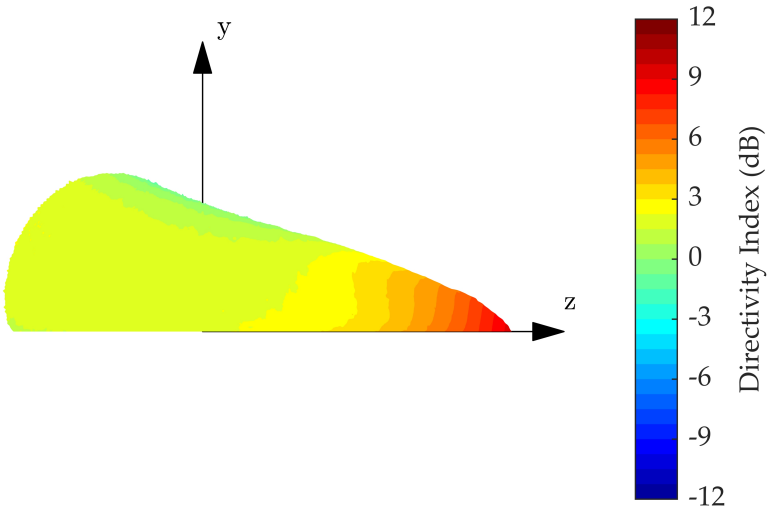

(d) Combining the thermal and convective effects ($\vec{v_0}(\vec{x}) \neq 0$, $T_j = 500\,°C$, $R = 5$)

Figure 3.58: Visualising the 3-D directivity radiation pattern for four different propagation media: (a) isothermal stationary field with no JICF, (b) convective effects only with the JICF at ambient temperature, (c) temperature effects only with the heated jet and cooler cross-flow, and (d) combining the temperature and convective effects for a heated jet in cooler cross-flow. The 3-D directivity radiation was conducted along a hemisphere with a radius $r = 32D$, and at $ka = 0.8$. The cross-flow for (b), (c) and (d) is flowing parallel to the Z-axis, going from left to right. Values of DI less than $-12\,dB$ are saturated dark blue.

to the ground affects the sound radiation; for the ground-level JICF and elevated JICF the position of the acoustic lobe downwind is at 90° and 80°, respectively. By placing the reflective boundary condition of the ground at ±90° the sound has now been reflected, and with the presence of the plume causes the lobe to form at 90°. By elevating the exhaust stack the sound can radiate below ±90° and changes the concentration of sound downwind to form a lobe at a higher position, 80°. It is also important to note that the definition of DI is slightly different for both cases (using Equations (3.26) and (3.29), respectively), and for the ground surface, a 'Robin' radiation boundary condition was used for the elevated JICF and a hard reflective boundary condition was used for the ground-level JICF.

3.5 Conclusion

The results from this study have shown that the steady-state convective and thermal gradients found within the plumes of ground-level and elevated JICF plumes significantly impact the propagation of sound from the stack. The ground-level JICF the sound radiation in the absence of steady-state thermal and velocity gradients resembles the directivity pattern for a baffled piston, and for an elevated JICF the sound radiation resembles a directional pattern, with a lobe forming on-axis. However, when there is a JICF that has either a steady-state convective flow, or is hotter than ambient, or combination of both, the resulting sound propagation becomes asymmetric, due to the redistribution of acoustical energy, as sound is refracted by the thermal and velocity gradients in the shear layer.

The key results from this study are:

- In the presence of the plume and cross-flow, the sound radiation pattern is complicated and axisymmetric.
- The directivity of sound is dependent on the distance from the duct outlet, with the directivity near the duct outlet (at $r = 2D$) showing spherical radiation and at a radial distance of $r = 32D$ the directivity becomes very asymmetric.

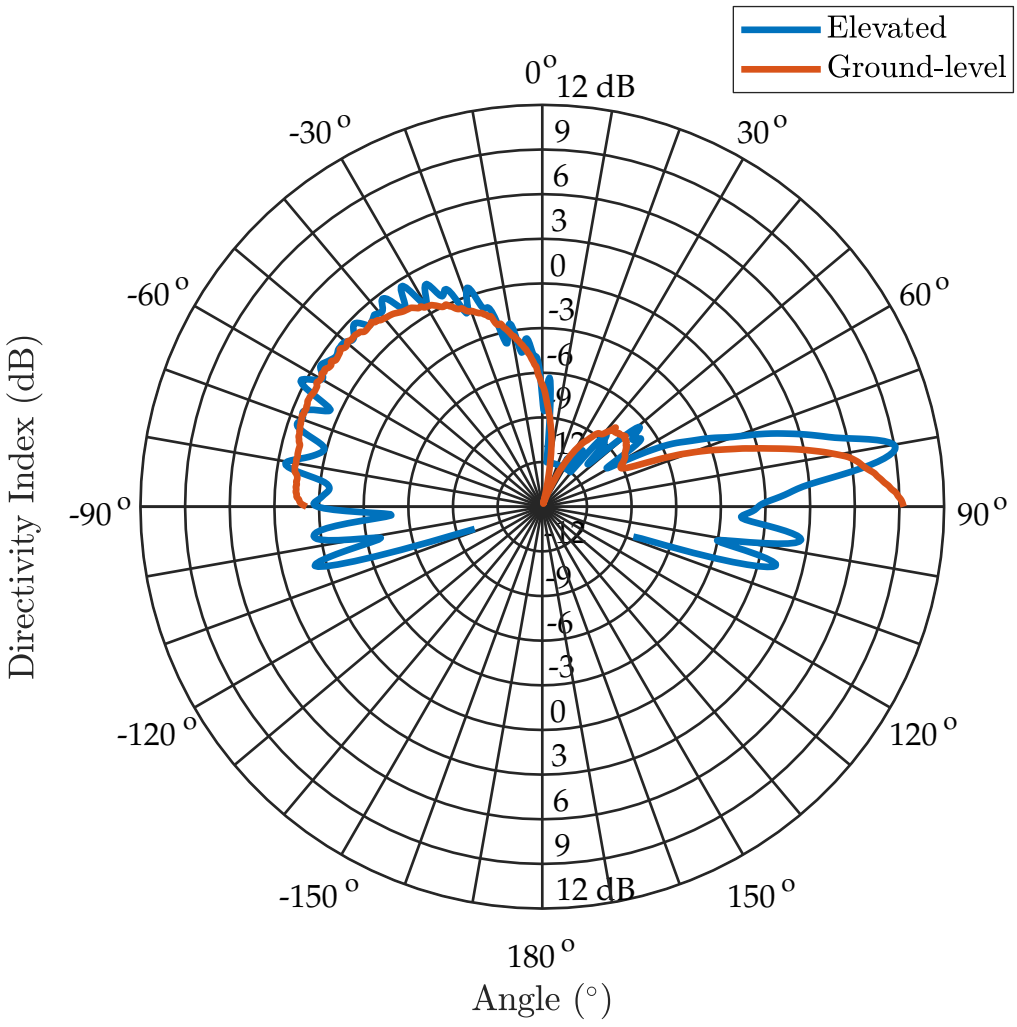

Figure 3.59: Comparison of the DI for an elevated JICF and a ground-level JICF at a radius of $32D$ along the Y-Z plane (of symmetry) for sound propagation from a source with $ka = 0.8$ and flow conditions $T_j = 500\,°C$, $R = 5$, and $\vec{v_0}(\vec{x}) \neq 0$).

- The change in sound propagation path depends significantly on the Helmholtz number ka, with a higher value of ka more likely to cause sound to interact with the plume, with an increase in the DI magnitude observed downwind of the stack in the acoustic lobe.
- A dominant factor in sound refraction is the thermal gradient within the plume, which causes a strong, slightly elevated, 'lobe' of sound to form downwind.
- The steady-state velocity gradients associated with the plume cause an increase in the SPL downwind with the sound energy more likely to be concentrated at ground-level.
- Upwind of the jet there is an upward refraction of sound caused by the velocity gradients in the incoming boundary layer.
- The plume causes a strong 'cusp' to initially form near the axis of the duct centreline. As the jet is deflected by the cross-flow and the position of the 'cusp' rotates downstream with increasing distance from the stack.
- When both the steady-state fluid flow and the temperature effects are present for the ground-level JICF, a significant increase in DI of up to 11 dB is observed downwind at ground-level.
- The increase in the downwind SPL at ground-level is dependent on the cross-flow ratio, R, where an increase in the cross-flow ratio (decrease in the cross-flow velocity) causes the sound to strike the ground further downwind.
- The sound directivity for the elevated JICF is dependent on the ground-level boundary condition, where the hard reflective boundary conditions lead to sound directivity plots possessing complex acoustic radiation patterns from diffraction and reflections.
- The sound radiation through an elevated stack does not spread uniformly with a monopole assumption.

- The sound directivity through an elevated stack produces axisymmetric sound, with a concentration of sound on-axis forming a lobe.
- Sound propagation through the thermal and velocity gradient from a non-isothermal elevated JICF, leads to the formation of an acoustic lobe downwind of the exhaust stack.
- When the sound source is elevated with the inclusion of the stack, the acoustic lobe downwind of the stack shows an increase in the Helmholtz number ka. There is an increase in the DI magnitude downwind and an angular shift towards 0°.
- The elevated source with the current domain, the downwind lobe, has yet to impact the ground, whereas for the ground-level JICF, the refraction of sound leads to a drastic increase in SPL at ground-level.
- Tonal results for sound radiation through the exhaust stack with and without an elevated JICF shows numerical artefacts from the numerical mesh, which can be smoothed by averaging the acoustic results over multiple discrete frequencies in a one-third octave band.

Future work can be undertaken to investigate the influence of steady-state convective and thermal effects from non-isothermal JICF on far-field sound propagation ($r > 32D$). In investigating the far-field sound propagation, the current numerical domain size would need to be substantially increased. Additional work can be undertaken for sound propagation for $ka > 0.8$, which can be achieved by increasing the FEM mesh density in the current domain. While this study investigated two cross-flow ratios, R, a more in-depth study involving a wider range of R should be conducted. The numerical study has shown that significant sound refraction occurs downwind of the exhaust stack, as a result of the sound interacting with the hot exhaust plume being deflected by the cooler cross-flow. The refraction of sound downwind leads to the redirection of SPL to form an acoustic lobe of increased sound level. Hence, practitioners and engineers should account for this when predicting community noise from hot exhaust stacks, such

as these found in OCGTs. It is possible that popular models such as CONCAWE or ISO 9613-2:1996 [88] will significantly under predict hot exhaust noise under certain conditions.

Chapter 4

Experimental measurements of sound propagation through jets in cross-flow

4.1 Outline

Chapter 3 presented the numerical results for sound radiation through non-isothermal hot exhaust jets in cooler cross-flow. This chapter contains the companion experimental measurements of the cases examined in Chapter 3. The experimental campaign in this thesis was conducted using a purpose-built exhaust rig and instrumentation. Experiments were conducted at two different facilities: the Anechoic Chamber and the Thebarton Wind Tunnel at The University of Adelaide. Testing in the Anechoic Chamber was conducted for two cases shown in Figure 4.1, to ensure the data acquisition system was operating correctly. The acoustic results from these tests are presented in Appendix D. Subsequent tests were then conducted at the Thebarton Wind Tunnel, as the facility provides a cross-flow that is perpendicular to the discharge of the jet. Figure 4.2 shows the three cases investigated at the Thebarton Wind Tunnel. This chapter focuses on the acoustic results for testing at the Thebarton Wind Tunnel.

This chapter comprises several sections. Section 4.2 outlines the method for the experimental measurements and the experimental apparatus used. Section 4.3 discusses the flow and temperature measurements for a non-isothermal exhaust

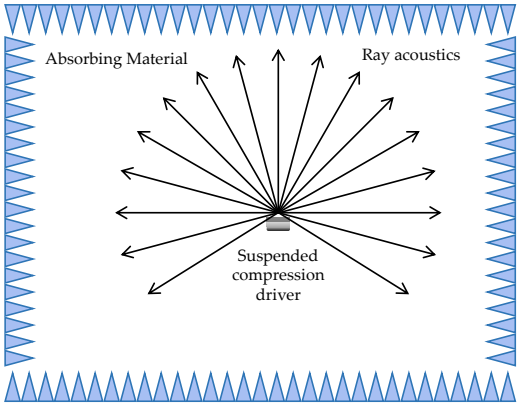

(a) Free-standing compression driver

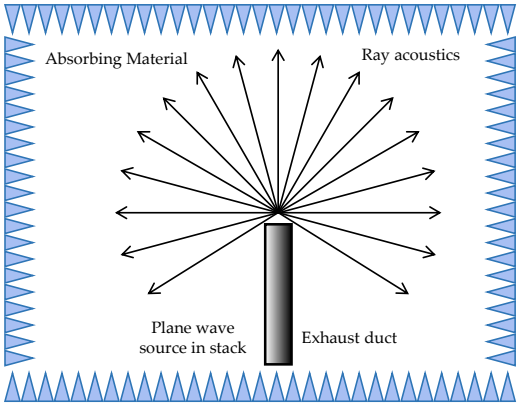

(b) Exhaust stack sound propagation

Figure 4.1: Schematics of the experimental acoustic testing in the Anechoic Chamber of two different systems; (a) a free-standing compression driver, and (b) sound propagation from an exhaust stack.

jet in cross-flow. The flow and temperature measurements show similar features to those seen in Chapter 3 and in the literature. The experimental acoustic results are discussed in Section 4.4, with details of the following discussed in subsequent subsections:

- Sound radiation in a homogeneous isothermal field (in the absence of the JICF), where the acoustic results show axisymmetric sound radiation with a lobe forming along the duct centreline.
- Sound radiation in the presence of a non-isothermal jet without cross-flow. The acoustic directivity results show axisymmetric sound radiation with a 'cusp' forming along the duct centreline and acoustic lobes off-axis.
- Sound radiation in the presence of a non-isothermal JICF at a single cross-flow ratio, $R = 5$. The acoustic results show the effects of the heated plume, with refraction being a prominent factor in increasing the sound levels downwind of the exhaust stack.

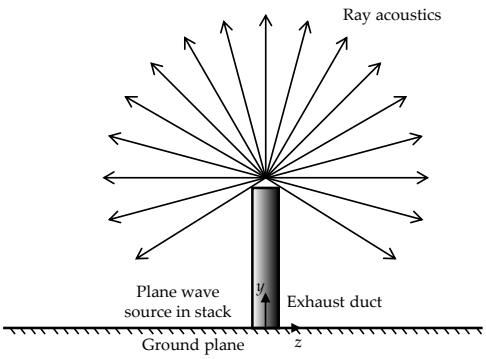

(a) Isothermal exhaust stack with no cross-flow sound propagation

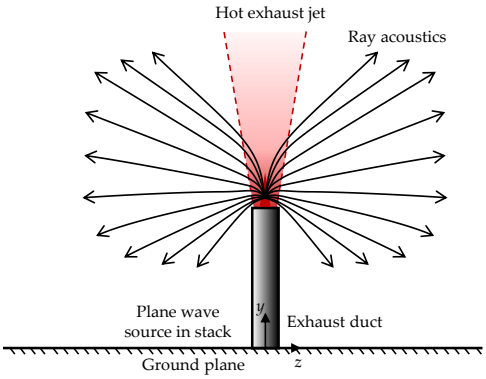

(b) Sound propagation with a heated jet

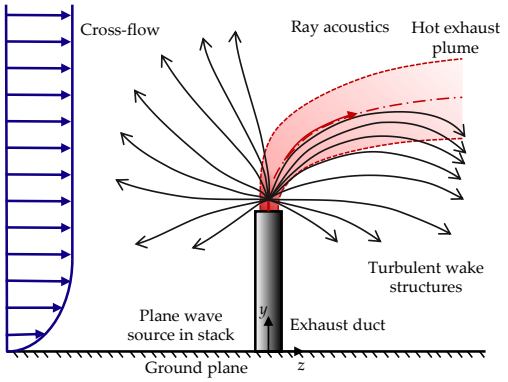

(c) Sound propagation with a heated JICF

Figure 4.2: Schematics of the experimental acoustic testing in the Thebarton Wind Tunnel of three systems; (a) sound propagation from an isothermal exhaust stack in the absence of flow, (b) sound propagation through a heated jet with no cross-flow, and (c) sound propagation through a non-isothermal heated JICF.

- Sound radiation cross-flow sensitivity study for non-isothermal JICF, with $R = [5, 7.5, 10, 12.5]$. The change in the jet to cross-flow momentum flux ratio alters the acoustic lobe downwind of the exhaust stack.

The experimental results are interpreted further and are outlined in Section 4.5. Section 4.6 summarises the key findings in the experimental study.

4.2 Methodology and experimental apparatus

Experiments on a full-scale operating OCGT are complex due to the practicalities of controlling flow and speed, as well as the difficulties associated with measurement of flow temperature, flow speed, and sound pressure. This research aims to simulate the flow, temperature and acoustic parameters of a full-scale OCGT with a small-scale exhaust rig, where the relevant parameters can be controlled. This section discusses the scale-model experimental apparatus representative of a full-scale OCGT, the commissioning of the experimental apparatus at the University of Adelaide Anechoic Chamber, the commissioning of the experimental apparatus at the University of Adelaide Wind Tunnel (rendered image shown in Figure 4.3), the required instrumentation, and the signal processing techniques used to process the acoustic data.

The experimental apparatus for simulating the exhaust flow and sound is shown in Figures 4.4 and 4.5. The exhaust was designed to achieve the parameters in Table 4.1. It should be noted that the exhaust rig was designed based on non-dimensional acoustic parameters relevant to full-scale OCGTs, but where possible the non-dimensional fluid dynamic parameters were also considered. A centrifugal blower (Leister Airpack) was used to generate the flow in the duct network. The inlet and outlet of the blower were connected to an acoustic silencer on each end to minimise the sound from the blower affecting acoustic measurements. The flow travelled through a stainless-steel duct network with an outer diameter of 50.8 mm and an inner diameter of 47.6 mm (D), which is approximately $1:100$ scale of a real 160 MW OCGT. The flow from the outlet silencer to the Airpack blower was split into a Y-junction and was passed through two 16 kW Leister 61L System Air

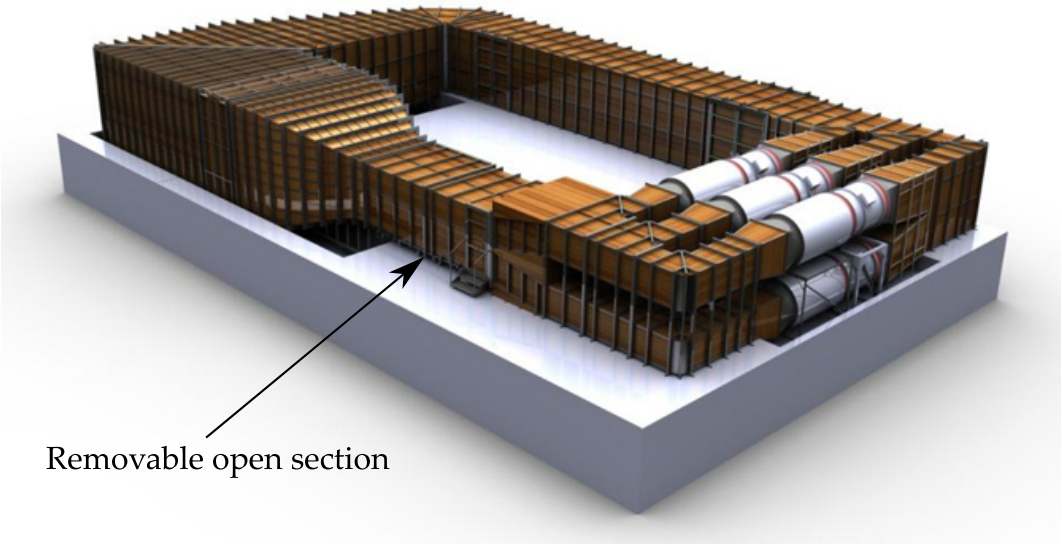

Figure 4.3: Illustration of the closed-loop four-sided University of Adelaide Wind Tunnel. The purpose-built small-scale exhaust rig was commissioned in the removable open section of the wind tunnel.

Heaters capable of variable temperature control, and then joined again with a 45° Y-junction into a single flow. Two heaters were used in lieu of a single unit due to the lower cost and practicality of delivering the required electricity. The flow in the duct network was measured with a pitot tube coupled to a differential pressure transducer (ManyYear Technology MPT-721). The temperature in the duct network was measured using k-type thermocouples. The flow then passed through a 90° bend to change the direction of flow to vertical before entering an automotive catalytic converter, which comprises of Corning Celcor with square pores, that acted to straighten the flow. The flow beyond the catalytic converter passed through a straight vertical section of pipe before exiting as a jet. The exhaust network was clad with Rockwool sectional pipe insulation to reduce the heat loss in the pipe network and attenuate structural acoustic radiation.

Figures 4.6a and 4.6b show the experimental setup in the University of Adelaide's Thebarton Wind Tunnel. A wooden decking, acting as a ground plane, was placed over the heater and blower of the exhaust rig. Acoustic foam (50 mm thick Dacron) was placed on the wooden decking to reduce acoustic reflections from the

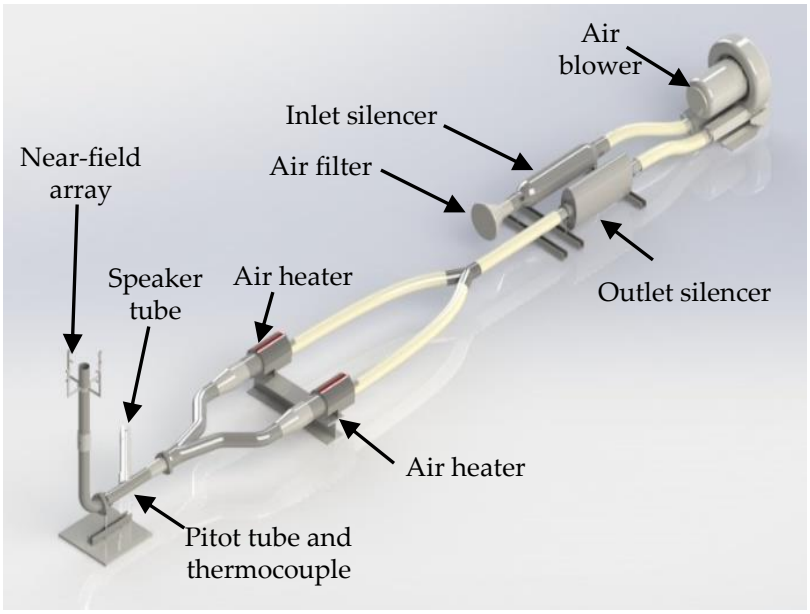

Figure 4.4: Illustration of the reduced-scale exhaust network experimental setup.

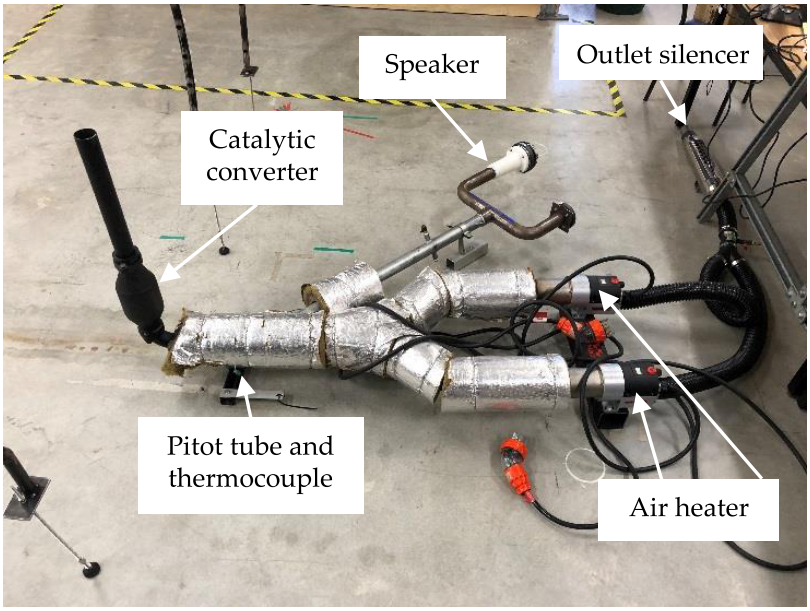

Figure 4.5: Photo of the reduced-scale exhaust network experimental setup to be installed in the Thebarton Wind Tunnel, without the blower or inlet silencer.

Table 4.1: Physical parameters for the experimental tests.

Parameters	Equation/Expression	Value
Inner diameter	D	47.6 mm
Mach number	$M = \frac{u_j}{c_j}$	0.1
Jet temperature	T_j	27 °C - 500 °C
Exhaust vertical duct length	$L = 8D$	381 mm
Jet to cross-flow momentum flux ratio	$R = \sqrt{\frac{\rho_j {u_j}^2}{\rho_{cf} {u_{cf}}^2}}$	5 - 12.5
Reynold's number	$Re = \frac{u_j D \rho_j}{\mu_j}$	3.31×10^4 - 1.04×10^5
Cut-on frequency	$f_{co} = \frac{c_j}{D}$	4226 Hz - 6818 Hz
Helmholtz number	$ka = \frac{\pi f D}{c_j}$	0.27 - 2.7

ground plane and to provide an anechoic surface above 500 Hz, thereby reducing the complexity of the sound field so that the effect of the plume, cross-flow and sound interaction could be more easily examined. The wooden decking was used so that only the exhaust stack interacts with the flow, with the rest of the apparatus shielded from the flow and thus more closely representing the traditional elevated JICF. The cross-sectional area of the wind tunnel is 2.75 m $\times$ 2 m and the available test section ground area covers a span of 3.5 m $\times$ 5.5 m.

The experimental campaign required acoustic instrumentation for data acquisition and sound source generation. The sound pressure measurements were taken with 62 1/4" G.R.A.S. 40PH Free-Field Microphones along two circular arrays with radii 14D (0.67 m) and 28D (1.33 m) from the exhaust stack outlet, as depicted in Figure 4.7. The microphones, according to the manufacturer, have a flat frequency response ($\pm$1 dB) within a frequency range of 20 Hz to 10 kHz. Microphone wind screens (G.R.A.S. AM0071 Windscreen) designed for the 1/4" G.R.A.S. 40PH Free-Field Microphones were used to minimise the flow induced noise. It should also be

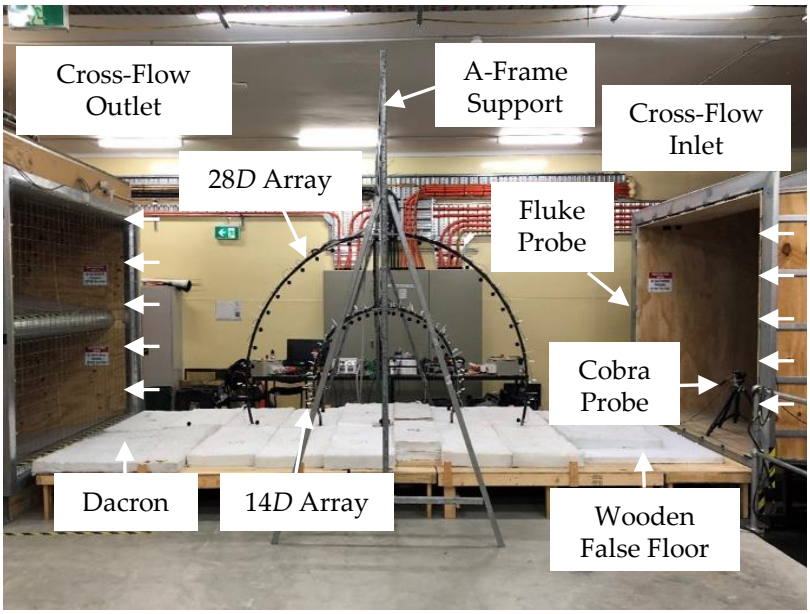

(a) Photo of the setup with both arrays and the cross-flow going from right to left.

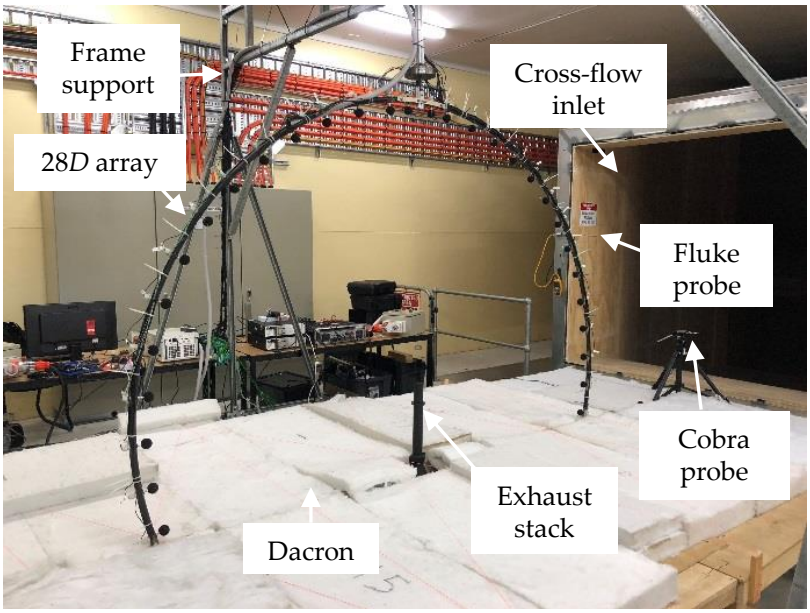

(b) Photo of the setup with only the 28D array. The cross-flow is going from top right to bottom left.

Figure 4.6: Photo of the experimental set up at the University of Adelaide's Wind Tunnel showing the test set up with (a) both arrays, and (b) the 28D array only.

noted that further signal processing of the acoustic measurements was undertaken to minimise the effects of flow induced noise from measuring the acoustic pressure in the wind tunnel with the jet flow and cross-flow present. The signal processing techniques will be discussed later in this section. The microphones in Figures 4.6a, and 4.6b were placed along a circular arc spanning $\pm 105°$, with each microphone spaced 7.5°, except for the centre microphone at 0° being replaced by two microphones at $\pm 2.5°$ for the $14D$ array arc and for the $28D$ arc the centre microphone at 0° was removed to accommodate the vertical support. The microphone arrays were positioned parallel to the cross-flow free-stream. The microphone arrays were supported by a frame incorporating a circular cross-section and acoustically absorptive material to minimise acoustic reflections, designed to have minimal flow and acoustic impact, as shown in Figures 4.6a, and 4.6b. The microphone signals were recorded by four NI (National Instruments) PXIe-4499 Sound and Vibration Modules in an 8-slot NI PXIe 1082 Chassis. Each NI PXIe-4499 was DC coupled with 16 analogue inputs. Each analogue input had an inbuilt anti-aliasing filter, 24-bit quantisation resolution and a maximum input range of ± 10 V. A broadband uniform white noise, generated from NI LABVIEW using a ± 10 V analogue output from a NI PXI-6221 Multifunction I/O Module was used as a sound source. A sampling frequency of 25.6 kHz was used. The broadband noise was passed through a dual channel analogue 4-pole Butterworth filter (Krohn-Hite Model 3362 Dual Channel Filter) designed with a low-pass and a high-pass filter to give a broadband excitation frequency range of 1 kHz-10 kHz. The sound was generated using two compression drivers, a 50.8 mm (2 inch) DS18 PRO-DKH1 1000 W compression driver and a 50.8 mm (2 inch) Timpano TPT-DH2000 400 W compression driver. The two compression drivers were needed to generate sufficient SPL over the desired bandwidth.

The acoustic data was post-processed in the frequency domain using MATLAB. The spectral analysis used a Hanning window with an FFT length of 4096, with 50% overlap to provide 1500 averages over a 120 second period. The corresponding frequency bin size was 6.25 Hz. The degree of linearity between the acoustic-electrical signal generated by the DAQ (x) and the acoustic pressures measured at

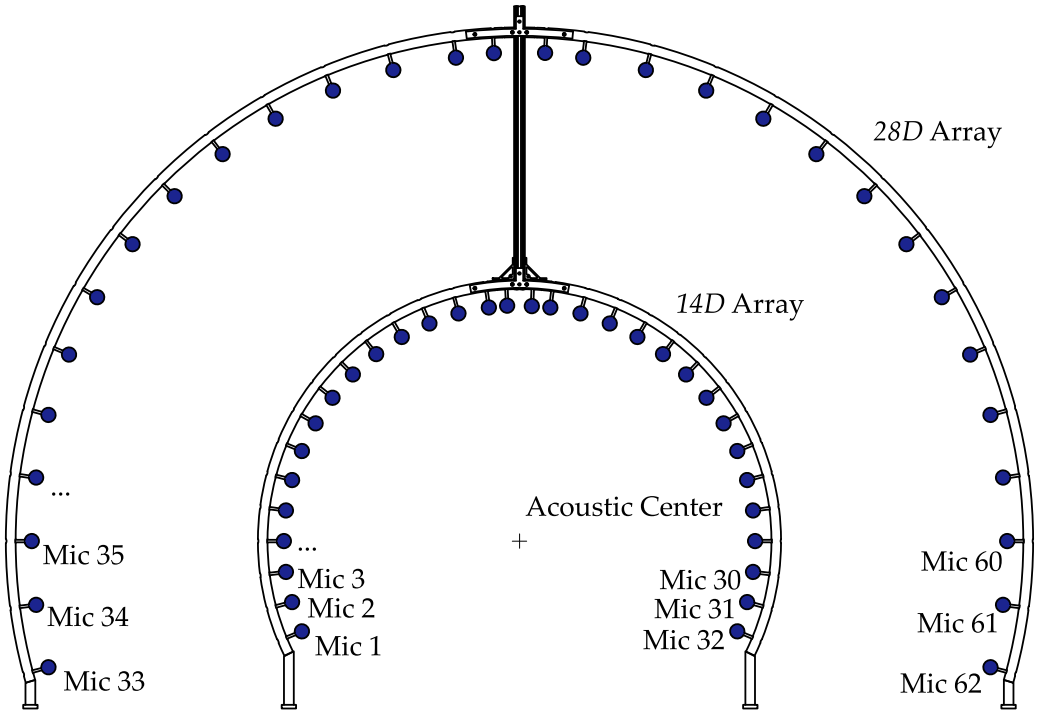

Figure 4.7: Schematic of the microphone arrays showing the microphone locations and corresponding reference numbers.

the microphones (y) may be quantified using the coherence function [22]:

$$\gamma_{xy}{}^2(f) = \frac{|G_{xy}(f)|^2}{G_{xx}(f)G_{yy}(f)}, \tag{4.1}$$

where f is the frequency of interest, G_{xy} is the cross-power spectra of the acoustic-electrical signal into the speaker and the microphone acoustic pressures, G_{xx} is the power spectra of the acoustic-electrical signal into a speaker and G_{yy} are the power spectra of the microphone acoustic pressures. The results in this chapter are presented as the coherent output power (COP) at each microphone given by the following formula:

$$\mathrm{COP}(f) = G_{yy} \times \gamma_{xy}{}^2, \tag{4.2}$$

The coherent output power was used, rather than raw sound pressure levels, so that only sound correlated with the loudspeaker is analysed, and noise from the blowers, wind tunnel fan and flow-induced noise may be ignored. The acoustic

results for directivity presented in Section 4.4 are calculated as:

$$\mathrm{DI}(f,\theta) = \frac{\mathrm{COP}(f,\theta)}{\mathrm{COP}_{av}}, \tag{4.3}$$

where DI is the directivity index based on the coherent output power and not the standard formulation involving sound intensity [25], θ is the angular position from the centreline of the duct, and COP_{av} is the average coherent output power along the directivity arc. This method of presenting the coherent results was chosen to ensure that the sound presented was coherent with the loudspeaker only, and the incoherent sound from external sources was eliminated.

Figure 4.8 shows the experimental setup for measuring flow and temperature. A Dantec three-axis transverse was used to position the flow and temperature instrumentation accurately. The flow velocity was measured with a Turbulent Flow Instrumentation Cobra Probe 209 at various positions in the flow, and a Fluke 922 airflow meter was placed at a fixed position upwind of the exhaust stack and used as a reference velocity for the cross-flow. The Cobra Probe 209 is a dynamic multi-hole pressure probe that can measure all three Cartesian velocity components, and the corresponding pressures. The air velocity measurements from the Cobra Probe 209 were used to calculate three Cartesian components of velocity (u, v, and w) and the turbulence intensities (TI) for each Cartesian component using:

$$I_{uu} = \frac{\sqrt{\overline{u'^2}}}{\overline{V}} = \frac{\sigma_u}{\overline{V}}, \tag{4.4}$$

$$I_{vv} = \frac{\sqrt{\overline{v'^2}}}{\overline{V}} = \frac{\sigma_v}{\overline{V}}, \tag{4.5}$$

$$I_{ww} = \frac{\sqrt{\overline{v'^2}}}{\overline{V}} = \frac{\sigma_v}{\overline{V}}, \tag{4.6}$$

where u' is the fluctuating velocity in the span-wise direction, V is the speed of the air, σ_u is the standard deviation of the velocity in the span-wise direction, v' is the fluctuating velocity in the vertical direction, σ_v is the standard deviation of the velocity in the vertical direction, w' is the fluctuating cross-flow free-stream

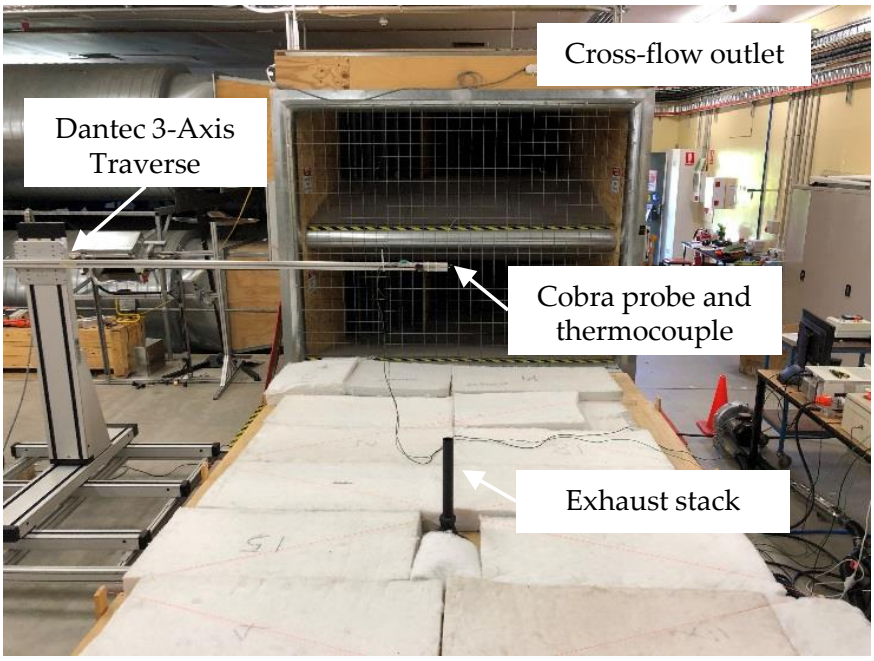

Figure 4.8: Photo of the exhaust rig including the Dantec 3-Axis traverse for flow and temperature measurements at the Thebarton Wind Tunnel.

velocity, and σ_w is the standard deviation of the cross-flow free-stream velocity. The cross-flow turbulence intensity, based on all three Cartesian components, was calculated as:

$$I_{uvw} = \frac{\sqrt{\frac{1}{3}(\overline{u'^2} + \overline{v'^2} + \overline{w'^2})}}{\overline{V}}. \tag{4.7}$$

It should be noted that there are limitations to measuring velocities using a Cobra Probe 209. Due to the orientation of the Cobra Probe, only positive velocities can be measured for w, the cross-flow free-stream direction. This is due to the position of the holes at the head of the Cobra Probe for pressure measurements. Therefore, reverse flow measured for w saturates the signal and returns $0\,\mathrm{m\,s^{-1}}$ for those measurements. Additionally, the velocity limit of the sensor was $35\,\mathrm{m\,s^{-1}}$, and this velocity limit is near the maximum velocity of the isothermal jet, with Mach number 0.1. Therefore it should be noted that velocity measurements in the immediate vicinity of the duct outlet may exceed the velocity limits of the probe.

Temperatures outside the duct and in the domain were measured using three k-type thermocouples. The three unique positions of the thermocouples are upwind of the exhaust stack at the Fluke 922 airflow meter, at the end of the Dantec three-axis traverse with the Cobra Probe 209, and downwind of the exhaust stack at the cross-flow outlet of the Thebarton Wind Tunnel. Due to the limitations of the Thebarton Wind Tunnel, the ambient cross-flow temperature could not be held constant throughout the testing campaign. Testing was conducted on days with large temperature variations, with cross-flow temperatures varying from 26 °C to 36 °C. The large changes in temperature were not evident for small durations of measurements but were evident over multiple hours. Hence, to account for changes in the ambient temperature, a dimensionless temperature parameter, Θ, was formed based on an expression from Kamotani and Greber [92] and has been modified slightly to produce the following equation:

$$\Theta = \frac{T - T_{cf}}{T_j - T_{cf}}, \tag{4.8}$$

where T is the measured temperature from the thermocouple at a point, T_j is the jet temperature from a thermocouple in the duct, and T_{cf} is the measured cross-flow temperature. The main difference in Equation (4.8) and the equation in Kamotani and Greber [92] is that T_j is replaced with $T_{\max}$, which is the maximum temperature measured in that particular temperature profile or temperature contour plane.

4.3 Experimental flow and temperature results

In this section, the experimental results of flow and temperature measurements are presented. The results are separated into two cases: isothermal (ambient jet) and non-isothermal (heated jet) JICF. Flow measurements were not taken for the non-isothermal JICF to prevent the Cobra Probe 209 from being damaged by the hot plume.

4.3.1 Experimental flow results

The experimental results for the reduced-scale isothermal JICF are presented in this section. The flow measurements are presented as vertical (varying y) profiles at various positions upwind and downwind of the exhaust stack, along the Y-Z plane intercepting the centre of the duct ($x = 0$). Additional span-wise flow measurements were undertaken with varying heights ($y/D = [17, 18, 21]$) at $z/D = 8$ downwind of the exhaust stack. The span-wise measurements were limited to only three profiles due to the limited time available in the Thebarton Wind Tunnel. The experimental flow results for this section are presented with two different flow statistics: time-averaged velocity components and turbulence intensities.

The time-averaged velocity components (Cartesian) were measured to understand the isothermal JICF bulk fluid dynamics. Figure 4.9 shows the velocity profiles at various distances upwind and downwind of the duct outlet ($z/D = [-8, -4, 1, 2, 4, 8, 16]$), with the measurement along the Y-Z plane intercepting the centre of the duct ($x = 0$). The u, v, and w velocity components are the span-wise velocity, vertical velocity, and cross-flow free-stream velocity components, respectively. For the upwind ($z/D = [-8, -4]$) velocity profiles, the velocity components are all relatively uniform, with small variations in the boundary layer. Figure 4.9c shows downwind, with w the progression of the plume. As the plume propagates downwind from the exhaust stack, from $z/D = 1$ to $z/D = 16$ the w component shows the following trends:

- a decrease in the maximum w velocity from $w \approx 18.4\,\mathrm{m\,s^{-1}}$ to $w \approx 7.2\,\mathrm{m\,s^{-1}}$,
- the increase in position of maximum w from $y/D = 13$ to $y/D = 19.5$, and
- an increase in the vertical (y) size of the plume.

All three trends listed are consistent with previous studies [1, 5, 6, 90]. The following phenomena can explain these trends; as the plume propagates downwind, the plume spatially spreads and dissipates, with the entrainment of the cross-flow. The dissipation of the plume leads to the flow eventually resembling the cross-flow free-stream profiles in Figure 4.9c at $z = [-8D, -4D]$. Figure 4.9a shows the

presence of the plume, but there is a strong span-wise bias in the flow along the negative direction ($u \approx -2.5$). This discrepancy in the flow asymmetry in the measurements could be from several factors, including misalignment of the Cobra Probe 209 leading to a bias in the span-wise direction, so that the flow exiting from the duct was not perfectly axisymmetric and exhibited a slight bias towards one end, and/or the geometry of the closed-loop four-sided wind-tunnel with flow favouring one side.

It should be taken into consideration that the current flow measurements in Figure 4.9 do not accurately represent the reverse flow. As discussed in Section 4.2, the measurements for negative velocities along the cross-flow free-stream saturate at $w = 0\,\mathrm{m\,s^{-1}}$. The data points in orange represent mean velocity measurements with more than 50% transient velocity data saturated at $0\,\mathrm{m\,s^{-1}}$. Interestingly, the flow measurements behind the exhaust stack at $z/D = [1, 2]$ show the majority of the orange data points. This suggests that this region contains reverse flow, which is consistent with other cases in the literature [1, 5, 6, 78, 80–82, 84, 141, 142]. The reverse flow in these regions is due to the recirculation of the flow in the geometric near-field, behind the jet, and the stack. As the plume propagates, the region for reverse flow reduces, and this can be seen in Figure 4.9, with $z/D = [4, 8, 16]$.

Figure 4.10 shows the turbulence intensities used to quantify the fluctuations in the velocity, with vertical profiles at various positions ($z/D = [-8, -4, 1, 2, 4, 8, 16]$) along the Y-Z plane intercepting the centre of the duct ($x = 0$). Upwind of the stack ($z/D = [-8, -4]$) the TI is relatively uniform in the cross-flow free-stream and shows an increase in TI along the boundary layer. The increase in the TI in the boundary layer is expected and is due to the vorticity in the boundary layer. It should be noted that the TI from the exhaust stack in the reduced-scale model is relatively low (0.5% to 1.5%) in comparison with the incoming TI from real atmospheric boundary layers (ABL) in nature. Hence in real OCGT, the diffusion of the plume is likely to be faster than the diffusion of the plume in the experimental realm. The same conclusion applies to the numerical results with steady-state fluid dynamics and steady-state sound radiation. This is supported by the study completed by Andreopoulos [5, 6].

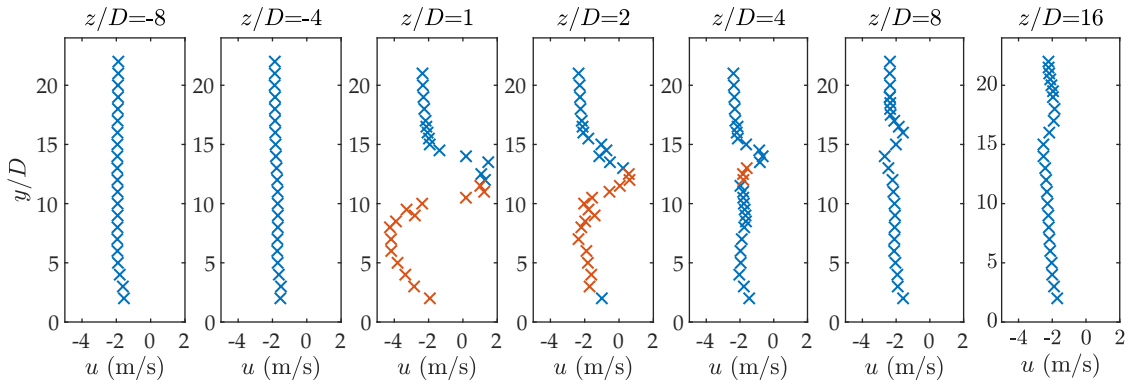

(a) u

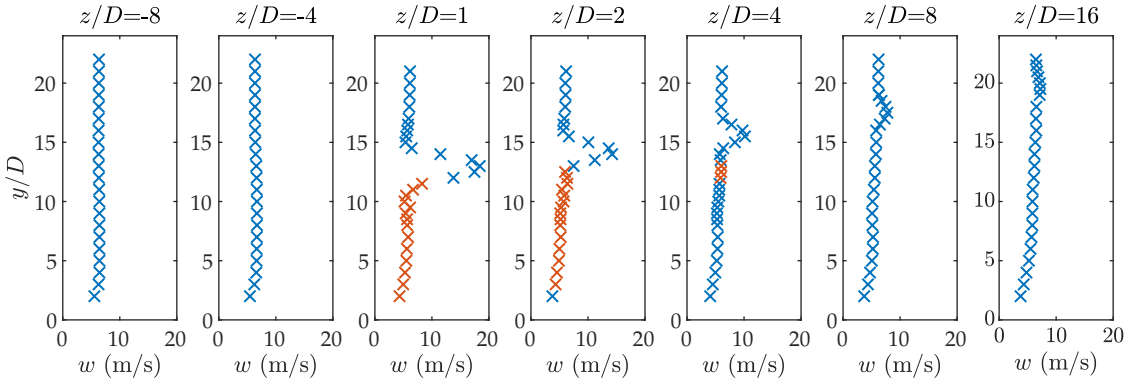

(b) v

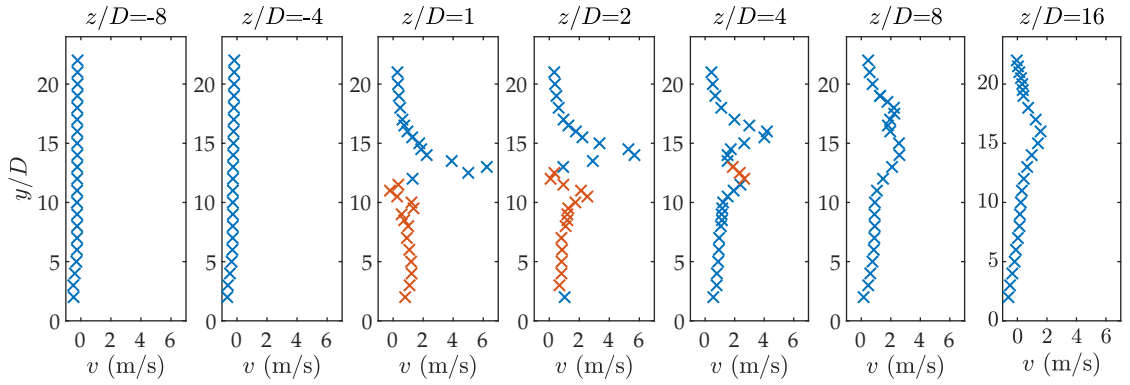

(c) w

Figure 4.9: Vertical velocity profiles at each velocity component, with (a) u, the span-wise velocity, (b) v, the vertical velocity, and (c) w, the cross-flow free-stream velocity. The vertical velocity profiles are at varying distances downwind and upwind ($z/D = [-8, -4, 1, 2, 4, 8, 16]$), and measured along a plane with $x = 0$ (along the duct centreline). The duct centreline is at $z/D = 0$, and the duct outlet height is at $y/D = 8$. The data points with more than 50% of the transient velocity data saturated by the Cobra Probe 209, due to the reverse flow, have been set to orange, and the other data points are blue.

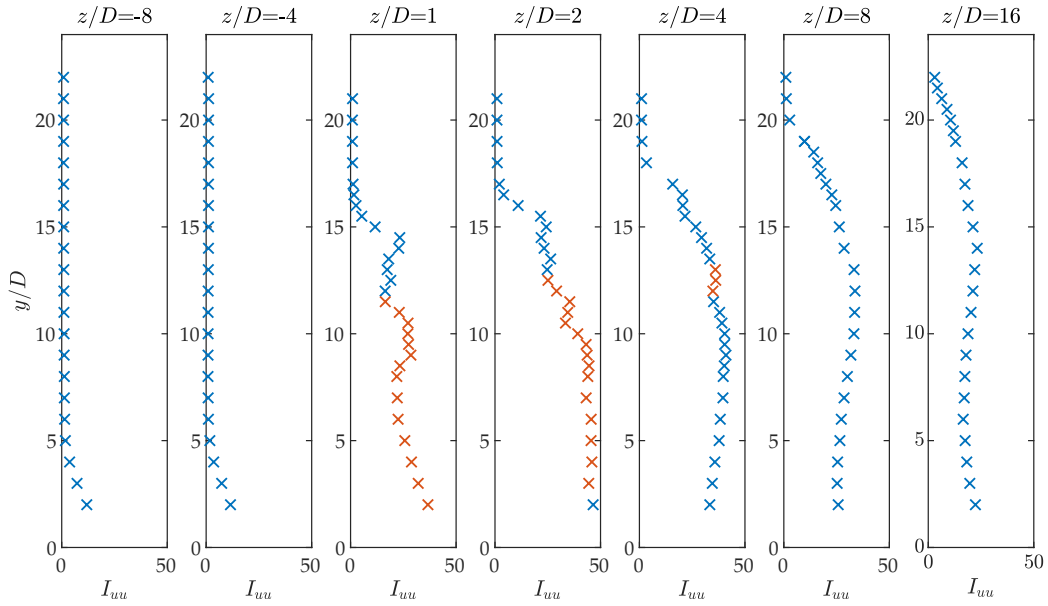
z/D=-8
z/D=-4
z/D=1
z/D=2
z/D=4
z/D=8
z/D=16
y/D
I_uu

(a) TI_{uu}

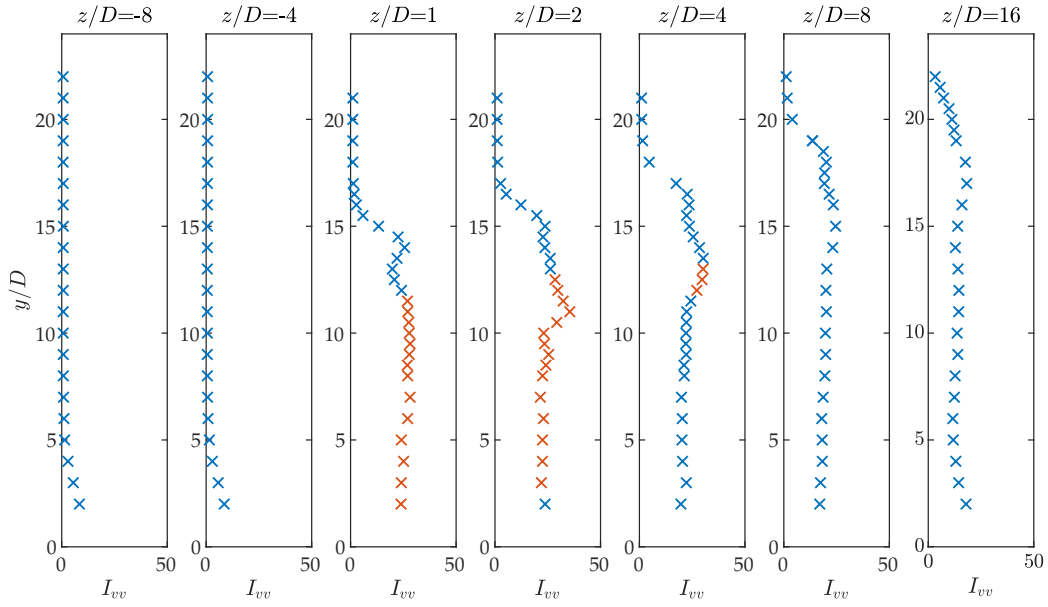
z/D=-8
z/D=-4
z/D=1
z/D=2
z/D=4
z/D=8
z/D=16
y/D
I_vv

(b) TI_{vv}

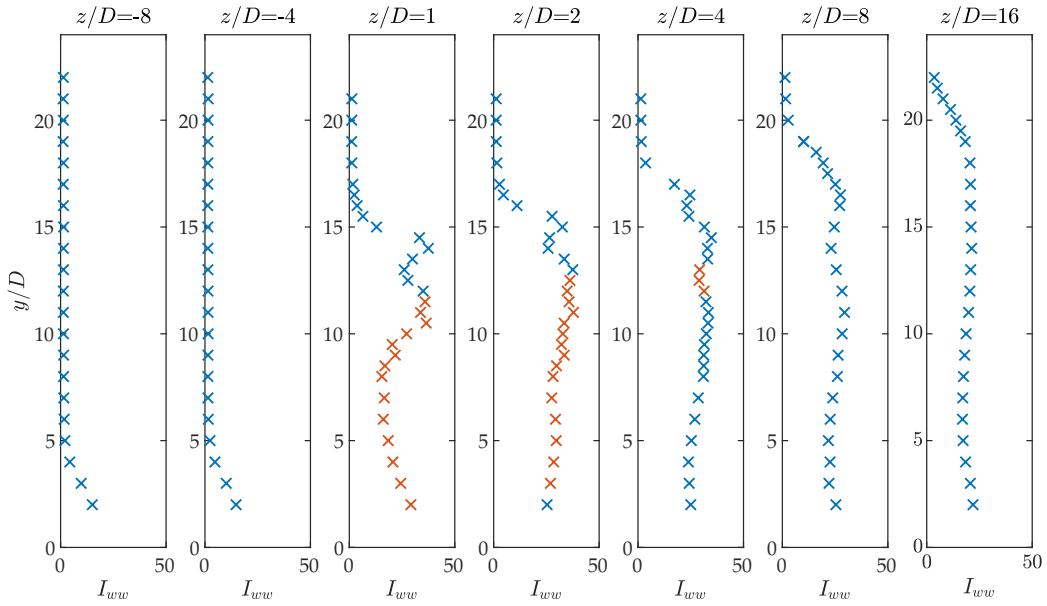

(c) TI_{ww}

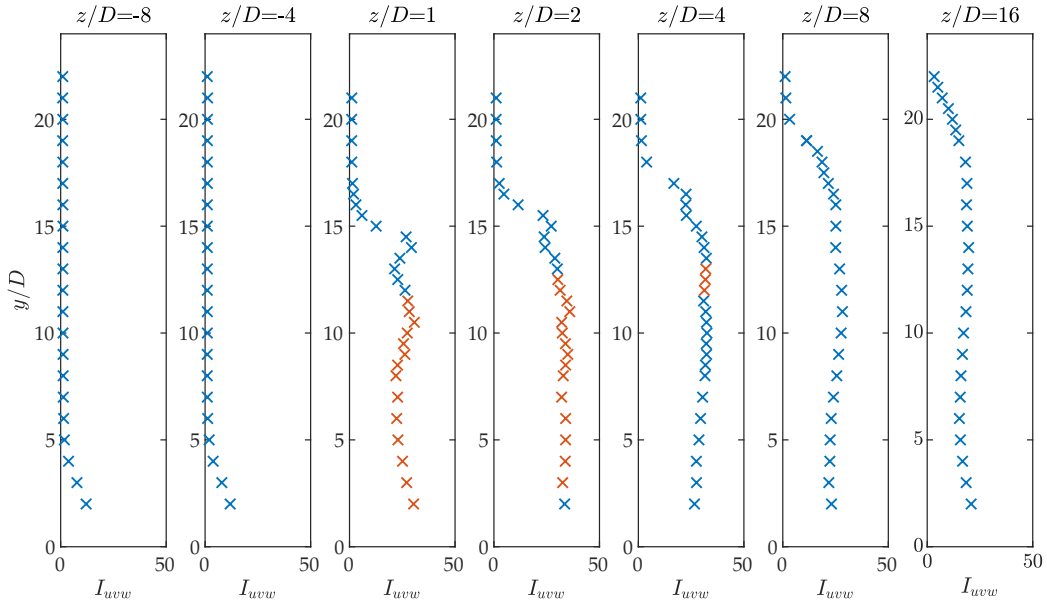

(d) TI_{uvw}

Figure 4.10: Vertical TI profiles, with (a) I_{uu}, (b) I_{vv}, and (c) I_{ww}, and (d) I_{uvw}. The vertical TI profiles are at varying distances downwind and upwind ($z/D = [-8, -4, 1, 2, 4, 8, 16]$) of the exhaust stack, and measured along a plane with $x = 0$ (along the duct centreline). The duct centreline is at $z/D = 0$ and the duct outlet height is at $y/D = 8$. The data points with more than 50% of the transient velocity data saturated by the Cobra Probe, due to the reverse flow, have been set to orange, and the other data points are blue.

The interaction of the cross-flow with the elevated exhaust jet leads to complex features downwind of the exhaust stack and is evident from the different flow structures that can be observed with TI measurements. Figure 4.10 shows that TI has significantly increased downwind of the duct ($z/D = [1, 2, 4, 8, 16]$), in comparison with upwind of the duct outlet ($z/D = [-8, -4]$). This is due to the incoming cross-flow interacting with the stack and jet to produce the three key fluid dynamic features observed in Figure 2.4, namely the plume, jet-wake, and stack-wake. Downwind of the exhaust stack there is also a distinguishing difference in the TI for the plume and cross-flow free-stream, where the cross-flow free-stream TI is approximately 1%. From this, it can be ascertained that as the plume propagates, the position of the plume increases in height downwind due to momentum and buoyancy. Although the TI is presented for values in the jet-wake and stack-wake at $z/D = [1, 2]$, the values presented are an underestimation of the actual value due to the reverse flow measurements for u being omitted in the calculations for I_{uu}, I_{vv}, I_{ww}, and I_{uvw}, as the Cobra Probe saturates when $u < 0\,\mathrm{m\,s^{-1}}$. By omitting the reverse flow measurements, the overall fluctuating component of velocity is reduced, as is the corresponding TI. However, even though a large portion of the fluctuating velocity components were removed when calculating the TI, the intensities in Figure 4.10 at $z/D = [1, 2]$, show a smooth trend. For the TI at $z/D = [4, 8, 16]$ the overall TI reduces as the plume propagates and dissipates into the cross-flow. The current set of TI measurements shows that the plume persists for the entire experimental domain. It would be ideal in the future to measure flow profiles further downwind of the exhaust stack ($z/D > 16$) to investigate the distance before the plume dissipates into the cross-flow.

From the literature and the numerical results in Chapter 3, the plume downwind of the exhaust stack has a finite width in the span-wise direction. Figure 4.11 shows the span-wise velocity measurements at three heights ($y/D = [17, 18, 21]$), and with a fixed distance downwind of the exhaust stack ($z/D = 8$). The three heights for the velocity measurements were chosen based on the velocity profiles at $z/D = 8$, shown in Figure 4.9, whereby $y/D = 17$ was expected to intercept the centre plume in the span-wise direction. As can be seen in Figure 4.9, all the plots show that

the measurements are plane-symmetric about the Y-Z plane ($x/D = 0$), with slight discrepancies in some of the measurements. Interestingly, the span-wise velocity measurements for u show a peak and a trough in the measurements that represent the peaks in the counter-rotating vortex. It should be noted that Figures 4.9a and 4.11a show there is a bias of $u \approx -2.5\,\mathrm{m\,s^{-1}}$. Figures 4.11b and 4.11c, show similar trends, with the peak in the velocity measurements along the plane of Y-Z plane of symmetry ($x/D = 0$). The peak in the v and w was as expected at the centre of the plume. All three velocity components show the increase in height from $y/D = 17$ to $y/D = 21$. The peak velocity in the span-wise profiles reduces and approaches cross-flow free-stream conditions. If more time were available for testing at the Thebarton Wind Tunnel, additional measurements for span-wise profiles would have been undertaken to investigate the development of the plume at different heights and positions downwind of the exhaust stack. However, the span-wise profiles show that the experimental reduced-scale exhaust rig reproduces key fluid dynamic features seen in the literature and numerically in Chapter 3.

The span-wise profiles can be further interpreted with TI at varying heights and a fixed distance downwind of the exhaust stack at $z/D = 8$, to show fluid dynamic details of the plume. Figure 4.12 shows the span-wise measurement of TI for three heights ($y/D = [17, 18, 21]$) at $z/D = 8$, downwind of the exhaust stack . All three span-wise profiles show the following trends:

- a peak in TI along the Y-Z plane that intercepts the duct centreline ($x/D = 0$) and was, as expected, at the centre of the plume,
- the plume is symmetrical along the Y-Z plane, with the symmetrical span-wise profiles showing symmetry in TI,
- a reduction in the peak TI with the increase in height from $y/D = 17$ to $y/D = 21$, and
- a slight asymmetry in the span-wise profile that favours $x/D > 0$.

It is difficult to determine the reason for the slight asymmetry in the span-wise profiles for TI. It could possibly be due to either: the geometry of the closed-

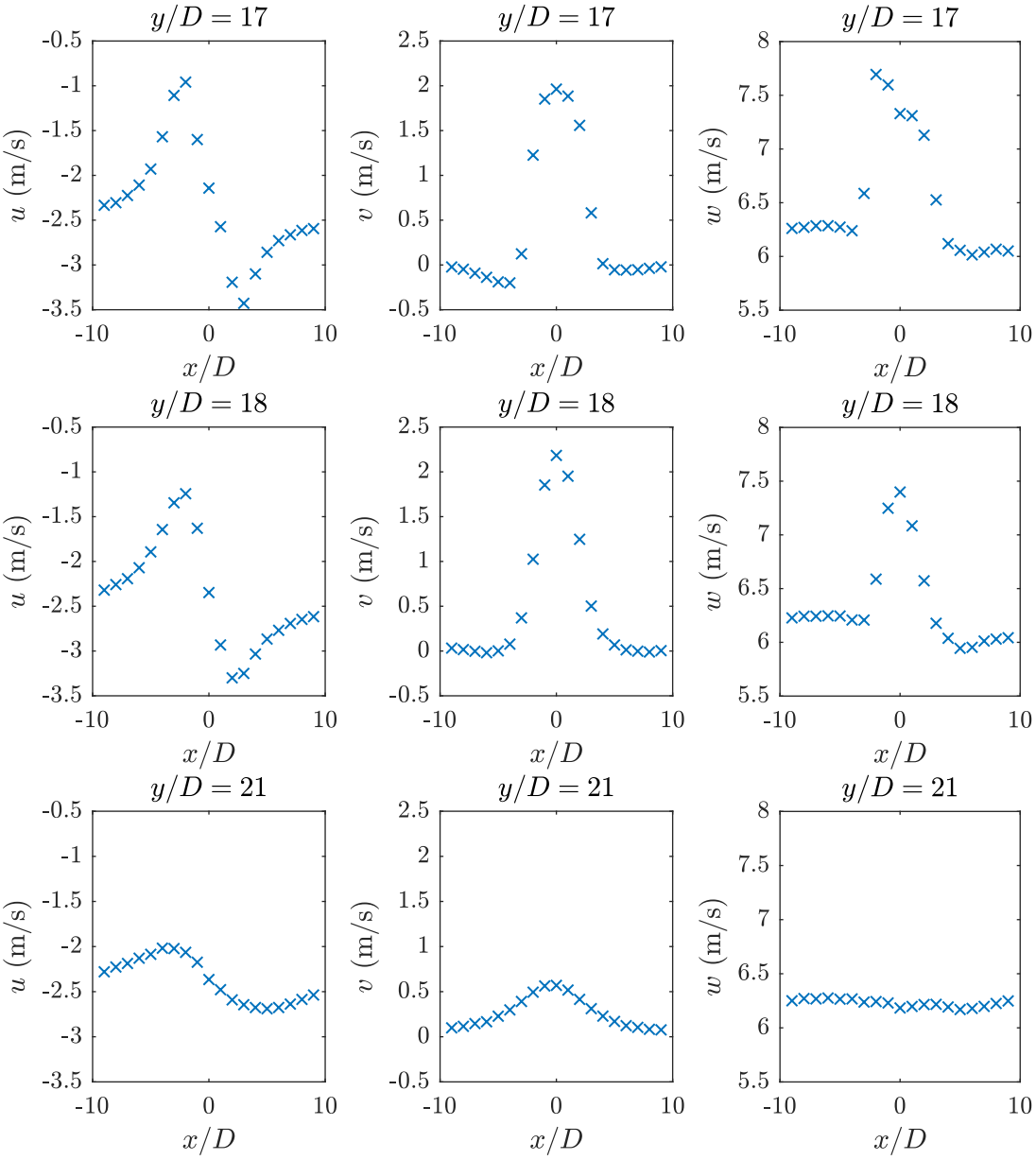

(a) u (b) v (c) w

Figure 4.11: Span-wise velocity profiles at each velocity component, with (a) u, the span-wise velocity, (b) v, the vertical velocity, and (c) w, the cross-flow free-stream velocity. The span-wise velocity profiles are at three heights (y/D = [17, 18, 21]), at a single position downstream of the exhaust stack at z/D = 8.

loop four-sided Thebarton Wind Tunnel biasing flow towards to the centre of the wind tunnel (as seen in Figure 4.3), the 90° bend in the exhaust stack causing non-axisymmetric flow exiting the exhaust stack favouring one side ($x/D > 0$), and/or the uneven Dacron surface for the incoming cross-flow surface. Hence, the span-wise profiles for TI show the presence of the fluctuating velocity in the plume, with a concentration of TI along the centreline, and a reduction in TI at certain heights outside of the plume.

4.3.2 Experimental temperature measurement

As discussed in Section 4.2, the temperature field was measured using the traverse. The temperature gradients downwind of the exhaust stack are complex due to the non-isothermal plume, as shown in Chapter 3. The first set of temperature results presented are vertical (y) temperature profiles at different positions upwind and downwind of the exhaust stack, with all the measurements along the Y-Z plane that intercepts the centre of the duct ($x = 0$). The second set of temperature results are contour plots along the X-Y planes at various distances downwind of the exhaust stack ($z/D = [8, 16]$).

Figure 4.13 shows the vertical profiles at various distances upwind and downwind of the exhaust stack along the Y-Z plane that intercepts the centre of the duct ($x = 0$). Upwind of the duct outlet, the temperature is approximately uniform, with $\Theta = 0$. However, downwind of the exhaust stack the temperature of the plume is not uniform and exhibits the following trends, with the propagation of the plume downwind:

- a decrease in maximum temperature from $\Theta \approx 0.19$ to $\Theta \approx 0.075$,
- increase in the vertical position of the maximum temperature from $y/D = 14$ to $y/D = 16.5$, and
- increase in the spatial size of the plume.

The results of the temperature measurements in Figure 4.13 show a similar trend with Figure 4.9. The temperature results reflect the work of Johnson et al. [90], who

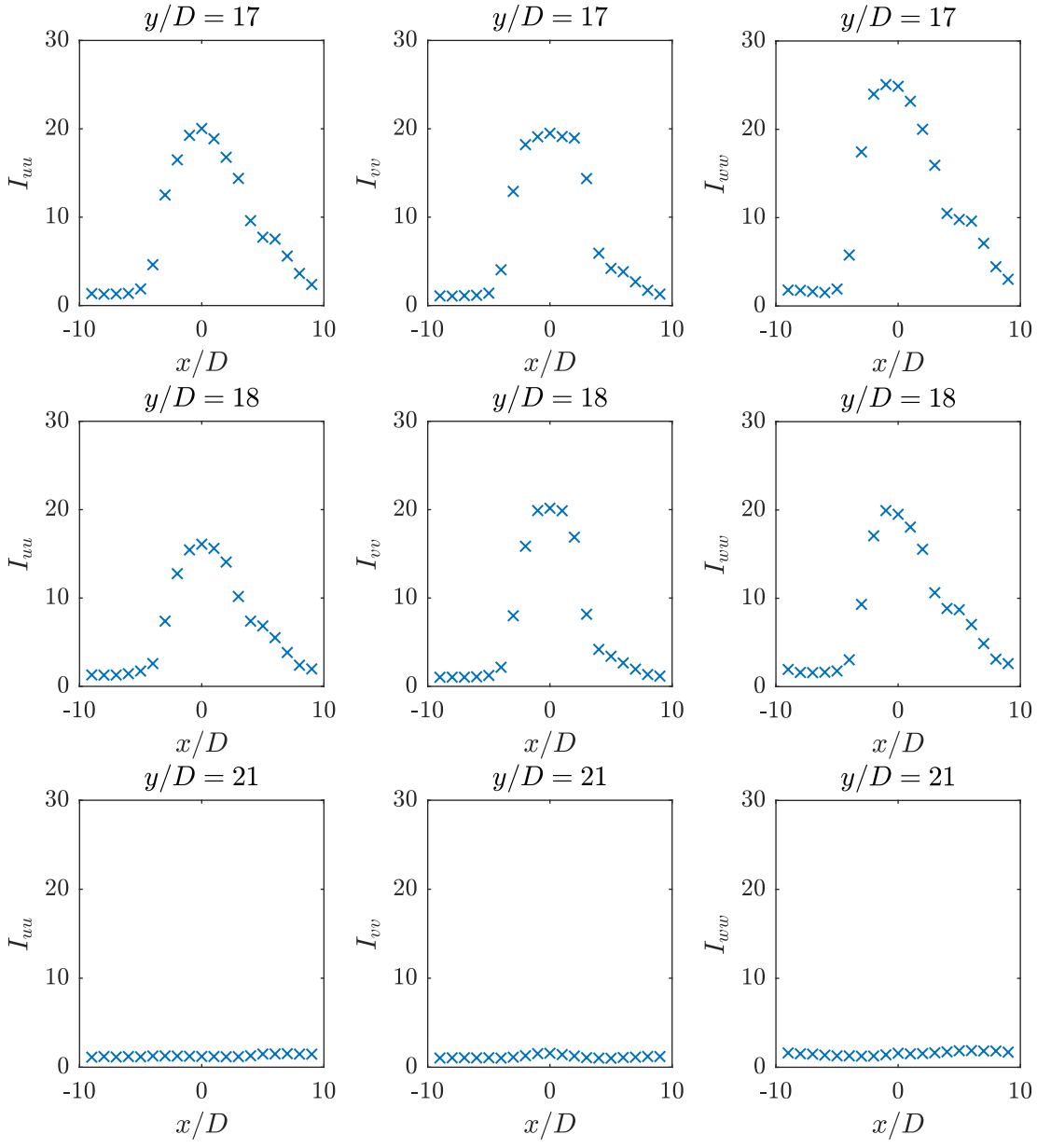

(a) I_{uu} (b) I_{vv} (c) I_{ww}

Figure 4.12: Span-wise turbulence intensity profiles at each component, with (a) I_{uu}, (b) I_{vv}, and (c) I_{ww}. The span-wise turbulence intensity profiles are at three heights (y/D = [17, 18, 21]) and at single position downwind of the exhaust stack at z/D = 8.

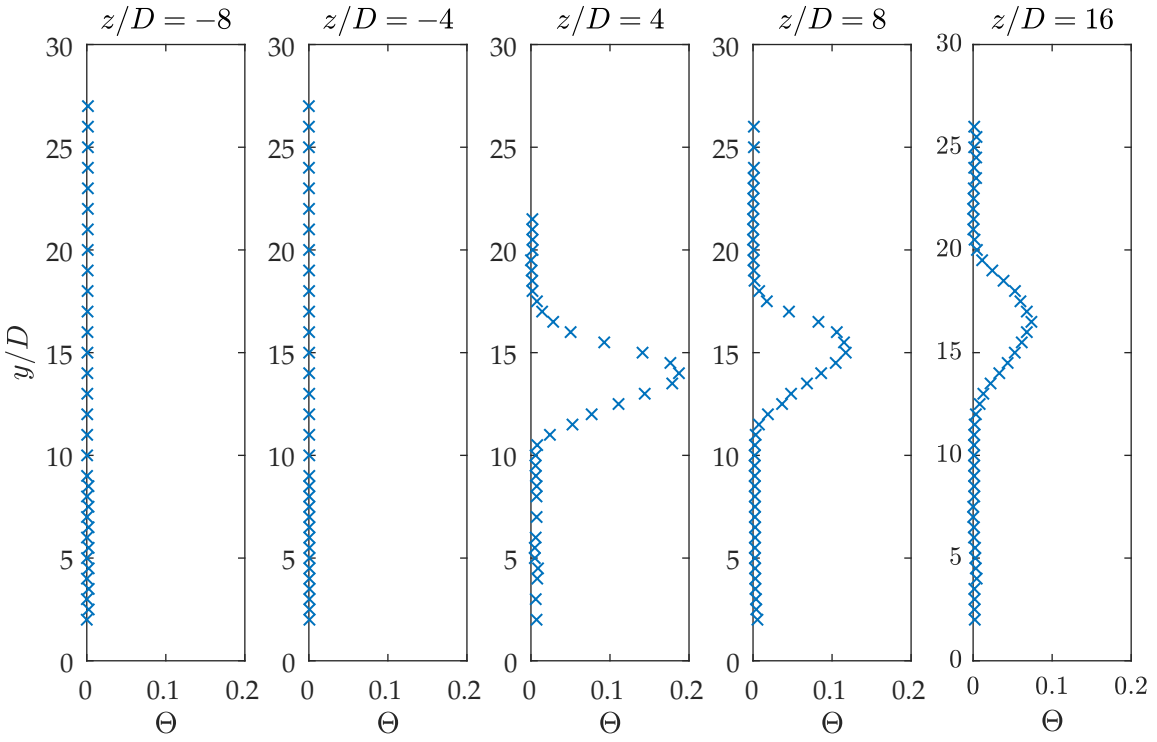

Figure 4.13: Vertical temperature profiles at five distances downwind and upwind ($z/D = [-8, -4, 4, 8, 16]$), measured along the plane $x = 0$ (the duct centreline).

show a similar finding, with the decrease in temperature and increase in the height of the plume, as the plume propagates downwind from the exhaust stack.

Downwind of the exhaust stack, the plume has a finite width in the span-wise direction, which was observed in both the velocity (shown in Figures 4.11 and 4.12) and temperature measurements. Figure 4.14 shows the temperature distribution as a contour plot along the X-Y plane at two positions downwind ($z/D = [8, 16]$). Figures 4.14a and 4.14b show similar features, with the increase in distance from the exhaust stack downwind: a decrease in the maximum temperature of the plume, an increase in the height of the plume, and an increase in the spatial size of the plume. From the temperature distribution it can be seen that the shape of the counter-rotating vortex pairs in Figure 4.14 is similar to the counter-rotating vortex pairs observed in the literature [90]. However, Figure 4.14 shows that the maximum temperature was not in the middle of the counter-rotating vortex, as

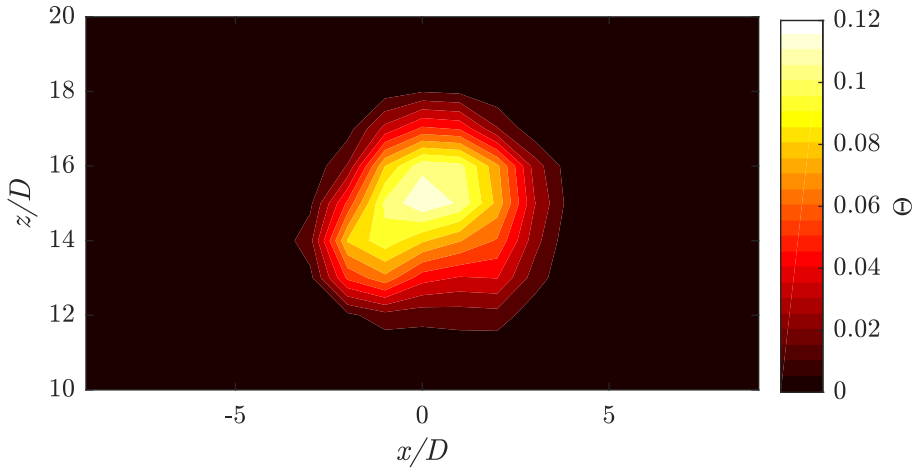

(a) v

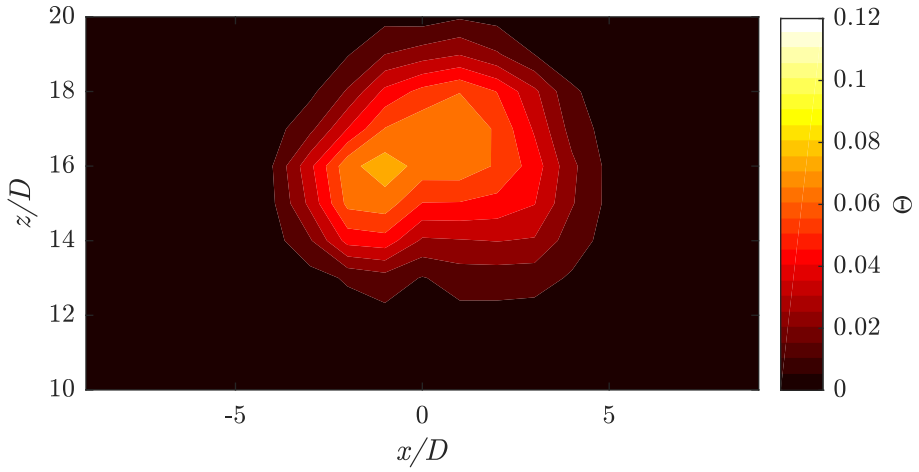

(b) w

Figure 4.14: Experimental temperature contour plot from the non-isothermal JICF at two distances downwind from the exhaust stack (a) z/D = 8, and (b) z/D = 16, with R = 5, and T_j = 500 °C.

observed by Johnson et al. [90]. One of the reasons for this could simply be random experimental errors in measuring the plume. Additionally, due to the discretised measurement, there could be a discretisation error in measuring the temperature at $1D$ intervals. Moreover, the duration for each temperature measurement may be insufficient. Furthermore, the asymmetric bias in the counter-rotating vortex pairs could be related to asymmetry in the cross-flow or the jet.

In summary, the temperature downwind of the exhaust stack shows a thermal gradient. The thermal gradient has a finite size and is propagated downwind of the exhaust stack. The experimental temperature measurements show that with jet spreading and entrainment of the cooler cross-flow, there is a reduction in the temperature gradients with the distance downstream. The results were only measured up to $16D$ due to time constraints when accessing the wind tunnel. All the measurements show the presence of a thermal gradient, and if additional measurements were taken further downwind of the exhaust, the plume would dissipate further, and the temperature downwind would converge to the cross-flow free-stream temperature. Future measurements will need to be taken to investigate the distance required for the plume to dissipate, and this is discussed further in Chapter 6.

4.4 Acoustic results

The key findings in the experimental acoustic results will be discussed in this section. A discussion on the following experimental sound radiation cases is presented:

- sound radiation in the absence of the JICF (isothermal stationary field),
- sound radiation in the presence of a non-isothermal jet without cross-flow,
- sound radiation in the presence of a non-isothermal JICF at a single cross-flow ratio, $R = 5$, and varying jet temperatures, $T_j = [27\,°C, 100\,°C, 300\,°C, 500\,°C]$, and
- sound radiation cross-flow sensitivity study for non-isothermal JICF, with $R = [5, 7.5, 10, 12.5]$.

4.4.1 Sound radiation in the absence of the jet and cross-flow

This section discusses the experimental acoustic results for sound radiation through the duct network in the absence of the jet and the cross-flow, which will be referred

to as the isothermal stationary field. The aim of these results was to provide a benchmark case where the sound propagates through a homogeneous medium and to investigate the validity of the monopole radiation assumption. The acoustic verification study in the Anechoic Chamber is presented in Appendix D and this section outlines the experimental acoustics results in the Thebarton Wind Tunnel.

With the array and exhaust rig characterised in the Anechoic Chamber (Appendix D), it was relocated to the Thebarton Wind Tunnel. The tunnel presents new challenges, in particular, strong acoustic reflections from hard surfaces and significant background noise levels from plant equipment, including tunnel fans. The acoustic tests undertaken in the Anechoic Chamber were repeated in the wind tunnel to investigate such issues. The following acoustic results are presented and discussed:

- SPL measurements at two microphones with and without the sound from the exhaust stack outlet,
- coherence results between the electro-acoustic signal and the acoustic pressure,
- COP for the acoustic pressure at two microphones, and
- band-averaged one-third octave band directivity plots with the sound radiating from the exhaust stack outlet.

Figure 4.15 shows the SPL plots for two different cases: background noise levels, without the fans, with a generator or Airpack blower operating, and then with sound only radiating from the exhaust stack in an isothermal stationary field. The SPL responses show that the sound levels are sufficiently higher than the background noise levels for adequate signal to noise ratios. Comparing the shape of the SPL responses between Figures D.7 and 4.15, the responses are similar. Apart from a large drop in SPL at 2.5 kHz, the two SPL responses are almost identical, which indicates that the Dacron and the false floor provide an adequate anechoic environment for the sound at ground level. Furthermore, the reflections from the wall, wind tunnel and other instrumentation are significantly less than the

contribution from the direct path, and hence, the contributions of the reflections to the directivity plot are minimal. In order to screen the effects of the dips in SPL associated with higher order duct modes, reflections, diffraction and other external unwanted noise, the results have been band-averaged over a one-third octave band, similar to the previous section.

Figure 4.16b shows the coherence, γ^2_{xy}, between the electro-acoustic signal and the acoustic pressures. Again, the coherence results for Figures D.3 and 4.16, taken in the Anechoic Chamber and in the wind tunnel, show similar results, with a strong degree of linearity in similar regions. However, as seen in Figure 4.15, the drop in SPL at 2.5 kHz is also observed in 4.16, and is only present in testing at the Thebarton Wind Tunnel. The reduction of coherence in these regions is suspected to be a signal to noise ratio issue and could be from one of, or a combination of, multiple multipath sources of sound such as: structural acoustic radiation from the ductwork, acoustic reflections, diffraction from the duct, all other surfaces reflecting sound and reducing the coherence drastically.

The coherence and the SPL are similar for the sound propagation through the duct in both the Anechoic Chamber and the Thebarton Wind Tunnel. Consequently, the COP should show a similar trend, but it does not. Figure 4.15 shows the COP at two microphones for sound propagation through the duct in an isothermal stationary field at the Thebarton Wind Tunnel. For the high frequency region above the cut-on (f_{co} = 4.23 kHz), the COP are very similar for the Anechoic Chamber and Thebarton Wind Tunnel, when comparing Figures D.7 and 4.15, respectively. As expected from the results in Figures D.7 and D.6, at approximately 2.5 kHz the reduction in SPL and coherence, respectively, are also consistent in the COP plot in Figure 4.15a.

Figure 4.17 shows the experimental, band-averaged sound directivity in an isothermal stationary field for four band-averaged one-third octave bands with centre frequencies, ka = [0.85, 1.08, 1.35, 1.70], at a distance of 14D and 28D. As expected for the 4 kHz one-third octave band ($ka \approx 1.1$), the sound directivity is axisymmetric and elliptical, with a lobe forming along the centreline of the duct axis at 0°. The results in Figure 4.17 show very similar trends to the results in the

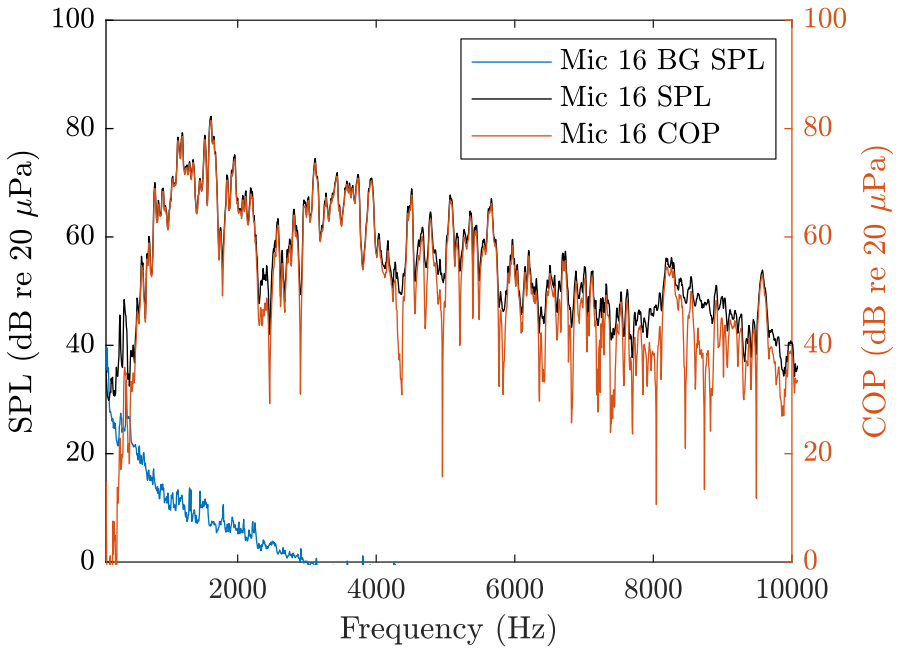

(a) Microphone at $-2.5°$ on the 14D array (Mic 16).

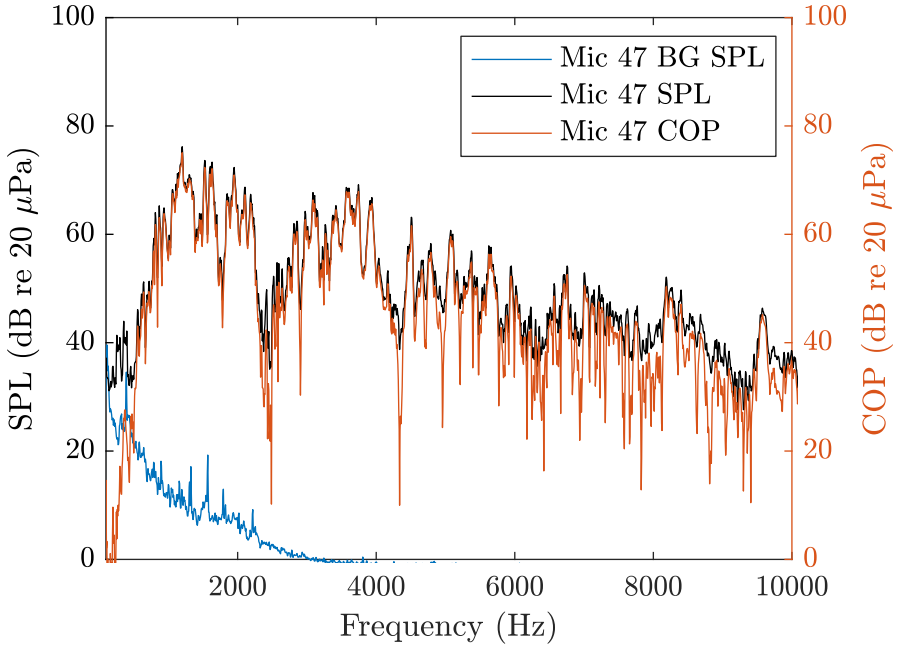

(b) Microphone $-7.5°$ on the 28D array (Mic 47).

Figure 4.15: The SPL measurement at two microphones at the top of the 14D and 28D array. The test was conducted in the Thebarton Wind Tunnel in an isothermal stationary field. The background measurements are taken with the plant equipment not operating, and the sound is propagating through the duct network. BG refers to the background noise levels. Relevant coherence is plotted in Figure 4.16.

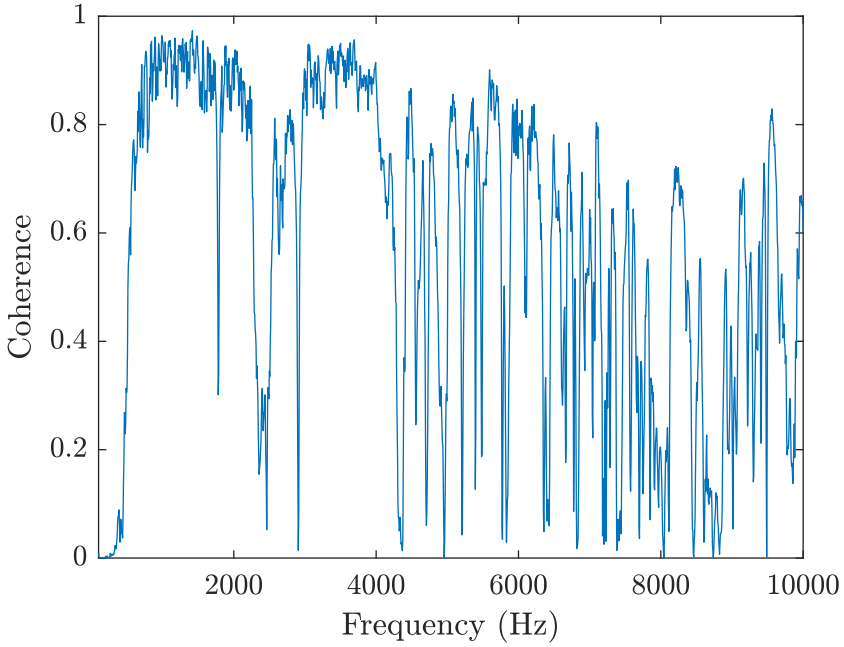

(a) Microphone at $-2.5°$ on the $14D$ array (Mic 16).

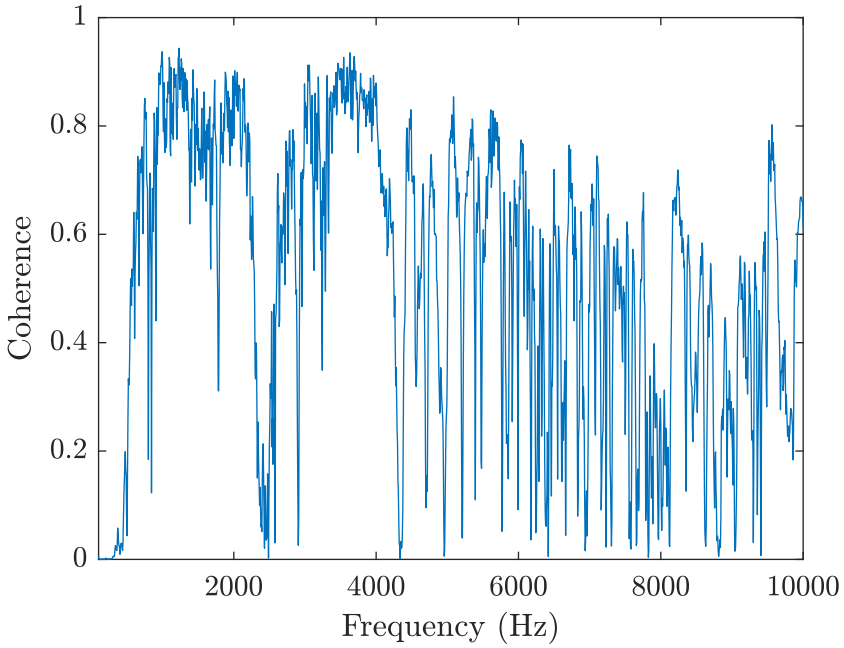

(b) Microphone at $-7.5°$ on the $28D$ array (Mic 47).

Figure 4.16: The coherence, γ^2_{xy}, between the electro-acoustic signal into the compression driver and microphone SPL response for two microphones at the top of the $14D$ and $28D$ array. The test was taken in the Thebarton Wind Tunnel with an isothermal stationary field and the plant equipment not operating. Sound is propagating through the duct network.

literature for the sound directivity for an exhaust stack in an anechoic environment [25]. In Figure 4.17, the elliptical lobe shows a reduction in sound levels of up to 4.5 dB at ±90° compared to on-axis. Hence, for predictions of ground-level SPLs, the monopole assumption is likely to be conservative. In the absence of the flow, it is commonly assumed that the sound power can be estimated with ISO-10494 [87] in the near-field and then propagated using ISO-9613 [88], where a monopole assumption is used, which approximates the sound radiation of a piston in an infinite plane. This is not the case in the experimental results, and it can be observed that with the hard duct exterior and the anechoic ground, the sound radiation is elliptical with a lobe forming on-axis (0°).

4.4.2 Sound radiation in the presence of a jet without cross-flow

The inclusion of a non-isothermal heated jet provides an inhomogeneous medium for complex sound propagation. The purpose of investigating sound radiation through an axisymmetric non-isothermal jet is to analyse the sound directivity in the absence of the cross-flow and reproduce qualitative features in the directivity plot seen in work conducted by Atvars et al. [14, 15] and Grande [66]. The sound radiation through the velocity and thermal gradients produced by the shear layer of a non-isothermal axisymmetric jet has shown to refract sound and form acoustic lobes off-axis [14, 15, 66]. This section will discuss the results from sound radiating through the non-isothermal jet and plot the SPL, coherence and COP response. Subsequently, directivity results for band-average one-third octave bands are presented. It should be noted that the experimental results in this study were measured at a lower jet temperature (T_j = 350 °C) than commonly seen in OCGT exhaust stacks. The lower temperature used in the tests is a limitation of the experimental setup, where the microphones on the 28D arc are in the heated jet flow arc, where testing with $T_j > 350$ °C would lead to an air temperature exceeding the maximum temperature rating of the microphones (60 °C). Furthermore, it was desirable to measure the directivity at 14D to observe the effects of distance on the sound propagation, in particular, the refraction of sound as a result of the jet shear layer, but, unfortunately, the microphone temperature limits were exceeded

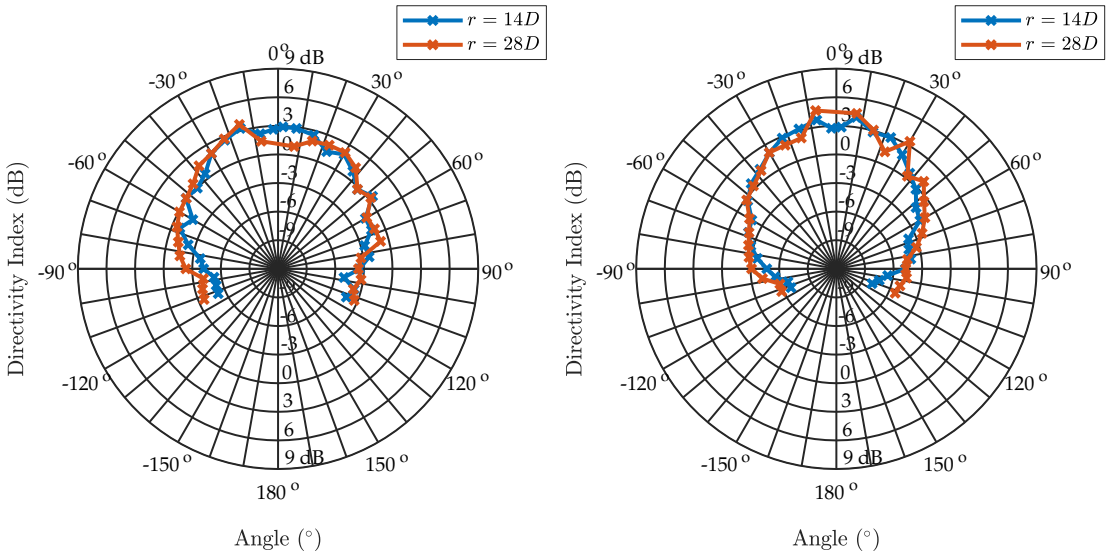

(a) ka = 0.85.

(b) ka = 1.08.

(c) ka = 1.35.

(d) ka = 1.70.

Figure 4.17: The DI for sound propagation in an isothermal stationary field for band-averaged one-third octave bands with centre frequency ka = [0.85, 1.08, 1.35, 1.70] (f = [3.15 kHz, 4 kHz, 5 kHz, 6.3 kHz]) at two radii (14D and 28D). The results are from tests conducted at the Thebarton Wind Tunnel.

necessitating their removal. As discussed earlier in Section 4.2, even though the microphones are subjected to the jet flow, both wind screens and COP analysis were used to reduce impact of the flow induced noise from the jet flow.

Figure 4.18 shows the SPL measurements with the speaker on and those for the background sound levels at two different microphones (Microphones 47 and 60) on the $28D$ array, while $T_j = 350\,°\text{C}$ and $M_j = 0.1$. The SPL measurements show an appreciable difference between background SPL and the measured SPL. However, the microphone on-axis at 7.5° (microphone 47) shows a significant reduction in SPL, where there is insufficient sound in the high-frequency region for an appropriate signal to noise ratio ($\geq 20\,\text{dB}$). The background SPL measurements show an overall increase in SPL with the Airpack blower and heaters on, which can be seen when comparing Figures 4.15 and 4.18. Additionally, the background SPL measurements in Figure 4.18 show the presence of harmonic tones at approximately 1.9 kHz, 3.8 kHz, 5.7 kHz, and 7.6 kHz. These harmonic tones in the background SPL measurements are not obvious in the SPL measurement with the compression drivers on.

To complement the SPL plots, the coherence results are presented in Figure 4.19 to show the regions of coherent sound in the measurements. The coherence plots in Figure 4.19 show that the coherence is dependent on the position of the microphones and the acoustic frequency. Both coherence plots show that there is a reduction in the coherence in the high frequency range above 1.8 kHz and 4 kHz for Figures 4.19a and 4.19b, respectively. The reduction in coherence for the microphone at $-7.5°$ (Microphone 47) and the microphone at 90° (Microphone 60), will be explained later in this section, from analysis of the directivity plots in Figure 4.20. Furthermore, due to the fine frequency bins in Figure 4.19 the results are not smooth and it is hard to determine if the operation of the Airpack blower and heater, with the presence of the harmonic tones shown in Figure 4.18, affected the results.

Interestingly, Figure 4.18 show the COP at two different microphones (Microphones 47 and 60), where the presence of the non-isothermal jet introduces further complexity to the COP measurements. As expected from the results in Figure 4.19,

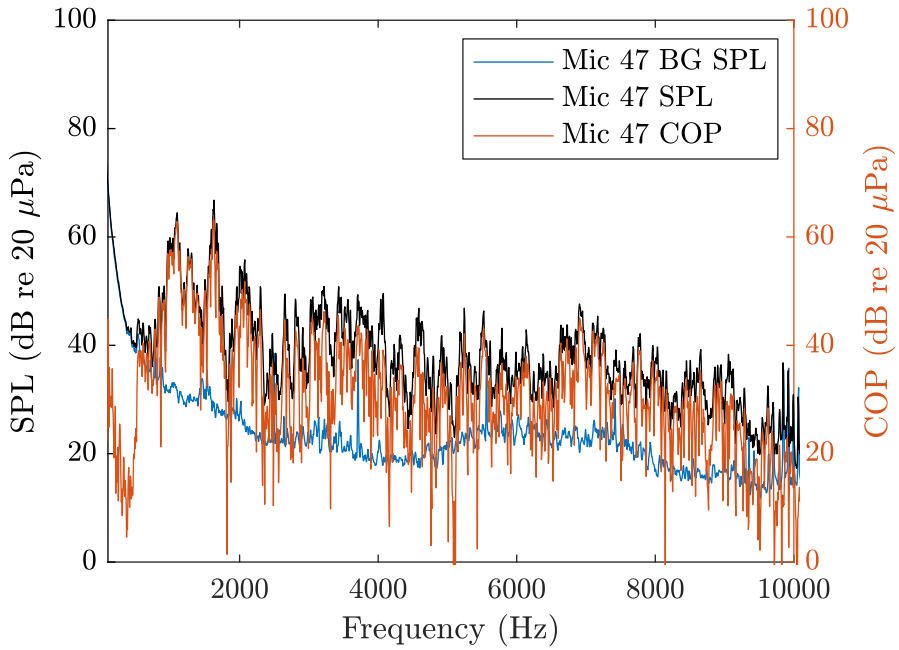

(a) Microphone at −7.5° (Mic 47) or on-axis.

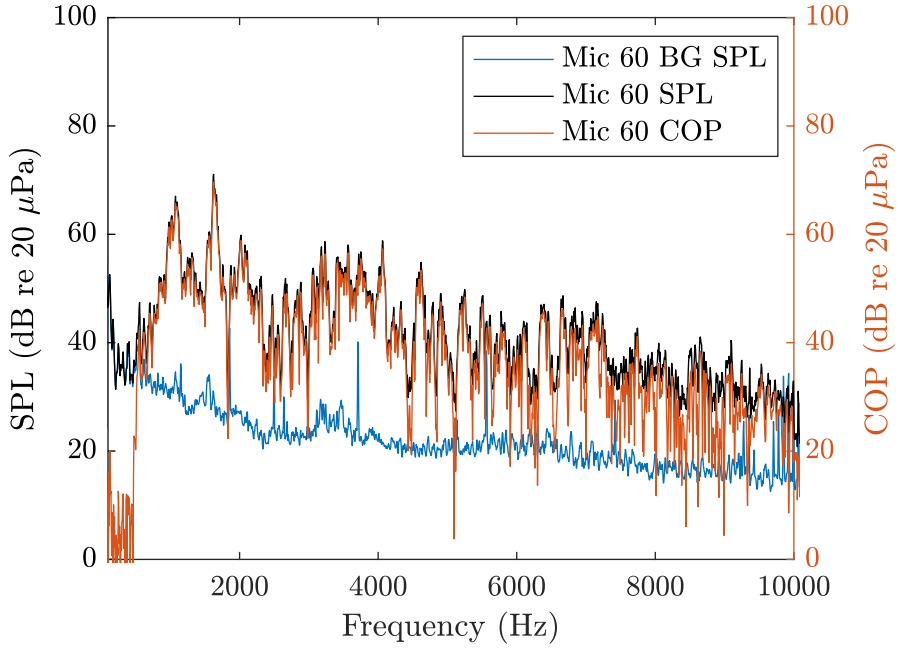

(b) Microphone at 90° (Mic 60) or horizontal to the duct outlet.

Figure 4.18: The SPL response at two microphones (on the vertical and horizontal axis) on the 28D array for sound propagating through a non-isothermal jet with T_j = 350 °C and M = 0.1. BG refers to the background noise levels. Relevant coherence is plotted in Figure 4.19.

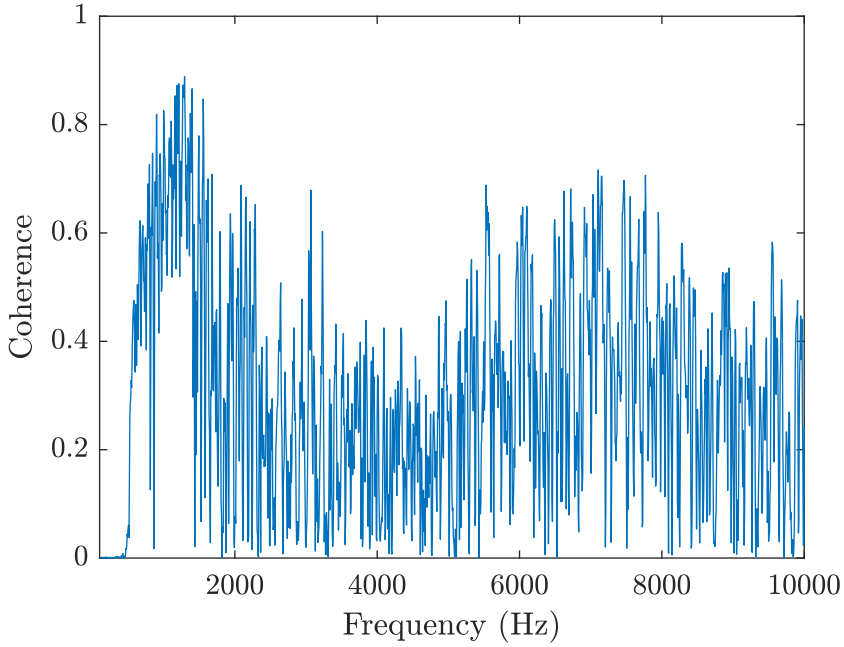

(a) Microphone at −7.5° (Mic 47) or on-axis.

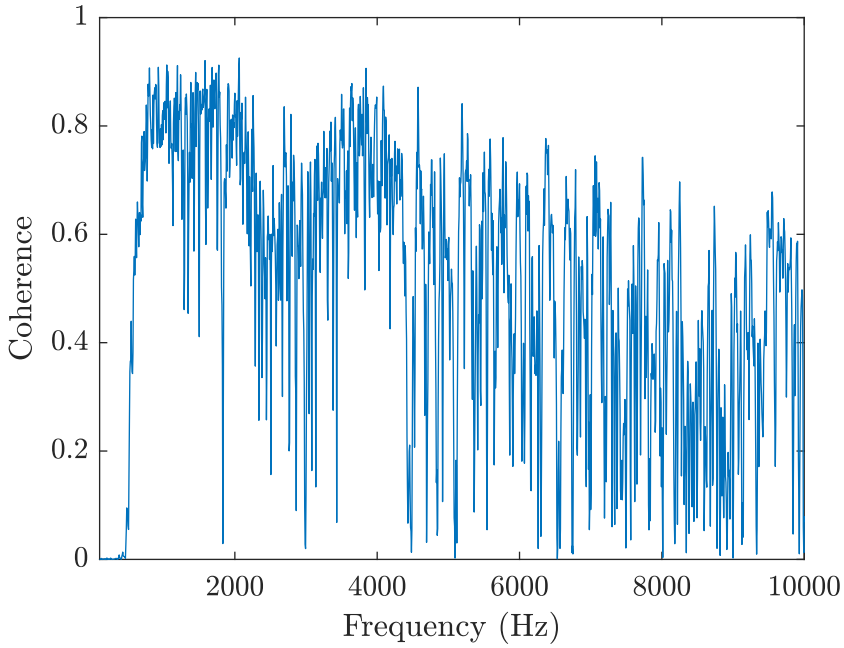

(b) Microphone at 90° (Mic 60) or horizontal to the duct outlet..

Figure 4.19: The coherence, γ^2_{xy} between the electro-acoustic signal into the compression driver and microphone SPL response for two microphones (on the vertical and horizontal planes) on the $28D$ array for sound propagating through a non-isothermal jet with $T_j = 350\,°\text{C}$ and $M = 0.1$.

the results in Figure 4.18 also show reduced COP levels for frequencies above 1.8 kHz and 4.2 kHz for microphones at angles of $-7.5°$ and 90° (Microphones 47 and 60, respectively). Comparing the microphone on-axis and off-axis shows a reduction in Figure 4.19, where the coherence has dropped drastically on-axis. This will be later explained with the directivity plot in Figure 4.20.

The temperature and flow from non-isothermal, heated jets are known to produce unique directivity plots governed by refraction, as investigated by Atvars et al. [15] and experimental results investigating this phenomenon will be discussed. Figure 4.20 shows the experimental results for the band-averaged sound directivity at four one-third octave bands, with centre frequencies, ka = [0.85, 1.08, 1.35, 1.70], at $28D$, for sound propagating through the non-isothermal, heated jet. The directivity plots show that the sound is axisymmetric about the vertical axis, with a shadow zone or 'cusp' forming along the centreline of the duct axis (0°). The acoustic cusp has a DI of approximately -12 dB. The acoustic energy that was originally on-axis (0°) has been refracted by the jet shear layer to form acoustic lobes off-axis at approximately symmetrical locations of $\pm 50°$. The SPL of the lobes off-axis has increased by approximately 3 dB, compared with Figure 4.17. These results are qualitatively consistent with the results by [14] and [27]. As indicated by Atvars et al. [15], the higher frequencies lead to a reduction in the acoustic wavelength and cause the sound to interact earlier with the spatially growing shear layer, hence leading to enhanced refraction in the far-field.

4.4.3 Sound radiation with the jet and cross-flow

In this section, the sound radiation through a non-isothermal JICF is discussed. The inclusion of the cross-flow introduces complexities to the acoustic results. This section is structured as follows. Firstly, the SPL results are presented with and without sound for the case with a non-isothermal, heated JICF. Next, the coherence between the electro-acoustic signal and the acoustic microphone response is shown. Presented next is the COP at two different microphones downwind. Lastly, directivity results are presented, showing the complex sound radiation

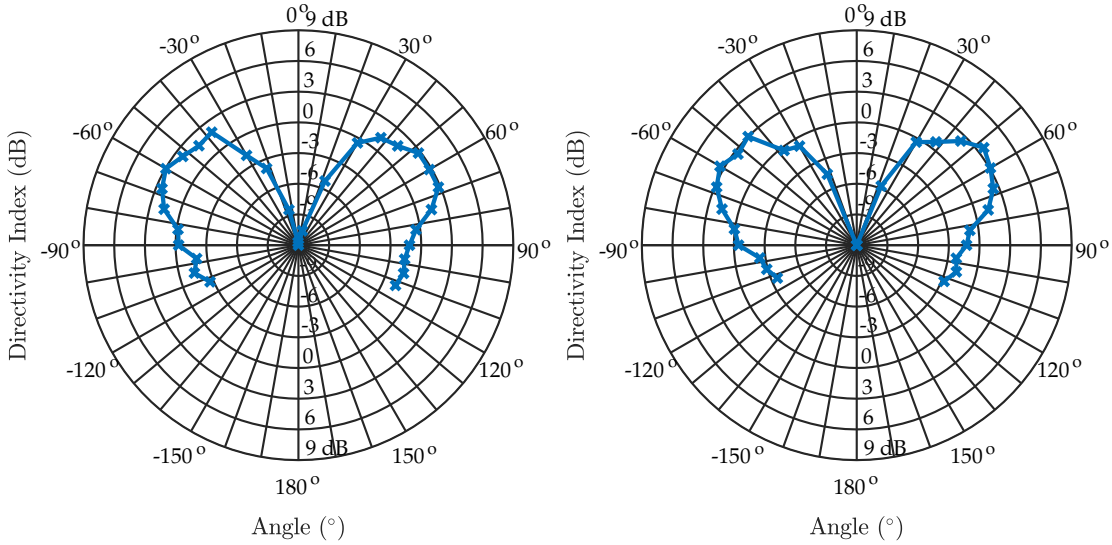

(a) $ka = 0.85$.

(b) $ka = 1.08$.

(c) $ka = 1.35$.

(d) $ka = 1.70$.

Figure 4.20: The DI along the Y-Z plane (of symmetry) for sound propagation through a non-isothermal jet for band-averaged one-third octave bands with centre frequencies $ka = [0.85, 1.08, 1.35, 1.70]$ ($f = [3.15\,\text{kHz}, 4\,\text{kHz}, 5\,\text{kHz}, 6.3\,\text{kHz}]$) at $r = 28D$, $T_j = 350\,°\text{C}$, and $M = 0.1$.

for non-isothermal, heated JICF. The directivity for three cases is analysed in this section for sound propagation through a non-isothermal JICF:

- DI sound propagation through a non-isothermal JICF at four band-average one-third octave bands with centre frequency, ka = [0.85, 1.08, 1.35, 1.70] with the following parameters: R = 5, T_j = 500 °C, and r = [14D, 28D],
- DI sound propagation through a non-isothermal JICF with varying band-averaged one-twelfth octave bands, with the following parameters: R = 5, T_j = 500 °C, and r = [28D],
- a reduction in the peak TI with the increase in height from y/D = 17 to y/D = 21, and
- jet temperature sensitivity for DI sound propagation through non-isothermal JICF with varying jet temperatures (T_j = [27 °C, 100 °C, 300 °C, 500 °C]), with the following parameters: ka = [0.85, 1.08, 1.35, 1.70], R = 5, T_j = 500 °C, and r = 28D.

The SPL measurements for sound radiation through a non-isothermal JICF with R = 5 and T_j = 500 °C are presented in Figure 4.21. It can be seen in Figure 4.21 that the background noise levels have increased with the non-isothermal, heated JICF, compared with the cases without the wind tunnel operating in Figures 4.15 and 4.18. The background SPL measurements show the presence of the wind tunnel fan tones and corresponding harmonics at approximately 2.5 kHz, 5 kHz, and 7.5 kHz. Furthermore the tone and corresponding harmonics from the blower, seen in Figure 4.18, are also present in Figure 4.21, but are suppressed. Even though there is an increase in background noise levels, there is still a sufficient difference between the speaker induced SPLs and background levels for accurate COP measurements. Additionally, for all the cases with sound propagating through the duct , shown in Figures D.7, 4.15, and 4.18, there are various dips in the SPL response and a roll-off in SPL in the high frequency region above 4 kHz. The complex non-uniform SPL response necessitates the band-averaged one-third octave results.

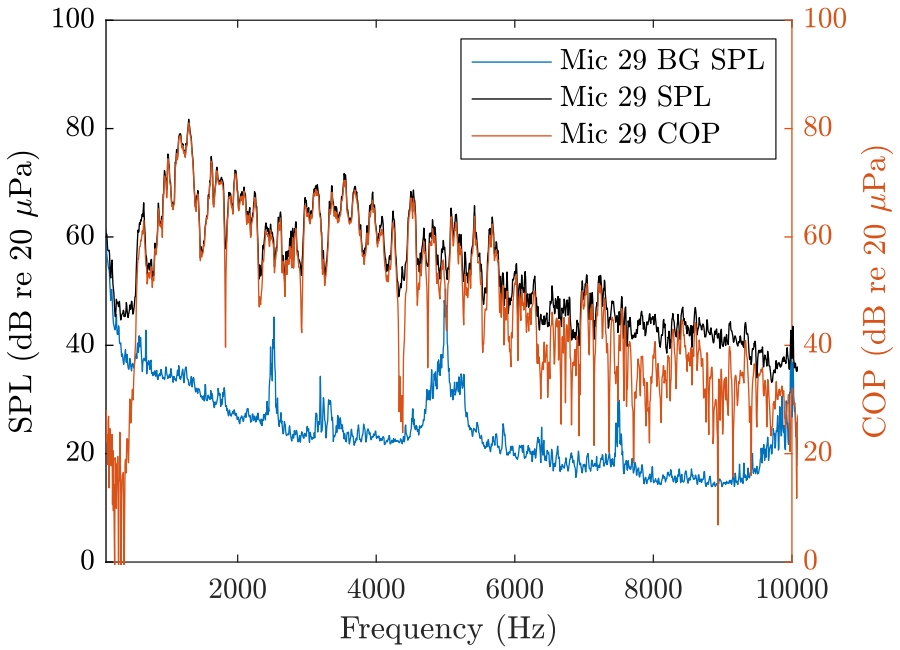

(a) Microphone at 90° downwind on the 14D array (Mic 29).

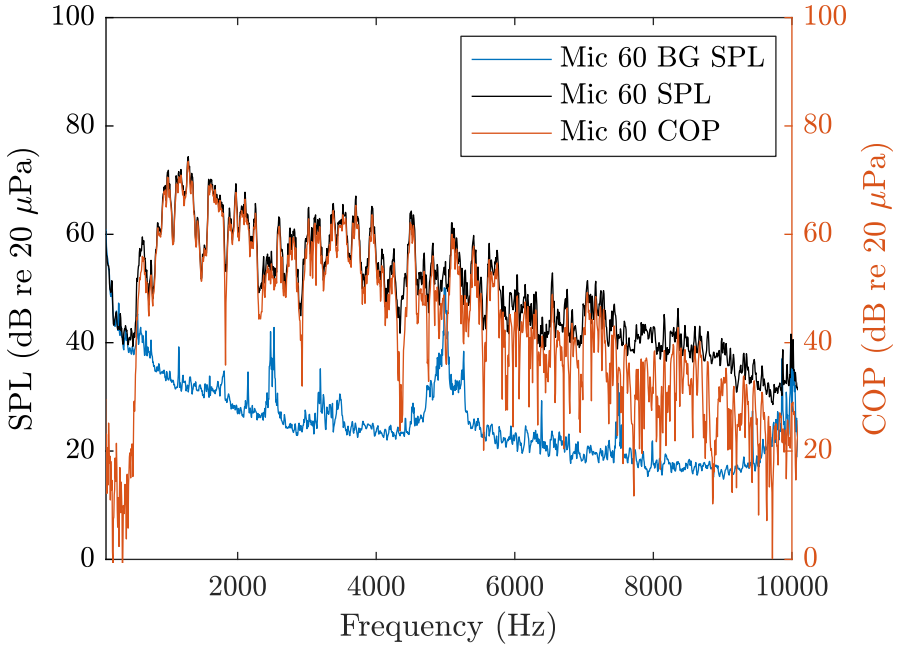

(b) Microphone at 90° downwind on the 28D array (Mic 60).

Figure 4.21: The SPL response for the acoustic pressure at two microphone locations from sound radiating through a non-isothermal JICF with $R = 5$ and $T_j = 500\,°C$. BG refers to the background noise levels. Note that both microphones are horizontal (90°) downwind. Relevant coherence is plotted in Figure 4.22.

The addition of the cross-flow introduces complexities to the sound measurement and the coherence shows these effects. Figure 4.22 shows the coherence, ${\gamma_{xy}}^2$ between the electrical-acoustic signal into the compression driver and the acoustic pressure at two different microphones along the $14D$ and $28D$ array. The results in Figure 4.22 show that below 4 kHz the coherence is high (near unity). However, above 4 kHz, there is a reduction in coherence (towards zero) with the increase in frequency. The coherence plots also show multiple regions of 'poor' coherence, which are at approximately 1.8 kHz, 3 kHz, and 4.5 kHz. It is difficult to identify the reason for the decrease in coherence at these tones, but external sources could reduce the coherence in specific regions. These sources of uncorrelated noise could be from a combination of the following: fan noise from the wind tunnel fans, noise from the Airpack blower, fan noise from the data acquisition hardware, fan noise from the compression driver speaker amplifier, electrical switching noise from the wind tunnel fan controllers, reflections from other hard surfaces, and/or the multi-modal response for the sound propagating through the duct above cut-on frequency (f_{co} = 6.82 kHz).

Figure 4.21 shows the COP at two different microphones on the $14D$ and $28D$ array, with sound propagating through the non-isothermal JICF. The overall responses for Figure 4.21, show that the SPL and COP show similar trends. However, there is a slight reduction in overall magnitude for the COP for all frequencies, when compared with the SPL plots. At the higher frequency range (above 4 kHz) there is a reduction in magnitude when comparing the SPL and COP in Figure 4.21, and this is due to the reduction in coherence, as shown in Figure 4.22.

Figure 4.23 shows the experimental results for the band-averaged sound directivity of a heated JICF at four one-third octave bands, with centre frequencies ka = [0.85, 1.08, 1.35, 1.70], while the jet Mach number is 0.1, T_j = 500 °C, R = 5, and r = [$14D$, $28D$]. Note that the cross-flow permitted higher stack exhaust temperatures compared with the results in Section 4.4.2, while remaining under the 60 °C temperature limit at the microphone locations. By comparing Figures 4.17, 4.20, and 4.23, it can be observed that with the heated plume and cross-flow, the sound directivity is no longer elliptical or axisymmetric about 0°. The directivity

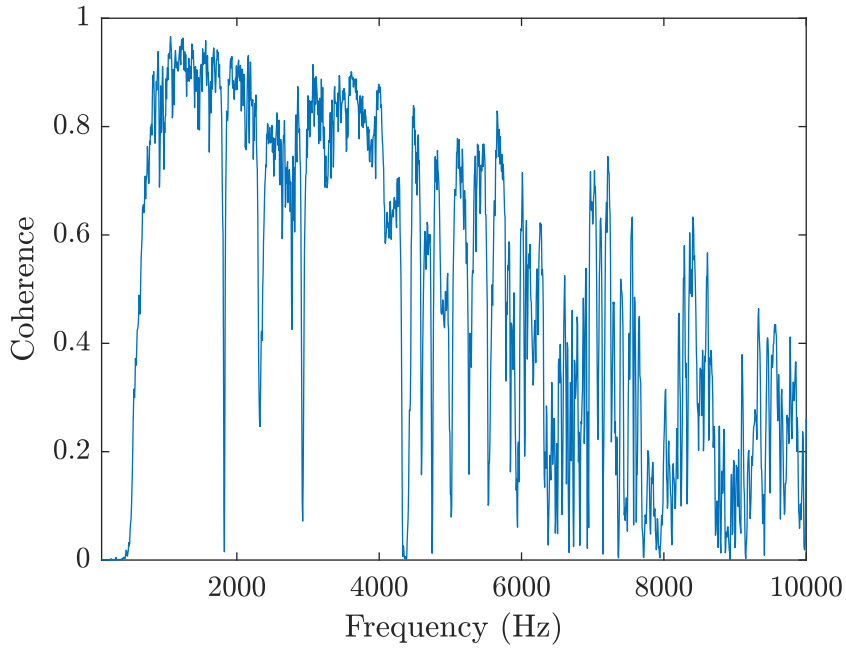

(a) Microphone at 90° downwind on the 14D array (Mic 29).

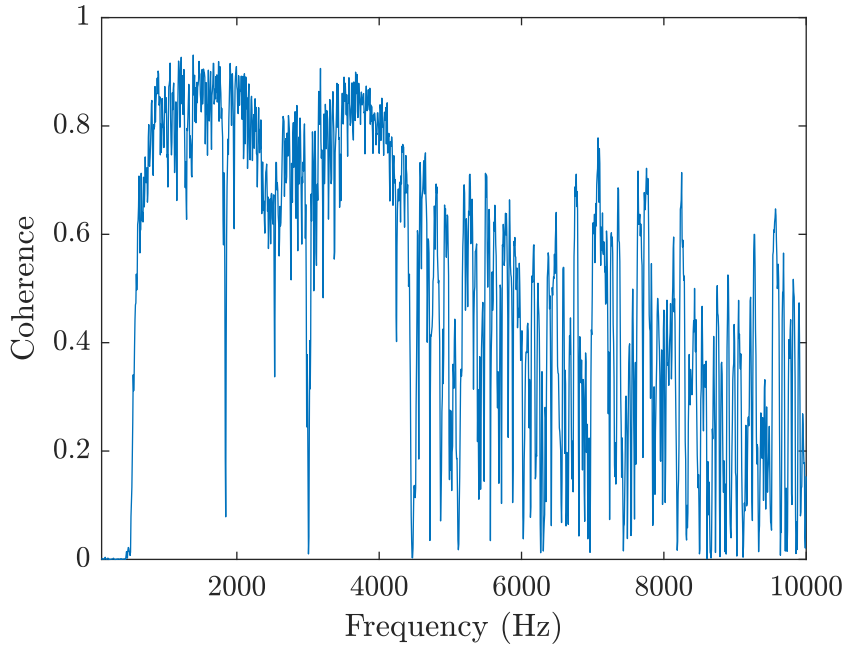

(b) Microphone at 90° downwind on the 28D array (Mic 60).

Figure 4.22: The coherence, γ^2_{xy} between the electro-acoustic signal into the compression driver and microphone SPL response from sound radiating through a non-isothermal JICF with $r = [14D, 28D]$, $R = 5$ and $T_j = 500\,°\text{C}$. Note that both microphones are horizontal (90°) downwind.

of sound becomes biased towards the leeward side (or downwind) of the exhaust duct. The cross-wind shifts the peak observed in the downwind lobe from an angle of 67.5° at 14D to 90° for the 28D array. It can also be observed that as the sound propagates downwind, the width of the lobe decreases from 40° to 25° for the 14D and 28D arcs, respectively. The downwind lobe becomes narrower, with the energy more concentrated and increasing in amplitude from 4.5 dB at 14D to 6.5 dB at 28D. However, upwind of the exhaust duct, the sound directivity patterns remain similar for the 14D and 28D arcs. The position of the acoustic 'cusp' or shadow zone shifted from 0° in Figure 4.20 in the absence of the cross-flow to 10° at 14D and 20° at 28D with the cross-flow present in Figure 4.23. It must be noted that the angular resolution of the directivity measurements is 7.5° increments and this may be insufficient to capture the fine detail in the directivity pattern. The directivity results in Figure 4.23 at the 28D array show that the downwind lobe may not be fully resolved for the current angular spacing of the microphones but, for this research, it is sufficient for investigating the change in sound levels downwind of the exhaust duct. As sound propagates downwind, it can be observed that the plume has a greater influence on the propagation path. The temperature gradients strongly govern the influence on the propagation path of sound in the plume, which causes the sound to refract as it propagates downwind.

Apart from the asymmetric directivity plots in Figure 4.23 due to the cross-flow, there are also acoustic frequency dependent details. Figure 4.23, shows the band-average directivity results at four one-third octave bands. The directivity results for $r = [14D, 28D]$ show that with the increase in ka there are key features: the width of the acoustic lobes upwind and downwind of the exhaust stack reduce in size, there is an increase in the DI magnitude of the lobe downwind of the exhaust stack, and there is seen a slight change in the position of the maximum SPL downwind of the exhaust stack. The width of the acoustic lobe downwind of the exhaust stack reduces from 30° to 50° and 20° to 30° for 14D and 28D, respectively. For the increase in the band-averaged one-third octave band, the DI magnitude for the lobe downwind of the exhaust increases from 4.5 dB to 7.5 dB for the 14D array. Similarly, with the increase in the frequency (band-averaged one-third octave band)

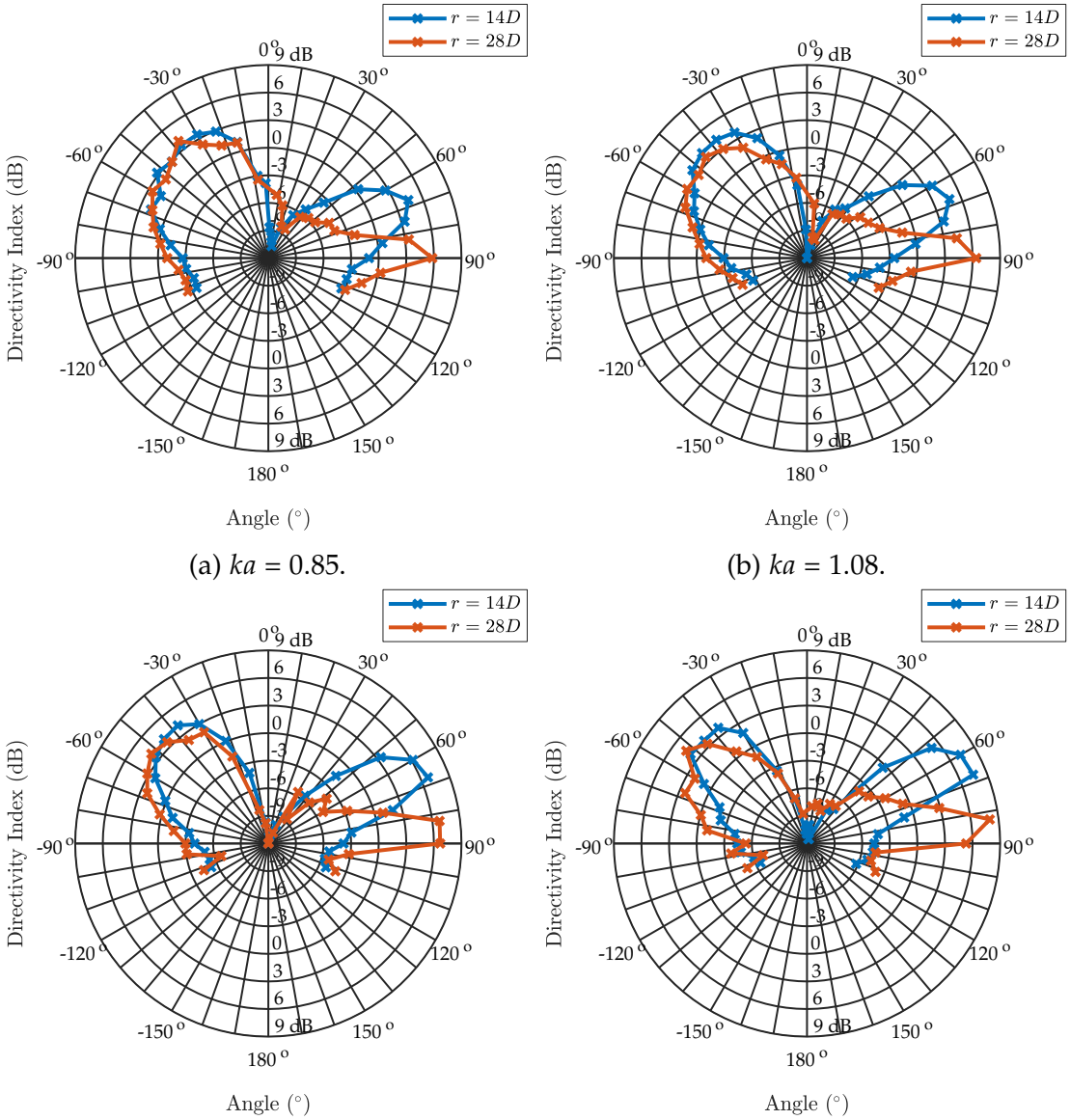

(a) ka = 0.85.

(b) ka = 1.08.

(c) ka = 1.35.

(d) ka = 1.70.

Figure 4.23: The band-averaged DI along the Y-Z plane (of symmetry) for sound propagation through a non-isothermal JICF for one-third octave bands with centre frequencies ka = [0.85, 1.08, 1.35, 1.70] (f = [3.15 kHz, 4 kHz, 5 kHz, 6.3 kHz]) at two radii (14D and 28D) while R = 5 and T_j = 500 °C. The cross-flow is from left to right.

for the $28D$ array the magnitude for the acoustic lobe downwind of the exhaust stack increases from 6 dB to 8.5 dB.

The acoustic directivity results presented previously were for one-third octave. It is also insightful to show the results as band-averaged one-twelfth octave bands. Over a frequency range of 2650 Hz to 6300 Hz there are 20 one-twelfth octave bands, whereas a comparison of one-third octave bands there are only four one-third octave bands over this frequency range. The finer frequency resolution also reveals spatial details in the directivity plot that can provide additional insight into the acoustic directivity details in-between each microphone, as the angular resolution of the microphone array is 7.5°. The spatial resolution of the directivity plots is limited by the number of microphones available and the number of channels available for data acquisition with the four NI PXIe-4499 Sound and Vibration Modules in an 8-slot NI PXIe 1082 Chassis. The justification for using one-twelfth octave bands for analysis is supported with Figures 3.36 and 3.53, which both show an increase in the DI magnitude and decrease in angular position of the acoustic lobe downwind of the jet, with the increase in ka. Figure 4.24, shows the band-averaged directivity results for one-twelfth octave bands at 20 frequency bands, with the presence of the non-isothermal JICF. The increase in narrowband frequency shows a gradual change in the acoustic lobe downwind of the exhaust stack, with the increase in the maximum SPL from 6 dB to 9 dB, and the change in the maximum SPL angular position from 90° to 82.5° (microphones 60 to 59). These findings are qualitatively consistent with the numerical work in Chapter 3, shown in Figures 3.36 and 3.53.

Jet temperature has been shown to influence sound radiation downwind of the jet outlet in Chapter 3 for ground-level JICF, and this parameter is experimentally investigated for non-isothermal, elevated JICF. Figure 4.25 shows the band-averaged one-third octave directivity for the non-isothermal JICF, with varying jet temperatures (T_j = [27 °C, 100 °C, 300 °C, 500 °C]). Although the jet temperature was altered, there are key features that remain the same in the directivity plot: the presence of a cusp at approximately 7.5°, a broad acoustic lobe upwind of the exhaust stack, and a concentration of sound downwind of the exhaust stack with a narrow acoustic

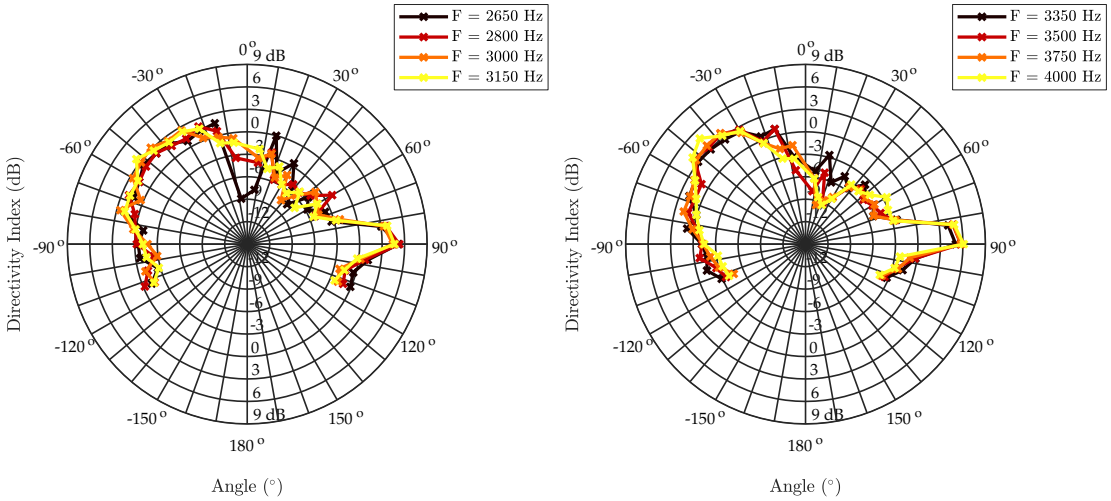

(a) ka = 0.85.

(b) ka = 1.08.

(c) ka = 1.35.

(d) ka = 1.70.

Figure 4.24: The band-averaged DI along the Y-Z plane (of symmetry) for sound propagation through a non-isothermal JICF at 20 one-twelfth octave bands. The test conditions were $r = 28D$, $R = 5$ and $T_j = 500\,°C$. The cross-flow is from left to right.

lobe. The increase in jet temperature shows unique jet temperature dependent features in the directivity plots, such as the following:

- the acoustic lobe position downwind of the exhaust stack shifts from approximately 50° to 90° with increasing temperature,
- the magnitude of the acoustic lobe downwind of the exhaust stack increases with temperature and can increase by up to approximately 4 dB,
- the depth of the cusp at approximately 7.5° to 22.5° increases with the jet temperature, and
- upwind of the exhaust stack, the magnitude of the lobe increases with the jet temperature.

All the features listed are consistent for all the different band-averaged one-third octave bands investigated in Figure 4.25. Therefore, the jet temperature influences the directivity of sound, but in particular the refraction of sound downwind of the exhaust stack, with the hottest jet temperature (T_j = 500 °C) showing the most significant increase in sound downwind up to 9 dB.

4.4.4 Cross-flow sensitivity study

In the thesis thus far, it has been shown that the fluid dynamics of the plume play a critical role in the downwind sound propagation, with the plume dependent on R, as shown through the numerical simulations in Figure 3.40. The acoustic results in this section aim to investigate the sound radiation from different jet to cross-flow momentum flux ratios. The acoustic directivity for four jet to cross-flow momentum flux ratios ranging from R = 5 to 12.5 will be presented. Additionally, an analysis of the effects of acoustic frequency on the sound radiation with varying R will be investigated.

Figure 4.26 shows the band-averaged directivity for sound propagating through non-isothermal jet in cross-flow with varying jet to cross-flow momentum flux ratios (R = [5, 7.5, 10, 12.5]) and for varying one-third octave bands (f = [3.15 kHz,

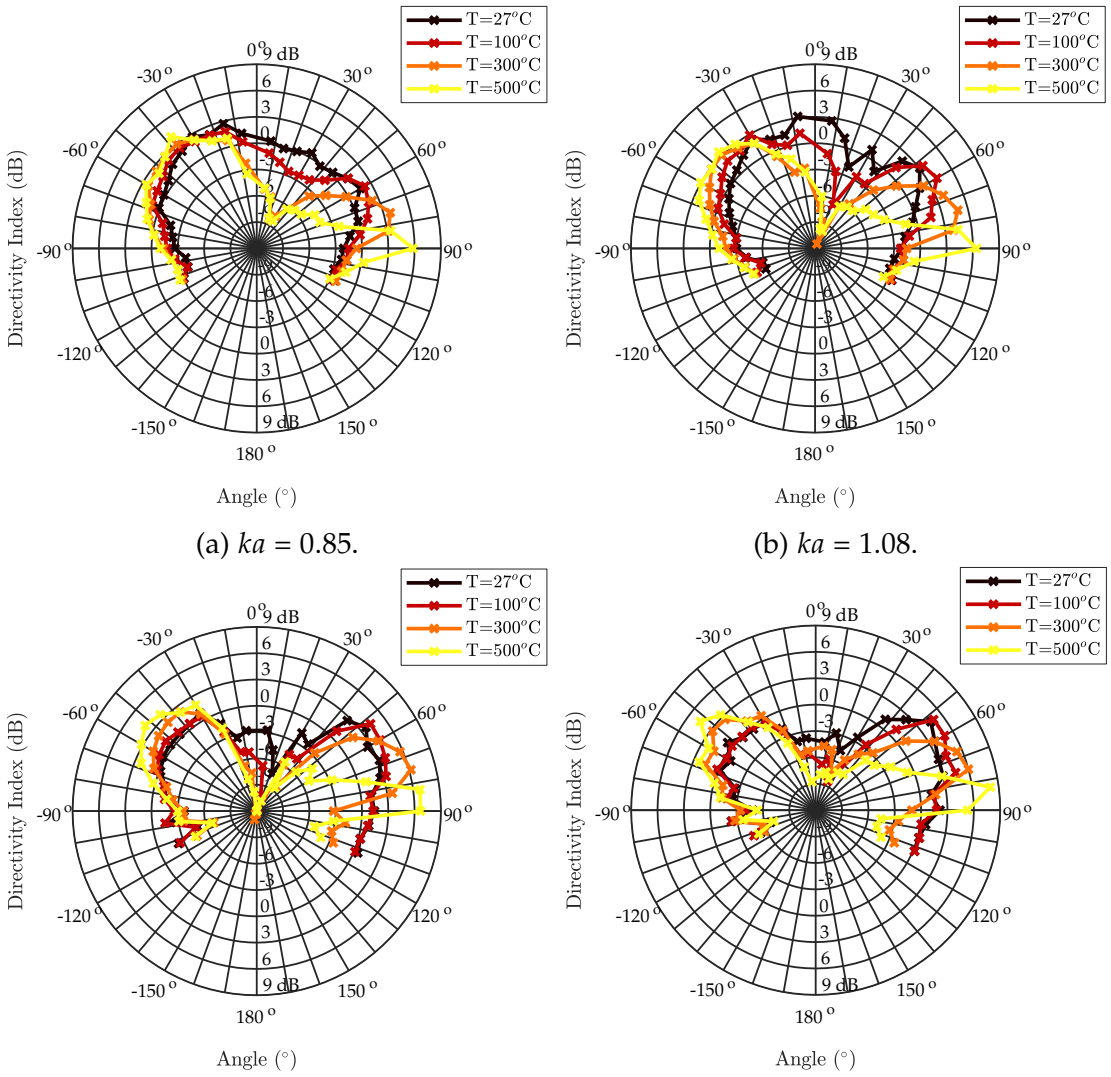

(a) ka = 0.85.

(b) ka = 1.08.

(c) ka = 1.35.

(d) ka = 1.70.

Figure 4.25: The band-averaged DI along the Y-Z plane (of symmetry) as a function of jet temperature (T_j = [27 °C, 100 °C, 300 °C, 500 °C]) for sound propagation through a non-isothermal JICF. The test conditions were for ka = [0.85, 1.08, 1.35, 1.70] (f = [3.15 kHz, 4 kHz, 5 kHz, 6.3 kHz]), $r = 28D$ and $R = 5$. The cross-flow is from left to right.

4 kHz, 5 kHz, 6.3 kHz] or ka = [0.85, 1.08, 1.35, 1.70]). The jet conditions remained consistent at M = 0.1 and T_j = 500 °C, while the cross-flow free-stream velocity (u_{cf}) was varied to give the different values of R. All four directivity plots show that with the increase in R from 5 to 12.5, the position of the acoustic lobe downwind shifts from 90° to 60°. The increase in R towards 12.5 in Figure 4.26 shows that the position of the acoustic lobe position downwind becomes more axisymmetric about the jet centreline axis at 0°. The acoustic directivity for R = 12.5 almost resembles the sound directivity of Figure 4.20, for r = 28D. The reason for the similar directivity arcs is that with the reduction in cross-flow speed or increase in R, a plume downwind is produced that becomes more 'jet dominant'. Hence, since the plume is still in the 'jet dominant' regime for the directivity at 28D, the directivity arc for Figure 4.26 at R = 12.5 closely resembles the directivity in Figure 4.20 (no cross-flow). In the relative near-field the sound radiation at lower values of R or higher cross-flow values leads to an increase in SPL at ground level (28D). In the far-field it is expected that the sound radiation for lower cross-flow velocities and higher R would be the dominant regime or case for inducing sound amplification downwind.

For all four ka values in Figure 4.26, the cross-flow momentum flux ratio, R = 7.5, produces the highest magnitude acoustic lobe downwind of the exhaust stack. The increase in ka for R = 7.5 shows a change in DI magnitude of the acoustic lobe downwind of the exhaust stack from 6 dB to 9.5 dB. However, this may not be the exact case as the spatial resolution of the microphones was only 7.5° separation and the full resolution of the acoustic lobe may not be captured. This can also be supported by the results from Section 3.3.2. Hence, the full SPL magnitude of the acoustic lobe, as well as other acoustic features, may not have been captured with the current array configuration.

Figure 4.26 shows the directivity plots for the plume with varying ka or acoustic frequencies in one-third octave bands. It can be observed from the increase in acoustic frequency in Figures 4.26a to 4.26d that the lobe downstream is 'narrower'. Furthermore, the increase in R also exhibits a similar behaviour for all the plots, and that is the increase in the lobe position downstream, as well as the lobe

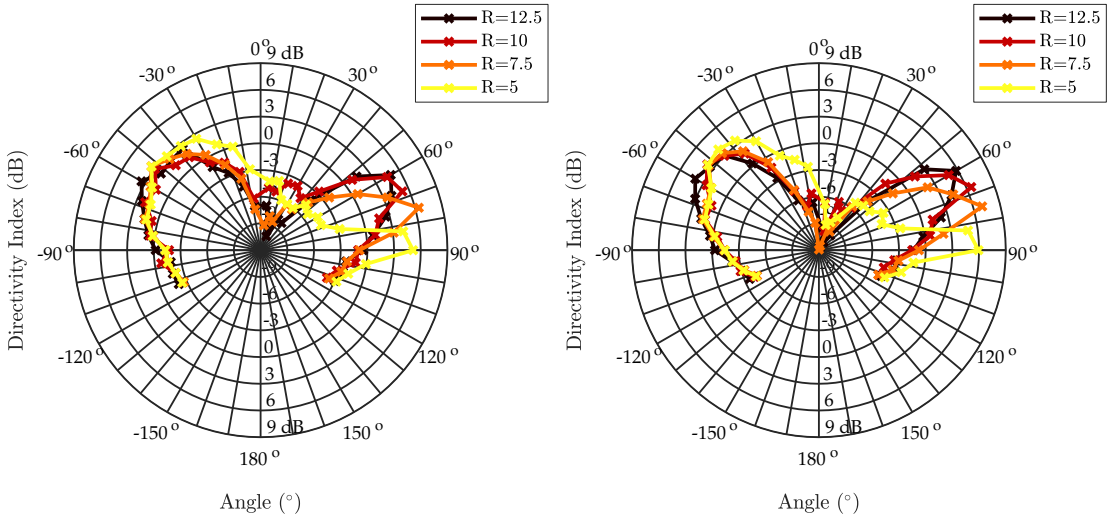

(a) ka = 0.85.

(b) ka = 1.08.

(c) ka = 1.35.

(d) ka = 1.70.

Figure 4.26: The band-averaged DI along the Y-Z plane (of symmetry) for sound propagation through a non-isothermal JICF with $R = [5, 7.5, 10, 12.5]$, while the one-third octave bands of interest are $ka = [0.85, 1.08, 1.35, 1.70]$ (f = [3.15 kHz, 4 kHz, 5 kHz, 6.3 kHz]). The test conditions were $r = 28D$, $R = 5$ and $T_j = 500\,°C$. The cross-flow is from left to right.

downstream becomes wider. Additionally, it can be seen in Figure 4.26 that the sound directivity plot for the case with R = 10 and R = 12.5 for all these cases seems to be quite similar. This is true as the cross-flow ratio indicates that the change in cross-flow velocity is minimal and that the plume is more likely still in the 'jet dominated' regime. In order to quantify the effects of the plume at these higher values of R, it is critical to increase the experimental domain spatially, but with the current facilities, this is not possible.

Whilst the cross-flow sensitivity study gives some insight into the shape of the plume, there are other factors that change the position of the plume downwind, which include the terrain downstream and the turbulence intensity in the incoming flow. It was observed in the research by Andreopoulos [5, 6] that for elevated jets in cross-flow, the incoming turbulence intensity highly governs the diffusion of the plume, as well as the span-wise and vertical flapping motion of the plume in the incoming flow. Hence, the vertically flapping plume will cause the sound trajectory to change also and, subsequently, the downwind lobe position would also vary.

The research work to date analysed the time-average response of the sound, temperature and flow for the elevated jet in cross-flow. The work conducted in the numerical Chapter 3 also analysed the steady-state sound propagation. Hence, the transient effects of the sound interacting with the flapping plume was not quantified for this research.

4.5 Discussion

In this experimental study it has been shown that the bent-over non-isothermal plume has changed the sound propagation path, with refraction being the dominant mechanism for asymmetric sound radiation. The acoustic refraction downwind is due to the temperature and velocity gradients in the plume that alter the speed of sound (c) of the air. Figure 4.25 shows that the majority of the refraction arises from the temperature gradients, causing a change in the speed of sound ($\Delta c \propto \sqrt{\Delta T}$), as opposed to the convective effects of the flow ($\Delta c = c + \Delta u_{\text{flow}}$) [128]. The CFD work presented in Chapter 3 showed the counter-rotating vortex pairs produce thermal

and velocity gradients. In Chapter 3, the numerical work has shown that acoustic refraction happens over the entire computational domain. Figure 4.26 shows the directivity results for a single radius ($r = 28D$), and shows qualitative similarities for the acoustic refraction downwind, with the directivity results in Chapter 3. Further experimental investigations will need to examine the directivity at radii greater than $28D$ to quantify the far-field magnitude of the directivity index. The flow and temperature field associated with the experimental small-scale model will need to be measured in the far-field ($> 16D$) to gain a better understanding of the extent of the fluid dynamic and temperature effects that govern the propagation path of sound.

In Figure 4.23, the experimental results have shown that there is a downstream lobe forming, causing an increase in sound levels of up to 6.5 dB. The increase in downstream sound level, shown in Figure 4.23, was calculated using the average coherent output power (COP_{av}) of that measurement arc. The results can be directly compared with the case without flow, seen in Figure 4.17, which results in an elliptical sound radiation pattern. In Figure 4.17, the sound downstream at 90° is approximately -4.5 dB, whereas the sound levels in Figure 4.23 with the bent-over non-isothermal plume are 6.5 dB. Hence, the plume has caused an 11 dB increase in the sound level parallel to the ground plane when compared with the isothermal stationary field case.

Figure 4.27 shows a comparison between the numerical results from Section 3.3.3.2 and the experimental results from Section 4.4.3. The results in Figure 4.27 are for the propagation of sound through a heated jet with cooler cross-flow with $R = 5$, $T_j = 500\,°\text{C}$, and for a one-third octave band of $ka = 0.85$ ($f = 3.15$ kHz). Qualitatively, the results between the two methods show similar trends with

- a cusp forming near the centreline axis of the duct,
- upwind of the exhaust stack the sound directivity shows spherical spreading,
- downwind of the exhaust stack there is a concentration of sound in the form of an acoustic lobe, and

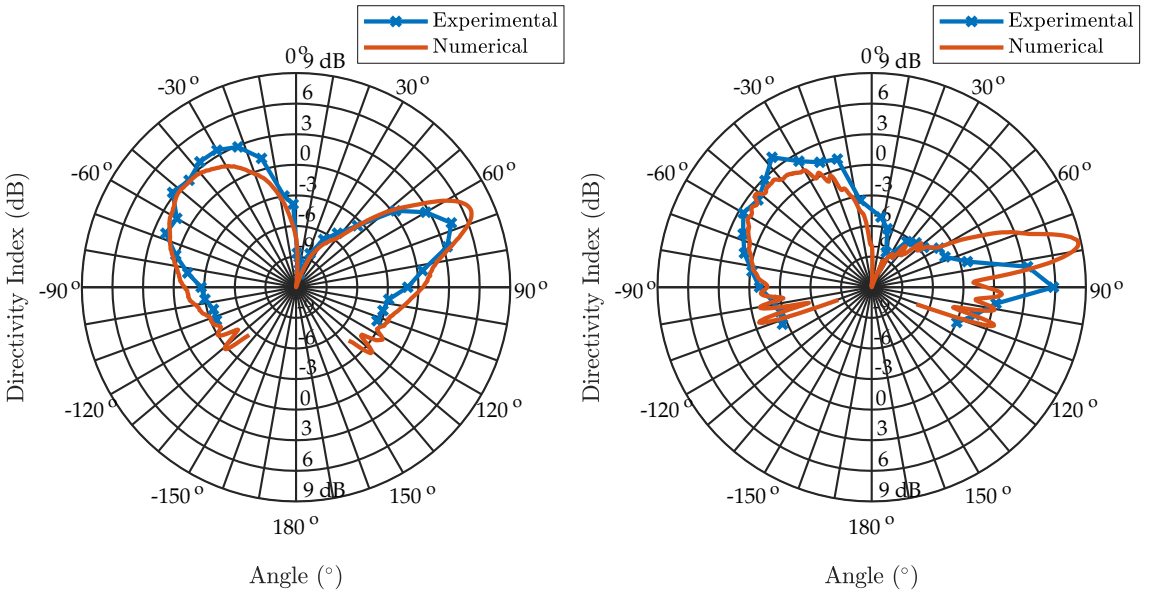

(a) $r = 14D$. (b) $r = 28D$.

Figure 4.27: A comparison between the numerical and experimental results for the band-averaged DI along the Y-Z plane (of symmetry) for sound propagation through a non-isothermal JICF for two directivity radii, $r = [14D, 28D]$, with $R = 5$. The one-third octave bands of interest, $ka = 0.85$ ($f = 3.15\,\text{kHz}$), and $T_j = 500\,°\text{C}$. The cross-flow is from left to right. The results are saturated at $-12\,\text{dB}$.

- with the increase in radial distance for the directivity plots, the angular position of the lobe downwind shifts clockwise and moves towards the ground.

Although there are qualitative similarities between the experimental and numerical results in Figure 4.27, there are slight quantitative differences. In Figure 4.27 there is approximately a 3 dB difference upwind and downwind of the exhaust stack in acoustic magnitude. At $r = 28D$, the position of the acoustic lobe downwind is higher in the numerical results at approximately 77.5°, whereas for the experimental results the acoustic lobe is at approximately 90°.

These are a number of reasons why these difference are observed. For the numerical study the exhaust duct is $10D$ long and for the experimental study the exhaust duct is $8D$ long. The flow and temperature conditions are also slightly different between the numerical and experimental results. The incoming cross-flow

conditions are similar, but not identical between the numerical domain and flow in the wind tunnel over the ground-surface. This is also similar for the exhaust jet with the temperature and flow for the exhaust jet measured at a point in the exhaust duct. Furthermore, modelling the flow with a steady-state RANS model, a realisable k-ϵ model for the turbulence, does not accurately predict the temperature and flow from a heated exhaust jet in cooler cross-flow. Due to the limited access of the HPC Phoenix at the University of Adelaide, only five frequencies were used to calculate the band-average one-third octave band for the numerical results in Figure 4.27. However, the experimental work uses in the order of 100 FFT frequency bins for the band-average one-third octave band results. With the finite number of microphones, there is also limited spatial resolution in the experimental results, and it is unclear whether the maximum peak in DI magnitude was measured downwind of the exhaust stack. From all these differences it is expected that there will be small differences in the experimental and numerical acoustic results. However, ultimately the results presented in this thesis shows important reproducible trends from sound radiation through heated exhaust jets in cooler cross-flow.

The geometry of the reduced-scale mode exhaust stack is a simple straight duct section that protrudes $8D$ into the flow. In real OCGTs, the geometry of the plant is considerably more complex, thereby affecting the cross-flow and consequently the sound refraction. This simplification of the model is appropriate for scientific investigation, as it resembles the elevated jets in cross-flow seen in the literature and reduces the acoustic and fluid dynamic complexity in the model. The primary purpose of the research is to investigate the sound interaction with the plume and observe non-axisymmetry of the acoustic directivity, as well as quantify the increase in sound level downwind, which was confirmed in the experimental results here, and previously in numerical studies.

In the experimental work presented in this chapter, measurements were taken with an anechoic ground to simulate an absorptive surface surrounding the stack. This is generally not the case for OCGTs, as complex structures and hard reflective surfaces typically surround the exhaust stacks. These reflective surfaces would change the sound directivity pattern, and hence the experimental setup used

here may not be an accurate representation of real installations. Work completed in Chapter 3 suggests that a complex acoustic pattern occurs when a reflective ground is included. As a result, all the directivity plots in Section 4.4 show 'smooth' directivity patterns in the absence of diffraction and reflections from other surfaces. Additionally, the sound directivity results in this thesis are presented as band-averaged to reduce the complexity of the results. Further tests over several band-averaged one-third octave bands should be undertaken to examine the relationship of the plume and the downwind sound levels.

4.6 Summary of the findings

The results of the experimental study undertaken on the reduced-scale exhaust rig have shown that a non-isothermal elevated JICF changes the propagation path of sound to produce complex sound radiation patterns. The flow and temperature associated with the non-isothermal elevated JICF were measured and showed reproducible trends with both the published literature and the numerical work presented in Chapter 3. Different cases were investigated for the sound radiation, which included the following:

- sound radiation in the absence of the JICF (the isothermal stationary field),
- sound radiation in the presence of the non-isothermal jet without cross-flow,
- sound radiation in the presence of a non-isothermal JICF at a single R, $R = 5$, and with varying jet temperatures, $T_j = [27\,°C, 100\,°C, 300\,°C, 500\,°C]$, and
- sound radiation cross-flow sensitivity study for non-isothermal JICF, with $R = [5, 7.5, 10, 12.5]$.

The key findings for the flow, temperature and acoustic results will be outlined in this section. The flow and temperature measurements for the reduced-scale exhaust rig subjected to cross-flow shows complex bulk fluid dynamic and thermal features. Upwind of the exhaust stack, the flow and temperature are relatively uniform, with a slight difference in the incoming boundary layer. Additionally,

the magnitude and profile for the incoming turbulence intensity are lower than seen in the literature and for ABL, which affects the dispersion of the plume downwind of the exhaust stack [5, 6]. Downwind of the exhaust stack, the velocity and temperature measurements show complex profiles, with the following features observed:

- there are definitive velocity and thermal gradients in the measurements downwind of the exhaust stack from the complex interaction of the cross-flow with the stack and heated jet,
- there is a distinguishable difference between the plume and the cross-flow free-stream,
- the centre position of the plume increases in height as it propagates downwind of the exhaust stack,
- the plume grows spatially with the increase in distance downwind from the exhaust stack,
- the velocity and temperature gradients reduce as the plume travels downwind due to the entrainment of the cooler cross-flow and the dissipation of the plume,
- the plume has spanned the entire domain,
- the stack-wake is complex, with the region near the stack exhibiting reverse flow as a result of recirculation,
- the plume is approximately symmetrical about the Y-Z plane ($x/D = 0$), and
- the flow and temperature measurements show the presence of a counter-rotating vortex pair.

Various experimental cases were explored in this chapter, and can be depicted in Figure 4.2, but one of the most simplified cases investigated is the sound radiation through the reduced-scale exhaust network in an isothermal stationary field. The

results were presented in Section 4.4.1 and show consistency in the acoustic results for testing in the Anechoic Chamber (results presented in Appendix D) and the Thebarton Wind Tunnel, even though the testing in the wind tunnel introduces complexities with increased background noise levels and multiple reflection surfaces. The sound directivity results for sound propagation through the duct network in the absence of the jet and cross-flow exhibits approximately axisymmetric acoustic radiation, with a lobe forming on-axis (0°). The experimental sound directivity plot is consistent with work in the published literature [25] and the numerical results presented in Chapter 3.

For the case of the non-isothermal jet, the sound radiation was still axisymmetric, but no longer spherical or elliptical, with a cusp forming on-axis and strong lobes forming off-axis. The band-average directivity plot has shown an increase in the DI magnitude off-axis of up to 4.5 dB. The results are due to the refraction of the propagating sound through the jet shear layer and are consistent with the work completed by Atvars et al. [14]. However, it should be noted that the jet temperature was limited to T_j = 350 °C and it is expected that with higher jet temperatures (T_j = 500 °C) the maximum DI magnitude off-axis would be higher than the measured 4.5 dB.

The case for sound propagation through the non-isothermal elevated JICF has produced an asymmetrical directivity plot, with the results presented in Section 4.4.3. It can be observed that the sound radiation upwind is approximately elliptical and resembles the band-average directivity for the non-isothermal jet without cross-flow. Downwind of the exhaust stack, the thermal and velocity gradients have refracted the sound, leading to the concentration of acoustic energy forming a narrow 'lobe'. The cusp previously seen on-axis has now changed position to approximately 5°. Downwind of the exhaust stack, the non-isothermal JICF can increase the observed DI by up to 11 dB when compared with either the isothermal stationary field, or the non-isothermal jet without cross-flow. The overall magnitude increase is qualitatively consistent with the numerical work completed previously in Chapter 3 and that the thermal and velocity gradient in the plume governs the refraction of sound downwind of the exhaust stack.

The band-averaged directivity results with one-twelfth octave bands, show frequency dependent details that are similarly observed in Chapter 3 with tonal directivity results. Figure 4.24 shows with such an increase in the band-averaged one-twelfth octave bands, there is an increase in the maximum DI magnitude observed downwind of the exhaust stack by up to 2 dB. Additionally, the increase in the one-twelfth octave band shows a shift in the position of the acoustic lobe from 90° to 82.5°, which is also consistent with the tonal directivity results in Chapter 3. However, the directivity measurements have a discrete angular resolution of 7.5° and the maximum DI observed in the acoustic lobe downwind of the exhaust stack cannot be perfectly resolved, even with the shift in the position of the acoustic lobe.

It has been shown in this chapter and Chapter 3 that the jet temperature for elevated JICF impacts the sound directivity, whereby the hottest jet temperature (T_j = 500 °C) shows the greatest asymmetry in the directivity plot. The change in the directivity plot is from the refraction of sound, arising from the large change in temperature leading to the significant difference in the speed of sound ($\Delta c \propto \sqrt{\Delta T}$). The elevated temperature observed in the plume was measured and presented in Section 4.3.2. For the acoustic results, the impact of the increase in T_j can be summarised with the following:

- an increase in the DI magnitude for the acoustic lobe downwind of the exhaust stack,
- downwind of the exhaust stack there is a shift in the position of the acoustic lobe towards the ground plane,
- a downward shift in the position of the acoustic cusp, and
- upwind of the exhaust stack, the directivity lobe remains relatively unchanged with changes in jet temperature.

The sound radiation downwind is affected by the thermal and velocity gradient associated with the plume, and therefore the trajectory of the plume alters the sound radiation. The DI plots in Figure 4.26 have shown that, with a decrease in R, there is an increase in the angular position of the acoustic lobe downwind of the

exhaust stack. This indicates that if the cross-flow is varying, then the acoustic lobe downwind would also be varying, giving different points of impact at ground level for the acoustic lobe. The increase in R causes the acoustic lobe in the directivity plot to broaden spatially. Furthermore, in the experimental domain of up to $28D$, the sound radiation converges at $R = 10$ to 12.5 and the sound radiation closely resembles the jet directivity in Figure 4.20. Hence, for higher R the plume is in the 'jet dominant' regime which causes almost axisymmetric spreading. Therefore to quantify the effects of lower cross-flow speeds, a larger experimental domain would need to be considered for future testing.

Chapter 5

Prototype exhaust stack noise mitigation

5.1 Introduction

In Chapter 3 and 4 it was shown that the plume from hot exhaust stacks causes a drastic change in the sound radiation downwind. This chapter explores different methods for mitigating this phenomenon, thereby reducing the sound downwind from the exhaust stack. The investigation involves three different embodiments of prototype sound mitigation devices.

This chapter details an investigation into the theoretical premise of using nozzles at the end of an exhaust stack for noise mitigation in the far-field and a proposal to replace sections of acoustically hard, reflective duct with an acoustically transparent section, that is impervious to fluid flow. A description of the three designs will be discussed in Section 5.4. Section 5.5 investigates the performance of one of the designs numerically. Subsequent experimental analyses of the three prototype nozzles are presented in Section 5.6. A discussion summarising the performance of the nozzles and the implementation of the nozzle on real systems is presented in Section 5.7. The key findings are summarised in Section 5.8.

5.2 Previous work on exhaust nozzle design

All previous research into controlling noise directivity from stack outlets has used hard-reflective surfaces to redirect the sound away from sensitive areas. Rigid-walled nozzles have been investigated experimentally in the literature by Björk [27] and have been summarised in Section 2.2.1. Björk [27] designed two rigid-walled nozzles, Figure 2.1, which were to (a) extend a section of the exhaust stack with half of the existing circumference, or (b), place a conical section at the duct outlet. The rigid-walled nozzles were designed for a reduced-scale (1:20) open cycle gas turbine exhaust stack. Both rigid-walled nozzles were designed to increase the acoustic 'shadow region' downwind of the exhaust stack, with the directivity results showing slight reductions in the sound observed at ground level.

However, there were limitations to the rigid-walled nozzles experimental study by Björk [27] and the technology itself. Firstly, the directivity measurements were conducted in the geometric near-field ($r = 3D$) and more extensive measurements needed to be completed in the geometric far-field ($r > 200D$) to more closely resemble the scenario of real OCGT and communities. It is expected that the rigid-walled nozzles increase the acoustic 'shadow region' in the geometric near-field, but this effect diminishes in the far-field, as a rigid-walled nozzle increases the vertical height of the acoustic source slightly, in comparison with the propagation distance. Additionally, rigid-walled nozzles change the exiting exhaust stack flow, and this was not discussed in the work by Björk [27]. From the research in Chapters 3 and 4, the exiting flow condition is a critical factor in predicting the sound levels downwind of the exhaust stack.

5.3 Acoustically transparent, impervious to flow nozzles

An alternative nozzle concept for reducing the downwind sound level is proposed here. The idea is to use an acoustically transparent nozzle that is impervious to bulk flow. This concept is perhaps counter-intuitive, as one would not expect

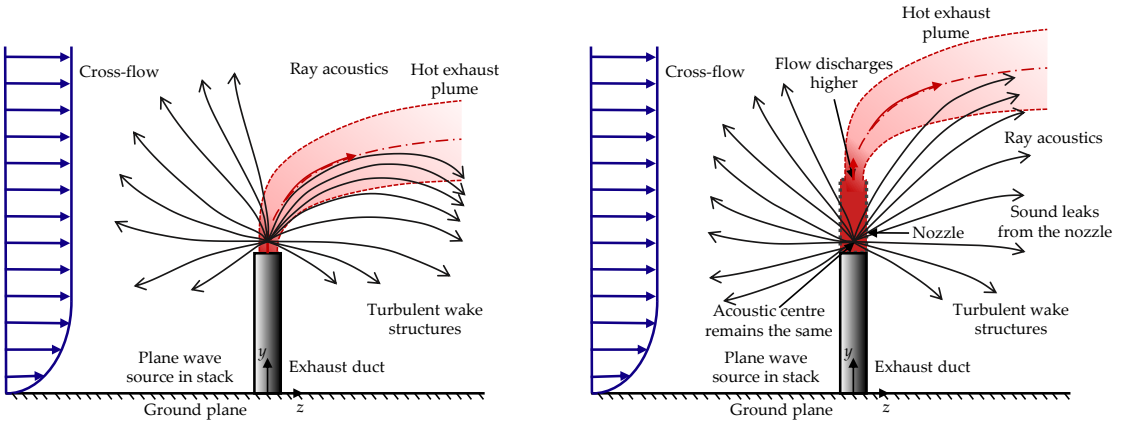

(a) Sound propagation without the nozzle (b) Sound propagation with the nozzle

Figure 5.1: Acoustic ray propagation for the sound propagation through non-isothermal elevated JICF (a) a hard-walled exhaust stack and (b) with the straight acoustically transparent nozzle. The acoustic rays are shown with grey lines. The exterior of the nozzle is symbolised by a black dashed line and filled in with red to show the constrained flow.

that 'releasing' acoustic energy could possibly lead to reducing downwind sound levels. The following discussion, computational and experimental investigations demonstrate that this technique leads to a reduction in downwind sound levels. Figure 5.1 shows a schematic that summarises the acoustic interaction with the hot exhaust plume with and without the flow impervious, acoustically-transparent nozzle. The straight section nozzle constrains the flow to the interior of the nozzle and causes the fluid to exit the duct at a higher vertical height. The acoustically transparent nozzle allows for the acoustic centre of the duct to remain unaltered. This concept allows the acoustic energy to be 'released' or 'leaked' from the protruding vertical exhaust stack at an earlier stage. Hence, less sound interacts with the hot plume deflected by the cooler cross-winds. The reduction in sound interacting with the hot plume leads to a reduction in the amount of sound refracted by the plume and, ultimately, a reduction in the maximum SPL observed downwind of the exhaust stack.

Three prototype nozzles were designed for the reduced-scale exhaust rig in an attempt to alter the sound radiation downwind of the exhaust stack. Figure 5.2

(a) Nozzle 1 (b) Nozzle 2 (c) Nozzle 3

Figure 5.2: Schematics of the three prototype noise mitigation nozzles, where (a) Nozzle 1 is a straight section nozzle, (b) Nozzle 2 is a conical section nozzle with 5° expansion, and (c) Nozzle 3 is a venturi section nozzle. The nozzles are shown in grey and the exhaust ducts are shown in black.

shows the three nozzle designs: a straight section nozzle, conical section nozzle and venturi section nozzle. Next, discussions in this chapter focus on expanding the concept of using nozzles that are acoustically transparent, but impervious to bulk flow. Section 5.4 outlines the construction of the three nozzles, with varying geometries, for a purpose built reduced-scale exhaust rig.

5.4 Prototype nozzle designs

The material for the nozzle construction must be sufficiently stiff to maintain the desired shape; a cylindrical or conical shape; while supporting the self-weight of the structure. Furthermore, the material must be impervious to heated jet flow, and have a high melting point to prevent the nozzle from reaching a malleable state and bending under its own self-weight in heated conditions (often around 600 °C). In addition, the material must also be acoustically transparent. The nozzle

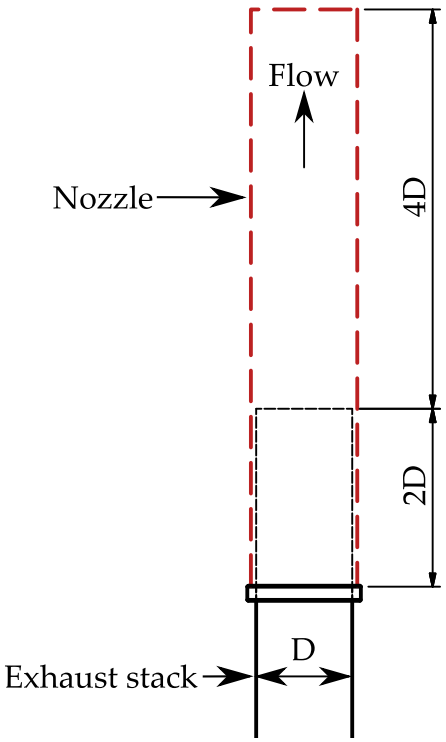

Figure 5.3: A schematic of the straight section nozzle showing the non-dimensional geometry, where the red dash line represents the nozzle and the black line represents the exhaust duct.

was constructed from two different layers of stainless steel mesh. One layer was a stainless steel mesh with a 300 grade (0.05 mm open hole sizing and 0.05 mm thickness) fine mesh for high flow resistivity (impervious to flow), and a coarse 50 grade (0.282 mm open hole sizing and 0.2 mm thickness) stainless steel mesh to form the shape of the nozzle. The acoustic and flow properties for the nozzles will be verified and discussed in detail in Section 5.6.

The first prototype design was a straight section nozzle (Nozzle 1) shown in Figure 5.2a. The dimensions of the straight section nozzle are shown in Figure 5.3 and the nozzle protrudes $4D$ into the domain from the duct outlet. As discussed in Section 5.3, the nozzle constrains the bulk flow, while 'releasing' or 'leaking' the sound through the acoustically transparent nozzle. The purpose of the nozzle is to reduce the acoustic interaction with the hot exhaust plume, and reduce the sound level observed downwind of the exhaust stack, as shown in Chapters 3 and 4.

Another prototype design for the nozzle was inspired by Björk's [27] with a conical shaped nozzle, the geometry for which was discussed briefly in Section 2.2.1. Figures 5.2b and 5.4 show a prototype nozzle with a conical expansion (Nozzle 2). The nozzle in Figures 5.2b and 5.4 has a different geometry and material construction from the nozzle by Björk [27], as seen in Figure 2.1. The nozzle designed by Björk [27] was designed using the theory of increasing the shadow region downwind of the exhaust stack, which could be accomplished with an acoustically hard reflective nozzle and the nozzle geometry shown in Figure 2.1. The nozzle design in Figure 5.2b was constructed out of acoustically transparent material that is impervious to bulk fluid flow. The design choice for the nozzle material was to release the acoustic energy at the duct outlet, while containing the fluid flow. Figure 5.4 shows the non-dimensional geometry for the conical nozzle designed for this research, where the key difference from the nozzle designed by Björk [27] and the conical extension in this thesis, is the inclination angle α, where $\alpha = 20°$ and $\alpha = 5°$, respectively. Again, the cone angle α was different for the two designs, because Björk [27] designed the nozzle purely on the acoustic radiation and increasing the acoustic shadow zone, whereas the nozzle geometry was designed for a smooth transition for the expanding flow in the nozzle. It should be noted that the length of the conical nozzle in Figure 5.2b was $6D$. Hence, the conical nozzle prototype and in this work is similar to Björk's [27] but uses a different ideology for noise mitigation than the conical extension in this chapter.

The prototypes for the straight section and conical nozzles in Figures 5.2a and 5.2b have been extended to a nozzle design that resembles a venturi (Nozzle 3). The design for the venturi is shown in Figures 5.2c and 5.5 and can be separated into three sections: converging, straight and diverging sections. Using the same material as the previous prototype designs in this chapter, the venturi nozzle was designed to be acoustically transparent so that the acoustic centre would remain adjacent to the duct outlet. Figure 5.5 shows the initial part of the nozzle is a converging section for entraining cooler ambient flow with the heated non-isothermal jet exiting the duct. Due to the conservation of fluid momentum and the change in nozzle diameter, the flow would be accelerated in the converging section.

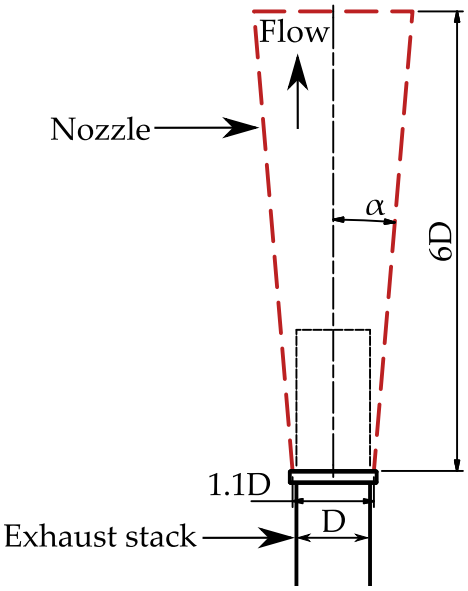

Figure 5.4: A schematic of the conical expansion nozzle showing the non-dimensional geometry, where α is the inclination angle of the cone. The red dash line represents the nozzle and the black line represents the exhaust duct.

Subsequently, in the diverging section, the flow would expand and decelerate with the increase in nozzle diameter. The desired end outcome would be a jet exiting the nozzle with a significantly lower jet temperature when compared with the jet temperature for the exhaust jet without the nozzles, which, as shown in Chapters 3 and 4, leads to a reduction in sound refraction. Figure 5.6 shows the non-dimensional geometry for the venturi nozzle.

Of the three prototype nozzle designs, only the straight section nozzle has been investigated numerically due to the effort required for the modelling, whereas, all three nozzles were experimentally investigated. In Section 5.5 the numerical investigation for the straight section nozzle is discussed. The straight section nozzle was chosen for analysis due to the simplicity of modelling the nozzle. Section 5.6 discusses the acoustic results from the experimental tests performed on each nozzle.

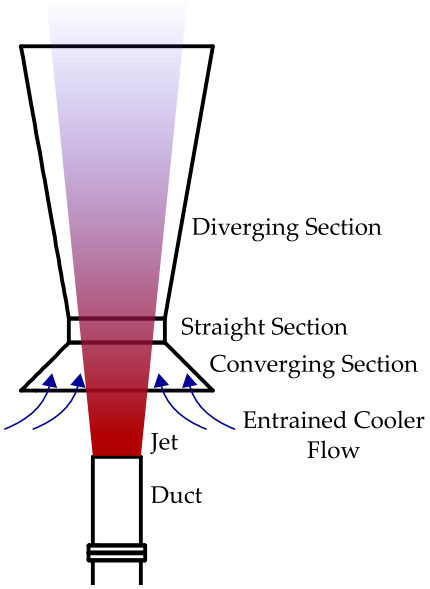

Figure 5.5: A schematic for the venturi nozzle to show the three different sections and the region for enhanced entrained cooler flow. The supports for the nozzle are omitted from the graphic to help with the visualisation of the cooler ambient flow.

5.5 Numerical validation of the acoustically transparent duct section

The numerical techniques of CFD and FEM were used to model the three-dimensional sound radiation in the absence of a hard rigid-wall for an elevated JICF. The purpose of this numerical study was to investigate replacing the hard wall section of the duct with an acoustically transparent section while maintaining consistent flow and temperature conditions. This study replicates this by replacing a section of the exhaust duct with an acoustically transparent section that is impervious to flow. The length of the acoustically hard reflective walls for the duct was varied for two different scenarios: the benchmark case for sound radiation through the existing stack ($L = 10D$) and the case with a shorted stack ($L = 6D$), as shown in Figure 5.2a. The numerical methods for this section are the same as previously used and presented in Chapter 3. The boundary conditions for the CFD and acoustic FEM simulations are presented in Figure 5.7. The flow conditions for

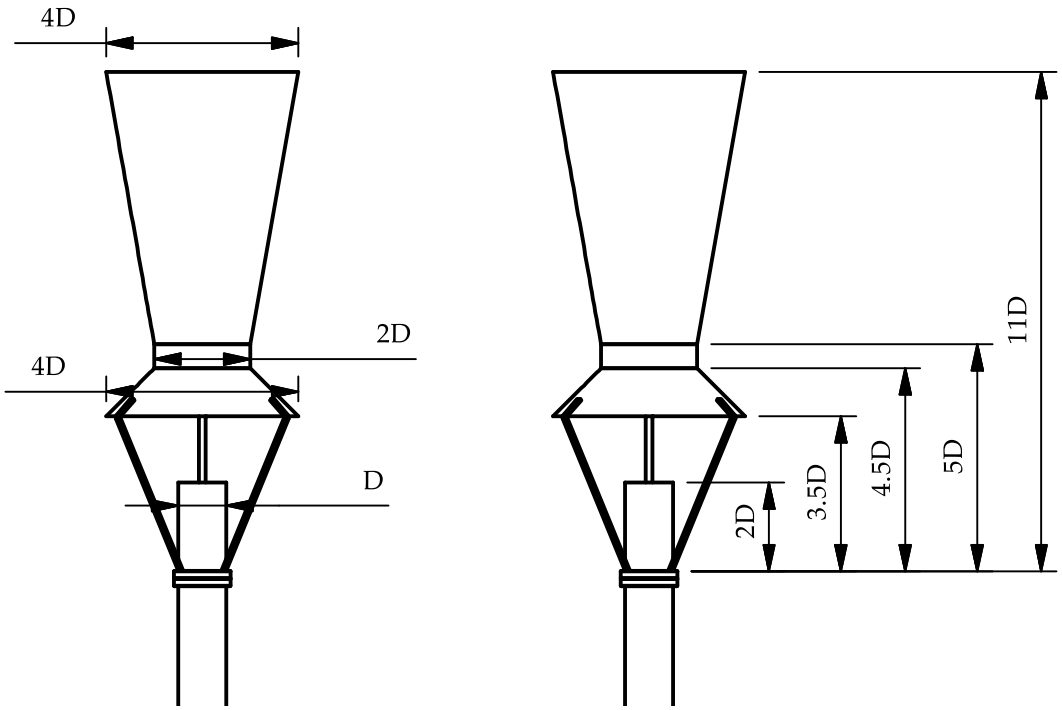

Figure 5.6: Two views of the venturi nozzle (Nozzle 3) illustrating the non-dimensional geometry. Both nozzles in the figure are identical in scale and are used to show the geometry of each nozzle section.

this case study were produced previously using CFD, detailed in Section 3.3.1.2, and were identical for all cases presented in this section. Along the ground surface at the base of the exhaust stack, two different boundary conditions are used to represent realistic boundary conditions near real OCGT exhaust stacks: a hard reflective surface representing hard structures and cement surroundings (a wall with the absorptive coefficient, $\alpha_s = 0$), and absorptive surface representing grass and other vegetation ($\alpha_s = 1$). The simulations with the hard reflective boundary condition are a more accurate representation of a real OCGT, however as was seen in Section 3.3.3, the sound radiation patterns become complex. Furthermore, the experimental results presented in Section 5.6 are with an anechoic ground surface to minimise reflections off the ground surface and to assist the analysis for determining the direct path of sound from the exhaust stack. Hence, to reduce the complexity and to investigate in more detail the impact the plume has on altering

the sound propagation path, an anechoic boundary condition was implemented for the ground surface. This anechoic boundary condition is the Robin radiation boundary condition defined by Equation (3.31), which is discussed in detail in Section 3.2.2.2 and with acoustic results including this boundary condition are presented in Section 3.3.3. The following acoustic results for the two different duct lengths ($L = 10D$ and $L = 6D$) were visualised with the following:

- SPL contour plots along the Y-Z plane of symmetry,
- directivity line plots along the Y-Z plane of symmetry for the band-averaged one-third octave band at various radii ($r = [2D, 8D, 16D, 32D]$), and
- 3-D radiation directivity patterns for the band-averaged one-third octave band with centre frequency $ka = 0.85$ at $r = 32D$.

Figure 5.8 shows the SPL contour plots for the hard reflective ground surface, and two different rigid-walled duct lengths: $L = 10D$ (Figure 5.8a), and $L = 6D$ (Figure 5.8b). The results show that replacing a $4D$ length of stack with an acoustically transparent section that is impervious to flow has changed the sound radiation observed downwind of the exhaust stack. In Figure 5.8a, the acoustic lobe observed downwind of the stack is less prominent than in Figure 5.8b. Interestingly, comparing Figures 5.8a and 5.8b shows that the latter produces an acoustic radiation that is approximately symmetrical about the duct centreline with little evidence of refraction. Although Figures 5.8a and 5.8b show the dominant effects of the acoustic diffraction and reflections, it is difficult to ascertain detailed acoustic features, which necessitates analysis of the results for an anechoic ground surface.

Replacing the hard reflective ground surface with an anechoic ground surface reduces the complexity for visualising the acoustic radiation from the elevated JICF. Figure 5.9 shows the SPL contour plots along the Y-Z plane for two different duct lengths, $L = 10D$ and $L = 6D$, with an anechoic ground surface. Reducing the rigid-walled duct from $L = 10D$ to $L = 6D$ reduces the asymmetry in the acoustic radiation about the duct centreline. In particular, it can be seen that the acoustic lobe previously observed downwind of the exhaust stack in Figure 5.9a has reduced drastically in Figure 5.9b. Qualitatively, the reduction in the acoustic lobe observed

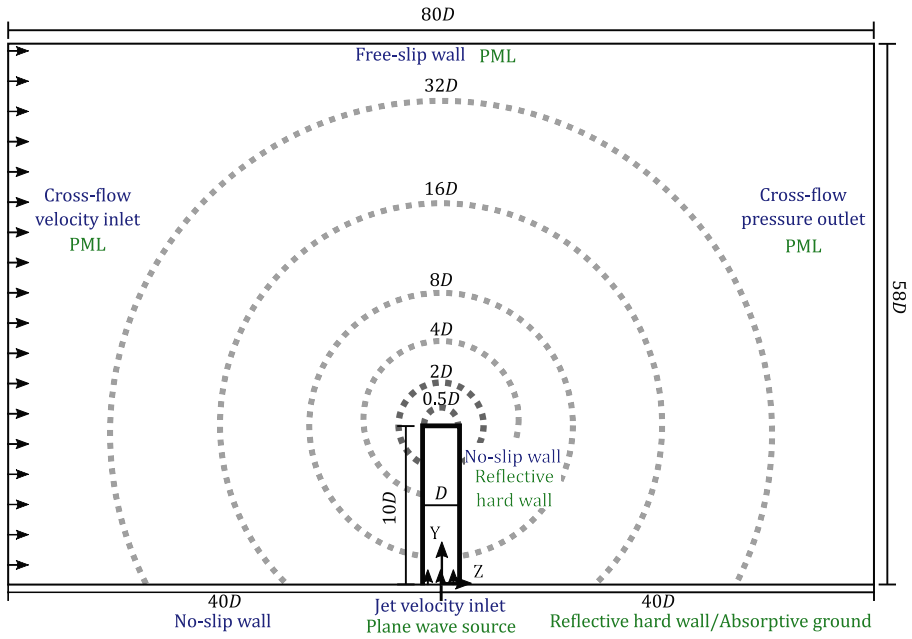

(a) $L = 10D$

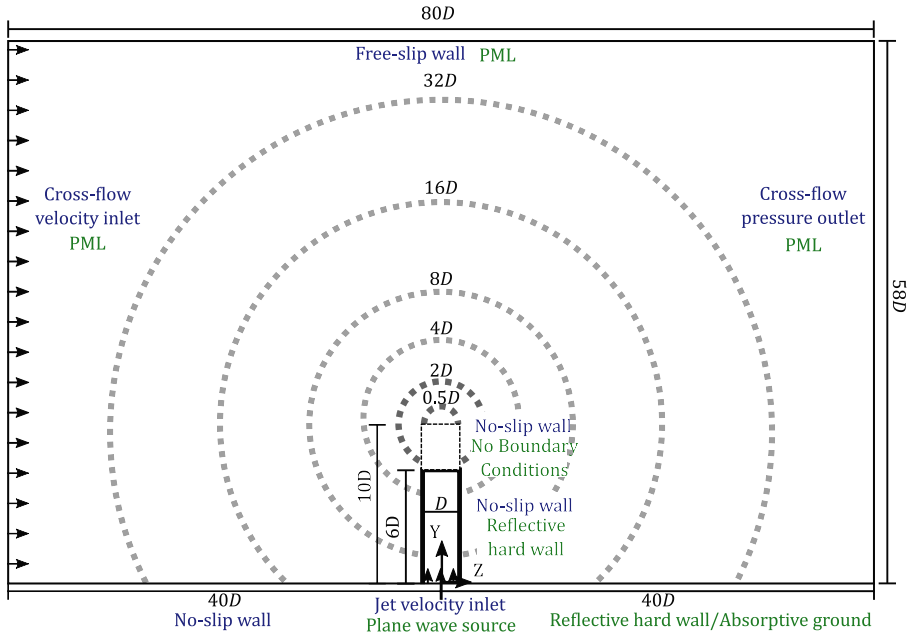

(b) $L = 6D$

Figure 5.7: Schematics to illustrating the case for sound propagation through the non-isothermal elevated JICF with two different rigid-walled duct lengths (a) $L = 10D$ and (b) $L = 6D$ along the Y-Z plane (of symmetry). Blue text represents the fluid dynamics boundary conditions and green text represents the acoustic boundary conditions. PML refers to a Perfectly Matched layer.

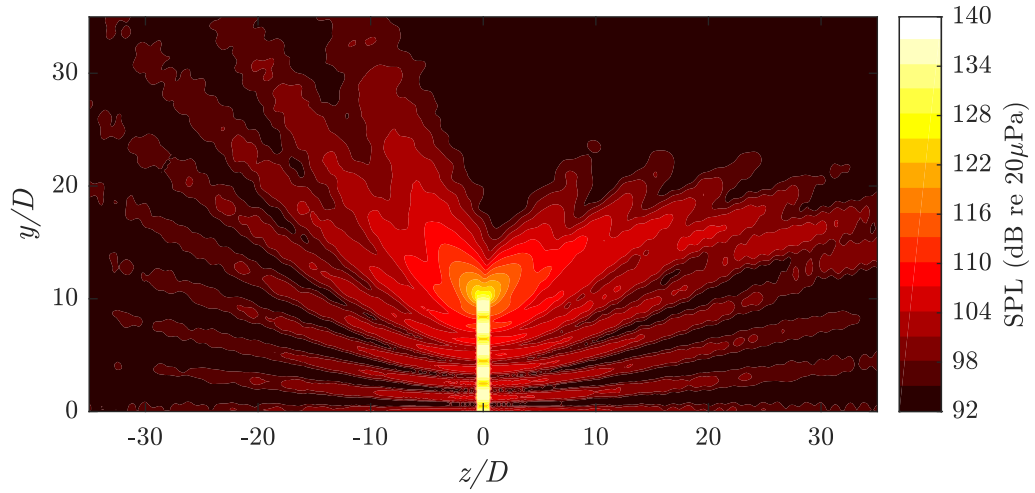

(a) $L = 10D$

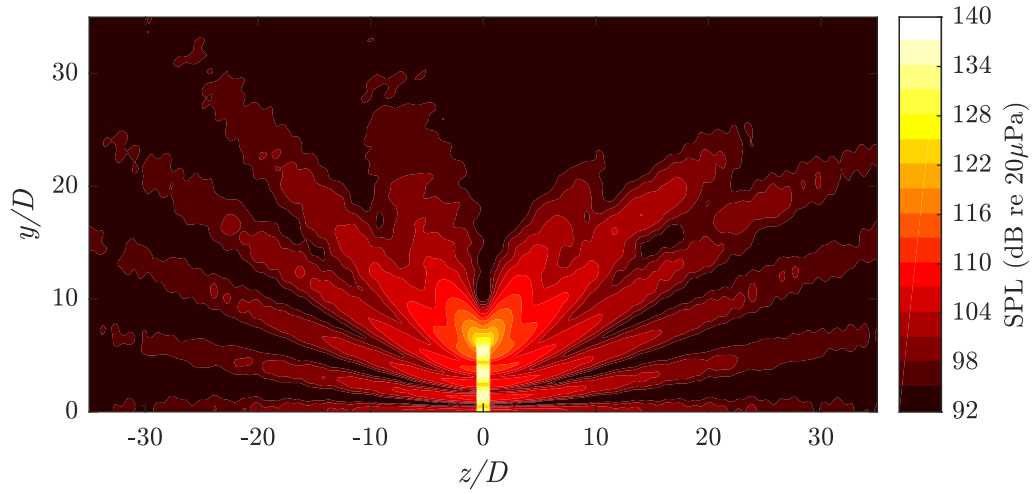

(b) $L = 6D$

Figure 5.8: Contour plots for sound pressure levels for elevated JICF with a hard reflective ground surface at two rigid-walled duct lengths (a) $L = 10D$ and (b) $L = 6D$. The results are along the Y-Z plane (of symmetry) for sound propagation through the non-isothermal velocity and thermal gradients from a JICF with $\alpha_s = 0$, $R = 5$, $T_j = 500\,°\text{C}$, $\vec{v}_0(\vec{x}) \neq 0$, and $ka = 0.8$. The cross-flow is from left to right in the figure. Values 48 dB less than the maximum SPL are saturated black.

downwind of the exhaust stack is a promising finding in the mitigation of sound pressure levels downwind of an exhaust stack.

The sound radiation can be interpreted with sound directivity plots to quantify the mean normalised sound pressure levels for each case with varying rigid-walled duct lengths. Due to the change in the acoustically rigid-walled duct length from $L = 10D$ to $L = 6D$, the acoustic centre at the rigid-walled duct outlet also changes in height. The centre for the directivity results presented in this section is at the duct centreline and was depicted in Figure 5.7. Figure 5.10 shows the sound directivity with two different rigid-walled duct lengths, $L = 10D$ to $L = 6D$. The directivity results in Figure 5.10 are displayed over a band-averaged one-third octave with a centre frequency $ka = 0.85$ ($f = 3150\,\text{Hz}$). Band-averaged results have been used to reduce the ripples in the results from the numerical artefacts previously seen and discussed in Chapter 3. The sound directivity plots in Figure 5.10 show that the sound radiation is dependent on the radii directivity distance ($r = [2D, 8D, 16D, 32D]$). Figure 5.10a show that the sound radiation at $r = 2D$ for varying duct lengths $10D$ and $6D$ is almost identical. The sound radiation is approximately axisymmetric and resembles the sound radiation from a non-isothermal jet, as shown in Figure 4.20a and the work completed by Atvars et al. [15]. With the increase in distance ($r \geq 4D$), the sound directivity plots show the effects of changing duct length and, in particular, the change in sound radiation asymmetry. The results of sound directivity when reducing the duct length from $L = 10D$ to $L = 6D$ for directivity radii, $r \geq 4D$, can be summarised as follows:

- a cusp has formed on-axis of the duct from the refraction of sound,
- upwind of the exhaust stack the sound directivity plots are relatively similar,
- there has been a reduction in the acoustic lobe downwind from the exhaust stack by approximately 3 dB to 4.5 dB,
- a change in the position of the acoustic lobe downwind of the exhaust stack towards 0°, and
- spatial broadening of the acoustic lobe downwind of the exhaust stack.

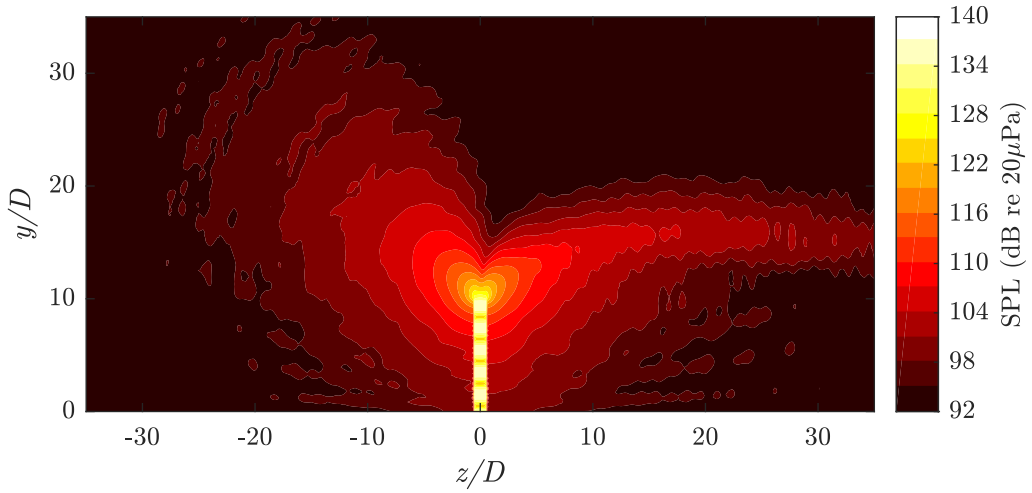

(a) $L = 10D$

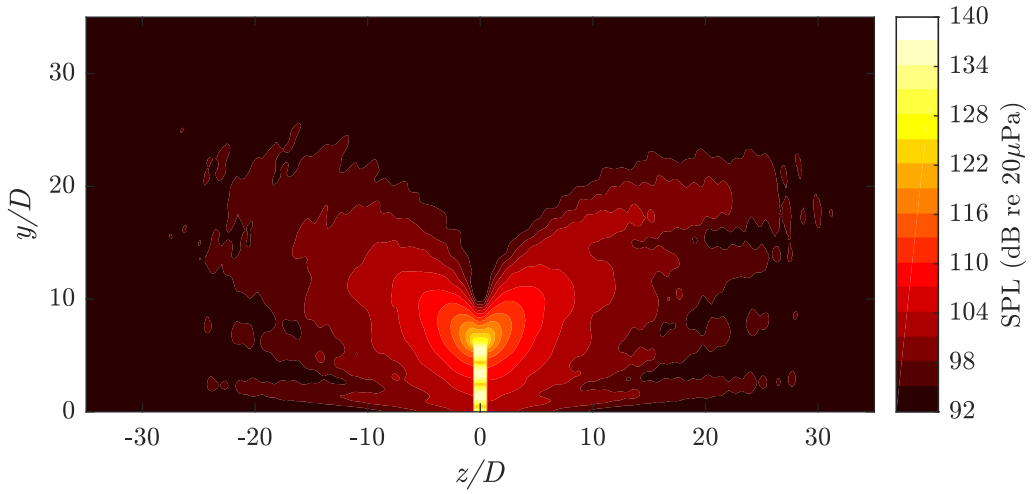

(b) $L = 6D$

Figure 5.9: Contour plots of sound pressure levels for elevated JICF with an anechoic ground surface at two rigid-walled duct lengths (a) $L = 10D$ and (b) $L = 6D$. The results are along the Y-Z plane (of symmetry) for sound propagation through an elevated JICF with $\alpha_s = 1$, $R = 5$, $T_j = 500\,°\text{C}$, $\vec{v}_0(\vec{x}) \neq 0$, and $ka = 0.8$. The cross-flow is from left to right in the Figure. Values 48 dB less than the maximum SPL are saturated black.

The directivity plots have shown quantitatively the change in the sound radiation with the decrease in the acoustically hard duct length from $L = 10D$ to $L = 6D$, whereby there is a reduction in the DI magnitude of the acoustic lobe downwind of the exhaust stack.

The acoustic radiation with the shorter exhaust duct ($L = 6D$) can be presented with a 3-D directivity radiation pattern to show complex details that are not visible with line plots or 2-D planar contour plots. Figure 5.11 shows the band-averaged one-third octave result for the 3-D directivity radiation pattern with a duct length of $L = 6D$ for the non-isothermal JICF at a radius of $r = 32D$, centre frequency $ka = 0.85$, $r = 32D$, cross-flow ratio $R = 5$, and jet temperature $T_j = 500\,°\text{C}$. It can be seen that downwind of the exhaust stack there is a slight presence of an acoustic lobe. On-axis of the duct outlet, an axisymmetric cusp has formed from the refraction of sound. Upwind of the exhaust stack, the sound spreads approximately spherically with a uniform colour band. The features are consistent with the previous plots in this section, however Figure 5.11 highlights the complex 3-D radiation pattern of the sound.

The 3-D directivity radiation pattern can be visualised from a different perspective to highlight different acoustic details for the cases with a varying rigid-walled duct length, $L = 10D$ and $L = 6D$. Figure 5.12 shows the 3-D directivity radiation pattern for the two different cases with, $L = 10D$ and $L = 6D$, while viewing the acoustic results along the Y-Z plane. The acoustic results for the reduction in the rigid-walled duct length can be summarised as follows:

- a relatively more spherical acoustic radiation pattern,
- a reduction in the DI magnitude of the acoustic lobe downwind of the exhaust stack,
- spatial broadening of the acoustic lobe downwind of the exhaust stack,
- an increase in the height of the acoustic lobe downwind of the exhaust stack,

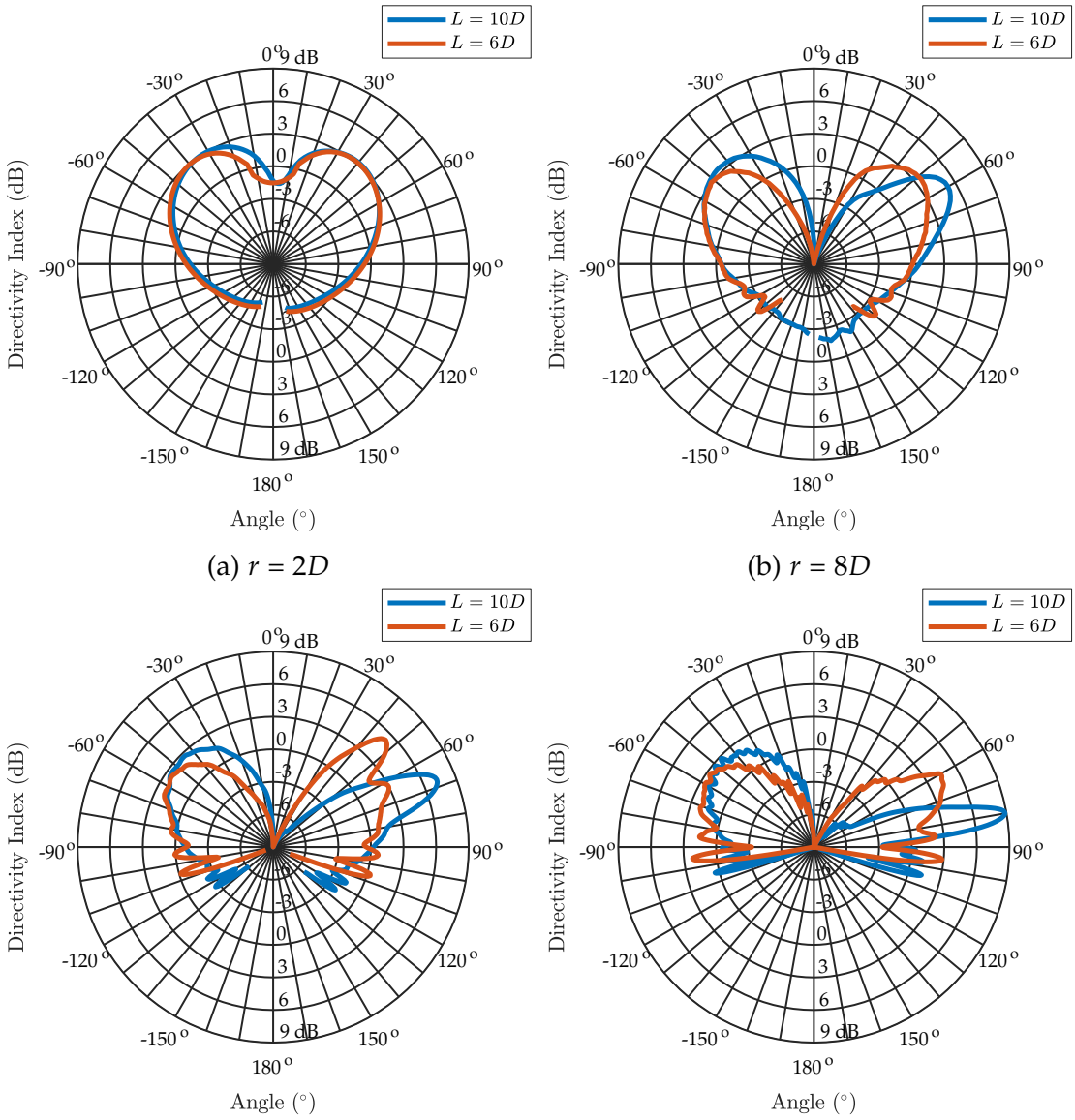

(a) $r = 2D$ (b) $r = 8D$

(c) $r = 16D$ (d) $r = 32D$

Figure 5.10: The DI along the Y-Z plane (of symmetry) as a function of radial distance from the outlet, $r = [2D, 8D, 16D, 32D]$. For sound propagation through the non-isothermal JICF, with a rigid-walled duct length at $6D$ and $10D$, while $\alpha_s = 1$, $ka = 0.85$, $R = 5$ and $T_j = 500\,°\text{C}$. The cross-flow is from left to right.

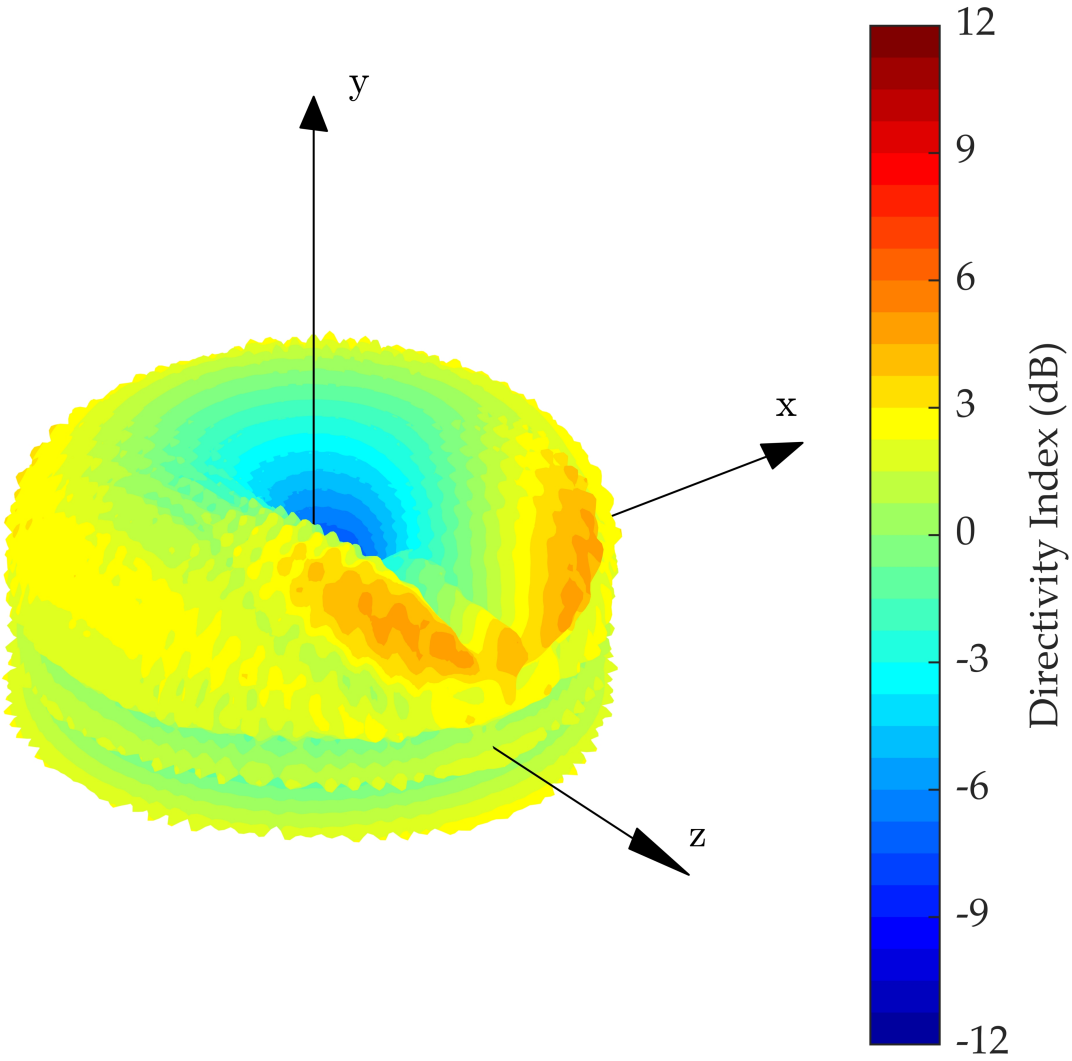

Figure 5.11: The one-third octave band-average 3-D directivity radiation pattern for sound propagation through a non-isothermal elevated JICF at a radius $r = 32D$ with $R = 5$, $T_j = 500\,°\text{C}$, $\vec{v}_0(\vec{x}) \neq 0$, and centre frequency $ka = 0.85$ (3150 Hz). The cross-flow is flowing parallel to the Z-axis, towards the positive direction. Values of DI less than $-12\,\text{dB}$ are saturated dark blue.

- there are clear, coherent acoustic radiation patterns below the Z-axis, which could be related to diffraction patterns from the duct edge or the acoustic reflections from the stack, and
- upwind of the exhaust stack the sound radiation differs slightly, with the shorter rigid-walled duct length leading to a relatively more spherical sound radiation pattern.

The results in Figure 5.12 reinforce the numerical findings that replacing a length of $4D$ of the exhaust stack with an acoustically transparent section that is impervious to flow changes the sound radiation, where the broadening of the acoustic lobe downwind of the exhaust stack reduces the maximum DI observed downwind.

5.6 Experimental tests on exhaust nozzles

Experiments were conducted on the three prototype nozzles illustrated in Figure 5.2. Figure 5.13 shows photographs of each of the nozzles at the duct outlet taken during experimental testing at the Thebarton Wind Tunnel. The experimental apparatus and methodology for testing at the Thebarton Wind Tunnel were discussed previously in Section 4.2. The following cases for each nozzle will be discussed: sound radiation in an isothermal stationary field, and sound radiation through a non-isothermal, heated elevated JICF. The isothermal stationary field tests were conducted to ensure that the construction was acoustically transparent. The tests conducted on the non-isothermal, heated elevated JICF were used to assess the performance of the nozzle in reducing or redirecting the downwind acoustic energy.

Each of the three nozzles in Figures 5.2 and 5.13 were designed to be easily interchangeable on the duct outlet, and the vertical position of each nozzle can be shifted. However, each nozzle was experimentally tested for a single mounting position at the duct outlet and future work can investigate the noise mitigation performance for each nozzle with varying mounting heights. The test campaign was limited due to the availability of the Thebarton Wind Tunnel.

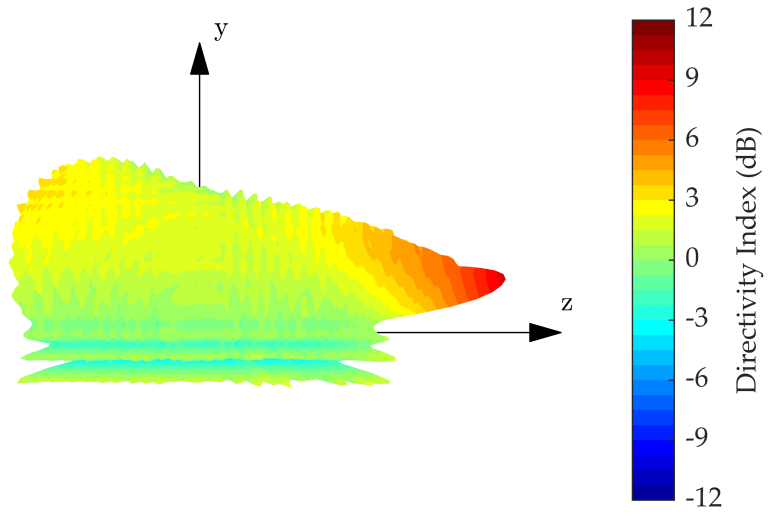

(a) $L = 10D$

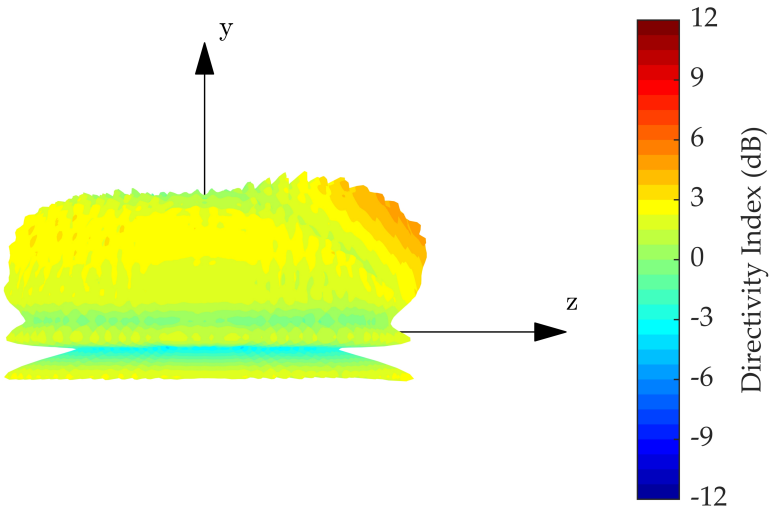

(b) $L = 6D$

Figure 5.12: The one-third octave band-average 3-D directivity radiation pattern for sound propagation through a non-isothermal elevated JICF for two rigid-walled duct lengths (a) $L = 10D$ and (b) $L = 6D$. Both configurations had a radius $r = 32D$ with $R = 5$, $T_j = 500\,°\text{C}$, $\vec{v}_0(\vec{x}) \neq 0$, and centre frequency $ka = 0.85$ (3150 Hz). The cross-flow is flowing parallel to the Z-axis, towards the negative direction. Values of DI less than $-12\,\text{dB}$ are saturated dark blue.

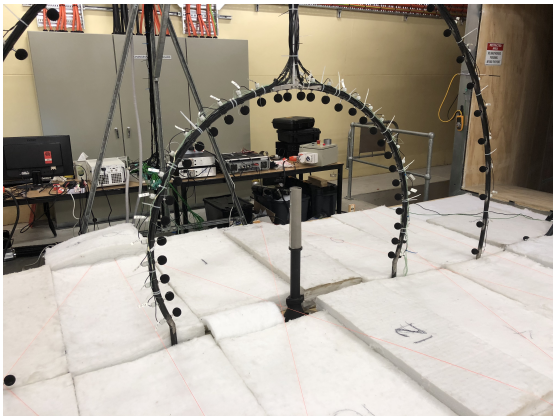

(a) Straight section nozzle (Nozzle 1)

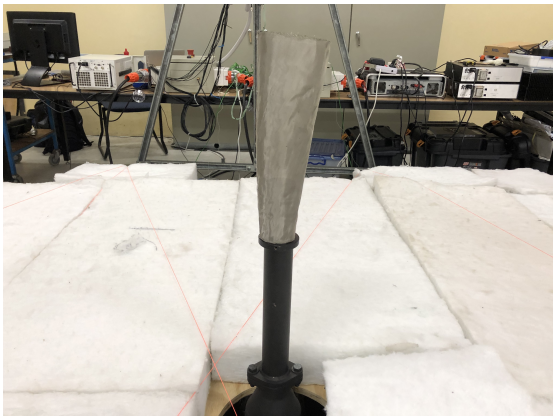

(b) Conical section nozzle (Nozzle 2)

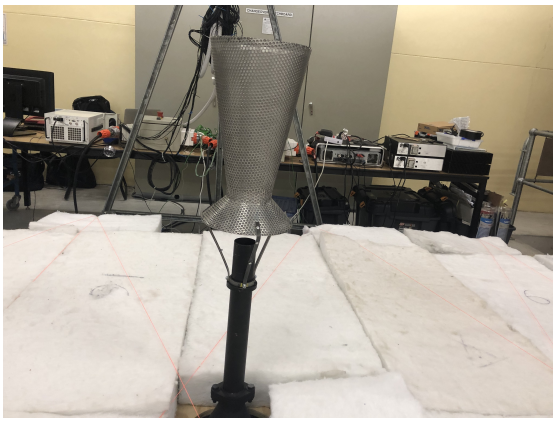

(c) Venturi section nozzle (Nozzle 3)

Figure 5.13: Photos of the experimental setup with three nozzles attached to the reduced-scale exhaust rig at the Thebarton Wind Tunnel, where: (a) is the straight section nozzle (Nozzle 1), (b) is the conical section nozzle (Nozzle 2), and (c) is the venturi section nozzle (Nozzle 3).

5.6.1 Experimental validation of the acoustically transparent nozzles

This section describes the investigation of the acoustic insertion loss of the nozzles in the absence of heat or flow. If the nozzles are acoustically transparent, the acoustic centre of the system remains unchanged for testing in an isothermal stationary field, in the absence of a jet and cross-flow. The unchanged acoustic centre, with and without the nozzles, allows a direct comparison for each directivity plot.

Figure 5.14 shows the directivity for sound radiation through the exhaust stack, with and without the nozzles in an isothermal stationary field, at four band-average one-third octave bands with centre frequencies $ka = [0.85, 1.08, 1.35, 1.70]$ ($f = [3.15\,\text{kHz}, 4\,\text{kHz}, 5\,\text{kHz}, 6.3\,\text{kHz}]$). The directivity results show that the sound propagation with and without the nozzles is identical with experimental errors, and therefore it can be concluded that the nozzles are acoustically transparent and the acoustic centre for each case remains the same.

It should be noted that the sum of the sound pressures intercepting the microphone array at $28D$ was also calculated for each band-averaged one-third octave band. For the same signal source and power into the compression drivers, the total sound pressure for each one-third octave band with and without the nozzles was almost identical, with variations of approximately $\pm 0.5\,\text{dB}$ and within the measurement tolerance of the microphones. The equivalence in the total sound pressure shows that the nozzles are acoustically transparent, the sound power from the exhaust stack is essentially equal, and the acoustic centre remains fixed and independent of the nozzles.

5.6.2 Experimental investigation of the nozzles in the presence of a non-isothermal elevated JICF

This section presents the experimental acoustic results for sound radiation through the non-isothermal elevated JICF with and without the three nozzles. The acoustic radiation for each nozzle is presented in the form of directivity plots. For analysing

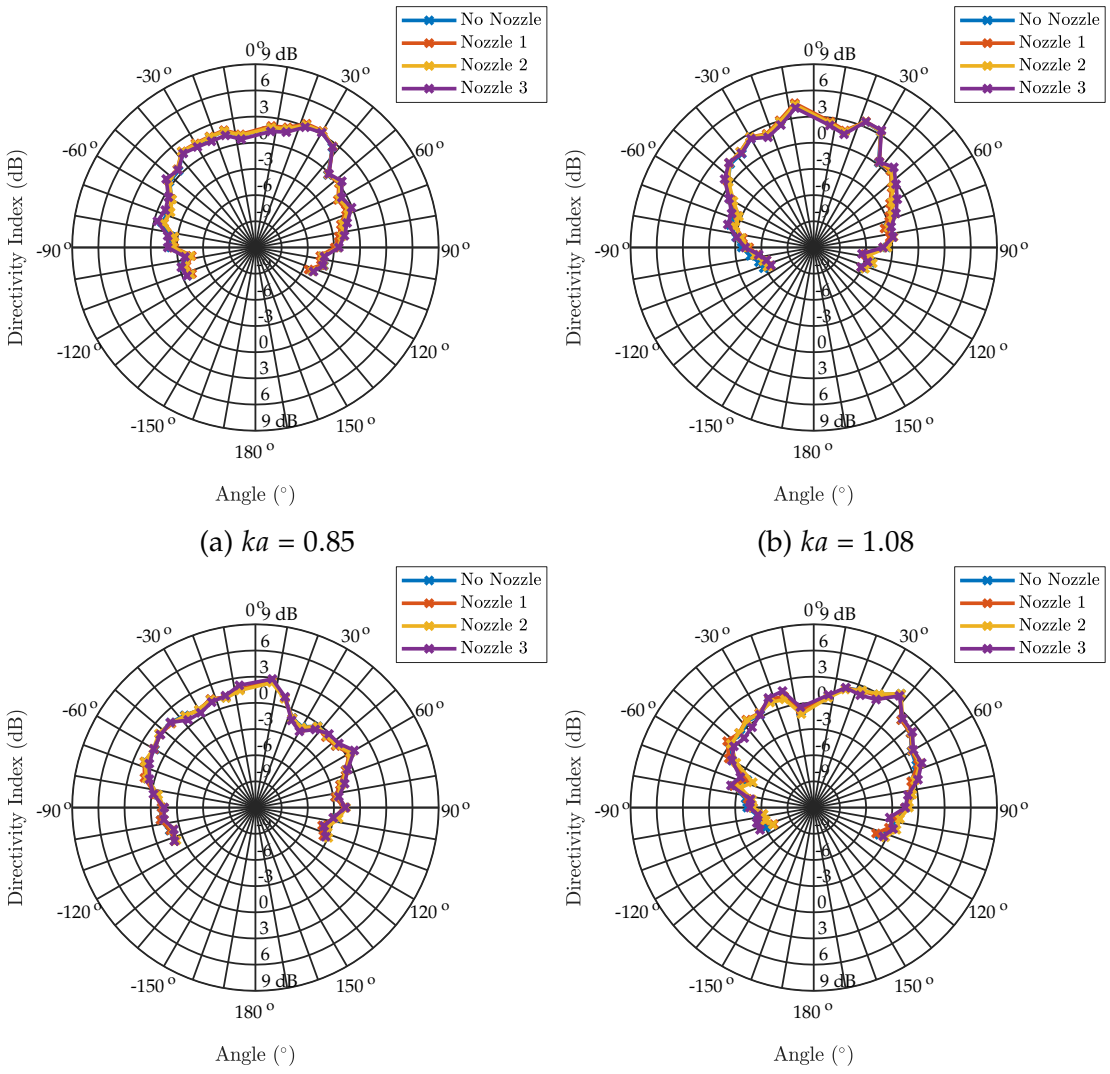

(a) $ka = 0.85$ (b) $ka = 1.08$

(c) $ka = 1.35$ (d) $ka = 1.70$

Figure 5.14: The band-averaged DI along the Y-Z plane (of symmetry) for sound propagation in the absence of a non-isothermal JICF, with and without the three nozzles. The test conditions were $ka = [0.85, 1.08, 1.35, 1.70]$, $r = 28D$, $R = 5$ and $T_j = 500\,°\text{C}$.

the sound directivity, four band-averaged one-third octave bands, with centre frequencies $ka = [0.85, 1.08, 1.35, 1.70]$ or $f = [3.15\,\text{kHz}, 4\,\text{kHz}, 5\,\text{kHz}, 6.3\,\text{kHz}]$, are presented for each case, with three cross-flow ratios ($R = [5, 7.5, 10]$) and jet temperature, $T_j = 500\,°\text{C}$.

Figure 5.15 shows the directivity results with and without the nozzles for $R = 5$, $T_j = 500\,°\text{C}$, $r = 28D$ and $ka = [0.85, 1.08, 1.35, 1.70]$. The results show that each of the nozzles produce unique directivity patterns, with the intended goal of reducing the maximum SPL downwind of the duct. For Nozzles 1 and 2, the acoustic directivity is almost identical, with a spatial broadening in the acoustic lobe downwind, when compared with the case with no nozzle. The spatial broadening of the acoustic lobe downwind leads to the reduction in maximum downwind SPL, with Nozzle 1 showing a greater reduction in SPL downwind of approximately 1 dB to 2.5 dB. The difference in the downwind SPL between Nozzles 1 and 2 can be from 0.5 dB to 1 dB at different frequencies. Figures 5.15a, 5.15b, and 5.15c show that Nozzle 3 produces two acoustic lobes downwind of the exhaust stack at approximately 60° and 90°. The two acoustic lobes lead to a broadening of the directivity plot downwind and an overall reduction of the downwind SPL by approximately 2 dB to 2.5 dB. Figure 5.15d shows the greatest reduction in the maximum downwind SPL for all three nozzles, with Nozzles 1 and 3 showing a decrease of up to 3 dB. At $ka = 1.70$ ($f = 6.3\,\text{kHz}$), Nozzle 3 does not have two acoustic lobes downwind and is now a broad single acoustic lobe. In summary, the nozzles change the sound directivity pattern downwind of the exhaust stack, with Nozzle 1 and 3 showing the greatest reduction in maximum SPL downwind.

Section 4.4.4 showed that the sound directivity is dependent on the cross-flow ratio. Figures 5.16 and 5.17 present the sound directivity results for sound propagation through non-isothermal elevated JICF at two cross-flow ratios ($R = [7.5, 10]$), with and without the three nozzles. In comparing the directivity results from Figures 5.15, 5.16, and 5.17, key acoustic features can be seen with the increase in R:

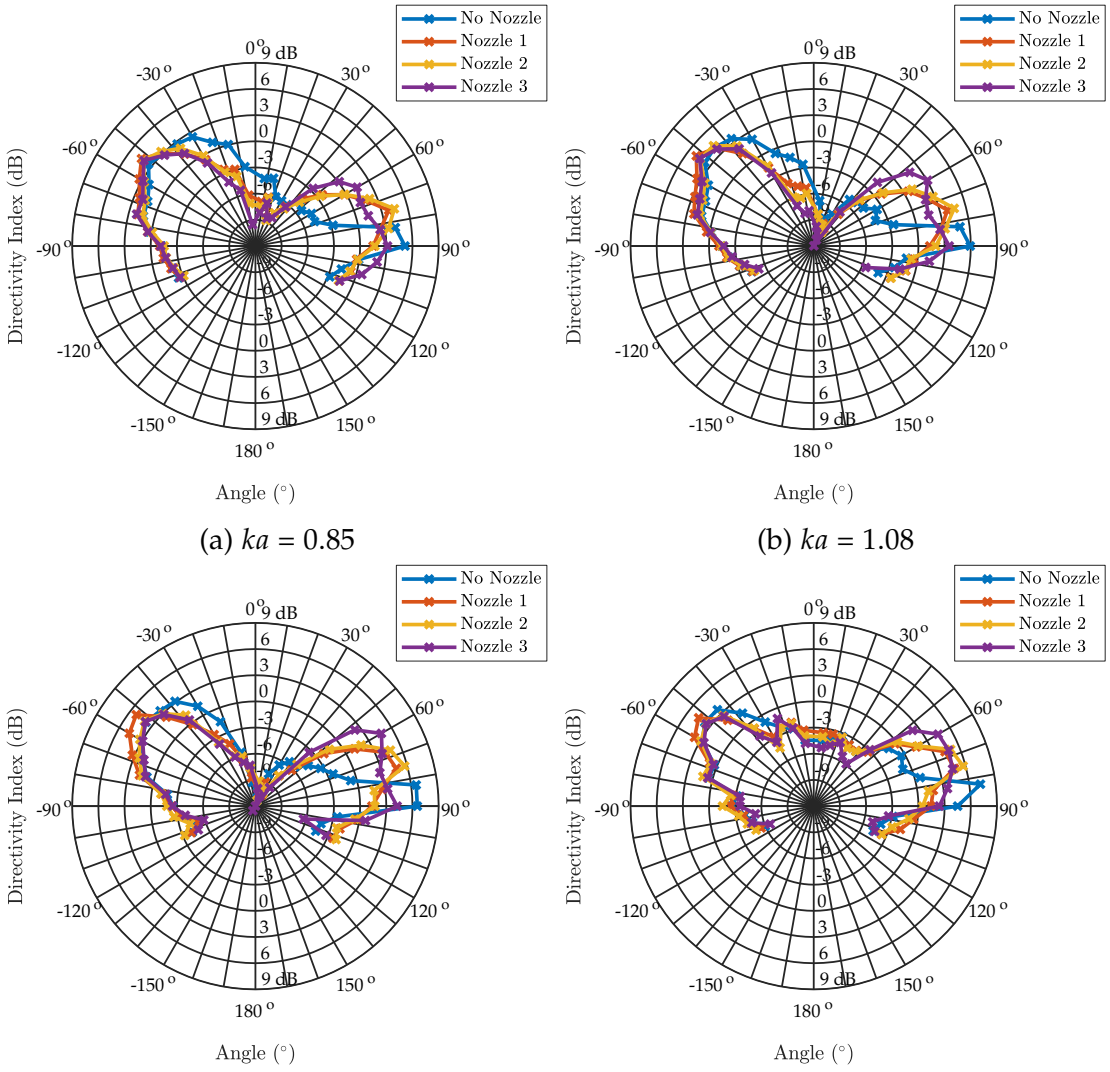

(a) ka = 0.85 (b) ka = 1.08

(c) ka = 1.35 (d) ka = 1.70

Figure 5.15: The band-averaged DI along the Y-Z plane (of symmetry) for sound propagation with the non-isothermal JICF, with and without the three nozzles. The test conditions were $ka = [0.85, 1.08, 1.35, 1.70]$, $r = 28D$, $R = 5$ and $T_j = 500\,°\text{C}$. The cross-flow is from left to right.

- the sound directivity of the nozzles shows a reduction in the maximum DI observed downwind of the exhaust stack when compared with the sound directivity without the nozzles,
- all three directivity results with the nozzles show the reductions in the maximum DI observed downwind of the exhaust stack are dependent on the centre frequency of the one-third octave band, with an increase in ka leading to an increase in sound reduction downwind,
- the attachment of a nozzle to the duct spatially broadens the acoustic lobe downwind of the exhaust stack, when compared with the case without the nozzles,
- the acoustic lobe downwind of the exhaust stack with and without the nozzles shifts towards 0° with the increase in R,
- all cases presented in this experimental section show a cusp forming on-axis of the duct centreline as the total sound power is conserved but is redistributed, and
- upwind of the stack the difference in sound directivity is small, with and without the nozzles.

Interestingly, Figure 5.15 shows an important feature that Nozzle 3 produces two acoustic lobes downwind of the exhaust stack, but for Figures 5.16, and 5.17, the sound directivity for Nozzle 3 shows a broadening of a single acoustic lobe downwind of the exhaust stack.

The acoustic directivity results in Figures 5.15, 5.16, and 5.17 can be further analysed to show the reduction in maximum DI downwind of the exhaust stack. Tables 5.1, 5.2, and 5.3 summarise the quantitative reduction in maximum DI downwind of the exhaust stack for the three nozzles. Firstly, it should be noted that Tables 5.1, 5.2, and 5.3 show that each nozzle has different levels of downwind sound reduction for each cross-flow ratio (R) and one-third octave centre frequency (ka). The results in Table 5.1 show that for $ka = [0.85, 1.08]$, Nozzle 3 has the largest

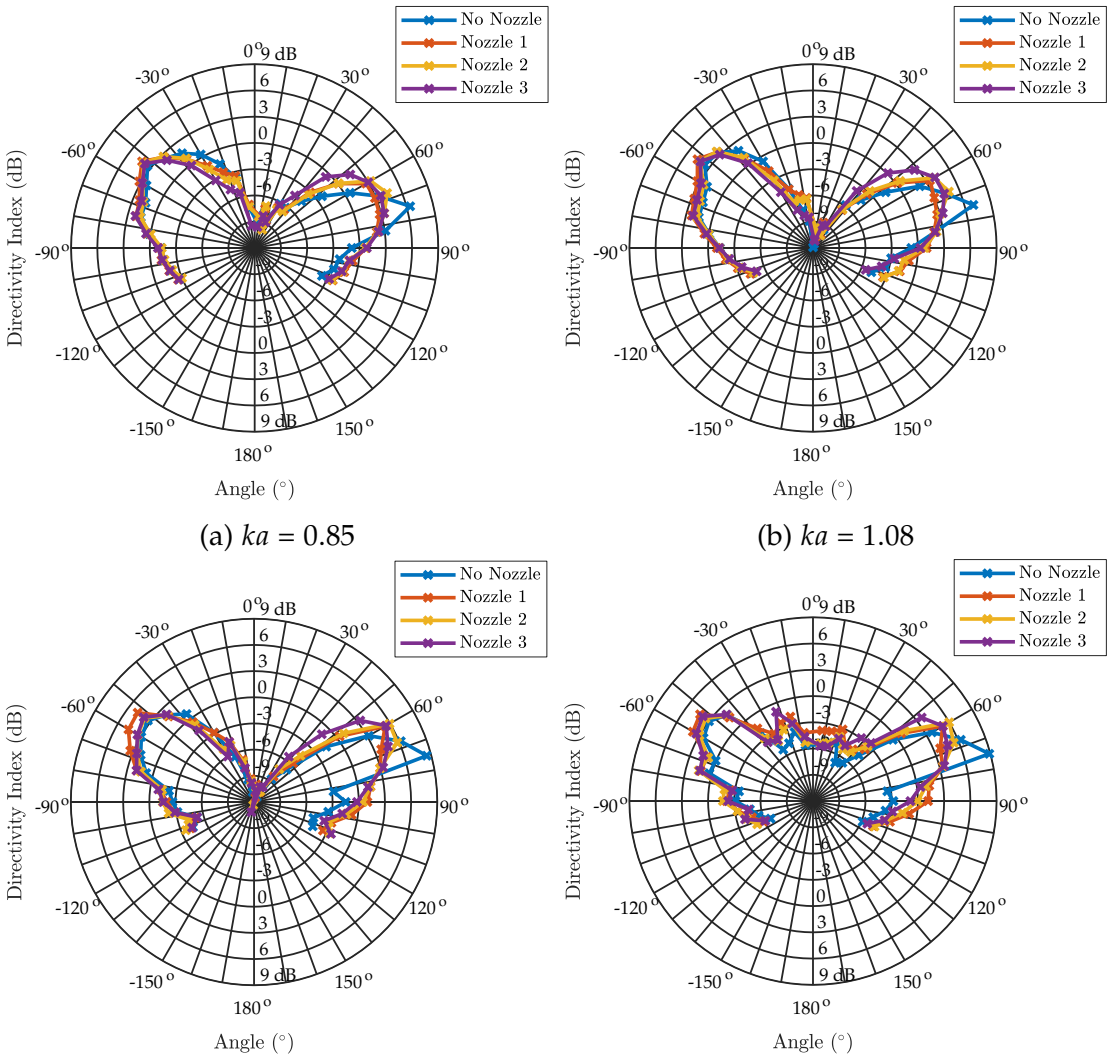

(a) $ka = 0.85$ (b) $ka = 1.08$

(c) $ka = 1.35$ (d) $ka = 1.70$

Figure 5.16: The band-averaged DI along the Y-Z plane (of symmetry) for sound propagation with the non-isothermal JICF, with and without the three nozzles. The test conditions were $ka = [0.85, 1.08, 1.35, 1.70]$, $r = 28D$, $R = 7.5$ and $T_j = 500\,°\text{C}$. The cross-flow is from left to right.

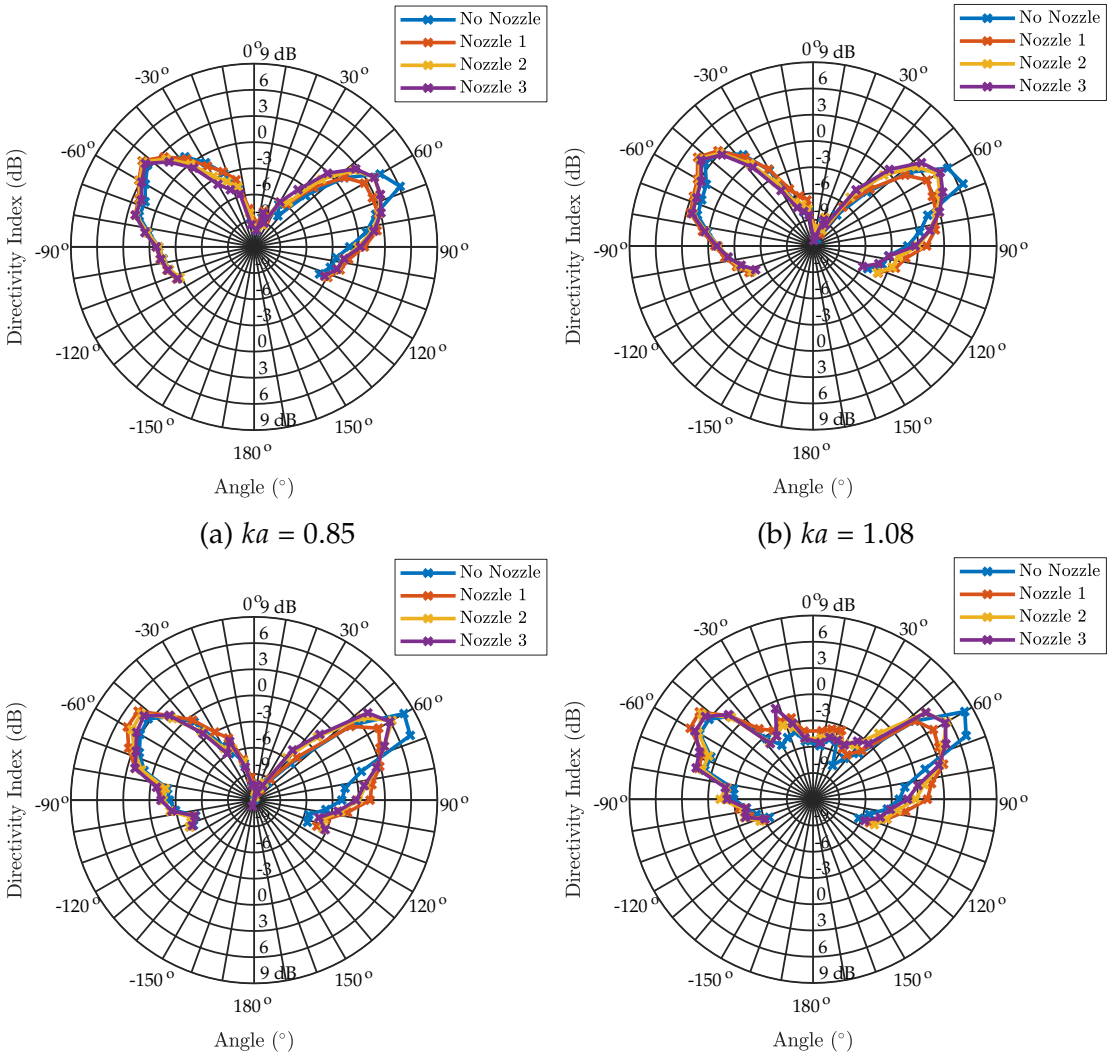

(a) $ka = 0.85$ (b) $ka = 1.08$

(c) $ka = 1.35$ (d) $ka = 1.70$

Figure 5.17: The band-averaged DI along the Y-Z plane (of symmetry) for sound propagation with the non-isothermal JICF, with and without the three nozzles. The test conditions were $ka = [0.85, 1.08, 1.35, 1.70]$, $r = 28D$, $R = 10$ and $T_j = 500\,°\text{C}$. The cross-flow is from left to right.

Table 5.1: The reduction in maximum DI for the acoustic lobe downwind of the exhaust stack where the three nozzles for the case with $R = 5$. The ka in the left column is the band-averaged one-third octave centre frequency.

	$R = 5$		
ka	Nozzle 1 (dB)	Nozzle 2 (dB)	Nozzle 3 (dB)
0.85	1.3	0.7	2.0
1.08	2.1	1.3	2.4
1.35	1.9	0.9	1.9
1.70	2.6	1.5	2.5

Table 5.2: The reduction in maximum DI for the acoustic lobe downwind of the exhaust stack where the three nozzles for the case with $R = 7.5$. The ka in the left column is the band-averaged one-third octave centre frequency.

	$R = 7.5$		
ka	Nozzle 1 (dB)	Nozzle 2 (dB)	Nozzle 3 (dB)
0.85	3.5	2.0	2.8
1.08	3.6	2.2	2.8
1.35	3.1	2.6	3.0
1.70	3.7	2.9	3.7

reduction in downwind DI, and for $ka = [1.35, 1.70]$, Nozzles 1 and 3 show very similar levels of reduction downwind. Table 5.2 shows a slightly different outcome, with Nozzle 1 showing the greatest reduction in maximum DI downwind for $ka = [0.85, 1.08, 1.35]$. However, Table 5.2 also shows that for $ka = 1.70$, Nozzles 1 and 3 have similar levels of reduction downwind DI. Interestingly, Table 5.3 shows that for $R = 10$, Nozzle 1 shows the largest reduction in downwind sound, of approximately 3.4 dB to 4.2 dB.

Table 5.3: The reduction in maximum DI for the acoustic lobe downwind of the exhaust stack where the three nozzles for the case with $R = 10$. The ka in the left column is the band-averaged one-third octave centre frequency.

	$R = 10$		
ka	Nozzle 1 (dB)	Nozzle 2 (dB)	Nozzle 3 (dB)
0.85	3.4	2.2	2.2
1.08	3.5	2.1	1.8
1.35	3.4	1.6	1.9
1.70	4.2	2.4	2.3

5.7 Discussion on noise mitigation and real life implementation

All three nozzles have produced unique directivity plots, with the change in sound directivity downwind of the exhaust stack. This section discusses the performance of each nozzle in detail and future considerations for reducing the maximum downwind DI. Additionally, this section discusses the limitations of the research outcomes for the nozzles and the drawbacks of implementing the technology on a full-scale exhaust stack, but in particular exhaust stacks for OCGT.

Figure 5.18 shows a summary of the results for the straight section nozzle, with qualitative similarities between the numerical results presented in Section 5.5 and the experimental results in Section 5.6. With the non-isothermal elevated JICF, the experimental and numerical work shows qualitative similarities for the sound radiation. Importantly, both the experimental and numerical work show that downwind of the exhaust stack, the straight section nozzle spatially broadens the acoustic lobe and reduces the maximum DI. In quantitative comparisons of the reduction in maximum downwind DI from the straight section nozzle for the numerical and experimental results, are 4.5 dB and 1.5 dB respectively for the same one-third octave band. The quantitative discrepancy could be from:

- the acoustic centre at the duct outlet, as the experimental and numerical results are different for the straight section nozzle,

- the thermal gradients for the plume downwind of the exhaust stack is over predicted as a result of modelling turbulence using the RANS model, discussed in Chapter 3,
- the band-averaged one-third octave results for the numerical case use five discrete tones for the average, but experimentally more frequencies are used for the band-averaged one-third octave results, and
- discrete spatial measurements for the experimental results misses the 'peak' observed downwind.

In summary, the experimental and numerical results for the straight section nozzle differ quantitatively, but qualitatively the results show a similar trend with the broadening of the acoustic lobe downwind of the exhaust stack and subsequently the reduction in maximum DI.

The results in Section 5.6.2 show that Nozzles 1 and 3 have similar reductions in the maximum DI downwind of the exhaust stack, where in some cases Nozzle 1 showed a more significant reduction, which was not expected when designing the nozzles. As discussed in Section 5.4, Nozzle 1 was designed to increase the duct length for the flow to exit at a higher height, whereas Nozzle 3 was designed to not only increase the height for the exhaust flow but to enhance the entrainment of the cooler fluid with the venturi. The entrainment of the cooler cross-flow would significantly reduce the temperature of the exiting jet, subsequently reducing the thermal gradients in the plume downwind of the exhaust stack. Since the speed of sound is proportional to the square root of temperature ($\Delta c \propto \sqrt{\Delta T}$), the reduction in thermal gradients should lead to a reduction in acoustic refraction downwind, but this was not observed in Section 5.6.2, with the acoustic results indicating a minimal reduction in the thermal gradient in the plume, when comparing Nozzles 1 and 3. During the experimental tests with Nozzle 3, it was identified that the nozzle was not impervious to flow and the venturi nozzle did not completely contain the hot exhaust flow. Hence, the nozzle did not perform as expected with the entrainment in the converging section. As discussed previously in this section, additional flow and temperature measurements downwind of the exhaust stack

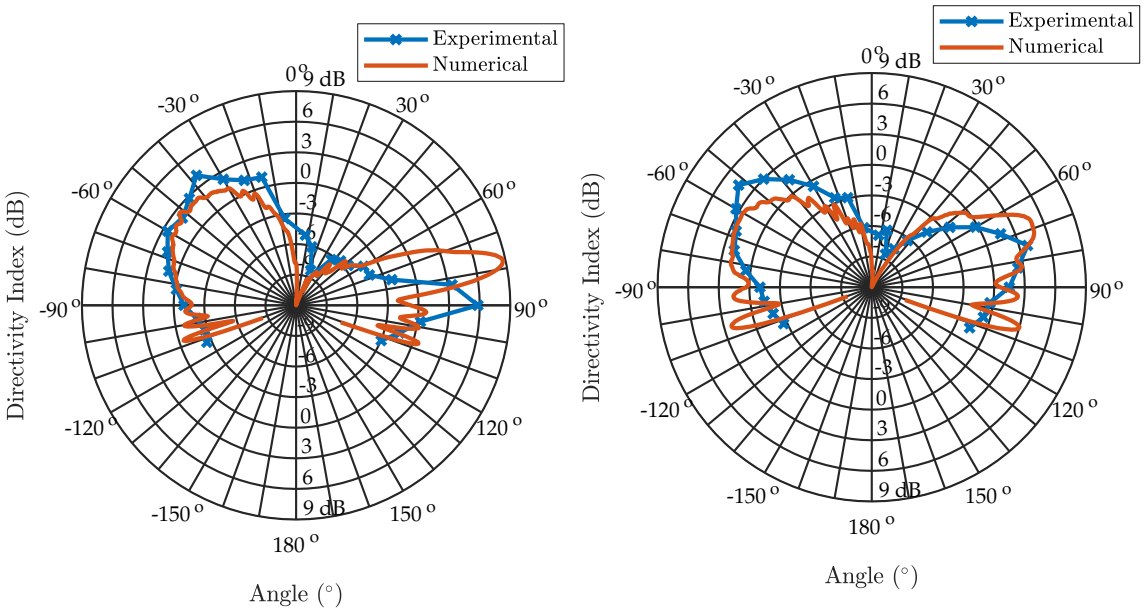

(a) No nozzle

(b) Acoustically transparent straight section nozzle

Figure 5.18: Comparing the numerical and experimental results for the band-averaged DI along the Y-Z plane (of symmetry) for sound propagation through a non-isothermal JICF for the case without a nozzle, and with a transparent section straight nozzle that is $4D$ long, with $R = 5$, $r = 28D$, the one-third octave bands of interest, $ka = 0.85$ ($f = 3.15\,\text{kHz}$), and $T_j = 500\,°\text{C}$. The cross-flow is from left to right. The results are saturated at $-12\,\text{dB}$.

would show deficiencies in the design for Nozzle 3 in enhancing the entrainment of the cooler cross-flow.

It should be pointed out that during the experimental study the maximum DI observed downwind of the exhaust stack without the nozzle was most likely not captured due to the discrete spatial measurements on the acoustic array. Hence, when comparing the cases with and without the nozzles, the reduction in the maximum DI observed in the acoustic lobe downwind of the exhaust stack could be underpredicted. Section 4.5 discusses the limitations of the experiments with a discrete number of microphones spaced at 7.5° apart on the array, which could lead to the underprediction of the maximum DI observed downwind in the acoustic lobe. It is expected that if a greater number of microphones in the array were used, the results in Section 5.6.2 would show better spatial fidelity, and therefore a

greater reduction in the maximum DI observed downwind of the exhaust stack with the nozzles.

It is important to note that the experimental results presented in Chapter 4 and Section 5.6.2 are constrained by the distance of the microphone array from the stack outlet. As discussed in Chapter 4, the experimental domain is limited by the size of the Thebarton Wind Tunnel, with a maximum radius for acoustic directivity of $r = 28D$. Ideally, the sound radiation at $r \gg 28D$ would be investigated to observe further the sound radiation from the nozzle, and the relationship with distance from the exhaust stack and the reduction in maximum DI. Alternatively, with the nozzle at the duct outlet and the propagation of sound further downwind of the exhaust stack ($r > 28D$), the reduction in sound levels may stop reducing in comparison with the case without a nozzle. Future tests would need to be completed at a different facility with a larger wind tunnel or outside to investigate sound radiation in the outer far-field ($r > 28D$).

In the experimental study, the non-dimensional scale, geometry and position of the nozzles were not investigated in depth due to the research being a preliminary study and the limited testing duration available at the Thebarton Wind tunnel. Firstly, the three nozzle geometries could be redesigned with different non-dimensional scales to explore how each design affects the fluid mechanics at the outlet of the exhaust stack and consequently the interaction of sound with the modified flow dynamics. In particular, the venturi nozzle could be redesigned with different diameters for the converging, straight, and diverging sections. Similar to the previous point, the vertical position of each nozzle could be shifted to change the fluid dynamics at the duct outlet, which is an essential parameter for the venturi nozzle. For the venturi nozzle, the vertical spacing between the nozzle and the duct outlet would affect the rate of entrainment of cooler ambient flow into the nozzle. Future work would involve a detailed analysis into varying the nozzle geometry and mounting position on the duct outlet, for the change in acoustic radiation.

An important consideration with the nozzles designed in this chapter is that the nozzles are impervious to bulk flow and attaching the nozzles at the duct outlet

extends the exhaust flow. The change in the flow and temperature downwind of the exhaust stack was not quantified. For a more in-depth analysis of the temperature and flow effects of attaching the nozzle onto the exhaust stack, and consequently altering the sound radiation, the temperature and flow should be measured as for the work completed in Chapter 4. By measuring the flow and temperature downwind of the exhaust stack with the nozzles, the fluid flow and temperature effects on the sound radiation can be quantified. Due to the limited time for testing at the Thebarton Wind Tunnel, an extensive experimental campaign for measuring the velocity and temperature downwind of the exhaust stack was not possible and should be completed in the future.

Although nozzles can be used for altering the fluid dynamics for the non-isothermal elevated JICF, and subsequently the sound radiation, little consideration was taken of the analysis of pressure drops or back pressure in the reduced-scale exhaust rig with the inclusion of nozzles. It is well known that any changes to the exhaust duct network would introduce a pressure drop and could be quantified with pressure measurements in the duct network at two locations, ideally one pressure measurement near the duct outlet and the other early in the duct network (close to the AIRPACK centrifugal blower). The pressure difference between the two pressure measurements quantifies the pressure drop in the duct network and any additional elements to the duct network would theoretically increase this pressure drop. For this reduced-scale exhaust experiment, the pressure drop was not an essential parameter to measure, but for real-scale OCGTs this would not be the case. Not only does the addition of the nozzle at the duct outlet introduce a pressure drop, but it can also lead to the increase back pressure acting on the turbines. The pressure drop could reduce the efficiency of the turbines in terms of power generation, or increase the load on the turbines. Therefore, the pressure drops in the duct network are an essential consideration when designing nozzles for noise mitigation.

For the reduced-scale exhaust rig, the nozzles were tested in a clean environment with the exhausting jet and cross-flow being air, but in practice the exhaust gas and environmental cross-flow conditions for real-scale OCGTs are different. Due to

the presence of impurities from combustion, the performance of the nozzles may degrade as the impurities settle on the interior wall of the nozzles. Additionally, debris from the cross-flow or other environmental factors could also affect the acoustic performance of the nozzle over time. Therefore, the long term acoustic performance of the nozzles installed on a real-scale exhaust stack would need to be considered.

The ideal case for noise mitigation based on the current nozzle design is a scenario where the sound is radiating in the absence of the jet and cross-flow, in a stationary isothermal field. The results for sound radiation in an isothermal stationary field have been investigated extensively in Chapter 4 and Section 5.6.1. In order to further mitigate the sound downwind of the exhaust stack, alternative methods would need to be considered. Some ideas include active noise control, acoustic absorption (acoustic liners or large baffles), injecting significantly cooler flow into the exhaust duct network, or redirection of the radiated sound.

5.8 Summary of noise mitigation

The sound radiation from an elevated JICF can be altered using varied nozzle designs at the duct outlet. The research to date investigates the feasibility of using nozzles for sound redirection, with walls that are acoustically transparent but impervious to bulk flow. The investigation in this chapter focused on the nozzles, which were explored both numerically with CFD and FEM, and experimentally with a reduced-scale exhaust rig in the Thebarton Wind Tunnel. Preliminary numerical work has been completed for a straight section nozzle to investigate the viability of altering the sound radiation path. The numerical simulations showed that reducing the hard reflective duct length by $4D$, with walls that are acoustically transparent and impervious to flow, changes the sound directivity downwind of the exhaust stack. The numerical results have shown that the acoustically transparent, flow impervious, nozzle changes the acoustic lobe observed downwind, with a spatial broadening of the acoustic lobe, leading to the reduction in maximum SPL magnitude.

Three nozzles have been designed and experimentally investigated, using a reduced-scale exhaust rig at the Thebarton Wind Tunnel. Initial testing has verified that the nozzles are acoustically transparent with the directivity plots for sound propagation through an isothermal stationary field being identical for the cases with and without the nozzles. All three nozzles have shown promising results for reducing the maximum downwind DI. The acoustic radiation for the reduced-scale exhaust rig with and without the nozzles can be summarised as:

- the three prototype nozzles alter the sound radiation downwind of the exhaust stack, with a spatial broadening of the acoustic lobe downwind,
- the spatial broadening of the acoustic lobe downwind of the exhaust stack reduces the maximum DI observed downwind,
- the reduction in maximum DI downwind of the exhaust with different nozzles was dependent on the centre-frequency of the one-third octave bands,
- the reduction in maximum DI downwind of the exhaust stack with different nozzles was dependent on R, with the increase in R shifting the acoustic lobe downwind towards the 0° axis, and
- each nozzle has shown different levels of sound reduction downwind of the exhaust stack, where Nozzles 1 and 3 are the most effective for different cases.

Therefore, it can be concluded that nozzles attached to exhaust stacks with sound radiating through a non-isothermal elevated JICF can reduce the maximum levels of sound observed downwind.

The investigation into the use of nozzles for reducing sound levels downwind of the exhaust stack was a preliminary study, and further work should be completed to expand the field of research. The limitations of the research at the Thebarton Wind Tunnel were highlighted in Section 5.7, as well as future considerations for the research. Moreover, due to the limited time, only a small set of nozzle geometries and mounting arrangements were investigated during this preliminary study. It

has also been noted that the research mainly focused on the sound radiation from a reduced-scale exhaust rig with sound propagating through a non-isothermal elevated JICF, but for real-scale exhaust stacks, such as exhaust stacks for 160 MW OCGT, other factors will need to be considered when increasing the scale of the technology. Nevertheless, three prototype nozzles have been shown in this preliminary study to reduce the maximum sound levels observed downwind for a non-isothermal elevated JICF.

Chapter 6

Conclusions

6.1 Summary of the findings

In this thesis, the complex sound radiation patterns resulting from sound propagating through a non-isothermal jet in cross-flow (JICF) was investigated. It was hypothesised, in Sections 1.2 and 2.6, that the hot exhaust plume alters the propagation path of the sound, leading to asymmetric acoustic radiation in the plane parallel to the incoming cross-flow free stream velocities. The results in Chapters 3 and 4, show asymmetric sound radiation patterns that were observed in both the numerical and experimental results, which strongly supports the hypothesis. Chapter 5 described results from numerical analyses and experimental tests that demonstrated the viability off attaching nozzles at the duct outlet to reduce the sound levels observed downwind of the exhaust stack and showed promising results. The key findings of this thesis are summarised below.

6.1.1 Numerical steady-state simulation for sound propagation through non-isothermal JICF

Chapter 3 explored the sound radiation propagating from a ground level JICF and elevated JICF. The phenomenon was investigated using a combination of CFD and acoustic FEM to understand the effects of the thermal and velocity gradients from

a ground level JICF and an elevated JICF on sound radiation. The numerical cases investigated were:

- sound propagation through a duct flanged at the outlet with a homogeneous isothermal stationary field at ambient temperature,
- sound propagation through a non-isothermal, ground level JICF,
- sound propagation through a duct protruding from a ground plane with an isothermal stationary field at ambient temperature, and
- sound propagation through non-isothermal elevated JICF.

The key acoustic features seen in the directivity results for the ground-level JICF and elevated JICF are summarised schematically with Figures 6.1 and 6.2, respectively. The acoustic features outlined are based on the acoustic directivity at $r = 32D$ and $ka = 0.8$. For the heated jet in cooler cross-flow cases presented in Figures 6.1c and 6.2b, the jet temperature and cross-flow momentum flux ratio were $T_j = 500\,°\text{C}$, and $R = 5$, respectively. The key findings from the numerical study are summarised below.

Section 3.3.2.1 presented the results for sound propagation through an isothermal field, with sound radiation from the exhaust duct with a plane at the outlet. The corresponding sound radiation pattern is shown in Figure 6.1a and resembles the sound radiation from the baffled piston. The sound radiation is axisymmetric with a single lobe forming along the duct centreline. The sound directivity from the 'baffled' exhaust duct was shown to be frequency dependent. This is to be expected as there are similarities to the well understood radiation from a point source in a plane baffle, and a point source at the end of a pipe in an infinite domain.

Section 3.3.2 investigated the effects of temperature and convection on the sound propagation through non-isothermal JICF for three cases: temperature effects only, convective effects only, and a combination of both the temperature and convective effects, with all cases showing asymmetric sound radiation. Figure 6.1b and 6.1c show the key acoustic features graphically for the acoustic directivity results.

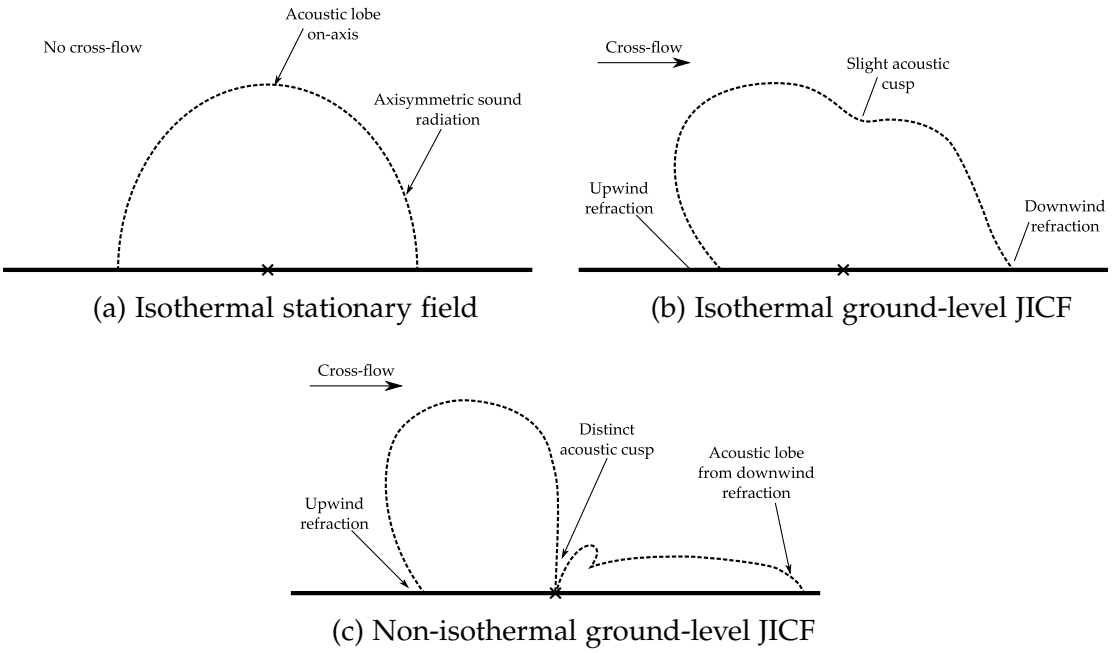

(a) Isothermal stationary field

(b) Isothermal ground-level JICF

(c) Non-isothermal ground-level JICF

Figure 6.1: Schematics of the numerical acoustic directivity results for three different cases; (a) sound propagation through an isothermal stationary field, (b) sound propagation through an isothermal ground-level JICF, and (c) sound propagation through a ground-level, heated jet with cooler cross-flow. The dash line is the acoustic radiation pattern. The cross-flow is from left to right.

The important findings from the numerical study for sound radiation through non-isothermal ground level JICF are:

- the temperature gradients from the plume cause refraction of sound downwind of the exhaust stack and the formation of an acoustic lobe,
- the concentration of sound, leading to an increase in sound downwind, is influenced by the jet temperature, acoustic frequency and cross-flow velocity,
- the convective effects cause further sound refraction downwind, with the acoustic lobe shifting towards ground-level,
- the sound directivity in the far-field is dependent on the radial distance from the stack, with the DI levels increasing for the downwind acoustic lobe with increasing distance,

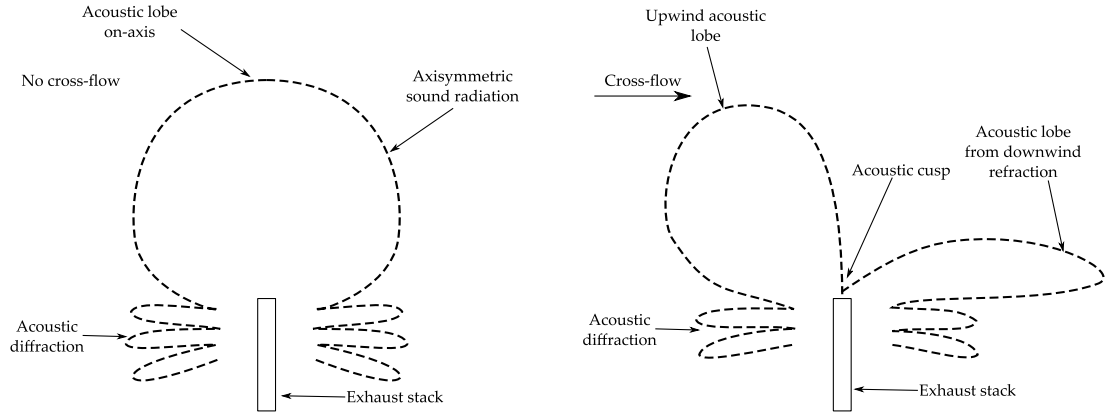

(a) Isothermal stationary field (b) Non-isothermal elevated JICF

Figure 6.2: Schematics of the numerical acoustic directivity results for two different cases; (a) sound propagation through an exhaust stack in an isothermal stationary field, and (b) sound propagation through an elevated, heated jet with cooler cross-flow. The dash line is the acoustic radiation pattern. The cross-flow is from left to right. The base plane is acoustically absorptive with $\alpha_s = 1$

- the sound directivity is related to the non-dimensional frequency, ka, and shows an increase in the magnitude of the downwind acoustic lobe, increasing with acoustic frequency,
- the 3-D representation of the acoustic radiation at a radius of $r = 32D$ shows complex non-axisymmetric sound radiation, and
- the position of the acoustic lobe downwind is dependent on the cross-flow ratio (R), with the increase in R shifting the acoustic lobe higher above the ground level and towards the duct centreline.

Consequently, of all scenarios investigated in the numerical simulations, the case with the highest cross-flow ($R = 5$), highest jet temperature ($T_j = 500\,°C$) at the highest frequency ($ka = 0.8$) and the furthest distance from the exhaust stack ($r = 32D$), exhibited the largest downstream SPLs.

The numerical work for sound propagation through the ground level JICF was extended for sound propagation through an elevated JICF, with the results presented in Section 3.3.3. The inclusion of the duct changed the sound radiation

in an isothermal stationary field, with the complexity of the sound radiation increasing with different boundary conditions along the ground surface. When the ground surface is a hard reflective boundary condition, then duct outlet edge diffraction and reflections off the ground surface dominated the sound radiation. Replacing the ground with an anechoic boundary condition simplified the sound radiation pattern, and showed a distinct acoustic lobe forming along the duct centreline, with a toroidal sound radiation pattern.

The sound field of the elevated JICF showed similar trends to the ground level JICF, as well as several unique features. Common to both cases, the thermal and velocity gradients from the ground level and elevated JICF plumes lead to the refraction of sound and asymmetric sound radiation. The key features observed in the acoustic results are a broad lobe resembling elliptical spreading upwind, a cusp along the duct centreline, and downwind a lobe with an increase in sound level. The sound directivity for the ground level JICF and the elevated JICF, show a dependency with the distance from the duct outlet (r), and the acoustic frequency (ka). The main difference in sound directivity between the ground level and elevated JICF was the position of the acoustic lobe downwind of the exhaust stack, with the elevated stack increasing the height of the downwind acoustic lobe. The increase in the vertical height for the downwind acoustic lobe necessitates investigation of the distance required for the refracted sound to strike the ground.

Another important observation from the numerical results for sound propagation through the non-isothermal elevated JICF was the presence of numerical artefacts. The acoustic results show ripples in the contour plots of the sound level and these become more pronounced as the frequency and distance from the exhaust stack increases. By band-averaging over one-third octaves using five discrete frequencies, the results showed a significant reduction in the ripples and numerical artefacts. With the reduction in the ripples, the key acoustic features are more pronounced, with a clear acoustic lobe observed downwind. Furthermore, 3-D directivity radiation patterns show that below the duct outlet there are apparent, coherent acoustic features that appear to be either edge diffraction from the duct outlet, or reflections from the sidewalls of the exhaust stack. In summary, the

one-third octave sound directivity results show the key acoustic features from the sound interacting more clearly with the non-isothermal elevated JICF.

6.1.2 Experimental results for sound propagation through non-isothermal JICF

In Chapter 4, the sound field measured experimentally from the scale-model, elevated JICF was complex and showed qualitative similarities with the numerical results in Chapter 3. The research employed a purpose-built reduced-scale exhaust rig for investigating the sound radiation through non-isothermal elevated JICF, with non-dimensional parameters similar to the exhaust flow observed from a 160 MW OCGT. The flow and temperature results from testing the non-isothermal elevated JICF in a wind tunnel were presented in Section 4.3. The validation tests were conducted by examining the sound radiation in an anechoic chamber and were shown in Appendix D. The results validated the acoustic acquisition in a controlled environment, absent of hard reflections. Acoustic testing was conducted at the Thebarton Wind Tunnel with the following results presented in this thesis:

- sound radiation in the absence of the JICF (the isothermal stationary field),
- sound radiation in the presence of the non-isothermal jet without cross-flow,
- sound radiation in the presence of a non-isothermal JICF at a single cross-flow ratio, $R = 5$, and varying jet temperature, $T_j = [27\,°C, 100\,°C, 300\,°C, 500\,°C]$, and
- sensitivity of sound radiation to cross-flow sensitivity study, with $R = [5, 7.5, 10, 12.5]$.

The key acoustic features from the experimental campaign can be summarised using the directivity plots in Figure 6.3.

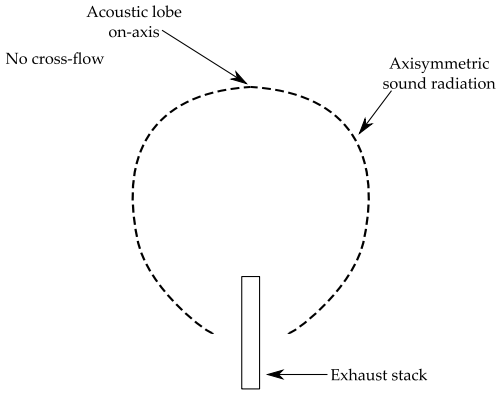

(a) Isothermal stationary field

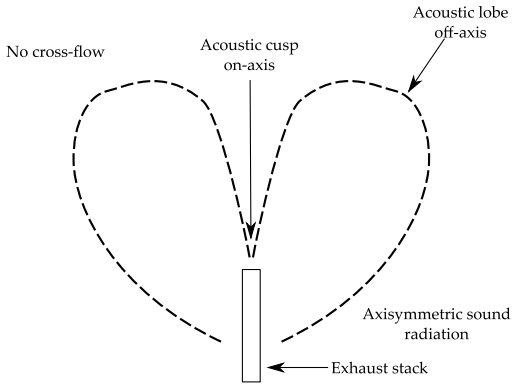

(b) Non-isothermal heated jet

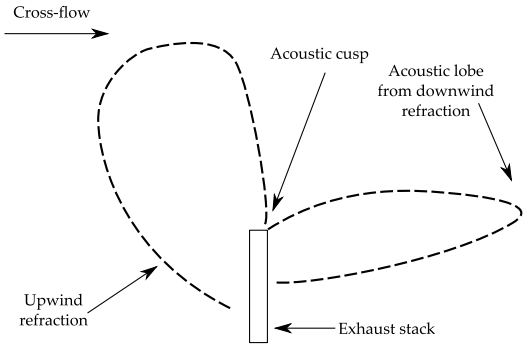

(c) Non-isothermal elevated JICF

Figure 6.3: Schematics of the experimental acoustic directivity results for three different cases; (a) sound propagation through an isothermal stationary field, (b) sound propagation through a non-isothermal, heated jet, and (c) sound propagation through an elevated, heated jet with cooler cross-flow. The dash line is the acoustic radiation pattern. The cross-flow is from left to right.

6.1.2.1 Experimental flow and temperature results for the non-isothermal elevated JICF

For the reduced-scale non-isothermal elevated JICF, the flow and temperature results show key features, which have also been observed in the literature [1, 5, 6, 90], namely:

- upwind of the exhaust stack, the cross-flow free-stream velocity was uniform and showed that a boundary layer formed along the ground surface,
- the incoming cross-flow turbulence intensity from the wind tunnel was approximately 1%,
- the temperature and velocity results show the presence of the deflected jet and the plume downwind of the exhaust stack,
- as the distance from the exhaust stack increases, the velocity gradient downstream reduces,
- the temperature gradients downwind of the exhaust stack show a similar trend to the velocity gradients,
- the height of the plume increases as the plume propagates downwind,
- the turbulence intensity shows the position of the plume and wake structure behind the exhaust stack clearly,
- the temperature, velocity and turbulence intensity results clearly show the counter-rotating vortex pairs of finite width,
- the temperature gradients with increasing distance downwind show an increase in the height of the plume, a reduction in the magnitude, with the entrainment of the cooler cross-flow, and the plume spreading spatially.

Hence, it can be concluded that the temperature and velocity results show key features that would affect the sound radiation, and in particular, govern the refraction of sound downwind of the exhaust stack.

6.1.2.2 Experimental acoustic results for sound propagation through the non-isothermal elevated JICF

Stationary field

The experimental results for the sound radiation in an isothermal stationary field at ambient temperature are presented in Section 4.4.1, and exhibit similar results to published work by Bies et al. [25]. Figure 6.3a summarises the key acoustic features seen in the directivity plots. The sound radiation of the exhaust duct in the anechoic environment exhibited a single axisymmetric acoustic lobe aligned with the axis of the duct. The acoustic directivity results show similar trends to those detailed in the literature [25]. It is important to note that the sound radiation pattern differs from the common monopole assumption. Comparing the results by Bies et al. [25] there were slight discrepancies in the sound directivity results, which could be from the acoustic modal response of the sound exiting the duct ($ka > 1$), the imperfections in the duct network, reflections from the array or other surfaces in the Thebarton Wind Tunnel, and the experimental accuracy of the microphones, which were ± 0.5 dB.

Jet with no cross-flow

Section 4.4.2 presented the results for sound propagation in the presence of a heated exhaust jet. The key acoustic features are summarised in Figure 6.3b. As expected, the thermal and velocity gradients along the jet shear layer caused the sound to refract, with the band-averaged sound directivity results displaying axisymmetric sound radiation with acoustic lobes forming off-axis, and an acoustic cusp forming along the duct centreline. The increase in the off-axis sound lobes and the presence of the acoustic cusp along the duct centreline are qualitatively similar to the work in Atvars et al. [15]. This finding was investigated with the band-averaged sound directivity for four one-third octave bands, with all four showing consistent results. Therefore, the sound directivity for sound propagation through a non-isothermal jet exhibits similarities to the literature and the presence of acoustic refraction from the jet shear layer.

It is important to note the sound directivity from a heated exhaust jet is axisymmetric, but differs drastically from the common monopole assumption used

for estimating the sound radiating from OCGT exhaust stacks. There is a reduction in the sound levels along the duct centreline, which is contrary to the uniform sound distribution with the monopole assumption and different from the acoustic lobe seen on-axis in Section 4.4.1. The highest levels of sound are observed off-axis as a result of the acoustic refraction from the jet shear layer, with an increase in DI of approximately 4.5 dB. Hence, the exiting jet flow must be considered for OCGT exhaust stacks when measuring the sound in the far-field. Additionally, multiple measurements in numerous locations, not just the near-field as per ISO 10494:1993 [87], should be taken in order to quantify the sound directivity and power from exhaust stacks with hot exhaust flows.

Jet in cross-flow

A research gap outlined from the literature review was the lack of understanding of the sound propagation through non-isothermal elevated JICF with varying conditions, and Chapter 4.4.3 explained the results. The introduction of the cross-flow was investigated for a non-isothermal JICF with $R = 5$ and $T_j = 500\,°C$, and the key acoustic features are summarised graphically in Figure 6.3c. Upstream of the duct outlet, the sound radiation for a hot jet with or without cross-flow are similar. Along the duct centreline, there is an acoustic cusp formed from the acoustic refraction. However downwind, the sound has been refracted by the deflected plume to concentrate the sound into a narrower acoustic lobe. Additionally, the position of the acoustic lobe on the leeward side of the duct has moved towards the ground level. The position of the lobe, magnitude of the lobe, and the spatial width of the lobe is also dependent on the one-third octave band frequency. At the highest centre-frequency (6.3 kHz, $ka = 1.70$) that was investigated, the sound directivity exhibited a narrow lobe and the largest increase in sound (13 dB) when compared with the case for sound propagation through a duct in an isothermal stationary field at ambient temperature.

As expected from the numerical results in Section 3.3.3.2, the acoustic results are position dependent, and this was observed in Section 4.4.3. Figure 6.4a schematically represents the directivity plot with two different radial distances from the duct outlet, r, while $T_j = 500\,°C$ and $R = 5$. Even though the experimental campaign

investigated two directivity radii (r = [14D, 28D]), the results show that the angle and geometry of the downwind acoustic lobe are dependent on the distance from the duct outlet. The increase in distance from the duct outlet shifts the downwind acoustic lobe towards the ground level, which is consistent with the numerical results observed in Section 3.3.3.2. It should be noted that for OCGT exhaust stacks with cooler cross-winds, there are limited studies in the literature investigating the effect of distance from the exhaust stack on the acoustic measurement from the exhaust stack. The experimental and numerical acoustic results contribute to the new understanding that for a heated exhaust jet with cooler cross-flow, the acoustic radiation pattern alters significantly with distance from the exhaust stack.

The change in jet temperature was also investigated in Chapter 4.4.3, where the results showed a significant impact on the sound directivity downwind of the exhaust stack. Figure 6.4b graphically summarises the effects of jet temperature on sound directivity, whereby an increase in jet temperature leads to a change in the acoustic radiation, from approximately spherical to non-axisymmetric sound radiation. The increase in jet temperature showed the prominence of the sound refraction, with the acoustic lobe being spatially narrowed and an increase in sound levels downwind. For the research in this thesis, the scenario with the most significant increase in sound level observed downwind was when T_j = 500 °C. For OCGT, the exhaust jet temperature ranges from T_j = 500 °C to 650 °C, and therefore the sound directivity results are a precursor of the acoustic results in the far-field for real OCGT exhaust stacks with cooler cross-flows.

The sensitivity of sound directivity to the cross-flow ratio was investigated in this thesis, with the results explained in Chapters 3 and 4.4.4. The literature review described in Chapter 2, identified that the cross-flow ratio influences the trajectory and fluid dynamics of the plume. Figure 6.4c summarises the effect of cross-flow ratio, R, on the sound directivity downwind of the exhaust stack. The increase in cross-flow ratio changes the sound directivity downwind of the exhaust stack, with the angular position of the acoustic lobe increasing in height above the ground level. The variability in the trajectory of the plume with the change in the cross-flow ratio would also cause the sound in the lobe downwind to oscillate and, in some cases,

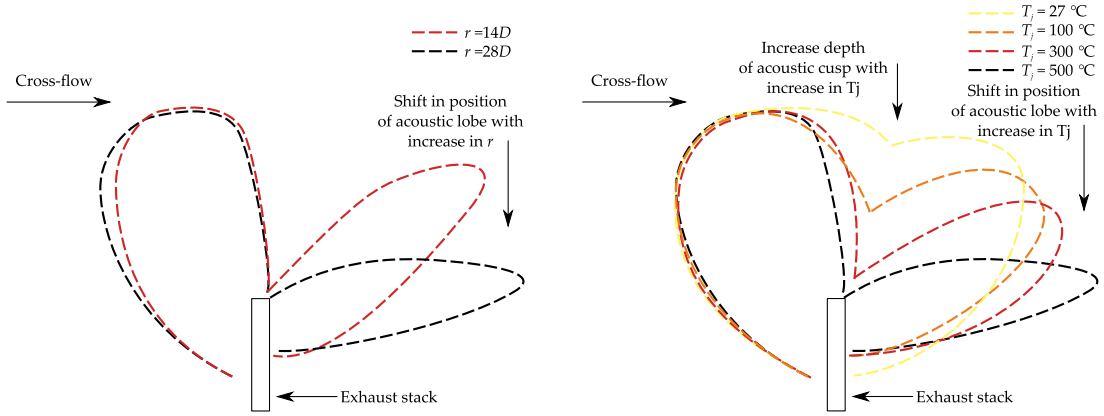

(a) Directivity as a function of r

(b) Directivity as a function of T_j

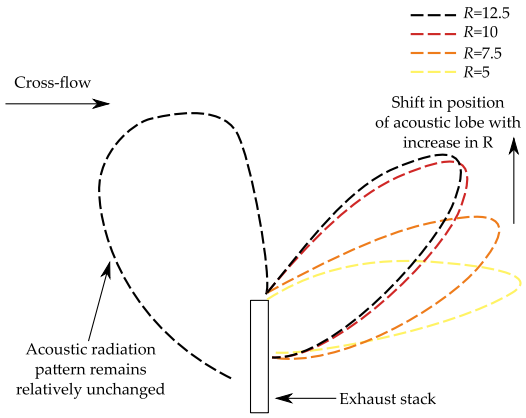

(c) Directivity as a function of R

Figure 6.4: Schematics of the experimental acoustic directivity results for varying parameters; (a) the distance from the duct outlet, r, (b) the jet temperature, T_j, and (c) the jet to cross-flow momentum flow ratio, R. The dash line is the acoustic radiation pattern. The cross-flow is from left to right.

causes a 'modulation' in the sound observed downwind, which has been observed by acoustic consultants in the field. The acoustic results in Section 4.4.4 indicate that for OCGT exhaust stacks the variation in the meteorological conditions would affect the sound observed downwind in the far-field. Therefore, the cross-wind conditions are critical in predicting the sound levels downwind of the exhaust stacks for OCGT.

6.1.3 Downwind sound reduction with prototype nozzles

It was shown in Chapter 5 that attaching a nozzle to the duct is a viable method for reducing the maximum sound observed downwind of the exhaust. The numerical work in Section 5.5 and experimental work in Section 5.6 investigated replacing portions of the rigid-walled duct with acoustically transparent duct lengths that are impervious to the mean flow. From the numerical simulation results presented in Section 5.5, and the experimental test results presented in Section 5.6, there are qualitative similarities for the band-averaged sound directivity downwind of the exhaust stack. With the band-averaged directivity results, the straight section nozzle (Nozzle 1) changed the acoustic radiation pattern downwind of the exhaust stack by broadening the acoustic lobe and thereby reducing the maximum DI observed in the acoustic lobe.

Two other nozzles geometries were assessed for the reduction in maximum sound observed downwind, as seen in Figure 5.2. All three nozzles were experimentally tested at the Thebarton Wind Tunnel, with the acoustic results presented as band-averaged sound directivity plots in Section 5.6. The nozzles caused a change in the sound directivity downwind of the exhaust stack when compared with the case without a nozzle. The nozzles cause spatial broadening of the acoustic lobe and reduce the maximum sound observed downwind. There were slight differences in the reductions of maximum sound observed downwind, with the straight section nozzle (Nozzle 1) and venturi section nozzle (Nozzle 3) showing the best performance, conditionally.

The sound directivity with and without the nozzles was further analysed with varying cross-flow ratios (R) and various one-third octave bands. The results for the reduction in maximum sound downwind with the nozzles were summarised in Tables 5.1, 5.2, and 5.3. The band-averaged sound directivity results show that the one-third octave bands with centre frequency $ka = 1.70$ (6.3 kHz) exhibit the most considerable reductions in the maximum downwind sound. Additionally, the sound directivity results for Nozzles 1 and 3 with $R = [5, 7.5]$ show similar performance for the reduction in the maximum sound downwind. However, for the case with $R = 10$, Nozzle 3 shows the largest reductions in the maximum sound

downwind. Each nozzle causes a unique level of sound reduction for different cross-flow ratios and one-third octave bands. It can be concluded that nozzles at the duct outlet can reduce the maximum sound observed downwind of the exhaust stack.

The concept of nozzles at the duct outlet reducing the downwind noise levels showed promising results for the reduced-scale purpose-built exhaust stack. This noise mitigation concept should be further explored for application to OCGT exhaust stacks to reduce noise for nearby communities.

6.2 Future work

This section discusses the time frame limitations faced whilst undertaking the research presented in this thesis, as well as the future work that can be conducted in this field of research to extend the work of the thesis. The discussion on future work can be separated into the following topics:

- numerical sound propagation through ground level JICF,
- numerical sound propagation through elevated JICF,
- experimental sound propagation through non-isothermal elevated JICF, and
- noise mitigation downwind with nozzles.

6.2.1 Ground level jet in cross-flow

This section discusses recommendations for further investigating numerical sound propagation through ground level JICF in Chapter 3.

Due to the technical limitations for the numerical work, the computational domain was at the limit practical for the software and the super-computing infrastructure available for this project. The acoustic results were presented for $r \leq 32D$ and show complex acoustic features. Nevertheless, the aim of measuring the sound at radii greater than $32D$ is to closely resemble the sound propagating towards communities near OCGT, which are in the order of $100D - 500D$ (600 m to 3000 m

in real life) away from the exhaust stack. Different acoustic phenomena may occur during sound radiation at these distances, which may include further acoustic refraction downwind or dissipation of the plume, which may then cease the acoustic refraction after a certain distance from the exhaust stack.

The number of mesh nodes for the acoustic FEM computational domain was limited by the computational resources available and, with advancements in technology, an increase in the number of mesh nodes would enable the investigation of sound radiation at frequencies higher than $ka = 0.8$. The analyses were conducted at $ka < 0.8$, but it would be interesting to inspect the effects of the plume with sound at a frequency of $ka > 0.8$. The research only conducted numerical simulations for two cross-flow ratios, but additional cross-flow ratios should be investigated. Altering the jet to cross-flow momentum flux ratio would provide an insight into the variability of the lobe downwind. Additionally, frequencies could have also been analysed to obtain more accurate one-third octave band averaged levels, which would reduce the numerical artefacts.

6.2.2 Elevated jet in cross-flow numerical modelling

The numerical simulations showed in Chapter 3 that the ground level JICF and elevated JICF exhibit similar limitations with their modelling methodology and results, leading to similar recommendations for future work. The inclusion of an exhaust stack protruding from ground level introduces complexities with the acoustic results but the majority of the key features are common in the sound directivity between the ground level JICF and elevated JICF. However, the sound directivity for elevated JICF showed unique features that can be explored further in future work.

The numerical mesh for the ground level JICF and elevated JICF are different for the acoustic FEM simulations, which slightly alter the acoustic results. The ground level JICF uses a combination of a highly symmetric, structured mesh and unstructured mesh. The region of structured numerical mesh for the ground level JICF was for the duct, spherical region of interest ($r \leq 32D$), and in the PML. For the buffer region between the last spherical surface and the PML, an

unstructured mesh was implemented for the acoustic FEM. Improvements in the acoustic results for the elevated JICF can be achieved for the numerical mesh by using a combination of structured and unstructured hexahedra elements for the acoustic FEM simulations, in particular for the duct and in the domain near the duct outlet. Increasing the mesh density for the elevated JICF with structured hexahedra elements should reduce the ripples from the numerical artefacts and increase the axisymmetric acoustic results for the sound propagation through an isothermal stationary field.

Similar to the ground level JICF, the computational resources available for this project limited the size of the computational domain for the elevated JICF and the highest ka value for sufficient resolution of the acoustic results. As discussed in the previous section, the acoustic results were presented for $r \leq 32D$, and showed salient acoustic features for asymmetric sound radiation. Nevertheless, the aim is to measure sound at radii in the order of $100D - 500D$ (600 m to 3000 m in real life) away from the exhaust stack to reveal far-field acoustic features downwind. With an advancement or increase in computational resources, simulations with a higher number of mesh elements would allow for the investigation of sound radiation at $ka > 0.8$. The research concentrated on $ka < 0.8$, but it would be interesting to inspect the effects of the hot exhaust plume with sound at a $ka > 0.8$. The research conducted numerical simulations for a single cross-flow ratio, but additional cross-flow ratios should be investigated for the elevated JICF case.

Using the experimental results obtained in Chapter 4 for the fluid dynamics and acoustics, the results could be reproduced in numerical simulations to gain a better understanding of the propagation path of sound. The velocity and temperature at each node for the elevated JICF were mapped from CFD simulations, and the results could be modelled more closely with the experimental results obtained in this thesis to investigate the mechanisms that affect sound refraction downwind. By using temperature and velocity results more closely resembling the experimental measurements, a closer comparison between the numerical and experimental sound directivity can be made to show the quantitative similarities between the two scenarios. A more realistic representation of the numerical results would

improve the reliability of the acoustic results in the regions not verifiable with experimental measurements.

Additionally, an alternative method for modelling the acoustic interaction between the plume and the sound would be to model the transient scale resolving simulation in CFD. Scale resolving simulations would resolve the transient vertical and span-wise flapping motions of the plume. The flapping motion of the plume would change the propagation path of sound, hence the variability in the sound experienced at the ground level.

6.2.3 Experimental sound propagation through non-isothermal elevated JICF

The experimental results presented in Chapter 4 showed an important original contribution to the understanding of sound propagation through non-isothermal elevated JICF. However, the experiments can be further expanded to provide more detailed results or find new features related to the problem. The discussion in this section highlights recommended future work to improve the understanding of sound propagation through non-isothermal elevated JICF.

The experimental results in Chapter 4 on flow and temperature distribution provide insights into the sound radiation from a non-isothermal elevated JICF. However, the experiments were constrained by time frame limitations and the size of the wind tunnel. The current results from the flow and temperature measurements show features as seen in the literature. To further confirm the presence of the counter-rotating vortex pairs with the finite spatial width and changes in the height of the plume, additional flow and temperature measurements should be conducted. Moreover, the previously published literature [1, 5, 6, 90] suggests that the plume downwind of the exhaust stack would dissipate in the far-field, outside of the current experimental domain. In order to quantify the extent of the thermal and velocity gradients of the plume downwind, experiments should be conducted in a larger wind tunnel or possibly outside. It is hypothesised that the sound would further refract for $r > 28D$, with the presence of the thermal and velocity gradients from the hot exhaust plume.

Furthermore, for a more accurate representation of sound propagation from OCGT exhaust stacks, an atmospheric boundary layer, rather than uniform velocity profiles should be utilised for the incoming cross-flow, by accurately replicating the wind velocity profile and the turbulence intensity profiles recorded in the literature. By altering the wind velocity profiles and the turbulence intensities, the plume would develop differently but, in particular, the turbulence intensity would change the dissipation rate of the plume.

A limitation for the acoustic measurements was the discrete number of microphones on the array. The acoustic directivity measurements use a finite number of microphones to achieve an angular resolution of 7.5°. The angular resolution for the experimentally measured sound directivity showed a lack of detail in resolving the downwind acoustic lobe. The sound directivity analysed using band-average one-twelfth octave bands provided more detail about the acoustic lobe in between the microphone locations. The band-averaged sound directivity results showed that for the current angular resolutions with the microphone array, more detail of the maximum sound downwind can be revealed using one-twelfth octave results. However, better results would be obtained by using a microphone array with a finer spatial resolution, which would help to resolve the maximum sound levels observed downwind.

For future experimental studies, the use of a larger wind tunnel for acoustic measurements would be desirable to investigate the sound directivity at array radii greater than $28D$. The purpose of measuring the sound at radii greater than $28D$ is to resemble the real-life situation of sound propagating towards communities near OCGT, which are in the order of $100D - 500D$ away from the exhaust stack. Different acoustic phenomena may occur during the sound radiation at these distances that are yet to be explored.

6.2.4 Noise mitigation

Chapter 5 described the results of using prototype nozzles to reduce sound levels downwind. However, there were limitations with this study and recommendations

for future work were outlined in Section 5.7. The following paragraphs reiterate the discussion in Section 5.7 and propose future work.

The preliminary measurements with the nozzles were conducted in a controlled experimental environment with a reduced-scale, non-isothermal elevated JICF in the wind tunnel. The purpose of the research is to develop solutions that address challenges with real-life open cycle gas turbines. Hence, a full-scale nozzle needs to be manufactured and commissioned on a real open cycle gas turbine. Its acoustic performance needs to be measured over extended periods, under various meterological and operating conditions, with field measurements for validation of the results presented in this thesis.

As discussed in the previous section, the sound directivity measurements for the reduced-scale exhaust rig at the Thebarton Wind Tunnel were limited by the size of the test section. The experimental measurements could only be conducted up to a radius of $r = 28D$, with the reduction in maximum sound observed downwind only quantified for this constrained distance. Hence, future research needs to be undertaken at a larger wind tunnel to investigate the sound directivity with prototype nozzles at distances greater than $r > 28D$.

The geometry for the nozzles investigated for this thesis was limited to three designs, due to this research being a preliminary study and the limited availability of the Thebarton Wind Tunnel. Continuation of the existing research would expand on the three existing nozzle geometries and the impact they have on altering the far-field sound directivity. Furthermore, the existing test setup with current nozzles could be further analysed with different mounting positions, as the height of the nozzles at the duct outlet can be shifted vertically along the exhaust duct.

The proposed noise control device was a nozzle that is attached at the duct outlet, where the walls of the nozzle are acoustically transparent yet impervious to mean flow. These conditions could be verified with flow and temperature measurements. All the nozzles were validated experimentally for acoustical transparency, achieving the same sound directivity. The acoustic results with the nozzles fitted to the heated jet show a change in the sound directivity, which is believed to be a change in the flow and temperature of the plume downwind. In order to

determine the change in velocity and temperature downwind of the exhaust stack when a nozzle is attached to the duct outlet, an extensive testing campaign for flow and temperature measurements would need to be undertaken. Therefore, flow and temperature measurements could reveal the mechanisms behind the sound propagation caused by the nozzles and confirm that the nozzles are altering the thermal and velocity gradients from the plume downwind of the exhaust stack.

The acoustic results for Nozzle 3 were expected to show the most reduction in the maximum sound downwind. However, the experimental results showed that this did not occur. During testing, it was noted that Nozzle 3 was not impervious to bulk flow, and it did not constrain the flow within the test section. As discussed previously, the flow and temperature field with the nozzles present should be measured to quantify if they are impervious to flow. If it is proven that Nozzle 3, or any other nozzle, were not impervious to flow, then the nozzle would be shrouded with an additional layer of finer stainless steel mesh.

This thesis has contributed to a better understanding of sound refraction from an elevated JICF, and proposed a noise mitigation concept to reduce noise downstream.

References

[1] M.S. Adaramola, D. Sumner, and D.J. Bergstrom. "Effect of velocity ratio on the streamwise vortex structures in the wake of a stack". In: *Journal of Fluids and Structures* 26.1 (2010), pp. 1–18. DOI: 10.1016/j.jfluidstructs.2009.07.007. URL: http://dx.doi.org/10.1016/j.jfluidstructs.2009.07.007.

[2] A. Agarwal and P. J. Morris. "Calculation of sound propagation in nonuniform flows: Suppresion of instability waves". In: *American Institute of Aeronautics and Astronautics Journal* 42.1 (Jan. 2004), pp. 80–88. DOI: 10.2514/1.619. URL: https://doi.org/10.2514/1.619.

[3] R.K. Amiet. "Refraction of sound by a shear layer". In: *Journal of Sound and Vibration* 58.4 (1978), pp. 467–482. ISSN: 0022-460X. DOI: 10.1016/0022-460x(78)90353-x. URL: http://dx.doi.org/10.1016/0022-460X(78)90353-X.

[4] J. Andreopoulos. "On the structure of jets in a crossflow". In: *Journal of Fluid Mechanics* 157 (1985), pp. 163–197. ISSN: 1469-7645. DOI: 10.1017/S0022112085002348. URL: http://dx.doi.org/10.1017/S0022112085002348.

[5] J. Andreopoulos. "Wind tunnel experiments on cooling tower plumes: Part 1—in uniform crossflow". In: *Journal of Heat Transfer* 111.4 (1989), pp. 941–948. ISSN: 0022-1481. DOI: 10.1115/1.3250809. URL: http://dx.doi.org/10.1115/1.3250809.

[6] J. Andreopoulos. "Wind tunnel experiments on cooling tower plumes: Part 2—in a nonuniform crossflow of boundary layer type". In: *Journal of Heat Transfer* 111.4 (1989). 10.1115/1.3250810, pp. 949–955. ISSN: 0022-1481. DOI: 10.1115/1.3250810. URL: http://dx.doi.org/10.1115/1.3250810.

[7] J. Andreopoulos and W. Rodi. "Experimental investigation of jets in a crossflow". In: *Journal of Fluid Mechanics* 138.-1 (1984), pp. 93–127. ISSN: 1469-7645. DOI: 10.1017/s0022112084000057. URL: http://dx.doi.org/10.1017/s0022112084000057.

[8] ANSYS. *ANSYS Mechanical APDL Acoustic Analysis Guide*. 18.0. ANSYS, Inc. 2600 ANSYS Drive, Canonsburg, PA 15317, Jan. 2017.

[9] ANSYS. *ANSYS Mechanical APDL Theory Reference*. 18.0. ANSYS, Inc. 2600 ANSYS Drive, Canonsburg, PA 15317, Jan. 2017.

[10] D.F.J. Arago. "Resultats des experiences faites en 1822, par ordre du Bureau des Longitudes, por la determination de la vitesse du son dans l'atmosphere". In: *Annales de Chimie et de Physique* 20 (1822), p. 210.

[11] R. J. Astley and W. Eversman. "Wave envelope elements for acoustical radiation in inhomogeneous media". In: *Computers and structures* 30.4 (1988). Special Issue: Computational Engineering Mechanics, pp. 801–810. ISSN: 0045-7949. DOI: https://doi.org/10.1016/0045-7949(88)90108-3. URL: http://www.sciencedirect.com/science/article/pii/0045794988901083.

[12] K. Attenborough. "Sound propagation close to the ground". In: *Annual Review of Fluid Mechanics* 34.1 (2002), pp. 51–82. DOI: 10.1146/annurev.fluid.34.081701.143541. eprint: https://doi.org/10.1146/annurev.fluid.34.081701.143541. URL: https://doi.org/10.1146/annurev.fluid.34.081701.143541.

[13] K. Attenborough, S. Taherzadeh, H.E. Bass, X. Di, R. Raspet, G.R. Becker, A. Güdesen, A. Chrestman, G.A. Daigle, and A. L'Espérance. "Benchmark cases for outdoor sound propagation models". In: *The Journal of the Acoustical Society of America* 97.1 (1995), pp. 173–191. DOI: 10.1121/1.412302. URL: http://dx.doi.org/10.1121/1.412302.

[14] J. Atvars, L.K. Schubert, E. Grande, and H.S. Ribner. *Refraction of sound by jet flow or jet temperature*. Book. University of Toronto: Institute for Aerospace Studies, 1965.

[15] J. Atvars, L.K. Schubert, and H.S. Ribner. "Refraction of sound from a point source placed in an air jet". In: *The Journal of the Acoustical Society of America* 37.1 (1965), pp. 168–170. ISSN: 0001-4966. DOI: 10.1121/1.1909297. URL: http://dx.doi.org/10.1121/1.1909297.

[16] R. Baccouche, M. Ben Tahar, and S. Moreau. "Perfectly Matched Layer for Galbrun's aeroacoustic equation in a cylindrical coordinates system with an axial and a swirling steady mean flow". In: *Journal of Sound and Vibration* 378 (2016), pp. 124–143. ISSN: 0022-460X. DOI: https://doi.org/10.1016/j.jsv.2016.05.024. URL: http://www.sciencedirect.com/science/article/pii/S0022460X16301572.

[17] S. Bagheri, P. Schlatter, P.J. Schmid, and D.S. Henningson. "Global stability of a jet in crossflow". In: *Journal of Fluid Mechanics* 624 (2009), pp. 33–44. ISSN: 1469-7645. DOI: 10.1017/s0022112009006053. URL: https://doi.org/10.1017/S0022112009006053.

[18] C. Bailly and D. Juve. "Numerical solution of acoustic propagation problems using linearized euler equations". In: *American Institute of Aeronautics and Astronautics Journal* 38.1 (2000), pp. 22–29. DOI: https://doi.org/10.2514/2.949. URL: https://doi.org/10.2514/2.949.

[19] E.H. Barton. "On the refraction of sound by wind". In: *The London, Edinburgh, and Dublin Philosophical Magazine and Journal of Science* 1.1 (1901), pp. 159–165. DOI: 10.1080/14786440109462599. URL: http://dx.doi.org/10.1080/14786440109462599.

[20] Klaus-Jürgen Bathe. *Finite element procedures*. Klaus-Jurgen Bathe, 2006.

[21] A. Bayliss and L. Maestrello. "On the interaction of a sound pulse with the shear layer of an axisymmetric jet, II: Heated jets". In: *Journal of Sound and Vibration* 86.3 (1983), pp. 395–409. ISSN: 0022-460X. DOI: 10.1016/0022-

460X(83)90584-9. URL: http://dx.doi.org/10.1016/0022-460X(83)90584-9.

[22] J.S. Bendat and A.G. Piersol. *Engineering applications of correlation and spectral analysis*. Ed. by John Wiley & Sons. 2nd. John Wiley & Sons, 1993.

[23] L.L. Beranek, T.J. Mellow, and A.J. Zuckerwar. "Acoustics: Sound fields and transducers". In: *The Journal of the Acoustical Society of America* 134.3 (2013), p. 2337. ISSN: 00014966. DOI: 10.1121/1.4816547. URL: http://dx.doi.org/10.1121/1.4816547.

[24] P.G. Bergmann. "The wave equation in a medium with a variable index of refraction". In: *The Journal of the Acoustical Society of America* 17.4 (1946), pp. 329–333. DOI: 10.1121/1.1916333. eprint: https://doi.org/10.1121/1.1916333. URL: https://doi.org/10.1121/1.1916333.

[25] D.A. Bies, C.H. Hansen, and C.Q. Howard. *Engineering Noise Control: Theory and Practice*. Ed. by CRC Press. 5th. CRC Press, 2017.

[26] A. Bissuel, G. Allaire, L. Daumas, S. Barré, and F. Rey. "Linearized Navier–Stokes equations for aeroacoustics using stabilized finite elements: Boundary conditions and industrial application to aft-fan noise propagation". In: *Computers & Fluids* 166 (2018), pp. 32–45. ISSN: 0045-7930. DOI: https://doi.org/10.1016/j.compfluid.2018.01.011. URL: http://www.sciencedirect.com/science/article/pii/S0045793018300112.

[27] E.A. Björk. "Experimental study of measures to reduce noise radiated from power-station exhaust stacks". In: *Noise Control Engineering Journal* 42.5 (1994), pp. 171–178. DOI: 10.3397/1.2828354. URL: https://doi.org/10.3397/1.2828354.

[28] R. Blumrich and D. Heimann. "A linearized Eulerian sound propagation model for studies of complex meteorological effects". In: *The Journal of the Acoustical Society of America* 112.2 (2002), pp. 446–455. DOI: 10.1121/1.1485971. URL: http://dx.doi.org/10.1121/1.1485971.

[29] C.H. Bosanquet and J.L. Pearson. "The spread of smoke and gases from chimneys". In: *Transactions of the Faraday Society* 32 (1936), pp. 1249–1263.

[30] N. Broner. "The effects of low frequency noise on people - A review". In: *Journal of Sound and Vibration* 58.4 (1978), pp. 483–500. ISSN: 0022-460X. DOI: 10.1016/0022-460X(78)90354-1. URL: http://dx.doi.org/10.1016/0022-460X(78)90354-1.

[31] N. Broner. "A simple criterion for low frequency noise emission assessment". In: *Journal of Low Frequency Noise, Vibration and Active Control* 29.1 (2010), pp. 1–13. DOI: 10.1260/0263-0923.29.1.1. URL: https://doi.org/10.1260/0263-0923.29.1.1.

[32] N. Broner. "A simple outdoor criterion for assessment of low frequency noise emission". In: *Acoustics Australia* 39.1 (2011), pp. 7–14. ISSN: 08146039.

[33] N. Broner. "Power to the people". In: *15th International Meeting on Low Frequency Noise and Vibration and its Control*. Ed. by Vibration Low Frequency Noise and Active Control. Low Frequency Noise, Vibration and Active Control. Stratford upon Avon, United Kingdom: Low Frequency Noise, Vibration and Active Control, 2012, pp. 1–10.

[34] E.H. Brown and F.F. Hall. "Advances in atmospheric acoustics". In: *Reviews of Geophysics* 16.1 (1978), pp. 47–110. DOI: 10.1029/rg016i001p00047. eprint: https://agupubs.onlinelibrary.wiley.com/doi/pdf/10.1029/RG016i001p00047. URL: https://agupubs.onlinelibrary.wiley.com/doi/abs/10.1029/RG016i001p00047.

[35] L.M.B.C. Campos and M.H. Kobayashi. "On the reflection and transmission of sound in a thick shear layer". In: *Journal of Fluid Mechanics* 424 (2000), pp. 303–326. ISSN: 1469-7645. DOI: 10.1017/s0022112000002068. URL: https://doi.org/10.1017/S0022112000002068.

[36] L.M.B.C. Campos and M.H. Kobayashi. "Sound transmission from a source outside a nonisothermal boundary layer". In: *American Institute of Aeronautics and Astronautics Journal* 48.5 (2010), pp. 878–892. ISSN: 0001-1452.

[37] S.M. Candel. "Acoustic transmission and reflection by a shear discontinuity separating hot and cold regions". In: *Journal of Sound and Vibration* 24.1

(1972), pp. 87–91. ISSN: 0022-460X. DOI: 10.1016/0022-460x(72)90124-1. URL: http://dx.doi.org/10.1016/0022-460X(72)90124-1.

[38] S.M. Candel, A. Julienne, and A. Guedel. "Refraction and scattering of sound in an open wind tunnel flow". In: *6th International Congress on Instrumentation in Aerospace Simulation Facilities*. Ed. by 6th International Congress on Instrumentation in Aerospace Simulation Facilities. 6. 1975, pp. 288–300.

[39] A.M. Cargill. "Sound propagation through fluctuating flows - Its significance in aeroacoustics". In: *American Institute of Aeronautics and Astronautics Conference 83* 697 (1983), pp. 11–13. DOI: 10.2514/6.1983-697. URL: https://doi.org/10.2514/MAERO83.

[40] D. Casalino. "Finite element solutions of a wave equation for sound propagation in sheared flows". In: *American Institute of Aeronautics and Astronautics Journal* 50.1 (2012), p. 37. ISSN: 0001-1452. DOI: 10.2514/1.j050772. URL: https://doi.org/10.2514/1.j050772.

[41] S. Cheinet, L. Ehrhardt, D. Juvé, and P. Blanc-Benon. "Unified modeling of turbulence effects on sound propagation". In: *The Journal of the Acoustical Society of America* 132.4 (2012), pp. 2198–2209. DOI: 10.1121/1.4748584. URL: https://doi.org/10.1121/1.4748584.

[42] G. Chochua, W. Shyy, S. Thakur, J. Brankovic A. Lienau, L. Porter, and Lischinsky D. "A computational and experimental investigation of turbulent jet and crossflow interaction". In: *Numerical Heat Transfer, Part A: Applications* 38.6 (2000), pp. 557–572. DOI: 10.1080/104077800750021134. eprint: https://doi.org/10.1080/104077800750021134. URL: https://doi.org/10.1080/104077800750021134.

[43] R. Cortelezzi and A.R. Karagozian. "On the formation of the counter-rotating vortex pair in transverse jets". In: *Journal of Fluid Mechanics* 446 (2001), pp. 347–373. DOI: 10.1017/S0022112001005894. URL: http://dx.doi.org/10.10177/S0022112001005894.

[44] D. Crabb, D.F.G. Durao, and J.H. Whitelaw. "A round jet normal to a crossflow". In: *Journal of Fluids Engineering* 103.1 (1981). 10.1115/1.3240764, pp. 142–153. ISSN: 0098-2202. DOI: 10.1115/1.3240764. URL: http://dx.doi.org/10.1115/1.3240764.

[45] A. Cummings. "High temperature effects on the radiation impedance of an unflanged duct exit". In: *Journal of Sound and Vibration* 52.2 (1977), pp. 299–304. ISSN: 0022-460X. DOI: 10.1016/0022-460X(77)90648-4. URL: http://dx.doi.org/10.1016/0022-460X(77)90648-4.

[46] P.R.E Cutler. "On the structure and mixing of a jet in crossflow". PhD thesis. Adelaide: University of Adelaide, Dec. 2002.

[47] G. A. Daigle, T. F. W. Embleton, and J. E. Piercy. "Propagation of sound in the presence of gradients and turbulence near the ground". In: *The Journal of the Acoustical Society of America* 79.3 (1986), pp. 613–627. DOI: 10.1121/1.393451. eprint: https://doi.org/10.1121/1.393451. URL: https://doi.org/10.1121/1.393451.

[48] A. Day and B. Bennett. "Directivity of sound from an open ended duct". In: *Acoustics 2008*. Ed. by Australian Acoustical Society. Australian Acoustical Society. Australian Acoustical Society, Nov. 2008.

[49] A. Day, C. Hansen, and B. Bennett. "Duct directivity index applications". In: *Acoustics Australia* 37.3 (Dec. 2009), pp. 93–97.

[50] F. Delaroche. "Sur l'influence que le Vent exerce dans la Propagation du Son, sous le rapport de son Intensité". In: *Annales de Chimie* 1 (1816), p. 76.

[51] O.S. Eiff, J.G. Kawall, and J.F. Keffer. "Lock-in of vortices in the wake of an elevated round turbulent jet in a crossflow". In: *Experiments in Fluids* 19.3 (1995), pp. 203–213. ISSN: 0723-4864. DOI: 10.1007/bf00189709. URL: https://doi.org/10.1007/BF00189709.

[52] O.S. Eiff and J.F. Keffer. "On the structures in the near-wake region of an elevated turbulent jet in a crossflow". In: *Journal of Fluid Mechanics* 333 (1997), pp. 161–195. ISSN: 1469-7645. DOI: 10.1017/s0022112096004314. URL: http://dx.doi.org/10.1017/s0022112096004314.

[53] O.S. Eiff and J.F. Keffer. "Parametric investigation of the wake-vortex lock-in for the turbulent jet discharging from a stack". In: *Experimental Thermal and Fluid Science* 19.1 (1999), pp. 57 –66. ISSN: 0894-1777. DOI: https://doi.org/10.1016/S0894-1777(99)00010-2. URL: http://www.sciencedirect.com/science/article/pii/S0894177799000102.

[54] T.F.W. Embleton. "Tutorial on sound propagation outdoors". In: *The Journal of the Acoustical Society of America* 100.1 (1996), pp. 31–48. DOI: http://dx.doi.org/10.1121/1.415879. URL: http://scitation.aip.org/content/asa/journal/jasa/100/1/10.1121/1.415879.

[55] Energy XPRT. *Clyde Bergemann Power Group - Gas Turbine Exhaust Systems*. URL: https://www.energy-xprt.com/products/gas-turbine-exhaust-systems-348809.

[56] M. Esmaeili, A. Afshari, and F.A. Jaberi. "Turbulent mixing in non-isothermal jet in crossflow". In: *International Journal of Heat and Mass Transfer* 89 (2015), pp. 1239–1257. DOI: 10.1016/j.ijheatmasstransfer.2015.05.055. URL: http://dx.doi.org/10.1016/j.ijheatmasstransfer.2015.05.055.

[57] R. Ewert and W. Schröder. "Acoustic perturbation equations based on flow decomposition via source filtering". In: *Journal of Computational Physics* 188.2 (2003), pp. 365–398. ISSN: 0021-9991. DOI: 10.1016/S0021-9991(03)00168-2. URL: http://www.sciencedirect.com/science/article/pii/S0021999103001682.

[58] R. Fearn and R.P. Weston. "Vorticity Associated with a Jet in a Cross Flow". In: *American Institute of Aeronautics and Astronautics Journal* 12.12 (Dec. 1974), pp. 1666–1671. DOI: 10.2514/3.49576. URL: https://doi.org/10.2514/3.49576.

[59] X. Feng, M. Ben Tahar, and R. Baccouche. "The aero-acoustic Galbrun equation in the time domain with perfectly matched layer boundary conditions". In: *The Journal of the Acoustical Society of America* 139.1 (2016), pp. 320–331.

DOI: 10.1121/1.4939965. eprint: https://doi.org/10.1121/1.4939965. URL: https://doi.org/10.1121/1.4939965.

[60] T.F. Fric and A. Roshko. "Vortical structure in the wake of a transverse jet". In: *Journal of Fluid Mechanics* 279 (1994), pp. 1–47. ISSN: 1469-7645. DOI: 10.1017/s0022112094003800. URL: http://dx.doi.org/10.1017/s0022112094003800.

[61] J. Fröhlich, J. Denev, and H. Bockhorn. "Large eddy simulation of a jet in crossflow". In: *Proceeding 4th ECCOMAS Conference*. Jyväskylä, Finland, 2004, pp. 24–28.

[62] G. Gabard, R. J. Astley, and M. Ben Tahar. "Stability and accuracy of finite element methods for flow acoustics. II: Two-dimensional effects". In: *International Journal for Numerical Methods in Engineering* 63.7 (2005), pp. 974–987. DOI: 10.1002/nme.1319. eprint: https://onlinelibrary.wiley.com/doi/pdf/10.1002/nme.1319. URL: https://onlinelibrary.wiley.com/doi/abs/10.1002/nme.1319.

[63] G. Gabard, F. Treysséde, and M. Ben Tahar. "A numerical method for vibro-acoustic problems with sheared mean flows". In: *Journal of Sound and Vibration* 272.3 (2004), pp. 991–1011. ISSN: 0022-460X. DOI: https://doi.org/10.1016/j.jsv.2003.03.007. URL: http://www.sciencedirect.com/science/article/pii/S0022460X03008514.

[64] F.C.C. Galeazzo, G. Donnert, C. Cárdenas, J. Sedlmaier, P. Habisreuther, N. Zarzalis, C. Beck, and W. Krebs. "Computational modeling of turbulent mixing in a jet in crossflow". In: *International Journal of Heat and Fluid Flow* 41 (2013), pp. 55–65. DOI: 10.1016/j.ijheatfluidflow.2013.03.012. URL: https://doi.org/10.1016/j.ijheatfluidflow.2013.03.012.

[65] F.C.C. Galeazzo, G. Donnert, P. Habisreuther, N. Zarzalis, R.J. Valdes, and W. Krebs. "Measurement and simulation of turbulent mixing in a jet in crossflow". In: *Journal of Engineering for Gas Turbines and Power* 133.6 (2011), p. 061504. DOI: 10.1115/1.4002319. URL: https://doi.org/10.1115/1.4002319.

[66] E Grande. "Refraction of injected sound by a very cold nitrogen jet". In: *The Journal of the Acoustical Society of America* 38.6 (1965), pp. 1063–1064. DOI: 10.1121/1.1909848. URL: http://dx.doi.org/10.1121/1.1909848.

[67] E. Grande. *Refraction of sound by jet flow and jet temperature II*. Report. University of Toronto, 1966.

[68] C.R. Hart, N.J. Reznicek, D.K. Wilson, C.L. Pettit, and E.T. Nykaza. "Comparisons between physics-based, engineering, and statistical learning models for outdoor sound propagation". In: *The Journal of the Acoustical Society of America* 139.5 (2016), pp. 2640–2655. DOI: 10.1121/1.4948757. eprint: https://doi.org/10.1121/1.4948757. URL: https://doi.org/10.1121/1.4948757.

[69] G. He, G. Guo, and Hsu. A.T. "The effect of Schmidt number on turbulent scalar mixing in a jet-in-crossflow". In: *International Journal of Heat and Mass Transfer* 42.20 (1999), pp. 3727 –3738. ISSN: 0017-9310. DOI: https://doi.org/10.1016/S0017-9310(99)00050-2. URL: http://www.sciencedirect.com/science/article/pii/S0017931099000502.

[70] G.F. Hessler Jr. "Proposed criteria in residential communities for low-frequency noise emissions from industrial sources". In: *Noise Control Engineering Journal* 52.4 (2004), pp. 179–185. ISSN: 0736-2501. DOI: 10.3397/1.2839748. URL: https://doi.org/10.3397/1.2839748.

[71] G.F. Hessler Jr. "Proposed criteria for low frequency industrial noise in residential communities". In: *Low Frequency Noise, Vibration and Active Control* 24.2 (2005), pp. 97–106. ISSN: 0263-0923. DOI: 10.1260/0263092054530957. URL: https://doi.org/10.1260/0263092054530957.

[72] R. Hetzel and R.A. Putnam. "Sources and rating criteria of low frequency gas turbine exhaust noise - via case study". In: *INTER-NOISE and NOISE-CON Congress and Conference Proceedings, 2009*. Ed. by Institute of Noise Control Engineering. Ontario, Canada, 2009, pp. 1600–1607.

[73] A. Hirschberg and M. Hoeijmakers. "Comments on the low frequency radiation impedance of a duct exhausting a hot gas". In: *The Journal of the Acoustical Society of America* 136.2 (2014), pp. 84–89. DOI: 10.1121/1.4885540. eprint: https://doi.org/10.1121/1.4885540. URL: https://doi.org/10.1121/1.4885540.

[74] A. Hoda and S. Acharya. "Predictions of a film coolant jet in crossflow with different turbulence models". In: *Journal of Turbomachinery-Trans. ASME* 122.3 (2000), pp. 558–569. ISSN: 0889-504X. DOI: 10.1115/1.1302322. URL: https://doi.org/10.1115/1.1302322.

[75] A. Holmberg, A. Kierkegaard, and C. Weng. "A frequency domain linearized Navier–Stokes method including acoustic damping by eddy viscosity using RANS". In: *Journal of Sound and Vibration* 346 (2015), pp. 229–247. ISSN: 0022-460X. DOI: https://doi.org/10.1016/j.jsv.2015.02.030. URL: http://www.sciencedirect.com/science/article/pii/S0022460X15001649.

[76] M. Hornikx, R. Waxler, and J. Forssén. "The extended Fourier pseudospectral time-domain method for atmospheric sound propagation". In: *The Journal of the Acoustical Society of America* 128.4 (2010), pp. 1632–1646. DOI: 10.1121/1.3474234. URL: https://doi.org/10.1121/1.3474234.

[77] C.Q. Howard and B.S. Cazzolato. *Acoustic analyses using MATLAB® and Ansys®*. CRC Press, 2014. ISBN: 1482223252.

[78] C. M. Hsu and R. F. Huang. "Comparisons of flow and mixing characteristics between unforced and excited elevated transverse jets". In: *Journal of Mechanics* 30 (01 Feb. 2014), pp. 87–96. ISSN: 1811-8216. DOI: 10.1017/jmech.2013.74. URL: http://journals.cambridge.org/article_S1727719113000749.

[79] C.M. Hsu and R.F. Huang. "Effects of crossflow on puff and oscillation modes of a pulsed elevated transverse jet". In: *European Journal of Mechanics-B/Fluids* 31 (2012), pp. 140–148. ISSN: 0997-7546. DOI: 10.1016/j.euromechflu.2011.09.003. URL: https://doi.org/10.1016/j.euromechflu.2011.09.003.

[80] J.F. Huang, M.J. Davidson, and R.I. Nokes. "Two-dimensional and line jets in a weak cross-flow". In: *Journal of Hydraulic Research* 43.4 (2005), pp. 390–398. ISSN: 0022-1686. DOI: 10.1080/00221680509500134. URL: http://dx.doi.org/10.1080/00221680509500134.

[81] R.F. Huang and R.H. Hsieh. "An experimental study of elevated round jets deflected in a crosswind". In: *Experimental Thermal and Fluid Science* 27.1 (2002), pp. 77–86. ISSN: 0894-1777. DOI: 10.1016/s0894-1777(02)00217-0. URL: https://doi.org/10.1016/S0894-1777(02)00217-0.

[82] R.F. Huang and R.H. Hsieh. "Sectional flow structures in near wake of elevated jets in a crossflow". In: *American Institute of Aeronautics and Astronautics Journal* 41.8 (2003), pp. 1490–1499. ISSN: 0001-1452. DOI: 10.2514/2.2099. URL: https://doi.org/10.2514/2.2099.

[83] R.F. Huang and C.M. Hsu. "Turbulent flows of an acoustically excited elevated transverse jet". In: *American Institute of Aeronautics and Astronautics Journal* 50.9 (2012), pp. 1964–1978. ISSN: 0001-1452. DOI: 10.2514/1.j051595. URL: https://doi.org/10.2514/1.J051595.

[84] R.F. Huang and J. Lan. "Characteristic modes and evolution processes of shear-layer vortices in an elevated transverse jet". In: *Physics of Fluids* 17.3 (2005), p. 034103. ISSN: 1070-6631. DOI: 10.1063/1.1852575. URL: http://dx.doi.org/10.1063/1.1852575.

[85] Uno Ingård. "A review of the influence of meteorological conditions on sound propagation". In: *The Journal of the Acoustical Society of America* 25.3 (1953), pp. 405–411. DOI: 10.1121/1.1907055. eprint: https://doi.org/10.1121/1.1907055. URL: https://doi.org/10.1121/1.1907055.

[86] International Organization for Standardization. *ISO 9613-1:1993 Acoustics - Attenuation of sound during propagation outdoors – Part 1: Calculation of the absorption by the atmosphere*. Standard. International Organization for Standardization, 1993a.

[87] International Organization for Standardization. *ISO 10494:1993 Gas turbines and turbine sets- Measurement of emitted airborne noise – Engineering/ survey method*. Standard. International Organization for Standardization, 1993b.

[88] International Organization for Standardization. *ISO 9613-2:1996 Acoustics - Attenuation of sound during propagation outdoors – Part 2: General method of calculation*. Standard. The standard was reconfirmed in 2017. International Organization for Standardization, 1996.

[89] International Organization for Standardization. *ISO 10494:2018 Gas turbines and turbine sets- Measurement of emitted airborne noise – Engineering/ survey method*. Standard. International Organization for Standardization, 2018.

[90] B.E. Johnson, G.S. Elliott, and K.T. Christensen. "Structural characteristics of a heated jet in cross-flow emanating from a raised, circular stack". In: *Experiments in Fluids* 54.6 (2013), p. 1543. ISSN: 1432-1114. DOI: 10.1007/s00348-013-1543-1. URL: https://doi.org/10.1007/s00348-013-1543-1.

[91] W.P. Jones and M. Wille. "Large-eddy simulation of a plane jet in a cross-flow". In: *International Journal of Heat and Fluid Flow* 17.3 (1996), pp. 296 –306. ISSN: 0142-727X. DOI: https://doi.org/10.1016/0142-727X(96)00045-8. URL: http://www.sciencedirect.com/science/article/pii/0142727X96000458.

[92] Y Kamotani and I Greber. "Experiments on a turbulent jet in a cross flow". In: *American Institute of Aeronautics and Astronautics Journal* 10.11 (1972), pp. 1425–1429. DOI: 10.2514/3.50386. URL: http://dx.doi.org/10.2514/3.50386.

[93] R.M. Kelso, T.T. Lim, and A.E. Perry. "New experimental observations of vortical motions in transverse jets". In: *Physics of Fluids* 10.9 (1998), pp. 2427–2429. ISSN: 1070-6631. DOI: 10.1063/1.869761. URL: http://dx.doi.org/10.1063/1.869761.

[94] R.M. Kelso, T.T. Lim, A.E. Perry, and A.E. Lim. "An experimental study of round jets in cross-flow". In: *Journal of Fluid Mechanics* 306.1 (1996),

pp. 111–144. ISSN: 00221120. DOI: 10.1017/s0022112096001255. URL: http://dx.doi.org/10.1017/s0022112096001255.

[95] R.M. Kelso and A.J. Smits. "Horseshoe vortex systems resulting from the interaction between a laminar boundary layer and a transverse jet". In: *Physics of Fluids* 7.1 (Jan. 1995), pp. 153–158. DOI: 10.1063/1.868736. URL: https://doi.org/10.1063/1.868736.

[96] A. Kierkegaard, S. Boij, and G. Efraimsson. "A frequency domain linearized Navier–Stokes equations approach to acoustic propagation in flow ducts with sharp edges". In: *The Journal of the Acoustical Society of America* 127.2 (2010), pp. 710–719. DOI: 10.1121/1.3273899. eprint: https://doi.org/10.1121/1.3273899. URL: https://doi.org/10.1121/1.3273899.

[97] K.E. Kinsler, A.R. Frey, A.B. Coppens, and J.V. Sanders. *Fundamentals of Acoustics*. Ed. by John Wiley & Sons. 4th. John Wiley & Sons, 1999.

[98] H. Klug. "Sound-speed profiles determined from outdoor sound propagation measurements". In: *The Journal of the Acoustical Society of America* 90.1 (1991), pp. 475–481. DOI: http://dx.doi.org/10.1121/1.401272. URL: http://dx.doi.org/10.1121/1.401272.

[99] A.R. Kriebel. "Refraction and attenuation of sound by wind and thermal profiles over a ground plane". In: *The Journal of the Acoustical Society of America* 51.1A (1972), pp. 19–23. DOI: 10.1121/1.1912816. eprint: https://doi.org/10.1121/1.1912816. URL: https://doi.org/10.1121/1.1912816.

[100] G. Kroeff. "Low frequency noise generated by industrial gas turbines". PhD thesis. Loughborough University, 2004.

[101] G. Kudernatsch. "Combustion turbine exhaust systems-low frequency noise reduction". In: *INTER-NOISE 2000, The 29th International Congress and Exhibition on Noise Control Engineering*. Ed. by Institute of Noise Control Engineering. Nice, France, 2000, pp. 1–6.

[102] A. L'Espérance, J. Nicolas, D.K. Wilson, D.W. Thomson, Y. Gabillet, and G. Daigle. "Sound propagation in the atmospheric surface layer: Comparison of experiment with FFP predictions". In: *Applied Acoustics* 40.4 (1993), pp. 325–346. DOI: 10.1016/0003-682X(93)90092-K. URL: https://doi.org/10.1016/0003-682X(93)90092-K.

[103] A. L'Espérance, J.R. Nicolas, P. Herzog, and G.A. Daigle. "Heuristic model for outdoor sound propagation based on an extension of the geometrical ray theory in the case of a linear sound speed profile". In: *Applied Acoustics* 37.2 (1992), pp. 111 –139. ISSN: 0003-682X. DOI: http://dx.doi.org/10.1016/0003-682X(92)90022-K. URL: http://www.sciencedirect.com/science/article/pii/0003682X9290022K.

[104] H. Levine and J. Schwinger. "On the radiation of sound from an unflanged circular pipe". In: *Physical review* 73.4 (1948), p. 383. DOI: 10.1103/physrev.73.383. URL: https://journals.aps.org/pr/abstract/10.1103/PhysRev.73.383.

[105] M.J. Lighthill. "On sound generated aerodynamically. I. General theory". In: *Proceedings of the Royal Society of London A: Mathematical, Physical and Engineering Sciences* 211.1107 (1952), pp. 564–587. ISSN: 0080-4630. DOI: 10.1098/rspa.1952.0060. eprint: http://rspa.royalsocietypublishing.org/content/211/1107/564.full.pdf. URL: http://rspa.royalsocietypublishing.org/content/211/1107/564.

[106] M.J. Lighthill. "On sound denerated aerodynamically. II. Turbulence as a source of sound". In: *Proceedings of the Royal Society of London A: Mathematical, Physical and Engineering Sciences* 222.1148 (1954), pp. 1–32. ISSN: 0080-4630. DOI: 10.1098/rspa.1954.0049. eprint: http://rspa.royalsocietypublishing.org/content/222/1148/1.full.pdf. URL: http://rspa.royalsocietypublishing.org/content/222/1148/1.

[107] T.T. Lim, T.H. New, and S.C. Luo. "On the development of large-scale structures of a jet normal to a cross flow". In: *Physics of Fluids* 13.3 (2001),

pp. 770–775. DOI: 10.1063/1.1347960. URL: http://scitation.aip.org/content/aip/journal/pof2/13/3/10.1063/1.1347960.

[108] J. Ling, A. Ruiz, G. Lacaze, and J. Oefelein. "Uncertainty analysis and data-driven model advances for a jet-in-crossflow". In: *Journal of Turbomachinery* 139.2 (2016), pp. 1–9. DOI: 10.1115/1.4034556. URL: http://dx.doi.org/10.1115/1.4034556.

[109] W. C. Lucas and G. F. Hessler Jr. "The reduction of low frequency gas turbine exhaust noise: A case study". In: *ASME 1996 International Gas Turbine and Aeroengine Congress and Exhibition*. Vol. Volume 4: Heat Transfer Electric Power Industrial and Cogeneration. Turbo Expo: Power for Land, Sea, and Air. Birmingham, UK., June 1996. DOI: 10.1115/96-GT-010. URL: https://doi.org/10.1115/96-GT-010.

[110] G.R. MacGregor, H.S. Ribner, and H. Lam. ""Basic" jet noise patterns after deletion of convection and refraction effects: Experiments vs. Theory". In: *Journal of Sound and Vibration* 27.4 (1973), pp. 437–454. ISSN: 0022-460X. DOI: 10.1016/s0022-460x(73)80356-6. URL: http://dx.doi.org/10.1016/S0022-460X(73)80356-6.

[111] L. Maestrello, A. Bayliss, and E. Turkel. "On the interaction of a sound pulse with the shear layer of an axisymmetric jet". In: *Journal of Sound and Vibration* 74.2 (1981), pp. 281–301. ISSN: 0022-460X. DOI: 10.1016/0022-460X(81)90510-1. URL: http://dx.doi.org/10.1016/0022-460X(81)90510-1.

[112] P. Majander and T. Siikonen. "Large-eddy simulation of a round jet in a cross-flow". In: *International Journal of Heat and Fluid Flow* 27.3 (2006), pp. 402–415. ISSN: 0142-727X. DOI: 10.1016/j.ijheatfluidflow.2006.01.004. URL: https://doi.org/10.1016/j.ijheatfluidflow.2006.01.004.

[113] C.M. Mak. "A prediction method for aerodynamic sound produced by multiple elements in air ducts". In: *Journal of Sound and Vibration* 287.1 (2005), pp. 395–403. ISSN: 0022-460X. DOI: 10.1016/j.jsv.2005.01.048. URL: https://doi.org/10.1016/j.jsv.2005.01.048.

[114] F.R. Menter. "Two-equation eddy-viscosity turbulence models for engineering applications". In: *American Institute of Aeronautics and Astronautics Journal* 32.8 (1994), pp. 1598–1605. DOI: 10.2514/3.12149. URL: http://dx.doi.org/10.2514/3.12149.

[115] C.L. Morfey and P.F. Joseph. "Shear layer refraction corrections for off-axis sources in a jet flow". In: *Journal of Sound and Vibration* 239.4 (2001), pp. 819–848. ISSN: 0022-460X. DOI: 10.1006/jsvi.2000.3218. URL: http://dx.doi.org/10.1006/jsvi.2000.3218.

[116] F. Muldoon and S. Acharya. "Direct Numerical Simulation of pulsed jets-in-crossflow". In: *Computers & Fluids* 39.10 (2010), pp. 1745 –1773. ISSN: 0045-7930. DOI: https://doi.org/10.1016/j.compfluid.2010.04.008. URL: http://www.sciencedirect.com/science/article/pii/S0045793010000848.

[117] P. Mungur, H.E. Plumblee, and P.E. Doak. "Analysis of acoustic radiation in a jet flow enviroment". In: *Journal of Sound and Vibration* 36.1 (1974), pp. 21–52. ISSN: 0022-460X. DOI: 10.1016/S0022-460X(74)80341-X. URL: http://dx.doi.org/10.1016/S0022-460X(74)80341-X.

[118] M.L. Munjal. *Acoustics of ducts and mufflers with application to exhaust and ventilation system design*. John Wiley & Sons, 1987. ISBN: 0471847380.

[119] S. Muppidi and K. Mahesh. "Study of trajectories of jets in crossflow using direct numerical simulations". In: *Journal of Fluid Mechanics* 530 (2005), pp. 81–100. ISSN: 0022-1120. DOI: 10.1017/S0022112005003514. URL: http://dx.doi.org/10.1017/S0022112005003514.

[120] S. Muppidi and K. Mahesh. "Two-dimensional model problem to explain counter-rotating vortex pair formation in a transverse jet". In: *Physics of Fluids (1994-present)* 18.8 (2006), p. 085103. ISSN: 1070-6631. DOI: 10.1063/1.2236304. URL: http://dx.doi.org/10.1063/1.2236304.

[121] S. Muppidi and K. Mahesh. "Direct numerical simulation of round turbulent jets in crossflow". In: *Journal of Fluid Mechanics* 574 (2007), pp. 59–84. ISSN:

0022-1120. DOI: 10.1017/S0022112006004034. URL: http://dx.doi.org/10.1017/S0022112006004034.

[122] National Aeronautics and Space Administration. *Fourth computational aeroacoustics (CAA) workshop on benchmark problems*. Tech. rep. NASA Glenn Research Center; Cleveland, OH, United States: National Aeronautics and Space Administration, 2004.

[123] P.A. Nelson and C.L. Morfey. "Aerodynamic sound production in low speed flow ducts". In: *Journal of Sound and Vibration* 79.2 (1981), pp. 263–289. ISSN: 0022-460X. DOI: https://doi.org/10.1016/0022-460X(81)90372-2. URL: http://www.sciencedirect.com/science/article/pii/0022460X81903722.

[124] J. R. Newman and K. I. McEwan. "Low frequency gas turbine noise". In: *Journal of Engineering for Power* 108.2 (1980), pp. 476–481. DOI: 10.1115/1.3230280. URL: http://dx.doi.org/10.1115/1.3230280.

[125] J.R. Newman and K.I. McEwan. "Low frequency gas turbine noise". In: *ASME 1979 International Gas Turbine Conference and Exhibit and Solar Energy Conference*. American Society of Mechanical Engineers. 1979, pp. 1–12.

[126] NS Energy. *Gas turbine modernisation: looking at the options*. https://www.nsenergybusiness.com/features/featuregas-turbine-modernisation-looking-at-the-options/. Accessed: 16-01-2020. July 2016.

[127] Origin Energy Limited. *Uranquinty Power Station 2014 Annual Environmental Management Report*. Tech. rep. Origin Energy Limited, 2015.

[128] V.E. Ostashev and D.E. Wilson. *Acoustics in moving inhomogeneous media*. CRC Press, 2015. ISBN: 9780415564168.

[129] V.E. Ostashev, D.K. Wilson, L. Liu, D.F. Aldridge, N.P. Symons, and D. Marlin. "Equations for finite-difference, time-domain simulation of sound propagation in moving inhomogeneous media and numerical implementation". In: *The Journal of the Acoustical Society of America* 117.2 (2005), pp. 503–517. DOI: 10.1121/1.1841531. URL: https://doi.org/10.1121/1.1841531.

[130] H. Peters, U.J. Kurze, and H. Nurnberger. "Model tests on flow noise in exhaust stacks of gas turbine power stations". In: *Proceedings of the 36th Annual Meeting of German Acoustical Society*. Ed. by Deutsche Jahrestagung für Akustik DAGA Berlin. Berlin, 2010.

[131] A.D. Pierce. "Wave equation for sound in fluids with unsteady inhomogeneous flow". In: *The Journal of the Acoustical Society of America* 87.6 (1990), pp. 2292–2299. DOI: 10.1121/1.399073. eprint: https://doi.org/10.1121/1.399073. URL: https://doi.org/10.1121/1.399073.

[132] J.E. Piercy, T.F.W. Embleton, and L.C. Sutherland. "Review of noise propagation in the atmosphere". In: *The Journal of the Acoustical Society of America* 61.6 (1977), pp. 1403–1418. DOI: http://dx.doi.org/10.1121/1.381455. URL: http://scitation.aip.org/content/asa/journal/jasa/61/6/10.1121/1.381455.

[133] H.E. Plumblee and P.D. Dean. "Sound measurements within and in the radiated field of an annular duct with flow". In: *Journal of Sound and Vibration* 28.4 (1973), 715–IN1. ISSN: 0022-460X. DOI: 10.1016/s0022-460x(73)80145-2. URL: https://doi.org/10.1016/S0022-460X(73)80145-2.

[134] K.B. Rasmussen. "Outdoor sound propagation under the influence of wind and temperature gradients". In: *Journal of Sound and Vibration* 104.2 (1986), pp. 321–335. ISSN: 0022-460X. DOI: 10.1016/0022-460x(86)90271-3. URL: http://www.sciencedirect.com/science/article/pii/0022460X86902713.

[135] J.W.S. Rayleigh. *The theory of sound*. Dover, New York, 1945.

[136] O. Reynolds. "On the refraction of sound by the atmosphere". In: *Proceedings of the Royal Society of London* 22.148-155 (1873), pp. 531–548.

[137] O. Reynolds. "On the refraction of sound by the atmosphere". In: *Philosophical Transactions of the Royal Society of London* (1876), pp. 315–324.

[138] G. Ross and R. C. Chivers. "A note on the Helmholtz equations for acoustic waves in inhomogeneous media". In: *The Journal of the Acoustical Society of America* 80.5 (1986), pp. 1536–1539. DOI: 10.1121/1.394362. eprint: https://doi.org/10.1121/1.394362. URL: https://doi.org/10.1121/1.394362.

[139] A.M. Ruiz, G. Lacaze, and J.C. Oefelein. "Flow topologies and turbulence scales in a jet-in-cross-flow". In: *Physics of Fluids* 27.4 (2015), p. 045101. DOI: 10.1063/1.4915065. eprint: https://doi.org/10.1063/1.4915065. URL: https://doi.org/10.1063/1.4915065.

[140] D. Rusch, L. Blum, A. Moser, and T. Roesgen. "Turbulence model validation for fire simulation by CFD and experimental investigation of a hot jet in crossflow". In: *Fire Safety Journal* 43.6 (2008), pp. 429–441. DOI: 10.1016/j.firesaf.2007.11.005. URL: http://dx.doi.org/10.1016/j.firesaf.2007.11.005.

[141] N.M. Saïd, H. Mhiri, G. Le Palec, and P. Bournot. "Experimental and numerical analysis of pollutant dispersion from a chimney". In: *Atmospheric Environment* 39.9 (2005), pp. 1727–1738. ISSN: 1352-2310. DOI: 10.1016/j.atmosenv.2004.11.040. URL: https://doi.org/10.1016/j.atmosenv.2004.11.040.

[142] N.M. Said, S. Habli, H. Mhiri, H. Bournot, and G. Le Palec. "Flow field measurement in a crossflowing elevated jet". In: *Journal of Fluids Engineering* 129.5 (2007), pp. 551–562. ISSN: 0098-2202. DOI: 10.1115/1.2717614. URL: http://dx.doi.org/10.1115/1.2717614.

[143] P. Schlatter, S. Bagheri, and D. Henningson. "Self-sustained global oscillations in a jet in crossflow". In: *Theoretical Computational Fluid Dynamics* 25.1-4 (2010), pp. 129–146. ISSN: 0935-4964. DOI: 10.1007/s00162-010-0199-1. URL: http://dx.doi.org/10.1007/s00162-010-0199-1.

[144] R.H. Schlinker and R.K. Amiet. *Refraction and scattering of sound by a shear layer*. Book. National Aeronautics, Space Administration, Scientific, and Technical Information Branch, 1980.

[145] L.K. Schubert. "Numerical study of sound refraction by a jet flow. I. Ray acoustics". In: *The Journal of the Acoustical Society of America* 51.2A (1972), pp. 439–446. ISSN: 0001-4966. DOI: 10.1121/1.1912861. URL: http://dx.doi.org/10.1121/1.1912861.

[146] L.K. Schubert. "Numerical study of sound refraction by a jet flow. II. Wave acoustics". In: *The Journal of the Acoustical Society of America* 51.2A (1972), pp. 447–463. ISSN: 0001-4966. DOI: 10.1121/1.1912862. URL: http://dx.doi.org/10.1121/1.1912862.

[147] S.A. Sherif and R.H Pletcher. "Measurements of the thermal characteristics of heated turbulent jets in crossflow". In: *Journal of Heat Transfer* 111.4 (1989), p. 897. DOI: 10.1115/1.3250803. URL: http://dx.doi.org/10.1115/1.3250803.

[148] S.A. Sherif and R.H. Pletcher. "Jet-wake thermal characteristics of heated turbulent jets in crossflow". In: *Journal of Thermophysics and Heat Transfer* 5.2 (1991), pp. 181–191. DOI: 10.2514/3.246. URL: http://dx.doi.org/10.2514/3.246.

[149] T-H. Shih, W.W. Liou, A. Shabbir, Z. Yang, and J. Zhu. "A new k-ϵ eddy viscosity model for high reynolds number turbulent flows". In: *Computers and Fluids* 24.3 (1995), pp. 227–238. ISSN: 00457930. DOI: 10.1016/0045-7930(94)00032-T. URL: http://dx.doi.org/10.1016/0045-7930(94)00032-T.

[150] Siemens. *We power the world with innovative gas turbines - Siemens gas turbine portfolio*. Data sheet. 2019.

[151] A.R. da Silva, G.P. Scavone, and A. Lefebvre. "Sound reflection at the open end of axisymmetric ducts issuing a subsonic mean flow: A numerical study". In: *Journal of Sound and Vibration* 327.3 (2009), pp. 507–528. ISSN: 0022-460X. DOI: 10.1016/j.jsv.2009.06.027. URL: https://doi.org/10.1016/j.jsv.2009.06.027.

[152] S.H. Smith and M.G. Mungal. "Mixing, structure and scaling of the jet in crossflow". In: *Journal of Fluid Mechanics* 357 (1998), pp. 83–122. ISSN: 1469-7645. DOI: 10.1017/s0022112097007891. URL: http://dx.doi.org/10.1017/s0022112097007891.

[153] S. Stephenson. "Predicting environmental noise form industrial exhaust stacks". In: *Acoustics bulletin* 38.1 (Jan. 2013), pp. 37–41.

[154] G.G. Stokes. "On the effect of wind on the intensity of sound". In: *Brit. Assoc. Report* (1857), p. 22.

[155] L.K. Su and M.G. Mungal. "Simultaneous measurements of scalar and velocity field evolution in turbulent crossflowing jets". In: *Journal of Fluid Mechanics* 513 (2004), pp. 1–45. ISSN: 1469-7645. DOI: 10.1017/s0022112004009401. URL: https://doi.org/10.1017/S0022112004009401.

[156] W. Sutherland. "LII. The viscosity of gases and molecular force". In: *The London, Edinburgh, and Dublin Philosophical Magazine and Journal of Science* 36.223 (1893), pp. 507–531. DOI: 10.1080/14786449308620508. URL: http://dx.doi.org/10.1080/14786449308620508.

[157] S. Taherzadeh, K.M. Li, and K. Attenborough. "Some practical considerations for predicting outdoor sound propagation in the presence of wind and temperature gradients". In: *Applied Acoustics* 54.1 (1998), pp. 27–44. ISSN: 0003-682X. DOI: 10.1016/s0003-682x(97)00069-8. URL: http://www.sciencedirect.com/science/article/pii/S0003682X97000698.

[158] C.K.W. Tam and L. Auriault. "Mean flow refraction effects on sound radiated from localized sources in a jet". In: *Journal of Fluid Mechanics* 370 (1998), pp. 149–174. ISSN: 0022-1120. DOI: 10.1017/s0022112098001852. URL: https://doi.org/10.1017/S0022112098001852.

[159] F. Treysséde and M. Ben Tahar. "Comparison of a finite element model with a multiple-scales solution for sound propagation in varying ducts with swirling flows". In: *The Journal of the Acoustical Society of America* 115.6 (2004), pp. 2716–2730. DOI: 10.1121/1.1707084. eprint: https://doi.org/10.1121/1.1707084. URL: https://doi.org/10.1121/1.1707084.

[160] F. Treysséde, G. Gabard, and M. Ben Tahar. "A mixed finite element method for acoustic wave propagation in moving fluids based on an Eulerian-Lagrangian description". In: *The Journal of the Acoustical Society of America* 113.2 (2003), pp. 705–716. DOI: 10.1121/1.1534837. eprint: https://doi.org/10.1121/1.1534837. URL: https://doi.org/10.1121/1.1534837.

[161] I.L. Ver. "Prediction scheme for the self-generated noise of silencers". In: *INTER-NOISE and NOISE-CON Congress and Conference Proceedings, 1972*. Ed. by Institute of Noise Control Engineering. Washington, D.C., 1972, pp. 294–298.

[162] M. West, K. Gilbert, and R. West. "A tutorial on the parabolic equation (PE) model used for long range sound propagation in the atmosphere". In: *Applied Acoustics* 37.1 (1992), pp. 31 –49. ISSN: 0003-682X. DOI: https://doi.org/10.1016/0003-682X(92)90009-H. URL: http://www.sciencedirect.com/science/article/pii/0003682X9290009H.

[163] M.J. White and K.E. Gilbert. "Application of the parabolic equation to the outdoor propagation of sound". In: *Applied Acoustics* 27.3 (1989), pp. 227 –238. ISSN: 0003-682X. DOI: https://doi.org/10.1016/0003-682X(89)90062-5. URL: http://www.sciencedirect.com/science/article/pii/0003682X89900625.

[164] D.K. Wilson. "Use of wave-number-domain windows in fast field programs". In: *The Journal of the Acoustical Society of America* 89.1 (1991), pp. 448–450. DOI: 10.1121/1.400480. URL: https://doi.org/10.1121/1.400480.

[165] D.K. Wilson. "Wind gusts or scattering by turbulence: Which is more important for near-ground propagation?" In: *The Journal of the Acoustical Society of America* 108.5 (2000), pp. 2650–2650. DOI: http://dx.doi.org/10.1121/1.4743881. URL: http://scitation.aip.org/content/asa/journal/jasa/108/5/10.1121/1.4743881.

[166] D.K. Wilson. "The sound-speed gradient and refraction in the near-ground atmosphere". In: *The Journal of the Acoustical Society of America* 113.2 (2002), pp. 750–757. DOI: http://dx.doi.org/10.1121/1.1532028. URL: http:

//scitation.aip.org/content/asa/journal/jasa/113/2/10.1121/1.1532028.

[167] D.K. Wilson, E.L Andreas, J.W. Weatherly, C.L. Pettit, E.G. Patton, and P.P. Sullivan. "Characterization of uncertainty in outdoor sound propagation predictions". In: *The Journal of the Acoustical Society of America* 121.5 (2007), EL177–EL183. DOI: 10.1121/1.2716159. URL: http://dx.doi.org/10.1121/1.2716159.

[168] D.K. Wilson, M.S. Lewis, J.W. Weatherly, and E.L. Andreas. "Dependence of predictive skill for outdoor narrowband and broadband sound levels on the atmospheric representation". In: *Noise Control Engineering Journal* 56.6 (2008), pp. 465–477. DOI: 10.3397/1.3010733. URL: https://doi.org/10.3397/1.3010733.

[169] D.K. Wilson, J.M. Noble, and Coleman M.A. "Sound propagation in the nocturnal boundary layer". In: *Journal of Atmospheric Sciences* 60.20 (2003), pp. 2473–2486. DOI: 10.1175/1520-0469(2003)060<2473:SPITNB>2.0.CO;2. URL: https://doi.org/10.1175/1520-0469(2003)060<2473:SPITNB>2.0.CO;2.

[170] D.K. Wilson, C.L. Pettit, V.E. Ostashev, and S.N. Vecherin. "Description and quantification of uncertainty in outdoor sound propagation calculations". In: *The Journal of the Acoustical Society of America* 136.3 (2014), pp. 1013–1028. DOI: http://dx.doi.org/10.1121/1.4890644. URL: http://asa.scitation.org/doi/full/10.1121/1.4890644.

[171] D.K. Wilson, C.L. Pettit, V.E. Ostashev, and S.N. Vecherin. "Sound propgation in the atmospheric boundary layer". In: *Acoustics Today* 11.2 (2015), pp. 44–53.

[172] L.L. Yuan and R.L. Street. "Trajectory and entrainment of a round jet in crossflow". In: *Physics of Fluids* 10.9 (1998), pp. 2323–2335. DOI: doi:http://dx.doi.org/10.1063/1.869751. URL: http://scitation.aip.org/content/aip/journal/pof2/10/9/10.1063/1.869751.

[173] L.L. Yuan, R.L. Street, and J.H. Ferziger. "Large-eddy simulations of a round jet in crossflow". In: *Journal of Fluid Mechanics* 379 (1999), pp. 71–104. ISSN: 1469-7645. DOI: 10.1017/S0022112098003346. URL: https://doi.org/10.1017/S0022112098003346.

[174] L. Zhang and V. Yang. "Flow dynamics and mixing of a transverse jet in crossflow - Part 1: Steady crossflow". In: *Journal of Engineering for Gas Turbines and Power* 139.8 (2017), pp. 1–14. DOI: 10.1115/1.4035808. URL: https://doi.org/10.1115/1.4035808.

[175] L. Zhang and V. Yang. "Flow dynamics and mixing of a transverse jet in crossflow - Part 2: Oscillating crossflow". In: *Journal of Engineering for Gas Turbines and Power* 139.8 (2017), pp. 1–13. DOI: 10.1115/1.4035809. URL: https://doi.org/10.1115/1.4035809.

[176] J. Ziefle and L. Kleiser. "Large-eddy simulation of a round jet in crossflow". In: *American Institute of Aeronautics and Astronautics Journal* 47.5 (2009), pp. 1158–1172. ISSN: 0001-1452. DOI: 10.2514/1.38465. URL: https://doi.org/10.2514/1.38465.

Appendix A

Reduced scale mathematical calculations

This document contains all the preliminary calculations for both the experimental and numerical simulation work in the research.

A.1 Numerical Calculations for a Real-Scale Exhaust Stack

The following calculations are based on a real exhaust stack with a 160 MW Siemens V94.2 gas turbine and its superseded model Siemens SGT5-2000E gas turbine [126, 150]. Furthermore, Siemens [150] provides data sheets for the performance characteristics of their industrial simple cycle gas turbines. It should be noted that Siemens provide a wide range of industrial gas turbines for power generation with simple cycle power outputs ranging from 4 MW to 593 MW [150]. For range of gas turbines offered by Siemens [150], the temperature of the exhaust flow varies from 430 °C-680 °C. Similarly, depending on the gas turbines the exhaust mass flow rate also varies from 15.4 kg/s-1050 kg/s.

Table A.1: Parameters for a typical exhaust stack for an OCGT

Description	Parameter	Value	Units
Temperature in duct	T_j	809.15	K
Duct diameter	D_j	6	m
Heat capacity ratio in duct	γ_j	1.357	-
Ideal gas constant in duct	R_{air}	287.0586	$\text{J/kg} \cdot \text{K}$
Dynamic viscosity in duct	μ_j	3.9288×10^{-5}	$\text{N} \cdot \text{s/m}^2$
Exhaust flow	$\dot{M}_j$	558	kg s^{-1}
Temperature in cross-flow	T_{cf}	300.15	K
Heat capacity ratio in cross-flow	γ_{cf}	1.4	-
Dynamic viscosity in cross-flow	μ_{cf}	1.846×10^{-5}	$\text{N} \cdot \text{s/m}^2$
Speed of sound in cross-flow	c_{cf}	347.24	m s^{-1}
Minimum velocity in cross-flow (based on minimum average from www.bom.gov.au)	$u_{cf,\text{min}}$	1.67	m s^{-1}

Minimum cross-flow momentum flux ratio (wind speeds can exceed this ratio, but will be neglected)	$r_{cf,\max}$	3	-
Atmospheric pressure	p_{atm}	101325	Pa
Duct height	H_{duct}	60	m
Maximum acoustic frequency	$f_{\max}$	100	Hz
Minimum acoustic frequency	$f_{\min}$	16	Hz

A.1.1 Heated Stack Speed of Sound

The speed of sound in the duct will be dependent on the maximum desired temperature in the OCGT exhaust stack, 809.15 K.

$c_j = \sqrt{\gamma_j R_{air} T_j}$

$c_j = 561.4224\,\text{m/s}$

A.1.2 Air Density (Ideal Gas Formulation)

These calculations are for the density in the exhaust duct and cross-flow.

A.1.2.1 Heated Stack Air Density

The density of the gas in the stack will be dependent on the temperature based on the performance of the gas turbine.

$\rho_j = \frac{p_{atm}}{R_{\text{air}} T_j}$

$\rho_j = 0.4362\,\text{kg/m}^3$

A.1.2.2 Cross-Flow Air Density

The cross-flow air density is based on the cross-flow temperature.

$\rho_{cf} = \frac{p_{atm}}{R_{\text{air}} T_{cf}}$

$\rho_{cf} = 1.1766\,\text{kg/m}^3$

A.1.3 Exhaust Stack Jet Speed

The jet speed for the OCGT exhaust stack is dependent on the exhaust temperature and exhaust mass flow from the turbine.

$\dot{M} = \frac{\pi {D_j}^2 u_j \rho_j}{4}$

$u_j = \frac{4\dot{M}}{\pi {D_j}^2 \rho_j}$

$u_j = 45.2402\,\mathrm{m/s}$

It should be noted that in the above calculation the duct diameter chosen was the outer diameter of a typical exhaust stack, but the calculation should use the inner diameter of the exhaust stack. By taking into consideration the thickness of the exhaust stack and the acoustic tiles or lining, D_j would be closer to 5.7 m.

$\dot{M} = \frac{\pi {D_j}^2 u_j \rho_j}{4}$

$u_j = \frac{4\dot{M}}{\pi {D_j}^2 \rho_j}$

$u_j = 50.1277\,\mathrm{m/s}$

A.1.4 Mach Number

The Mach number for the exhaust duct is dependent on the exhaust flow velocity and calculated previously, there could be two different Mach numbers depending on the definition of the duct diameter.

$M_j = \frac{u_j}{c_j}$

$M_j = 0.0806$

$M_j = \frac{u_j}{c_j}$

$M_j = 0.0893$

The Mach number for the jet is $M_j \approx 0.08 - 0.09$ and subsequent analysis in the thesis will use a rounded value of $M_j = 0.1$.

A.1.5 Jet Reynolds Number

The following is the Reynolds number for the OCGT exhaust stack.

$$\mathrm{Re}_j = \frac{\rho_j u_j D_j}{\mu_j}$$
$$\mathrm{Re}_j = 3.1723 \times 10^6$$

A.1.6 Maximum Cross-Flow Velocity Ratio

$$R_{\min} = \sqrt{\frac{\rho_j u_j^2}{\rho_{cf} u_{cf,\min}^2}}$$
$$R_{\min} = 20.4296$$

A.1.7 Minimum Cross-Flow Velocity

$$R_{\min} = \sqrt{\frac{\rho_j u_j^2}{\rho_{cf} u_{cf,\max}^2}}$$
$$u_{cf,\max} = \sqrt{\frac{\rho_j u_j^2}{\rho_{cf} R_{\min}^2}}$$
$$u_{cf,\max} = 11.3540\,\mathrm{m/s}$$

A.1.8 Maximum Cross-Flow Momentum Flux Ratio

The maximum cross-flow momentum flux ration is based on the minimum cross-flow velocity.

$$R_{\max} = \sqrt{\frac{\rho_j u_j^2}{\rho_{cf} u_{cf,\min}^2}}$$
$$R_{\max} = 18.2764$$

A.1.9 OCGT Duct Cut on Frequency

$$f_{\mathrm{co}} = 0.586 \frac{c_j}{D_j}$$
$$f_{\mathrm{co}} = 56.7307\,\mathrm{Hz}$$

A.1.10 Acoustic Limits for OCGT Exhaust Stacks

This section calculates the non-dimensional frequencies (ka) for the problematic region. From acoustic consultants and the literature the problematic region is $f = 16.5\,\mathrm{Hz}$ to $100\,\mathrm{Hz}$. The following calculations will use $D_j = 5.7\,\mathrm{m}$.

$ka_{\min} = \frac{\pi f_{\min} D_j}{c_j}$
$ka_{\min} = 0.5263$
$ka_{\max} = \frac{\pi f_{\max} D_j}{c_j}$
$ka_{\max} = 3.1896$

A.2 AWT Non-Isothermal Experimental Testing

The following parameters and calculations were conducted for experimental testing in the Adelaide Wind Tunnel. These calculations are based on the duct diameter 0.0476 m. It should be taken into consideration that the conditions derived in Table A.2 were from calculations based on A.1. Values for the jet Mach number and jet temperature were rounded to $M_j = 0.1$ and 500 °C, for simplicity, respectively.

Table A.2: Parameters for experimental testing in AWT

Description	Parameter	Value	Units
Max temperature in duct	T_j	773.15 K	
Mach number in duct	M_j	0.1	-
Duct diameter	D_j	0.0476	m
Heat capacity ratio in duct	γ_j	1.357	-
Ideal gas constant in duct	R_{air}	287.0586	$\text{J/kg} \cdot \text{K}$
Dynamic viscosity in duct	μ_j	3.6400×10^{-5}	$\text{N} \cdot \text{s/m}^2$
Maximum blower volumetric flow rate at 20 °C	$Q_{\max}$	3.9	m^3/min
Frequency converter blower speed factor	FC_{factor}	1.2	-
Temperature in cross-flow	T_{cf}	300.15	K
Heat capacity ratio in cross-flow	γ_{cf}	1.4	-
Specific heat of ambient air	C_p	1006	$\text{N m kg}^{-1}\text{K}^{-1}$
Dynamic viscosity in cross-flow	μ_{cf}	1.846×10^{-5}	$\text{N} \cdot \text{s/m}^2$
Cross-flow momentum flux ratio	r_{cf}	$5 - 10$	-
Atmospheric pressure	p_{atm}	101325	Pa
Heating power from each air heater	$P_{\text{individual}}$	16	kW
Maximum heating power from both heaters	$P_{\max}$	32	kW

Duct height	H_{duct}	0.476	m
Decking height	H_{deck}	0.4	m
Experimental rig height	H_{rig}	0.908	m
Total rig height with array	H_{total}	2.3304	m
Inner microphone array radius	$r_{\text{array},i}$	$14D_j$	-
Outer microphone array radius	$r_{\text{array},o}$	$28D_j$	-
Wind tunnel open jet section dimensions	$H_{\text{jet}} \times W_{jet}$	2×2	m $\times$ m
Wind tunnel height	H_{tunnel}	4.2	m
Wind tunnel width	W_{tunnel}	3.5	m
Minimum Helmholtz number	ka_{max}	0.5263	-
Maximum Helmholtz number	ka_{max}	3.1896	-
Desired acquisition Frequency	f_{desire}	10000	Hz
FFT length	$NFFT$	2^{12}	-
Number of averages	N_{averages}	128	-

A.2.1 Speed of Sound

These calculations are for the speed of sound in the duct with varying temperature options and cross-flow.

A.2.1.1 Heated Stack Speed of Sound

The speed of sound in the duct will be dependent on the maximum desired temperature in the duct.

$c_{j,\text{min}} = \sqrt{\gamma_j R_{\text{air}} T_{j,\text{min}}}$

$c_{j,\text{min}} = 548.79\,\text{m/s}$

However, CFD, assumes that the heat capacity ratio of air is constant. In which, the speed of sound may be over predicted, as follows. The speed of sound will be assumed in further research to have a heat capacity ratio constant with ambient air. The experimental testing will assume the heat capacity ratio is varying with temperature.

A.2.1.2 Cross-Flow Speed of Sound

$c_{cf} = \sqrt{\gamma_{cf} R_{\text{air}} T_{cf}}$
$c_{cf} = 347.24\,\text{m/s}$

A.2.2 Air Density (Ideal Gas Formulation)

These calculations are for the density in the duct and cross-flow.

A.2.2.1 Heated Stack Air Density

The density of the gas in the stack will be dependent on the temperature achievable by the blower.
$\rho_j = \frac{p_{atm}}{R_{\text{air}} T_{j,\text{min}}}$
$\rho_j = 0.4565\,\text{kg/m}^3$

A.2.2.2 Cross-Flow Air Density

$\rho_{cf} = \frac{p_{atm}}{R_{\text{air}} T_{cf}}$
$\rho_{cf} = 1.1766\,\text{kg/m}^3$

A.2.3 Jet Speed

The jet speed will vary in the stack, depending on temperature.
$M_j = \frac{u_j}{c_j}$
$u_j = M_j c_j$
$u_j = 54.879\,\text{m/s}$

A.2.4 Jet Reynolds Number

$\text{Re}_j = \frac{\rho_j u_j D_j}{\mu_j}$
$\text{Re}_j = 3.2761 \times 10^4$

A.2.5 Cross-Flow Velocity

In the experiments, the exhaust gas flow will remain at a constant speed and temperature for all the experiments. The parameter that will be varied for the cross-flow sensitivity analysis will be the cross-flow velocity from the wind tunnel. The following calculations will calculate the upper and lower boundary of the cross-flow velocity. Each section will be based on the different temperatures in the duct.

A.2.5.1 Cross-Flow Velocity Based on Desired Duct Temperature

The following calculations will be based on the desired duct temperature.

$$r_{\min} = \sqrt{\frac{\rho_j u_j^2}{\rho_{cf} u_{cf,\max}^2}}$$

$$u_{cf,\max} = \sqrt{\frac{\rho_j u_j^2}{\rho_{cf} r_{\min}^2}}$$

$$u_{cf,\max} = 5.9970\,\mathrm{m/s}$$

$$r_{\max} = \sqrt{\frac{\rho_j u_j^2}{\rho_{cf} u_{cf,\min}^2}}$$

$$u_{cf,\min} = \sqrt{\frac{\rho_j u_j^2}{\rho_{cf} r_{\max}^2}}$$

$$u_{cf,\min} = 3.4183\,\mathrm{m/s}$$

These cross-flow velocities that were calculated are the upper and lower bound of the cross-flow velocities that will be tested experimentally, which are $6.8366\,\mathrm{m/s}$ and $3.4183\,\mathrm{m/s}$, respectively.

A.2.6 Cross-Flow Reynolds Number Based on Flow Across the Duct

The following calculations for the Reynolds number are based on the duct diameter.

$$\mathrm{Re}_{cf,\min} = \frac{\rho_{cf} u_{cf,\min} D_j}{\mu_{cf}}$$

$$\mathrm{Re}_{cf,\min} = 1.1068 \times 10^4$$

$$\mathrm{Re}_{cf,\max} = \frac{\rho_{cf} u_{cf,\max} D_j}{\mu_{cf}}$$

$$\mathrm{Re}_{cf,\max} = 1.9417 \times 10^4$$

A.2.7 Maximum Jet Speed Based on AIRPACK Blower Capabilities

This set of calculations are for the maximum velocity possible in the duct, based on the original blower design specifications. The calculations will be based on the mass-flow continuity equation. The first set of calculation will also assume the duct in the system is based on the desired temperature with subsequent calculations based on the achievable realistic temperature.

$\dot{m}_{\text{inlet}} = \dot{m}_{\text{outlet}}$

$\rho_{\text{ambient}}\dot{Q}_{\text{max}} = \rho_j \dot{Q}_j$

$\frac{\dot{Q}_{\text{max}} p_{atm}}{R_{\text{air}} T_{\text{ambient}}} = \rho_j u_j A_j$

$u_j = \frac{\dot{Q}_{\text{max}} p_{atm}}{R_{\text{air}} T_{\text{ambient}} \rho_j A_j}$

$u_j = 94.1442\,\text{m}\,\text{s}^{-1}$

The next set of calculations are based on the capacity of the variable frequency driver to increase the flow rate from the blower by 20%.

$\dot{m}_{\text{inlet}} = \dot{m}_{\text{outlet}}$

$1.2\rho_{\text{ambient}}\dot{Q}_{\text{max}} = \rho_j \dot{Q}_j$

$\frac{1.2\dot{Q}_{\text{max}} p_{atm}}{R_{\text{air}} T_{\text{ambient}}} = \rho_j u_j A_j$

$u_j = \frac{1.2\dot{Q}_{\text{max}} p_{atm}}{R_{\text{air}} T_{\text{ambient}} \rho_j A_j}$

$u_j = 112.9730\,\text{m}\,\text{s}^{-1}$

From these calculations the blower rate can be determined to meet the desired experimental speed in the duct.

$\dot{Q}_{\text{max}} = \frac{R_{\text{air}} T_{\text{ambient}} \rho_j A_j u_j}{p_{atm}}$

$\dot{Q}_{\text{max}} = 0.037\,89\,\text{m}^3/\text{s}$

$\dot{Q}_{\text{max}} = 2.2734\,\text{m}^3/\text{min}$

From this we can calculate the flow rate through each heater.

$\dot{Q}_{\text{heater}} = Q_{\text{max}}/4$

$\dot{Q}_{\text{heater}} = 0.5684\,\text{m}^3/\text{min}$

The next set of calculations will be the maximum operable speed from the blower at ambient condition.

$\dot{m}_{\text{inlet}} = \dot{m}_{\text{outlet}}$
$1.2\rho_{\text{ambient}}\dot{Q}_{\text{max}} = \rho_{cf}\dot{Q}_j$
$\frac{\dot{Q}_{\text{max}} p_{atm}}{R_{\text{air}} T_{\text{ambient}}} = \rho_{cf} u_j A_j$
$u_j = \frac{1.2\dot{Q}_{\text{max}}}{A_j}$
$u_j = 25.5507\,\text{m}\,\text{s}^{-1}$
It can be seen that the reduction in duct diameter will lead to an increase in the possible flow speed in the duct.

A.2.8 Heater Parameters

In order to meet the requirements of the experiments, the maximum power required will be calculated. This will be followed by a calculation for the maximum achievable temperature.

A.2.8.1 Power Required

The following is the maximum power necessary for heating the fluid from the blower at maximum output.
$P_{\text{max}} = 1.2\rho_{cf}\dot{Q}_{\text{max}} C_p \Delta T$
$P_{\text{max}} = 43.6265\,\text{kW}$

A.2.8.2 Maximum Possible Duct Temperature at Maximum Flow Rate

The following calculations will assume that the blower will operate at maximum speed and the heater is at maximum power output.
$P_{\text{max}} = 1.2\rho_{cf}\dot{Q}_{\text{max}} C_p \Delta T$
$\Delta T = \frac{P_{\text{max}}}{1.2\rho_{cf}\dot{Q}_{\text{max}} C_p}$
$\Delta T = 346.7768\,^{\circ}\text{C}$
$T_{j,\text{max}} = 386.7768\,^{\circ}\text{C}$
This temperature will show that there is a definitive temperature gradient in the shear layer that will cause refraction of sound. However, it does not meet the desired thermal gradients, as seen in real exhaust stacks. The next set of calculations will be based on $M = 0.1$.

$P_{\max} = \rho_{cf} \dot{Q_{\max}} C_p \Delta T$
$P_{\max} = 24.1612\,\text{kW}$
From the calculations it can be seen that in an ideal system, the heaters can achieve the desired temperature. However, this will need to be evaluated again, as heat loss mechanisms will need to be considered.

A.2.9 Experimental Duct Cut-On Frequency

The following is based on the equation from the literature [25, 97] to calculate the cut-on frequency in a round duct :
$f_{\text{co}} = 0.586 \frac{c_j}{D_j}$
$f_{\text{co}} = 6617.0975\,\text{Hz}$

A.2.10 Experimental Acoustic Limits

The experimental acoustics limits were determined based on the maximum Helmholtz number for the simulation and the minimum frequency possible with temporal gating.

A.2.10.1 Maximum Experimental Frequency

The maximum experimental acoustic frequency is determined by the maximum Helmholtz number commonly seen in exhaust stacks. This Helmholtz number is typically $ka_{\max} = 3.1896$.
$ka_{\max} = \frac{2\pi f_{\max} D_j}{2c_j}$
$f_{\max} = \frac{c_j ka_{\max}}{D_j \pi}$
$f_{\max} = 11\,705.381\,89\,\text{Hz}$

A.2.10.2 Minimum Experimental Frequency

The minimum experimental acoustic frequency is determined by the minimum Helmholtz number commonly seen in exhaust stacks. This Helmholtz number is typically $ka_{\min} = 0.5263$.

$ka_{\min} = \frac{2\pi f_{\min} D_j}{2c_j}$
$f_{\min} = \frac{c_j ka_{\min}}{D_j \pi}$
$f_{\min} = 1931.4467\,\text{Hz}$

A.2.10.3 Minimum Experimental Frequency from Gating

The height of the AWT can limit the low frequency performance of the measurements with temporal gating. The height of the AWT ceiling is 4.2 m.
The calculations are based on the wind tunnel height of 4.2 m.
$\Delta T_{\min} = \frac{2(H_{\text{tunnel}} - H_{\text{total}})}{c_{cf}}$
$\Delta T_{\min} = 0.010\,77\,\text{s}$
$f_{\min} = \frac{1}{\Delta T_{\min}}$
$f_{\min} = 92.8647\,\text{Hz}$
$ka_{\min} = \frac{2\pi f_{\min} D_j}{2c_j}$
$ka_{\min} = 0.02701$
$\therefore$ From the calculations it is clear the minimum ka and f are 0.02701 and 92.8647 Hz.

A.2.11 Acoustic Data Acquisition and Signal Processing

The following are calculations based on the data acquisition capabilities of the NI DAQ and the required acoustic frequencies based on the exhaust stack used in the industry.

A.2.11.1 Sampling Frequency

The sampling frequency is based on the desired frequency multiplied by a factor to take into consideration the aliasing and the anti-aliasing filter.
$f_s = 2.56 f_{\text{desire}}$
$f_s = 25\,600\,\text{Hz}$

A.2.11.2 FFT Bin Width

The FFT bin width is the resolution of the processed signal in the frequency domain.
$\Delta f = \frac{f_s}{NFFT}$
$\Delta f = 6.25\,\text{Hz}$

A.2.11.3 Total Time for Acoustic Acquisition

The time it takes for a single full power spectrum to be achieved will be calculated.
$\Delta T = \frac{1}{\Delta f}$
$\Delta T = 0.16\,\text{s}$
The total time necessary for acoustic data acquisition is based on the number of averages necessary for adequate coherence.
$T = N_{\text{averages}} \Delta T$
$T = 20.48\,\text{s}$

A.2.11.4 Maximum Number of Acoustic Averages

The total duration for the sampling is $T_{\text{total}} = 120\,\text{s}$ and the overlap for the power spectrum is $n_{\text{overlap}} = 50\%$.
$N_{\text{averages}} = \frac{T_{\text{total}}}{n_{\text{overlap}} \Delta T}$
$N_{\text{averages}} = 1500$

A.3 Numerical Simulations - Non-Isothermal Ground Level JICF

This section of the calculation will be for Chapter 3 and will be the parameters for the non-isothermal ground level JICF. These parameters will be similar to the parameters conducted in the experiments.

Table A.3: Parameters for non-isothermal ground level JICF numerical simulations

Description	Parameter	Value	Units

Temperature in duct	T_j	773.15	K
Heat capacity ratio in duct	γ_j	1.357	-
Ideal gas constant in duct	R_{air}	287.0586	$\text{J/kg} \cdot \text{K}$
Dynamic viscosity in duct	μ_j	3.6400×10^{-5}	$\text{N} \cdot \text{s/m}^2$
Density in duct	ρ_j	0.4565	kg/m^3
Speed of sound in duct	c_j	548.76	m s^{-1}
Mach number in duct	M_j	0.1	-
Velocity in duct	u_j	54.876	m s^{-1}
Reynolds number in duct	Re_j	3.4963×10^4	-
Duct diameter	D_j	0.0476	m
Maximum Helmholtz number in the duct (typical value is 3.42)	$ka_{\max}$	1	-
Minimum Helmholtz number in the duct (typical value is 0.5354)	$ka_{\min}$	0.3	-
Temperature in cross-flow	T_{cf}	300.15	K
Heat capacity ratio in cross-flow	γ_{cf}	1.4	-
Dynamic viscosity in cross-flow	μ_{cf}	1.846×10^{-5}	$\text{N} \cdot \text{s/m}^2$
Density in cross-flow	ρ_{cf}	1.1766	kg/m^3
Speed of sound in cross-flow	c_{cf}	347.24	m s^{-1}
Cross-flow momentum flux ratio	r_{cf}	$5 - 10$	-
Maximum velocity in cross-flow	$u_{cf,\max}$	5.9970	m s^{-1}
Minimum velocity in cross-flow	$u_{cf,\min}$	3.4183	m s^{-1}
Boundary layer 80 displacement thickness	$\delta_{80\%,cf}$	$1.32D_j$	-
Atmospheric pressure	p_{atm}	101325	Pa
Courant–Friedrichs–Lewy number	CFL	< 1	-
Stream-wise total domain length	L_x	$56D_j$	-
Span-wise total domain length	W_y	$48D_j$	-
Height total domain length	H_z	$48D_j$	-
Duct length	L_j	$10D_j$	-

A.3.1 Cross-Flow Reynolds Number

This Reynolds number will be based on the inlet cross-section minimum length, $L_{cf} = 64D_j$.

$\text{Re}_{cf} = \frac{\rho_{cf} u_{cf} L_{cf}}{\mu_{cf}}$

$\text{Re}_{cf} = 1164442.70$

Cross-flow Reynolds number can also be calculated using the distance travelled along the plate, until it impedes the jet. This is using $L_{cf} = 33D_j$.

$\mathrm{Re}_{cf} = \frac{\rho_{cf} u_{cf} L_{cf}}{\mu_{cf}}$

$\mathrm{Re}_{cf} = 600415.77$

A.3.2 Cross-Flow Mach Number

$M_{cf} = \frac{u_{cf}}{c_{cf}}$

$M_{cf} = 0.01727$

A.3.3 Cross-Flow Boundary Layer Displacement Thickness

$\delta_{80\%,cf} = 1.32D_j$

$\delta_{80\%,cf} = 0.063\,\mathrm{m}$

A.3.4 Numerical Simulation Duct Cut on Frequency

$f_{\mathrm{co}} = 0.586\frac{c_j}{D_j}$

$f_{\mathrm{co}} = 6756.11\,\mathrm{Hz}$

A.3.5 Minimum Acoustic Frequency for Simulation

The minimum Helmholtz number chosen for analysis is in a region where it is possible to measure experimentally in the AWT and well below the cut-on frequency of the duct. This is to ensure that acoustic spreading is spherical at these low Helmholtz numbers.

$ka_{\mathrm{min}} = \frac{2\pi f_{\mathrm{min}} D_j}{2c_j}$

$f_{\mathrm{min}} = \frac{c_j ka_{\mathrm{min}}}{D_j \pi}$

$f_{\mathrm{min}} = 1100.9577\,\mathrm{Hz}$

A.3.6 Maximum Acoustic Frequency for Simulation

Due to the limited computational resources presented in the research, a maximum Helmholtz number of 1 will be explored.

$ka_{\max} = \frac{2\pi f_{\min} D_j}{2c_j}$
$f_{\max} = \frac{c_j ka_{\max}}{D_j \pi}$
$f_{\max} = 3669.8589\,\mathrm{Hz}$

A.3.7 First Layer Height for Cross-Flow Boundary Layer Resolution

The first layer height will be calculated using various equations.
$C_f = (2\log_{10}(\mathrm{Re}_{cf}) - 0.65)^{-2.3}$
$C_f = 0.006640$
$\tau_w = \frac{1}{2} C_f \rho_{cf} u_{cf}^2$
$\tau_w = 0.036\,54\,\mathrm{Pa}$
$u_* = \sqrt{\frac{\tau_w}{\rho_{cf}}}$
$u_* = 0.1762\,\mathrm{m\,s^{-1}}$
$\Delta y_{\text{first}} = \frac{y^+ \mu_{cf}}{\rho_{cf} u_*}$
$\Delta y_{\text{first}} = 8.9088 \times 10^{-5}\mathrm{m}$
Based on this calculation for the first layer height, there is an approximate calculation for the number of elements in the boundary layer.
$\text{Elements} = \frac{0.00594}{\Delta y_{\text{first}}}$
$\text{Elements} = 66.6756$

A.3.8 First Layer Height for Duct Boundary Layer Resolution

The first layer height will be calculated using various equations. The first solution assumes the free-stream velocity is the same as the bulk jet velocity.
$C_f = (2\log_{10}(\mathrm{Re}_j) - 0.65)^{-2.3}$
$C_f = 7.4088 \times 10^{-3}$
$\tau_w = \frac{1}{2} C_f \rho_j u_j^2$
$\tau_w = 5.0924\,\mathrm{Pa}$
$u_* = \sqrt{\frac{\tau_w}{\rho_j}}$
$u_* = 3.3400\,\mathrm{m\,s^{-1}}$

$\Delta y_{\text{first}} = \frac{y^+ \mu_j}{\rho_j u_*}$
$\Delta y_{\text{first}} = 2.3873 \times 10^{-5}\text{m}$

A.3.9 Fluid Dynamic CFL for Implicit

From the calculations thus far, the minimum element size and maximum velocity will be used for calculating the fluid dynamic Courant-Freidrichs-Lewy (CFL) number.
$CFL = \frac{u_j \times \Delta t_{\text{min}}}{\Delta x_{\text{min}}}$
$\Delta t_{\text{min}} = \frac{CFL \times \Delta x_{\text{min}}}{u_j}$
$\Delta t_{\text{min}} = 4.8685 \times 10^{-7}\text{s}$

A.3.10 Time for Transience in Implicit Simulation

In order to wash out the transient behaviour in the simulation, the simulation will be conducted for 50 cycles. This cycle is dependent on each time the cross-flow fluid passes through the cross-section of the duct. The minimum time step that will be used for all the simulations to achieve the highest *ka* resolution.
$t_{\text{trans}} = \frac{50 \times D_j}{\Delta u_{cf}}$
$t_{\text{trans}} = 0.6275\,\text{s}$
$\Delta t_{\text{step}} = \frac{t_{\text{trans}}}{\Delta t_{\text{min}}}$
$\Delta t_{\text{step}} = 1\,288\,962\,\text{steps}$
This solution will need to be reviewed again, as this task is not physically possible with the resources available.

A.3.11 Acoustic CFL for Explicit

The time step for the acoustic explicit simulations will be based on the acoustic CFL, $CFL_{\text{acoustics}} < 1$. This is to ensure, for every time step, that the fluid propagated will not surpass a single cell.

$$CFL_{\text{acoustics}} = \frac{u_j \Delta t_{\text{explicit}}}{\Delta x_{\text{min}}}$$
$$\Delta t_{\text{explicit}} = \frac{\Delta x_{\text{min}}}{CFL_{\text{acoustics}} c_j}$$
$$\Delta t_{\text{explicit}} = 4.8685 \times 10^{-8}\text{s}$$

A.3.12 Nodal Mesh Density for Acoustic Simulations

The number of elements per wavelength for the acoustic FEM simulations is important for accurate resolution of the acoustic wave. It is recommended by Howard and Cazzolato [77] that for quadratic elements (elements with mid-side nodes), six elements per wavelength are used. Therefore, the minimum elements size (x_{min}) would be calculated:

$$x_{\text{min}} = \frac{\lambda}{6}$$
$$x_{\text{min}} = \frac{c_{cf}}{6 \times f_{\text{max}}}$$
$$x_{\text{min}} = 0.015\,59\,\text{m}$$

However, due to the limitations with the number of nodes in the mesh, the minimum element size is $x_{\text{min}} = 0.024\,94\,\text{m}$. With this information the maximum recommended frequency can be calculated:

$$f_{\text{max}} = \frac{c_{cf}}{6 \times x_{\text{min}}}$$
$$f_{\text{max}} = 2293\,\text{Hz}$$
$$ka_{\text{max}} = 0.625$$

It should be noted that a maximum non-dimensional frequency, $ka_{\text{max}} = 0.625$, is calculated to be the recommended upper limit of the mesh [77]. However, it has been shown in Chapter 3 and Section C.10 that the acoustic FEM code can adequately model sound up to $ka_{\text{max}} = 0.8$.

A.3.13 Perfectly Matched Layers Minimum Frequency

The minimum acoustic frequency for attenuation with PML elements can be calculated:

$$f_{\text{min}} = \frac{c_{cf}}{16 \times D_j}$$
$$f_{\text{min}} = 450.7\,\text{Hz}$$

$$ka_{\min} = \frac{\pi f_{\min} D_j}{c_j}$$
$$ka_{\min} = 0.1228$$

Appendix B

Mathematical formulation for sound propagation with finite element model

The numerical acoustic simulations were conducted with a 3-dimensional (3-D) linearised acoustic wave equation method that is discretised and solved with the FEM package ANSYS Mechanical [8, 9]. This section will discuss the governing equations that were used in the acoustic simulations, as well as a brief outline in discretisation of the model to be solved with FEM. Two different acoustic wave equations are available in ANSYS Mechanical; a stationary medium case and non-stationary medium with mean fluid flow. The formulation for the acoustic wave equation through a stationary medium used by ANSYS Mechanical ANSYS [8, 9], will be discussed first, and it is based on the derivation in literature by Bergmann [24], Pierce [131], and Ross and Chivers [138]. The second derivation is for the acoustic wave equation in a non-stationary medium with mean fluid flow, and it is similar to the work by Ostashev et al. [129] and Pierce [131], which differs slightly with the inclusion of a source term in the formulation, and the final solution for the FEM solver is in the frequency domain.

B.1 Stationary acoustic wave equation

The following formulation of the acoustic wave equation for the numerical work in this research uses a number of common assumptions. Namely, the fluid is compressible with relatively no large changes in the bulk pressure. The body force and the effects of gravity will be ignored in the acoustic wave equation formulation. The propagating medium is 'frozen' or stationary in time, with only small perturbations in acoustic pressure taken into consideration. It is also assumed that the fluid is irrotational. Additionally, it is assumed that the gas is ideal, inviscid, adiabatic and reversible. Furthermore, the following derivation in this appendix is a first order approximation of the linearised acoustic wave equation with the second and higher order terms neglected.

The following is a 3-D formulation in Cartesian coordinates, with four governing equations used for acoustic modelling; they are the flow continuity equation, Navier-Stokes equations for fluid momentum, conservation of entropy, and equa-

tion of state, respectively given by:

$$D_t(\rho) + \nabla \cdot (\rho \vec{v}) = \rho Q, \tag{B.1}$$

$$\rho D_t(v) + \nabla p = \frac{\vec{F}}{\rho}, \tag{B.2}$$

$$D_t(s) = 0, \tag{B.3}$$

$$p = IP(\rho, s), \tag{B.4}$$

where ρ is the density, t is time, $\vec{v}$ is the velocity vector, Q is the mass source, p is the pressure, $\vec{F}$ is the body force, $D_t = \frac{\partial}{\partial t} + \vec{v} \cdot \nabla$ is the material derivative (also known as the substantial derivative or what Pierce [131] refers to as the time derivative following the ambient flow[1]) and IP is the relation function. In Equations (B.1) and (B.2), ρ, p, and $\vec{v}$ are spatially dependant on position $\vec{x} = (x, y, z)$. Furthermore, the assumption of a 'frozen' or stationary propagating medium leads to the assumption that ρ is time-invariant or the time-averaged statistics is used. As discussed previously it is assumed that there are no body forces ($\vec{F} = 0$).

Equations (B.1) to (B.4) can be further simplified, based on the assumptions outlined above and linearised to form the following states:

$$\rho = \rho_0(x, y, z) + \epsilon \rho'(x, y, z, t), \tag{B.5a}$$

$$p = p_0(x, y, z) + \epsilon p'(x, y, z, t), \tag{B.5b}$$

$$s = s_0(x, y, z) + \epsilon s'(x, y, z, t), \tag{B.5c}$$

$$\vec{v} = \vec{v_0}(x, y, z) + \epsilon \vec{v}'(x, y, z, t), \tag{B.5d}$$

[1] An important note is that in different literature the material derivative is expressed in different forms with ANSYS Mechanical using $\frac{D_0}{dt}$ [8, 9], Bergmann [24] using $\frac{D}{Dt}$, Ostashev et al. [129] and Ross and Chivers [138] using $\frac{d}{dt}$, and Pierce [131] using D_t, which is the notation used in this appendix.

$$Q \approx \epsilon Q(x, y, z, t), \tag{B.5e}$$

where the parameters with the subscript 0 represents the local steady-state or time-averaged quantity, ϵ is the small perturbation in the quantity, and the $'$ notation represents the unsteady perturbation in that particular quantity. The word local refers to the time-averaged value at position $\vec{x}$. It should be noted that for the rest of the derivation all unsteady terms with fluctuating components will be replaced with subscript a, to represent the unsteady acoustic perturbation. The linearisation of Equations (B.1), (B.2), and B.4 are as follows

$$D_t(\rho_0(\vec{x})) + \rho_a(\vec{x}) \cdot \nabla \vec{v_0}(\vec{x}) + \rho_0(\vec{x}) \nabla \cdot \vec{v_a}(\vec{x}) + \vec{v_a}(\vec{x}) \cdot \nabla \rho_0(\vec{x}) = \rho_0(\vec{x}) Q(\vec{x}), \tag{B.6}$$

$$D_t(\vec{v_a}(\vec{x})) + \vec{v_a}(\vec{x}) \cdot \nabla \vec{v_0}(\vec{x}) + \frac{1}{\rho_0(\vec{x})} \nabla p_a(\vec{x}) - \frac{\rho_a(\vec{x})}{\rho_0(\vec{x})^2} \nabla p_0(\vec{x}) = 0, \tag{B.7}$$

$$D_t(s_a(\vec{x})) + \vec{v_a}(\vec{x}) \cdot \nabla s_0(\vec{x}) = 0, \tag{B.8}$$

where $D_{t,0} = \frac{\partial}{\partial t} + \vec{v_0}(\vec{x}) \cdot \nabla$ is the material derivative (or substantial derivative with respect to the local steady-state velocity or bulk velocity, v_0). Equations (B.6), (B.7), and (B.8) are identical to the linearised equations presented in Pierce [131] (no source terms in the proof) and Ostashev et al. [129] (with source terms), with the exception of different notation between the derivation presented in this appendix and the reference listed.

Linearisation of the equation of state or Equation (B.4), can be further elaborated:

$$dp(\rho(\vec{x}), s(\vec{x})) = \left(\frac{\partial IP(\rho(\vec{x}), s(\vec{x}))}{\partial \rho(\vec{x})} \right)_s d\rho + \left(\frac{\partial IP(\rho(\vec{x}), s(\vec{x}))}{\partial s(\vec{x})} \right)_\rho ds, \tag{B.9}$$

$$c^2(\vec{x}) = \left(\frac{\partial IP}{\partial \rho(\vec{x})} \right)_\rho ds, \tag{B.10}$$

$$dp(\rho(\vec{x}), s(\vec{x})) = c^2(\vec{x}) d\rho(\vec{x}) \implies \frac{d(\rho(\vec{x}), s(\vec{x}))}{dt} = c^2(\vec{x}) \frac{d\rho(\vec{x})}{dt}, \tag{B.11}$$

$$c^2(\vec{x}) \frac{d\rho(\vec{x})}{dt} = c^2(\vec{x}) [\rho(\vec{x}) Q(\vec{x}) - \rho(\vec{x}) \nabla \cdot \vec{v}(\vec{x})], \tag{B.12}$$

$$\frac{dp(\rho(\vec{x}), s(\vec{x}))}{dt} + c^2(\vec{x})\rho(\vec{x})\nabla \cdot \vec{v}(\vec{x}) = c^2(\vec{x})\rho(\vec{x})Q(\vec{x}). \tag{B.13}$$

The linearised states for $\rho(\vec{x})$ and $s(\vec{x})$ are shown in Equations (B.5a) and (B.5c), and can be substituted into Equation (B.10) to form

$$c^2(\vec{x}) = \frac{\partial IP(\rho_0(\vec{x}) + \rho_a(\vec{x}), s_0(\vec{x}) + s_a(\vec{x}))}{\partial \rho_a(\vec{x})}, \tag{B.14}$$

$$\begin{aligned} c^2(\vec{x}) = \frac{\partial}{\partial \rho_a(\vec{x})} \Bigg(& IP(\rho_0(\vec{x}), s_0(\vec{x})) + \rho_a(\vec{x}) \frac{\partial IP(\rho_0(\vec{x}), s_0(\vec{x}))}{\partial \rho_a(\vec{x})} + \\ & s_a(\vec{x}) \frac{\partial IP(\rho_0(\vec{x}), s_0(\vec{x}))}{\partial s_a(\vec{x})} \Bigg), \end{aligned} \tag{B.15}$$

$$c^2(\vec{x}) = c_0^2(\vec{x}) + \frac{\partial}{\partial \rho_a(\vec{x})} \left(\frac{\partial IP(\rho_0(\vec{x}), s_0(\vec{x}))}{\partial \rho_a(\vec{x})} \rho(\vec{x}) + \frac{IP(\rho_0(\vec{x}) s_0(\vec{x}))}{\partial s_a(\vec{x})} s_a(\vec{x}) \right), \tag{B.16}$$

$$c^2(\vec{x}) = c_0^2(\vec{x}) + \rho_a(\vec{x}) \frac{\partial^2 IP(\rho_0(\vec{x}), s_0(\vec{x}))}{\partial \rho_a^2(\vec{x})} + s_a(\vec{x}) \frac{\partial^2 IP(\rho_0(\vec{x}), s_0(\vec{x}))}{\partial \rho_a(\vec{x}) \partial s_a(\vec{x})}, \tag{B.17}$$

$$c^2(\vec{x}) = c_0^2(\vec{x}) + \left\{ \rho_a(\vec{x}) \frac{\partial^2 IP(\rho_0(\vec{x}), s_0(\vec{x}))}{\partial \rho_a^2(\vec{x})} + s_a(\vec{x}) \frac{\partial^2 IP(\rho_0(\vec{x}), s_0(\vec{x}))}{\partial \rho_a(\vec{x}) \partial s_a(\vec{x})} \right\}, \tag{B.18}$$

The term in the parenthesis represents the variation in the speed of sound due to the passage of the wave. It is often noted that:

$$(c_0^2(\vec{x}))' = \left\{ \rho_a(\vec{x}) \frac{\partial^2 IP(\rho_0(\vec{x}), s_0(\vec{x}))}{\partial \rho_a^2(\vec{x})} + s_a(\vec{x}) \frac{\partial^2 IP(\rho_0(\vec{x}), s_0(\vec{x}))}{\partial \rho_a(\vec{x}) \partial s_a(\vec{x})} \right\}, \tag{B.19}$$

which leads to the following linearised equation for the speed of sound:

$$c^2(\vec{x}) = c_0^2(\vec{x}) + (c_0^2(\vec{x}))'. \tag{B.20}$$

Let us now introduce the perfect gas assumption, whereby the equation of state is given by:

$$p(\rho_a(\vec{x}), s_a(\vec{x})) = A\rho^\gamma(\vec{x}) e^{\frac{(\gamma-1)s(\vec{x})}{r}}, \tag{B.21}$$

where A is a constant, $\gamma = \frac{c_p}{c_v}$ is the ratio of specific heats, c_p is the specific heat capacity at constant pressure, c_v is the specific heat capacity at constant volume,

$r = \frac{R}{M_0}$ is the specific gas constant, R is the universal gas constant, and M_0 is the molar mass. Using the perfect gas example the following expressions can be used:

$$c_0^2(\vec{x}) = p_0(\vec{x})\frac{\gamma}{\rho_0(\vec{x})}, \tag{B.22}$$

$$\left(\frac{\partial IP}{\partial s}\right)_{\rho_0} = \frac{(\gamma-1)}{\gamma}p_0(\vec{x}). \tag{B.23}$$

From the assumption of a perfect gas, Equation (B.19) can be further expanded to form

$$(c_0^2(\vec{x}))' = \left\{\left(\frac{\gamma(\gamma-1)}{\rho_0^2(\vec{x})}\right)\rho_a(\vec{x}) + \left(\frac{\gamma(\gamma-1)}{\rho_0(\vec{x})r}\right)s_a(\vec{x})\right\}p_0(\vec{x}). \tag{B.24}$$

Equation (B.13) with the perfect gas assumption can be linearised with Equations (B.5), and (B.20).[2]

$$\begin{aligned}\frac{d(p_0(\vec{x})+p_a(\vec{x}))}{dt} + (c_0^2(\vec{x})+c_a^2(\vec{x}))(\rho_0+\rho_a)(\nabla\cdot\vec{v_0}(\vec{x})+\nabla\vec{v_a}(\vec{x}))\\ = (c_0^2(\vec{x})+c_a^2(\vec{x}))(\rho_0(\vec{x})+\rho_a(\vec{x}))Q_a(\vec{x}).\end{aligned} \tag{B.25}$$

By expanding the previous equation and taking only the first order terms, one obtains:

$$\begin{aligned}D_{t,0}(p_a(\vec{x})) + \vec{v_a}(\vec{x})\nabla p_0(\vec{x}) + c_0^2(\vec{x})(\rho_0(\vec{x})\nabla\cdot\vec{v_a}(\vec{x}) + \rho_a(\vec{x})\nabla\cdot\vec{v_0}(\vec{x}))\\ +c_a^2(\vec{x})\rho_0(\vec{x})\nabla\cdot\vec{v_0}(\vec{x}) = c_0^2(\vec{x})\rho_0(\vec{x})Q(\vec{x}).\end{aligned} \tag{B.26}$$

This is the same as Equation (12) of Ostashev et al. [129].

In solving for the case of a inhomogeneous medium without mean flow ($\vec{v_0}(\vec{x}) = 0 \implies D_{t,0} = \frac{\partial}{\partial t}$) and using the previous assumptions, Equations (B.6), (B.7), and (B.26) can be manipulated to give the following:

$$\frac{\partial\rho_0(\vec{x})}{\partial t} + \nabla\cdot(\rho_0(\vec{x})\vec{v_a}(\vec{x})) = \rho_0(\vec{x})Q(\vec{x}), \tag{B.27}$$

$$\frac{\partial\vec{v_a}(\vec{x})}{\partial t} + \frac{1}{\rho_0(\vec{x})}\nabla p_a(\vec{x},t) = 0, \tag{B.28}$$

[2]It should be noted that the subscript a is the fluctuating term, where terms such as $(c_0{}^2)'$ has been replaced with $c_a{}^2$ for notation consistency in the rest of the appendix.

$$\frac{1}{\rho_0(\vec{x})c_0^2(\vec{x})}\frac{\partial p_a(\vec{x},t)}{\partial t} + \nabla \cdot \vec{v}_a(\vec{x}) = Q(\vec{x}), \tag{B.29}$$

where $\vec{v}_a(\vec{x})$ is the acoustic particle velocity, $c_0(\vec{x})$ is the local speed of sound, and $\rho_0(\vec{x})$ and the local fluid density. It should also be noted that $\vec{v}_a$ is dependent on position $\vec{x}$. Equations (B.29) and (B.28) can be further manipulated to reduce the two independent equations. If the partial derivative with respect to time is taken for Equation (B.29) and the grad is taken for Equation (B.28), then both equations have a common term, $\nabla \cdot \frac{\partial \vec{v}_a}{\partial t}$, which can be reduced to the following acoustic wave equation

$$\nabla \cdot \left(\frac{1}{\rho_0(\vec{x})}\nabla p_a(\vec{x},t)\right) - \frac{1}{\rho_0(\vec{x})c_0^2(\vec{x})}\frac{\partial^2 p_a(\vec{x},t)}{\partial t^2} = -\frac{\partial Q(\vec{x})}{\partial t}. \tag{B.30}$$

The time dependent Equation (B.30) is now given in terms of time dependent acoustic pressure. Equation (B.30) was first derived by Bergmann [24] and also later revisited by Ross and Chivers [138]. In order to solve for the harmonic normalised wavenumber, the following harmonically varying pressure formulation can be used:

$$p_a(\vec{x},t) = \mathrm{Re}[p_a(\vec{x})e^{j\omega t}], \tag{B.31}$$

where Re refers to the real component of the expression, $\omega = 2\pi f$ is the angular frequency of interest in rad/s and f is the linear frequency of interest in Hz. Equation (B.31) was also used by Ross and Chivers [138] and substituted into Equation (B.30), to represent the time dependent acoustic wave equation as a harmonic solution. This harmonic equation is also presented by Bergmann [24] and Ross and Chivers [138], and is given by:

$$\omega^2 \underbrace{\frac{p_a(\vec{x})}{\rho_0(\vec{x})c_0^2(\vec{x})}}_{M_p} + \underbrace{\nabla \cdot \left(\frac{1}{\rho_0(\vec{x})}\nabla p_a(\vec{x})\right)}_{K_p} = -j\omega \underbrace{Q(\vec{x})}_{f_p}, \tag{B.32}$$

where M_p is the term for the 'acoustic fluid mass' for acoustic pressure, K_p is the term for the 'acoustic stiffness' for acoustic pressure, and f_p is the 'acoustic fluid load' for the acoustic pressure.

The harmonically varying acoustic wave equation is suitable for modelling sound propagation through an ideal gas medium that is stationary with local $\rho_0(\vec{x})$ and $c_0(\vec{x})$. ANSYS Mechanical [8, 9] has stated that the local $\rho_0(\vec{x})$ and $c_0(\vec{x})$ can vary with position and this is consistent with assumption used in earlier work by Bergmann [24] and Ross and Chivers [138]. To account for temperature variations, the ideal gas law can be used to relate the speed of sound, $c_0(\vec{x})$, and density, $\rho_0(\vec{x})$, with local absolute temperature, $T(\vec{x})$. The following equations were used to calculate the $c_0(\vec{x})$ and $\rho_0(\vec{x})$ with the change in temperature, respectively:

$$c_0(\vec{x}) = \sqrt{\gamma R_{\text{gas}} T(\vec{x})}, \tag{B.33a}$$

$$\rho_0(\vec{x}) = \frac{P_{\text{state}}(\vec{x})}{R_{\text{gas}} T(\vec{x})}, \tag{B.33b}$$

where γ is the ratio for specific heats, R_{gas} is the universal gas constant, and P_{state} is the absolute pressure of the gas measured in atmosphere at a location $\vec{x}$. However, ANSYS [8, 9] uses a variation of Equations (B.33a) and (B.33b) with

$$c_0(\vec{x}) = c_{\text{ref}} \sqrt{\frac{T(\vec{x})}{T_{\text{ref}}}}, \tag{B.34a}$$

$$\rho_0(\vec{x}) = \frac{P_{\text{state}}(\vec{x}) \rho_{\text{ref}} T_{\text{ref}}}{T(\vec{x})}, \tag{B.34b}$$

where the subscript, ref, refers to the reference state for the ambient environmental conditions and $P_{\text{state}}(\vec{x})$ is the static pressure based on the local temperature $T(\vec{x})$ and calculated using ideal gas law assumption. Table B.1 elaborates further on the fixed parameters used in Equations (B.34a) and (B.34b) by ANSYS [9] for ambient environmental conditions in the ideal gas law assumption. Therefore, the governing equation for numerical acoustic simulations with temperature variations in the domain are given by Equation (B.32), with the exception that Equations (B.33a) and (B.33b) are used for $\rho_0(\vec{x})$ and $c_0(\vec{x})$ [8, 9].

Table B.1: Values for the reference state at environmental conditions for the formulation of the ideal gas law assumption from ANSYS [8, 9]

Variable name	Nomenclature	Value
Temperature	T_{ref}	22 °C
Reference static pressure	P_{ref}	101 325 Pa
Density	ρ_{ref}	1.2041 kg m^{-3}
Speed of sound	c_{ref}	343.24 m s^{-1}

B.2 Non-stationary acoustic wave equation with mean fluid flow

The prior derivation of the acoustic wave equation assumes that the medium is stationary. However, recent developments with ANSYS Mechanical means it is possible to account for the non-stationary mean fluid flow using the following derivation of the acoustic wave equation [8]. The acoustic wave equation with the non-stationary convective effects used by ANSYS Mechanical is almost identical to the equations developed by Pierce [131]. The following is a simplified derivation of the formulation used by ANSYS Mechanical [8], with a similar outcome to Pierce [131], however there is a slight difference in the final formulation and will be discussed later. A more detailed derivation of the non-stationary acoustic wave equation with mean fluid flow is provided by Pierce [131].

The formulation for the acoustic wave equation with non-stationary mean fluid flow by incorporating the linearised continuity equation and the Navier-Stokes equation for fluid momentum to give

$$\nabla \cdot \vec{v}_a = -\frac{1}{\rho_0(\vec{x})c_0^2(\vec{x})}\frac{\partial p_a(\vec{x},t)}{\partial t} + \frac{Q(\vec{x})}{\rho_0(\vec{x})}, \tag{B.35}$$

$$\frac{\partial \vec{v}_a(\vec{x})}{\partial t} = -\frac{1}{\rho_0(\vec{x})}\nabla p_a(\vec{x},t). \tag{B.36}$$

It should be noted that Equations (B.35) and (B.36) are identical to Equations (B.28) and (B.29), with slight manipulation of terms.

The acoustic particle velocity, $\vec{v_a}(\vec{x})$, and acoustic pressure, $p_a(\vec{x})$, can also be interpreted based on the relationship derived by Pierce [131] with

$$\vec{v_a}(\vec{x}) = -\frac{A}{\rho_0(\vec{x})}\nabla\phi(\vec{x},t), \tag{B.37}$$

$$p_a(\vec{x},t) = AD_t\phi(\vec{x},t), \tag{B.38}$$

where A is a constant one can choose and it is related to $\rho_0(\vec{x})$ and $c_0(\vec{x})$, $\phi(\vec{x},t)$ is the velocity potential or scalar flow potential that is dependent on time, t, and position, $\vec{x}$, and $D_t = \frac{\partial}{\partial t} + \vec{v_0}(\vec{x}) \cdot \nabla$ is the material derivative (also known as the substantial derivative or derivative along the ambient flow). In the derivation by Pierce [131], the author proposes two different values of A; $A = -1$ or $A = -\rho_0(\vec{x})$, where it leads to two different formulations of the linearised acoustic wave equation with mean flow using the scalar flow potential. Both formulations will be discussed later in this section. ANSYS Mechanical effectively uses $A = -1$ to give the following:

$$\vec{v_a} = \frac{1}{\rho_0(\vec{x})}\nabla\phi(\vec{x},t), \tag{B.39}$$

Equation (B.39), can be substituted into Equation (B.36) and manipulated to give

$$p_a(\vec{x},t) = -\left(\frac{\partial\phi(\vec{x},t)}{\partial t} + \vec{v_0}(\vec{x}) \cdot \nabla\phi(\vec{x},t)\right), \tag{B.40}$$

$$p_a(\vec{x},t) = -D_t\phi(\vec{x},t). \tag{B.41}$$

Equation (B.41) is the same as Equation (B.38) by Pierce [131], with $A = -1$. Substituting Equations (B.41) and (B.39) into (B.35) leads to the linearised continuity equation with mean fluid flow given by

$$-\frac{1}{\rho_0(\vec{x})c_0^2(\vec{x})}\frac{\partial}{\partial t}D_t\phi(\vec{x},t) + \nabla \cdot \left(\frac{1}{\rho_0(\vec{x})}\nabla\phi(\vec{x},t) - \frac{\vec{v_0}(\vec{x})}{\rho_0(\vec{x})c_0^2(\vec{x})}D_t\phi(\vec{x},t)\right) = \frac{q(\vec{x})}{\rho_0(\vec{x})}, \tag{B.42}$$

where q is

$$q(\vec{x}) = Q(\vec{x}) - \frac{1}{c_0^2(\vec{x})}D_t(\rho_0(\vec{x})\phi(\vec{x},t)). \tag{B.43}$$

Equation (B.42) can be rearranged and expressed as

$$-\frac{1}{\rho_0(\vec{x})c_0^2(\vec{x})}\frac{\partial}{\partial t}D_t\phi(\vec{x},t) - \nabla\cdot\frac{\vec{v_0}(\vec{x})}{\rho_0(\vec{x})c_0^2(\vec{x})}D_t\phi(\vec{x},t) + \left(\nabla\cdot\frac{1}{\rho_0(\vec{x})}\nabla\phi(\vec{x},t)\right) = \frac{q(\vec{x})}{\rho_0(\vec{x})}. \tag{B.44}$$

By grouping the common terms, $\frac{1}{\rho_0(\vec{x})c_0^2(\vec{x})}D_t\phi(\vec{x},t)$, the following is formed

$$-\left(\frac{\partial}{\partial t}+\vec{v_0}(\vec{x})\cdot\nabla\right)\left(\frac{1}{\rho_0(\vec{x})c_0^2(\vec{x})}D_t\phi(\vec{x},t)\right)+\nabla\cdot\left(\frac{1}{\rho_0(\vec{x})}\nabla\phi(\vec{x},t)\right)=\frac{q(\vec{x})}{\rho_0(\vec{x})}, \tag{B.45}$$

$$\nabla\cdot\left(\frac{1}{\rho_0(\vec{x})}\nabla\phi(\vec{x},t)\right)-D_t\left(\frac{1}{\rho_0(\vec{x})c_0^2(\vec{x})}D_t\phi(\vec{x},t)\right)=\frac{q(\vec{x})}{\rho_0(\vec{x})}. \tag{B.46}$$

Equation (B.46) is the time dependent acoustic wave equation taking into consideration the unsteady non-stationary mean fluid flow and is used by ANSYS Mechanical. It is important to note that Equation (B.46) is almost identical to the formulation by Pierce [131] shown as

$$\nabla\cdot\left(\frac{1}{\rho_0(\vec{x})}\nabla\phi(\vec{x},t)\right)-\rho_0(\vec{x})D_t\left(\frac{1}{\rho_0^2(\vec{x})c_0^2(\vec{x})}D_t\phi(\vec{x},t)\right)=0. \tag{B.47}$$

Equations (B.46) and (B.47) are identical as a first order approximation, however the second terms in both equations showing exhibit differences. The second terms on the left hand side in Equations (B.46) and (B.47) differ by $\rho_0(\vec{x})$, which introduces a first order change of $O(L^{-1})+O(T^{-1})$, where L is the length scale and T is the time scale. An important consideration and limitation for the acoustic wave equation in Equations (B.30), (B.46), and (B.47) assumes that there is no vorticity in the pressure perturbation.

Pierce [131] has two different formulations for the linearised acoustic wave equation with mean flow and a scalar flow potential, which is dependent on the definition of A. For most of the work in this section $A=-1$, for the derivation of Equation (B.46) by ANSYS Mechanical or Equation (B.47) by Pierce [131]. An

alternative formulation by Pierce [131] assumes $A = -\rho_0(\vec{x})$, and this is the author's preferred assumption of the constant, A. This leads to the author's preferred form

$$\frac{1}{\rho_0(\vec{x})}\nabla\cdot(\rho_0(\vec{x})\nabla\phi(\vec{x},t)) - D_t\left(\frac{1}{c_0^2(\vec{x})}D_t\phi(\vec{x},t)\right) = 0. \tag{B.48}$$

Pierce [131] has stated that even though there are two possible outcomes for the linearised acoustic wave equation with mean flow and scalar flow potential shown in the article and expressed in Equations (B.47) and (B.48), there are other possible formulations based on the choice of the constant A. Pierce [131] has also noted that Equations (B.47) and (B.48) are both valid first order approximations. However, the preferred form of Equation (B.48) is slightly more attractive, as the formulation is "exact" under the condition that the ambient medium has constant entropy per unit mass and when the flow is irrotational and steady.

For a harmonic solution of Equation (B.46) a harmonically varying velocity potential is introduced

$$\phi(\vec{x},t) = \mathrm{Re}[\phi(\vec{x})e^{j\omega t}]. \tag{B.49}$$

For harmonic analyses, Equation (B.49) may be substituted into Equation (B.42) to give the acoustic wave equation, which accounts for mean fluid flow and temperature variations as

$$\begin{aligned}\frac{\omega^2}{\rho_0(\vec{x})c_0^2(\vec{x})}\phi(\vec{x}) - j\omega\nabla\cdot\frac{\vec{v_0}(\vec{x})}{\rho_0(\vec{x})c_0^2(\vec{x})}\phi(\vec{x}) - j\omega\frac{\vec{v_0}(\vec{x})}{\rho_0(\vec{x})c_0(\vec{x})^2}\cdot\nabla\phi(\vec{x})\\ -\frac{\vec{v_0}(\vec{x})}{\rho_0(\vec{x})c_0^2(\vec{x})}\vec{v_0}(\vec{x})\nabla\phi(\vec{x}) + \nabla\cdot\frac{1}{\rho_0(\vec{x})}\nabla\phi(\vec{x}) = \frac{q(\vec{x})}{\rho_0(\vec{x})}.\end{aligned} \tag{B.50}$$

With further manipulation of Equation (B.50), the potential flow formulation of the acoustic wave equation with mean flow can be represented as

$$\begin{aligned}\omega^2\underbrace{\frac{\phi(\vec{x})}{\rho_0(\vec{x})c_0^2(\vec{x})}}_{M_\phi} - j\omega\underbrace{\left(\nabla\cdot\frac{\vec{v_0}(\vec{x})}{\rho_0(\vec{x})c_0^2(\vec{x})}\phi(\vec{x}) + \frac{\vec{v_0}(\vec{x})}{\rho_0(\vec{x})c_0^2(\vec{x})}\cdot\nabla\phi(\vec{x})\right)}_{C_\phi}\\ \underbrace{-\frac{\vec{v_0}(\vec{x})}{\rho_0(\vec{x})c_0^2(\vec{x})}\vec{v_0}(\vec{x})\nabla\phi(\vec{x}) + \nabla\cdot\frac{1}{\rho_0(\vec{x})}\nabla\phi(\vec{x})}_{K_\phi} = \frac{q(\vec{x})}{\rho_0(\vec{x})},\end{aligned} \tag{B.51}$$

where M_ϕ is the term for the 'acoustic fluid mass' for the acoustic velocity potential, C_ϕ is the term for the 'acoustic fluid damping' for the acoustic velocity potential, K_ϕ is the term for the 'acoustic fluid stiffness' for the acoustic velocity potential, and f_ϕ is the term for the 'acoustic fluid load' for the acoustic velocity potential.

B.3 Discretised acoustic wave equation for FEM

Equations (B.32) and (B.51) can be discretised using the Galerkin procedure [20] for finite element formulation. For the case without mean flow, Equation (B.32) is multiplied by testing function w and integrated over the volume of the domain with some manipulation to yield:

$$\begin{aligned}\iiint_{\Omega_F} \frac{w\omega^2 p_a(\vec{x})}{\rho_0(\vec{x})c_0^2(\vec{x})}\,\mathrm{d}V + \iiint_{\Omega_F} wj\omega\left(\frac{Q(\vec{x})}{\rho_0(\vec{x})}\right)\mathrm{d}V + \iiint_{\Omega_F} \nabla w\cdot\left(\frac{1}{\rho_0(\vec{x})}\nabla p_a(\vec{x})\right)\mathrm{d}V \\ - \oiint_{\Gamma_F} w\frac{1}{\rho_0(\vec{x})}\hat{n}\cdot\nabla p_a(\vec{x},t)\,\mathrm{d}S = 0,\end{aligned} \tag{B.52}$$

where Ω_F is the volume of the acoustic domain, Γ_F is the acoustic surface domain boundary, $\mathrm{d}V$ is the volume differential for the acoustic domain Ω_F, $\mathrm{d}S$ is the surface differential for the acoustic domain boundary Γ_F, and $\hat{n}$ is the outward normal unit vector to the boundary Γ_F.

Similarly to Equation (B.52), Equation (B.51) can be discretised using the Galerkin procedure with the linear potential flow and manipulated to yield:

$$\begin{aligned}
&\iiint_{\Omega_F} \frac{w\omega^2\phi(\vec{x})}{\rho_0(\vec{x})c_0^2(\vec{x})}\,\mathrm{d}V - \iiint_{\Omega_F} \nabla w \frac{j\omega\vec{v}_0(\vec{x})}{\rho_0(\vec{x})c_0^2(\vec{x})}\phi(\vec{x})\,\mathrm{d}V + \\
&\qquad \iiint_{\Omega_F} \frac{j\omega w}{\rho_0(\vec{x})c_0^2(\vec{x})}\vec{v}_0(\vec{x})\cdot\nabla\phi(\vec{x})\,\mathrm{d}V \\
&+ \iiint_{\Omega_F} \nabla w \cdot \left(\frac{1}{\rho_0(\vec{x})}\nabla\phi(\vec{x}) - \frac{\vec{v}_0(\vec{x})}{\rho_0(\vec{x})c_0^2(\vec{x})}\vec{v}_0(\vec{x})\cdot\nabla\phi(\vec{x})\right)\mathrm{d}V \\
&- \oiint_{\Gamma_F} w\left(\frac{1}{\rho_0(\vec{x})}\nabla\phi(\vec{x}) - \frac{j\omega\vec{v}_0(\vec{x})}{\rho_0(\vec{x})c_0^2(\vec{x})}\phi(\vec{x}) - \frac{\vec{v}_0(\vec{x})}{\rho_0(\vec{x})c_0^2(\vec{x})}\vec{v}_0(\vec{x})\cdot\nabla\phi(\vec{x})\right)\cdot\hat{n}\,\mathrm{d}S \\
&\qquad = \iiint_{\Omega_F} w\omega\left(\frac{q(\vec{x})}{\rho_0(\vec{x})}\right)\mathrm{d}V.
\end{aligned} \tag{B.53}$$

In modelling the sound, the following non-symmetric formulation is used for the linearised acoustic wave equation both without and with mean fluid flow, respectively:

$$(-\omega^2[M_p] + j\omega[C_p] + [K_p])\{p\} = f_p, \tag{B.54a}$$

$$(-\omega^2[M_\phi] + j\omega[C_\phi] + [K_\phi])\{\phi\} = f_\phi, \tag{B.54b}$$

$[M_p]$ is the acoustic fluid mass matrix for acoustic pressures, $[C_p]$ is the acoustic damping matrix for acoustic pressures, $[K_p]$ is the acoustic stiffness matrix for acoustic pressures, f_p is the acoustic fluid load vector for acoustic pressures, $[M_\phi]$ is the acoustic fluid mass matrix for ϕ, $[C_\phi]$ is the acoustic damping matrix for ϕ, $[K_\phi]$ is the acoustic stiffness matrix for ϕ, f_ϕ is the acoustic fluid load vector for ϕ. It should be noted that for the case of inviscid flow, the $[C_p]$ is non-existent for the formulation that uses the Helmholtz equation without mean fluid flow. The two equations are very similar in their implementation in ANSYS Mechanical, with; Equations (B.54a) and (B.54b), are in terms of a single degree of freedom for pressure p and a single degree of freedom velocity potential ϕ, respectively.

The acoustic pressure data from Equation (B.50) are derived using Equation (B.41). The matrix Equations (B.54a) and (B.54b), are solved directly with the 'Sparse' matrix solver in ANSYS as the matrices in Equations (B.54a) and (B.54b) have poor numerical conditioning. The matrix formulation for the solver treats the full domain as a matrix, which is solved using the 'Shared Memory Parallel' mode. The 'Shared Memory Parallel' mode requires less Random Accessible Memory (RAM) being necessary to solve for Equations (B.54a) and (B.54b) using FEM with ANSYS Mechanical, compared with a model with the domain being partitioned. Hence, using ANSYS Mechanical with the 'Shared Memory Parallel' mode provides the ability to solve models that have a large number of nodes, a requirement for accurate propagation of sound through non-isotropic media.

Appendix C

Numerical validation

Table C.1: The numerical validation cases investigated using acoustic FE modelling in ANSYS Mechanical.

Section number	Description	References
C.1	Sound propagation through ducts in 2-D	[77]
C.2	Sound propagation through ducts in 3-D	[77]
C.3	Sound radiation from an infinitely thin rectangular baffled piston in 2-D	[23]
C.4	Sound radiation from a circular baffled piston in axisymmetry	[25, 97]
C.5	Sound propagation through the thermal gradients in a plane jet in 2-D	-
C.6	Sound radiation from a circular unbaffled piston in axisymmetry	-
C.7	Sound radiation from a point source with uniform mean flow in 2-D	[18]
C.8	Sound radiation from a point source with a finite thickness sheared flow in 2-D	[57, 59]
C.9	Sound radiation from a point source with a heated, subsonic, non-expanding jet in 2-D	[2, 122]
C.10	Sound propagation from an infinitely baffled circular piston in 3-D	[97]

This appendix addresses the numerical validation conducted in this thesis. The different numerical cases investigated in this appendix are presented in Table C.1. The different numerical cases investigated in this thesis are supplementary to the substantial numerical validation work conducted by Howard and Cazzolato [77] for acoustic FE modelling with ANSYS Mechanical.

C.1 Sound Propagation through Ducts in 2-D

This section discusses the results for sound propagation through a 2-D duct. It is expected that when the Helmholtz number, $ka < 1$, the sound will propagate as a plane wave at some distance from the source. This study investigates two different

Helmholtz numbers, $ka = [0.63, 1.26]$. Several key parameters for the simulations are presented in Table C.2.

The numerical simulation results in this section have been validated using two different methods. The first method compares the maximum analytical acoustic pressure, and analytical SPL with the numerical maximum acoustic pressure, and numerical SPL. The second method compares the analytical acoustic wavelength with the numerical acoustic wavelength.

The numerical simulation results will be validated using analytical acoustic pressure and acoustic SPL results.

$P_{\text{acoustics,max}} = c_j u_a \rho_j$

$P_{\text{acoustics,max}} = 41.33\,\text{Pa}$

$P_{SPL} = 20\log_{10}(\frac{c_j u_a \rho_j}{\sqrt{2}\times 20\times 10^{-6}})$

$P_{SPL} = 123.29\,\text{dB re } 20\,\mu\text{Pa}$

From the analytical results and the results in Figures C.1, and C.2 there is good agreement between the results.

Furthermore, the numerical propagation through the duct can be validated with the acoustic wavelength, λ.

$\lambda/W_j = \frac{c_j}{f\times W_j}$

$\lambda/W_j = 2.5$ and 5

Table C.2: Parameters for isothermal stationary field in a duct

Description	Parameter	Value	Units
Duct width	W_j	0.0476	m
Duct length	L_j	$15W_j$	-
Density in duct	ρ_j	1.2041	kg/m^3
Speed of sound in duct	c_j	343.24	m s^{-1}
Acoustic velocity	u_a	0.1	m s^{-1}
Acoustic frequency	f	$1442.19 - 2884.37$	Hz
Atmospheric pressure	p_{atm}	101325	Pa
Ideal gas constant in duct	R_{air}	286.71	$\text{J/kg}\cdot\text{K}$

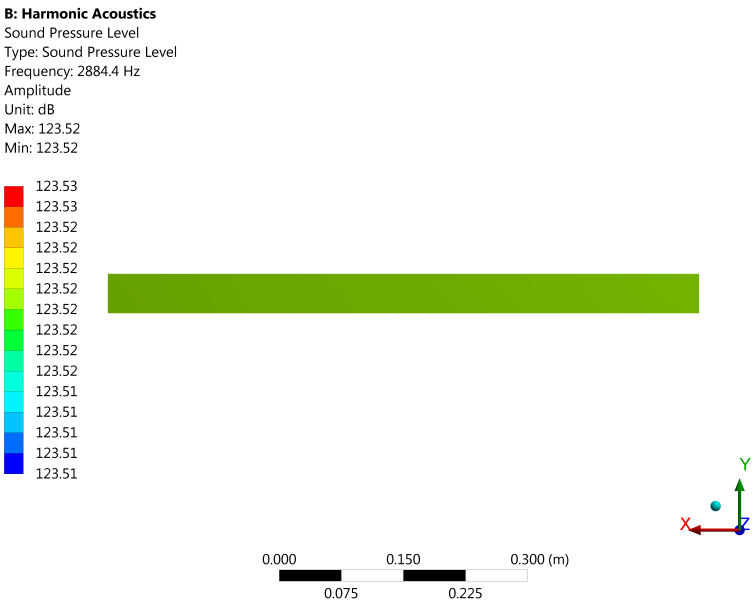

Figure C.1: SPL contour for 2-D plane wave propagation from left to right. The propagation medium is an isothermal stationary field at ambient temperature.

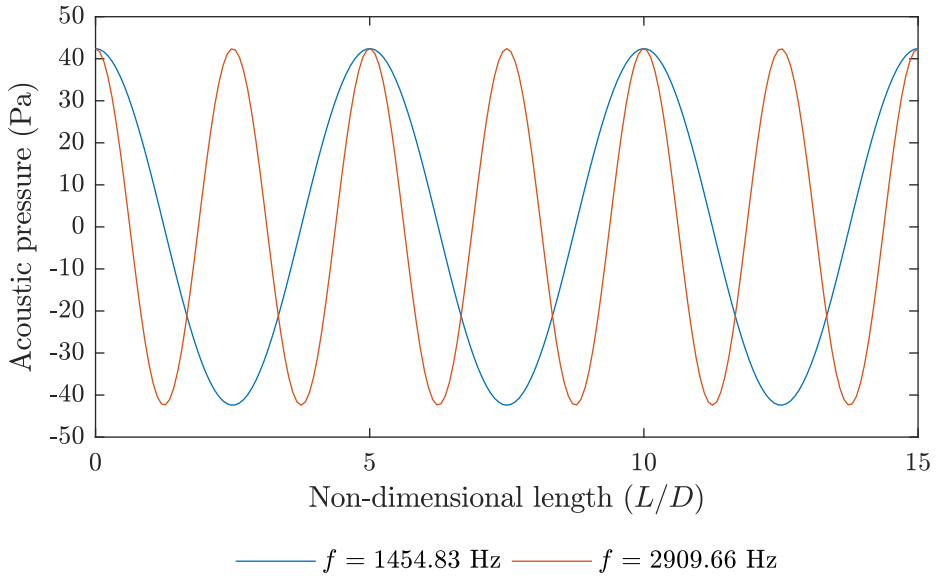

Figure C.2: Acoustic pressure along the duct centreline for 2-D plane wave propagation. The propagation medium is an isothermal stationary field at ambient temperature.

Using MATLAB to calculate the numerical wavelength based on the results presented in Figure C.2, there is a good agreement between the numerical and analytical result, with an error of approximately 1.66×10^{-6}%. Furthermore, from the results in Figure C.2 it is evident that the sound propagates through the 2-D duct in a plane wave.

C.2 Sound Propagation through Ducts in 3-D

The results that followed are sound propagation through a 3-D duct with varying propagation mediums. The different propagation mediums in the ducted investigated are the:

- isothermal stationary field,
- isothermal uniform flow at ambient temperature,
- non-isothermal, heated duct with no flow,
- heated duct with uniform flow,
- isothermal duct flow at ambient temperature, and
- non-isothermal heated duct flow.

All the cases investigated in this section adds a different level of complexity for sound propagation. The numerical work in this section uses both ANSYS Mechanical for acoustic FEM and ANSYS FLUENT for CFD.

C.2.1 Isothermal stationary field

The results are for the propagation of acoustic plane waves through 3-D ducts using ANSYS Mechanical. Some key parameters for the simulations are presented in Table C.3.

The numerical simulation results in this section will be validated using two different methods. The first method compares the maximum analytical acoustic pressure, the analytical SPL with the numerical maximum acoustic pressure, and numerical SPL. The second method compares the analytical acoustic wavelength with the numerical acoustic wavelength.

The numerical simulation results will be validated using analytical acoustic pressure and acoustic SPL results.

$P_{\text{acoustics,max}} = c_j u_a \rho_j$

$P_{\text{acoustics,max}} = 41.33\,\text{Pa}$

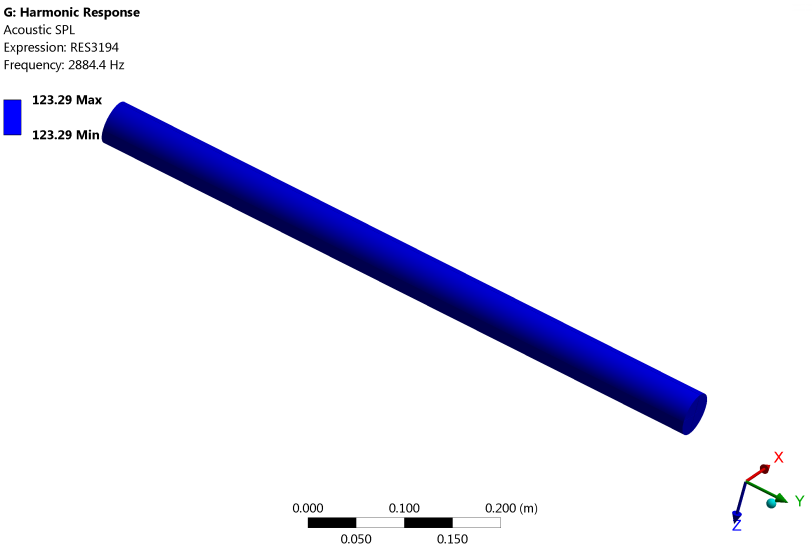

Figure C.3: SPL contour for 2-D plane wave propagation from top left to bottom right from ANSYS Mechanical. The propagation medium is an isothermal stationary field at ambient temperature.

$$P_{SPL} = 20\log_{10}\left(\frac{c_j u_a \rho_j}{\sqrt{2}\times 20\times 10^{-6}}\right)$$
$$P_{SPL} = 123.29\,\text{dB re } 20\,\mu\text{Pa}$$

From the analytical results and the results in Figures C.3, and C.4 there is good agreement between the results.

Table C.3: Parameters for isothermal stationary field in a duct

Description	Parameter	Value	Units
Duct diameter	D_j	0.0476	m
Duct length	L_j	$15D_j$	-
Density in duct	ρ_j	1.2041	kg/m^3
Speed of sound in duct	c_j	343.24	m s^{-1}
Acoustic velocity	u_a	0.1	m s^{-1}
Acoustic frequency	f	2884.37	Hz
Atmospheric pressure	p_{atm}	101325	Pa
Ideal gas constant in duct	R_{air}	286.71	$\text{J/kg}\cdot\text{K}$

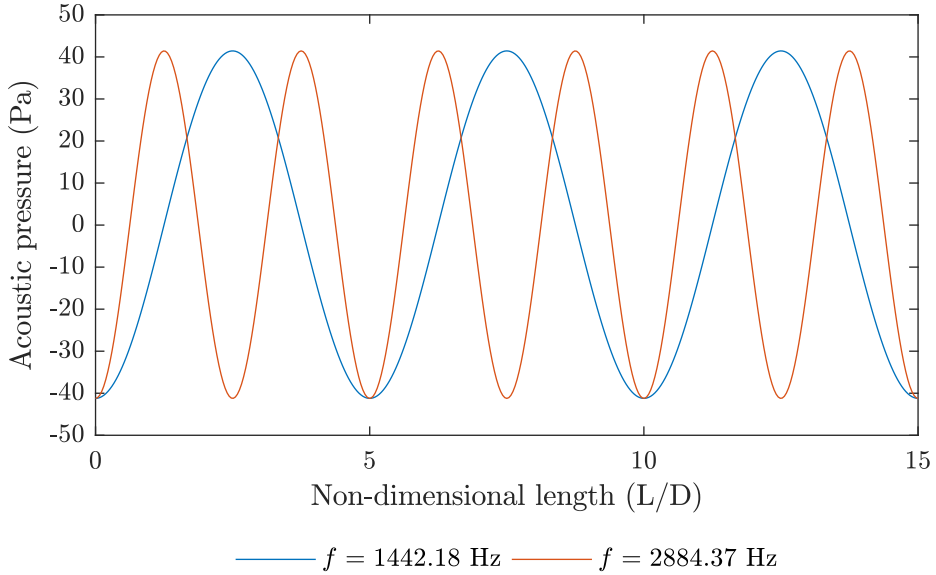

Figure C.4: Acoustic pressure along the duct centreline for 3-D plane wave propagation. The propagation medium is an isothermal stationary field at ambient temperature.

Furthermore, the numerical propagation through the duct can be validated with the acoustic wavelength, λ.
$\lambda/D_j = \frac{c_j}{f \times D_j}$
λ/D_j = 2.5 and 5

Using MATLAB to calculate the numerical wavelength based on the results presented in Figure C.4, there is a good agreement between the numerical and analytical result, with an error of approximately 1.66×10^{-6}%. Furthermore, as expected for the results in Figures C.2 and C.4, the acoustic pressures are almost identical, which is to be expected for plane wave propagation through ducts with $ka < 1$.

C.2.2 Isothermal uniform flow at ambient temperature

Sound propagation through a duct with uniform flow at ambient temperature was investigated. This case is a simplified case and does not take into consideration

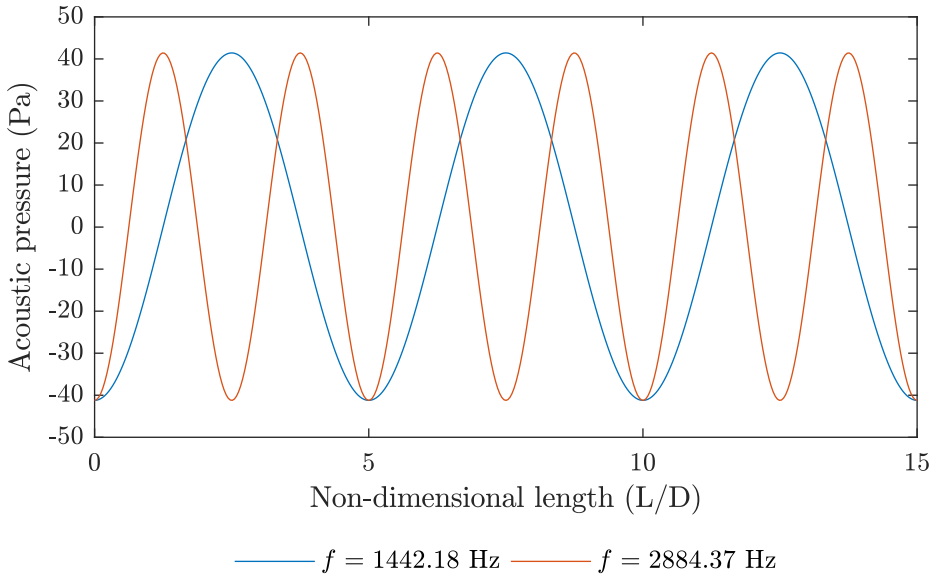

Figure C.5: Acoustic pressure along the duct centreline for 3-D plane wave propagation. The propagation medium is a duct with uniform bulk flow, $u_{flow} = 50\,\mathrm{m\,s^{-1}}$.

the boundary layer formed for flow in a duct. Alternatively, it can be assumed that a free-slip boundary condition was implemented along the duct walls. All the parameters for the case remain the same as presented in Table C.3, however the uniform flow has a bulk velocity, $u_{flow} = 50\,\mathrm{m\,s^{-1}}$, and a speed of sound of ,$c_j = 393.24\,\mathrm{m\,s^{-1}}$. It should be noted that the bulk flow is in the direction of the propagating sound.

The inclusion of the uniform bulk flow in the duct would alter the acoustic wavelength, λ, and can be calculated by

$\lambda/D_j = \frac{c_j}{f \times D_j}$

$\lambda/D_j = 2.86$ and 5.72

Using MATLAB to calculate the numerical wavelength based on the results presented in Figure C.4, there is a good agreement between the numerical and analytical result, with an error of approximately $6.22 \times 10^{-2}\%$ for both frequencies investigated.

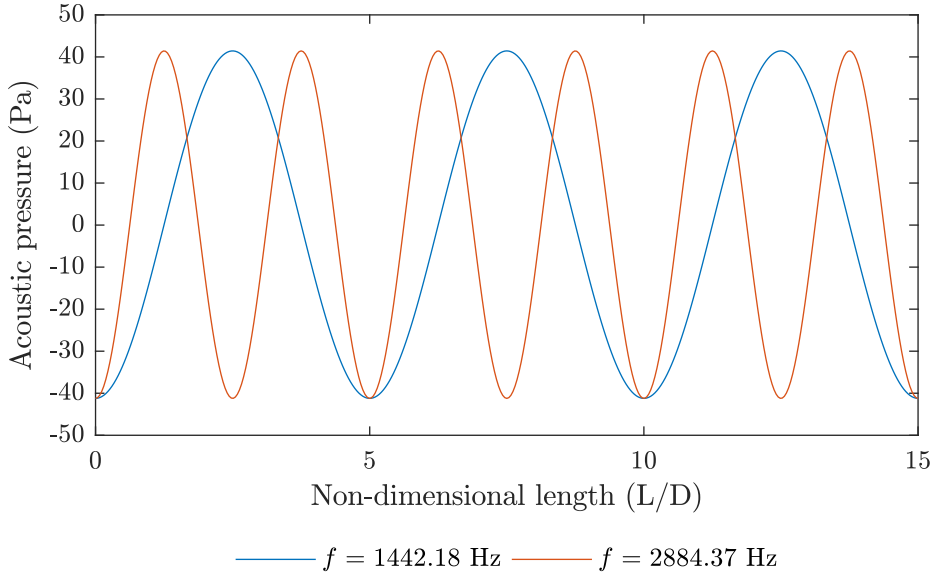

Figure C.6: Acoustic pressure along the duct centreline for 3-D plane wave propagation. The propagation medium is a heated duct, T_j = 500 °C, with no flow.

C.2.3 Heated duct with no flow

Sound propagation through a duct heated duct with no flow was investigated. This simplified case assumes the air in the duct is heated with no flow. All the parameters for the case remains the same as presented in Table C.3, however the duct temperature is T_j = 500 °C, and the speed of sound is c_j = 557.02 m s^{-1}. It should be noted that the bulk flow is in the direction of the propagating sound.

The change in the duct temperature would alter the acoustic wavelength, λ, and can be calculated.

$\lambda/D_j = \frac{c_j}{f \times D_j}$

λ/D_j = 4.04 and 8.09

Using MATLAB to calculate the numerical wavelength based on the results presented in Figure C.4, there is a good agreement between the numerical and analytical results, with an error of approximately 7.71×10^{-2}% for both frequencies investigated.

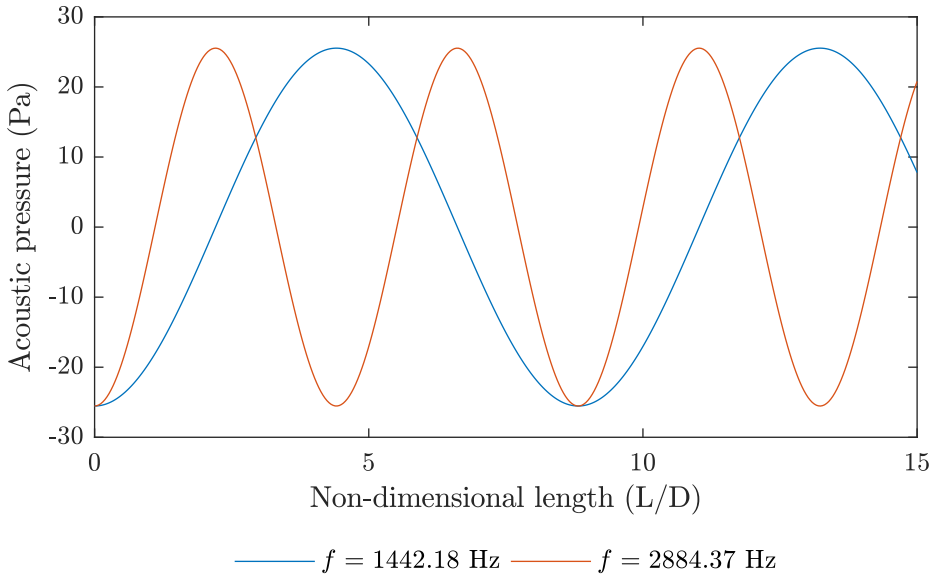

Figure C.7: Acoustic pressure along the duct centreline for 3-D plane wave propagation. The propagation medium is a duct with a uniform flow profile where the flow velocity is, $u_{flow} = 50\,\mathrm{m\,s^{-1}}$ and the temperature of the duct is $T_j = 500\,°\mathrm{C}$.

C.2.4 Heated duct with uniform flow

The next sound propagation case is a heated duct with a uniform velocity profile. This numerical case is the first where the superposition of the flow and temperature are considered for the acoustic propagation medium. The uniform duct velocity is $u_{flow} = 50\,\mathrm{m\,s^{-1}}$ and the temperature of the duct is $T_j = 500\,°\mathrm{C}$.

The inclusion of a non-uniform duct flow would alter the acoustic wavelength, λ, and can be calculated.

$\lambda/D_j = \frac{c_j}{f \times D_j}$

$\lambda/D_j = 4.41$ and 8.82

Using MATLAB to calculate the numerical wavelength based on the results presented in Figure C.7, there is a good agreement between the numerical and analytical result, with an error of approximately 0.22% for both frequencies investigated.

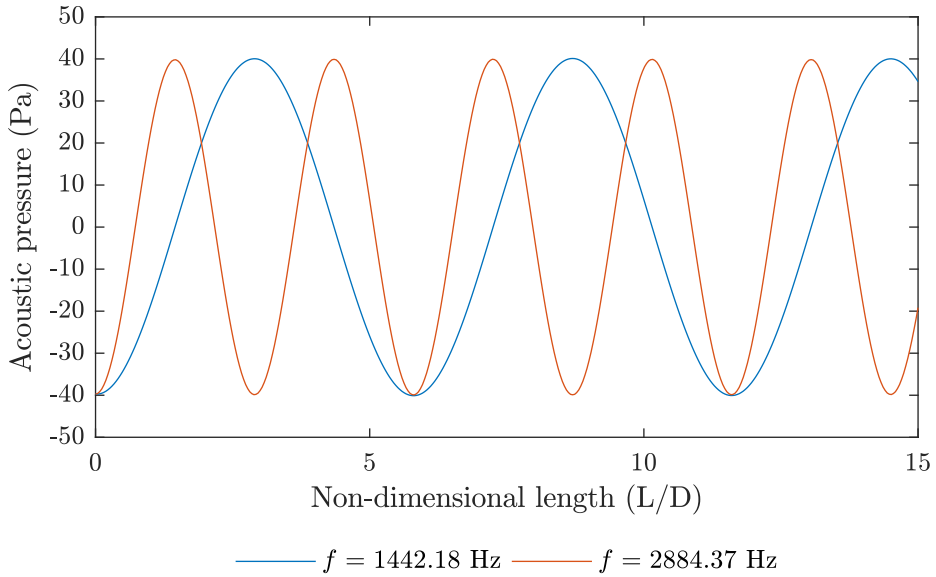

Figure C.8: Acoustic pressure along the duct centreline for 3-D plane wave propagation. The propagation medium is a duct with a non-uniform flow profile where the bulk velocity is, $u_{flow} = 55.11\,\mathrm{m\,s^{-1}}$.

C.2.5 Isothermal duct flow at ambient temperature

This section discusses the sound propagation in a duct with a non-uniform velocity profile. The temperature of the duct is isothermal at ambient temperature. For this particular case the bulk velocity in the duct was $u_{flow} = 55.11\,\mathrm{m\,s^{-1}}$.

The inclusion of the non-uniform duct flow would alter the acoustic wavelength, λ, and can be calculated.

$\lambda/D_j = \frac{c_j}{f \times D_j}$

$\lambda/D_j = 2.90$ and 5.81

Using MATLAB to calculate the numerical wavelength based on the results presented in Figure C.8, there is a good agreement between the numerical and analytical result, with an error of approximately 0.32% for both frequencies investigated.

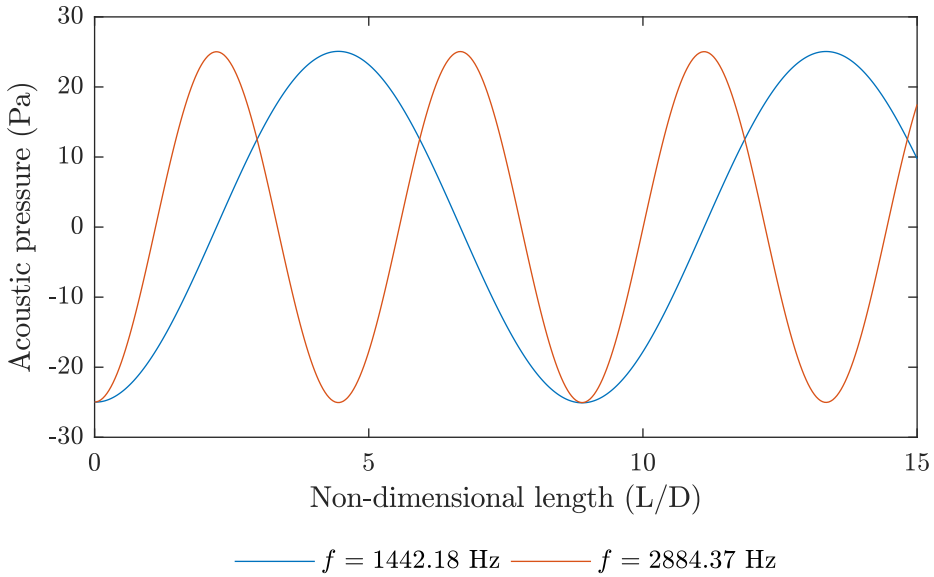

Figure C.9: Acoustic pressure along the duct centreline for 3-D plane wave propagation. The propagation medium is a duct with non uniform flow profile where the bulk velocity is, $u_{flow} = 55.11\,\mathrm{m\,s^{-1}}$ and the temperature of the duct is $T_j = 500\,°\mathrm{C}$.

C.2.6 Heated duct with wall bounded flow

The final numerical validation case for sound propagation through the duct is with a heated duct and non-uniform velocity profile. This numerical validation case is the most complex case investigated for sound propagation through a 3-D duct. The bulk duct velocity is $u_{flow} = 55.11\,\mathrm{m\,s^{-1}}$ and the temperature of the duct is $T_j = 500\,°\mathrm{C}$.

The inclusion of the non-uniform duct flow would alter the acoustic wavelength, λ, and can be calculated.
$\lambda/D_j = \frac{c_j}{f \times D_j}$
$\lambda/D_j = 4.45$ and 8.91

Using MATLAB to calculate the numerical wavelength based on the results presented in Figure C.9, there is a good agreement between the numerical and analytical result, with an error of approximately 0.11% for both frequencies investigated.

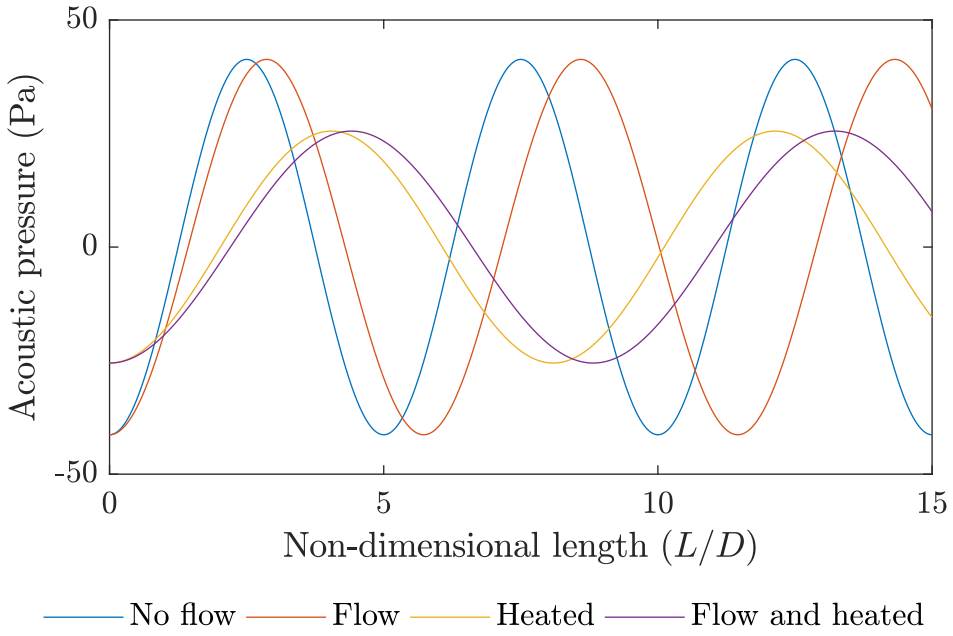

Figure C.10: Acoustic pressure along the duct centreline for 3-D plane wave propagation for four propagation conditions in the duct: an isothermal stationary field at ambient temperature, a uniform bulk flow at ambient temperature, a heated duct with no flow, and a heated duct with uniform bulk flow.

C.2.7 Summary of findings for sound propagation through 3-D ducts

The sound propagation through a 3-D duct with different propagation mediums have been investigated to validate the numerical code. Figure C.10 shows the results at four different propagation conditions in the duct, which are: an isothermal stationary field at ambient temperature, a uniform bulk flow at ambient temperature, a heated duct with no flow, and a heated duct with uniform bulk flow. It should be noted that the acoustic frequency was constant at $f = 1442.18\,\text{Hz}$, which is a $ka < 1$ for all cases. Investigating sound propagation with $ka < 1$ ensures the sound is propagating as a plane wave in the duct.

C.3 Sound Radiation from an Infinitely Thin Rectangular Baffled Piston in 2-D

Numerical simulations were explored using ANSYS Mechanical to explore the sound propagation from an infinitely thin rectangular piston and was analytically validated at the piston face. Figures C.11, C.12, C.13, and C.14 shows the SPL contour plot for sound radiation from an infinitely thin rectangular baffled piston in 2-D.

The impedance at the piston face for an infinitely long oscillating ribbon in infinite baffle can be used to verify the acoustic source with known a analytical solution [23]. The analytical solution for the radiation resistance, $R_r(2ka)$, and radiation reactance, $X_r(2ka)$, at the piston face is given by Beranek et al. [23]. Figure C.15 shows the numerical radiation impedance at the piston face and compares it with the analytical solution from Beranek et al. [23]. There is good agreement between the numerical and analytical solutions for radiation impedance.

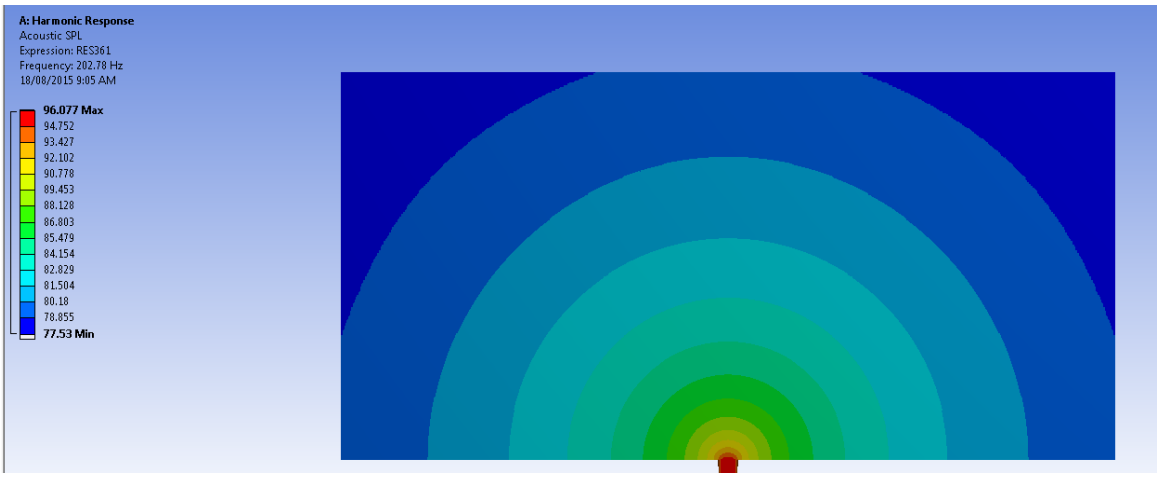

Figure C.11: ANSYS Mechanical simulation for the SPL (dB re 20 µPa) for a baffled rectangular piston at 202 Hz

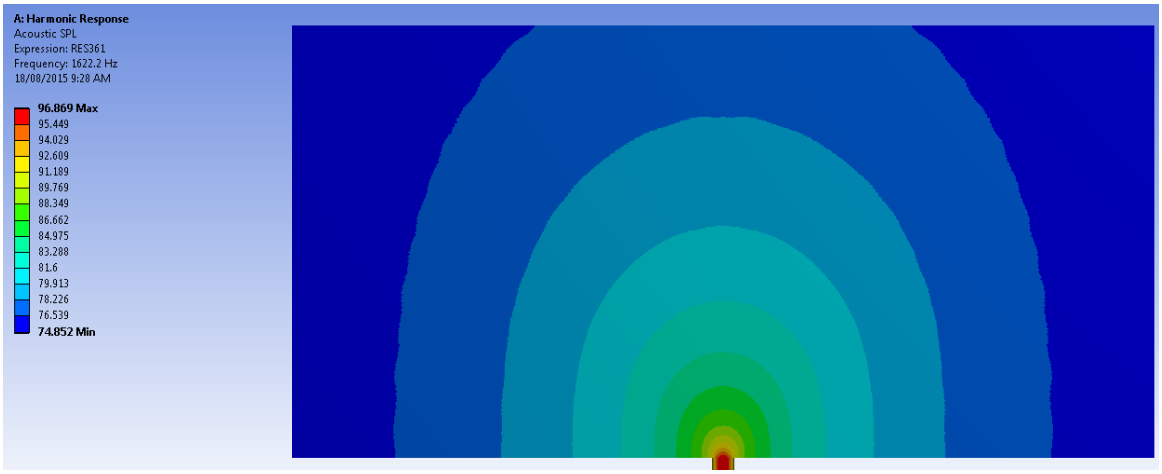

Figure C.12: ANSYS Mechanical simulation for the SPL (dB re 20 µPa) for a baffled rectangular piston at 1622 Hz

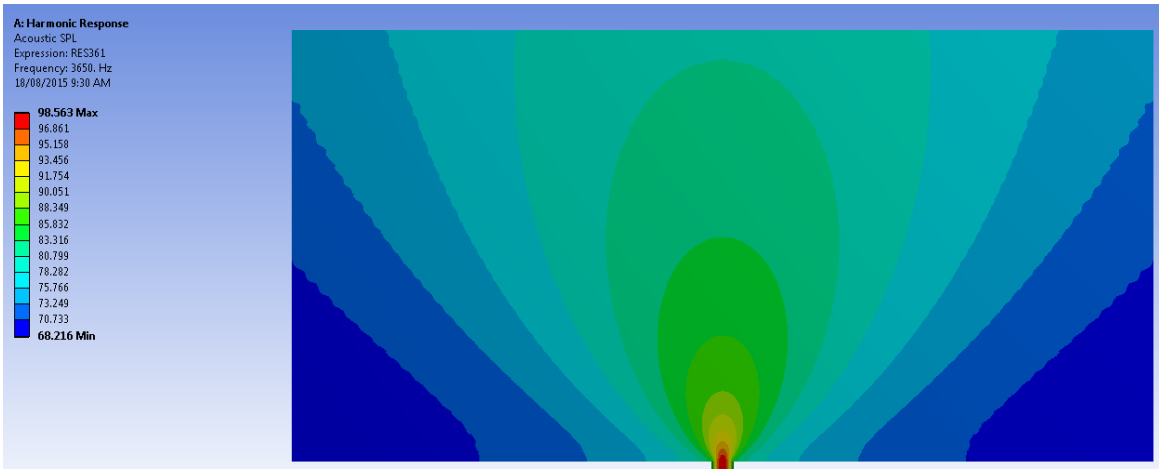

Figure C.13: ANSYS Mechanical simulation for the SPL (dB re 20 µPa) for a baffled rectangular piston at 3650 Hz

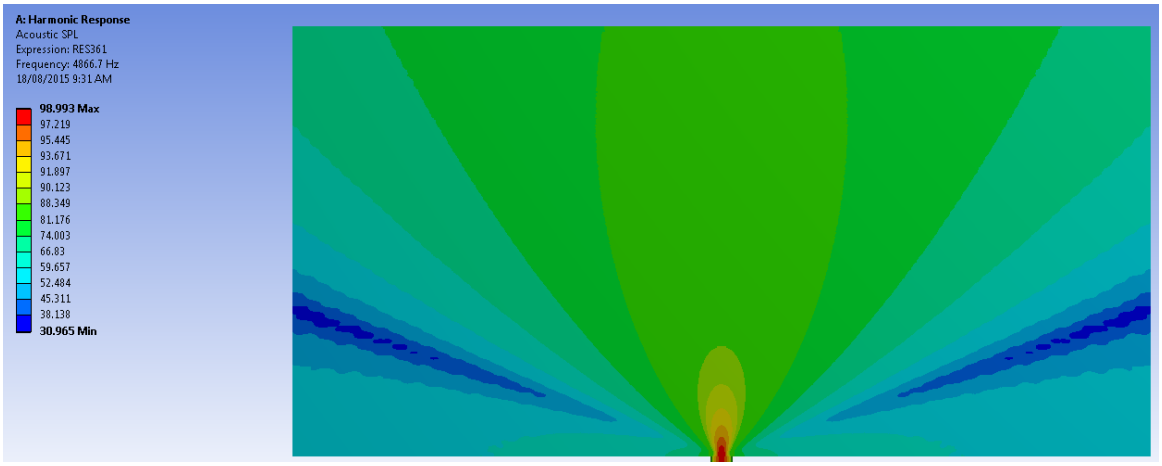

Figure C.14: ANSYS Mechanical simulation for the SPL (dB re 20 µPa) for a baffled rectangular piston at 4866 Hz

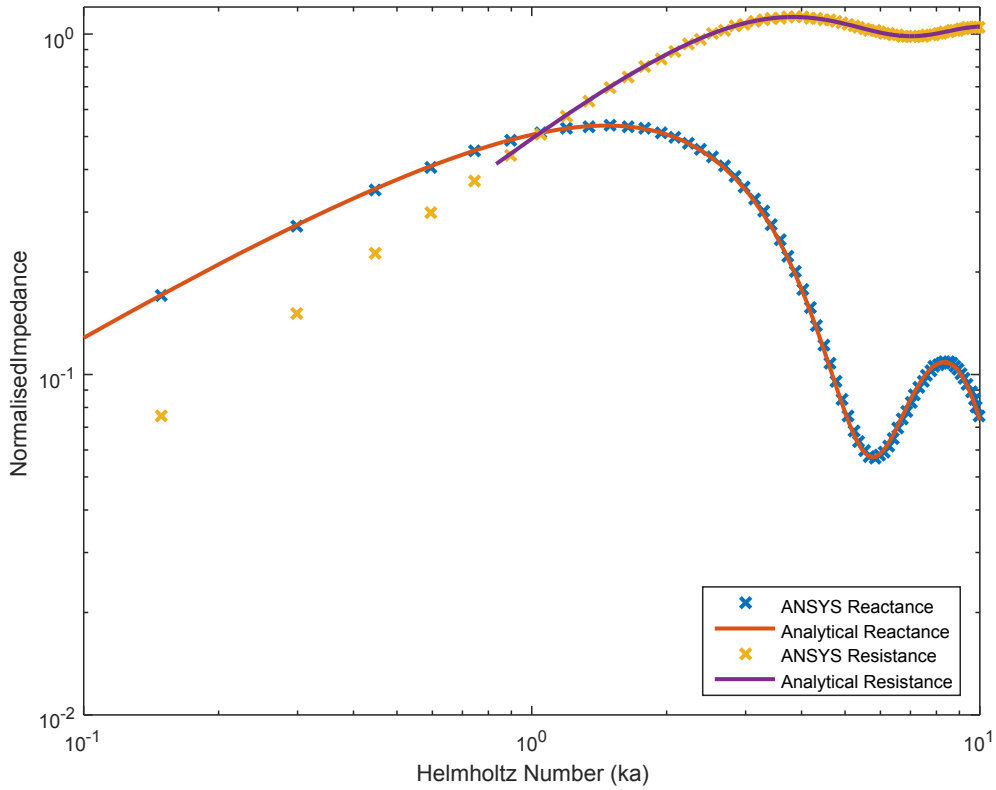

Figure C.15: Normalised acoustic impedance face for an infinitely baffled, infinitely thin rectangular piston

C.4 Sound Radiation from a Circular Baffled Piston in Axisymmetry

The numerical results for this section are for the sound radiation from an infinitely baffled piston in 2-D with ANSYS Mechanical. This simulation uses the axisymmetric boundary condition for modelling the sound radiation from an infinitely baffled piston, as it has been established in the literature that the sound radiation is axisymmetric about the duct centreline [25, 97].

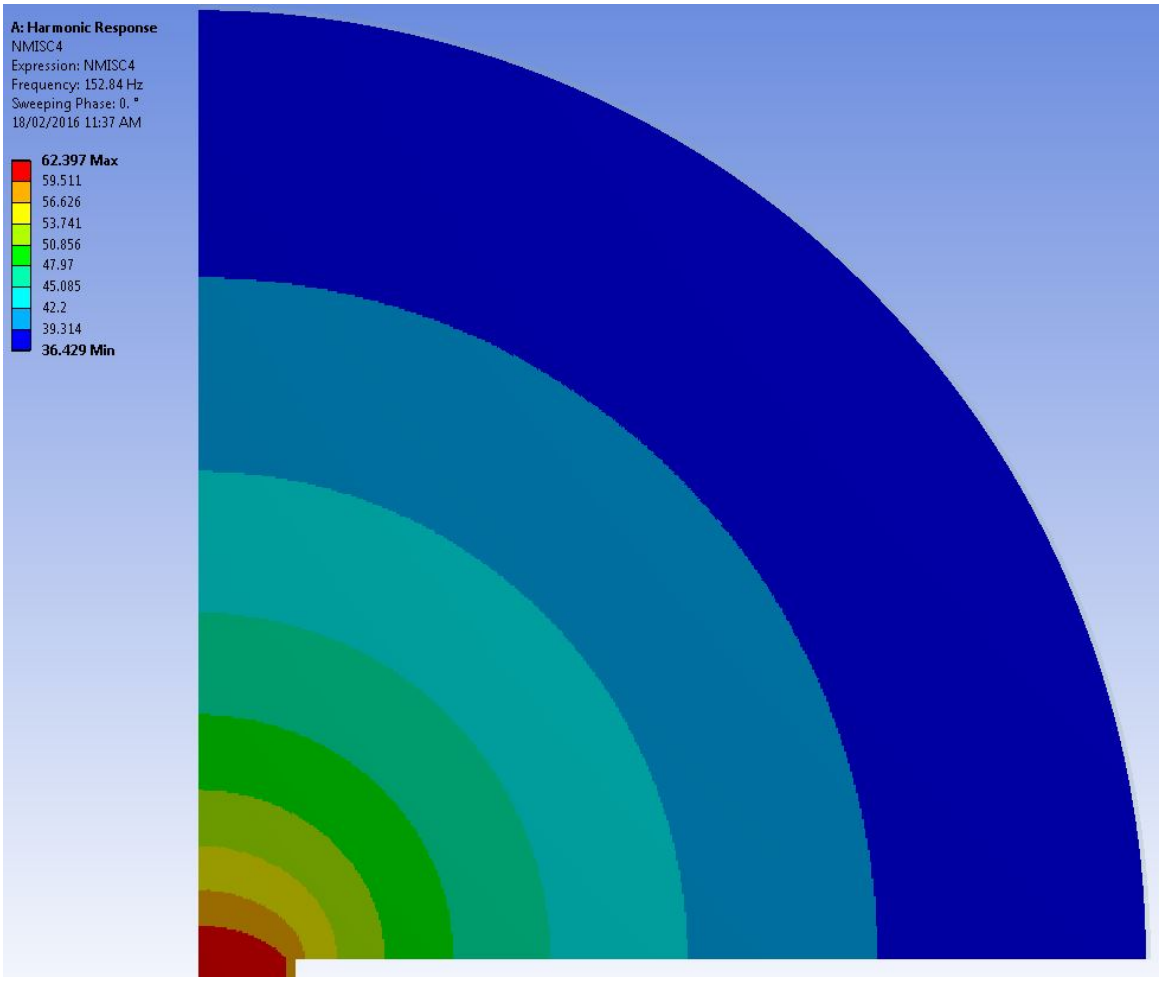

Figure C.16: ANSYS Mechanical simulation for the SPL (dB re 20 µPa) for a 2-D baffled circular piston at 152 Hz

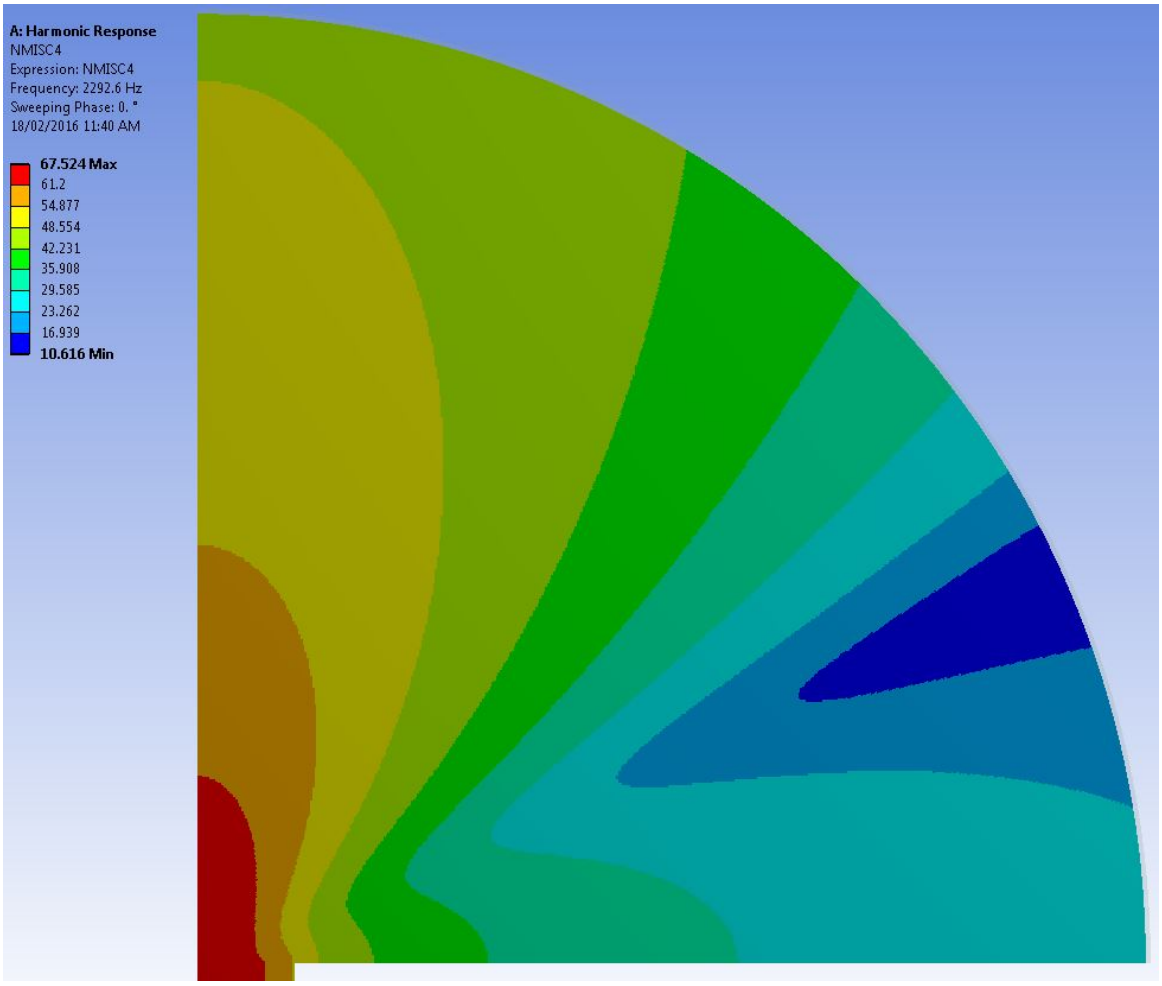

Figure C.17: ANSYS Mechanical simulation for the SPL (dB re 20 µPa) for a 2-D baffled circular piston at 2292 Hz

The impedance at the piston face can be used to verify the acoustic source with a known analytical solution [25, 97]. The analytical solution for the radiation resistance, $R_r(2ka)$, and radiation reactance, $X_r(2ka)$, at the piston face is given by Kinsler et al. [97]. Figure C.19 shows the numerical radiation impedance at the piston face and compares it with the analytical solution from Kinsler et al. [97]. There is good agreement between the numerical and analytical solutions for radiation impedance.

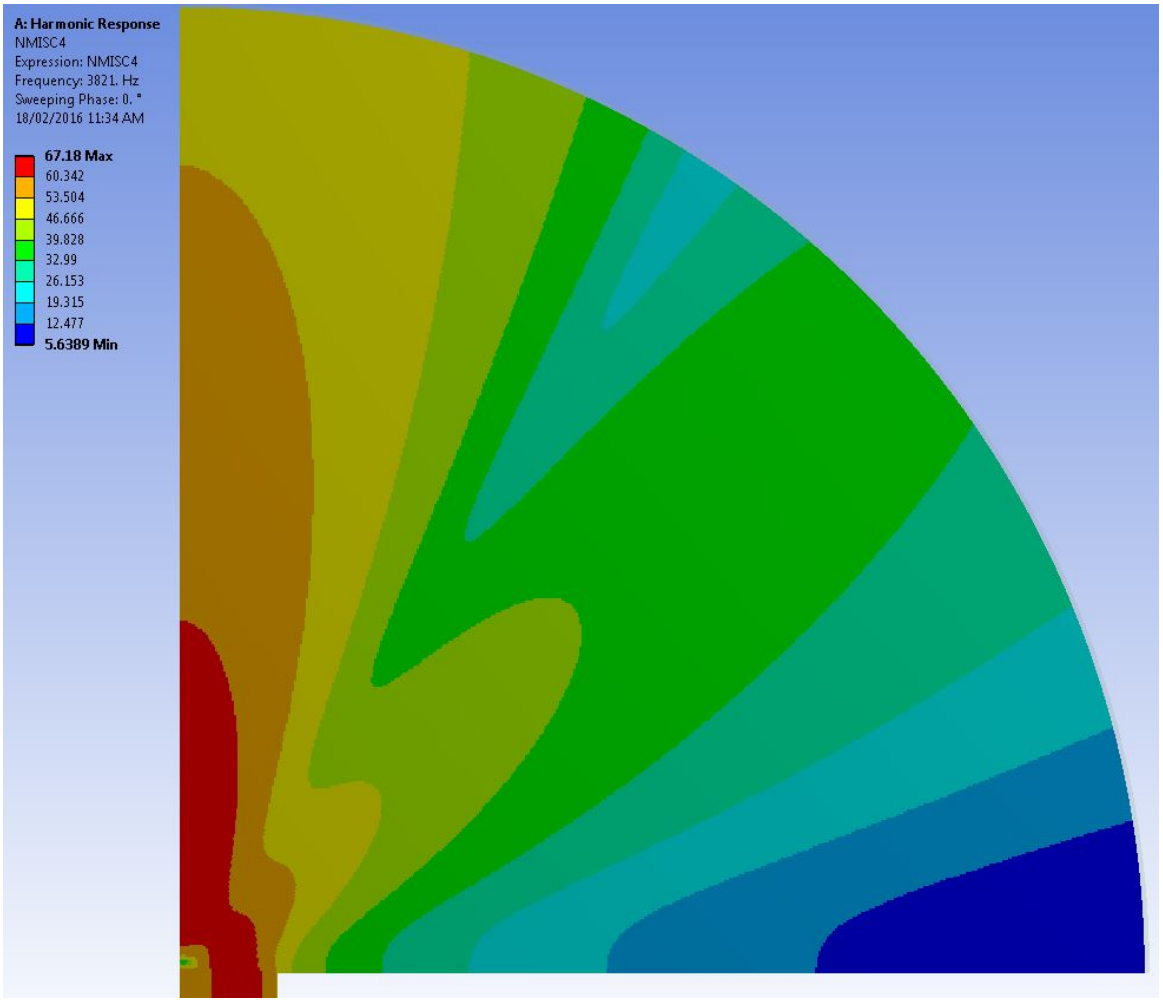

Figure C.18: ANSYS Mechanical simulation for the SPL (dB re 20 µPa) for a 2-D baffled circular piston at 3821 Hz

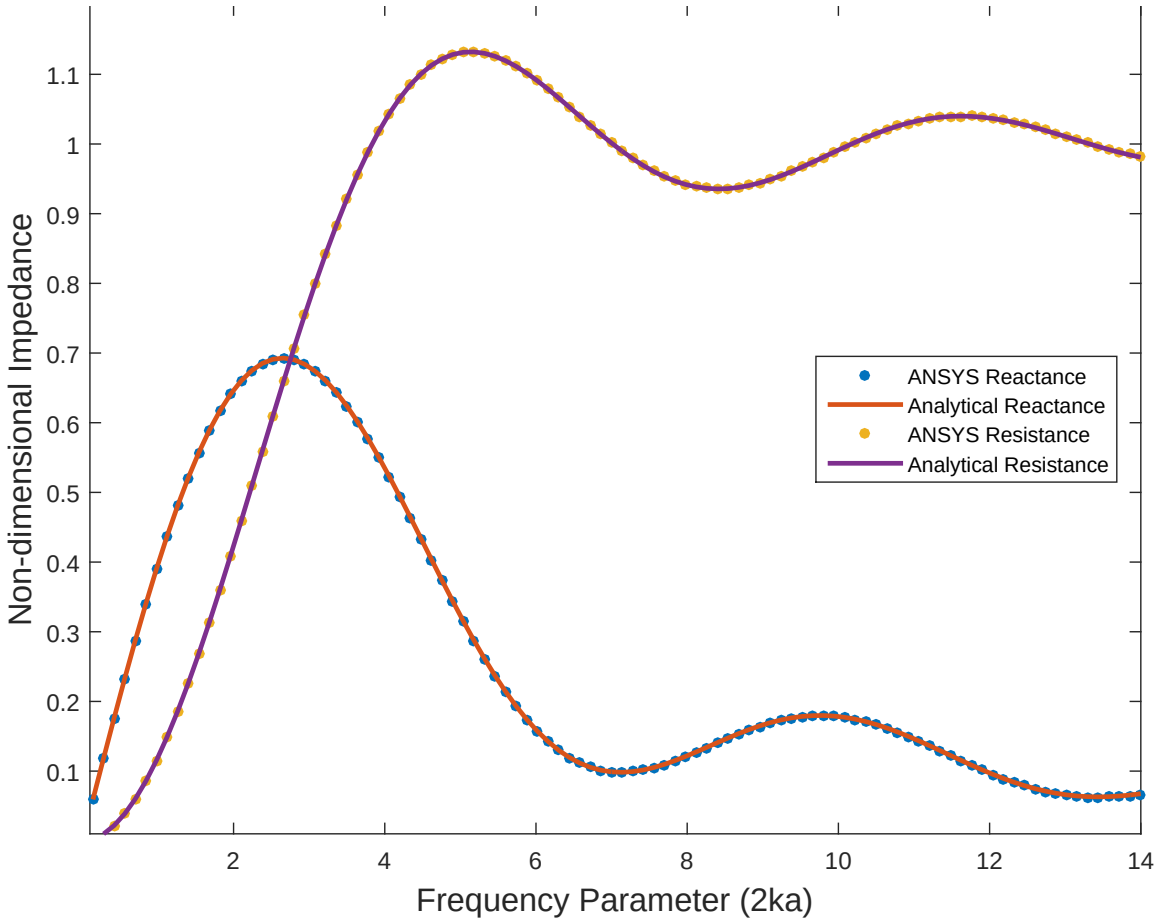

Figure C.19: The analytical and ANSYS Mechanical simulation results for the normalised acoustic impedance at the piston face

C.5 Sound Propagation through the Thermal Gradients in a Plane Jet in 2-D

This simulation of sound propagation through the thermal gradients of a plane jet in 2-D was a preliminary simulation investigating numerical simulation techniques. The purpose of this exercise was to generate the RANS generated temperature gradients using CFD and importing the temperature gradients into ANSYS Mechanical. Using ANSYS Mechanical Acoustic ACT Extension, the sound was numerically propagated through the thermal data using the acoustic FEM. The results show definitive sound refraction with the presence of the thermal gradients in 2-D.

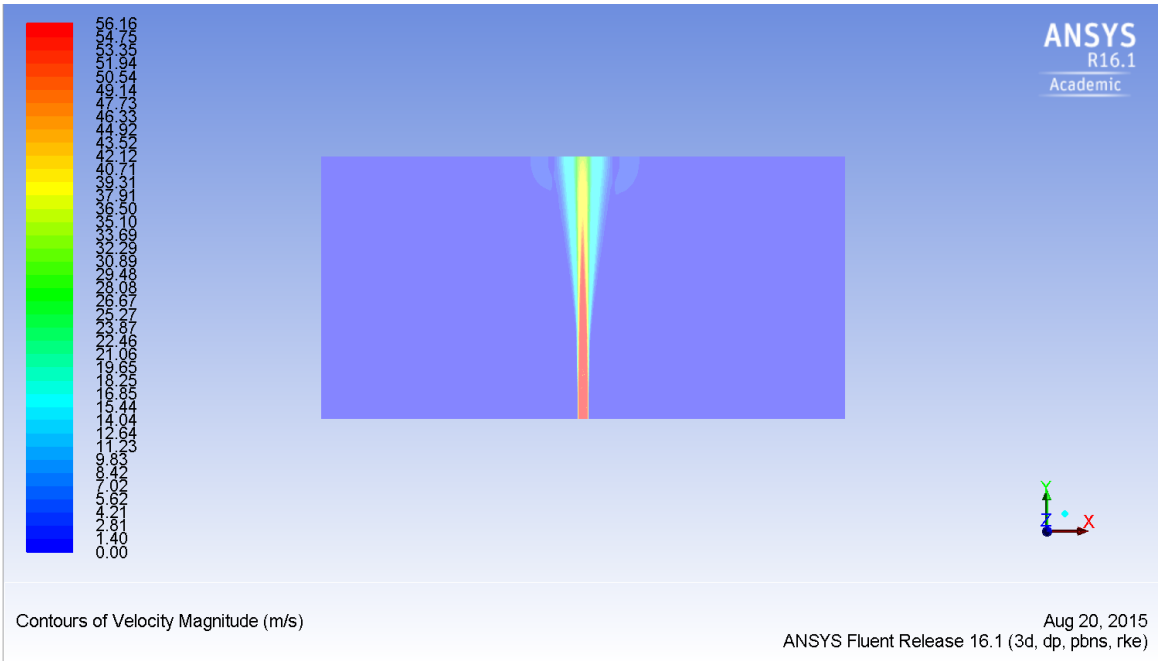

Figure C.20: Mean velocity magnitude contour plot from a non-isothermal plane rectangular jet

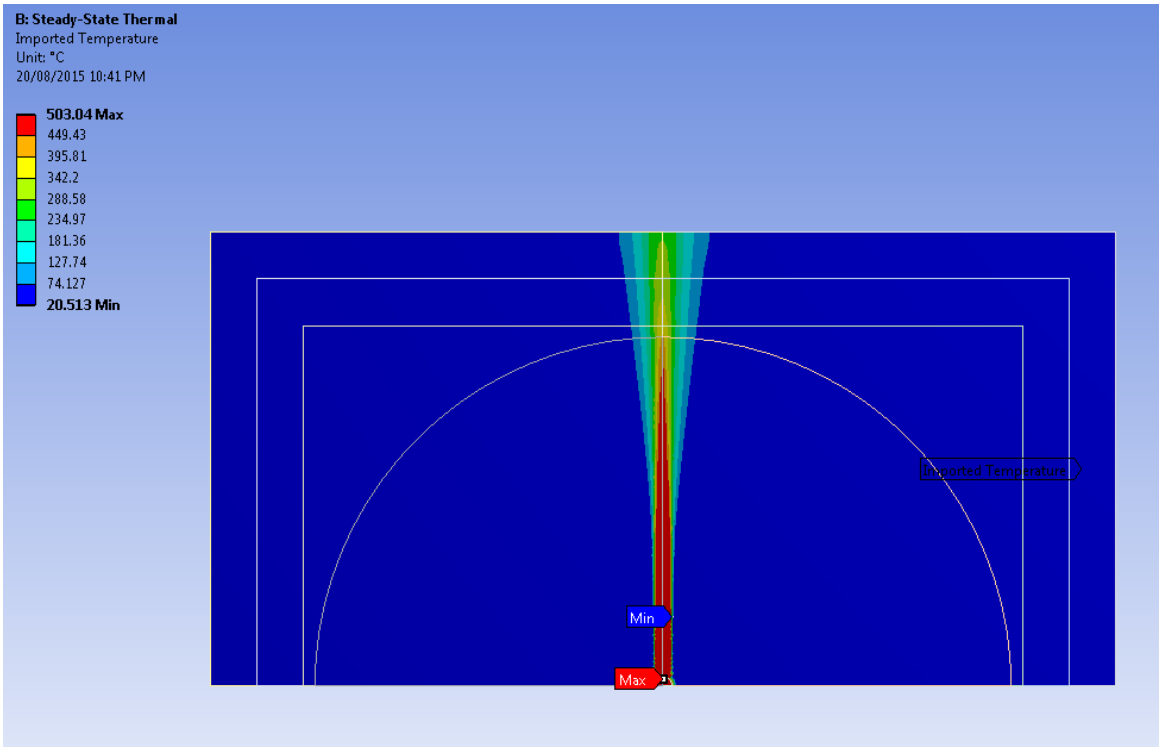

Figure C.21: Mean pressure contour plot from a non-isothermal plane rectangular jet

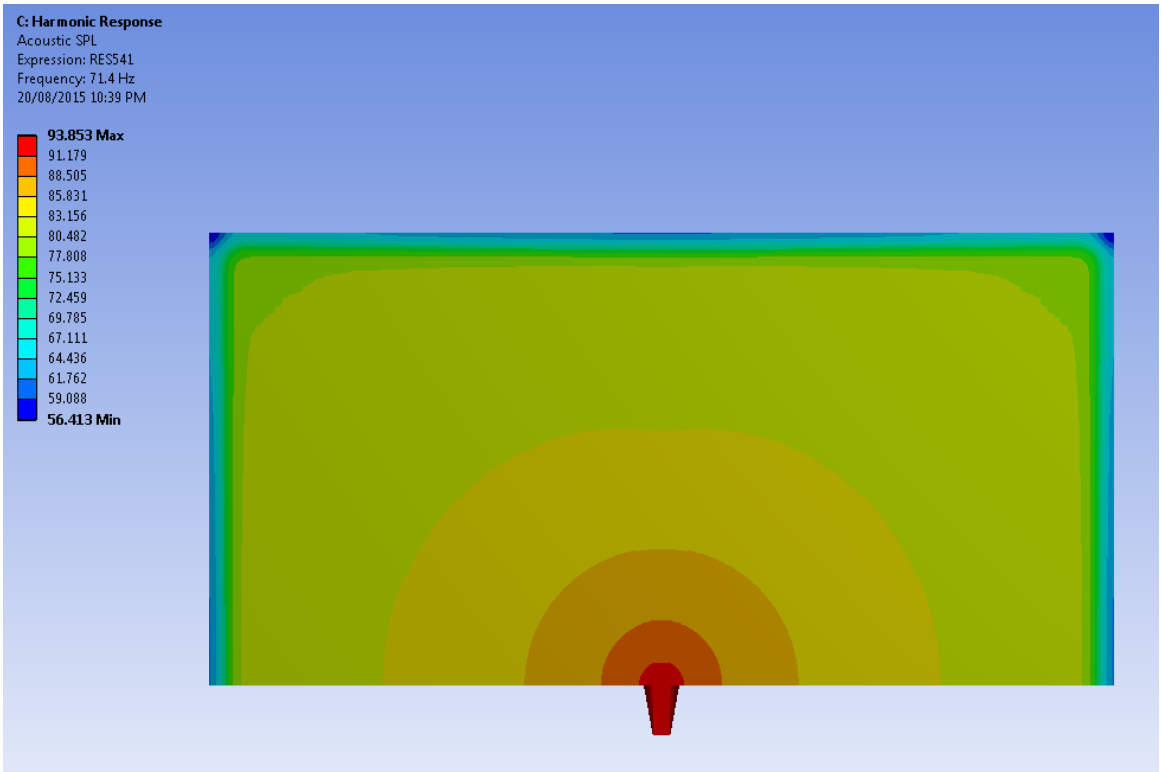

Figure C.22: Acoustic SPL (dB re 20 µPa) contour plot at 71Hz from a non-isothermal plane rectangular jet

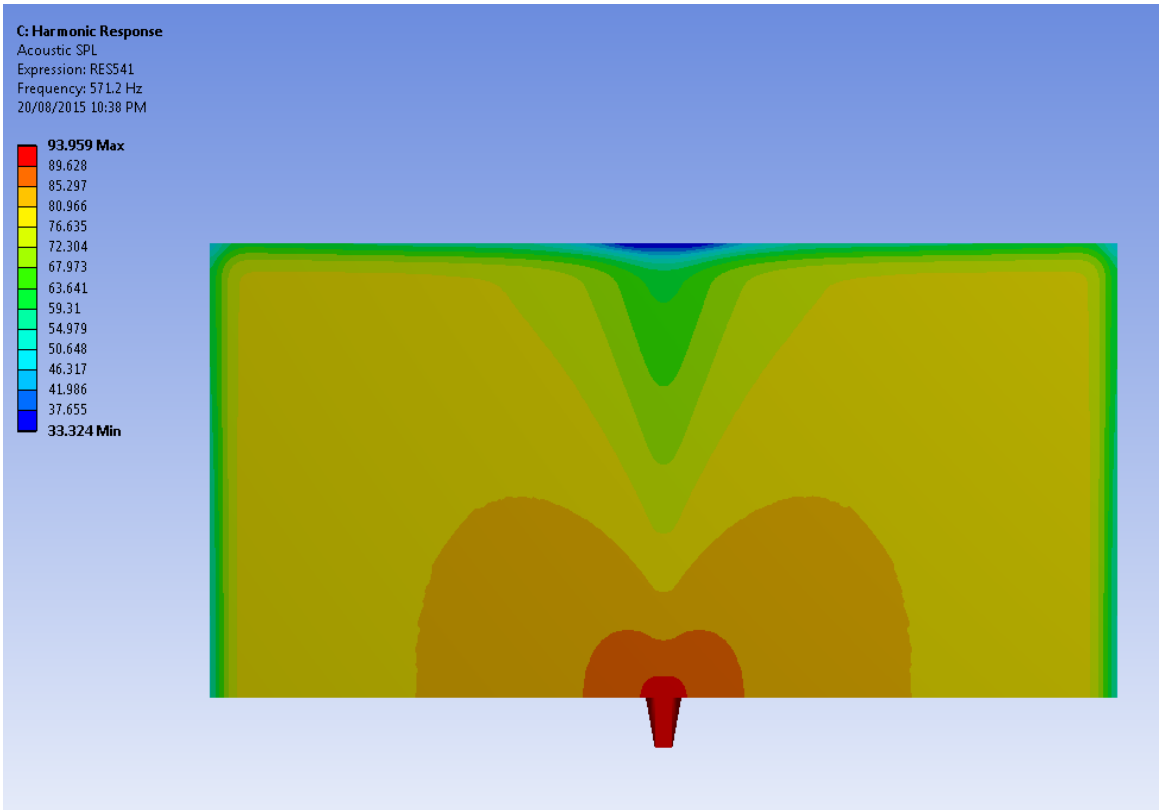

Figure C.23: Acoustic SPL (dB re 20 µPa) contour plot at 571Hz from a non-isothermal plane rectangular jet

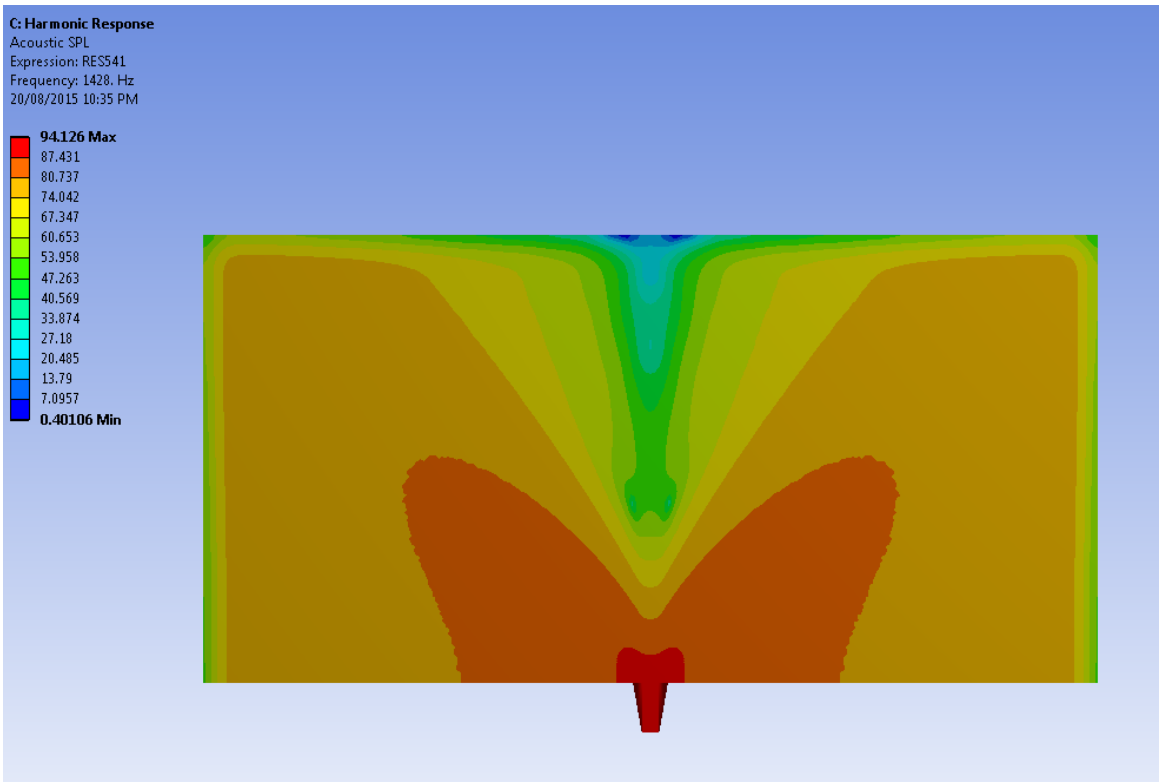

Figure C.24: Acoustic SPL (dB re 20 µPa) contour plot at 1428Hz from a non-isothermal plane rectangular jet

C.6 Sound Radiation from a Circular Unbaffled Piston in Axisymmetry

The results in this section are for a circular unbaffled piston in Axisymmetry. The simulation is in 2-D with the axisymmetric boundary condition employed. Figures C.25, C.26, C.27, C.28, C.29, and C.30 show the SPL contour plots for varying acoustic frequencies.

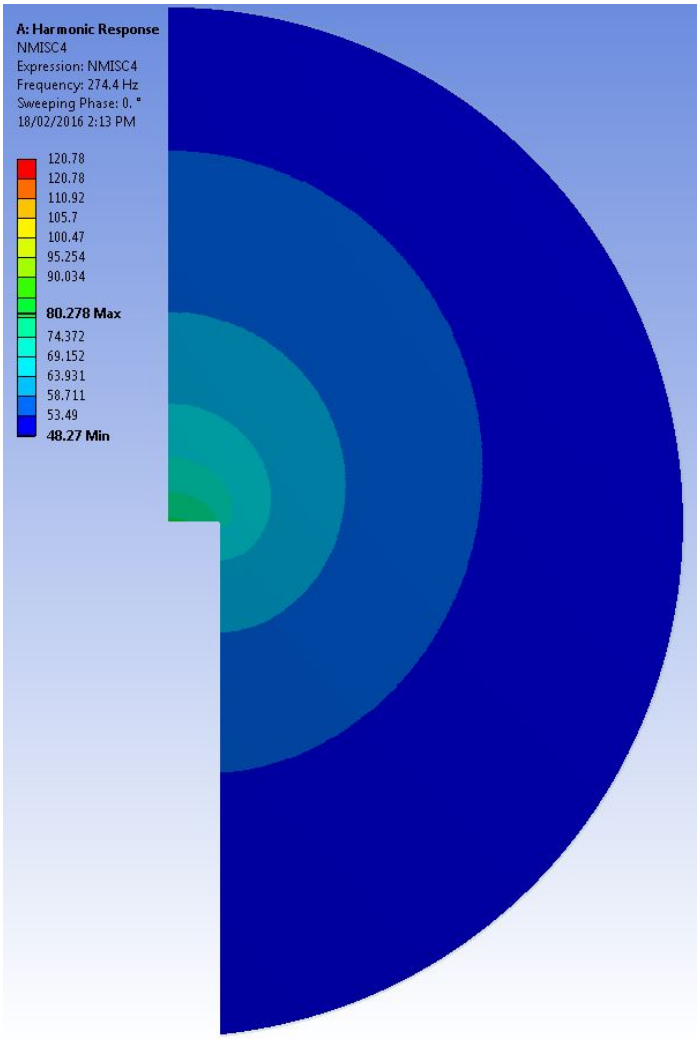

Figure C.25: SPL (dB re 20 µPa) contour plot with ANSYS Mechanical for a 2-D unbaffled circular piston at 274 Hz without the duct

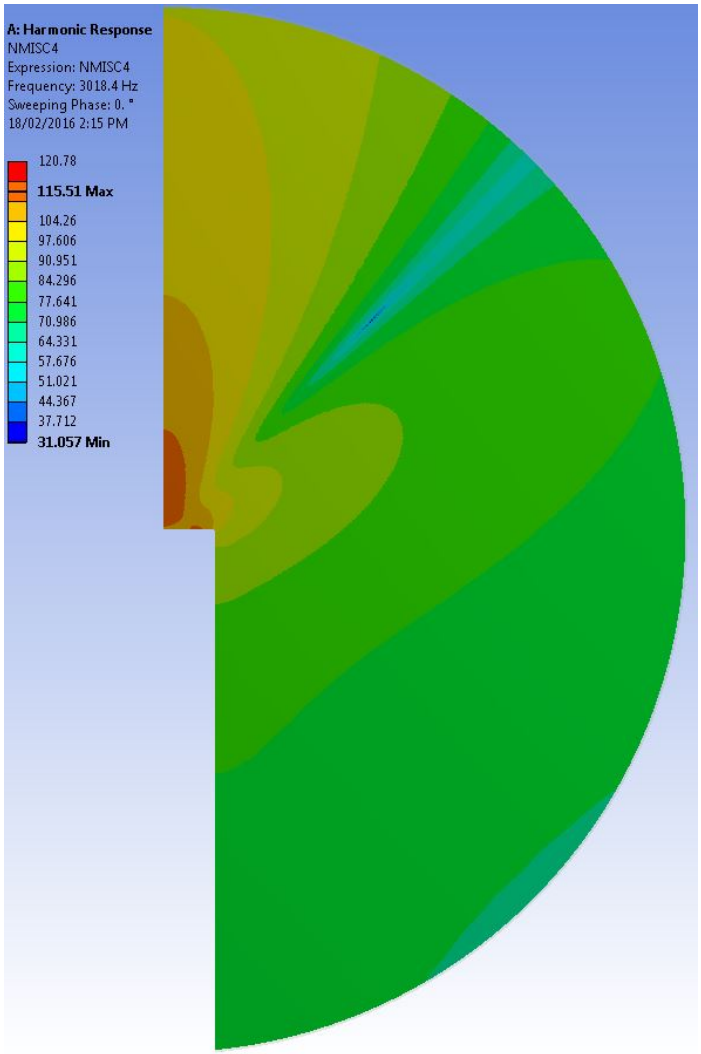

Figure C.26: SPL (dB re 20 µPa) contour plot with ANSYS Mechanical for a 2-D unbaffled circular piston at 3018 Hz without the duct

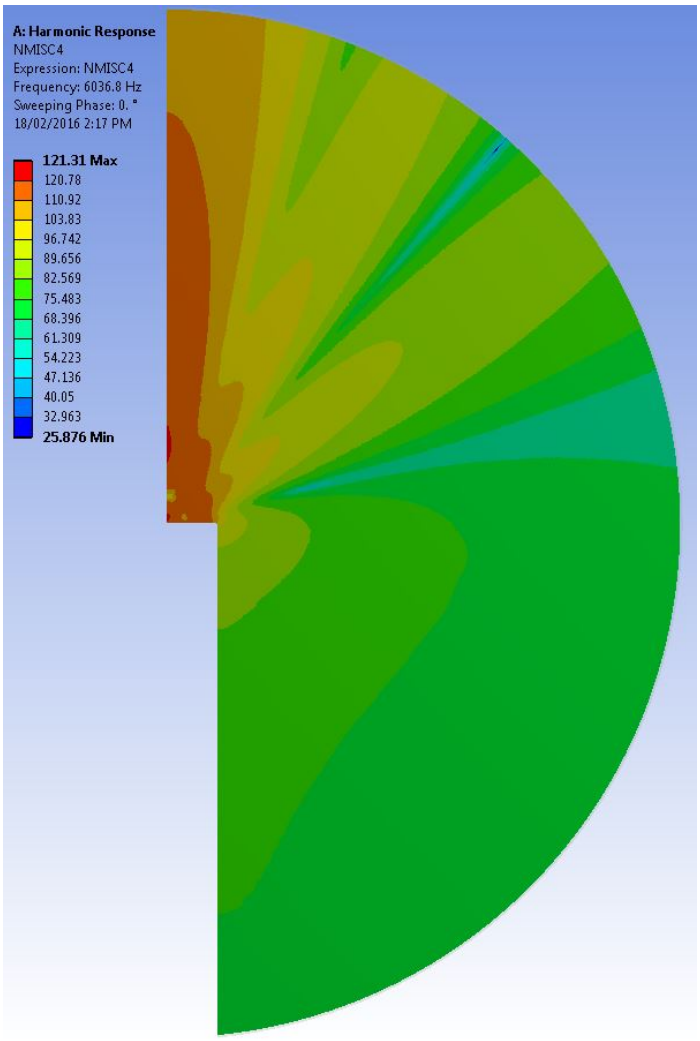

Figure C.27: SPL (dB re 20 µPa) contour plot with ANSYS Mechanical for a 2-D unbaffled circular piston at 6036 Hz without the duct

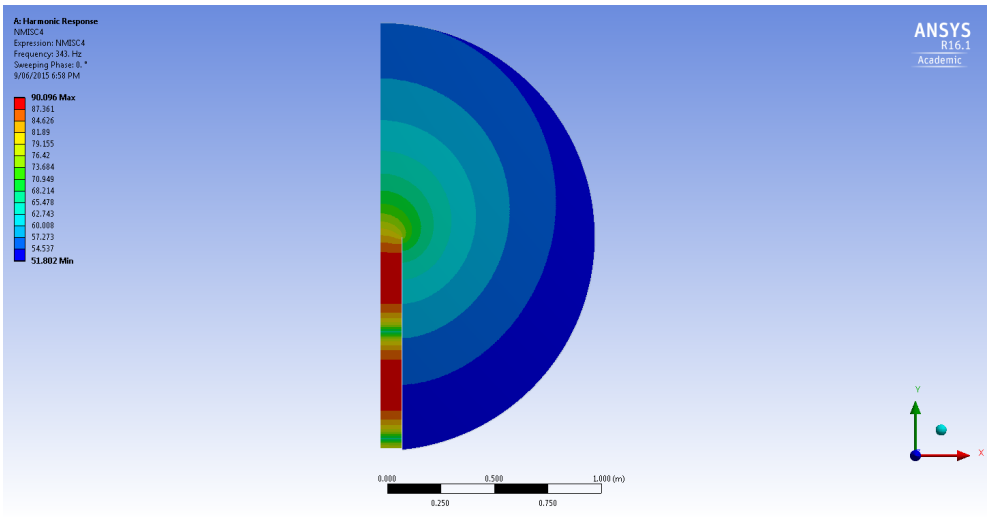

Figure C.28: SPL (dB re 20 µPa) contour plot with ANSYS Mechanical for a 2-D unbaffled circular piston at 343 Hz with the duct

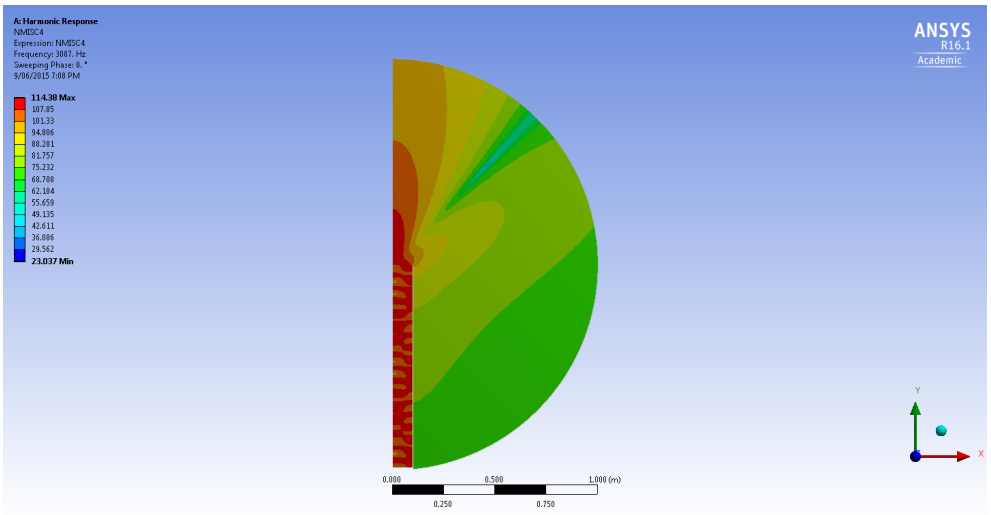

Figure C.29: SPL (dB re 20 µPa) contour plot with ANSYS Mechanical for a 2-D unbaffled circular piston at 3087 Hz with the duct

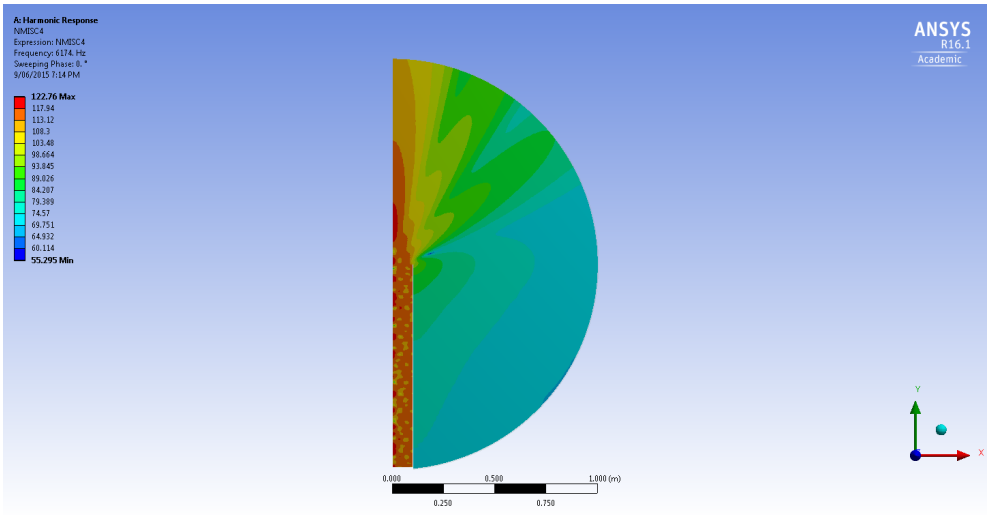

Figure C.30: SPL (dB re 20 µPa) contour plot with ANSYS Mechanical for a 2-D unbaffled circular piston at 6174 Hz with the duct

C.7 Sound propagation from a point source in uniform flow in 2-D

This section presents the results for sound propagation from a point source in 2-D convected by a uniform, subsonic mean flow. The problem at hand is based on a paper by Bailly and Juve [18], where the authors investigate this case analytically and numerically using the linearised Euler equations. The motivation for the work is to investigate if the linearised acoustic wave equation with convective effects using the scalar flow potential, described in Chapter 3 and elaborated in Appendix B, can be used to model the acoustic pressure field. ANSYS Mechanical was used as the acoustic FE solver with the linearised acoustic wave equation with mean flow using the scalar flow potential. Apart from comparing the results between the linearised acoustic wave equation with mean flow using the scalar flow potential and the linearised Euler equation from Bailly and Juve [18], additional cases were validated using the University of Technology of Compiègne's (UTC's) acoustic FE solver with Galbrun's equation. Details of the the acoustic FE solver with Galbrun's equation can be found follows: Baccouche et al. [16], Gabard et al. [62, 63], Treysséde and Ben Tahar [159], and Treysséde et al. [160]. The results and discussion in this section are presented as the following:

- background and description of the problem,
- numerical validation against the literature,
- numerical validation of the linearised acoustic wave equation with mean flow using the scalar flow potential and Galbrun's equations, and
- summary of findings.

C.7.1 Background and problem definition

The parameters and definition for the problem are based on the case presented in Bailly and Juve [18] and values defined for each parameters are described in

Table C.4. It should be noted that non-dimensional values are used to describe the speed of sound, c_0, and the density, ρ_0.

The schematic for the numerical domain is shown in Figure C.31. It should be noted that since non-dimensional values are used for c_0, and ρ_0, it can be assume that the dimensions for the domain is in dimensionless units. The acoustic domain is $L_x \times L_y$, 200×200, and the outer region of the domain is surrounded by PML elements, which is the shown in green and is 100 thick. The dimensions for the domain is identical to the case explored in the subsequent section, Section C.8.

Figure C.32 shows the numerical mesh for the acoustic FEM in ANSYS Mechanical, with the mesh comprising 230,400 second-order, hexahedra elements with mid-side nodes giving 1,617,603 nodes. It should also be noted that the mesh is structured and the elements are aligned with the Cartesian coordinate system. Even though the mesh in Figure C.32 is presented in 2-D the simulations were conducted in 2.5-D, with the mesh being one element thick.

Figure C.33 shows the acoustic mesh for the numerical simulations with Galbrun's equation using the UTC's FE solver. The mesh consists of linear triangular elements or otherwise known as either "4-3c", "$P^+ - P_1$", or "MINI" [159, 160]. The region with elements in blue represents the acoustic elements for modelling the sound propagation and the elements in orange are the PML elements for sound attenuation. The acoustic mesh consists of 346,622 nodes and 698,042 elements in total. It should be noted that the simulation has 1,039,866 degrees of freedom, and arises because each node has two acoustic displacement degrees of freedom and an acoustic pressure degree of freedom.

Table C.4: Parameters for the case with a point source submersed in a sheared flow.

Description	Parameter	Value	Units
Density in domain	ρ_0	1	
Speed of sound in domain	c_0	1	
Mach number	M	0.5	
Acoustic frequency	f	$\frac{1}{30}$	

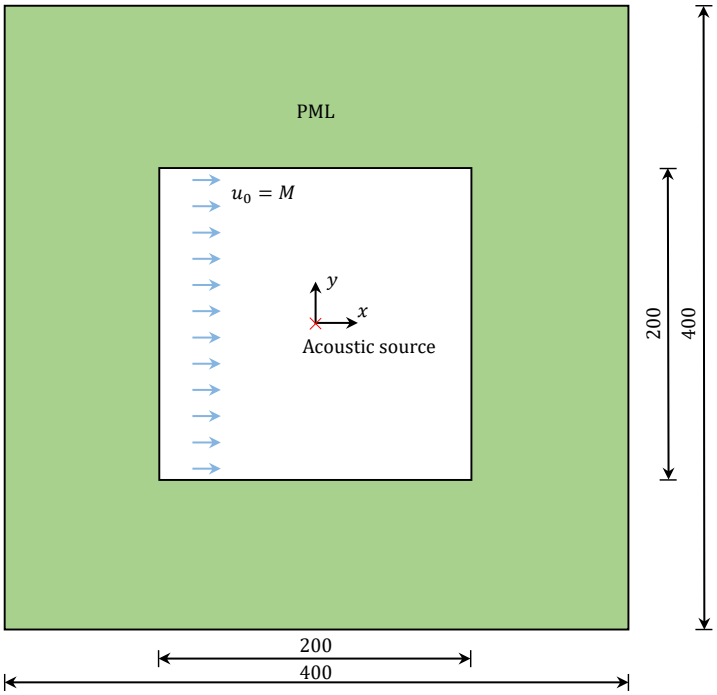

Figure C.31: The schematic for the case with a point source convected by a uniform mean flow, where the area in white is acoustic propagation domain, the area in green is the PML zone, the blue arrows represents the mean flow field throughout the acoustic domain, and the red cross at the origin represents the acoustic source.

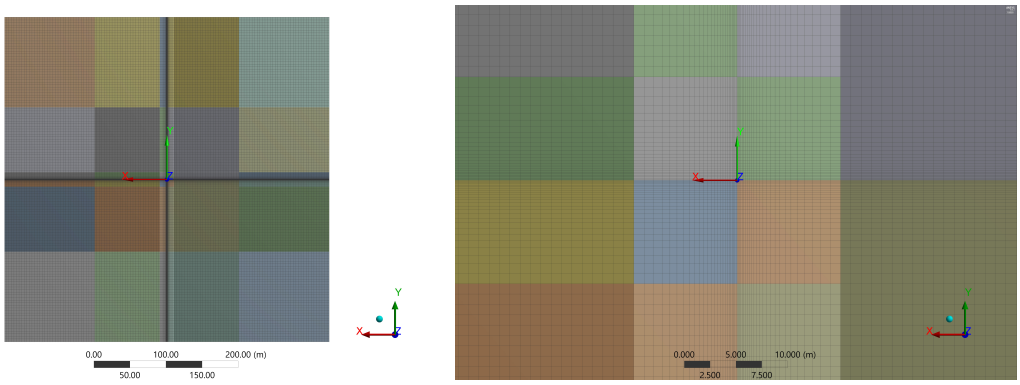

(a) Total Mesh (b) Mesh near the source

Figure C.32: The numerical mesh for the acoustic FEM with (a) showing the the total mesh, and (b) the mesh near the acoustic source a non-uniform grid and high spatial resolution to resolve the acoustic source.

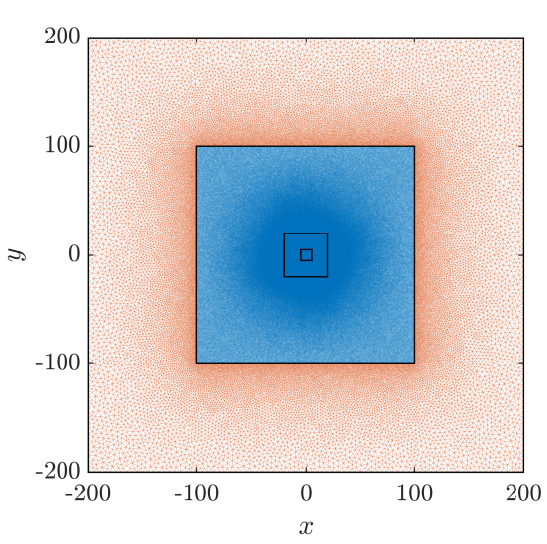

(a) Total mesh

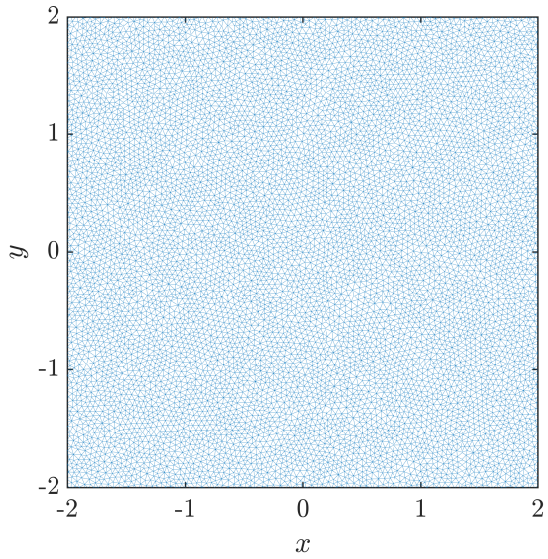

(b) Mesh near the acoustic source

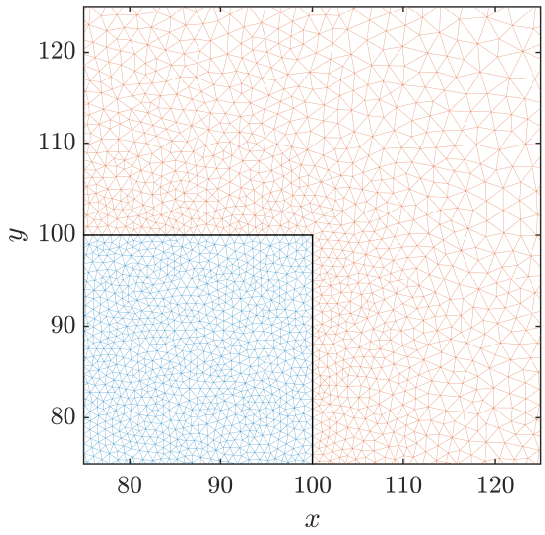

(c) Mesh at the PML interface

Figure C.33: The acoustic mesh generated by GMESH for solving the case with the point source convected by uniform, subsonic mean flow for solving using the UTC's FE solver and Galbrun's equation, where (a) is the total acoustic mesh, (b) is the mesh near the acoustic source at the origin, and (c) is the acoustic mesh at the interface between the acoustic propagating domain and the PML domain. The elements in blue represents the acoustic domain of interest and the elements in orange represents the domain with PML elements.

C.7.2 Numerical validation with literature

Figure C.34 shows the numerical results as a contour and isocontour plot for a point source submersed in uniform mean, subsonic flow. The numerical results were generated from the linearised acoustic wave equation with mean flow using the scalar flow potential,[1] described in Appendix B. The mean flow in each figure is going from left to right. The results are plotted with a linear and logarithmic scale, with the results in Figure C.34b showing qualitative similarity with the isocontour plot in Figure C.34c from the work by Bailly and Juve [18]. The key features of the contour plots in Figure C.34 is the reduction in acoustic wavelength upwind of the acoustic source and an increase in acoustic wavelength downwind of the acoustic source.

The results in Figure C.35 shows the acoustic pressure along $y = 0$, and compares the results from Bailly and Juve [18] and the linear acoustic wave equation with scalar flow potential from ANSYS Mechanical. Slight modifications were applied to the acoustic results from ANSYS Mechanical with the acoustic pressure being multiplied by a scaling factor to quantitatively match the results from Bailly and Juve [18]. There is a slight differences in Figure C.35 with the results downwind, which is explained in Section C.7.3. Even though the work conducted by Bailly and Juve [18] uses a time-dependent linearised Euler equation acoustic solver, a harmonic solver using linear acoustic wave equation with scalar flow potential can adequately reproduce the results. Additionally, the source term used by Bailly and Juve [18] and the acoustic FEM solver are different. Bailly and Juve [18] defines the acoustic source term as a Gaussian point source with the following definition:

$$f(x,y) = 0.5\exp\left(-\beta\ln(2)\left[x^2+y^2\right]\right), \tag{C.1}$$

where $f(x,y)$ is the Gaussian distribution function in space, and β is the coefficient governing the spread of the Gaussian distribution. However, ANSYS Mechanical defines the acoustic source as a line source in a 2.5-D by a Dirac delta function, δ, along an edge.

[1] To simplify the discussion for the reader, the linearised acoustic wave equation with mean flow using the scalar flow potential using ANSYS Mechanical has been refer to as ANSYS Mechanical in this section.

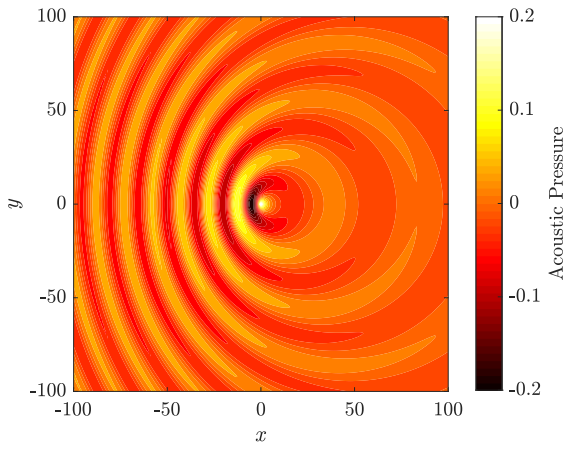

(a) Linear scale

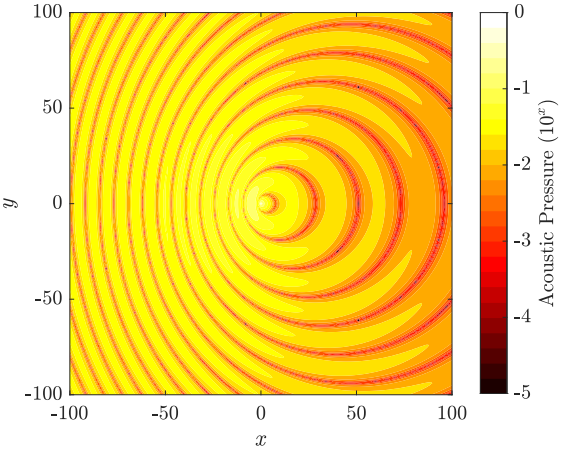

(b) Logarithmic scale

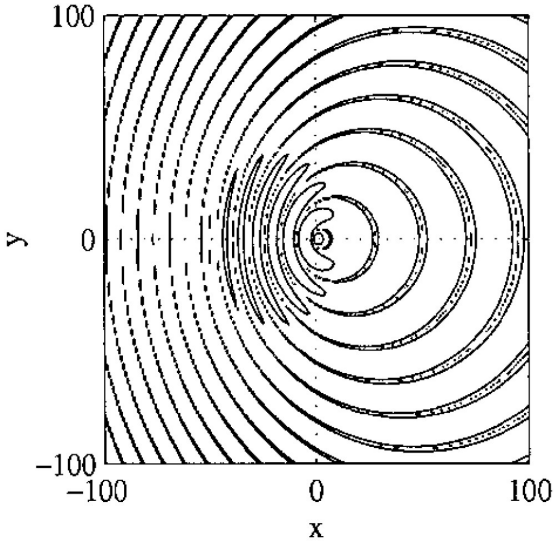

(c) Isocontour plot from Bailly and Juve [18]

Figure C.34: Acoustic pressure contour plots for a point source convected in uniform, subsonic flow with $M = 0.5$, and solved using a linearised acoustic wave equation with scalar potential flow formulation, with (a) showing the contour plot with a linear scale, (b) showing the contour plot with a logarithmic scale, and (c) showing the results from Bailly and Juve [18] as isocontour plots with the values ——, 10^{-1}, 10^{-2}, 10^{-3}; — — —, 10^{-4}; and ▪ ▪ ▪ ▪, 10^{-5}. The flow in the figures is going from left to right.

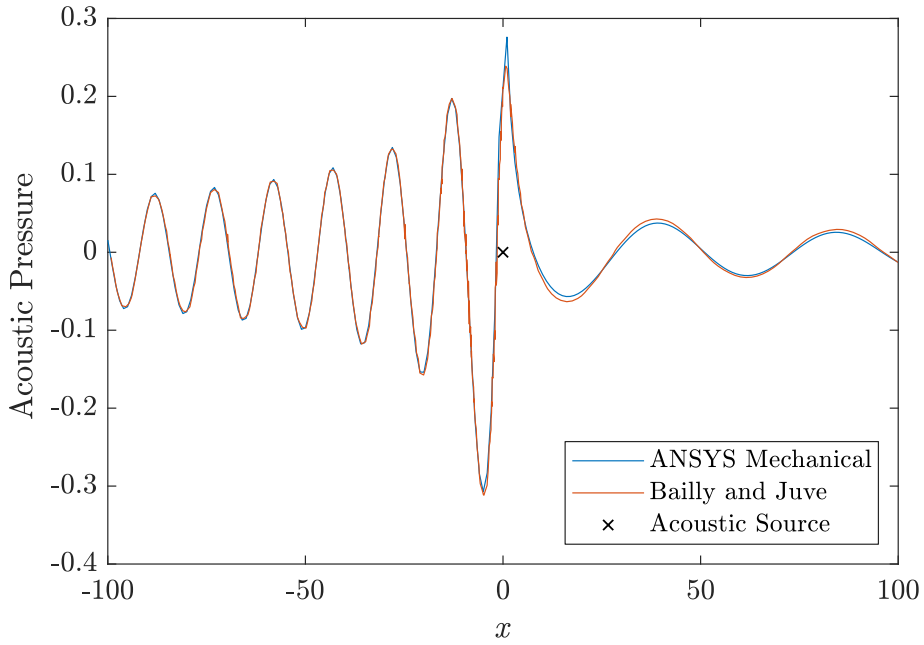

Figure C.35: The acoustic pressure along the line at $y = 0$ for a point source convected in uniform, subsonic flow with $M = 0.5$. The results compares two different acoustic FE methods, the linearised acoustic wave equation with mean flow using the scalar flow potential and the linearised Euler equation from Bailly and Juve [18]. The black cross represents the position of the acoustic source.

An additional note is that there is an analytical expression of the pressure field for this case and the results are presented in Bailly and Juve [18]. The analytical expression for pressure can be described with

$$p_a(x, y, t) = f(x, y) * \frac{dG(x, y, t)}{dt}, \tag{C.2}$$

where p_a is the acoustic pressure, $G(x, y, t)$ is the 2-D Greens function in time, described as

$$G(x, y, t) = \frac{i}{4} \frac{1}{c_0 \sqrt{1 - M^2}} H_0^{(1)} \left[\frac{k\sqrt{x^1 + (1 - M^2)y}}{1 - M^2} \right] \exp\left(\frac{-iM}{1 - M^2} kx - i\omega t \right), \tag{C.3}$$

where i is the imaginary number, c_0 is the speed of sound, M is the number, $H_0^{(1)}$ is the Hankel function, k is the acoustic wavenumber, and $\omega = 2\pi f$ is angular acoustic frequency. Solving the analytical expression for pressure in Equation (C.2) proved

difficult. Instead, the data for the analytical solution presented in Bailly and Juve [18] was used for comparison in Figure C.35. It was shown in Bailly and Juve [18] that their solution with the linearised Euler equation shows perfect agreement with their analytical expression, and hence the results for the numerical and analytical solution from Bailly and Juve [18] are presented as one plot in Figure C.35.

C.7.3 Numerical validation with Galbrun's equation

The results presented in this section uses two different acoustic FE methods to investigate the sound propagation from a point source in uniform, subsonic flow; the linearised acoustic wave equation with mean flow using the scalar flow potential, and Galbrun's equation. Figure C.36 shows the acoustic pressure at $y = 0$, using the two different acoustic FE methods for three different frequencies. The results show good agreement between the two different methods, with the exception of the acoustic pressure near the acoustic source, shown with a black cross. Similar to the results in Bailly and Juve [18], the acoustic source for Galbrun's equation uses a source with Gaussian point spread function given in Equation (C.1), whereas, ANSYS Mechanical uses a Dirac delta function. Therefore, acoustic pressure near the acoustic source may show slight discrepancies, but as the wave propagates the results show excellent agreement.

The results presented in Figure C.36 are different to Figure C.35, with the phase for the acoustic source, and the definition for the acoustic source with a Gaussian point spread function. A limitation to using the frequency domain solver with Galbrun's equation is that the phase of the acoustic source cannot be altered and remains at 0°, whereas the phase of the acoustic source in Bailly and Juve [18] is at 270°. Furthermore, for the Gaussian point spread function in Galbrun's equation the value for β in Equation (C.1) needs to be altered for Galbrun's equation to have good agreement with ANSYS Mechanical in Figure C.36. For the work conducted by Bailly and Juve [18], $\beta = 0.5$, whereas for the results in Figure C.36, $\beta = 0.05$. The difference in β suggests that the acoustic source in Galbrun's formulation will need to be 'stretched' to match the results with ANSYS Mechanical, when compared to the acoustic source using the linearised Euler equation. Figure C.37 supports the

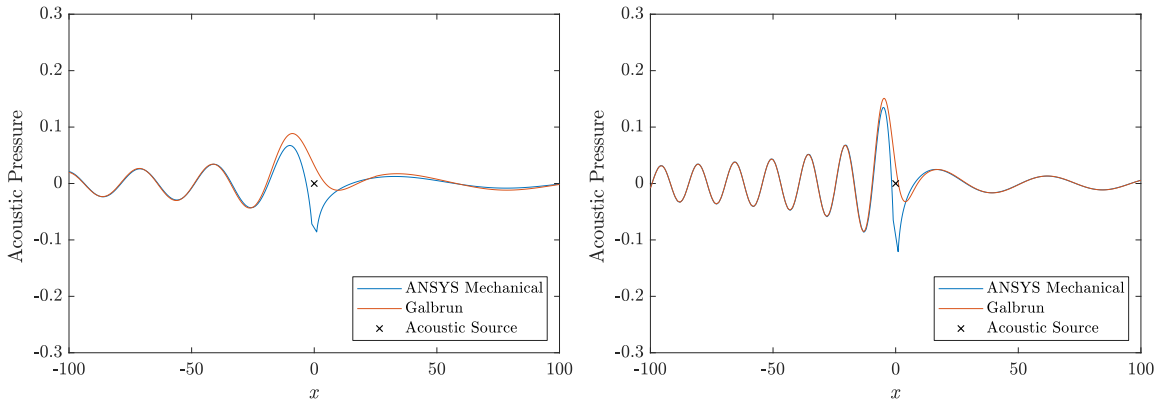

(a) Acoustic frequency, $f = 1/60$

(b) Acoustic frequency, $f = 1/30$

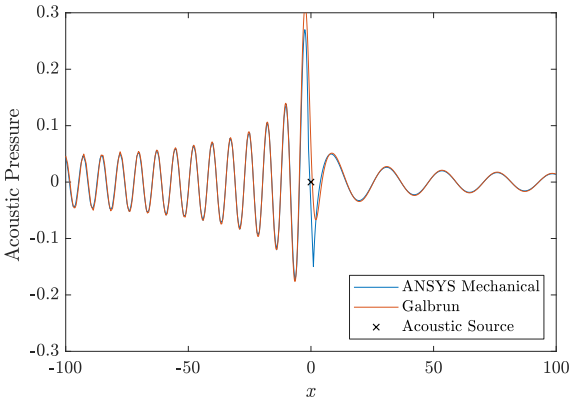

(c) Acoustic frequency, $f = 1/15$

Figure C.36: The acoustic pressure along the line at $y = 0$ for a point source convected in uniform, subsonic flow with $M = 0.5$. The acoustic results compare two different acoustic FE methods, the linearised acoustic wave equation with mean flow using the scalar flow potential and Galbrun's equation. The black cross represents the position of the acoustic source. The results presented are for three different frequencies, $f = [1/60, 1/30, 1/15]$, where f is normalised by c_0 and ρ_0.

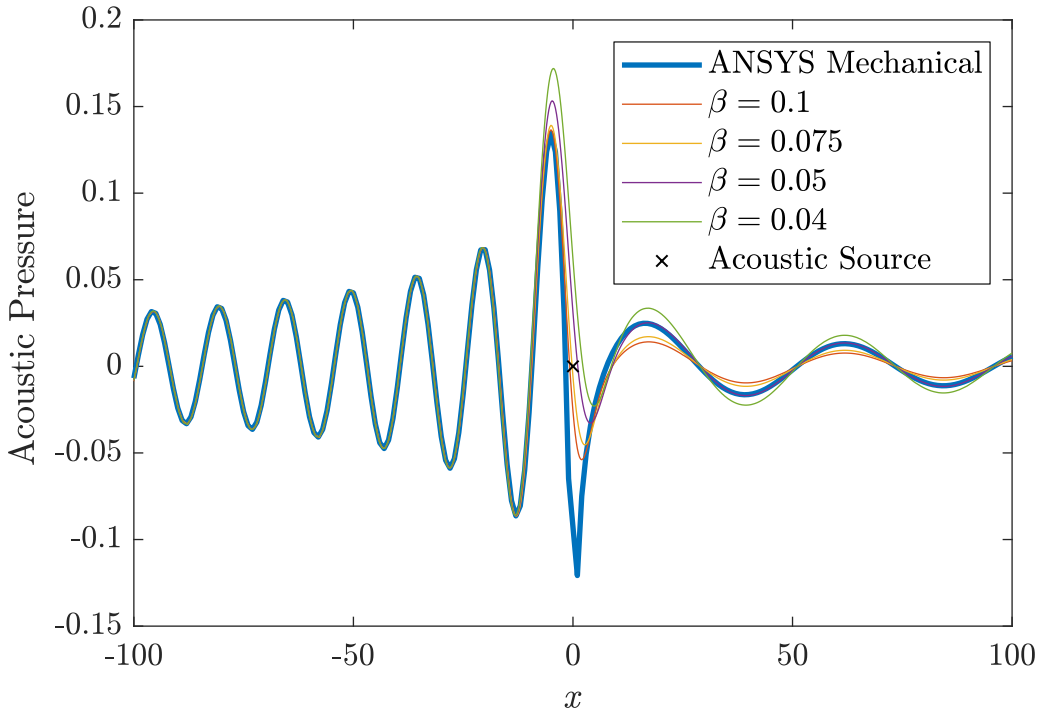

Figure C.37: The acoustic pressure along the line at $y = 0$ for a point source convected in uniform, subsonic flow with $M = 0.5$. The results from ANSYS Mechanical are compared to the results generated from Galbrun's equation with varying β from Equation (C.1). The black cross represents the position of the acoustic source.

need to alter β in Equation (C.1) to match the results from ANSYS Mechanical. It can also be seen in Figure C.37 that β dictates the amplitude of the acoustic wave downwind, but the acoustic wavelength is insensitive to the change in β.

Figure C.38 shows the acoustic pressure along the line at $y = 0$ for a point source convected in uniform, subsonic flow with four different flow velocities, $M = [0.1, 0.2, 0.3, 0.4]$. The results show good agreement between the scalar potential solution of ANSYS Mechanical and UTC's FE solver of Galbrun's equation for four different cases. This is an important result as it shows the linearised acoustic wave equation with convective flow using the scalar flow potential is capable of modelling sound propagation through different uniform flow conditions.

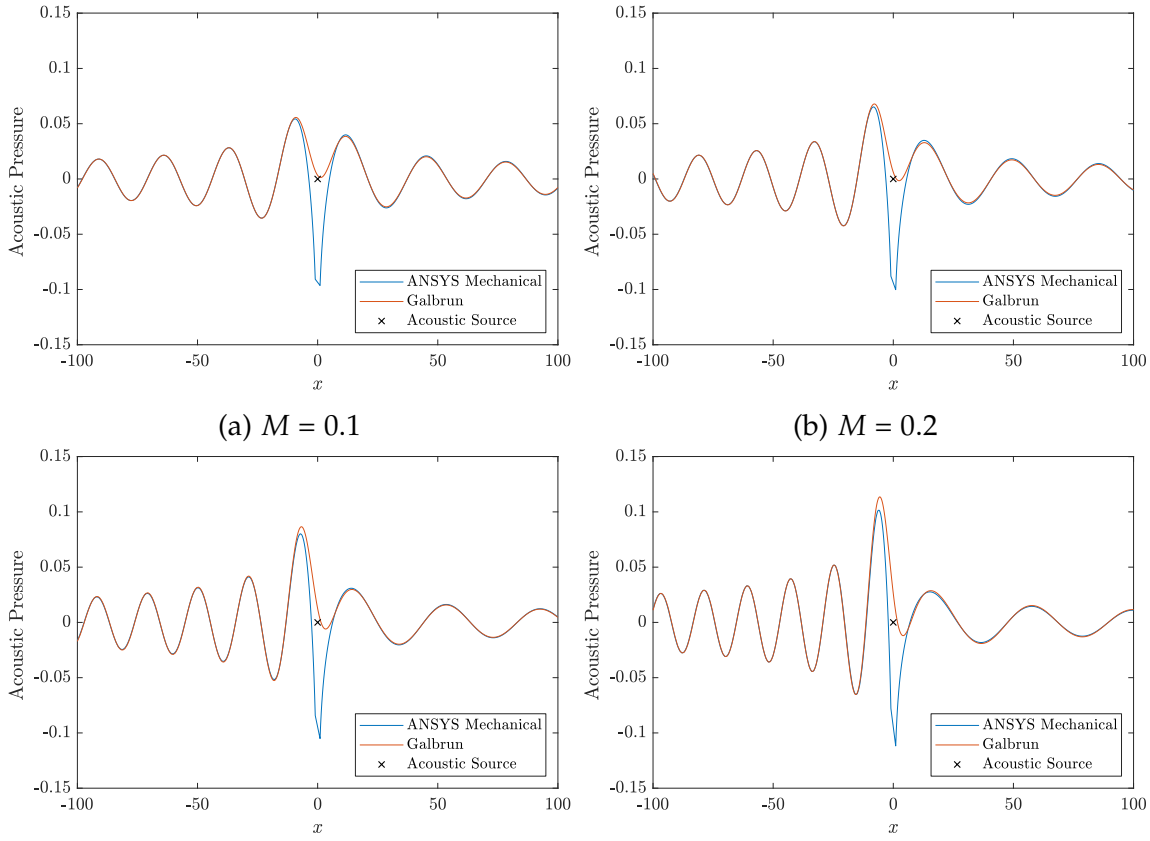

(a) $M = 0.1$ (b) $M = 0.2$

(c) $M = 0.3$ (d) $M = 0.4$

Figure C.38: The acoustic pressure along the line at $y = 0$ for a point source convected in uniform, subsonic flow at four different Mach numbers, $M = [0.1, 0.2, 0.3, 0.4]$. The acoustic results compare two different acoustic FE methods; the linearised acoustic wave equation with mean flow using the scalar flow potential and Galbrun's equation. The black cross represents the position of the acoustic source.

C.7.4 Summary of findings

Investigating the 2-D problem of a point source convected by a uniform, subsonic mean flow it has been shown that ANSYS Mechanical with the linearised acoustic wave equation with mean flow using the scalar flow potential can be used as a tool to model the instantaneous acoustic pressure under various conditions. Under certain circumstances ANSYS Mechanical which uses the linearised acoustic wave equation with mean flow using the scalar flow potential has shown good agreements with the linearised Euler equation and analytical solution from Bailly and Juve [18]. However, the results are only verified with Bailly and Juve [18] for the instantaneous acoustic pressure at a single acoustic frequency, single acoustic phase and the instantaneous along the vertical profile for $y = 70$, as shown in Figure C.35. Qualitative assessment with isocontour plots for the instantaneous acoustic pressure in Figure C.34 has also shown good qualitative agreement to show the necessary scientific outcomes for a point source convected by uniform, subsonic mean flow.

Further analysis of the linearised acoustic wave equation with mean flow using the scalar flow potential, has been completed by comparing the results from Galbrun's formulation with the UTC's FE solver. When comparing the two numerical methods the results in Section C.7.3 has shown good agreements with the two approaches under certain conditions. A key condition is the definition of the acoustic source with ANSYS Mechanical being a limiting factor, with ANSYS Mechanical limiting the acoustic source definition to a Dirac delta function. By changing the shape of the Gaussian distribution using β from Equation (C.1), the results from Galbrun's equation can match the results from ANSYS Mechanical. Additional analysis has shown that for a certain set of flow conditions ($M = [0.1, 0.2, 0.3, 0.4, 0.5]$) and for three acoustic frequencies there is good agreement between the two different numerical methods. Even though the cases explored are limited, the results from this section has shown that ANSYS Mechanical with the linearised acoustic wave equation with mean flow using the scalar flow potential can be used to model in 2-D the sound from a point source submersed in a uniform, subsonic mean flow.

C.8 Sound propagation from a point source in sheared flow in 2-D

In this section the case of the sound propagation from a 2-D point source submersed in a sheared flow is investigated and is based on published results from Ewert and Schröder [57] and Feng et al. [59]. Ewert and Schröder [57] and Feng et al. [59] both use a time-dependent acoustic FEM to investigate the same problem, however Ewert and Schröder [57] use both a linearised Euler equations and acoustic perturbation equation, whereas Feng et al. [59] use Galbrun's equation. The results from ANSYS Mechanical were solved using a frequency domain formulation and were validated against the time domain results in Ewert and Schröder [57] and Feng et al. [59]. The motivation for the work is to investigate if the linearised acoustic wave equation with mean flow using the scalar flow potential,[2] described in Chapter 3 and elaborated in Appendix B, can be used model the acoustic pressure in regions with shear (velocity gradient) and no rotational acoustic effects, as described in Feng et al. [59]. Finally, comparisons between two different frequency domain solvers, namely the linearised acoustic wave equation with mean flow using the scalar flow potential and Galbrun's equation, are presented in this section. Similar to Section C.7, the University of Technology of Compiègne's (UTC's) acoustic FE solver with Galbrun's equation will be used to compare the numerical outcomes from ANSYS Mechanical and the linearised acoustic wave equation with mean flow using the scalar flow potential. Details of the UTC's acoustic FE solver with Galbrun's equation can be found from the following references: Baccouche et al. [16], Gabard et al. [62, 63], Treysséde and Ben Tahar [159], and Treysséde et al. [160].

The presentation of the results of this section can be broken down into the following:

- background and description of the problem,

[2] To simplify the discussion for the reader, the linearised acoustic wave equation with mean flow using the scalar flow potential using ANSYS Mechanical has been refer to as ANSYS Mechanical in this section.

- numerical validation against the published literature,
- numerical validation of the linearised acoustic wave equation with mean flow using the scalar flow potential and Galbrun's equation, and
- summary of findings.

C.8.1 Background and problem definition

The parameters and definition for the problem are based on the case presented in Ewert and Schröder [57] and Feng et al. [59]. The parameters for the problem are described in Table C.5, and it should be noted that non-dimensional values are used to describe the speed of sound, c_0, and the density, ρ_0.

The schematic for the numerical domain is shown in Figure C.39, and the dimensions of the domain is identical to Figure C.31. The acoustic domain is $L_x \times L_y$, 200×200, and the outer region of the domain is surrounded by PML elements, which is the shown in green and is 100 thick. It should be noted that since non-dimensional values are used for c_0, and ρ_0, the domain is expressed in dimensionless units. Figure C.40a and C.40b shows the mean velocity as a profile, and a contour plot for the domain, where the mean velocity is a sheared flow of finite thickness defined as

$$u_0(y) = M \times \tanh\left(\frac{2y}{\delta}\right), \tag{C.4}$$

Table C.5: Parameters for the case with a point source submersed in a sheared flow.

Description	Parameter	Value	Units
Density in domain	ρ_0	1	
Speed of sound in domain	c_0	1	
Mach number	M	0.5	
Acoustic frequency	f	$\frac{1}{30}$	
Shear layer width	δ	50	

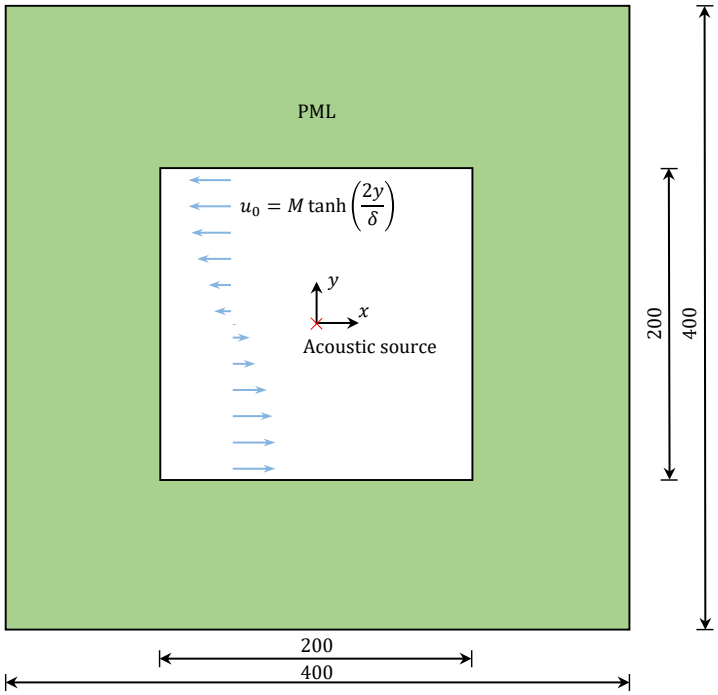

Figure C.39: The schematic for the case with a point source convected by a finite thickness shear layer, where the area in white is acoustic propagation domain, the area in green is the PML zone, the blue arrows represents the mean velocity field throughout the acoustic domain, and the red cross at the origin represents the acoustic source.

where u_0 is the horizontal bulk fluid velocity, y is the nodal location along the vertical axis, M is the Mach number, and δ is the width of the shear. The values used to define the velocity profile are given in Table C.5.

The acoustic mesh for the following work is the same as the previous example in Section C.7, and presented in Figure C.32. Again, the acoustic mesh has 230400 second-order, quadrilateral elements with mid-side nodes or 1617603 nodes.

Figure C.41 shows the acoustic mesh for the numerical simulations with Galbrun's equation using the UTC's FE solver. The mesh consists of linear triangular elements or otherwise known as either "4-3c", "$P^+ - P_1$", or "MINI" [159, 160]. The region with elements in blue represents the acoustic elements for modelling the sound propagation and the elements in orange are the PML elements for sound attenuation. The acoustic mesh consists of 500,527 nodes and 1,006,972 elements

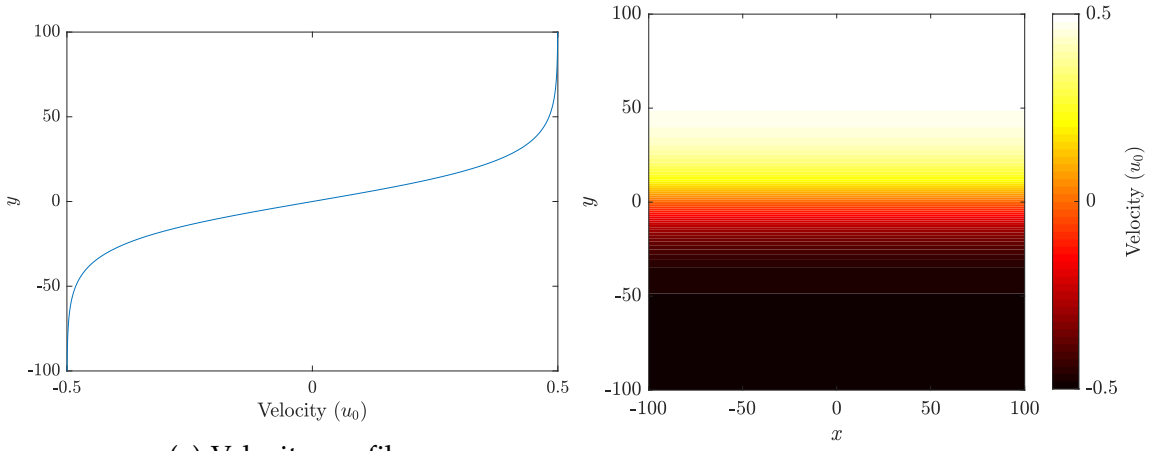

(a) Velocity profile

(b) Contour plot of velocity

Figure C.40: The velocity profile for the mean flow with a finite thickness shear layer, based on Equation (C.4), with (a) showing the velocity profile as a function of y, and (b) showing a contour plot of velocity for the domain.

in total. It should be noted that the simulation has 1,501,581 degrees of freedom, as each node has two acoustic displacement degrees of freedom and an acoustic pressure degree of freedom.

C.8.2 Numerical validation with literature

Figure C.42 shows the instantaneous acoustic pressure as a contour plot for sound propagation from a point source with a finite thickness shear layer from four different acoustic FE methods. The acoustic results shows the refraction of sound upwind and downwind of the acoustic source. Furthermore, since the direction of the shear layer is in the top and bottom half of the domain are opposite and symmetrical, as shown in Figure C.40, the acoustic results reflects the symmetry in the solution. Additional analysis of Figure C.42 shows that the acoustic pressure contour plot is qualitatively similar to the results by Feng et al. [59] in Figure C.42b and Ewert and Schröder [57] in Figure C.42c. It should be noted that Ewert and Schröder [57] and Feng et al. [59] solves the problem using a transient acoustic FE model with the linearised Euler equation and Galbrun's equation, respectively.

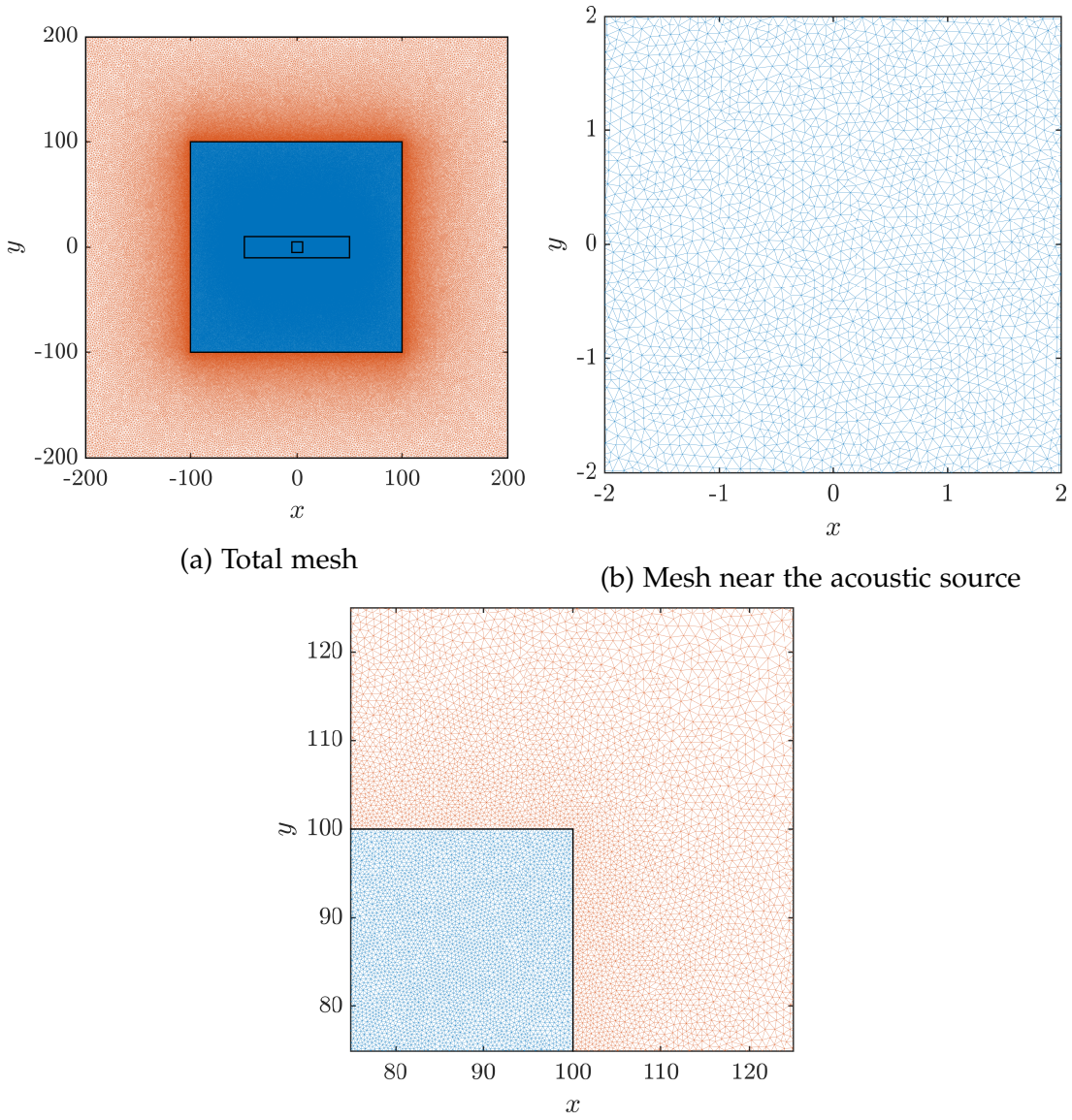

(a) Total mesh

(b) Mesh near the acoustic source

(c) Mesh at the PML interface

Figure C.41: The acoustic mesh generated by GMESH for solving the case with the point source convected by a finite thickness sheared flow for solving using the UTC's FE solver and Galbrun's equation, where (a) is the total acoustic mesh, (b) is the mesh near the acoustic source at the origin, and (c) is the acoustic mesh at the interface between the acoustic propagating domain and the PML domain. The elements in blue represents the acoustic domain of interest and the elements in orange represents the domain with PML elements.

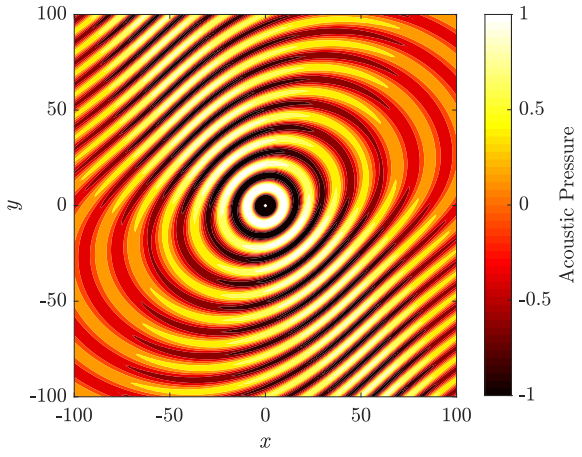

(a) Contour plot from ANSYS Mechanical

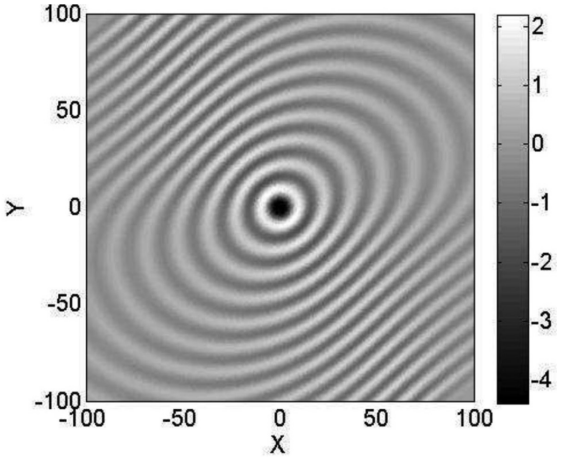

(b) Contour plot from Feng et al. [59]

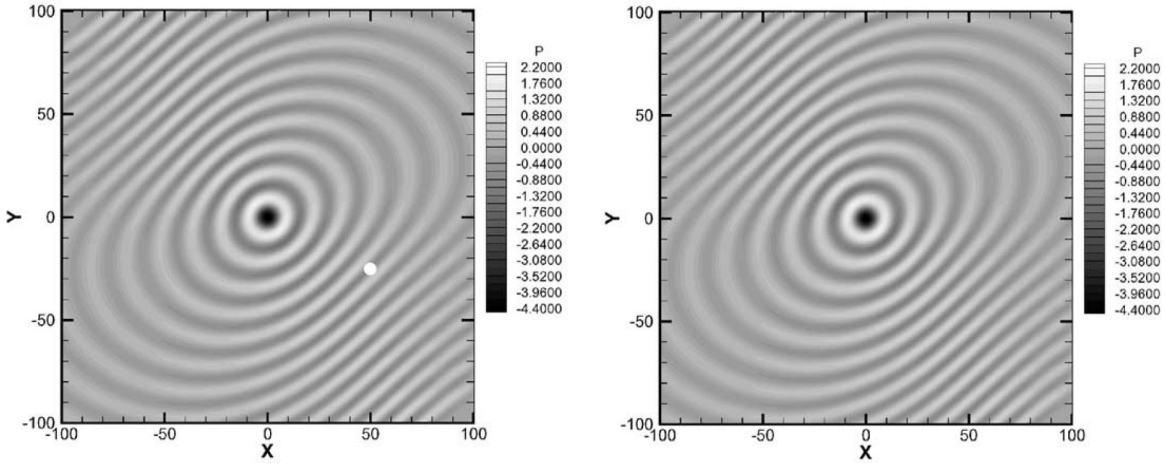

(c) Contour plot from Ewert and Schröder [57], where the left figure shows the results generated from the linearised Euler equations and the right figure shows the results generated from a variant of the acoustic perturbation equation.

Figure C.42: Acoustic pressure contour plots for a point source convected by a finite thickness shear flow defined by Equation (C.4), where (a) shows the results from ANSYS Mechanical generated using the linearised acoustic wave equation with mean flow using the scalar flow potential, (b) shows the time domain results from Feng et al. [59] with Galbrun's equation, and (c) shows the time domain results from Ewert and Schröder [57] with two different numerical methods: (left) the linearised Euler equations, and (right) a variant of the acoustic perturbation equation.

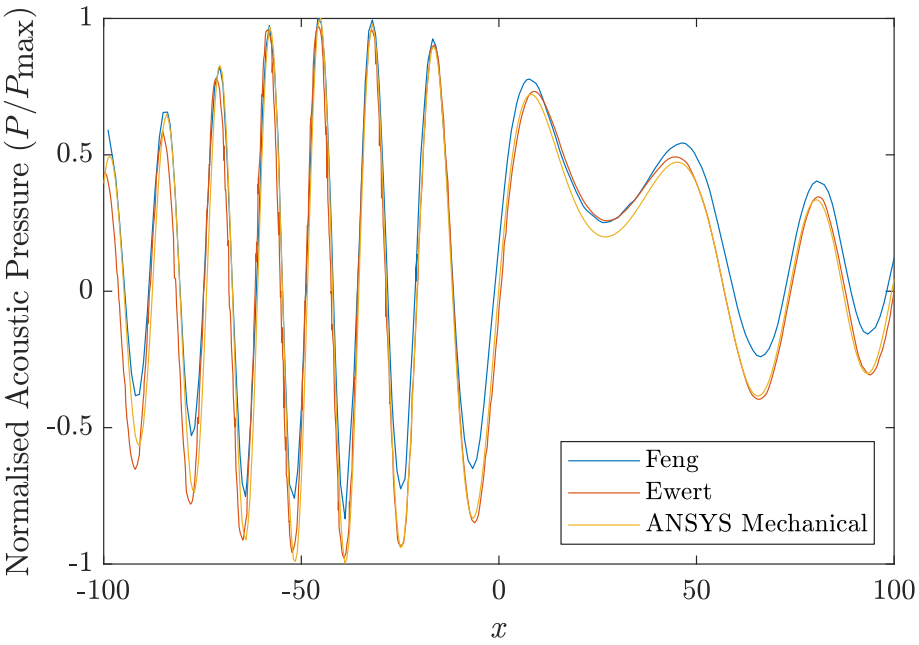

Figure C.43: The instantaneous acoustic pressure along the line at $y = 70$ for a point source convected by a finite thickness shear flow defined by Equation (C.4), comparing the results from the linearised acoustic wave equation with mean flow using the scalar flow potential, the linearised Euler equation from Ewert and Schröder [57], and Galbrun's equation from Feng et al. [59].

Figure C.43 show the instantaneous acoustic pressure at $y = 70$ for the sound propagation from an acoustic source within a finite thickness shear layer. The results were generated using three different numerical methods: the linearised acoustic wave equation with mean flow using the scalar flow potential, the linearised Euler equations [57], and Galbrun's equation [59]. The three different methods show good agreement with the results of Feng et al. [59] showing the greatest deviation in results. It should be noted that to generate the plot in Figure C.43 with ANSYS Mechanical the data needed to be scaled to account for the different source and the method for scaling results was to normalise the acoustic pressure by the maximum acoustic pressure.

Whilst the results in Figure C.43 show good agreement, some minor details will need to be considered when comparing the results between three different methods. Firstly, the results generated from the linearised acoustic wave equation

with mean flow using the scalar flow potential is a frequency domain solver and the phase for the acoustic source must be adjusted to match the phase of the acoustic source for the time-domain solutions from Ewert and Schröder [57] and Feng et al. [59]. Additionally, the definition for the acoustic sources are different; with ANSYS Mechanical defining the acoustic source as a Dirac delta function, as described in Section C.7.2, whereas Ewert and Schröder [57] and Feng et al. [59] defines the acoustic source as a Gaussian point source by the following function:

$$f(x,y) = \exp\left(-\ln(2)\left[\frac{x^2+y^2}{\sigma^2}\right]\right), \tag{C.5}$$

where $f(x,y)$ is the Gaussian distribution function in space, and $\sigma^2 = 9$ is the coefficient governing the spread of the Gaussian distribution. The results in Figure C.43 are presented outside of the sheared mean flow, where the rotational field of acoustic pressure is minimal as was described by Feng et al. [59]. This is very important, as a deficiency in the linearised acoustic wave equation with mean flow using the scalar flow potential is the assumption that the acoustic field is irrotational. Although, the assumption holds true for the linearised acoustic wave equation with mean flow using the scalar flow potential, the results show that it is appropriate to compare the acoustic results in the region outside of the shear layer, where the rotational components of the acoustic field would have minimal impact. This observation is important, and will be explored further in the subsequent section by investigating the acoustic instantaneous pressure in the shear layer by comparing the results with two different solvers: the linearised acoustic wave equation with mean flow using the scalar flow potential in ANSYS Mechanical and Galbrun's equation with the FE solver from the UTC.

C.8.3 Numerical validation with Galbrun's equation

In this section, the numerical results from the linearised acoustic wave equation with mean flow using the scalar flow potential solved using ANSYS Mechanical with results obtained using Galbrun's equation with the FE solver from the UTC, for the case with a point source convected by a finite thickness shear layer. Again, this is similar to the method in Section C.7.3. To aid in comparisons, the work

conducted in this section uses a frequency domain formulation of Galbrun's equation, whereas Feng et al. [59], uses a time domain formulation of Galbrun's equation. It should be noted that both formulations are from the UTC's FE solver. With access to the UTC's FE solver it is possible to further investigate the validity of using the linearised acoustic wave equation with the scalar flow potential in ANSYS Mechanical to model a point source convected by a finite thickness shear layer.

Figure C.44 shows the instantaneous acoustic pressure at $y = 70$ for sound propagation from a point source in sheared flow, with two different acoustic FE methods, the linearised acoustic wave equation with mean flow using the scalar flow potential and Galbrun's equations. Figure C.44 presents the results at three frequencies, $f = [1/(8\pi), 1/(4\pi), 1/(2\pi)]$. The parameters used for this simulation is expressed in Table C.5. Figure C.44 shows good agreement between the two method for all three frequencies. It should be noted that the pressure results had to be normalised by the maximum acoustic pressure to account for difference source amplitudes.

Figure C.45 shows the acoustic pressure along the line at $y = 70$ for a point source convected in a finite thickness shear layer flow with four different free-stream velocity, $M = [0.1, 0.2, 0.3, 0.4]$. The results show good agreement between the scalar potential solution of ANSYS Mechanical and the UTC's FE solver of Galbrun's equation for four different cases. This is an important result as it shows the linearised acoustic wave equation with convective flow using the scalar flow potential is capable of modelling sound propagation through different shear layers of varying velocity gradients, but more importantly it captures the sound refraction from the point source in the shear layer.

Figure C.46 shows the acoustic pressure at $y = 15$ with five different mesh densities used to solve the model with Galbrun's equation. The results with Galbrun's equation are compared against the results from ANSYS Mechanical. The results using Galbrun's equation shows numerical convergence in the acoustic pressure for the case from approximately $250,000$ nodes. There is good agreement with the converged solution from Galbrun's Equation and ANSYS Mechanical.

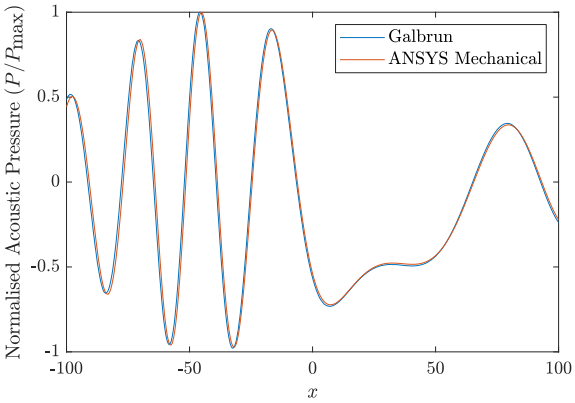

(a) Acoustic frequency, $f = 1/(8\pi)$

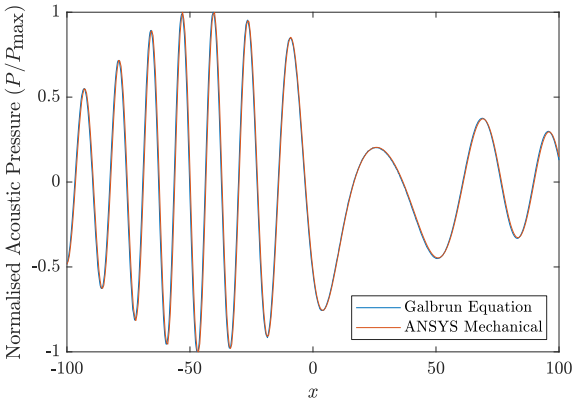

(b) Acoustic frequency, $f = 1/(4\pi)$

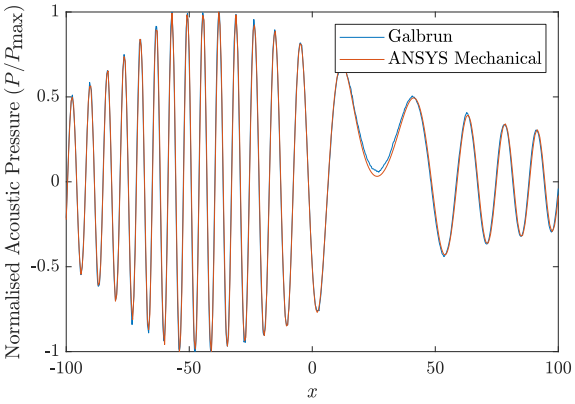

(c) Acoustic frequency, $f = 1/(2\pi)$

Figure C.44: The acoustic pressure along the line at $y = 70$ for a point source convected by a finite thickness shear flow defined by Equation (C.4), comparing the results from the linearised acoustic wave equation with mean flow using the scalar flow potential and Galbrun's equation. The results presented are for three different frequencies, $f = [1/(8\pi), 1/(4\pi), 1/(2\pi)]$.

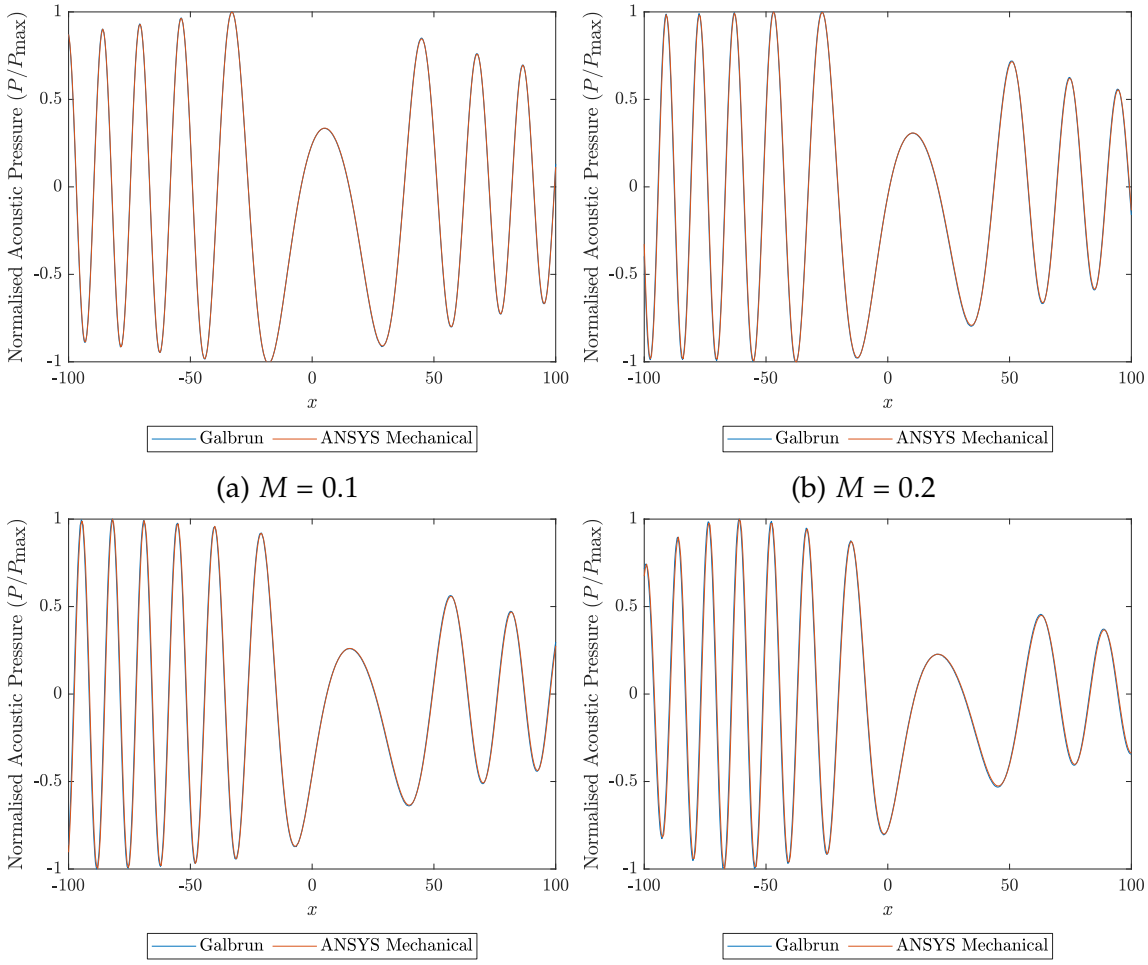

(a) $M = 0.1$ (b) $M = 0.2$

(c) $M = 0.3$ (d) $M = 0.4$

Figure C.45: The acoustic pressure along the line at $y = 70$ for a point source convected in a finite thickness shear layer flow defined by Equation (C.4) with four different Mach numbers, $M = [0.1, 0.2, 0.3, 0.4]$. The acoustic results compare two different acoustic FE methods, the linearised acoustic wave equation with mean flow using the scalar flow potential and Galbrun's equation.

Table C.6: Solution time and numerical grid size for the simulation of sound propagation from a 2-D point source in a finite thickness shear layer.

Solver	Nodes	Elements	DOF	Time (s)
Galbrun	83,297	169,452	249,891	230
Galbrun	185,128	374,054	555,384	460
Galbrun	257,234	518,466	771,702	625
Galbrun	500,527	1,006,972	1,501,581	1,281
Galbrun	1,120,959	2,251,116	3,362,877	3,347
ANSYS	1,617,603	230,400	1,617,603	137

Solving the model with Galbrun's equation to obtain the results in Figure C.46 can be used to determine the duration it takes to solve the model with an increased number of mesh nodes. The results are outlined in Table C.6, which shows a linear scaling in computational duration with the increase in numerical nodes and DOF. An important outcome is the solution using ANSYS Mechanical solution takes 134 s for a model with approximately 1,600,000 nodes, which is significantly less than the 3,347 seconds it takes to solve the model with Galbrun's equation for a system with approximately 1,100,000 nodes. It is important to note that for the same spatial accuracy (node density) in the FE model the duration needed to solve the two FE methods are drastically different, which can be attributed to multiple factors. One factor is that Galbrun's equation was solved using MATLAB, whereas the results for the linearised acoustic wave equation with mean flow using a scalar flow potential was solved using ANSYS Mechanical. The results show that ANSYS Mechanical is a much more efficient solver for parallel computing. Another factor is that a single DOF system per node is solved with ANSYS Mechanical, whereas Galbrun is a three DOF system. The increased number of DOFs needed to be solved means that for two models with the same nodal density there will be an increase in both computational resources and computational runtime, where the size of the matrices needed to be solved increases based on the square of the number of DOFs.

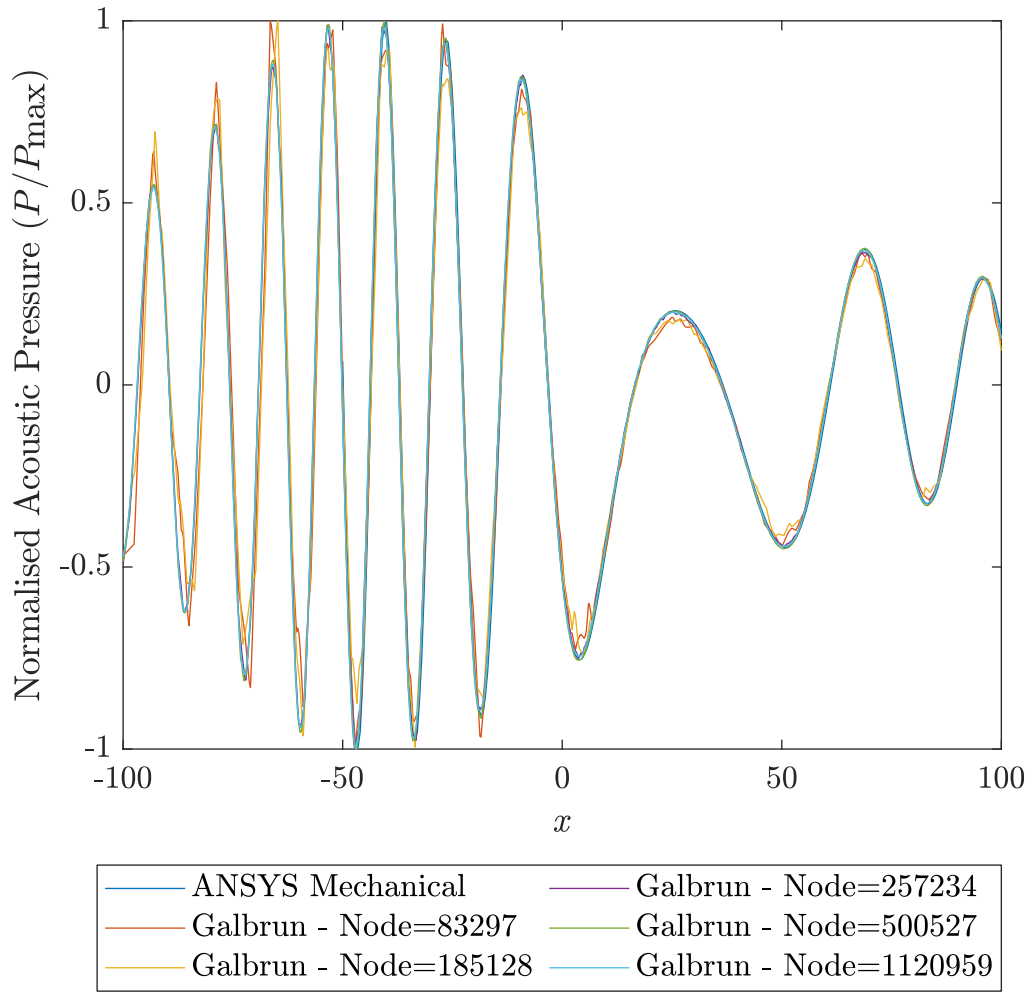

Figure C.46: A mesh independence study for the acoustic pressure along the line at $y = 70$ for a point source convected by a finite thickness shear flow defined by Equation (C.4), comparing the results from the linearised acoustic wave equation with mean flow using the scalar flow potential and Galbrun's equation.

C.8.4 Summary of findings

The numerical investigation of sound propagation from a point source in a finite thickness sheared flow shows important details about the linearised acoustic wave equation with mean flow using the scalar potential flow, when compared to other methods. Firstly, Section C.8.2 compares the results for the frequency dependant method in ANSYS Mechanical (the linearised acoustic wave equation with mean flow using the scalar flow potential), and three transient acoustic FE methods: the linearised Euler equations, acoustic perturbation equation, and Galbrun's equations. For a particular snapshot in time Figure C.43 shows good agreement between the four different methods, with Galbrun's equation showing the biggest different in instantaneous acoustic pressure. After further analysis and discussion in Section C.8.3, the difference is only seen in the published results by Feng et al. [59]. The major difference between the results in Feng et al. [59] and the results presented in Section C.8.3 for Galbrun's equation is that the former is a time-domain solver and the latter is a frequency domain solver.

After an indepth analysis it has been shown that in the frequency domain, the linearised acoustic wave equation with mean flow using the scalar flow potential and the UTC's FE solver using Galbrun's equation show almost identical outcomes, with some minor differences. Firstly, Figure C.44 has shown good quantitative agreement between the two numerical methods for three different frequencies. The results in Figure C.45 has also shown good agreement with the two numerical methods for different shear layers with four different free-stream velocities investigated.

Further analysis has shown a mesh independence study for Galbrun's equation for the acoustic pressure and compares the results with ANSYS Mechanical. The results from Galbrun's equation show convergence in the solution for a scenario with $2,500,000$ nodes. The mesh independence study also provides insight into the computational time required to solve these models, with a linear increase required for UTC's FE solver. When comparing ANSYS Mechanical to the UTC's FE solver, the latter would take significantly longer to solve a model with roughly similar

node counts, with ANSYS mechanical taking 137 s and the UTC's FE solver taking 3347 s.

Therefore, ANSYS Mechanical with the linearised acoustic wave equation with mean flow using the scalar flow potential can be used as a tool to model the sound propagation from a point source with a finite thickness shear layer in 2-D. The method has been verified for different cases in literature [57, 59] and with the UTC's FE solver using Galbrun's equation.

C.9 Sound propagation from a point source in a heated, non-expanding jet in 2-D

In this section, the sound radiation from a 2-D point source in a heated, non-expanding jet is investigated. The proposed case is a slightly different to the work conducted by Agarwal and Morris [2] and National Aeronautics and Space Administration [122], where smaller values for the Mach number, which are more representative of the OCGT exhaust speeds are investigated. Agarwal and Morris [2] and National Aeronautics and Space Administration [122] originally proposes a non-expanding jet with Mach number, $M = 0.756$. National Aeronautics and Space Administration [122] has shown that the sound propagation through the proposed flow condition is a difficult scenario to model the acoustic pressure, and this was shown with different numerical methods. Hence, the results presented here are for a modified case with reduced Mach numbers, $M = [0.1, 0.2]$, of the jet and compares the results between the linearised acoustic wave equation with mean flow using the scalar flow potential in ANSYS Mechanical and the University of Technology of Compiègne's (UTC's) FE solver using Galbrun's equations. The results show good agreement between the two numerical methods. The results and discussion in this section are presented as the following:

- background and description of the problem,
- numerical validation of the linearised acoustic wave equation with mean flow using the scalar flow potential against Galbrun's equations, and
- summary of findings.

C.9.1 Background and problem definition

The parameter and definition for the problem are based on the case presented in Agarwal and Morris [2] and National Aeronautics and Space Administration [122], with the key values shown in Table C.7. For the flow, density and temperature condition for the 2-D heated, non-expanding, subsonic jet, the profiles are based

Table C.7: Parameters for the case with a point source submersed in a 2-D heated, non-expanding, subsonic jet.

Description	Parameter	Value	Units
Specific gas constant for air	R_{air}	287	
Width of jet	b	1.3	m
Specific heat ratio	γ	1.4	-
Temperature in ambient fluid	T_{amb}	300	K
Temperature in jet	T_j	600	K
Speed of sound in ambient fluid	c_{amb}	347.2	m/s
Speed of sound in jet	c_j	491.0	m/s
Density in ambient	ρ_{amb}	1.2	kg/m^3
Density in jet	ρ_j	0.6	kg/m^3
Static pressure	p_0	103330	Pa
Mach number	M	0.1-0.2	
Acoustic frequency	f	$\frac{76}{2\pi}$	Hz

on the work by Agarwal and Morris [2] and National Aeronautics and Space Administration [122], but with a slight modification for the Mach number of the jet, where for the work in this section $M = [0.1, 0.2]$, whereas previously published literature a Mach number of $M = 0.756$ was used. The velocity, density, and temperature profiles can be described with

$$u_0(y) = Mc_j \exp\left(-\ln(2)\left(\frac{y}{b}\right)^2\right), \tag{C.6}$$

$$\frac{1}{\rho_0(y)} = -\frac{1}{2}\frac{\gamma-1}{\gamma p_0}[u_0(y) - Mc_j]u_0(y) + \frac{1}{\rho_j}\frac{u_0(y)}{Mc_j} + \frac{1}{\rho_{amb}}\frac{Mc_j - u_0(y)}{Mc_j}, \tag{C.7}$$

$$T_0(y) = \frac{P_0}{R_{air}\rho_0(y)}, \tag{C.8}$$

where the necessary parameters to evaluate these equation are provided in Table C.7. Figure C.47 shows the velocity, density, and temperature profiles for the domain, based on Equations (C.6), (C.7), and (C.8).

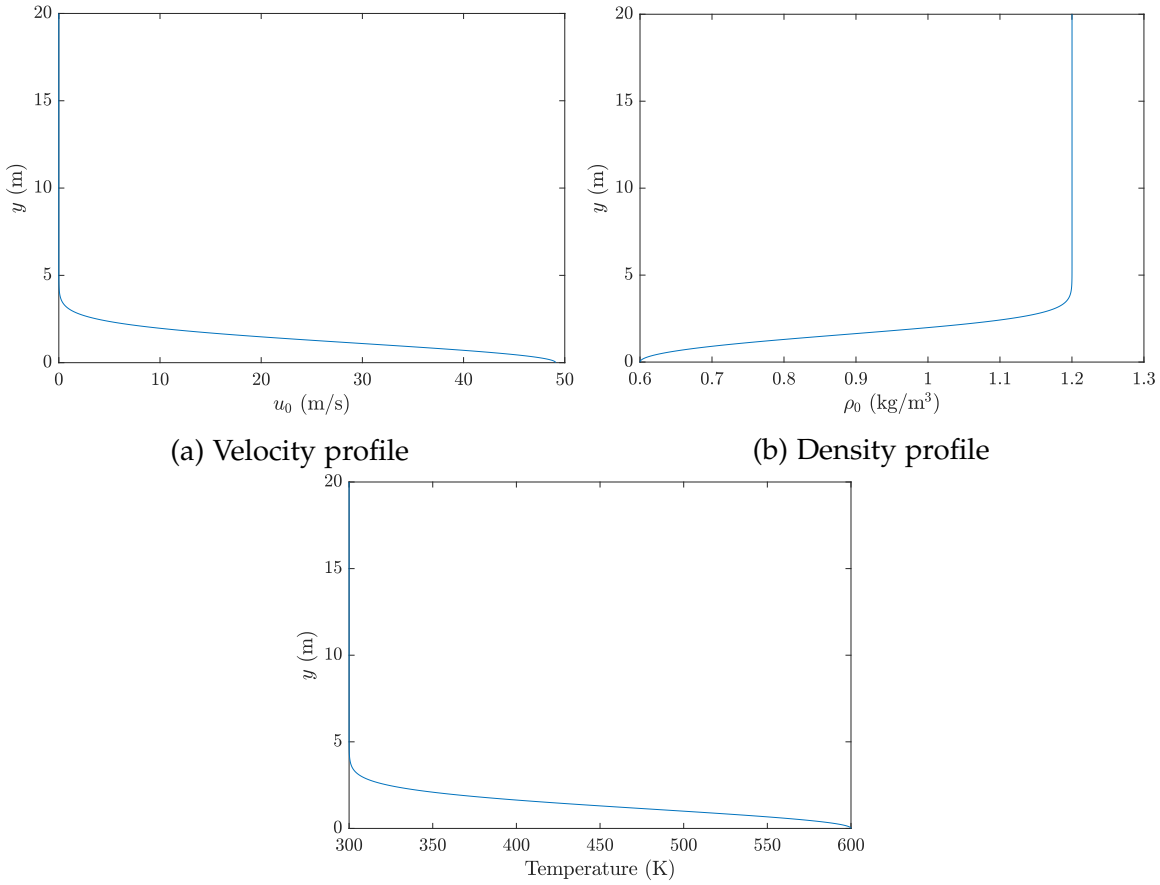

(a) Velocity profile

(b) Density profile

(c) Temperature profile

Figure C.47: The (a) velocity profile, (b) density profile, and (c) temperature profile for the 2-D heated, non-expanding, subsonic jet described by Agarwal and Morris [2].

The schematic for the numerical domain is shown in Figure C.48. The dimensions of the domain are different for the work in ANSYS Mechanical and the UTC's FE solver, where $L_x \times L_y = [x_{\min}, x_{\max}] \times [y_{\min}, y_{\max}] = [-60\,\text{m}, 160\,\text{m}] \times [0, 60\,\text{m}]$ and $L_x \times L_y = [x_{\min}, x_{\max}] \times [y_{\min}, y_{\max}] = [-200\,\text{m}, 200\,\text{m}] \times [0\,\text{m}, 150\,\text{m}]$, respectively. The outer region of the domain is surrounded by PML elements, which is the region shown in green and is 60 m thick for ANSYS Mechanical and 100 m thick for the UTC's FE solver. The work conducted using UTC's FE solver was conducted before the ANSYS Mechanical simulations, and a large domain was used to minimise the effects reflection near the PML region. It was later seen in

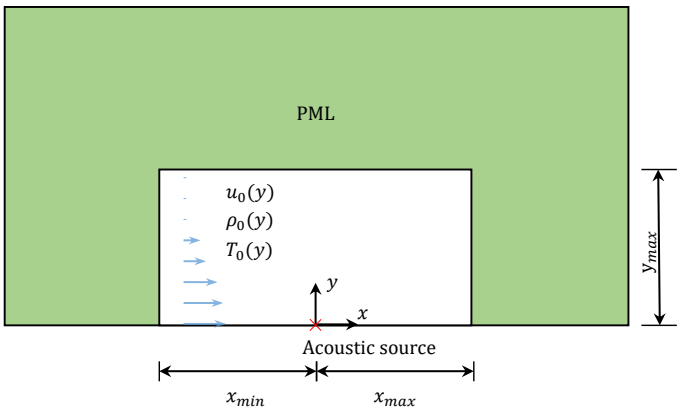

Figure C.48: The schematic for the case with a point source convected by a heated, non-expanding, subsonic, jet where the area in white is acoustic propagation domain, the area in green is the PML zone, the blue arrows represents the mean velocity field throughout the acoustic domain, and the red cross at the origin represents the acoustic source.

the ANSYS Mechanical simulation that the dimensions for the acoustic domain can be reduced and the reflection effects near the PML region have no effect on the acoustic pressure in the region of interest.

Figure C.49 shows the numerical mesh for the acoustic FEM in ANSYS Mechanical, with the mesh comprising of 212,800 second-order, hexahedra elements with mid-side nodes or 1,494,803 nodes. It should also be noted that the mesh is structured and the elements are aligned with the Cartesian coordinates. Even though the mesh in Figure C.49 is presented in 2-D the simulations were conducted in 2.5-D, with the mesh being one element thick.

Figure C.50 shows the acoustic mesh for the numerical simulations with Galbrun's equation using the UTC's FE solver. The mesh consists of linear triangular elements or otherwise known as either "4-3c", "$P^+ - P_1$", or "MINI" [159, 160]. The region with elements in blue represents the acoustic elements for modelling the sound propagation and the elements in orange are the PML elements for sound attenuation. The acoustic mesh consists of 180,760 nodes and 364,238 elements in total. It should be noted that the simulation has 542,280 degrees of freedom,

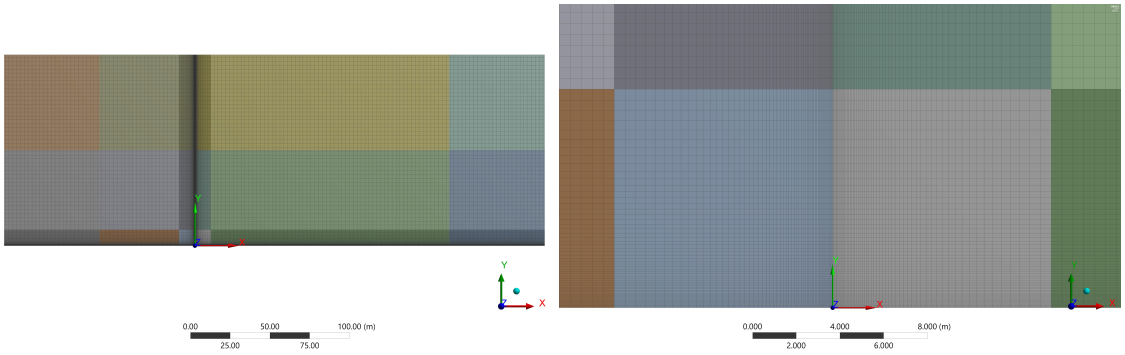

(a) Total Mesh (b) Mesh near the source

Figure C.49: The numerical mesh for the ANSYS acoustic FEM with (a) showing the the total mesh, and (b) the mesh near the acoustic source a non-uniform grid and high spatial resolution to resolve the acoustic source.

as each node has two acoustic displacement degrees of freedom and an acoustic pressure degree of freedom.

C.9.2 Numerical validation with Galbrun's equation

The results presented in this section compares two numerical methods: the linearised acoustic wave equation with mean flow using the scalar flow potential in ANSYS Mechanical and the UTC's FE solver using Galbrun's equations, for the case of a 2-D point source convected by a heated, non-expanding, subsonic jet.

Figure C.51 shows the contour plot for acoustic pressure for the two numerical methods. The results show similarities with qualitative features, and sound is refracted along the line of symmetry. However, the two contour plots are not quantitatively the same, and is due to the definition of the acoustic source. As discussed in Sections C.7 and C.8, the definition for the acoustic source with Galbrun's equation, a Gaussian distribution, is different to ANSYS Mechanical, which uses a Dirac delta function for the acoustic source. Hence, it was complicated to quantitatively scale the contour plots to show the same colour scale in the solution, especially near the acoustic source. Although, the contour plots in Figure C.51 shows quantitatively different results, they are qualitatively similar.

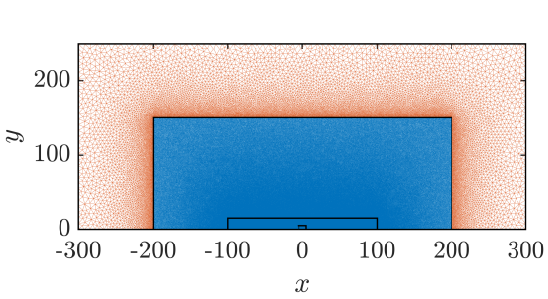

(a) Total mesh

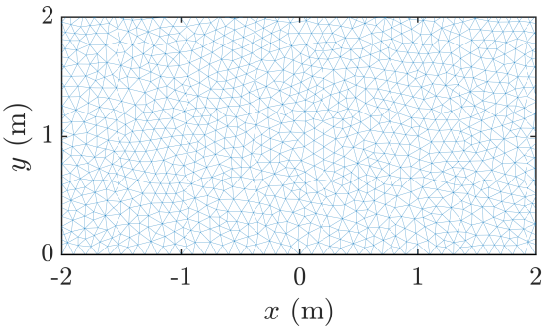

(b) Mesh near the acoustic source

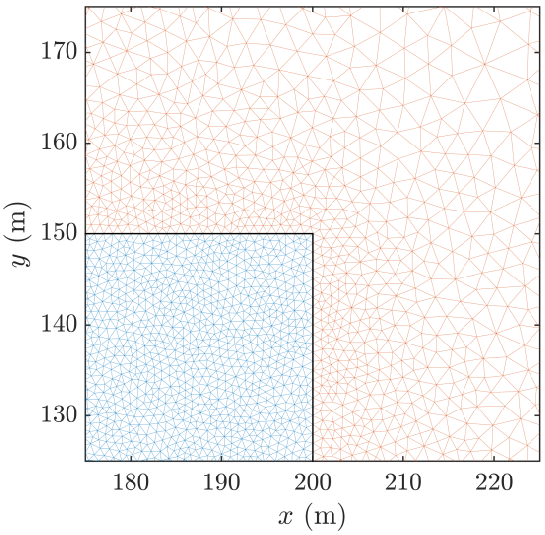

(c) Mesh at the PML interface

Figure C.50: The acoustic mesh generated by GMESH for solving the case with the point source convected by a heated, non-expanding, subsonic jet for solving using the UTC's FE solver and Galbrun's equation, where (a) is the total acoustic mesh, (b) is the mesh near the acoustic source at the origin, and (c) is the acoustic mesh at the interface between the acoustic propagating domain and the PML domain. The elements in blue represents the acoustic domain of interest and the elements in orange represents the domain with PML elements.

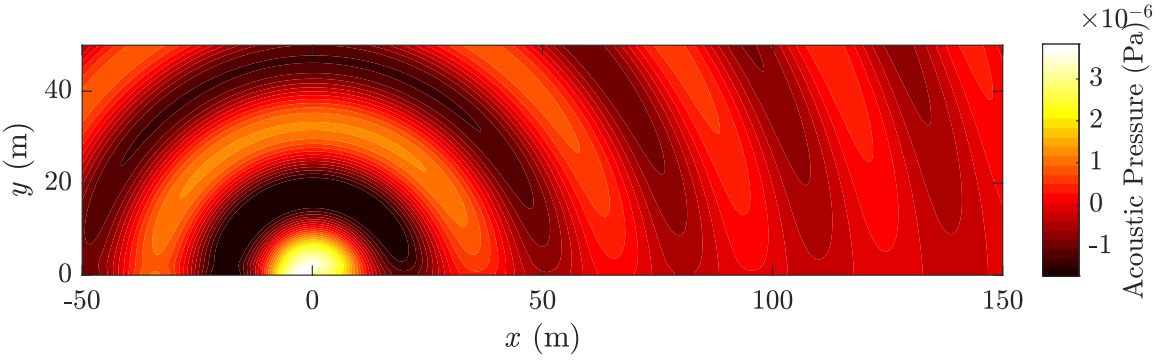

(a) ANSYS Mechanical

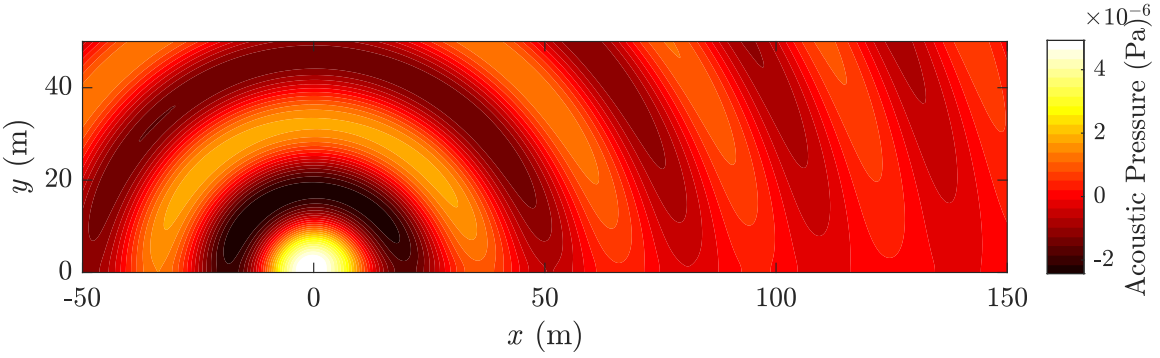

(b) Galbrun

Figure C.51: Contour plots of acoustic pressure for a 2-D point source convected by a heated, non-expanding, subsonic jet with the results from (a) ANSYS Mechanical, and (b) Galbrun's equation.

Figure C.52 shows the acoustic pressure as a line plots at $y = [15, 50]$, and with two flow Mach numbers, $M = [0.1, 0.2]$. Figure C.52 shows good quantitative agreement between ANSYS Mechanical and Galbrun's equation. Downwind of the acoustic source there are slight deviations in the amplitude and wavelength between the two numerical methods, with Mach numbers from 0.1 to 0.2. Furthermore, in the far-field, Figures C.52b and C.52d shows slight discrepancies in the acoustic pressure at $x = 0$, but good agreement outside of this region, which is due to the different acoustic source implemented for each method. The results in Figure C.52 are also normalised with the maximum acoustic pressure along that profile. The normalised results compensate for the different definitions for the acoustic sources between the two methods, and the results in Figure C.52 shows

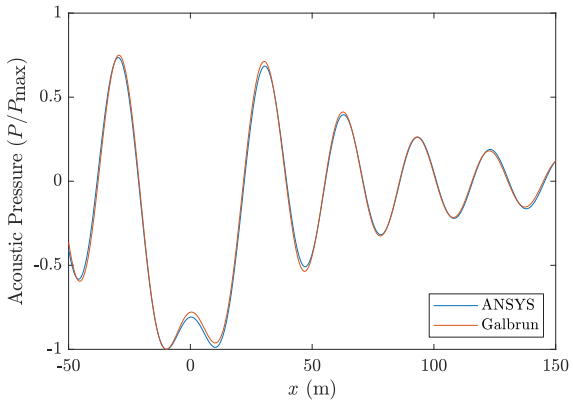

(a) Acoustic pressure at $y = 15$ and $M = 0.1$

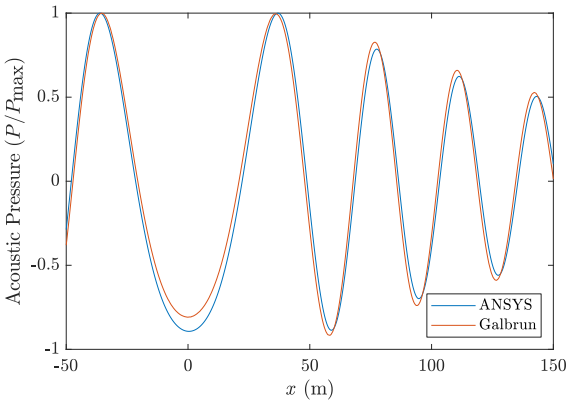

(b) Acoustic pressure at $y = 50$ and $M = 0.1$

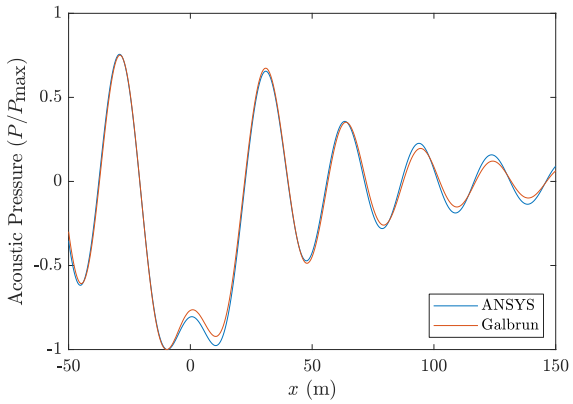

(c) Acoustic pressure at $y = 15$ and $M = 0.2$

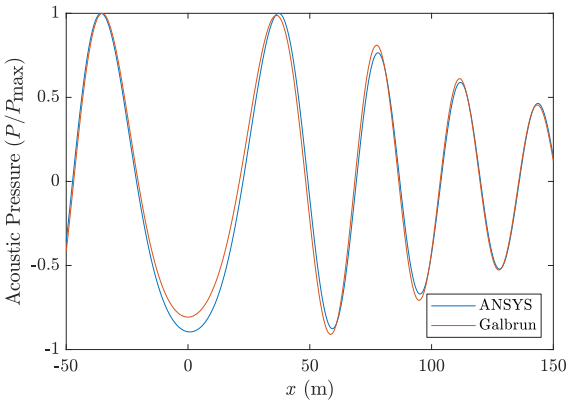

(d) Acoustic pressure at $y = 50$ and $M = 0.2$

Figure C.52: The acoustic pressure along the line at $y = 15$ and 30 for a point source convected in a finite thickness shear layer flow defined by Equation (C.4) with two Mach numbers for the jet, $M = [0.1, 0.2]$. The acoustic results compare two acoustic FE methods, the linearised acoustic wave equation with mean flow using the scalar flow potential and Galbrun's equation.

this is an appropriate method to scale the results. However, this is more difficult for Figure C.51, which shows the pressures in the near and far-field of the acoustic source.

The results presented in this section demonstrates that there is good qualitative agreement shown in Figure C.51 and excellent quantitative agreement shown in Figure C.52 for solutions in the far-field, with different flow conditions, there are limitations to the solution. Firstly, as discussed earlier in this chapter, the acoustic source when modelling with ANSYS Mechanical is limited to a Dirac

delta function, whereas numerical solvers in literature and Galbrun's equation prefers a Gaussian distribution. In the near field, the solution is somewhat different, however as the sound propagates from the source, the solutions for the acoustic pressure converge between ANSYS Mechanical and the cases in the literature. Unlike the flow conditions explored in Section C.7 with uniform, subsonic flow, or Section C.8 with a finite thickness shear-layer, the presence of heated, subsonic flow with spatially thin velocity gradients is a difficult case for all numerical methods, as stressed in National Aeronautics and Space Administration [122]. The work by National Aeronautics and Space Administration [122] differs to the work presented in this section, as it investigates a higher Mach number, $M = 0.756$, which leads to higher velocity gradients in the flow. With the different numerical methods as discussed in the report by National Aeronautics and Space Administration [122] there is no quantitative agreement to the problem, which in the end comes down to the acoustic frequency of interest, and the spatially thin gradients for velocity and temperature. The Mach numbers, $M = 0.1$ and 0.2, were chosen for this investigation as it reflects the flow conditions explored in Chapter 3 and emphasises the appropriateness of modelling with the linearised acoustic wave equation with mean flow using the scalar flow potential in ANSYS Mechanical by comparing it to a higher fidelity solver with increased numbers of degrees of freedom, such as the UTC's FE solver using Galbrun's equations.

Similar to the work conducted in Section C.8.3, Figure C.53 shows the acoustic pressure for models with a different number of mesh nodes and solved with UTC's FE solver using Galbrun's equations. Figure C.53 shows good agreement with ANSYS Mechanical against the results from Galbrun's Equation. Comparing Figures C.46 and C.53, the results in Figure C.53 shows the acoustic pressure for this particular case is quantitatively less sensitive to the change in mesh node density with convergence in the numerical solution shown for the case with approximately 800,000 nodes. Additionally, Table C.8 shows the computational duration for all the cases investigated in Figure C.53, with a linear relationship for the solution time and the increase in mesh nodes. Table C.8 shows that for two different methods with similar a similar number of DOFs, UTC's FE solver with Galbrun's equation takes

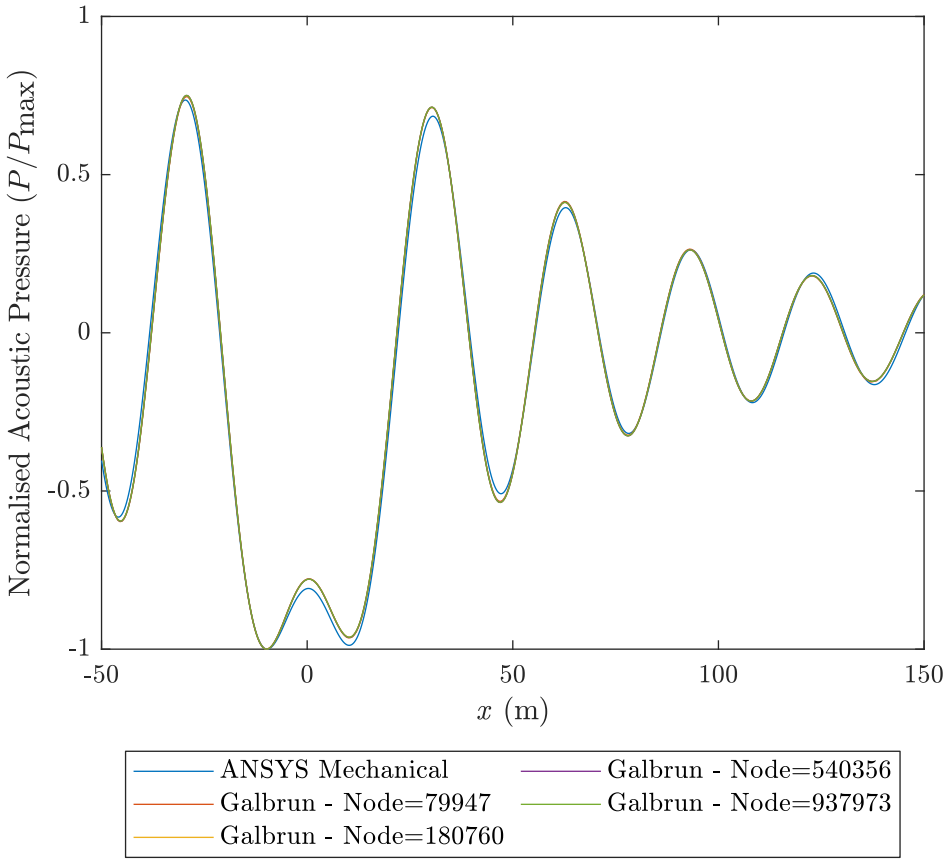

Figure C.53: A mesh independence study for the acoustic pressure along the line at $y = 15$ for a point source convected by 2-D heated, non-expanding, subsonic jet, comparing the results from the linearised acoustic wave equation with mean flow using the scalar flow potential and Galbrun's equation.

approximately 2201 s to solve model, whereas it only takes ANSYS Mechanical 144 s. It is emphasised that the increase in degree of freedoms solved will also increase both computational resources and computational runtime necessary, as the size of the matrices needed to be solved with an FE model increases in size based on the square of the number of DOFs.

C.9.3 Summary of findings

The results presented in this section have shown that the linearised acoustic wave equation with mean flow using scalar flow potential is a viable method for

Table C.8: Solution time and numerical grid size for the simulation of sound propagation from a 2-D point source in a heated, non-expanding, subsonic jet.

Solver	Nodes	Elements	DOF	Time (s)
Galbrun	79,947	161,680	239,841	197
Galbrun	180,760	364,238	542,280	511
Galbrun	543,056	1,090,950	1,629,168	2,201
Galbrun	937,973	1,882,384	2,813,619	5,160
ANSYS	1,494,803	212,800	1,494,803	144

modelling the sound radiation from 2-D point source convected by a heated, non-expanding, subsonic jet. The results from ANSYS Mechanical compare favourably to the results from a higher fidelity acoustic solver, such as UTC's FE solver with Galbrun's equations. The acoustic pressure results in this section show good agreement between the two numerical methods for two flow conditions, $M = [0.1, 0.2]$, and for two profiles along the horizontal line at $y = [15, 50]$. These flow conditions are not identical to the cases presented in literature from Agarwal and Morris [2] and National Aeronautics and Space Administration [122], but are reflective of the thermal and velocity gradients observed in Chapter 3 of the thesis.

The results for the mesh independence in Figure C.53 and Table C.8 shows the benefits in computational time with the linearised acoustic wave equation with mean flow using scalar flow potential for the acoustic problem presented in this section. The results for the acoustic pressure with ANSYS Mechanical and UTC's FE solver with Galbrun's equation shows good quantitative agreement. However, Table C.8 emphasises the difference in computational time needed to solve the model with similar mesh node count. This can be attributed (1) to the increase in DOF used for UTC's FE solver with Galbrun's equation and (2) the benefits of using a commercial software, ANSYS Mechanical, which was designed for efficient parallel computing for large FE models. Therefore, one needs to consider the benefits of numerical accuracy in a FE method and the computational time, and resource available for modelling.

C.10 Sound propagation from an infinitely baffled circular piston in 3-D

The numerical validation work in this section aims to validate an acoustic FEM (ANSYS Mechanical) solution for a 3-D infinitely baffled circular piston with a well-established analytical solution. The simulation employs the model to investigate the numerical work in Chapter 3. It should be noted that the propagation medium is a homogeneous stationary field at ambient temperature. The parameters used for this case is shown in Table C.9.

The boundary conditions used for the acoustic FEM simulation are shown in Figure C.54. The piston source is represented by a harmonically varying velocity condition. Elements with Perfectly Matched Layers surround the outer boundary of the simulation. It should be noted that the sound radiation from infinitely baffled piston is axisymmetric and only half the domain was modelled, with the symmetry boundary condition imposed along the Y-Z plane. Even though a 2.5-D simulation with the axisymmetric condition could be used for the numerical work, a 3-D simulation with a larger domain could be expanded for more complicated cases, as investigated in Chapter 3.

Figure C.55 shows the numerical mesh for the infinitely baffled piston. The numerical mesh shows the 3-D simulation and the complex domain. The number of nodes in the mesh is 12,282,853. It should be noted that the hybrid meshing scheme

Table C.9: Parameters for baffled piston.

Description	Parameter	Value	Units
Piston diameter	D_j	0.0476	m
Density in domain	ρ_0	1.2041	$\mathrm{kg/m^3}$
Speed of sound in domain	c_0	343.24	$\mathrm{m\,s^{-1}}$
Acoustic velocity	u_a	0.01	$\mathrm{m\,s^{-1}}$
Acoustic frequency	f	$1100.30 - 2934.12$	Hz
Atmospheric pressure	p_{atm}	101325	Pa
Ideal gas constant in duct	R_{air}	286.71	$\mathrm{J/kg \cdot K}$

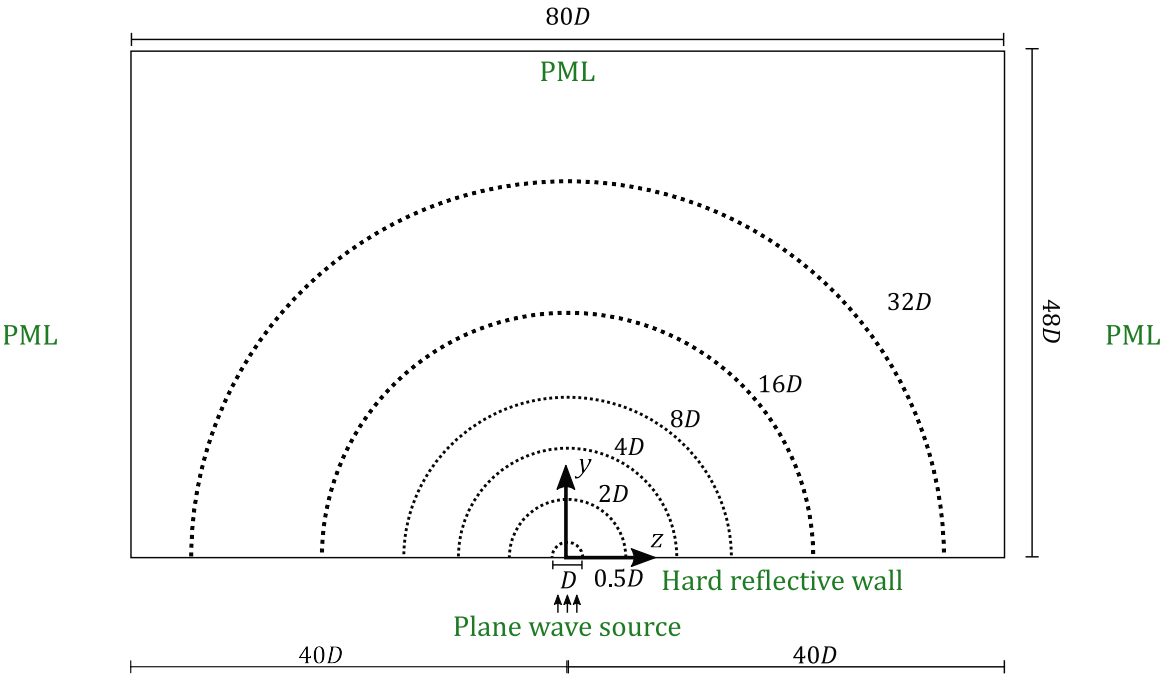

Figure C.54: Schematic and dimensions for the infinitely baffled piston simulations, where the green text represents the acoustic boundary conditions. PML refers to a Perfectly Matched Layer.

was used, with both structured hexahedra elements and unstructured tetrahedra. The acoustic region of crucial importance implemented structured hexahedra with 'FLUID 220' elements, otherwise known as quadratic elements with mid-side nodes. It should be noted that there are approximately 4.5 elements per wavelength for the maximum frequency (ka = 1.28) investigated in this section.

An essential factor in the baffled piston case is the non-dimensional acoustic frequency (Helmholtz number), ka. For the numerical validation work conducted in the chapter, the following formulation for ka was used

$$ka = \frac{\pi f D_j}{c_0} \quad , \tag{C.9}$$

where k is the non-dimensional wavenumber, a is the piston radius, f is the acoustic frequency, D_j is the piston diameter, and c_j is the speed of sound at ambient temperature. It should be noted that the speed of sound used in this section differs from the speed of sound in Chapter 3, where the speed of sound,

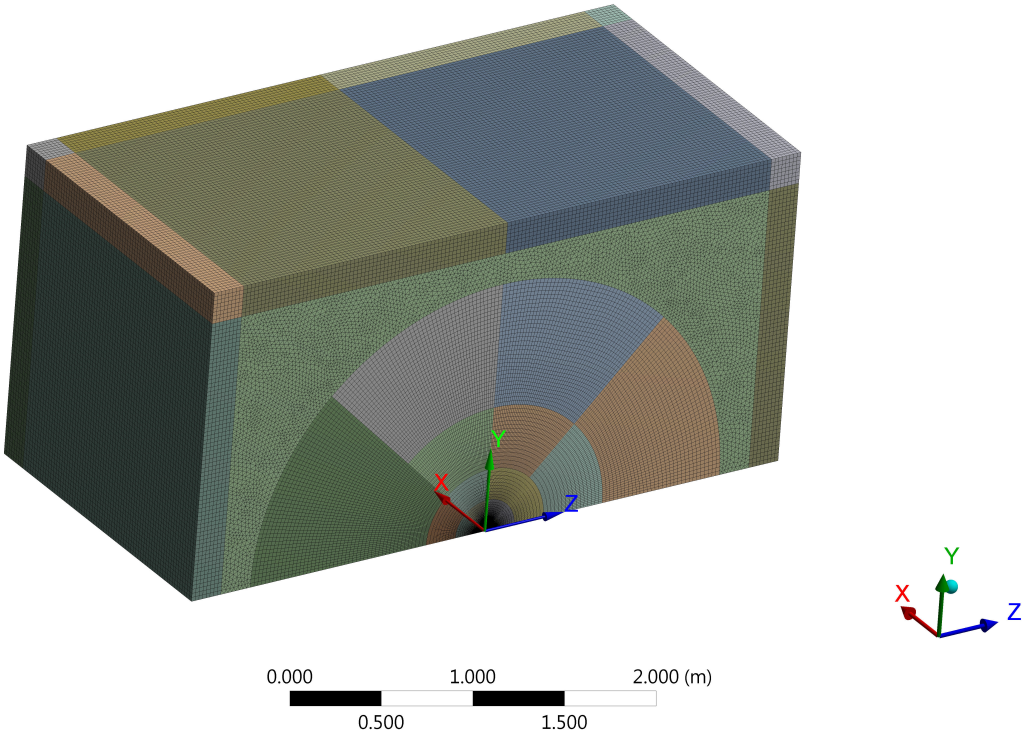

Figure C.55: Mesh for the FEM acoustic simulations.

c_j, is for a heated case with $T_j = 500\,°C$. For the work presented in this section, the non-dimensional acoustic frequencies investigated are $ka = 0.80$ to 1.28, but it should be noted that $ka < 0.80$ were investigated, showing similar results for $ka = 0.80$.

The piston with an infinite baffle is a well studied case with the known analytical solution for directivity [97]. The analytical solutions for the baffled piston of radius a are given by

$$I(\theta, ka, r) = \frac{\rho_0 c_0 \pi k^2 u_a^2 (\pi a^2)^2}{8\pi^2 r^2} \left(\frac{2J_1(ka\sin(\theta))}{ka\sin(\theta)} \right)^2, \tag{C.10}$$

where I is the acoustic intensity, θ is angle for directivity plot, r is the directivity radius from the piston outlet, u_a is the acoustic particle velocity, and J_1 is the Bessel function of the first kind. Equation (C.10) is used to calculate the intensity off-axis,

but on-axis (along the piston centreline) a different analytical solution for intensity can be used:

$$I(ka, r) = \frac{\rho_0 c_0 \pi k^2 u_a^2 (\pi a^2)^2}{8\pi^2 r^2}. \tag{C.11}$$

The acoustic results for the infinitely baffled piston are typically presented as a normalised directivity index (DI), using Equation (3.38) [25, 97].

Based on the analytical results for calculating the directivity index for infinitely baffled pistons, the numerical results obtained in ANSYS Mechanical in 3-D can be validated. Figures C.56 and C.57, show the DI polar plots at two radii ($r = [16D, 32D]$) and at four acoustic frequencies ($ka = [0.80, 0.96, 1.12, 1.28]$). In Figure C.56 the numerical results for directivity show good agreement with the analytical results from Equations (C.10) and (C.11). Hence, numerical simulations with acoustic FEM are appropriate for DI polar plots up to $r = 16D$ and for a maximum non-dimensional frequency, $ka = 1.28$. It should be noted that the numerical solution starts to deviate from the analytical result for the scenario with, $ka = 1.28$ and $r = 32D$. This is because at this directivity arc there are insufficient nodes to accurately resolve the acoustic wave for this particular frequency. With an increase in computational nodes for the numerical simulation, such that there are approximately 6 nodes per wavelength, it is expected that there would be good agreement between the numerical and analytical solution. This is possible by conducting the simulations with computational resources with higher amounts of RAM exceeding, 128 GB of RAM.

Figure C.57 shows the sound directivity for an infinitely baffled piston at $r = 32D$ for four non-dimensional acoustic frequencies ($ka = [0.80, 0.96, 1.12, 1.28]$). The numerical and analytical directivity results at $r = 32D$ show good agreement at all frequencies investigated. However, it can be observed that for Figures C.57c and C.57d there are slight discrepancies between the numerical results and the analytical solution. The slight discrepancies or ripples in the numerical results at higher frequencies show the numerical solution is near the upper limits of the numerical mesh, and to overcome this a finer mesh is necessary.

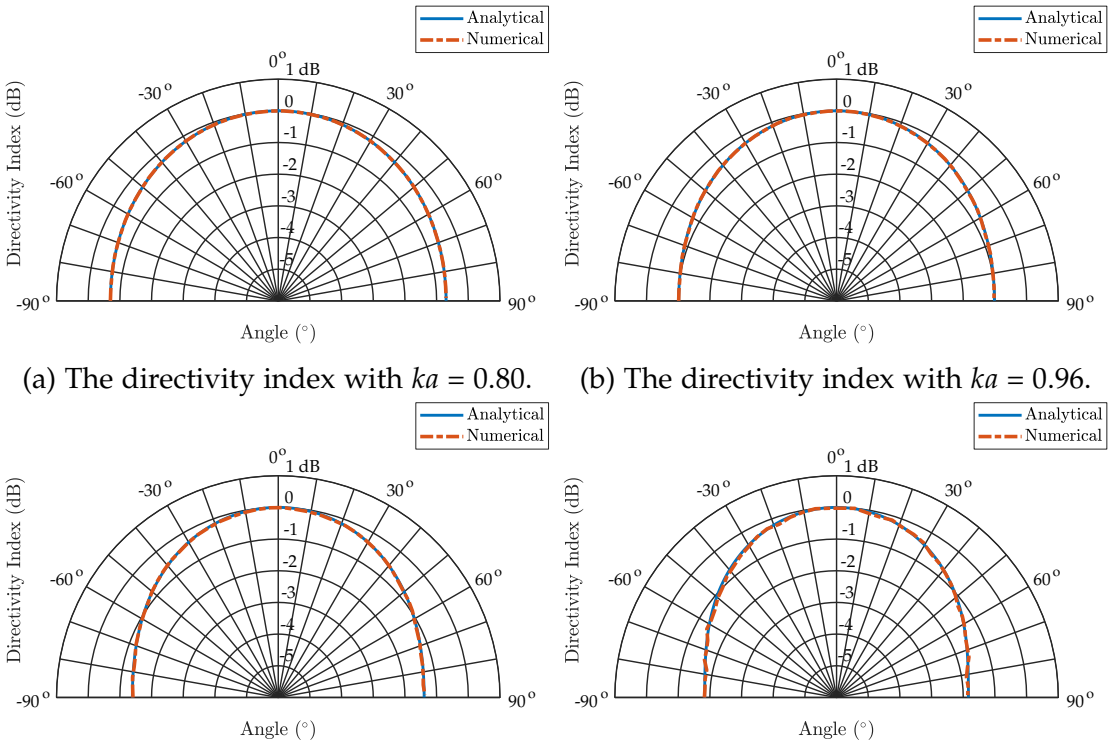

(a) The directivity index with $ka = 0.80$.

(b) The directivity index with $ka = 0.96$.

(c) The directivity index with $ka = 1.12$.

(d) The directivity index with $ka = 1.28$.

Figure C.56: Comparing the analytical and numerical solution for sound propagation from an infinitely baffled piston at four different Helmholtz numbers ($ka = [0.80, 0.96, 1.12, 1.28]$) along the Y-Z plane (of symmetry). The following parameters are used for the simulations $r = 16D$, and $\vec{v}_0(\vec{x}) = 0$.

In summary, acoustic FEM with ANSYS Mechanical is an appropriate method for modelling 3-D sound radiation from infinitely baffled pistons in an isothermal stationary field.

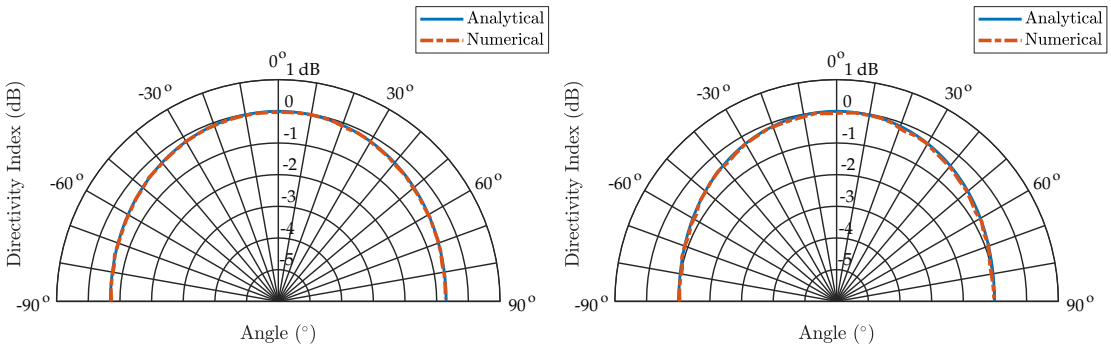

(a) The directivity index with $ka = 0.80$.

(b) The directivity index with $ka = 0.96$.

(c) The directivity index with $ka = 1.12$.

(d) The directivity index with $ka = 1.28$.

Figure C.57: Comparing the analytical and numerical solution for sound propagation from an infinitely baffled piston at four different Helmholtz numbers ($ka = [0.80, 0.96, 1.12, 1.28]$) along the Y-Z plane (of symmetry). The following parameters are used for the simulations $r = 32D$, and $\vec{v_0}(\vec{x}) = 0$.

Appendix D

Anechoic Chamber Acoustic Results

This Appendix presents the acoustic results for testing in the Anechoic Chamber to validate the acoustic acquisition and characterise the microphone array. The anechoic environment provides a controlled environment, minimising the complexity of the acoustic measurements and reflections. To remove the complexity of the sound radiation from the duct network, initial testing was undertaken using a single loudspeaker to characterise the microphone array (Figure D.1). With the array adequately characterised and calibrated, the single loudspeaker was subsequently removed and replaced with the exhaust stack (Figure D.2). Subsequent testing was for the sound radiation through the duct network, and the reflections off the duct network, as well as the duct acoustic response, were investigated.

Figures D.1 and D.2 show the two different experimental setups in the Anechoic Chamber used for validating the acoustic measurements in the anechoic environment. Figure D.1 shows the testing arrangement with a free-standing compression driver as the sound source. Testing with only the compression driver reduced the complexity of the sound source by eliminating the complex sound radiation from the duct outlet, including diffraction, reflections, and impedance changes. These tests were used to validate the acoustic data acquisition and characterise the array. Figure D.2 shows the subsequent testing arrangement, with the sound propagating through the duct network and introduces complexities to the measurement. Testing with the duct network in the Anechoic Chamber provided validation of the acoustic data acquisition system and provided results for a simplified case in an isothermal stationary field.

D.1 Anechoic chamber testing with a free-standing compression driver

A simple case to investigate the validity of the acoustic measurement and post-processing technique is to measure the radiation of sound from a compression driver suspended at the acoustic centre of the array. The electro-acoustic signal generated from NI Labview and used to excite the compression driver was a uniform white noise source. Figure D.3 shows the coherence between the electro-

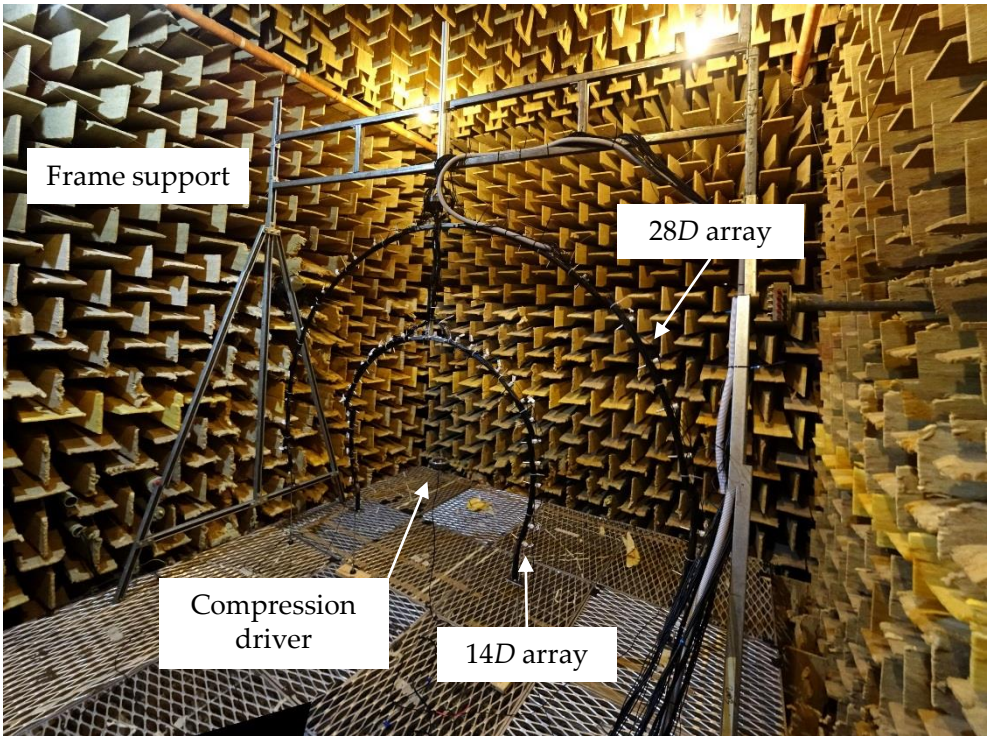

Figure D.1: Photo of the acoustic arrays in the University of Adelaide's Anechoic Chamber. The acoustic source is a free-standing compression driver suspended by a fishing line.

acoustic signal into the compression driver and the acoustic pressure at a single microphone near the centre of each of the circular arrays. The coherence results in Figure D.3 show a strong degree of linearity between the electro-acoustic signal and the acoustic pressure, with the coherence at almost unity, which is to be expected. This suggests that the acoustic pressure at the microphone is coherent with the speaker and that the reflections from the array have a minimal impact on the results. Note that strong reflections tend to result in periodic dips in coherence.

Figure D.4 shows SPL measurements along each of the circular arrays. The sound source for the measurements was from the free-standing compression driver. Figure D.4 shows that with broadband uniform white noise as the sound source, the acoustic response from the speaker is not perfectly uniform over the 100 Hz to 10 kHz range, with some decay in the speaker response from 4 kHz onwards. It should be noted that the compression driver has a rated performance

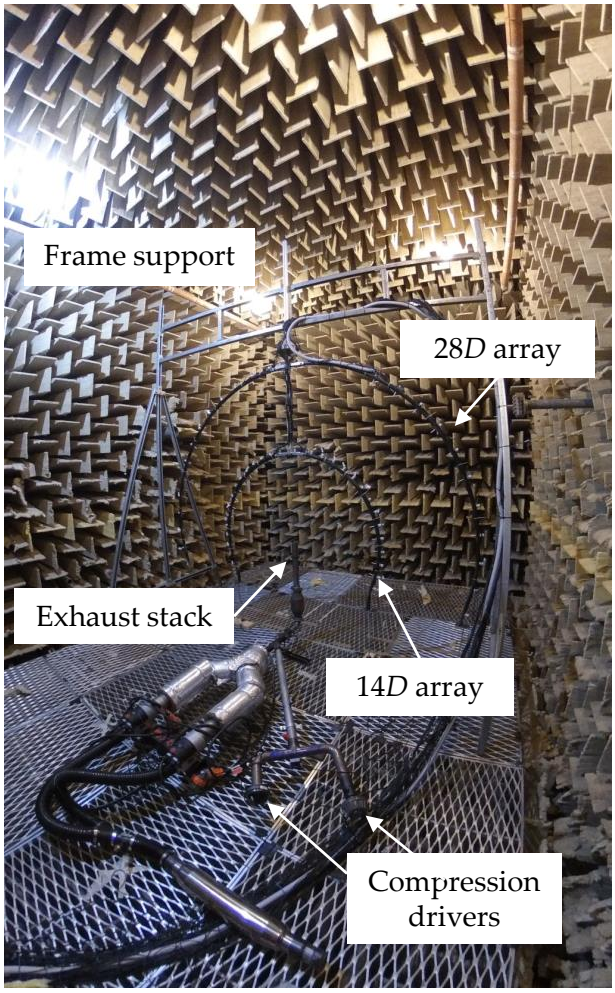

Figure D.2: Photo of the acoustic arrays and the exhaust rig in the University of Adelaide's Anechoic Chamber.

above 1 kHz and, to protect the speaker, a high pass filter was implemented for a cut-on frequency of 1 kHz. Figure D.4 shows the decay in SPL below the cut-on frequency of 1 kHz.

The coherent sound measured at the microphones in the Anechoic Chamber is presented in Figure D.4, which shows the COP at two different microphones for the sound propagating from the free-standing compression driver. Figures D.4 and D.4 show almost identical results, which is to be expected for a system with the strong coherence seen in Figure D.3. This shows that for the simplified case in

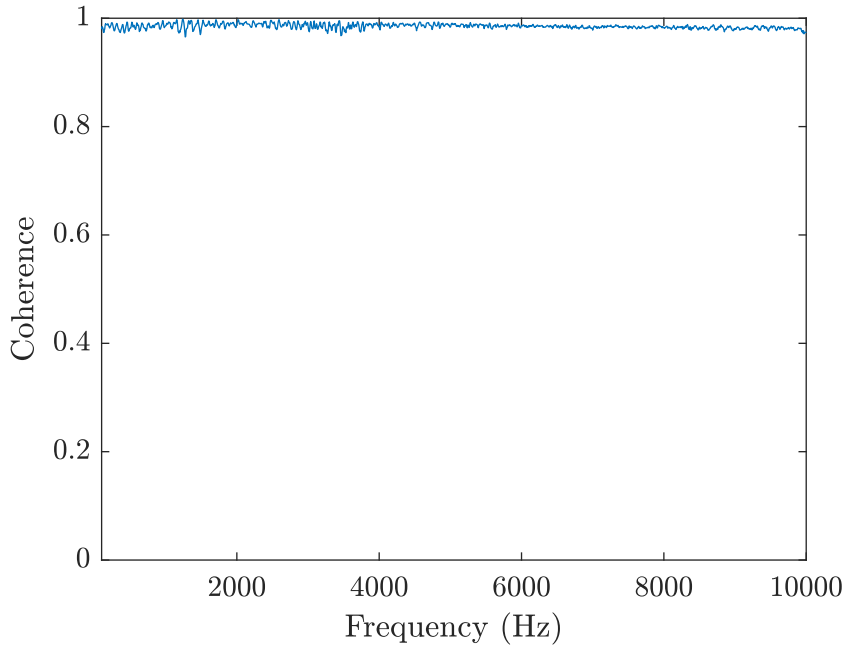

(a) Microphone at $-2.5°$ on the $14D$ array (Mic 16).

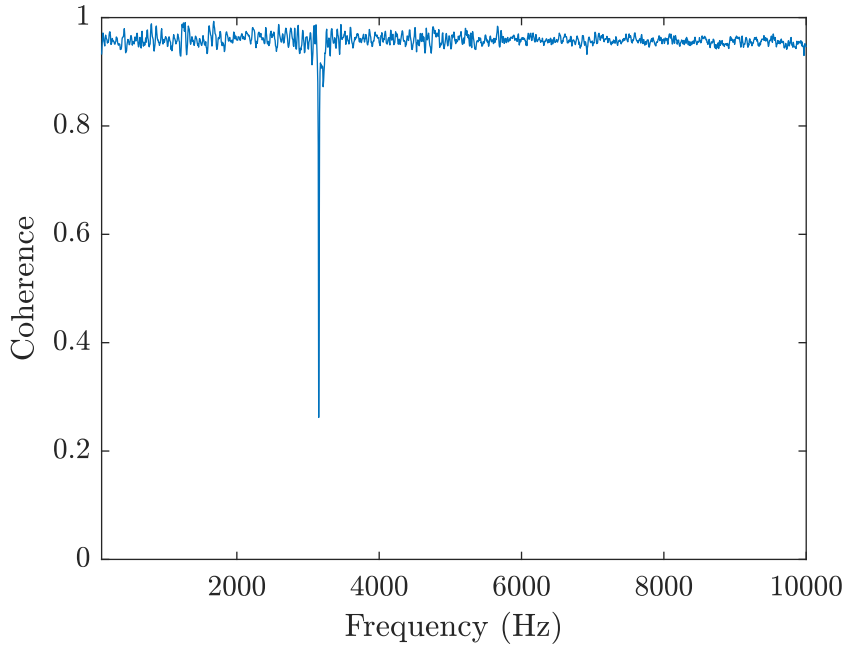

(b) Microphone at $-7.5°$ on the $28D$ array (Mic 47).

Figure D.3: The coherence, γ_{xy}^2, between the electro-acoustic signal into the compression driver and microphone SPL response for two different microphones at the top of the $14D$ and $28D$ array. The test was undertaken in the Anechoic Chamber with an isothermal stationary field. Sound is propagating from a free-standing compression driver.

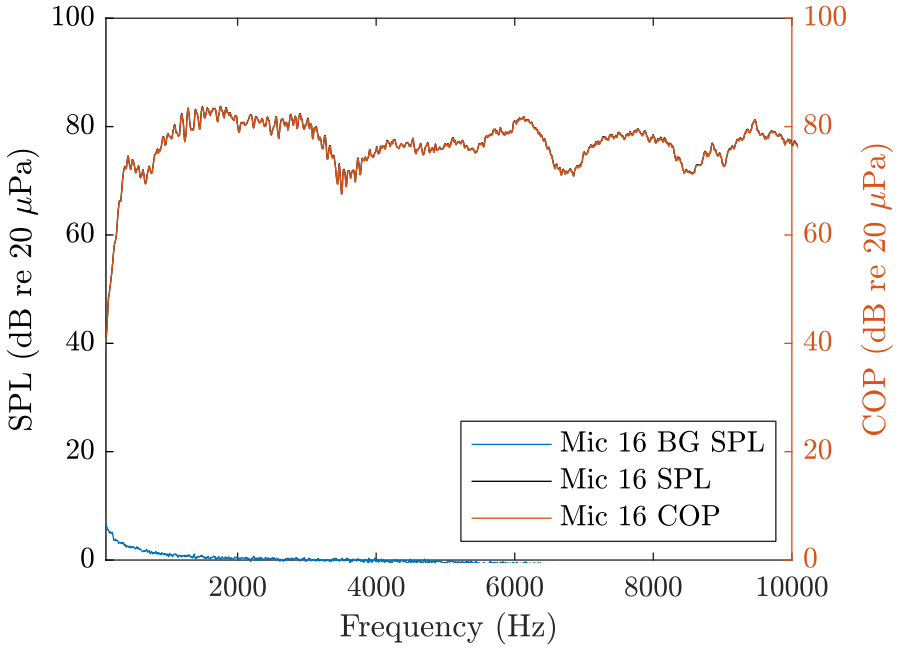

(a) Microphone at $-2.5°$ on the 14D array (Mic 16).

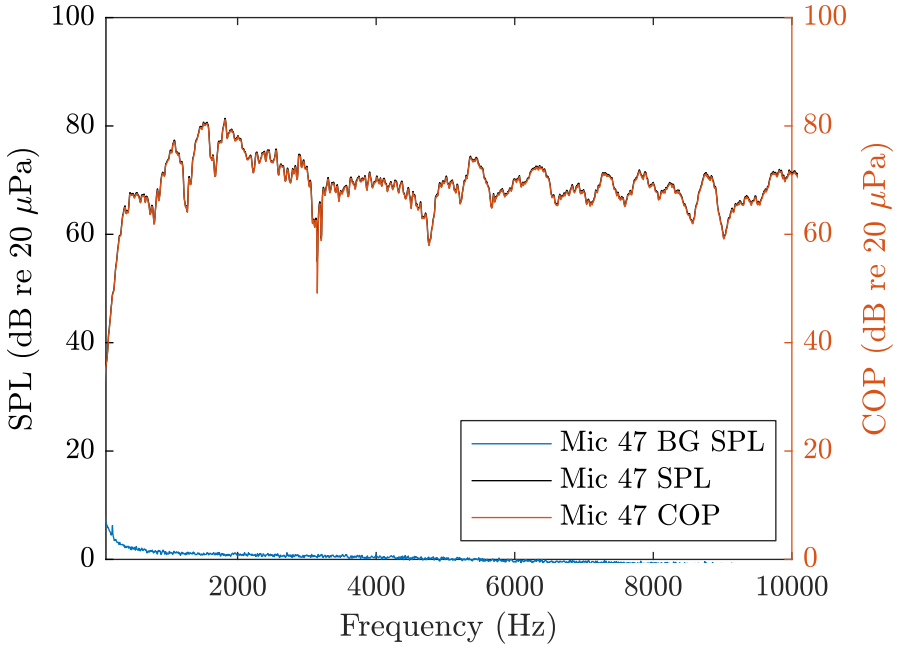

(b) Microphone at $-7.5°$ on the 28D array (Mic 47).

Figure D.4: The SPL and COP measurements for two different microphones at the top of the 14D and 28D array. The test was undertaken in the Anechoic Chamber with an isothermal stationary field. Sound is propagating from a free-standing compression driver. BG refers to background noise levels. Relevant coherence is plotted in Figure D.3.

the Anechoic Chamber with the free-standing compression driver in an isothermal stationary field, the acoustic measurement system shows predictable results for measurable coherent sound.

Figure D.5 shows the DI polar plots for sound propagating from the free-standing compression driver in the Anechoic Chamber. The DI polar plots are from measurements taken at two different array radii, $14D$ and $28D$, and at four band-averaged one-third octave bands with centre frequencies f = [3.15 kHz, 4 kHz, 5 kHz, 6.3 kHz] (ka = [0.85, 1.08, 1.35, 1.70]). Figure D.5 shows that for the DI polar plots, both circular arrays are approximately axisymmetric about the 0° (vertical) axis. The sound radiation from the suspended compression driver is also approximately elliptical, with an acoustic lobe centred around the 0° axis. As would be expected, Figure D.5 also shows that there is a reduction of DI below the horizontal plane of measurement ($\theta \leq -90$ and $\theta \geq 90$).

D.2 Anechoic chamber testing with an exhaust stack

The free-standing compression driver was removed and replaced with the exhaust system, and the acoustic measurements were repeated. Figure D.6 shows the coherence between the electro-acoustical signal and the acoustic pressure in the presence of the exhaust duct. It can be seen that there are regions with reduced coherence when compared with Figure D.3. The reduction in coherence is from the presence of the exhaust stack impacting on the linearity, since the exhaust stack is not only acting as a sound source through structural sound radiation, but also the sound is being diffracted at the duct edge, as well as being reflected by the hard reflective duct surface. The SPL plots show that the exhaust network has frequency regions where the duct significantly attenuates the sound as it propagates and radiates from the exhaust stack. These regions show that the duct network acts like a 'notch' filter in these regions. In order to overcome this issue, the results will be expressed as band-averaged one-third octave bands.

For the sound propagation through the duct network, the SPL was also measured and showed a non-uniform response. Figure D.7 shows the SPL measure-

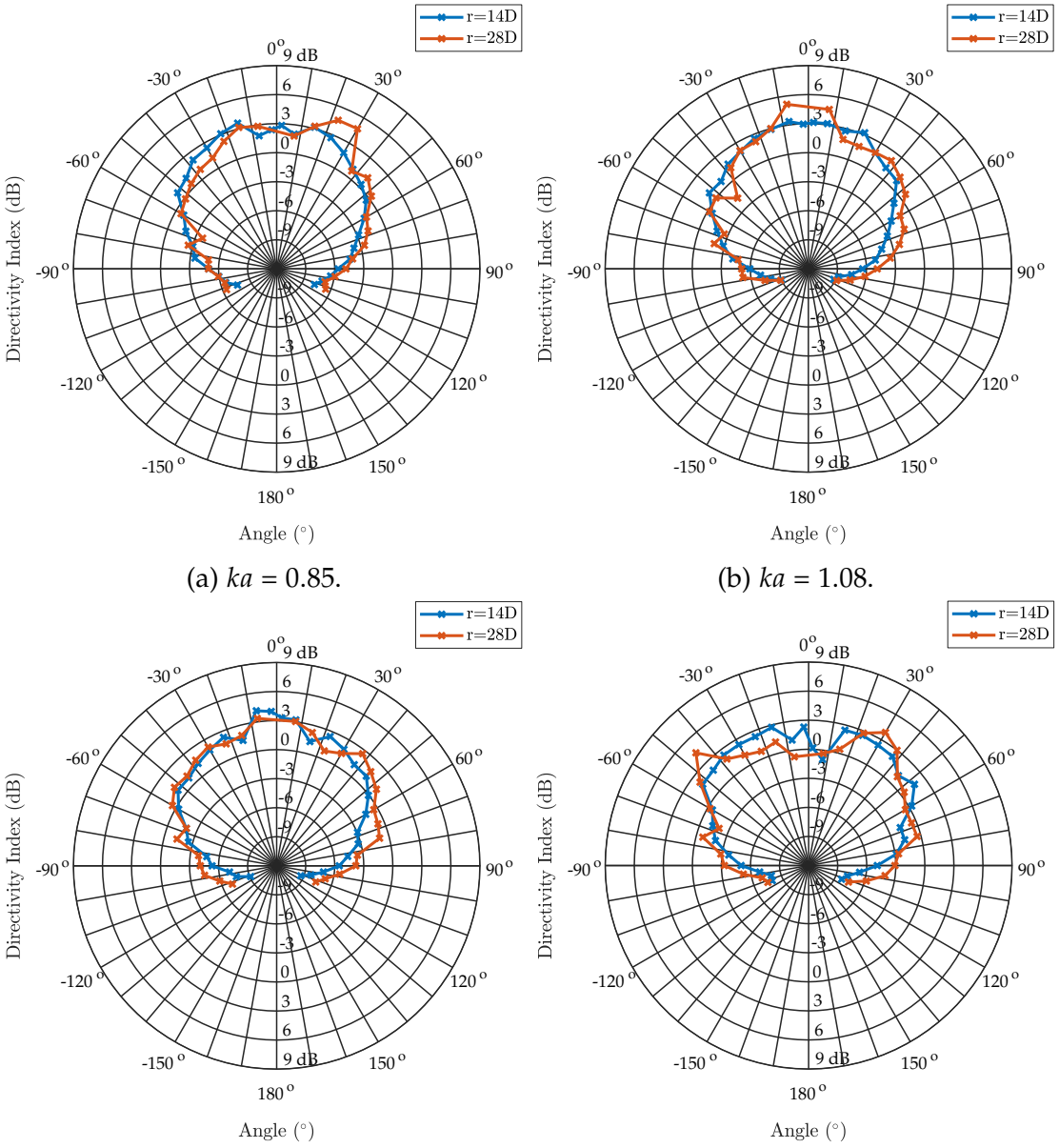

(a) $ka = 0.85$.

(b) $ka = 1.08$.

(c) $ka = 1.35$.

(d) $ka = 1.70$.

Figure D.5: The DI for sound propagation in an isothermal stationary field in the Anechoic Chamber for band-averaged one-third octave bands with centre frequencies $ka = [0.85, 1.08, 1.35, 1.70]$ ($f = [3.15\,\text{kHz}, 4\,\text{kHz}, 5\,\text{kHz}, 6.3\,\text{kHz}]$) at two different radii ($14D$ and $28D$). The results are from testing with a free-standing compression driver.

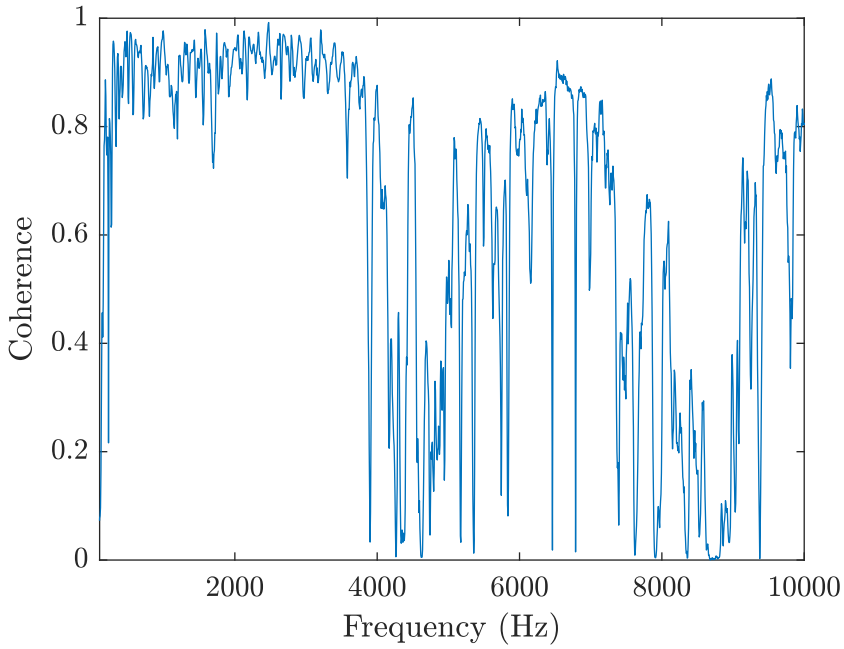

(a) Microphone at $-2.5°$ on the $14D$ array (Mic 16).

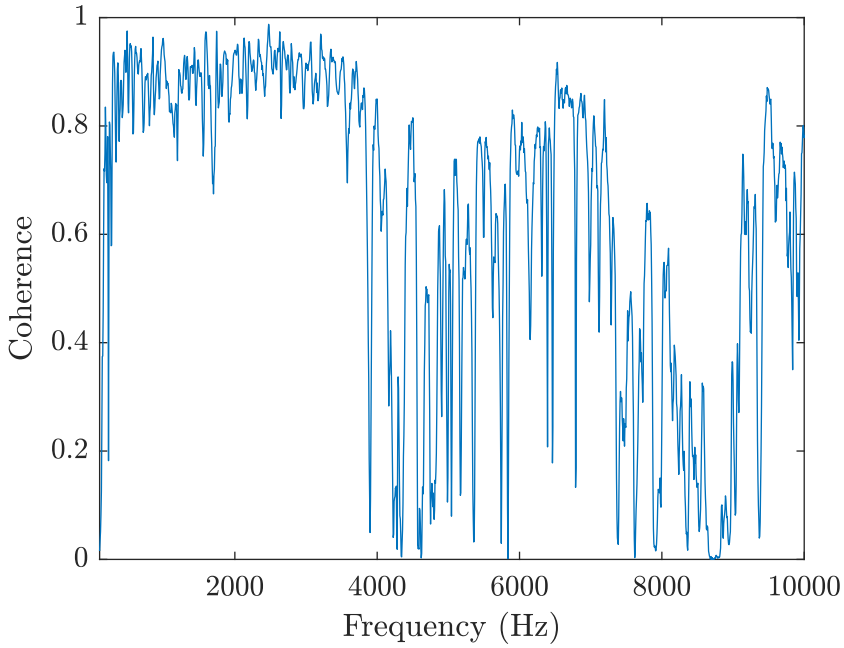

(b) Microphone $-7.5°$ on the $28D$ array (Mic 47).

Figure D.6: The coherence, γ^2_{xy}, between the electro-acoustic signal into the compression driver and microphone SPL response for two different microphones on the top of the $14D$ and $28D$ array. The test was undertaken in the Anechoic Chamber with an isothermal stationary field. Sound is propagating through the duct network.

ments at two different microphones at the top of the 14D and 28D array for sound propagation through the duct network. The SPL measurements show that when the sound is propagated through the duct network, the difference in SPL between the background noise levels and the sound through duct network is sufficient (>20 dB) to avoid signal to noise ratio issues. Comparing the results from Figures D.4 and D.7, the change from the free-standing compression driver to the inclusion of the duct network led to an overall reduction in the measured SPL, and an increased non-uniformity with dips in the response. The reduction in the overall SPL and non-uniform SPL response could be explained by the change in impedance from various parts of the duct network (bends, 'y-junctions', contractions, expansion, the flow straightener, and the duct outlet) or the response of higher order mode propagation, as f_{co} = 4.23 kHz for a duct at ambient temperature (27 °C).

The COP results for sound propagation through the duct represent the SPL, which is coherent with the sound from the electro-acoustic signal into the compression driver. Figure D.7 shows the COP at two different microphones at the top of the 14D and 28D array. The COP shows that below 3.9 kHz, there is significant coherent acoustic energy (approximately 50 dB to 60 dB). Above 3.9 kHz there are regions with significant reduction in COP levels, in particular around 4.2 kHz and 9 kHz. It should be noted that the first drop in COP is near the cut-on frequency, f_{co} = 4.23 kHz, for the system. The reduction in COP in the system above 4.2 kHz in certain regions is likely to be associated with one or more of the following issues: a multi-modal response of the duct, reflections, the duct network or array, and/or signal to noise ratio problems. The latter issue of a signal to noise ratio could be distortion from the compression driver, and is highly unlikely due to the insufficient SPLs measured at the microphones, as it can be seen in D.7 the SPL with the sound on is sufficiently higher than the background SPL.

In Figure D.8, the band-averaged sound directivity at four one-third octaves with centre frequencies f = [3.15 kHz, 4 kHz, 5 kHz, 6.3 kHz] is presented. The directivity plots show that the radiation pattern is approximately elliptical, with a lobe forming on-axis at 0° as the acoustic frequency increases. These results are qualitatively very similar to the results presented by Bies et al. [25] for the

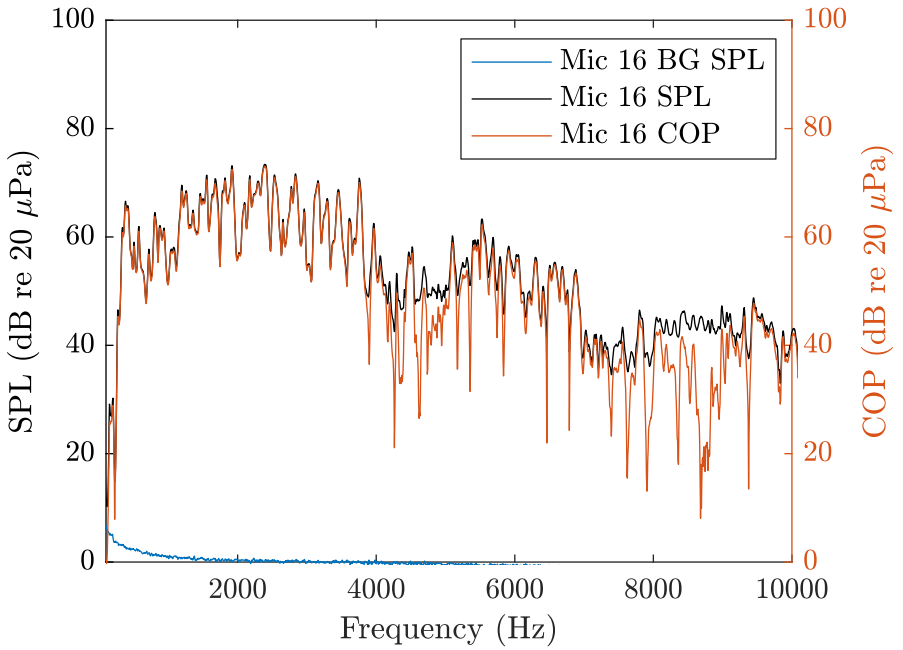

(a) Microphone at $-2.5°$ on the 14D array (Mic 16).

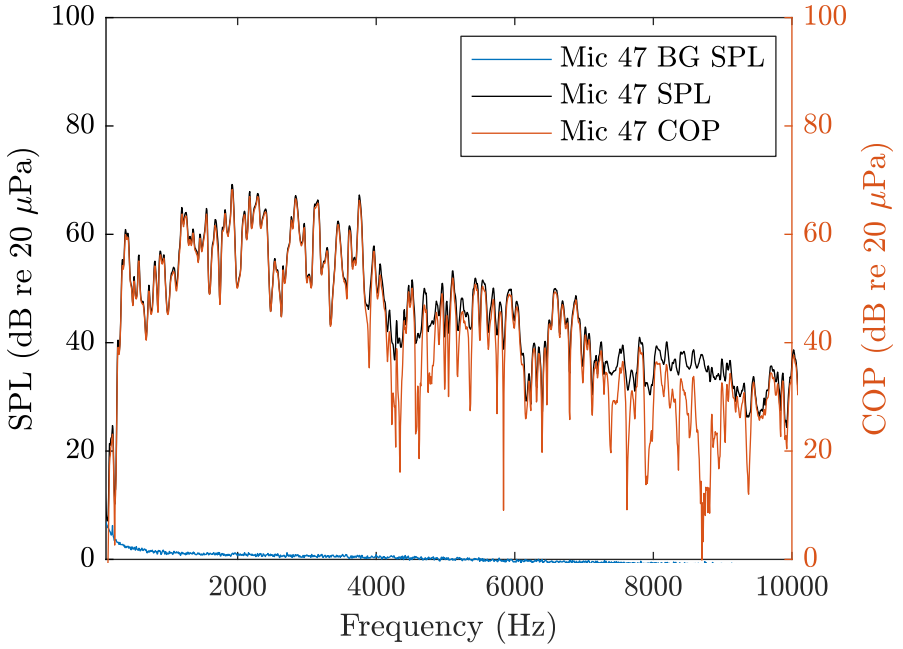

(b) Microphone at $-7.5°$ on the 28D array (Mic 47).

Figure D.7: The SPL and COP measurements at two different microphones at the top of the 14D and 28D array. The test was undertaken in the Anechoic Chamber with an isothermal stationary field. Sound is propagating through the duct network. BG refers to background noise levels. Relevant coherence is plotted in Figure D.6.

directivity results for sound propagation through an exhaust stack. The increase in sound on-axis has led to the reduction in the sound off-axis, but in particular there is a significant reduction in the sound outside of $\pm 90°$. This is an important observation, as it indicates that most of the acoustic energy is ejected vertically, instead of the common monopole assumption of uniform radiation. This leads to a more conservative sound prediction upwind and downwind of the exhaust stack at ground level in the far-field.

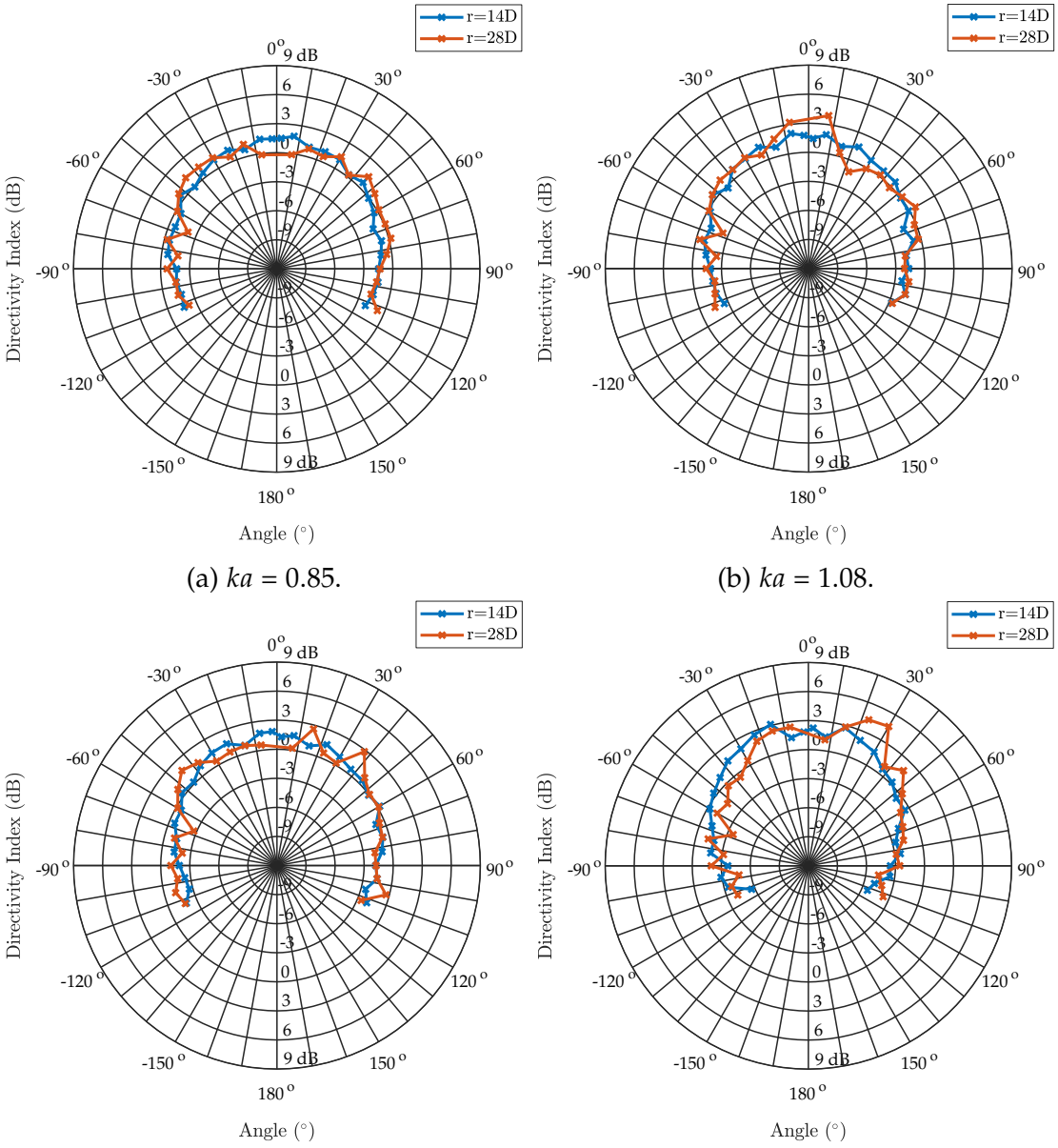

(a) ka = 0.85.

(b) ka = 1.08.

(c) ka = 1.35.

(d) ka = 1.70.

Figure D.8: The DI along the Y-Z plane (of symmetry) for sound propagation in an isothermal stationary field for band-averaged one-third octave bands with centre frequency ka = [0.85, 1.08, 1.35, 1.70] (f = [3.15 kHz, 4 kHz, 5 kHz, 6.3 kHz]) at two different radii (14D and 28D). The results are from testing in the Anechoic Chamber with sound propagation through the reduced-scale exhaust rig.

Appendix E

Sound propagation through 2D jet in cross-flow

Statement of Authorship

Title of Paper	Directivity analysis of sound in turbulent exhaust jets with laminar cross-flow: A numerical study
Publication Status	☑ Published ☐ Accepted for Publication ☐ Submitted for Publication ☐ Unpublished and Unsubmitted work written in manuscript style
Publication Details	Leav, O. Y., Cazzolato, B. S. and Howard, C. Q. (2015) "Directivity analysis of sound in turbulent exhaust jets with laminar cross-flow: A numerical study", Acoustics 2015 Australia, Hunter Valley, NSW, Australia, 15 - 18 November.

Principal Author

Name of Principal Author (Candidate)	Orddom Leav
Contribution to the Paper	Conducted the literature review, conducted all the CFD modelling, conducted all the acoustic FEM modelling, performed data processing and analysis, wrote the manuscript and acted as the corresponding author.
Overall percentage (%)	80
Certification:	This paper reports on original research I conducted during the period of my higher degree research candidature and is not subject to any obligations or contractual agreements with a third party that would constrain its inclusion in this thesis. I am the primary author of this paper.
Signature	Date 20/8/19.

Co-Author Contributions

By signing the Statement of Authorship, each author certifies that:

i. the candidate's stated contribution to the publication is accurate (as detailed above);

ii. permission is granted for the candidate in include the publication in the thesis; and

iii. the sum of all co-author contributions is equal to 100% less the candidate's stated contribution.

Name of Co-Author	Benjamin Seth Cazzolato
Contribution to the Paper	Supervised the development of work, helped in data interpreting, provided comments and edited manuscript.
Signature	Date 20/8/19

Name of Co-Author	Carl Quentin Howard
Contribution to the Paper	Supervised the development of work, helped in data interpreting, provided comments and edited manuscript.
Signature	Date 20/8/2019

DIRECTIVITY ANALYSIS OF SOUND IN TURBULENT EXHAUST JETS WITH LAMINAR CROSS-FLOW: A NUMERICAL STUDY

Orddom Y Leav[1], Benjamin S Cazzolato[1] and Carl Q Howard[1]

[1]School of Mechanical Engineering
University of Adelaide Australia, Adelaide SA 5005, Australia
Email: orddom.leav@adelaide.edu.au

Abstract

It is commonly assumed directivity of sound from exhaust stacks is axisymmetric, which is a reasonable assumption below cut-on and in the absence of flow or elevated stack temperatures. This paper shows that the sound directivity is non-spherical when there is a laminar cross-flow across the outlet of an exhaust stack that ejects hot subsonic gas. This computational study uses computational fluid dynamics to model the heated jet exhausting into a mean laminar cross-flow and the linearised Euler equations, solved using the finite element method, to model the propagation of sound. This non-spherical spreading is due to the refraction of sound in the shear layer and diffraction at the edge of the stack outlet. Furthermore, the laminar mean cross-flow causes asymmetric spreading of the acoustic field, as the exhaust flow is also non-axisymmetric. The implications of these findings suggest that community noise level predictions from stacks may be under-predicted due to the altered directivity of the exhaust stack caused by cross-flow and refraction effects from hot exhaust gases.

1. Introduction

Open cycle gas turbines (OCGT) are increasingly used for power generation as they are able to provide base loads in peaking or uncertain conditions and can respond quickly to power grid demands. However, some have been found to produce significantly higher community noise levels than is predicted using ISO Standard 10494 [1]. This issue of excessively high levels of low frequency noise from OCGT has been well documented internationally [2], [3], [4]. These excess levels of low frequency noise from OCGT can have the following effects: perceived annoyance of 'throbbing' from high intensity low frequency noise [3], 'beating' sensation in the chest [5], nausea [3] and acoustic excitation in structures with low resonant frequency, such as glass structures and wall panels [3]. The causes for the increased levels of low frequency noise in communities near OCGT is the subject of ongoing research. The source of excess low frequency noise from OCGT should be investigated in further detail in order to assist in the planning stages of such systems, as well as for the design of noise mitigation.

Currently, the ISO Standard 10494 for gas turbines assumes that the sound directivity from an exhaust stack is primarily from diffraction and does not take into consideration the flow effects [5]. In heated turbulent exhaust jets, flow mechanisms such as pressure gradient and temperature gradients in the shear layer can alter the sound propagation. Early research into the interaction of sound with a jet's shear layer has shown that plane waves will refract in an infinitesimally thin shear layer [6]. This work was expanded by the experimental work of Candel [7], and theoretical models developed by Cargil [8], which have shown that sound refraction occurs in a finite thickness shear layer. Further studies conducted by various other researchers into the phenomenon of shear layer refraction in jets has shown

that with modest Mach numbers (M=0.1) large dips (in excess of 20dB) in the directivity of the jet's centre line were observed [9], [10], [11]. Other affects such as radiation, scattering, reflections and acoustic spectrum broadening are also present in the shear layer's pressure gradient. The temperature gradients in the jet can also supplement the pressure gradient effects in the shear layer [12].

The presence of laminar cross-flow with turbulent exhaust jets is commonly seen in turbulent exhaust stacks and is a well-researched topic. The jet in cross-flow (JICF) problem is also seen in various applications such as oil film cooling for turbine blades, fuel injectors and dilution holes in gas turbine combustors [13]. Experimental analysis and computational fluid dynamics (CFD) simulations has shown that three-dimensional JICF can generate flow features such as shear layers, counter rotating vortex pairs, wake vortices and horse shoe vortices [13]. These features are not present in two-dimensional JICF where a recirculation zone forms on the leeward side of the exhaust jet instead [14], [15]. An additional feature that is present in two-dimensional JICF studies and not in three-dimensional JICF is the reattachment of the wake downstream [14], [15]. From the literature previously stated it is evident that shear layer and pressure gradient will cause refraction.

This paper analyses the effects that the thermal mixing of a hot turbulent jet exhaust with a cold laminar cross-flow has on the sound directivity of a turbulent subsonic heated exhaust stack. This study will use two-dimensional CFD and finite element analysis (FEA) to investigate the sound directivity in the following two scenarios: infinitely baffled infinitely thin rectangular (ribbon) pistons and heated JICF. The layout of the paper is as follows. The simplified computational model and boundary conditions of the computational mesh will be discussed in Section 2. Subsequently, the mathematical models that are used for the fluid flow simulations through CFD and acoustic propagation using linearised Euler equations (LEE) with FEA are explained. The analytical and simulation results from CFD and FEA are presented in Section 4, which shows the numerical fluid dynamics solution and the effects of temperature on the propagation of sound. The main conclusions of this paper and proposed future work are summarised in Section 5.

2. Details of Computational Model

2.1 Simplifications of the Computational Model

In this paper the complexity of modelling a realised OCGT exhaust stack has been simplified to ensure the modelling is computationally feasible. A schematic for simplified model is shown in Figure 1. Firstly, the computational model has been reduced to a two-dimensional simulation with an infinitely thin rectangular duct with finite length. The duct in the simulation is modelled as a straight duct with rigid no-slip walls. In a real exhaust stack the outlet of duct has finite dimension and contains complex geometries in the system such as baffles for sound attenuation, contractions, bends and other flow noise inducing mechanisms. Adjacent to the duct outlet is a half-space with a rigid reflective ground, which are similar to various studies previously completed [14],[15]. This assumption is adequate in analysing the basic fluid structures and reducing the complexity of the problem, but in reality the ducts are protruding and the flow in leeward side of the jet are not bounded by an adjacent wall. Since, the simulation is two-dimensional three-dimensional effects such as eddy formation, three dimensional flow features as described in Section 2.4.1 and three dimensional hemispherical spreading of sound cannot be captured in the simulation. A key limitation of this model is that sound is only generated from the harmonic source at the inlet and other flow generating mechanisms are neglected. Nevertheless, these limitations have been taken into consideration and the overall trend in sound propagation through thermal distribution of a jet in cross-flow can be ascertained.

In order to directly quantify the effects of the JICF it is essential to model the sound propagation with and without effects of flow and temperature. This study investigates the propagation of sound from a baffled infinitely thin rectangular piston with the absence of flow as the benchmark case. This benchmark case has well known trends for planar sources with low Helmholtz numbers and frequencies well below cut-on frequency. Subsequent sound propagation modelling initially involved CFD modelling for convective bulk fluid flow to generate the temperature distribution. The calculated temperature field is applied to the FEA model, which is used to vary the speed of sound appropriately.

An acoustic FEA is conducted to determine the sound pressure level (SPL) in the domain. The details and limitations of the CFD model and sound propagation models will be further discussed below.

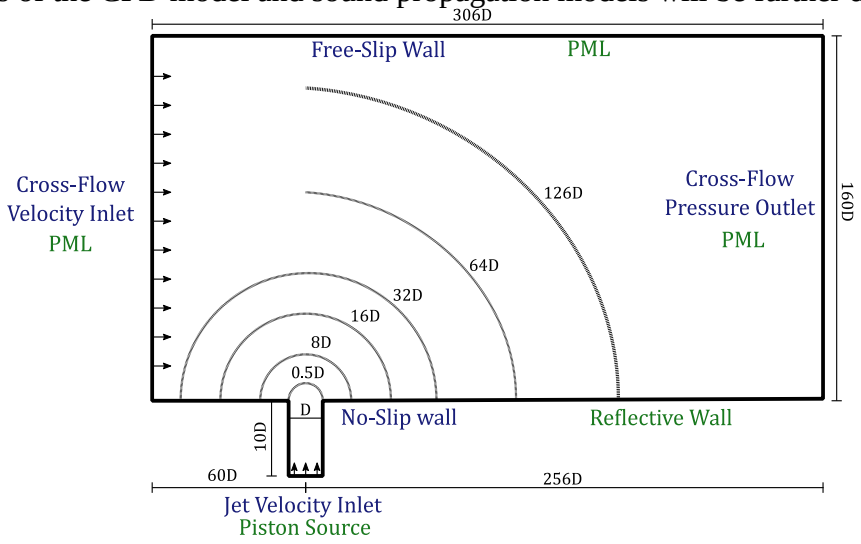

Figure 1. Schematic of two-dimensional JICF. Acoustic boundary conditions are in green, CFD boundary conditions are purple.

2.2 Boundary Conditions

Boundary conditions are essential in resolving both the CFD and computational acoustic solution accurately. The following will discuss the inlet boundary conditions and outlet conditions of the CFD simulation and computational acoustic simulations.

2.2.1 Inlet Boundary Conditions

Assumptions have been made for the inlet boundary conditions for the two-dimensional JICF CFD simulation and are based on recommendations in the literature [14]. The inlet conditions of the model are the turbulent jet inlet at the base of the duct and the laminar cross-flow on the windward side of the duct. For the jet inlet a flat mean velocity profile with a Reynolds Number, Re_{jet} of 51400 was chosen. A jet velocity to cross-flow velocity of 4 was chosen and the cross-flow inlet was prescribed with a constant mean velocity. To ensure the flow develops adequately the domain upstream of the jet and duct outlet were also extended some distance from the outlet. Both the Reynolds number of the jet and the jet velocity to cross-flow velocity were based on the numerical studies by Kavsaoglu and Arkmandor [14]. The resulting Mach number, M_{jet} for this simulation is approximately 0.1, which is the Mach number typically seen in many exhaust stacks. Heating was also added at the jet inlet and a temperature of 773K was chosen, as it resembles temperatures typically seen in OCGT exhaust stacks. The temperature at the cross-flow inlet was set to 300K. The walls adjacent to the duct inlet and outlet are also no-slip walls, resulting in a boundary layer along the wall which was resolved in the simulations.

In simulating the propagation of sound, the sound source was identical for the two cases considered here: with and without flow. The sound source was a planar harmonic source with a velocity amplitude of 0.1m/s. It is assumed in this study that the majority of sound is generated from the sound source and other flow generated noise mechanisms can be neglected. This can be justified by the fact, that the quadrupole terms from shear layer noise is dependent on M_{jet}^5, which is almost negligible for the Mach number in this study. The Helmholtz numbers solved for this paper range from 0.15-0.6, but the majority of the results are presented for the Helmholtz number of 0.3. These Helmholtz numbers were chosen as they are below one and are well below the cut-on frequency of the duct.

2.2.1 Outlet and Far-Field Boundary Conditions

In the far-field of the CFD model there are two different outlet conditions that are used. The first outlet condition is a free-slip wall boundary condition in the normal direction to the wall attached to the duct outlet and perpendicular to the cross-flow inlet. This was chosen to allow the shear stress along the wall to be to zero. This is the same as implementing a symmetry boundary condition. At the domain outlet, parallel to the cross-flow velocity inlet a pressure outlet condition is used. The temperature at the pressure outlet boundary condition was set to the same temperature as the cooler cross-flow inlet of 300K.

For the computational sound propagation simulation, the far-field condition is uniform for all boundary conditions. Perfectly matching layer (PML) elements are used for the far-field absorption of sound to simulate the half-space. The number of PML elements used is dependent on the duct width, D, and the wavelength of the lower frequency for analysis. Howard and Cazzolato [16] have recommended that the PML zone is at least one-quarter of the wavelength of the lowest frequency interest.

2.3 Domain and Meshing Details

The computational domain size for both the CFD and computational acoustic simulation are identical, but the mesh for each simulation differs. The computational domain has been scaled by jet width, D. The computational domain along the x-axis spans 256D downstream of jet's central axis and 60D upstream from the jet's central axis. The height of the simulation perpendicular to the wall attached to the outlet is 160D. The height and length of the simulation were sufficient to ensure that the majority of critical flow features were captured without effects of the top boundary condition. The large domain size also allows for acoustic measurements in the far-field and to analyse possible mechanisms that may alter the sound propagation path.

For the CFD simulations the mesh (shown in Figure 2) was refined in areas where necessary flow features were to be resolved with structruced hexahedrals elements. This mesh has 726,018 elements and 1,116,520 nodes. The cells with the smallest face area are situated in the duct, near-field region of the duct outlet and in the inflation layer near the bottom wall adjacent to the jet outlet. The non-dimensional wall distance, y^+, for this simulation is less than 13, which is acceptable for resolving the boundary layer in FLUENT with the scalable wall function. In the duct, geometric near field of the duct outlet and inflation layer elements are generated with structured hexahedras. Structured mesh in this region has a relativly slow growth rate to to ensure most of the elements in this region are isotropic to utilise the full capabilitiles of the third-order discretisation scheme, QUICK. In the geometric far-field where the flow characteristics are of less importance the mesh has been generated with unstructured triangular prism elements. Both element types used in FLUENT only specify nodes at the vertex of the element and is also known as 'brick' elements.

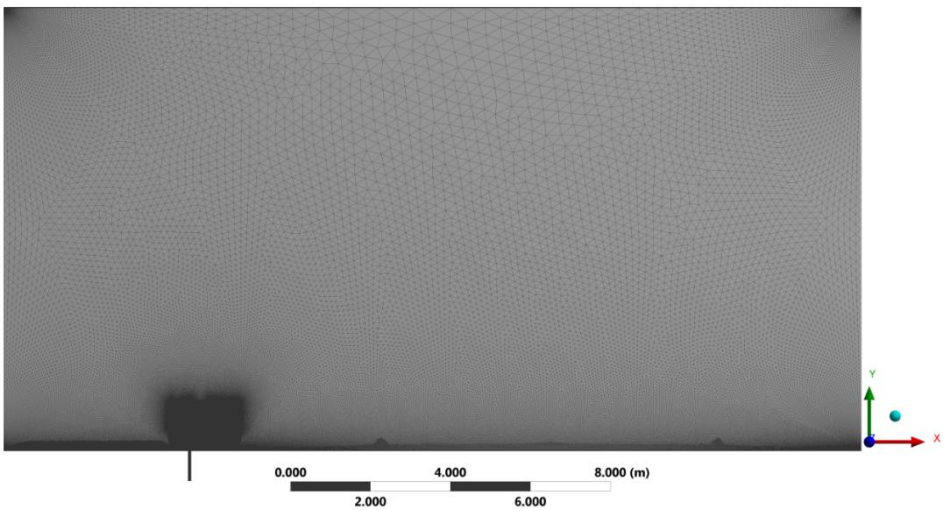

Figure 2. Meshing domain for CFD modelling a baffled rectangular jet with cross-flow

Mesh generation for modelling sound propagation with FEA has different requirements compared to meshing schemes for CFD simulation. Hence, an alternative mesh is necessary for computationally evaluating sound propagation with FEA and the final mesh is shown in Figure 3. In propagating acoustic waves it is desirable to use a structured mesh, ideally aligned in the planar direction of the wave [16]. As a result, the elements from the duct inlet to arcs seen in Figure 3 are structured hexahedra, as is the buffer region and the PML region on the outskirts of computational domain. There is however a small region at the duct outlet which is unstructured hexahedra, but due to the high mesh density and smooth growth rate in element size in that region the effects of the unstructured mesh are minimal. Quadratic FLUID 220 acoustic elements are used in the simulation. According to Howard and Cazzolato [16], at least six elements per wavelength are required for accurately resolving the acoustic pressure wave. Therefore, for the mesh shown in Figure 2 the maximum Helmholtz number achievable for this simulation is 0.66, and consequently all calculations will be conducted at Helmholtz numbers less than 0.6. The resulting acoustic element count is 448,484 and node count is 3,151,801.

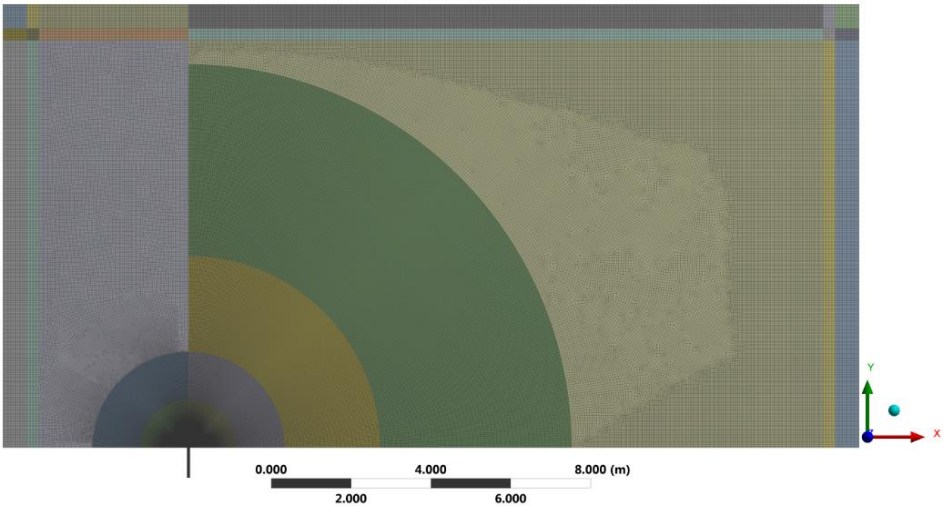

Figure 3. Meshing domain for acoustic FEA modelling sound propagation in a baffled duct with

2.4 Mathematical Models

This section will discuss the equations and models for both the CFD and sound propagation simulations.

2.4.1 Governing Models for Computational Fluid Mechanics

The fluid dynamics of the two-dimensional jet in cross-flow was simulated using ANSYS FLUENT [17]. The fluid flow in the model was computationally resolved using the compressible steady Reynolds Averaged Navier Stokes Equation (RANS). The fluid medium for this analysis is dry air. The density for the simulation was resolved using the ideal gas assumption for compressible analysis. The viscosity of the model was also calculated using the Sutherland approximation. The simulation also assumes the jet is non-buoyant. A pressure based solver with a "Coupled" setting for the pressure-velocity coupling was chosen. The spatial, pressure, energy and turbulent discretisation schemes chosen were a combination of the third-order QUICK scheme in isotropic cells and second-order upwind scheme in non-isotropic cells. The two equation realisable $\kappa - \epsilon$ model was chosen to resolve the turbulence [18]. This model is computationally less expensive than other more complicated RANS models and scale resolving turbulence models. Furthermore, the model is suitable for two-dimensional simulation as it does not resolve the three-dimensional eddies directly. However, there are limitations in the turbulence model: it assumes the eddy viscosity is isotropic; the turbulence can be modelled with two equations; the eddies in the models are not resolved with the average turbulence quantities being calculated in the shear layer; lack of prediction for flow separation at the jet inlet edge; and inaccurate prediction of the jet spreading and decay [18]. The boundary layer in the no-slip walls in the

model were resolved using scalable wall functions. For the CFD analysis in this paper, only the critical features of the flow will need to be reproduced and the compressible steady RANS model is sufficient.

2.4.2 Sound Propagation using Finite Element Analysis

Sound propagation simulations were conducted with ANSYS Mechanical by solving the LEE with FEA [19]. This type of analysis requires an Acoustic ACT extension to be used for solving these types of simulations [19]. In solving the LEE the following assumptions are made: the air medium is compressible, there are no mean flow on the fluid, the changes in density are small in comparison to the mean density, the viscous dissipation of the fluid is neglected and the acoustic pressure can be represented by the wave equation. Harmonic analyses were chosen for this modelling work, as it allows the system to be driven by a sinusoidal oscillating harmonic source. The elements in this simulation are set with the symmetric algorithms for faster solution times and is possible with the absence of fluid structural interaction between the propagated sound and the boundary conditions. The elements at the duct are set with the coupled symmetric algorithm to allow the fluid structure interaction at the inlet for acoustic source definition. The elements in the remaining domain are set with uncoupled symmetric algorithm. As discussed in Section 2.3, the higher order FLUID 220 elements are used for the simulation. Since, the model has large temperature gradients, the convective effects are neglected, as they only correspond to 10% of the temperature effects and will have little impact on the results.

3. Computational Results

3.1 Baffled Infinitely Thin Rectangular Piston

The acoustic radiation of a baffled infinitely thin rectangular piston was simulated and the results were used as a benchmark scenario for sound propagation in absence of heated flow. The results indicate that in the absence of heated flow the acoustic spreading from the duct outlet is spherical at the Helmholtz numbers of interest, as shown in Figure 4. This is to be expected of Helmholtz numbers significantly less than one and the frequency of the harmonic planar source is less than cut-on frequency of the duct. The computational acoustic power results in the far-field have also been compared with the acoustic power results from the methods used in the standard ISO 10494 [5]. Computational acoustic power results at a Helmholtz number of 0.3, in the far-field is approximately 103.0dB ref 10^{-12} W, whereas the acoustic power from the standards is 103.1dB ref 10^{-12} W. Since, the difference is minimal it can be concluded that the standards are adequate in estimating the sound power for sound propagation in exhaust stacks without heated flow. This has also been confirmed for higher Helmholtz numbers of up to 0.6.

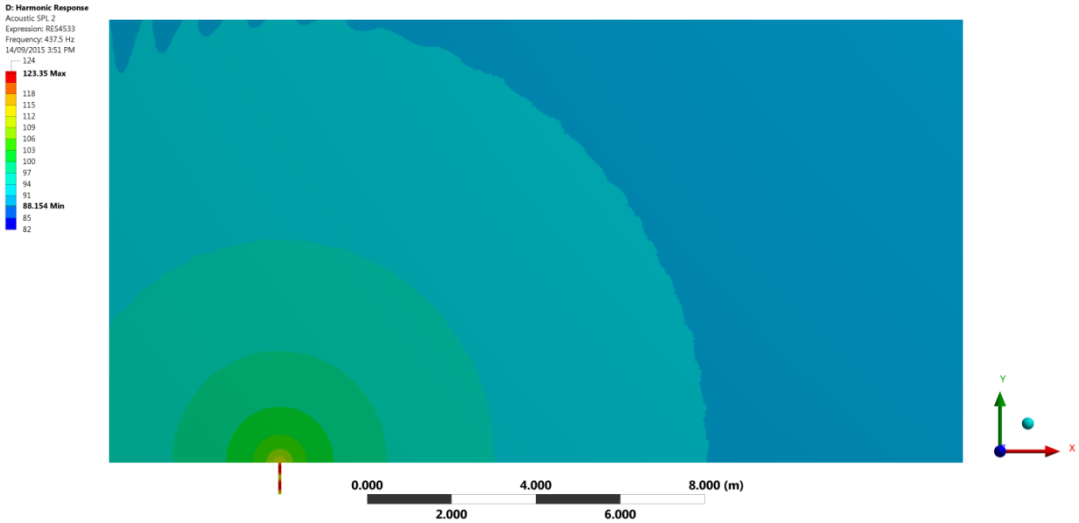

Figure 4. Acoustic SPL contour plot for a Helmholtz number of $ka = 0.3$ in the absence of flow

3.2 Heated Rectangular Jets in Cross-flow

3.2.1 Fluid Flow Features of Heated Rectangular Jets in Cross-Flow

The CFD simulations results for an infinitely thin heated rectangular JICF conducted in this study displays distinct flow features that have been witnessed in previous incompressible and ambient temperature studies. The velocity magnitude results from the CFD simulation are portrayed in Figures 4 and 5 with velocity streamlines and velocity vectors, respectively. These velocity streamlines in Figure 5 originate from either the turbulent jet inlet or laminar cross-flow inlet. A distinct feature seen in Figure 5 is that the there is a strong curvature in the jet, as a result of the cross-flow and a reattachment region further downstream. Since the velocity streamlines only display the streamlines originating from the inlets, there is a region near the jet outlet that is missing in Figure 5, but can be seen in the velocity vector results, shown in Figure 6. The distinct recirculation in this region is a contributing factor in the curvature and reattachment of the jet with the adjacent wall. These features are also observed in the incompressible and ambient temperature experimental study by Mikhail, Chu and Savage [15], and numerical study by Kavsaoglu and Akmandor [14]. Therefore, the CFD simulations conducted in this research have produced similar results to previous studies, and the presence of compressibility and temperatures have minor effects on the dominant flow features.

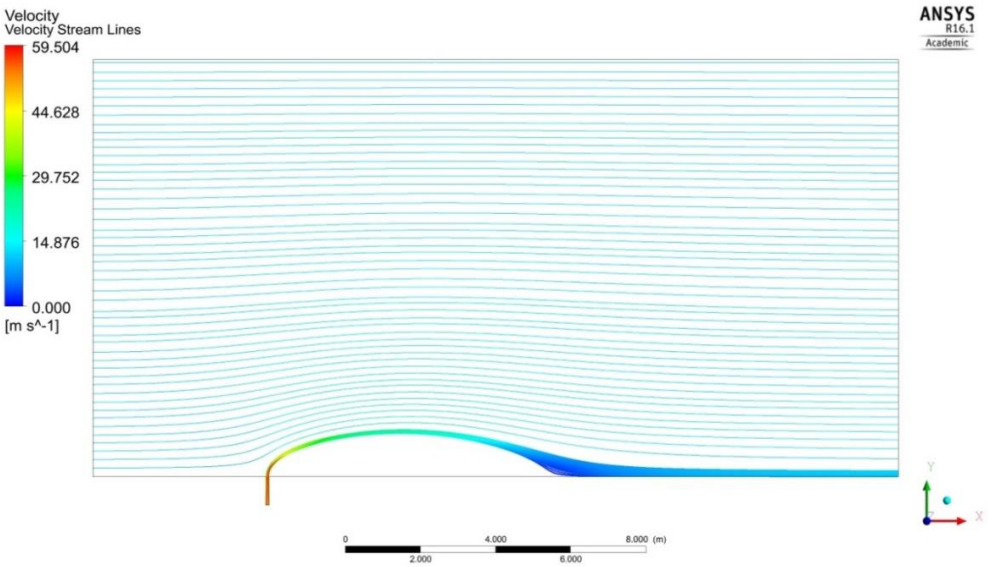

Figure 5. Two-dimensional JICF velocity streamline plot

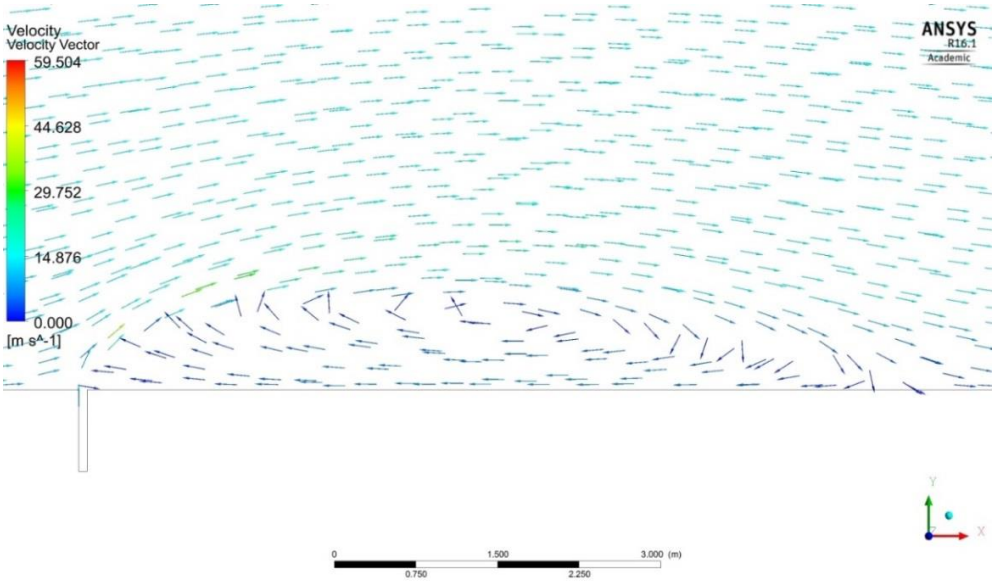

Figure 6. The velocity vector plot for the two-dimensional JICF in the recirculation region

The thermal results for the absolute temperature of the simulation show a dependence on the distinct convective flow features. The temperature distribution of the simulation is depicted with a temperature contour plot shown in Figure 7, where it is clearly shown that the region near the jet outlet possess the highest temperature. As the heated jet propagates further downstream entrainment with the cooler cross-flow occurs and the temperature of the overall plume continually decreases. There is also a strong correlation with the deflection of high temperature fluid in Figure 7 and the curvature in the velocity streamlines seen in Figure 5. It is also seen in Figures 6 and 7 that in the recirculation zone there are local minimums in both the velocity magnitude and temperature. Furthermore, the temperature gradients on the leading and leeward side of the plume are also correlated with the velocity gradient in the shear layer. Hence, there is evidence to suggest that the temperature distribution of the infinitely thin heated jet in cross-flow is dependent on the convective fluid flow.

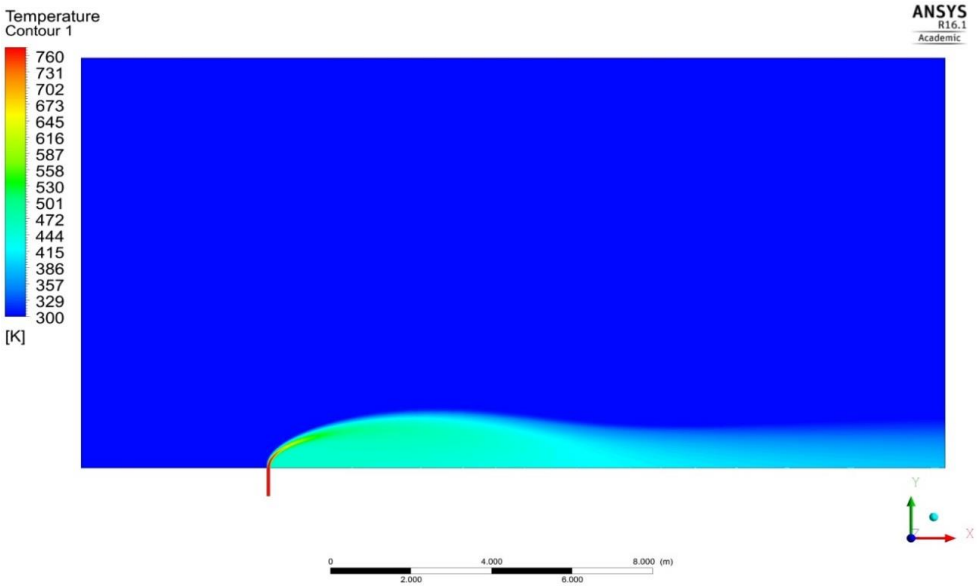

Figure 7. The temperature contour plot for the heated JICF

3.2.2 Sound Directivity of Heated Rectangular Jets in Cross-Flow

The thermal distribution from the CFD simulation was imported into the FE model and applied to the nodes. The FEA software models sound generation and propagation through the LEE, as described in Section 2.3.2. The resulting SPL for a Helmholtz number of 0.3 are shown in Figure 8. The SPL contour plot can be compared to Figure 4 where a significant change in the propagation path of sound can be seen. In the absence of temperature variation, the propagation of sound at these Helmholtz numbers exhibit hemi-spherical spreading from the duct outlet, as discussed in Section 3.1. However, this is not the case with the temperature distribution present and there are two distinct lobes forming. The lobe on the windward side of the jet is predominantly elliptical. On the leeward side the lobe is highly directive and is related to the deflected jet. With the presence of the temperature effects there is a strong increase in the sound levels perpendicular to the centre jet axis. Further downstream, sound is being reflected off the bottom wall and is 'beaming' off the wall. This reflection of sound is strongly dependant on the reattachment of the plume. The formation of the distinct lobes in relative near-field is from the refraction of sound in the temperature gradient, however in the far-field is a combination of directly refracted field and reflect field from the ground. The sound power has also been calculated based on the standards and compared with the numerical sound power in the far-field at a Helmholtz number of 0.3. The sound power based on the far-field numerical measurements and standards are 103.0dB ref 10^{-12} W and 102.8dB ref 10^{-12} W, respectively. Similar to the results in Section 3.1 the standards are sufficiently accurate in estimating the far-field sound power.

In addition to the SPL contour plots, directivity was analysed using normalised SPL polar plots at varying distances from the jet outlet. The result of the polar plot is for a Helmholtz number of 0.3 and is shown in Figure 9. The SPLs were normalised by the on-axis SPL for the simulation in the absence of the jet. The SPL results are taken from six different radial distances from the jet and have

been scaled with D. It can be seen in Figure 9 the normalised SPL in the absence of flow is relatively spherical for varying distances from the jet outlet, but this is definitely not the case with the thermal effects present. The results in the polar plot show that with increasing radial distances from the jet there are increases in the normalised SPL of the two side lobes. In particular, the normalised SPL in the side lobe of the leeward side of the JICF seems to be directly related to the radial distance with the results at $128D$ showing the largest lobe. There are also evidence of the reflective effects from the bottom wall in far-field ($128D$) and not in the relative near-field. From the analysis it can be seen that the normalised SPL for two-dimensional JICF are highly dependent on the radial arc of measurement. However, the normalised SPL for exhaust stacks without heated flow have relatively spherical distribution at most of the radial arcs in this study. As a result of the normalised SPL polar plots it can be seen that the thermal effects from the two-dimensional JICF has significantly altered sound propagation path and the results are strongly dependent on the radial location for measurements which is consistent with previous studies on sound propagation of sound in unheated axis-symmetric jets [9].

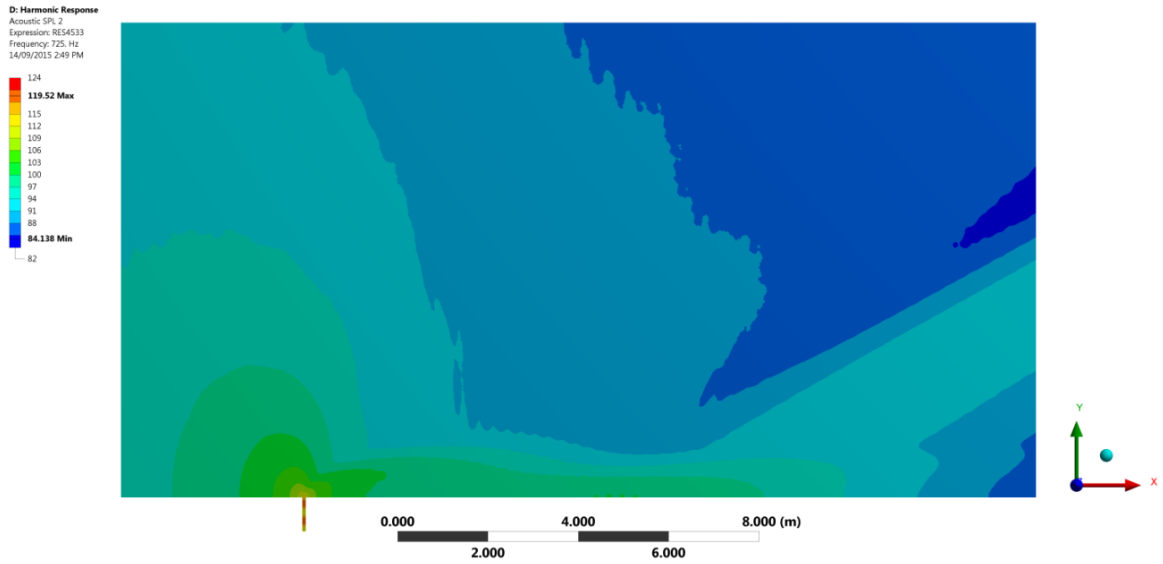

Figure 8. Acoustic SPL contour plot for a $ka = 0.3$ with the thermal distribution from the JICF

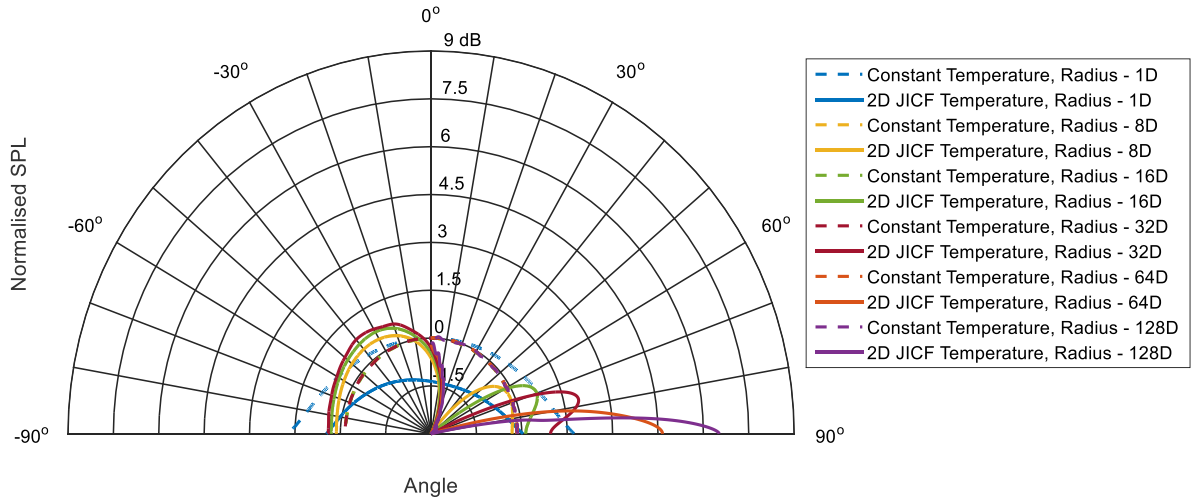

Figure 9. Normalised SPL polar plot at a $ka = 0.3$ with and without the thermal effects from the JICF

4. Conclusions and Future Work

The results from this study's simulations has shown that the temperature gradients from two-dimensional JICF can greatly affect the directivity of sound. The results have clearly indicated that in the absence of heated flow the propagation of sound from the duct is spherical. However, this is not the case with the temperature gradient from the two dimensional JICF, where the sound propagation is

now asymmetric due to refraction of the sound waves by the thermal gradients in the shear layer and subsequent edge diffraction at the jet exhaust. Further analysis has shown the normalised SPL is strongly dependant on the radial location of the measurements. Even though the standards are sufficient in calculating the total acoustic power of the system in the far-field, the altered directivity of the two-dimensional JICF has shown that off-axis sound may be under predicted in far field from the cross-flow and refraction effects from hot exhaust gases. The implications of these findings suggest that community noise level predictions from stacks may be under-predicted due to the altered directivity of the exhaust stack.

Future work will be further conducted in this area to build a higher fidelity computational model for better assessing community noise level predictions from OCGT exhaust stacks. The future computational study will involve the following: three dimensional simulations with a finite cylindrical jet, scale resolving simulations to analyse the effects of the vortical structures and resolution of the sound waves using direct computational acoustics. These models will later be validated with experimental test rig, which has been scaled using non-dimensional acoustic parameters.

References

[1] ISO 10494:1993 Gas turbines and turbine sets- Measurement of emitted airborne noise – Engineering/ survey method, *International Organization for Standardization*, Geneva, Switzerland, 2010.

[2] Broner, N. "A simple outdoor criterion for assessment of low frequency noise emission", *Acoustics Australia*, 39, 7-14, (2011).

[3] Broner, N. " Power to the people", *15th Int. meeting on low freq. noise & vib. & its control, 15th Int. meeting on low freq. noise & vib. & its control*, Stratford upon Avon, UK, May 2012.

[4] Hessler Jr, G. F. "Proposed criteria for low frequency industrial noise in residential communities", *Low Frequency Noise, Vibration and Active Control*, **24**, 97-106, (2005).

[5] Broner, N. "The effects of low frequency noise on people – A review", *Journal Sound and Vibration*, **58**, 483-500, (1978).

[6] Amiet, R. K. "Refraction of sound by a shear layer", *Journal of Sound and Vibration*, **58**, 467-482, (1978).

[7] Candel, S.M., Julienne, A. and Guedel, A. " Refraction and scattering of sound in an open wind tunnel flow", *6th International Congress on Instrumentation in Aerospace Simulation Facilities*, 288-300, 1975.

[8] Cargil, A.M. "Low frequency acoustic radiation from a jet pipe – a second order theory", *Journal of Sound and Vibration*, **83**, 339-354, (1982).

[9] Mungur, P., Plumblee, H.E., and Doak, P.E., "Analysis of acoustic radiation in a jet flow enviroment", *Journal Sound and Vibration*, **68**, 21-52, (1974).

[10] Savkar, S.D., "Radiation of cylindrical duct acoustic modes with flow mismatch", *Journal Sound and Vibration*, **42**, 363-386, (1975).

[11] Maestrello, L., Bayliss, A. and Turkel, E., "On the interaction of a sound pulse with the shear layer of an axisymmetric jet", *Journal Sound and Vibration*, **74**, 281-301, (1981).

[12] Candel, S.M., "Acoustic transmission and reflection by a shear layer discontinuity separating hot and cold regions", *International Journal of Aeroacoustics*, **8**, 199-230, (1972).

[13] Kelso, R.M., Lim, T.T. and Perry A.E., "An experimental study of round jets in crossflow", *Journal of Fluid Mechanics*, **306**, 111-144, (1996).

[14] Kavsaoglu, M.S. and Akmandor I.S., "Navier-Stokes simulation of two and three dimensional jets in crossflow", *American Institute of Aeronautics and Astronautics*, 1-20, (1991).

[15] Mikhai vgl, R., Chu, V.H. and Savage, S.B., " The reattachment of a two-dimensional turbulent jet in confined crossflow", *Proceedings of the 16th IAHR Congress*, Sao Paulo, Brazil, **3**, 414-415, (1975).

[16] Howard, C.Q. and Cazzolato, B.S. *Acoustic analysis using MATLAB and ANSYS*, CRC Press, 2014.

[17] ANSYS, *ANSYS FLUENT*, ver. 16.1, computer program, ANSYS Inc, Canonsburg, Pennsylvania, 2015.

[18] Shih, T-H., Liou, W.W., Shabbir, A., Yang, Z. and Zhu, J., "A new $\kappa - \epsilon$ eddy viscosity model for high Reynolds number turbulent flows", *Computer & Fluids*, **24**, 227-238, 1995.

[19] ANSYS, *ANSYS Mechanical*, ver. 16.1, computer program, ANSYS Inc, Canonsburg, Pennsylvania, 2015.

Appendix F

Numerical sound propagation through elevated jet in cross-flow

Statement of Authorship

Title of Paper	A computational analysis of sound directivity from sound propagation through non-isothermal, turbulent exhaust jets in cross-flow
Publication Status	☑ Published ☐ Accepted for Publication ☐ Submitted for Publication ☐ Unpublished and Unsubmitted work written in manuscript style
Publication Details	Leav, O. Y., Cazzolato, B. S., and Howard, C. Q. (2017) "A computational analysis of sound directivity from sound propagation through non-isothermal, turbulent exhaust jets in cross-flow", 24th International Congress of Sound and Vibrations, London, United Kingdom, 23 - 27 July.

Principal Author

Name of Principal Author (Candidate)	Orddom Leav		
Contribution to the Paper	Conducted the literature review, conducted all the CFD modelling, conducted all the acoustic FEM modelling, performed data processing and analysis, wrote the manuscript and acted as the corresponding author.		
Overall percentage (%)	80		
Certification:	This paper reports on original research I conducted during the period of my higher degree research candidature and is not subject to any obligations or contractual agreements with a third party that would constrain its inclusion in this thesis. I am the primary author of this paper.		
Signature		Date	20/8/19

Co-Author Contributions

By signing the Statement of Authorship, each author certifies that:

i. the candidate's stated contribution to the publication is accurate (as detailed above);

ii. permission is granted for the candidate in include the publication in the thesis; and

iii. the sum of all co-author contributions is equal to 100% less the candidate's stated contribution.

Name of Co-Author	Benjamin Seth Cazzolato		
Contribution to the Paper	Supervised the development of work, helped in data interpreting, provided comments and edited manuscript.		
Signature		Date	20/8/19

Name of Co-Author	Carl Quentin Howard		
Contribution to the Paper	Supervised the development of work, helped in data interpreting, provided comments and edited manuscript.		
Signature		Date	20/8/2019

24th INTERNATIONAL CONGRESS ON SOUND AND VIBRATION
23–27 July 2017, London

ICSV24
23-27JULY 2017
LONDON CALLING

A COMPUTATIONAL ANALYSIS OF SOUND DIRECTIVITY FROM SOUND PROPAGATION THROUGH NON-ISOTHERMAL, TURBULENT EXHAUST JETS IN CROSS-FLOW

Orddom Y. J. Leav, Benjamin S. Cazzolato and Carl Q. Howard
The University of Adelaide, School of Mechanical Engineering, Adelaide, South Australia, Australia
email: orddom.leav@adelaide.edu.au

When predicting community noise, it is commonly assumed that the directivity of sound from exhaust stacks is axisymmetric, which is appropriate in the absence of cross-flow. For real stacks, which typically carry hot exhaust gases this assumption is not valid. This paper analyses the effects of cooler cross-flow on the sound directivity of turbulent, heated, subsonic exhaust gas ejected from a stack. The analysis was first conducted using steady-state computational fluid dynamics to model the fluid dynamics associated with exhaust jets in cross-flow. The results of the computational fluid dynamics simulations, particularly the mean temperature and mean velocity components were then imported into a linearised Euler equation solver for conducting the sound propagation analysis. The flow conditions for this study were similar to conditions seen in large open-cycle gas-turbine exhaust-stacks, but scaled using non-dimensional acoustic and fluid dynamic parameters. The flow Mach number of the exhaust jet was approximately 0.1 and a jet velocity to cross-flow velocity ratio of 5 was chosen for analysis. Theoretically, an exhaust stack without flow would have spherical acoustic spreading at low frequencies at the duct outlet. However, the spreading is non-spherical due to the thermal gradient in the shear layer altering the propagation path of sound, as well as diffraction effects at the edge of the stack outlet. Furthermore, any cross-flow causes asymmetric spreading of the sound field. The computational results presented in this paper show that the presence of the turbulent non-isothermal, subsonic exhaust jet flow with cross-flow significantly alters the directivity of sound in the far-field (up to $3\,\mathrm{dB}$), thereby potentially impacting on nearby communities.

Keywords: Numerical sound propagation, exhaust jets in cross-flow, linearised Euler equations, computational fluid dynamics, sound directivity

1. Introduction

Open cycle gas turbines (OCGT) are increasingly been used for power generation as they are able to provide loads in peaking or uncertain conditions and can respond rapidly to power grid demands. However, there is considerable evidence suggesting that OCGT lead to higher noise levels than orthodoxy predicts [1, 2, 3, 4, 5]. This issue of low frequency gas turbine plant noise is almost entirely restricted to OCGT. Combined cycle gas turbines, which use the Brayton cycle and Rankin cycle, do not appear to suffer from the same issues. These excessive levels of low frequency noise from OCGT have caused documented detrimental effects to communities. The noise have previously lead to the following effects: perceived annoyance of ‘throbbing’ from high intensity low frequency noise [1], ‘beating’ sensation in the chest [6], nausea [1] and acoustic excitation in structures with low resonance frequencies, such as glass structures and wall panels [1].

Currently, the predicted sound levels from exhaust stacks is based on ISO 10494 [7] with a spherical source assumed at the exhaust stack outlet, and subsequent propagation predicted using ISO 9613 [8, 9]. However, in non-isothermal shear layers the propagation of sound can be altered due to the presence of velocity and temperature gradients in the shear layer [10, 11]. The study of shear layer sound refraction can be extended to the investigation of sound propagation through isothermal and non-isothermal jets, in which Atvars et al. [12] alluded that the non-isothermal jet shear layer can cause significant sound refraction. The refraction of sound due to the shear layer leads to the increase in off-axis SPL (sound pressure level) and a reduction in the on-axis SPL [12]. The effects of refraction are more pronounced with the increase in acoustic source frequency, thermal gradients from larger variations in jet temperature to ambient temperature, and velocity gradients from the increase in jet Mach number, M_j [12]. Mungur et al. [13] has also shown with isothermal jets that the measurement location for the sound directivity is also important, as the jet shear layer developing downstream can cause sound refraction many diameters from the stack outlet.

The fluid dynamics associated with exhaust chimney stacks can be simplified to a flush mounted circular duct in a ground plane, which is known in literature as an elevated jet in cross-flow (EJICF) [14]. This particular type of flow configuration has been experimentally studied by various researchers [14, 15]. There are also different type of flow regimes with unique, time-averaged flow structures for EJICF and are governed by the jet to cross-flow momentum flux ratio [14] defined by: $R = \sqrt{\frac{\rho_j u_j^2}{\rho_{cf} u_{cf}^2}}$, where the jet velocity is u_j, the jet density is ρ_j, the free stream cross-flow velocity is u_{cf}, and the free stream cross-flow density is ρ_{cf} [15]. Typically seen in OCGT are R in the jet dominated flow regime for EJICF [14]. For this type of flow regime, unique flow structures that form include the following: deflected jet, jet shear layer, counter rotating vortex pairs, and stack shear layer [14].

Leav et al. [16] has conducted a previous study into sound propagation through a two-dimensional (2D) heated rectangular jet in cross-flow (JICF). It was observed in this numerical study that the thermal gradients associated with the JICF can lead to strong refraction effects downstream, which leads to asymmetric spreading on the leeward side of the duct and the formation of a highly directed lobe of sound. On the windward side of the duct however, the sound still spreads elliptically. ISO 10494 [7] is sufficient in predicting the sound power emitted, but not the directivity of sound. The study conducted by Leav et al. [16] had the following limitations: only the mean thermal gradient effects on sound propagation were analysed, the simulations were 2D, the duct was a rectangular piston, and the fluid dynamics are drastically different between 2D JICF compared to three-dimensional (3D) EJICF.

This paper analyses the effects that the steady-state, non-isothermal, exhaust jet with a cooler cross-flow has on the sound directivity. Computational fluid dynamics (CFD) and finite element modelling (FEM) are used for the analysis. The layout of the paper is as follows. The simplified computational model and boundary conditions of the computational mesh will be discussed in Section 2. Subsequently, the mathematical models that are used for the fluid flow simulations through CFD and acoustic propagation using linearised Euler equations (LEE) with FEM are explained. The simulation results from CFD and FEM are presented in Section 3, which shows the numerical fluid dynamics solution and the effects of the temperature distribution on the propagation of sound. The main conclusions of this paper are summarised in Section 4.

2. Details of computational models

2.1 Simplifications of the computational models and domain

The CFD and acoustic modelling of a real OCGT is a complex task, so consequently a simplified model of a JICF has been employed for this study. A schematic of the computational domain with the dimensions and corresponding boundary conditions can be seen in Figure 1. Only half of the domain is modelled in this particular simulation with a symmetry condition along the y-z plane. Not shown in Figure 1 is that the domain also spans $40D$ in the x-axis perpendicular to jet's symmetry plane

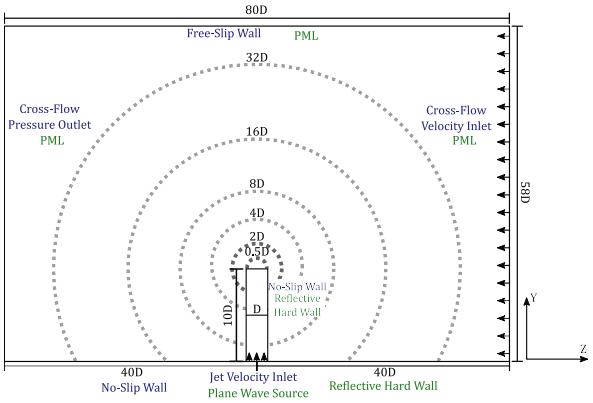

Figure 1: A schematic of the domain's geometry and boundary conditions, where D is the duct inner diameter

(into the page). This truncation in the domain is possible due to previous literature indicating that the steady-state flow field is plane symmetric and preliminary acoustic simulation's showing that the sound field is also plane symmetric [15].

2.2 Boundary conditions

The correct use of boundary conditions are essential in resolving both the CFD and computational acoustic solution accurately. The boundary conditions for the simulation can be seen in Figure 1. The following assumptions have been made for the inlet boundary conditions for the 3D CFD simulation. The inlet conditions for the model are the turbulent, heated jet inlet at the base of the duct and the cross-flow on the windward side of the duct. For the jet inlet, a developed duct velocity profile with a bulk Reynolds Number, Re_j of 38900 was chosen. The fully developed duct velocity profile was achieved by first conducting simulations with a duct $40D$ long duct and the developed velocity profile at the duct outlet is interpolated onto the EJICF jet inlet. The R chosen for this study is 5. A constant mean velocity profile was applied to the inlet boundary. The resulting M_j for this simulation is approximately 0.1 and is typical of exhaust stacks. The jet inlet temperature was $773\,\mathrm{K}$, and resembles temperatures typically seen in OCGT exhaust stacks. The temperature at the cross-flow inlet was set to $300\,\mathrm{K}$. The duct walls and the ground wall adjacent to the circular stack are also no-slip walls.

In the far-field of the CFD model there are two different outlet conditions that are used. The outlet at the top of the domain in Figure 1 is a free-slip wall boundary condition. This was chosen to allow the shear stress along the wall to be set to zero. At the domain outlet, parallel to the cross-flow velocity inlet shown on the left in Figure 1 a pressure outlet condition is used.

In simulating the propagation of sound, two cases are considered here: with and without temperature distribution. The sound source was a planar harmonic source with a particle velocity amplitude of $0.5\,\mathrm{m\,s^{-1}}$. It is assumed in this study that the majority of sound is generated from primary the sound source (turbine) and other flow generated noise mechanisms can be neglected. This can be justified by the fact, that the quadrupole terms from shear layer noise are dependent on M_{jet}^5, which is almost negligible for the Mach number in this study. A Helmholtz number, $ka = 0.6$, where k is the acoustic wave number based on the speed of sound, and a is inner radius of th duct, was chosen as it is a high enough such that it is comparable to the simulated plume's shear layer in Section 3.2.1 and is well below the cut-on frequency of the duct. Additionally, this was the highest ka that can be simulated with the computational resources available and ideally a higher ka closer to one would be better, at which the wavelength of sound would be small enough to interact with the shear layer.

For the computational sound propagation simulation, the far-field condition is uniform for all

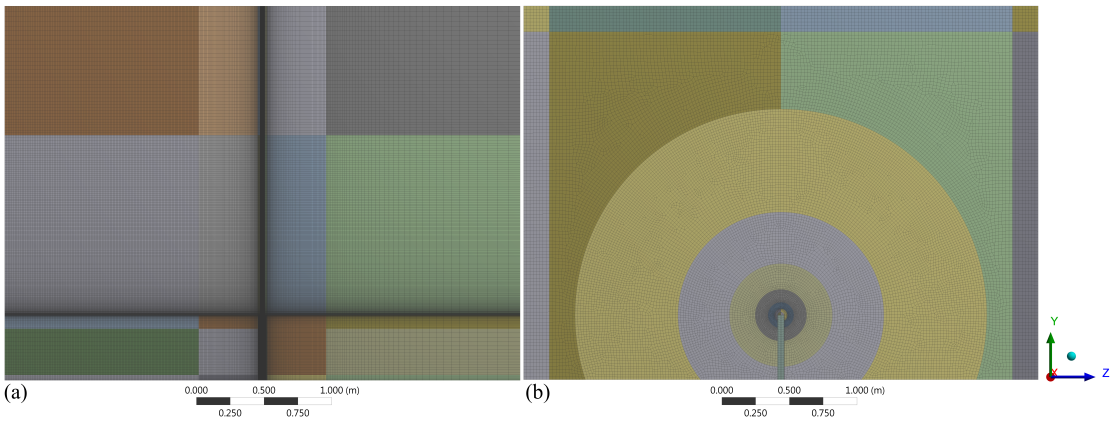

Figure 2: Non-isothermal EJICF mesh for CFD modelling (a) and mesh for LEE modelling with FEM (b)

boundary conditions. Perfectly matching layer (PML) elements are used for the far-field absorption of sound to simulate the free-field radiating condition. The number of PML elements used is dependent on the duct width, D, and the wavelength of sound. Howard and Cazzolato [17] have recommended that the PML zone is at least one-quarter of the wavelength wave length of sound.

2.3 Meshing details

For the CFD simulation the fluid dynamics were resolved using a mesh (shown in Figure 2) with structured hexahedra elements. Refinements were made in regions necessary for adequately resolving the critical flow features. This mesh has $15,250,000$ elements and $15,480,000$ nodes. The non-dimensional wall distance, y^+, for this simulation is more than 13, which is acceptable for resolving the boundary layer with the scalable wall function. In the geometric far-field where the flow characteristics are of less importance the mesh has been generated elements with high aspect ratio. The element type used in ANSYS FLUENT only specify nodes at the vertex of the element and is also known as 'brick' elements [18].

Mesh generation for modelling sound propagation with FEM has different requirements compared to the CFD simulation. The FEM mesh is shown in Figure 2. In propagating acoustic waves it is desirable to use a uniform mesh with minimal spatial changes in element size as it can cause numerical artefacts to form due to the minor impedance change, from different element sizes [17]. According to Howard and Cazzolato [17], at least six elements per wavelength are required for accurately resolving the acoustic pressure wave. Therefore, for the mesh shown in Figure 2 the ka achievable for this simulation is 0.6. The resulting acoustic element count is $1,280,000$ and node count is $4,850,000$. The mesh employs well defined arcs for ease of data post processing sound directivity at the radii of interest, structured hexahedra elements in the PML for the most effective attenuation of sound in the simulation [17].

2.4 Mathematical models

The fluid dynamics of the non-isothermal jet in cross-flow was simulated using ANSYS FLUENT [18]. The fluid flow in the model was computationally resolved using the compressible steady Reynolds Averaged Navier Stokes Equation (RANS). The fluid medium for this analysis is dry air. The density for the simulation was resolved using the ideal gas assumption. The viscosity of the model was calculated using the Sutherland approximation. A pressure based solver with a 'Coupled' setting for the pressure-velocity coupling was chosen. The spatial, pressure, energy and turbulent discretisation schemes chosen were a second-order upwind scheme. The two equation realisable $\kappa - \epsilon$

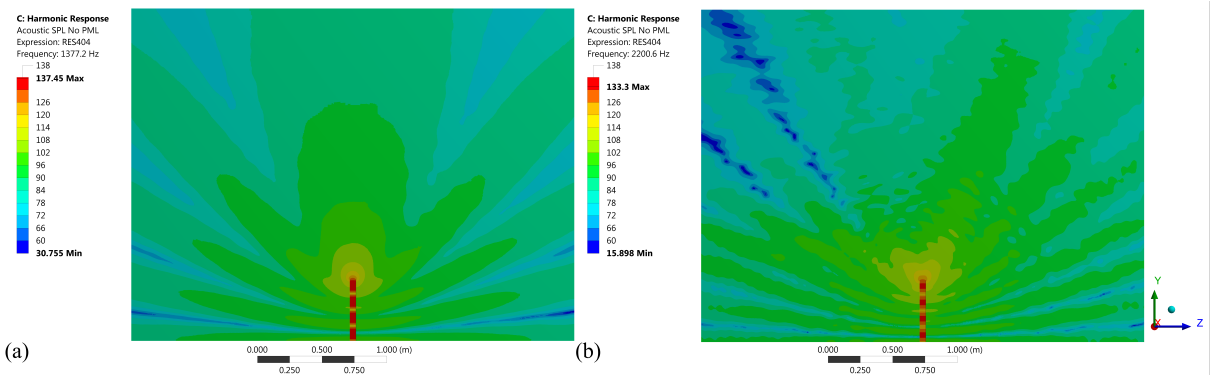

Figure 3: Acoustic SPL contour plot in a homogeneous medium (a) and in a media with temperature changes (b) along the y-z plane

model was chosen to resolve the turbulence [19]. This model is computationally less expensive than other more complicated RANS models and transient scale resolving turbulence models. However, there are limitations in the turbulence model: it assumes the eddy viscosity is isotropic; the turbulence can be modelled with two equations; the eddies in the models are not resolved with the average turbulence quantities being calculated in the shear layer; lack of prediction for flow separation at the jet inlet edge; and inaccurate prediction of the jet spreading and decay [19]. The boundary layer from the no-slip walls in the model were resolved using scalable wall functions. For the CFD analysis in this paper, only the critical steady-state features of the flow will need to be reproduced and the compressible steady RANS model is sufficient.

Sound propagation simulations were conducted by solving the LEE with FEM in ANSYS Mechanical with the Acoustic ACT extension [18]. In solving the LEE the following assumptions are made: the air medium is compressible, the changes in density are small in comparison to the mean density, the viscous dissipation of the fluid is neglected and the acoustic pressure can be represented by the wave equation. Harmonic analyses were chosen for this modelling work, as it allows the system to be driven by a sinusoidal oscillating harmonic source. The effect of temperature on propagation is modelled, however, the convective effects have been neglected as they have only minimal impact on refraction [16].

3. Computational Results

3.1 Absence of flow sound propagation

The sound propagating through the exhaust stack in the absence of mean flow was used as a benchmark case. The results indicate that in the absence of the heated mean flow, the acoustic spreading from the duct outlet is axisymmetric, as shown in Figure 3. However, due to the ground and duct walls being hard reflective surfaces there are reflections that propagate back into the domain and cause an increase in the SPL in the region below the duct outlet. This is to be expected when ka is significantly less than one and the frequency of the harmonic planar source is less than cut-on frequency of the duct. The computational acoustic power results in the far-field ($32D$) have also been compared with the acoustic power results from the methods used in the ISO 10494 [7], both were found to be $180\,\mathrm{dB}$ ref 10^{-12} W. Since, there is no difference it can be concluded that the standards are adequate in estimating the sound power from exhaust stacks without heated flow. However, it can be seen in Figure 3 that the radiation pattern is complex with the formation of pressure nodes. It can be observed in Figure 3, that the duct wall and the ground are causing the sound to reflect back into the domain. Hence, the spherical spreading assumption from ISO 9613 [8, 9] does not hold for this particular scenario, as the radiation pattern is now complex.

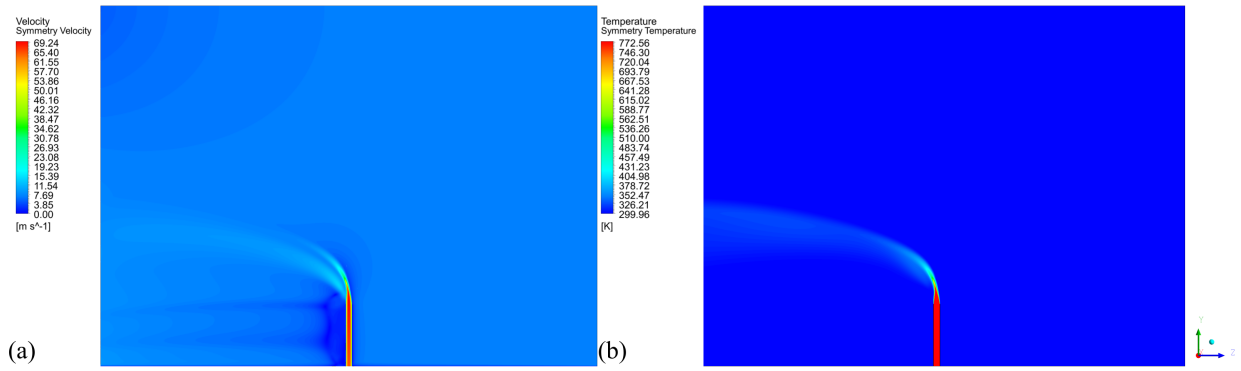

Figure 4: Velocity magnitude (a) and temperature (b) contour plots from modelling non-isothermal EJICF along the y-z plane, with the cross-flow from right to left

3.2 Non-isothermal elevated jet in cross-flow

3.2.1 Fluid features of non-isothermal elevated jets in cross-flow

It can be seen in Figure 4 that the fluid issued from the duct outlet initiates as a jet in the geometric near field. As the jet fluid propagates downstream the jet begins to deflect due to the presence of the cross-flow momentum. The deflected plume transitions from a jet to a counter rotating vortex. The counter rotating vortex further develops and forms, as the dominant vortical structure in the plume downstream. During the formation of the counter rotating vortex, fluid is entrained from both the cooler cross-flow and the wake behind the stack in the simulation. A shear layer is also formed on the leeward side of the stack, which is due to the stack acting as a bluff body.

Figure 4 shows the temperature contour plot for the EJICF in the y-z plane. It can be seen that at the geometric near field close to the duct outlet the temperature profile resembles a jet, with the hottest region residing in the jet potential core. As the jet propagates downstream the plume is deflected by the cooler cross-flow stream's momentum and enhanced mixing occurs. This mixing causes lower temperatures seen in the plume's thermal gradients as the plume develops downstream. As the plume propagates downstream the plume's development into a counter rotating vortex then enhances mixing with the cooler cross-flow and reduces the temperature in the plume. The hottest region in the plume is the centre of the counter rotating vortex. This development of the plume has lead to the formation of thermal gradients where refraction of sound can occur. The effect of the thermal gradient on sound refraction is investigated in the following section.

3.2.2 Sound directivity of non-isothermal jets in cross-flow

The steady-state, thermal distribution from the CFD simulation in Section 3.2.1 has been imported into the finite element model for sound propagation. The resulting SPL contour plot along the y-z plane is shown in Figure 4. In contrast to the case with a homogeneous media, the presence of the temperature distribution has drastically altered the propagation sound. Figure 3.1 shows that the sound radiation is no longer axisymmetric. There are now a distinct shift in lobes upstream and downstream, as well as the formation of a sound pressure null at $42\,\mathrm{deg}$. On the windward side, there is little changes to the acoustic radiation pattern and the spreading resembles the case in Section 3.1, which is to be expected as there are no significant fluid mechanic mechanisms that will change the sound propagation path. The lobes on the leeward side of the exhaust stack now differ from the previous lobes, concentrated closer towards the ground level of the domain. This change in acoustic radiation is a result of the thermal gradients associated with plume causing the sound to refract downstream and closer towards the ground. The sound power based on ISO 10494 [7] in the geometric near field has been calculated and compared with the sound power in the far-field. The sound power based on

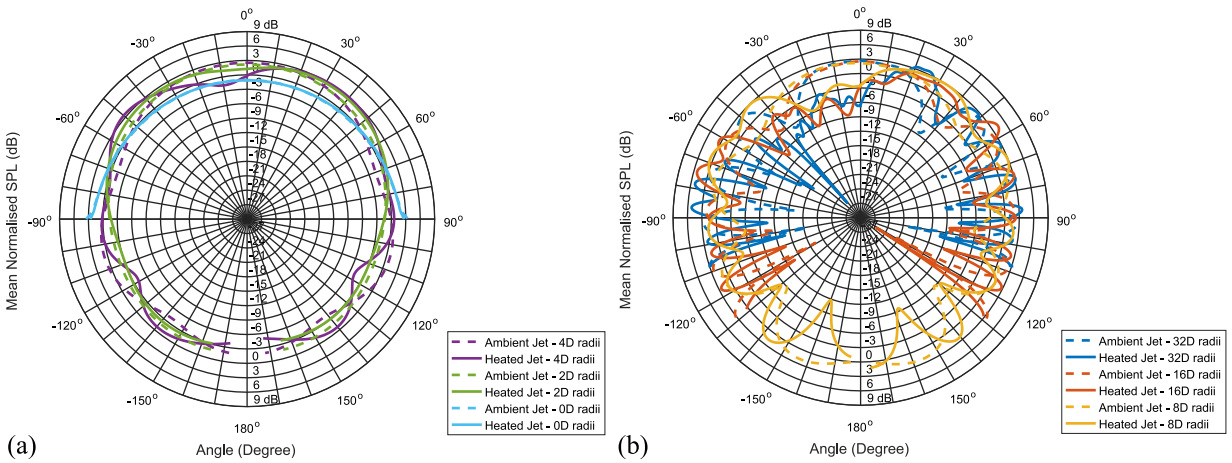

Figure 5: Mean normalised acoustic SPL directivity plots with varying radii from modelling with the EJICF thermal gradient's

the standards and far-field numerical measurements are both $180\,\mathrm{dB}$ ref $10^{-12}\mathrm{W}$.

In order to quantify the effects of refraction on the propagation path of sound, normalised SPL polar plots at varying spatial locations from the jet outlet were calculated and are shown in Figure 5. The results in each of the directivity plots are normalised with the mean SPL along the sphere with the same radii. Figure 5 indicates that at $0.5D$ there are edge diffraction effects due to the exhaust stack edge. For the sound directivity at the $2D$ and $4D$ arcs the acoustic spreading is almost spherical. This is the case as the plume's shear layer has yet grown spatially large enough for sound refraction. Figure 5 shows that as the arcs for sound directivity measurements increase in radii the sound becomes more directed downstream, with the magnitude in the lobe increasing by up to $3\,\mathrm{dB}$. This change in leeward side directivity is a result of the sound refraction becoming more prominent with the spatial growth in the non-isothermal shear layer. From the normalised SPL polar plots it can be seen that the EJICF has significantly altered the sound propagation path and the results are strongly dependent on the radial location for measurements, which is consistent with previous studies on sound propagation through unheated axisymmetric jets [13]. It was seen in early 2D studies [16], that further growth in SPLs along the horizontal can be expected at distances greater than investigated here.

4. Conclusion

The results from this study has shown that the thermal gradients in the plume from EJICF can affect the directivity of sound. The results have clearly indicated that in the absence of heated mean flow and without cross-flow, the propagation of sound from the duct is axisymmetric. However, this is not the case with the temperature distribution from the JICF, where the sound propagation is now asymmetric due to the sound refraction by the thermal gradients in the shear layer. Further analysis has shown the normalised SPL is strongly dependant on the radial location of the measurements. Even though the standards are sufficient in calculating the total acoustic power of the system in the far-field, the altered directivity of the 3D EJICF has shown that off-axis sound may be under predicted in the far field. The implications of these findings suggest that community noise levels from stacks may be under-predicted using ISO 9613 [8, 9] due to the altered directivity of sound from the exhaust stack.

REFERENCES

1. Broner, N. A simple outdoor criterion for assessment of low frequency noise emission, *Acoustics Australia*. **29** 1, 7–14, (2011).

2. Broner, N. Power to the people, *15th International Meeting on Low Frequency Noise & Vibration & its Control*, Stratford upon Avon, United Kingdom, 22–24 May, (2012).

3. Hessler Jr, G. F. Proposed criteria for low frequency industrial noise in residential communities, *Low Frequency Noise, Vibration and Active Control*, **52** 4, 179–185, (2004).

4. Hetzel, R. and Putnam, R. A. Sources and rating criteria of low frequency gas turbine exhaust noise - via case study, *INTER-NOISE and NOISE-CON, Congress and Conference Proceeding, 2009*, (2009).

5. Kudernatsch, G. Sources and rating criteria of low frequency gas turbine exhaust noise - via case study, *INTER-NOISE 2000, The 29th International Congress and Exhibition on Noise Control Engineering*, (2000).

6. Broner, N. The effects of low frequency noise on people - a review, *Journal of Sound and Vibration*, **58** 4, 483–500, (1978).

7. International Organization for Standardization. ISO 10494:1993 Gas turbines and turbine sets- Measurement of emitted airborne noise – Engineering survey method, *International Organization for Standardization*, Geneva, Switzerland, (1993).

8. International Organization for Standardization. ISO 9613-1:1993 Acoustics - Attenuation of sound during propagation outdoors – Part 1: Calculation of the absorption by the atmosphere, *International Organization for Standardization*, Geneva, Switzerland, (1993).

9. International Organization for Standardization. ISO 9613-2:1996 Acoustics - Attenuation of sound during propagation outdoors – Part 2: General method of calculation, *International Organization for Standardization*, Geneva, Switzerland, (1996).

10. Amiet, R. K. Refraction of sound by a shear layer, *Journal of Sound and Vibration*, **58** 4, 467–482, (1978).

11. Candel, S. M. Acoustic transmission and reflection by a shear layer discontinuity separating hot and cold regions, *Journal of Sound and Vibration*, **24** 1, 87–91, (1972).

12. Atvars, J., Schubert. L. K., and Ribner, H. S. Refraction of sound from a point source placed in an air jet, *American Institute of Aeronautics and Astronautics 2nd Aerospace Sciences Meeting*, (1965).

13. Mungur, P., Plumblee, H. E. and Doak, P. E. Analysis of acoustic radiation in a jet flow environment, *Journal of Sound and Vibration*, **36** 1, 21–52, (1974).

14. Adaramola, M. S., Sumner, D., and Bergstrom, D. J. Effect of velocity ratio on the streamwise vortex structures in the wake of a stack, *Journal of Fluids and Structures*, **26** 1, pp. 1–18, (2010).

15. Johnson, B. E. Elliot, G. E. and Christensen, K. T. Structural characteristics of a heated jet in cross-flow emanating from a raised, circular stack, *Experiments in Fluids*, **54** 6, 1543–1560, (2013).

16. Leav, O. Y. Cazzolato, B. S. and Howard, C. Q. Directivity analysis of sound in turbulent exhaust jets with laminar cross-flow: A numerical study. *Acoustics 2015 Hunter Valley*, (2015).

17. Howard, C. Q. and Cazzolato, B. S. *Acoustic analysis using MATLAB and ANSYS*, CRC Press, Boca Raton, Florida (2014).

18. ANSYS, *ANSYS Workbench 17.2*, ANSYS Inc, Canonsburg, Pennsylvania, (2016).

19. Shih, T-H., Liou, W. W., Shabbir, A., Yang, Z. and Zhu, J. A new κ–ϵ eddy viscosity model for high Reynolds number turbulent flows, *Computer & Fluids*, **24** 6, 227–238, (1995).

Appendix G

Experimental sound propagation through elevated jet in cross-flow

Paper was awarded the 'President's Prize for Best Overall Paper' at Acoustics 2018 from the Australian Acoustical Society.

Statement of Authorship

Title of Paper	Experimental analysis of sound directivity from sound propagation through non-isothermal, turbulent exhaust jets in cross-flow
Publication Status	☑ Published ☐ Accepted for Publication ☐ Submitted for Publication ☐ Unpublished and Unsubmitted work written in manuscript style
Publication Details	Leav, O. Y., Cazzolato, B. S., and Howard, C. Q. (2018) "Experimental analysis of sound directivity from sound propagation through non-isothermal, turbulent exhaust jets in cross-flow", Acoustics 2018 Australia, Adelaide, SA, Australia, 6 - 9 November.

Principal Author

Name of Principal Author (Candidate)	Orddom Leav
Contribution to the Paper	Conducted the literature review, conducted all the experimental testing, performed data processing and analysis, wrote the manuscript and acted as the corresponding author.
Overall percentage (%)	80
Certification:	This paper reports on original research I conducted during the period of my higher degree research candidature and is not subject to any obligations or contractual agreements with a third party that would constrain its inclusion in this thesis. I am the primary author of this paper.
Signature	Date 20/8/19

Co-Author Contributions

By signing the Statement of Authorship, each author certifies that:

i. the candidate's stated contribution to the publication is accurate (as detailed above);

ii. permission is granted for the candidate in include the publication in the thesis; and

iii. the sum of all co-author contributions is equal to 100% less the candidate's stated contribution.

Name of Co-Author	Benjamin Seth Cazzolato
Contribution to the Paper	Supervised the development of work, helped in data interpreting, provided comments and edited manuscript.
Signature	Date 20/8/19

Name of Co-Author	Carl Quentin Howard
Contribution to the Paper	Supervised the development of work, helped in data interpreting, provided comments and edited manuscript.
Signature	Date 20/8/2019

Experimental analysis of sound directivity from sound propagation through non-isothermal, turbulent exhaust jets in cross-flow

Orddom Yi Jie Leav (1), Benjamin Seth Cazzolato (1) and Carl Quentin Howard (1)

(1) School of Mechanical Engineering, University of Adelaide, Adelaide, Australia

ABSTRACT

The common assumption when predicting community noise levels from exhaust stacks is that the sound radiation is axisymmetric, which is appropriate for low Mach number, low temperature flows, and in the absence of cross-winds. However, this assumption is inaccurate when the conditions do not hold. This paper investigates experimentally the effects of a cooler cross-flow on the sound directivity of turbulent, heated exhaust gas from a stack. A small-scale experimental rig (1:100) has been built that reproduces the flow, temperature and acoustic conditions seen in large-scale open-cycle gas turbines. The University of Adelaide's Wind Tunnel was used to create cross-flows that resemble the cross-wind conditions observed near open-cycle gas turbines. The small-scale experimental rig and the test conditions were scaled using relevant non-dimensional fluid dynamics and acoustic parameters. Directivity measurements from the experiments have shown that the hot exhaust plume leads to an asymmetric acoustic radiation pattern from the exhaust stack. The experimental results presented in this paper shows that the presence of a hot exhaust plume and cross-flow alters sound directivity in the far-field downstream by increasing levels up to 11 dB, which has the potential to impact nearby communities.

1 INTRODUCTION

Sound propagation models for environmental noise prediction commonly assume that sound radiates as an elevated monopole source. However, when there are complex flow conditions affecting refraction, structures scattering and diffracting sound and meteorological effects, this assumption may not be appropriate. An example of such a case is modelling sound radiation from open-cycle gas turbines (OCGT), which has been shown in literature to produce higher than expected low frequency noise levels in communities (Bjork 1994, Broner 2010, 2011, 2012, Hessler Jr 2004, 2005, Hetzel and Putnam 2009, Kudernatsch 2000). It has been reported that the low frequency noise levels from OCGT have caused the following impact on communities: perceived 'annoyance' of throbbing (Broner 1978), 'beating' sensation in the chest (Hessler Jr 2004, 2005), nausea (Broner 1978), and acoustic excitation in structures with low resonance frequencies (Broner 1978). The higher than expected noise levels observed in OCGT are not typically seen in combined cycle gas turbines, which use the Brayton and Rankin cycle (Bjork 1994, Hetzel and Putnam 2009).

Sound levels in neighbourhoods near exhaust stacks are commonly predicted using multiple ISO standards (International Organization for Standardization 1993a, b, 1996). ISO 10494 is used to estimate the sound power from exhaust stacks (International Organization for Standardization 1993b). The sound propagation is modelled using ISO 9613-1 (International Organization for Standardization 1993a) and ISO 9613-2 (International Organization for Standardization 1996). For simple sound predictions ISO 9613-2 states that a simple monopole source can be used, but for more complex sound sources, a directivity correction factor can be applied. If a single monopole source cannot be used, then multiple monopole sources can be used to represent a discretised line source or discretised area sound source. A single value correction factor based on the meteorological conditions obtained from the 'local authorities' can be applied to the sound propagation model. These sound prediction models can also be extended using numerical software to include the atmospheric boundary layer (thermal and velocity gradients) and complex terrains. These approximations do not take into consideration the complex sound field from the exhaust stack and the acoustic interaction with the exhaust plume.

The fluid dynamics associated with non-isothermal exhaust stacks can be simplified to an elevated jet in cross-flow (JICF), which can be seen schematically in Figure 1 (Adaramola, Sumner, and Bergstrom 2010). The elevated JICF is a cylindrical duct protruding from a ground plane, with a jet flow exiting the duct. The flow structures associated with isothermal elevated JICF have been studied experimentally by various researchers in

the literature (Adaramola, Sumner, and Bergstrom 2010, Eiff, Kawall, and Keffer 1995, Eiff and Keffer 1997, Hsu and Huang 2012, 2014, Huang, Davidson, and Nokes 2005, Huang and Hsieh 2002, 2003, Huang and Hsu 2012, Huang and Lan 2005) and non-isothermal elevated JICF have also been investigated (Andreopoulos 1989a, b, Johnson, Elliott, and Christensen 2013). The fluid structures are governed by the JICF momentum flux ratio, defined as the following:

$$R = \sqrt{\frac{\rho_j u_j^2}{\rho_{cf} u_{cf}^2}}, \tag{1}$$

where ρ_j is the jet air density, ρ_{cf} is the cross-flow free stream air density, u_j is the average jet exit velocity, and u_{cf} is the cross-flow free stream velocity. The values for *R* in OCGT are typically in a 'jet-dominated' regime (Adaramola, Sumner, and Bergstrom 2010, Huang and Hsieh 2002, 2003, Johnson, Elliott, and Christensen 2013), in which the flow structures associated with this regime are shown in Figure 1. The unique flow structures that form for this regime are the following: deflected jet, jet shear layer, counter rotating vortex pairs, and stack shear layer (Adaramola, Sumner, and Bergstrom 2010).

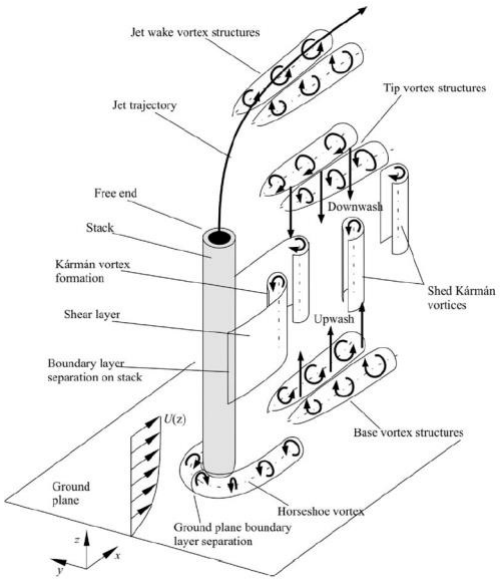

Source (Adaramola, Sumner, and Bergstrom 2010)

Figure 1: Flow structures schematic for elevated jets in cross-flow in the jet dominated regime

Research has shown that the radiation propagation from exhaust ducts may be quite complex. Bies, Hansen, and Howard (2017) showed that the sound radiation from exhaust ducts in the absence of flow in an anechoic environment is highly directed, with a lobe forming on-axis as the acoustic frequency increases. For non-isothermal exhaust duct flows a jet shear layer forms. It is known that with the presence of a shear layer sound refraction occurs (Amiet 1978, Candel 1972). The sound refraction due to the shear layer can be extended to non-isothermal jet shear layers, showing significant sound refraction (Atvars et al. 1965, Atvars, Schubert, and Ribner 1965, Grande 1965). The change in sound directivity from sound refraction becomes more pronounced with an increase in jet Mach number M_j, jet temperature T_j, and acoustic frequency. Mungur, Plumblee, and Doak (1974) showed that for isothermal jets, the location at which the sound directivity measurements are taken is also critical, with the developing jet shear layer downstream causing continual refraction many diameters from the exhaust outlet. This work on jet shear layer refraction was also extended to OCGT exhaust flow with near-field measurements by Bjork (1994). The research has shown that the sound is refracted by the jet shear layer and this was measured in both a real OCGT exhaust stack and in a scaled model (Bjork 1994).

It is hypothesised that sound radiating from OCGT exhaust stacks forms strong lobes, that under certain meteorological conditions, leads to the amplification of sound downstream as it interacts with the bent-over hot exhaust plume. Earlier work by Bjork (1994), stated that a bent-over hot exhaust plume with the thermal gradients and varying wind conditions would cause variations in sound levels downstream of up to $\pm$5 dB in the neighbourhood. However, Bjork (1994) only measured the sound in the near field; from the real exhaust stack at approximately 1.5*D* and approximately 3*D* with the small scale model, where *D* is the internal duct diameter. In the near-field the onset of refraction begins and cross-flow effects are yet to occur. Work previously done by Leav, Cazzolato, and Howard (2015, 2017) has shown numerically that the propagation path of sound is affected by the temperature of the plume for 2D non-isothermal ground level JICF and for 3D elevated JICF. Leav, Cazzolato and Howard (2015, 2017) have shown the propagation path of sound is dependent on the acoustic frequency and the distance from the exhaust outlet. Upstream of the exhaust stack the sound remains relatively unaffected by the cross-wind, with elliptical acoustic spreading observed (Leav, Cazzolato, and Howard 2017). Downstream of the exhaust stack for both the 2D non-isothermal ground level JICF and the 3D elevated JICF, the sound is altered and forms a highly directed lobe of sound. The numerical simulations were conducted using steady-state simulations with isotropic Reynolds-averaged Navier-Stokes equations (RANS) models which leads to limitations. The highly unsteady transient small-scale structures are not reproduced using RANS in Computational Fluid Dynamics (CFD). Furthermore, the steady state CFD model also produces coherent vortex structures downstream (counter rotating vortex pairs) that in reality would dissipate with the presence of the turbulence structures from the incoming cross-flow. The counter rotating vortex pairs downstream provide a thermal gradient that enables continuing refraction as the sound propagates downstream. For the 3-D elevated JICF, the acoustically reflective duct and ground produces complex sound diffraction patterns (Leav, Cazzolato, and Howard 2017).

This paper experimentally investigates the sound directivity of a non-isothermal, elevated hot exhaust jet in cooler cross-flow. A reduced scale (1:100) experimental rig to reproduce the flow and acoustic conditions of a 150 MW OCGT has been designed and commissioned at the University of Adelaide's Wind Tunnel. The experimental findings from the reduced scale experiments are used to analyse the effects of the plume on the propagation of sound. The layout of the paper is as follows. A description of the experimental set up and the signal processing techniques used for acoustic measurements are discussed in Section 2. In Section 3 the acoustic directivity measurements are detailed. A discussion of the experimental findings in relation to real OCGT is presented in Section 4. The main conclusions of the paper are summarised in Section 5.

2 APPARATUS AND METHODOLOGY

Measurements of OCGT are complex due to the practicality of controlling flow and speed, as well as taking measurements to characterise flow temperature, flow speed, and sound pressure. The aim of this research is to simulate the flow, temperature and acoustic parameters of a full-scale OCGT with a small-scale exhaust rig where the relevant parameters can be controlled. This section will discuss the experimental apparatus representing the OCGT, the commissioning of the experimental apparatus at the University of Adelaide Wind Tunnel, instrumentation, and the signal processing techniques used to process the acoustic data.

The experimental apparatus for simulating the exhaust flow and sound is shown in Figure 2. The exhaust was designed to achieve the parameters in Table 1. It should be noted that the exhaust rig was designed based on non-dimensional acoustic parameters relevant to OCGTs, but where possible the non-dimensional fluid dynamic parameters were also considered. An AIRPACK centrifugal blower was used to create the flow in the duct network. The inlet and outlet of the blower were connected to a silencer on each end. The flow travelled through a stainless-steel duct network with an outer diameter of 50.8 mm and an inner diameter of 47.6 mm (*D*), which is designed to be approximately 1:100 scale of a real 150 MW OCGT. The flow from the outlet silencer to the AIRPACK blower was split into a Y-junction and was passed through two 16kW LEISTER 61L System air heaters capable of variable temperature control, and then joined again with a 45° Y-junction into a single flow. The flow in the duct network was measured with a Pitot tube and a differential pressure transducer. The temperature in the duct network was measured with k-type thermocouples. The flow then passed through a 90° bend to a catalytic converter that acted to straighten the flow. The flow then passed through a straight vertical section of pipe before it exited as a jet. The exhaust network was clad with Rockwool SPI insulation to reduce the heat loss in the pipe network and attenuate structural acoustic radiation.

a)

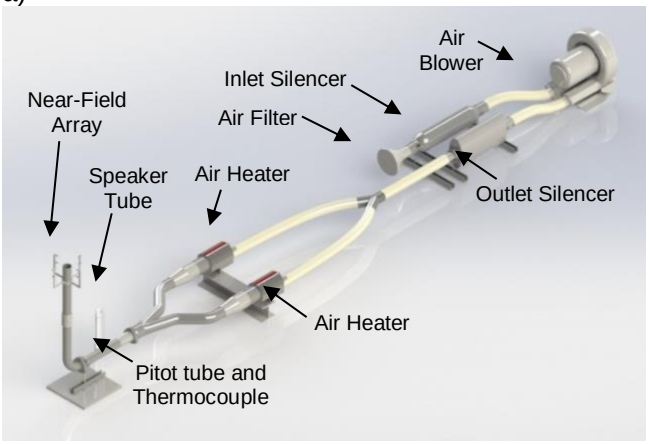

b)

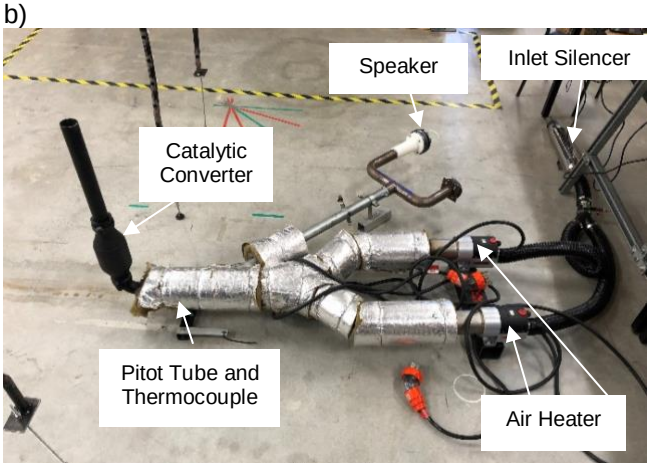

Figure 2: Images of the experimental setup of the reduced scale exhaust network, where a) is a computer aided design model of the exhaust, and b) is a photo of the exhaust network before installation of the false floor (blower not connected).

Table 1: Physical parameters for the experimental tests.

Parameters	Equation/Expression	Value
Mach number	$M = \frac{u_j}{c_j}$	0.1
Helmholtz number	$ka = \frac{\pi f D}{c_j}$	1.1
Jet temperature	T_j	500 °C
Exhaust vertical duct length	$L = 10D$	476 mm
Jet to cross-flow momentum flux ratio	$R = \sqrt{\frac{\rho_j u_j^2}{\rho_{cf} u_{cf}^2}}$	5

Figure 3 shows the experimental setup in the University of Adelaide's Wind Tunnel. A wooden decking, acting as a ground plane, was placed over the exhaust rig. Acoustic foam (50 mm thick Dacron) was placed on the wooden decking to reduce acoustic reflections from the ground plant and to provide an anechoic surface above 500 Hz, thereby reducing the complexity of the sound field so that the effect of the plume, cross-flow and sound interaction can be examined. The wooden decking is used so that only the exhaust stack interacts with the flow, with the rest of the apparatus shielded from the flow. The cross-sectional area of the wind tunnel cross-flow is 2.75 m × 2 m and the available test section ground area covers a span of 3.5 m × 5.5 m. The cross-flow wind velocity was measured with a Cobra Probe 209 and a Fluke 922 airflow meter at discrete points in the cross-flow freestream velocity. The Cobra Probe 209 air velocity measurements was used to calculate the incoming cross-flow free-stream turbulence intensity using the following equations:

$$I_{uu} = \frac{\sqrt{\overline{u'^2}}}{\bar{V}} = \frac{\sigma_u}{\bar{V}} \tag{1}$$

where u' is the fluctuating cross-flow free stream velocity, V is the speed of the air, and σ_u is the standard deviation of the cross-flow free stream velocity. The cross-flow turbulence intensity based on all three cartesian components was calculated using the following equation:

$$I_{uvw} = \frac{\sqrt{\frac{1}{3}(\overline{u'^2}+\overline{v'^2}+\overline{w'^2})}}{\bar{V}}, \quad (1)$$

where v' is the fluctuating velocity in the vertical direction, and w' is the fluctuating velocity in the span-wise direction.

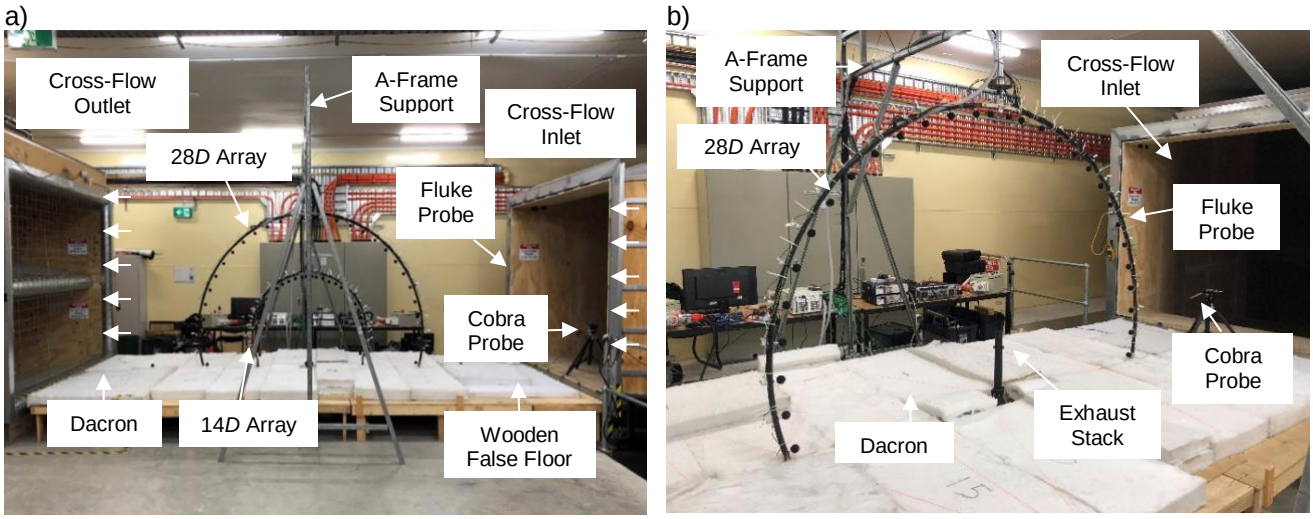

Figure 3: Photo of the experimental setup at the University of Adelaide's Wind Tunnel with the cross-flow going from right to left in all figures, where a) photo showing the full span of the commissioned test set up, b) the experimental set up with only the 28*D* microphone array.

The sound pressure was measured with 62 G.R.A.S. 40PH Free-Field Microphones along two circular arrays with radii 14*D* and 28*D* from the exhaust stack outlet. The microphones in Figure 3 were placed along a circular arc spanning $\pm$ 105°, with each microphone spaced 7.5°, except for the centre microphone at 0° being replaced by two microphones at $\pm$ 2.5° for the 14*D* array arc and for the 28*D* arc the centre microphone at 0° was removed to accommodate the vertical support. The microphone arrays were positioned parallel to the cross-flow free stream. The microphone arrays were supported by a frame, designed to have minimal flow and acoustic impact. The microphone signals were recorded by a NI (National Instruments) PXIe-4499 Sound and Vibration Module in a NI PXIe 1082 Chassis. The sound source used was uniform white noise, generated from NI LABVIEW and the electrical signal was generated using a NI PXI-6221 Multifunction I/O Module. The sampling frequency was 25.6 kHz. The uniform white noise was passed through a dual channel analogue 4-pole Butterworth filter (Krohn-Hite Model 3362 Dual Channel Filter) designed with low-pass and high-pass filter to give a 4kHz one-third octave ($ka \approx 1.1$). The sound was generated using two compression drivers, a 50.8 mm (2 inch) DS18 PRO-DKH1 1000 W compression driver and the 50.8 mm (2 inch) TIMPANO TPT-DH2000 400 W compression driver.

The acoustic data was post-processed in the frequency domain using MATLAB. The spectral analysis used a Hanning window with an FFT length of 8092 and 375 averages. The degree of linearity between the acoustic-electrical signal generated by the DAQ (x) and the acoustic pressures measured at the microphones (y) may be quantified using the coherence function:

$$\gamma_{xy}^2(f) = \frac{|G_{xy}(f)|^2}{G_{xx}(f)G_{yy}(f)}, \quad (2)$$

where f is the frequency of interest, G_{xy} is the cross power spectra of the acoustic-electrical signal into the speaker and the microphone acoustic pressures, G_{xx} is the power spectra of the acoustic-electrical signal into speaker and G_{yy} are the power spectra of the microphone acoustic pressures. The results in this paper are presented as the coherent output power at each microphone given by the following formula:

$$COP(f) = G_{yy}(f) \times \gamma_{xy}^2(f). \quad (3)$$

The coherent output power was used, rather than the sound pressure levels, so that only sound correlated with the loudspeaker is analysed, and noise from the blowers, wind tunnel fan and flow induced noise is ignored. The acoustic results for directivity presented in Section 3 are calculated as:

$$DI(f,\theta) = \frac{COP(f,\theta)}{COP_{av}}, \tag{4}$$

where DI is the directivity index based on the coherent output power and not the standard formulation involving sound intensity (Bies, Hansen, and Howard 2017), θ is the angular position from the centreline of the duct, and COP_{av} is the average coherent output power along the directivity arc. This method of presenting the coherent results was chosen to ensure that the sound presented was coherent with the loudspeaker only and the incoherent sound from external sources are 'screened out' and not considered.

3 EXPERIMENTAL RESULTS

The results for the sound directivity in the absence of the heated jet and cross-flow are discussed first. The results for the sound directivity for a heated jet with and without cross-flow are then presented for the 4 kHz one-third octave band.

Figure 4a shows the experimental results for the sound directivity at a distance of 28*D* in the absence of the heated jet and cross-flow. As expected for the 4 kHz one-third octave band ($ka \approx 1.1$), the sound directivity is axisymmetric and elliptical, with a lobe forming along the centreline of the duct axis at 0°. The results in Figure 4a show very similar trends to the results in literature for the open radiation of duct directivity in anechoic environments (Bies, Hansen, and Howard 2017). In the absence of the flow, it is commonly assumed that the sound power can be estimated with ISO 10494 (International Organization for Standardization 1993b) in the near field and then propagated using ISO 9613-2 (International Organization for Standardization 1996), where a monopole assumption is used, which approximates the sound radiation of a piston in an infinite plane. This is not the case seen in the experimental results, and it can be observed that with the hard duct exterior and the anechoic ground, the sound radiation is elliptical with a lobe forming on-axis (0 degrees). In Figure 4a, the elliptical lobe also causes a reduction in sound levels of up to 4.5 dB at ±90°. However, for predictions of ground-level SPLs, the monopole assumption is likely to be conservative.

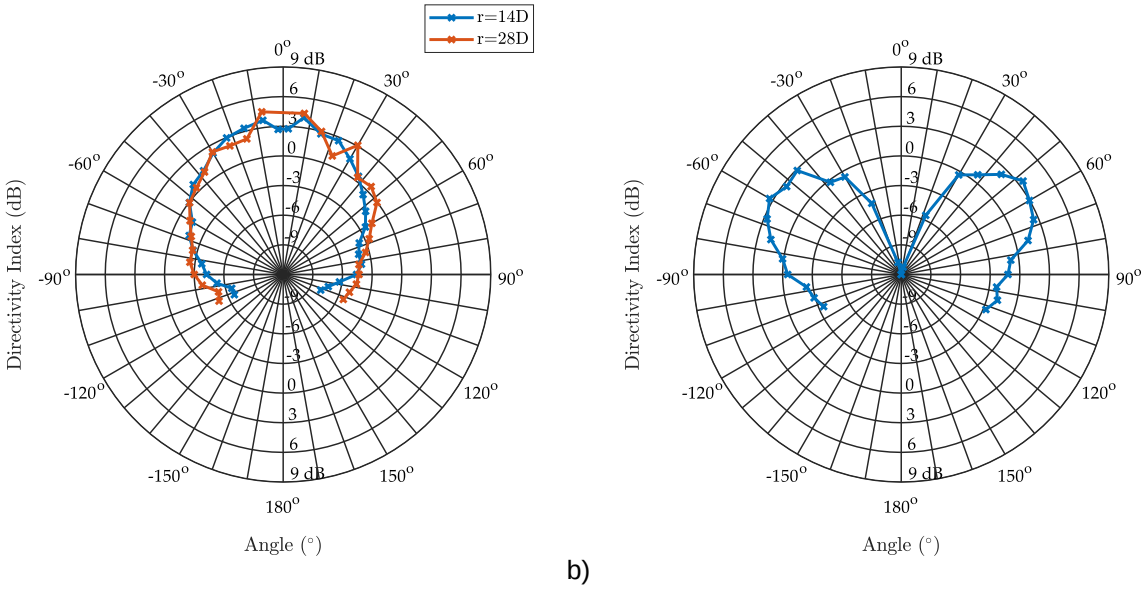

a) b)

Figure 4: The directivity of sound (a) in the absence of flow at two radii (14*D* and 28*D*), and (b) with a jet at 350°C and in the absence of cross-flow at a radius of 28*D*.

Figure 4b shows the experimental results for the sound directivity at 28*D* with a heated jet of Mach number 0.1 and T_j =350 °C. The directivity plot shows that the sound is axisymmetric about the vertical axis, with a shadow zone or 'cusp' forming along the centreline of the duct axis (0°). The acoustic cusp has a Directivity Index of approximately -12 dB. The acoustic energy that was originally in the on-axis region has been refracted by the jet shear layer to form acoustic lobes off-axis at approximately symmetrical locations of ±50°. The SPL of the lobes off-axis have increased by approximately 3 dB, compared with Figure 4a. These results are qualitatively consistent from the results by Atvars, Schubert, and Ribner (1965) and Bjork (1994). However, it should be noted that the experimental results in this study were measured at a lower jet temperature (T_j = 350°C) than commonly seen in OCGT exhaust stacks. The lower temperature used in the tests is a limitation of the experimental setup, where the air temperature at the microphones on the 28*D* arc could exceed the 60°C temperature rating of the microphones. Furthermore, it was desirable to measure the directivity at 14*D* to observe the effects of distance on the sound propagation, in particular the refraction of sound as a result of the jet shear layer, but unfortunately the microphone temperature limits were exceeded necessitating their removal.

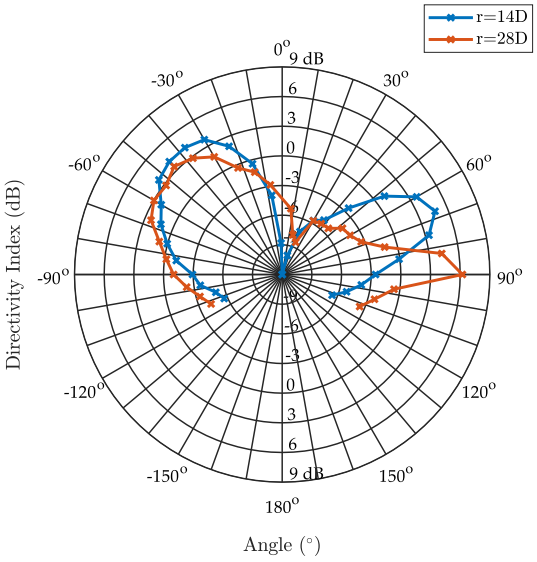

Figure 5: Directivity of sound at two different radii (14*D* and 28*D*), while *R* = 5 and the T_j = 500°C. The cross-flow is from left to right.

Figure 5 shows the experimental result for the sound directivity at 14*D* and 28*D* of a heated JICF with a Mach number of 0.1, T_j = 500°C and *R* = 5. Note that the cross-flow permitted higher stack exhaust temperatures whilst remaining under the 60°C temperature limit at the microphone locations. The incoming turbulence intensity measured at a single discrete location upstream are I_{uu} = 1.01% and I_{uvw} = 0.64%. By comparing Figure 4a, Figure 4b, and Figure 5, it can be observed that with the heated plume and cross-flow, the sound directivity is no longer elliptical or axisymmetric about 0°. The directivity of sound becomes biased towards the leeward side (or downstream) of the exhaust duct. The cross-wind shifts the peak observed in the downstream lobe from an angle of 50° to 65° and 90° for the 14*D* and 28*D* array, respectively. It can also be observed that as the sound propagates downstream the width of the lobe decreases from 40° to 25° for the 14*D* and 28*D* arcs, respectively. As the downstream lobe bends over and becomes narrower, the energy becomes more concentrated, increasing in amplitude by 4.5 dB at 14*D* and 6.5 dB at 28*D*. However, upstream of the exhaust duct, the sound directivity patterns remain similar for the 14*D* and 28*D* arcs. The position of the acoustic 'cusp' or shadow zone shifted from 0° in Figure 4b in absence of the cross-flow to 10° at 14*D* and 20° at 28*D* with cross-flow present. It must be noted that the angular resolution of the directivity measurements is 7.5° increments and this may be insufficient in capturing fine detail in the directivity pattern. The directivity results in Figure 5 at the 28*D* array show that the downstream lobe may not be fully resolved for the current angular spacing of the microphones, but for this research it is sufficient in investigating the change in sound levels downstream of the exhaust duct. In summary, the sound directivity is dependent on the arc radii with: the change in the width of the acoustic lobe downstream, the position of the acoustic lobe downstream and the shift in the position of the acoustic 'dip'. As sound propagates downstream, it can be observed that the plume has a greater influence on the propagation path. The influence on

the propagation path of sound is strongly governed by the temperature gradients in the plume, which causes the sound to continually refract as it propagates downstream.

4 DISCUSSION

The sound propagation downstream of the exhaust duct is altered significantly as it is refracted by the bent-over non-isothermal plume, with refraction being the dominant mechanism for altering sound propagation. The acoustic refraction downstream is due to the temperature and velocity gradients in the plume that alter the speed of sound (*c*) of the air. The majority of the refraction arises from the temperature gradients causing a change in the speed of sound ($\Delta c \propto \sqrt{\Delta T}$), as opposed to the convective effects of the flow ($\Delta c = c + \Delta u_{flow}$). Work previously conducted by Leav, Cazzolato, and Howard (2017) showed that the counter rotating vortex pairs produce thermal and velocity gradients. In their numerical work, the refraction continued for the entire computational domain. Figure 5 shows the relationship with the plume development, and acoustic refraction is consistent with the experimental directivity measurements in this paper at 14*D* and 28*D.* However, the diffusion of the plume downstream is dependent on the incoming cross-flow turbulence intensity, with the increase in turbulence intensity promoting plumes diffusion downstream (Andreopoulos 1989a, b). The distance the before the plume completes diffuses is unknown for the small-scale model and real OCGT, and needs to be quantified experimentally, with multiple turbulence intensity measurements. Currently for the small-scale model, a single discrete point measurement upstream for the turbulence intensity was measured, but from Andreopoulos (1989b) the incoming turbulence intensity profile for non-isothermal elevated JICF is complex. The flow and temperature field associated with the experimental small-scale model will need to be measured to gain a better understanding on the fluid dynamic and temperature effects that govern the propagation path of sound. Further experimental investigations will need to examine the directivity at radii greater than 28*D* to quantify far-field magnitude of the directivity index.

In Figure 5, the experimental results have shown that there is a downstream lobe forming causing an increase in sound levels of up to 6.5 dB. The increase in downstream sound level, shown in Figure 5, was calculated using the average coherent output power COP_{av} of that measurement arc. The results can be directly compared to the case without flow, seen in Figure 4a, which results in an elliptical sound radiation pattern. In Figure 4a, the sound downstream at -90° is approximately -4.5 dB, whereas the sound levels in Figure 5 with the bent-over non-isothermal plume is 6.5 dB. Hence, the plume has caused an 11 dB increase in the sound level parallel to the ground plane when compared to the sound radiation in the absence of flow.

The geometry of the reduced scale mode exhaust stack is a simple straight duct section that protrudes 10*D* into the flow. In real OCGTs, the geometry of the plant is considerably more complex, thereby affecting the cross-flow and consequently the sound refraction. This simplification of the model is appropriate for scientific investigation, as it resembles elevated jets in cross-flow seen in literature and reduces the acoustic and fluid dynamic complexity in the model. The main purpose of the research is to investigate the sound interaction with the plume and observe non-axisymmetry of the acoustic directivity, as well as quantity the increase in sound level downstream, which was confirmed in the experimental results here, and previously in numerical studies.

In the experimental worked conducted here, measurements were taken with an anechoic ground to simulate an absorptive surface surrounding the stack. This is generally not the case for OCGTs, as the exhaust stacks are typically surrounded by complex structures and hard reflective surfaces. These reflective surfaces would change the sound directivity pattern and hence the experimental setup used here may not be an accurate representation of real installations. Work completed by Leav, Cazzolato, and Howard (2017) suggests that a complex acoustic pattern occurs when a reflective ground is included. As a result, Figure 4a, Figure 4b and Figure 5 show ‘smooth’ directivity patterns in the absence of diffraction and reflections from other surfaces. Additionally, the sound directivity results in this paper are presented as a single one-third octave band average to reduce the complexity of the results. Further tests over several one-third octave bands should be undertaken to examine the relationship of the plume and the downstream sound levels.

5 CONCLUSIONS AND FUTURE CONSIDERATION

The results from this experimental study have shown that a non-isothermal jet with cooler cross-flow can significantly alter the directivity of sound. In the absence of the jet plume and the cross-flow, the sound is axisymmetric and elliptical with a lobe forming along the vertical axis and reflects current ISO standards. The directivity of sound with the jet shows that the sound is axisymmetric, but strong side lobes form due to sound

refraction because of the temperature gradients in the jet shear layer. The presence of a cooler cross-flow causes the sound to be asymmetric, with the sound biased towards the leeward side (downwind) of the exhaust stack. The sound refracts as it travels from the outlet. It was found from these experiments that sound was strongly refracted at a distance of 28*D* downstream from the exhaust duct, resulting in an 11dB increase in sound level, with the beam of sound being closer to the ground level and being more directed or 'narrow', compared to the case in the absence of jet and cross flows.

The current experimental work presented in this paper is a preliminary investigation into the problem and more work is planned to further understand this issue. Firstly, the sound propagation downstream is dependent on the acoustic frequency and other one-third octave bands should be investigated. The microphone arrays can be rotated through the vertical axis and measurements taken to explore the asymmetric spreading. The effects of cross-flow free stream velocity on the sound directivity should be investigated. In Section 3, it was noted that the acoustic results for the presence of the non-isothermal plume could be better resolved by increasing the number of microphones on the 28*D* array and reduce the angular separation between microphones. As discussed in Section 4, an investigation into a larger domain should be conducted to observe the limits of acoustic refraction. The flow and temperature field associated with the elevated JICF should be investigated to gain a better understanding on the mechanisms involved with changing the sound propagation path.

ACKNOWLEDGEMENTS

The author was sponsored by an Australian Government Research Training Program Scholarship from 2015 to 2018.The authors would like to thank Ben Wake, Carl Jungfer, and Lauren Manser for their effort as Engineering Honours Students in 2016 in designing and building the reduced scale experimental apparatus for testing at the Thebarton Wind Tunnel.

REFERENCES

Adaramola, M. S., D. Sumner, and D. J. Bergstrom. 2010. "Effect of velocity ratio on the streamwise vortex structures in the wake of a stack." *Journal of Fluids and Structures* 26 (1):1-18.

Amiet, R. K. 1978. "Refraction of sound by a shear layer." *Journal of Sound and Vibration* 58 (4):467-482.

Andreopoulos, J. 1989a. "Wind tunnel experiments on cooling tower plumes: Part 1 in uniform crossflow." *Journal of Heat Transfer* 111 (4):941-948.

Andreopoulos, J. 1989b. "Wind tunnel experiments on cooling tower plumes: Part 2 in a nonuniform crossflow of boundary layer type." *Journal of Heat Transfer* 111 (4):949-955.

Atvars, J., L. K. Schubert, E. Grande, and H. S. Ribner. 1965. Refraction of sound by jet flow or jet temperature. University of Toronto: Institute for Aerospace Studies.

Atvars, J., L. K. Schubert, and H. S. Ribner. 1965. "Refraction of sound from a point source placed in an air jet." *The Journal of the Acoustical Society of America* 37 (1):168-170.

Bies, D. A., C. H. Hansen, and C. Q. Howard. 2017. *Engineering Noise Control: Theory and Practice*. Edited by C. R. C. Press. 5th ed: CRC Press.

Bjork, E. A. 1994. "Experimental study of measures to reduce noise radiated from power-station exhaust stacks." *Noise Control Engineering Journal* 42 (5):171-178.

Broner, N. 1978. "The effects of low frequency noise on people - A review." *Journal of Sound and Vibration* 58 (4):483-500.

Broner, N. 2010. "A simple criterion for low frequency noise emission assessment." *Journal of Low Frequency Noise, Vibration and Active Control* 29 (1):1-13.

Broner, N. 2011. "A simple outdoor criterion for assessment of low frequency noise emission." *Acoustics Australia* 39 (1):7-14.

Broner, N. 2012. "Power to the People." 15th International Meeting on Low Frequency Noise and Vibration and its Control Stratford upon Avon, United Kingdom, 22-24 May.

Candel, S. M. 1972. "Acoustic transmission and reflection by a shear discontinuity separating hot and cold regions." *Journal of Sound and Vibration* 24 (1):87-91.

Eiff, O. S., J. G. Kawall, and J. F. Keffer. 1995. "Lock-in of vortices in the wake of an elevated round turbulent jet in a crossflow." *Experiments in Fluids* 19 (3):203-213.

Eiff, O. S., and J. F. Keffer. 1997. "On the structures in the near-wake region of an elevated turbulent jet in a crossflow." *Journal of Fluid Mechanics* 333:161-195.

Grande, E. 1965. "Refraction of injected sound by a very cold nitrogen jet." *The Journal of the Acoustical Society of America* 38 (6):1063-1064.

Hessler Jr, G. F. 2004. "Proposed criteria in residential communities for low-frequency noise emissions from industrial sources." *Noise Control Engineering Journal* 52 (4):179-185.
Hessler Jr, G. F. 2005. "Proposed criteria for low frequency industrial noise in residential communities." *Low Frequency Noise, Vibration and Active Control* 24 (2):97-106.
Hetzel, R., and R. A. Putnam. 2009. "Sources and rating criteria of low frequency gas turbine exhaust noise - via case study." INTER-NOISE and NOISE-CON Congress and Conference Proceedings, 2009, Ontario, Canada, 23-26 August.
Hsu, C. M., and R. F. Huang. 2012. "Effects of crossflow on puff and oscillation modes of a pulsed elevated transverse jet." *European Journal of Mechanics-B/Fluids* 31:140-148.
Hsu, C. M., and R. F. Huang. 2014. "Comparisons of flow and mixing characteristics between unforced and excited elevated transverse jets." *Journal of Mechanics* 30:87-96.
Huang, J. F., M. J. Davidson, and R. I. Nokes. 2005. "Two-dimensional and line jets in a weak cross-flow." *Journal of Hydraulic Research* 43 (4):390-398.
Huang, R. F., and R. H. Hsieh. 2002. "An experimental study of elevated round jets deflected in a crosswind." *Experimental Thermal and Fluid Science* 27 (1):77-86.
Huang, R. F., and R. H. Hsieh. 2003. "Sectional flow structures in near wake of elevated jets in a crossflow." *American Institute of Aeronautics and Astronautics Journal* 41 (8):1490-1499.
Huang, R. F., and C. M. Hsu. 2012. "Turbulent flows of an acoustically excited elevated transverse jet." *American Institute of Aeronautics and Astronautics Journal* 50 (9):1964-1978.
Huang, R. F., and J. Lan. 2005. "Characteristic modes and evolution processes of shear-layer vortices in an elevated transverse jet." *Physics of Fluids* 17 (3):034103.
International Organization for Standardization. 1993a. ISO 9613-1:1993 Acoustics - Attenuation of sound during propagation outdoors – Part 1: Calculation of the absorption by the atmosphere.
International Organization for Standardization. 1993b. ISO 10494:1993 Gas turbines and turbine sets-Measurement of emitted airborne noise – Engineering/ survey method.
International Organization for Standardization. 1996. ISO 9613-2:1996 Acoustics - Attenuation of sound during propagation outdoors – Part 2: General method of calculation.
Johnson, B. E., G. S. Elliott, and K. T. Christensen. 2013. "Structural characteristics of a heated jet in cross-flow emanating from a raised, circular stack." *Experiments in Fluids* 54 (6):1543. doi: 10.1007/s00348-013-1543-1.
Kudernatsch, G. 2000. "Combustion turbine exhaust systems-low frequency noise reduction." INTER-NOISE 2000, The 29th International Congress and Exhibition on Noise Control Engineering, Nice, France, 27-30 August.
Leav, O. Y., B. S. Cazzolato, and C. Q. Howard. 2015. "Directivity analysis of sound in turbulent exhaust jets with laminar cross-flow: A numerical study." Acoustics 2015, Hunter Valley, Australia, 15-18 November.
Leav, O. Y., B. S. Cazzolato, and C. Q. Howard. 2017. "A computational analysis of sound directivity from sound propagation through non-isothermal, turbulent exhaust jets in cross-flow." 24th International Congress of Sound and Vibration, London, United Kingdom, 23-27 July.
Mungur, P., H. E. Plumblee, and P. E. Doak. 1974. "Analysis of acoustic radiation in a jet flow enviroment." *Journal of Sound and Vibration* 36 (1):21-52.

Appendix H

Steady-state sound propagation through hot exhaust jets in cooler cross-flow: A computational study

Statement of Authorship

Title of Paper	Steady-state sound propagation through hot exhaust jets in cooler cross-flow: A computational study
Publication Status	☐ Published ☐ Accepted for Publication ☐ Submitted for Publication ☑ Unpublished and Unsubmitted work written in manuscript style
Publication Details	Leav, O. Y., Cazzolato, B. S., and Howard, C. Q. (2019). "Steady-state sound propagation through hot exhaust jets in cooler cross-flow: A computational study", Journal of Sound and Vibrations.

Principal Author

Name of Principal Author (Candidate)	Orddom Leav
Contribution to the Paper	Conducted the literature review, conducted all the CFD modelling, conducted all the acoustic FEM modelling, performed data processing and analysis, wrote the manuscript and acted as the corresponding author.
Overall percentage (%)	80
Certification:	This paper reports on original research I conducted during the period of my higher degree research candidature and is not subject to any obligations or contractual agreements with a third party that would constrain its inclusion in this thesis. I am the primary author of this paper.
Signature	Date 20/8/19

Co-Author Contributions

By signing the Statement of Authorship, each author certifies that:

i. the candidate's stated contribution to the publication is accurate (as detailed above);

ii. permission is granted for the candidate in include the publication in the thesis; and

iii. the sum of all co-author contributions is equal to 100% less the candidate's stated contribution.

Name of Co-Author	Benjamin Seth Cazzolato
Contribution to the Paper	Supervised the development of work, helped in data interpreting, provided comments and edited manuscript.
Signature	Date 20/8/19

Name of Co-Author	Carl Quentin Howard
Contribution to the Paper	Supervised the development of work, helped in data interpreting, provided comments and edited manuscript.
Signature	Date 20/8/2019

Steady-state sound propagation through hot exhaust jets in cooler cross-flow: A computational study

Orddom Yi Jie Leav[a,1], Benjamin Seth Cazzolato[a], Carl Quentin Howard[a], Mabrouk Ben Tahar[b]

[a] *School of Mechanical Engineering, University of Adelaide, North Terrace, Adelaide, South Australia, Australia*
[b] *Laboratoire Roberval UMR 6066, Secteur acoustique, Université de Technologie de Compiègne, Compiègne, France*

Abstract

An analysis has been carried out to investigate the sound radiation through a heated jet in cooler cross-flow using a hybrid steady-state computational fluid dynamics/ computational acoustic model. The mean flow and temperature fields are modelled using steady-state computational fluid dynamics, with the turbulence modelled using Reynolds Averaged Navier-Stokes equations. The corresponding mean flow and temperature fields are used in the computational sound propagation model with the discretised acoustic wave equation. The results determined from the computational simulations show that the flow significantly changes the sound propagation path and that there is an increase in sound levels downstream of the stack outlet. The dominant mechanism affecting the propagation of sound is the refraction arising from the plume's temperature and velocity gradients. The sound propagation is highly dependent on the proximity from the duct outlet, normalised wavenumber, temperature and the effective velocity ratio. This computational study is the first study to analyse the fluid-acoustic interaction for heated jets in cooler cross-flow to understand the complex spreading pattern that leads to increased sound levels downstream of the stack outlet.

Keywords: Sound propagation, Jets in cross-flow, Computational fluid

URL: orddom.leav@adelaide.edu.au (Orddom Yi Jie Leav)

dynamics, Finite element analysis, Acoustic wave equation, Sound refraction
2010 MSC: 00-01, 99-00

1. Introduction

Sound propagation from an acoustic source through inhomogeneous media is a complex phenomenon that exists in many systems. An example of this is the radiation of noise from the exit of a duct, which is of particular interest in fields such as aircraft jet exhausts, large HVAC systems, or large exhaust stacks. An example of radiating duct noise through inhomogeneous media is the noise from an open cycle gas turbine (OCGT) exhaust stack. There is considerable evidence showing that noise levels in the far-field from OCGTs are often higher than predicted [1–8]. This issue of significant levels of low frequency noise from OCGT has been well-documented [1–10], and have excessive levels of low-frequency noise can cause perceived annoyance from 'throbbing' from high-intensity low frequency noise [2], a 'beating' sensation in the chest [11], nausea [2] and acoustic excitation of structures with low resonance frequencies, such as glass structures and wall panels [2].

The underprediction of noise levels within communities near OCGT exhaust stacks is hypothesised to be related to the interaction between the sound emitted from the exhaust stack and the fluid dynamics associated with the plume. Earlier work by Björk [1], hypothesises a similar conjecture that a bent-over hot exhaust plume with the thermal gradients and varying wind conditions would cause variations in sound levels downstream of up to $\pm 5\,\mathrm{dB}$ in the neighbourhood. However, Björk [1] only measured the sound in the near field; from the real exhaust stack at approximately $1.5D$ and $3D$, where D is the internal duct diameter, with the small scale model.

As a first approximation, an OCGT exhaust stack can be modelled with a jet in cross-flow (JICF), which can be used to investigate the plume's effects on sound propagation. Fig. 1 shows, through ray acoustics, the expected sound radiation from a low frequency plane wave source within the stack with

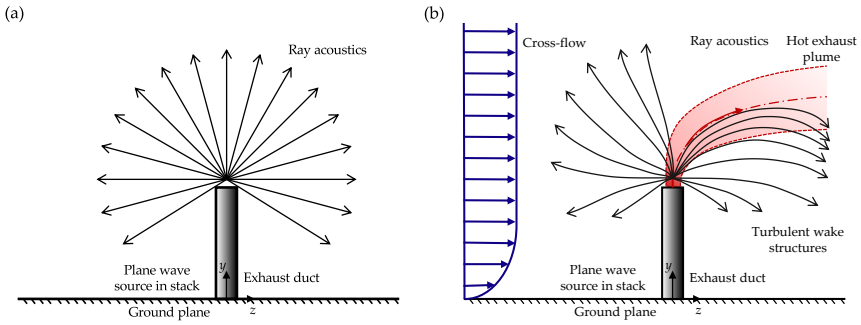

Figure 1: Schematic for the predicted acoustic ray representation, where (a) is without the presence of flow and temperature and (b) is with the presence of flow and temperature.

and without the plume. In Fig. 1(a), the sound radiation pattern resembles a monopole source in a homogeneous media, which is the common assumption in various models. The presence of a plume in Fig. 1(b) is hypothesised to increase the downstream sound levels as a result of sound refraction. The presence of the acoustical boundary layer plays a minor role, upward refracting the sound upstream, and downward refraction downstream of the stack. However, this meteorological effect, especially in the presence of a temperature inversions is less dramatic and occurs over a much larger domain than refraction through the plume. Leav et al. [12, 13] investigated the interaction of sound with the thermal gradients associated with a two-dimensional model of a ground-level JICF, and a three-dimensional model of an elevated JICF. Their results showed that whilst sound power is unaffected by the plume, it causes a dramatic re-distribution of acoustic energy away from the central axis of the stack, and a significant concentration downwind.

Experimental work has been investigated by Leav et al. [14–16] for the sound radiation from a hot exhaust jet in cooler cross-flow. The experimental study was based on the sound radiation from a reduced-scale model of a 190 MW OCGT exhaust stack (Siemens SGT5-2000E [17]). The results of the study has shown with a hot exhaust jet submersed in cooler cross-flow from the Adelaide Wind Tunnel has shown non-axisymmetric sound directivity. Downwind of the

exhaust stack Leav et al. [14–16] has shown an acoustic lobe forming downwind of the exhaust stack and when compared to the scenario with no jet or cross-flow, there is an increase of up to 9 dB. Further work by Leav et al. [15, 16] has shown the sound directivity results for a hot exhaust jet with cooler cross-flow is dependent on the distance from the duct outlet, acoustic frequency, jet temperature, and cross-flow momentum flux ratio (cross-flow speed). With the increase in jet temperature the refraction of sound downwind of the exhaust stack shows an increase in DI for the acoustic lobe downwind. The change in cross-flow momentum flux ratio has shown the position variability of the acoustic lobe downwind of the exhaust stack, whereby the highest cross-flow speeds causes the acoustic lobe downwind to refract closer towards ground-level. However, the results presented by Leav et al. [15, 16] are limited by a directivity radii of $28D$ due to the size of the Adelaide Wind Tunnel, and could be expanded upon using outdoor sound predictions.

Outdoor sound predictions will commonly use far-field atmospheric sound propagation models, where the meteorological and terrain effects must be considered. Early research [18, 19] has shown that the presence of atmospheric wind will alter the propagation path of sound. Since then, several literature reviews [20–23] identified that there are methods for quantifying atmospheric sound propagation. The typical sound propagation model aims to analyse the propagation of a monopole acoustic source with varying incoming velocity, turbulence, and temperature conditions, that resemble meteorological conditions [20–22, 24–33]. In analysing the far-field sound propagation from such effects, the dominant mechanism affecting the radiation of sound is the refraction of sound [20–22, 24–33]. This work has been extended with the analysis of sound propagation through the atmosphere with the addition of uncertainties from the atmospheric turbulence, which can cause further refraction, scattering and attenuation in the atmosphere [29, 31, 33]. While these sound propagation models account for the sound propagation in the far-field, they do not account for a local flow field, such as for the case with an exhaust stack. The exhaust plume will alter the propagation of sound, and the noise source may no longer resemble

an elevated monopole.

The effects of local flow and temperature field on sound propagation from exhausts are critical in determining far-field radiation. The gas flow exiting the stack resembles a jet, and there have been various experimental studies into the propagation of sound through jets [34–38]. It has been shown by Atvars et al. [34, 35] and Grande [36, 37] that the velocity and temperature of the jet affect the sound directivity, as a result of local sound refraction, resulting in a 'cone', 'zone', or 'cusp' of silence being formed along the centreline of the jet. An increase in flow Mach number and temperature of the jet has been shown experimentally to increase the depth of the 'cusp'. The subsequent refracted sound leads to the presence of strong lobes to form off-axis. These effects are supported numerically by Schubert's work [39, 40], who revealed with ray tracing and the numerical wave equation that some of the key features seen in the experimental directivity patterns could be reproduced. These features include the 'cusp' of silence and the increase in the SPL of the off-axis acoustic lobe. Mungur et al. [41] extended this work into a semi-numerical approach with the sound propagation through isothermal jets with varying Mach numbers $(0 - 0.9)$ and frequencies parameters $(ka = \pi/3 - 8\pi)$, where $k = \omega/c$ is the acoustic wavenumber, a is the nozzle radius, and c is the speed of sound. Schubert [39, 40] and Mungur et al. [41] showed that with an increase in jet Mach number and Helmholtz number (ka), the effects of refraction are more apparent, due to both the increase in velocity gradient and the reduction in the wavelength of sound. The experimental studies by Grande [36, 37] measured the acoustic directivity at a single radius, whereas numerical studies [39–41] have displayed the importance of the acoustic measurement radius from the source for quantifying sound directivity as the directivity changes with distance from the source.

Further numerical work was undertaken by Astley and Eversman [42], where they investigated numerically with an acoustic FE solver for sound radiation from a heated jet, based on the experimental study by Cummings [43]. The jet parameters used in the experimental study by Cummings [43], were based on

a reduced-scale boiler flue-gas stack, and investigated the radiation impedance and transmission loss for an unflanged exhaust duct with a heated exhaust jet ($T_j = 300\,^{\circ}\mathrm{C}$). Using an acoustic FE solver with the Helmholtz equation, Astley and Eversman [42] has shown with sound directivity results the refraction of sound from a heated jet at varying directivity radii ($1D < r < 40D$) and a Helmholtz number, ($ka = 2.0$). It is important to note that Astley and Eversman [42] neglected the flow effects from the jet in their acoustic modelling, as the effects of flow on the speed of sound is significantly less than temperature.

The majority of the literature on sound radiation from a jet investigates sound propagating from a source outside of the duct outlet yet in the region of the jet. There have also been subsequent simulations into the sound radiation from off-axis sound sources [44, 45]. However, in analysing sound propagation for OCGTs, the dominant sound source is from the turbine, and it is propagated and attenuated through the duct network before being radiated. There have been previous studies on sound propagation through straight ducts, with and without heated mean convective flow through a duct [43, 46–48], with the outlet boundary condition being an unflanged duct. These studies analysed the radiation efficiency of duct modes with various flow and temperature conditions by analysing the radiation impedance and reflection coefficient at the duct outlet. However, the effects of cross-flow over the stack outlet and the resulting sound directivity in the far-field is not of particular interest for a majority of the research in the previous literature. Hence, the analyses of sound radiation into a domain from a source located in an unflanged duct is a field of research that has yet to have significant attention and is the focus of the investigation described here.

From the literature reviewed above, the sound propagating through heated jets is complex. The main focus of these previous studies is to research the sound propagation for jets engines, which have Mach numbers of $M = 0.5$ to 2 [34–37, 39–41, 44, 45], that are much higher than what is commonly seen in exhaust stacks (where $M = 0.1$). Furthermore, the gas temperatures, in prior research is much cooler than what is commonly seen in the exhaust stacks of

open cycle gas turbines which can approach 600 ˚C.

The fluid dynamics of exhaust stack plumes has been researched extensively [49–54], and is generally referred to as an elevated jet in cross-flow (JICF). Adaramola et al. [55] showed that the fluid dynamics associated with elevated JICF is complicated due to the cross-flow interaction with the stack. The bluff-body flow behind the stack interacts with the plume exiting the stack outlet [56, 57]. A ground-level JICF is a simplification to the elevated JICF [56, 57], as the stack is removed from this particular case and only the plume is considered.

A typical ground-level JICF schematic is depicted in Fig. 2. The ground-level JICF does not include the interaction of the stack with the cross-flow. Ground-level JICF have been researched extensively both experimentally [58–66] and numerically [67–74]. However, research into the resulting acoustic response in the domain has yet to be investigated, and is the focus of the work presented here.

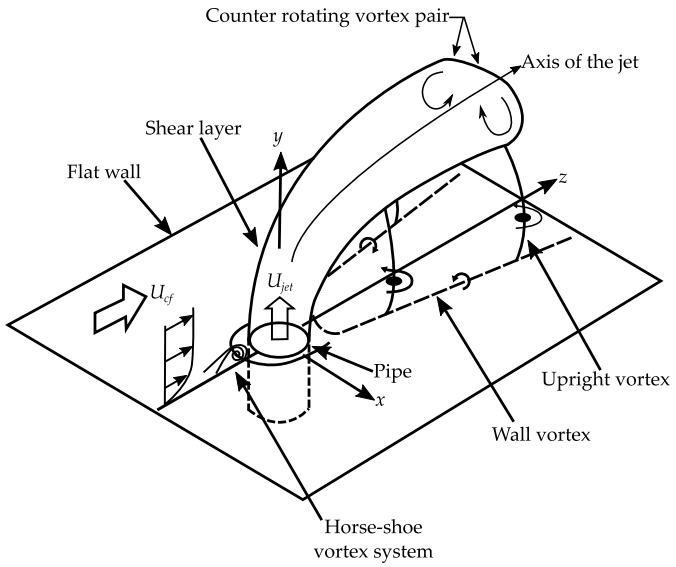

Figure 2: Schematic of the dominant fluid dynamic structures associated with JICF [62].

Simulations and experiments of jet in cross-flow are affected by the cross-flow momentum ratio, which is the ratio of the momentum of the gas in the jet

divided by the momentum of the gas in the cross-flow field. In the geometric near-field, at high cross-flow momentum flux ratios, flow is considered to be jet dominated with the flow exiting the outlet resembling a jet [61]. As the plume develops in the domain, the jet is deflected by the cross-flow momentum. The deflection in the jet then causes the plume to develop into a crescent-like structure [61]. In the far-field, the plume then transitions to counter-rotating vortex pairs [61]. The counter-rotating vortex pairs become the dominant flow structure in the plume. For high values of jet to cross-flow momentum ratios typically seen in exhaust stacks, the counter-rotating vortex pairs forms earlier in the plume than cases with lower jet to cross-flow momentum ratios [61, 75].

Studies using smoke visualisation have shown that the majority of the gas exiting the jet remains within the JICF plume [60, 62]. The counter-rotating vortex pairs in the far-field contain the hottest region in the plume. As the fluid is entrained by the counter-rotating vortex pairs, the overall temperature of the plume decreases as it develops downstream and eventually the temperature of the plume core slowly approaches the ambient temperature [61]. Previous experimental work has shown that the maximum vorticity in the plume is at the centre of the counter-rotating vortex pairs. Steady-state or time-averaged simulations have shown that the plume is symmetrical along a vertical plane along the z-axis (i.e. $x = 0$) in Fig. 2, with the smaller transient features (wake vortices and horseshoe vortices) not being visible in the domain. In the far-field, the dominant steady-state feature of the counter-rotating vortex pairs are plane-symmetric. Rusch et al. [74] showed that for a steady-state ground-level JICF, the smaller transient features, such as the horseshoe vortices and wake vortices are not modelled. By not modelling the smaller transient features, the entrainment of the cross-flow into the plume and enhance mixing in the plume are not adequately modelled leading to higher temperatures in the plume and a higher plume centreline trajectory than transient scale resolving simulations [74].

This study investigates the effects that a high temperature, exhaust jet, with a cooler cross-flow, has on the propagation of sound. Steady-state com-

putational fluid dynamics (CFD) and numerical acoustic simulations, using the finite element method (FEM), are used for the analyses. The layout of the paper is as follows. Section 2.1 describes the mathematical models that are utilised for the fluid flow simulations, which involve using CFD and acoustic propagation using the discretised acoustic wave equation with FEM. In Section 2.2, the domain and mesh used for the simulation are discussed. Section 3 describes the results from the CFD and acoustic FEA simulations. The main conclusions are summarised in Section 4.

2. Mathematical models, domain, and boundary conditions

The numerical research in this study is a hybrid computational aeroacoustic scheme that uses both steady-state CFD and the discretised acoustic wave equation, as shown in Fig. 3. Initially, a CFD model of the JICF in FLUENT was created to generate the nodal mean fluid velocity and nodal temperature. The nodal temperature and mean fluid velocity are mapped using MATLAB onto the acoustic FEM. The acoustic FEM model in ANSYS Mechanical was used to predict the acoustic pressures. This section of the paper will discuss these mathematical models and the governing equations, followed by a discussion of the domain geometry, boundary conditions, and mesh.

2.1. Mathematical models and governing equations

Initially a steady-state CFD model is conducted to obtain temperature and velocity fields. These are then mapped onto the Finite Element Model which is used to model the sound propagation. The numerical acoustic simulations were conducted using a 3-dimensional (3-D) linearised acoustic wave equation method that is discretised and solved with FEM. The model was implemented and solved using ANSYS Mechanical [76, 77]. A more detailed formulation of the governing equations that are presented in this paper is shown in Leav [16].

The formulation of the acoustic wave equation for the numerical work in this paper is based on a number of assumptions. The fluid is compressible with

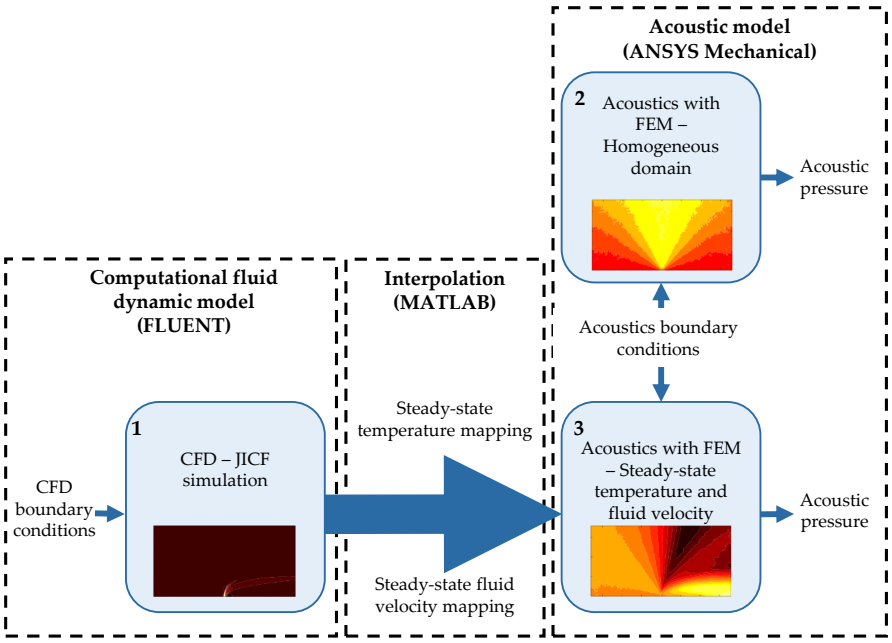

Figure 3: Simulation process for conducting the numerical simulations.

relatively no large changes in the bulk pressure. The propagating medium is 'frozen' or stationary in time with small perturbations in acoustic pressure taken into consideration. It is also assumed that the fluid is irrotational. Additionally, it is assumed that there are no body forces and the gas is ideal, adiabatic and reversible. The flow is also assumed to be inviscid. Furthermore, the following derivation in this paper is a first order approximation of the linearised acoustic wave equation with the second and higher order terms neglected.

Two different acoustic wave equations were used for different propagation conditions: a stationary field with or without temperature variations spatially, and an inhomogeneous domain which accounts for the local temperature and local mean fluid velocity. The following is a 3-D formulation in Cartesian co-ordinates, with four governing equations used for acoustic modelling; and they are the flow continuity equation, Navier-Stokes equations for fluid momentum,

conservation of entropy, and equation of state, respectively given by:

$$D_t(\rho) + \nabla \cdot (\rho \vec{v}) = \rho Q \tag{1}$$

$$\rho D_t(v) + \nabla p = \frac{\vec{F}}{\rho}, \tag{2}$$

$$D_t(s) = 0, \tag{3}$$

$$p = IP(\rho, s), \tag{4}$$

where ρ is the density, t is time, $\vec{v}$ is the velocity vector, Q is the mass source, p is the pressure, $\vec{F}$ is the body force, IP is the relation function, and $D_t = \frac{\partial}{\partial t} + \vec{v} \cdot \nabla$ is the material derivative (also known as the substantial derivative or as Pierce [78] describes, the time derivative following the ambient flow). An important note is that in different literature the material derivative is expressed in different forms with ANSYS Mechanical using $\frac{D_0}{dt}$[76, 77], Bergmann [79] using $\frac{D}{Dt}$, Ostashev et al. [26] and Ross and Chives[80] using $\frac{d}{dt}$, and Pierce [78] using D_t, which is the notation used in this paper. In Equations (1) and (2), ρ, p, and $\vec{v}$ are spatially dependant on position $\vec{x} = (x, y, z)$. Furthermore, the assumption of a 'frozen' or stationary propagating medium leads to the assumption that ρ is time invariant such that the time-averaged statistics are used. As discussed previously it is assumed that there are no body forces acting on the fluid ($\vec{F} = 0$).

Equations (1) to (4) can be further simplified, based on the assumptions outlined above and linearised to form the following states:

$$\rho = \rho_0(x, y, z) + \epsilon \rho'(x, y, z, t), \tag{5a}$$

$$p = p_0(x, y, z) + \epsilon p'(x, y, z, t), \tag{5b}$$

$$s = s_0(x, y, z) + \epsilon s'(x, y, z, t), \tag{5c}$$

$$\vec{v} = \vec{v_0}(x, y, z) + \epsilon\vec{v'}(x, y, z, t), \tag{5d}$$

$$Q \approx \epsilon Q(x, y, z, t), \tag{5e}$$

where the parameters with the subscript 0 represents the local steady-state or time averaged quantity, ϵ is the small perturbation in the quantity, and the $'$ notation represents the unsteady perturbation in that particular quantity. The word local refers to the time-averaged value at position $\vec{x}$. It should be noted that for the rest of the derivation all unsteady terms with fluctuating components will be replaced with subscript a, to represent the unsteady acoustic perturbation. The linearisation of Equations (1), (2), and (4) are shown next, with the resulting stationary acoustic wave equation used by ANSYS Mechanical [76, 77] being an identical formulation to the work by [79] and [80]. The time dependant stationary acoustic wave equation is

$$\nabla \cdot \left(\frac{1}{\rho_0(\vec{x})} \nabla p_a(\vec{x}, t) \right) - \frac{1}{\rho_0(\vec{x}) c_0^2(\vec{x})} \frac{\partial^2 p_a(\vec{x}, t)}{\partial t^2} = -\frac{\partial Q(\vec{x})}{\partial t}, \tag{6}$$

where $\rho_0(\vec{x})$ is the mean fluid density in kg/m^3, $c_0(\vec{x})$ is the speed of sound in m/s, $p_a(\vec{x})$ is the acoustic pressure in Pa, and $Q(\vec{x})$ is the mass source in kg/m^3.

In order to solve for the harmonic normalised wave number, the following harmonically varying pressure formulation can be used:

$$p_a(\vec{x}, t) = \mathrm{Re}[p_a(\vec{x}) e^{j\omega t}], \tag{7}$$

where Re refers to the real component of the expression, $\omega = 2\pi f$ is the angular frequency of interest in rad/s and f is the linear frequency of interest in Hz.

When solving the acoustic wave equation in a stationary field, the Helmholtz equation may be used, and is given by:

$$\omega^2 \underbrace{\frac{p_a(\vec{x})}{\rho_0(\vec{x}) c_0^2(\vec{x})}}_{M_p} + \underbrace{\nabla \cdot \left(\frac{1}{\rho_0(\vec{x})} \nabla p_a(\vec{x}) \right)}_{K_p} = -j\omega \underbrace{Q(\vec{x})}_{f_p}, \tag{8}$$

where M_p is the term for the 'acoustic fluid mass' for acoustic pressure, K_p is the term for the 'acoustic stiffness' for acoustic pressure, and f_p is the 'acoustic

fluid load' for the acoustic pressure. The homogeneous Helmholtz equation is suitable for modelling sound propagation through an ideal gas medium with uniform $\rho_0(\vec{x})$ and $c_0(\vec{x})$. It is also possible to account for temperature variations using the ideal gas law, which can be used to relate the speed of sound, $c_0(\vec{x})$, and the density, $\rho_0(\vec{x})$, with temperature, T. The following equations were used to calculate $c_0(\vec{x})$ and $\rho_0(\vec{x})$ as a function of temperature, respectively:

$$c_0(\vec{x}) = \sqrt{\gamma R_{\text{gas}} T(\vec{x})}, \tag{9a}$$

$$\rho_0(\vec{x}) = \frac{P_{\text{state}}(\vec{x})}{R_{\text{gas}} T(\vec{x})}, \tag{9b}$$

where γ is the ratio for specific heats, R_{gas} is the universal gas constant J/mol K, T is the absolute temperature in K at position $\vec{x}$, and P_{state} is the absolute pressure of the gas measured in fluid at a location $\vec{x}$. Therefore, the governing equation for numerical acoustic simulations with temperature variations in the domain are given by Eq. (8), using Equations (9a) and (9b) in lieu of $\rho_0(\vec{x})$ and $c_0(\vec{x})$, respectively.

The non-stationary formulation for the acoustic wave equation used by ANSYS Mechanical [76, 77] was almost identical to the formulation by [78], with a slight difference in the final time variant equation that will be discussed later. Pierce [78] presents two different formulations for the linearised acoustic wave equation with mean flow using a scalar potential flow, which is dependent on the definition of the acoustic particle velocity, $\vec{v_a}(\vec{x})$, and acoustic pressure, $p_a(\vec{x})$, with

$$\vec{v_a}(\vec{x}) = -\frac{A}{\rho_0(\vec{x})} \nabla \phi(\vec{x}, t), \tag{10}$$

$$p_a(\vec{x}, t) = A D_t \phi(\vec{x}, t), \tag{11}$$

where A is a constant one can choose and it is related to $\rho_0(\vec{x})$ and $c_0(\vec{x})$. In the derivation by Pierce [78], the author proposes two values of A; $A = -1$ or $A = -\rho_0(\vec{x})$, where it leads to two different formulation of the linearised acoustic wave equation with mean flow using a scalar potential flow. Both

formulations will be discussed later in this section. For the derivation used by ANSYS Mechanical, $A = -1$, and the acoustic velocity, $\vec{v_a}(\vec{x})$, and acoustic pressure, $p_a(\vec{x})$, are

$$\vec{v_a}(\vec{x}) = \frac{1}{\rho_0(\vec{x})} \nabla \phi(\vec{x}, t), \tag{12}$$

$$p_a(\vec{x}, t) = -D_t \phi(\vec{x}, t), \tag{13}$$

where $\phi(\vec{x}, t)$ is the velocity potential, and

$$D_t = \frac{\partial}{\partial t} + \vec{v_0}(\vec{x}) \cdot \nabla, \tag{14}$$

is the material derivative (or the time derivative following the ambient flow [78]), and $\vec{v_0}$ is the mean flow velocity. Further manipulation of the previous terms leads to the derivation for the time dependent non-stationary acoustic wave equation with mean flow is the equation given by:

$$\nabla \cdot \left(\frac{1}{\rho_0(\vec{x})} \nabla \phi(\vec{x}, t) \right) - D_t \left(\frac{1}{\rho_0(\vec{x}) c_0^2(\vec{x})} D_t \phi(\vec{x}, t) \right) = \frac{q(\vec{x})}{\rho_0(\vec{x})}, \tag{15}$$

where $q(\vec{x})$ is

$$q(\vec{x}) = Q(\vec{x}) - \frac{1}{c_0^2(\vec{x})} D_t(\rho_0(\vec{x}) \phi(\vec{x}, t)). \tag{16}$$

Eq. (15) is the time dependent acoustic wave equation taking into consideration the unsteady non-stationary mean fluid flow used by ANSYS Mechanical. It is important to note that Eq. (15) is almost identical to the formulation derived by [78] shown as

$$\nabla \cdot \left(\frac{1}{\rho_0(\vec{x})} \nabla \phi(\vec{x}, t) \right) - \rho_0(\vec{x}) D_t \left(\frac{1}{\rho_0^2(\vec{x}) c_0^2(\vec{x})} D_t \phi(\vec{x}, t) \right) = 0. \tag{17}$$

Equations (15) and (17) are identical as a first order approximation, with the second terms in both equations differing slightly. The equation by Pierce [78] does not include a mass source, q, but can be easily included in the formulation. The second term on the left hand side in Equations (15) and (17) differ by ρ_0, which introduces a first order change of $O(L^{-1}) + O(T^{-1})$, where L is the length scale and T is the time scale. An important consideration and limitation for the

acoustic wave equation in Equations (6), (15), and (17), it assumes that there is non vorticity in the pressure perturbation.

For the work presented in this paper, $A = -1$ for Equations (10) and (11), and with this chosen value for A, Eq. (15) by ANSYS Mechanical and Eq. (17) by Pierce [78] are derived. Another formulation by Pierce [78] assumes $A = -\rho_0(\vec{x})$, and this is the Pierce's preferred assumption of the constant, A. This leads to Pierce's [78] preferred form

$$\frac{1}{\rho_0(\vec{x})}\nabla \cdot (\rho_0(\vec{x})\nabla\phi(\vec{x},t)) - D_t\left(\frac{1}{c_0^2(\vec{x})}D_t\phi(\vec{x},t)\right) = 0. \tag{18}$$

Pierce [78] has stated that even though he presents two possible outcomes for the linearised acoustic wave equation with mean flow and using a scalar velocity potential shown in the article and expressed in Equations (17) and (18), there are other possible formulations based on the choice of the constant A. Pierce [78] has also noted that Equations (17) and (18) are equivalent to the first order approximation. However, the preferred form of Eq. (18) is slightly more attractive, as the formulation is "exact" under the condition that the ambient medium has constant entropy per unit mass and when the flow is irrotational and steady.

For a harmonic solution of Eq. (15) a harmonically varying velocity potential is introduced

$$\phi(\vec{x},t) = \mathrm{Re}[\phi(\vec{x}e^{j\omega t})], \tag{19}$$

whereby substituting Eq. (19) into (15) gives the following harmonically formulated acoustic wave equation

$$\begin{aligned}\frac{\omega^2}{\rho_0(\vec{x})c_0^2(\vec{x})}\phi(\vec{x}) - j\omega\nabla\cdot\frac{\vec{v_0}(\vec{x})}{\rho_0(\vec{x})c_0^2(\vec{x})}\phi(\vec{x}) - j\omega\frac{\vec{v_0}(\vec{x})}{\rho_0(\vec{x})c_0(\vec{x})^2}\cdot\nabla\phi(\vec{x}) \\ -\frac{\vec{v_0}(\vec{x})}{\rho_0(\vec{x})c_0^2(\vec{x})}\vec{v_0}(\vec{x})\nabla\phi(\vec{x}) + \nabla\cdot\frac{1}{\rho_0(\vec{x})}\nabla\phi(\vec{x}) = \frac{q(\vec{x})}{\rho_0(\vec{x})}.\end{aligned} \tag{20}$$

With further manipulation of Eq. (20), the potential flow formulation of the

acoustic wave equation with mean flow can be represented as

$$\omega^2 \underbrace{\frac{\phi(\vec{x})}{\rho_0(\vec{x})c_0^2(\vec{x})}}_{M_\phi} - j\omega \underbrace{\left(\nabla \cdot \frac{\vec{v_0}(\vec{x})}{\rho_0(\vec{x})c_0^2(\vec{x})}\phi(\vec{x}) + \frac{\vec{v_0}(\vec{x})}{\rho_0(\vec{x})c_0^2(\vec{x})} \cdot \nabla\phi(\vec{x})\right)}_{C_\phi} - \underbrace{\frac{\vec{v_0}(\vec{x})}{\rho_0(\vec{x})c_0^2(\vec{x})}\vec{v_0}(\vec{x})\nabla\phi(\vec{x}) + \nabla \cdot \frac{1}{\rho_0(\vec{x})}\nabla\phi(\vec{x})}_{K_\phi} = \underbrace{\frac{q(\vec{x})}{\rho_0(\vec{x})}}_{f_\phi}, \tag{21}$$

where M_ϕ is the term for the 'acoustic fluid mass' for the acoustic velocity potential, C_ϕ is the term for the 'acoustic fluid damping' for the acoustic velocity potential, K_ϕ is the term for the 'acoustic fluid stiffness' for the acoustic velocity potential, and f_ϕ is the term for the 'acoustic fluid load' for the acoustic velocity potential.

Equations (8) and (20) can be discretised using the Galerkin method for representation using FEM [81]. Detailed formulation for the discretisation of Equations (8) and (21) are provided in [77]. In modelling the sound, the following uncoupled, non-symmetric formulation is used for both the Helmholtz equation without and with mean fluid flow, respectively:

$$(-\omega^2[M_p] + j\omega[C_p] + [K_p])\{p\} = f_p, \tag{22a}$$

$$(-\omega^2[M_\phi] + j\omega[C_\phi] + [K_\phi])\{\phi\} = f_\phi, \tag{22b}$$

where $[M_p]$ is the acoustic fluid mass matrix for acoustic pressures, $[C_p]$ is the acoustic damping matrix for acoustic pressures, $[K_p]$ is the acoustic stiffness matrix for acoustic pressures, f_p is the acoustic fluid load vector for acoustic pressures, $[M_\phi]$ is the acoustic fluid mass matrix for ϕ, $[C_\phi]$ is the acoustic damping matrix for ϕ, $[K_\phi]$ is the acoustic stiffness matrix for ϕ, f_ϕ is the acoustic fluid load vector for ϕ. It should be noted that for the case of inviscid flow, the $[C_p]$ is non-existent for the formulation that uses Helmholtz equation without mean fluid flow. Equations (22a) and (22b) are very similar in their implementation in ANSYS Mechanical. Eq. (22a) is formulated using the single degree of freedom for pressure p and Eq. (22b) is formulated using the single

degree of freedom for the velocity potential ϕ. The acoustic pressure data from Eq. (20) are derived using Eq. (13). The matrix Equations (22a) and (22b), are solved directly with the 'Sparse' matrix solver in ANSYS as the matrices in Equations (22a) and (22b) have poor numerical conditioning. The matrix formulation for the solver treats the full domain as a matrix which is solved using the 'Shared Memory Parallel' mode. The 'Shared Memory Parallel' mode requires less Random Accessible Memory (RAM) to solve for Equations (22a) and (22b) using FEM with ANSYS Mechanical, compared with a model with the domain partitioned. Hence, using FEM with ANSYS Mechanical and the 'Shared Memory Parallel' mode provides the ability to solve models that have a large number of nodes, a requirement for the accurate propagation of sound through non-isotropic media.

It should be noted that there are different acoustic FEMs that could be used for the numerical study. These include the linearised Euler equations [82, 83], Galbrun's equations [84, 85], linearised Navier-Stokes [86, 87], Helmholtz equation [42, 79, 80] and the linearised acoustic wave equation with mean flow using a scalar flow potential [78]. Each FEM listed has their benefits for simulation and careful consideration needs to be taken based on the assumptions for each acoustic model and the computational requirements to solve higher fidelity models with multiple degrees of freedom. A benefit of the the Helmholtz equation and the linearised acoustic wave equation with mean flow using a scalar flow potential is that these methods are scalar formulation that solves for the pressure degree of freedom or scalar velocity potential, respectively. In contrast, for a 3-D simulation using the linearised Euler equations, linear Navier-Stokes or Galbrun's equation there are five, five (depending on assumptions it could be reduced to four) and four degrees of freedom, respectively. It is important to note that the dimensions of the matrices increases in size based on the square of the number of degree of freedoms. By only solving a single degree of freedom for an acoustic FE model it reduces the computational resources and computational runtime needed to solve a system, when compared to a higher fidelity model with multiple degrees of freedom. Hence, 3-D models with a larger number of

nodes can be computed with scalar formulations for the acoustic FE method, with the limited computational resources and computational runtime, which was also supported by Astley and Eversman [42]. However, there are limitations with a scalar pressure and scalar flow potential formulation, that needs to be considered when modelling aeroacoustic problems.

To support the validity of using Helmholtz equation [42, 79, 80] and the linearised acoustic wave equation with mean flow using a scalar flow potential [78] in ANSYS Mechanical, Howard and Cazzolato [88], and Leav [16] presents a number of cases from the literature that have been validated against the commercial package. In particular, Leav [16] has investigated the linearised acoustic wave equation with mean flow using a scalar flow potential for different flow and temperature conditions, which reflects the conditions in this paper. Further justification for using the the numerical method described in this section are presented in Section 3.2.

Modelling the steady-state fluid dynamics related to non-isothermal ground-level JICF, otherwise known as JICF for the rest of the paper, was undertaken using ANSYS FLUENT. The CFD simulation utilised the Reynolds Averaged Navier-Stokes (RANS) model Shear Stress Transport (SST) $\kappa - \omega$ [89]. This model was chosen on the recommendation of various researchers [68–70, 74], as it is the most appropriate RANS model for simulating the mixing characteristics in the plume downstream. Rusch [74] has also shown that accurate predictions of the temperatures downstream of a JICF can be made when using RANS SST $\kappa - \omega$ formulation. To model the temperatures in the plume adequately, the ideal gas law for density and Sutherland's law for dynamic viscosity were implemented to account for the temperature variations [90]. Furthermore, to capture the dynamics of the plume accurately the buoyancy of the gas was modelled. The CFD model uses a second-order upwind spatial discretisation scheme for all its variables and the 'Coupled' scheme for the pressure-velocity coupling.

The simulations conducted in this paper were solved using the University of Adelaide's Phoenix High-Performance Computing cluster. Each simulation used

Table 1: Relevant parameters for the Siemens SGT5-2000E gas turbine [17] and the reduced scale numerical simulations.

Description	Parameter	OCGT Value	Simulation Value	Units
Duct diameter	D	6	0.0476	m
Temperature in duct	T_j	809	300-773	K
Exhaust mass flow	$\dot{M}_j$	558	773	$\mathrm{kg\,s^{-1}}$
Exhaust velocity	u_j	45.2	773	$\mathrm{m\,s^{-1}}$
Mach number	M_j	0.08	0.1	-
Reynolds number	Re_j	3.17×10^6	773	-
Temperature in cross-flow	T_{cf}	300	300	K
Duct height	H_{duct}	60	0.476	m
Acoustic frequency range of interest	f	16-100	773	Hz
Helmholtz number	ka	0.53-3.19	0.3-0.8	-
Jet to cross-flow momentum flux ratio	R	3-20	5-7.5	-

a single node on the cluster, consisting of two Xeon E5-2698v3 CPU (central processing units), with 2.5 GHz. This configuration on the node leads to the availability of 32 CPU per node, with each node possessing 128 GB RAM.

2.2. Domain and boundary conditions

For the work conducted in the case study, the dimensions for the domain, parameters used for the fluid dynamics and acoustic simulations are based on a reduced scale (1:125) model of a 190 MW OCGT exhaust stack, Siemens SGT5-2000E gas turbine [17], and the experimental work presented in Leav [16] and Leav et al. [14, 15]. These values are presented in Table 1.

The geometry of the domain used in the case studies presented in this paper is shown in Fig. 4 and was consistent between the CFD and acoustic simulations. The domain had dimensions $48D \times 48D \times 80D$ ($L_x \times L_y \times L_z$), where $D = 0.0476\,\mathrm{m}$ is the duct diameter. This domain is plane-symmetric about the centreline of the duct, with the domain extending $40D$ upstream and downstream of the duct centre, in the direction of the cross-flow free stream. The

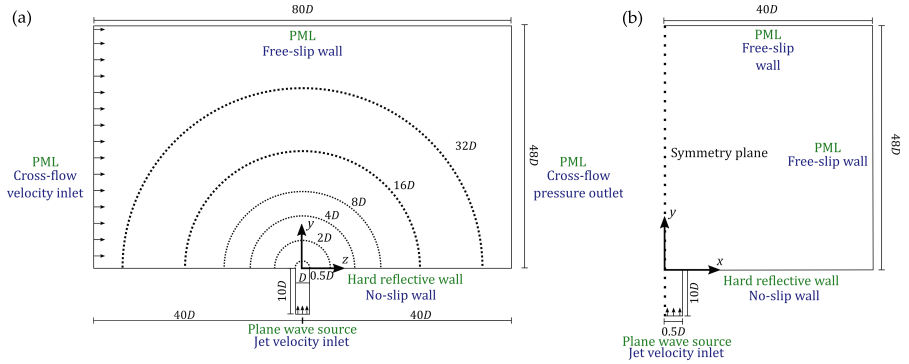

Figure 4: Schematic and dimensions for the simulations, where (a) shows the schematic along the Y-Z plane and (b) shows the schematic along the X-Y plane. The blue text represents the fluid dynamics boundary conditions and green text shows the acoustic boundary conditions.

length of the duct in these simulations is $10D$, and was chosen to allow the flow in the duct to develop and to account for the cross-flow effects on the duct outlet, as was shown to occur by Muppidi and Mahesh [71]. Furthermore, by including the duct itself in the computational acoustic simulations, the effects of diffraction at the edge of the duct outlet and the impedance change at the duct outlet are included.

The CFD mesh was generated using ANSYS and consisted of a fully structured mesh. The elements used are hexahedra 'brick' (first order, linear) elements with nodes residing on the vertices. The mesh also contains approximately 9.1 million elements and can be seen in Figs. 5(a) and (b). A mesh independence study was conducted in order to investigate mesh convergence, with the results showing that the current domain with 9.1 million elements is sufficient for solution convergence.

For the CFD simulations, the jet velocity at the duct inlet, u_j, was Mach $M = 0.1$, and had a fully developed pipe flow velocity profile. The temperature at the duct inlet, T_j, was either 27 °C (ambient), 250 °C or 500 °C. The cross-flow velocity, u_{cf}, and the quantitative value at the boundary were chosen to have varying cross-flow free-stream velocity. The velocities for u_{cf} were dependent on the effective velocity ratio, R, otherwise known as the square root of the jet

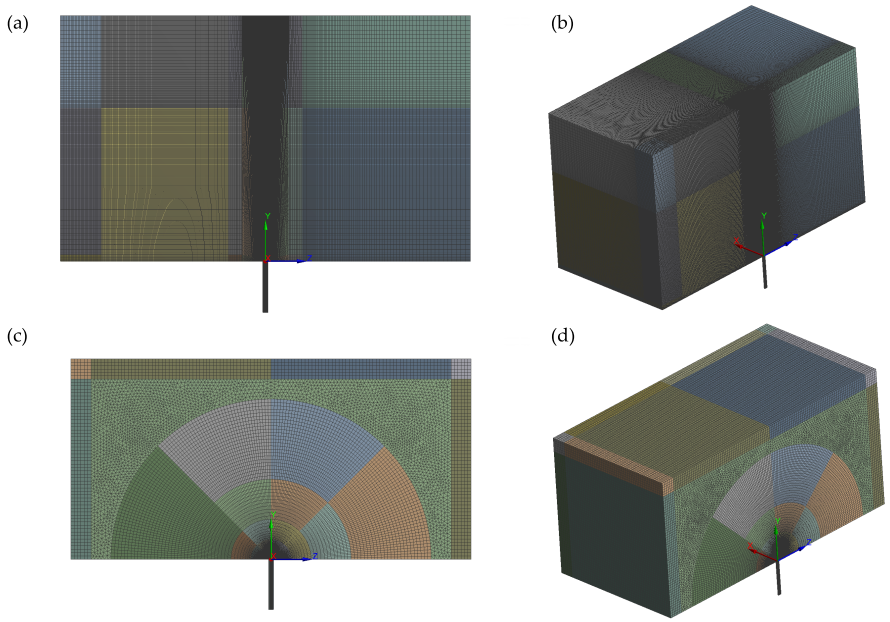

Figure 5: The meshes for CFD and FEA simulations, where (a) is the CFD mesh along the Y-Z plane, (b) is the CFD mesh at an angled view, (c) is the FEA mesh along the Y-Z plane, and (d) is the FEA mesh at an angled view. It should be noted that a planar half symmetry condition was used along the Y-Z plane in both CFD and FEA models.

to cross-flow momentum flux ratio, defined as:

$$R = \sqrt{\frac{\rho_j u_j^2}{\rho_{cf} u_{cf}^2}} \quad , \tag{23}$$

where ρ_j is the jet density, and ρ_{cf} is the free stream cross-flow density [91]. In this particular study, R was 5 and 7.5, as they closely resemble the conditions in real OCGT exhaust stacks. The cross-flow temperature was set 27 °C (ambient). A 'non-slip' wall boundary condition was used along the internal duct wall and the 'ground' (wall adjacent to the duct outlet), which assists in the formation of the boundary layer. Along the internal duct wall, the mesh was designed to resolve the wall boundary layer. However, Rusch et al. [74] suggested that the wall boundary layer along the 'ground' should not be resolved in the steady-state simulations for ideal convergence. It is known that resolving the boundary

layer along the 'ground' level can lead to global instabilities being triggered, and therefore leads to 'poor' convergence statistics. The outlet of the domain was a pressure outlet boundary condition. A 'free-slip' boundary condition was used along the centreline symmetry-plane and the remaining walls in the CFD simulations.

The mesh for the acoustic simulations can be seen in Figs. 5(c) and (d). The elements used in the acoustic simulation comprised a hybrid mesh with both structured hexahedra 'FLUID220' and unstructured tetrahedra 'FLUID221'. Both element types have mid-side nodes and are second-order (quadratic) elements. The nodal density of the acoustic simulation was derived using a rule of thumb of 11 nodes per wavelength, λ, at the highest frequency of interest [88], which resulted in a node count of approximately 6 million nodes. A mesh independence study has been conducted and showed the solution converged for the sound pressure in an isothermal stationary field. A more indepth mesh independence study for the sound pressure in an isothermal stationary field is presented in Leav [16].

The acoustic simulations used a harmonic velocity source at the base of the duct, with magnitude $u_a = 0.01\,\mathrm{m\,s^{-1}}$. The frequency for the acoustic source was defined as

$$ka = \frac{\pi f D}{c_j} \quad , \tag{24}$$

where f is the acoustic frequency of interest, and c_j is the speed of sound in the jet. The value of ka for these simulations ranges from $0.3 - 0.8$, which typically causes a hemispherical sound radiation pattern in the absence of the jet or cross-flow. A hard reflective wall boundary condition was used along the internal duct wall, the 'ground' wall (the surface adjacent to the duct outlet) and the symmetry-plane. The remaining exterior of the domain contained perfectly matched layer (PML) elements for simulating an infinite acoustic free-field. The PML was at least four elements thick and was larger than one-quarter of the acoustic wavelength (λ) of interest for the simulation, which in this case is a layer that is $4D$ thick [88].

The results in the acoustic FEM are calculated using acoustic pressure and can be represented using sound pressure level (SPL) and directivity index (DI). The SPL can be calculated from the root mean square (rms) of the acoustic pressure, p_{rms},

$$\text{SPL} = 20\log_{10}\left(\frac{p_{\text{rms}}(\vec{x})}{20\times10^{-6}}\right). \tag{25}$$

Another way to represent the results is with the directivity index (DI), and is given by [92]:

$$\text{DI}(\theta) = \frac{I(\theta)}{I_{av}}, \tag{26}$$

where θ is the angular position in spherical co-ordinates, I is the acoustic intensity, and I_{av} is the average acoustic intensity over a hemispherical surface in the acoustic domain. The acoustic intensity for a plane wave, I, can be calculated using the following formulation from Bies et al. [92]

$$I(\vec{x}) = \frac{p^2_{\text{rms}}(\vec{x})}{\rho_0(\vec{x})c_0(\vec{x})}. \tag{27}$$

Bies et al. [92] discuss that Eq. (27) can be used to to calculate the intensity in the far-field from a source, where the radius of curvature is ten times the acoustic wavelength. It should be noted that Eq. (27) may break down in the near-field. A more detailed representation of the co-ordinate system for DI is shown in Fig. 6. It should be noted that this definition for DI is used for this paper, with a slight exception for the DI presented in Section 3.2.1 and explained in detail later.

In Eq. (26) the average acoustic intensity, I_{av}, can be calculated using Eq. (27) to form the spatial average

$$I_{av} = \frac{1}{N}\sum_{i=1}^{N}\frac{p^2_{\text{rms},i}(\vec{x})}{\rho_{0,i}(\vec{x})c_{0,i}(\vec{x})}, \tag{28}$$

where N is the total number of nodes on a spherical surface, and i is the nodal number on the spherical surface. For calculating I_{av} at each radius from the stack outlet a, spatial average is taken with the expression in Eq. (28), over a quarter-sphere, shown in the acoustic mesh in Fig. 5. It should also be noted that for each surface over the quarter-sphere, the nodes are spaced evenly apart and the acoustic intensity at each node has equal weighting in calculating I_{av}.

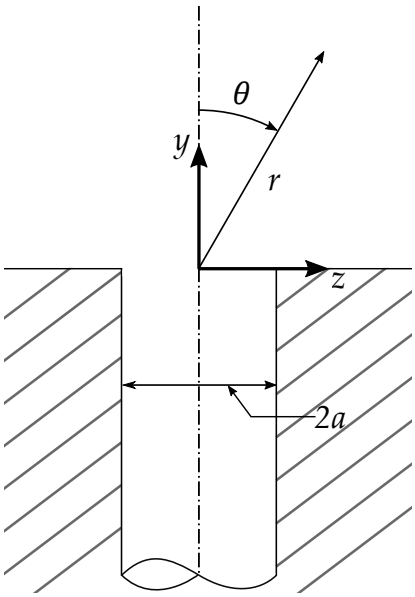

Figure 6: Schematic for the ground level JICF and the directivity definition from the duct outlet. The quantity a is the duct radius, θ is the directivity angle from the duct centreline, and r is the radius for the directivity arc from the centre of the duct outlet.

3. Results and discussion

This section will discuss the results and key findings from the numerical study. First, the steady-state RANS CFD simulation results will be discussed. Following this, a discussion on the following numerical sound radiation cases is presented:

- sound propagation at ambient temperature with no flow or otherwise known as isothermal stationary field,
- nodal temperatures and mean bulk fluid velocities from a CFD simulation of a non-isothermal (heated) JICF were applied to the FE model.

For these cases, three jet temperatures (T_j = 27 °C, 250 °C, and 500 °C), two cross-flow ratios ($R = 5$ and 7.5), and six Helmholtz numbers ($0.2 \leq ka \leq 0.8$) were considered.

3.1. Non-isothermal jets in cross-flow fluid dynamics

The results presented in this study are from steady-state simulations, and it will be shown that many of the important flow features seen in the literature are successfully reproduced. Fig. 7(a) shows a contour plot of the velocity magnitude along the Y-Z plane, and that the jet structure is dominant in the near-field close to the jet outlet adjacent to the ground wall. As the plume propagates, the cross-flow causes the jet to deflect, and the plume is bent over. Fig. 7(a) also shows that with the development of the plume, a velocity gradient formed by the shear layer develops as it propagates downstream. Similarly, Fig. 7(b) shows a contour plot of the temperature along the Y-Z plane. There are similar features between the temperature distribution and the velocity magnitude contour plot in Fig. 7(b). Fig. 7(b), shows that the elevated temperature follows the deflected plume itself. The highest temperature is observed near the duct outlet, with the temperature of the plume reducing as it propagates. The decrease in plume temperature is a result of the spatial growth of the plume and the entrainment of the cooler cross-flow [61].

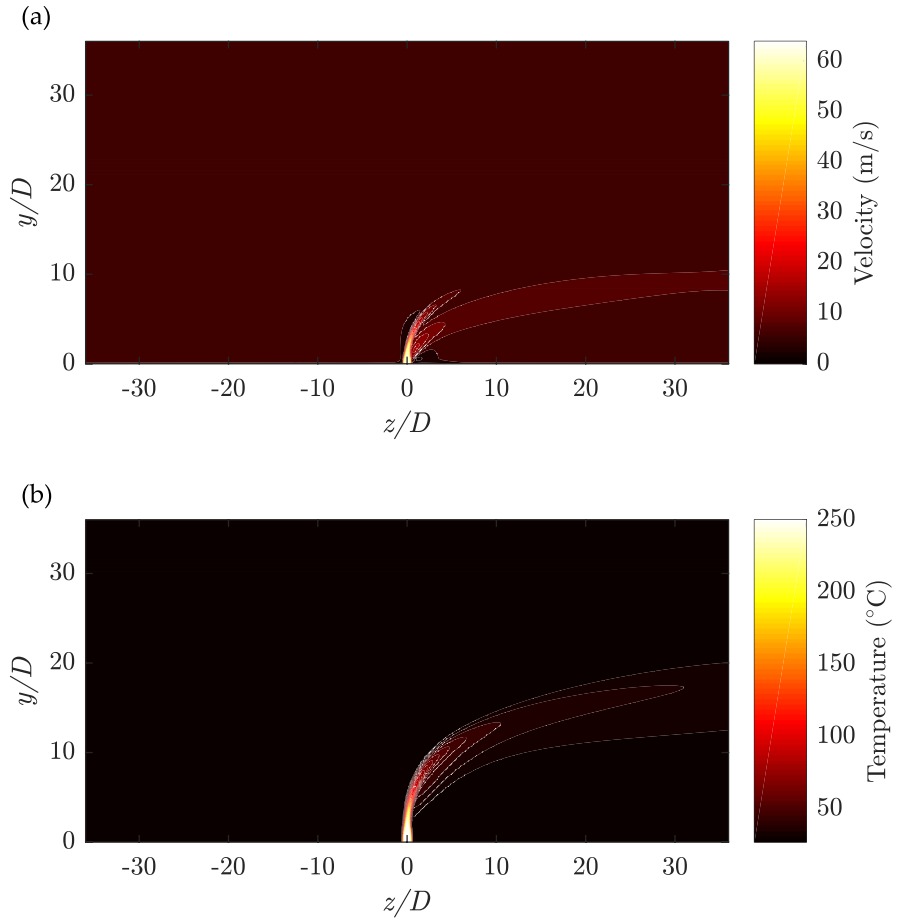

Figure 7: The CFD generated contour plots of (a) flow velocity and (b) temperature along the Y-Z plane (of symmetry), where $T_j = 500\,^{\circ}\mathrm{C}$ and $R = 5$. The cross-flow is from left to right.

Figs. 8(a) and (b) presents the fluid velocity at two locations; in the near-field of the jet and further downstream, and shows the span-wise development of the plume. Fig. 8(a) indicates that the deflected jet initiates downstream as a 'crescent' structure, which is the critical feature of the plume in the near-field. The plume's 'crescent' structure then transitions further to a counter-rotating vortex, which is shown in Fig. 8(b). For the cases studied in this research, it

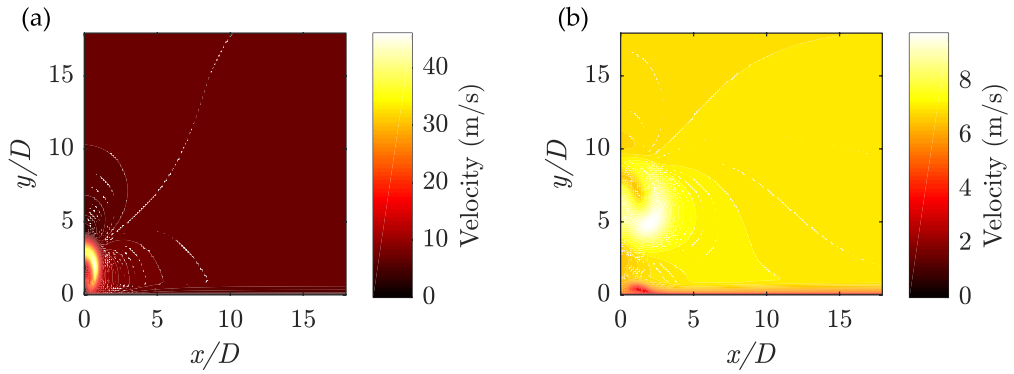

Figure 8: The velocity contour plot along the X-Y plane at (a) $z = 0.5D$ and (b) $z = 8D$, where $T_j = 500\,^{\circ}\mathrm{C}$ and $R = 5$.

can be seen that the counter-rotating vortex structure is the dominant flow feature downstream, as seen in previous studies [58–65, 68, 69, 71, 73, 74]. From the results of numerical simulations conducted here, it can be observed that the increase in cross-flow ratio, R, also causes the formation of the counter-rotating vortex to occur earlier in the plume as it propagates downstream, with lowest R in the study leading to the 'crescent' plume pertaining furthest downstream in all the cases studied. This observation in the spatial formation of the counter-rotating vortex in the plume is consistent with the observations made by Kamotani and Greber [61].

Figs. 9(a) and (b) show the contour plots of the nodal temperature along the X-Y planes at two distances downstream from the jet centreline. As previously observed by Kamotani and Greber [61], the centre of the 'crescent' and the counter-rotating vortex contains the hottest region in the plume. This observation with the plume's temperature was consistent with all the simulations presented in this study. Also observed in the results is a slight increase in the centre temperature of the plume, with an increase in R. This occurs as a result of the reduction in cross-flow momentum, which leads to a lack of cross-flow mixing downstream. The reduction in both the cross-flow momentum and ambient air entrainment downstream also changes the jet trajectory downstream,

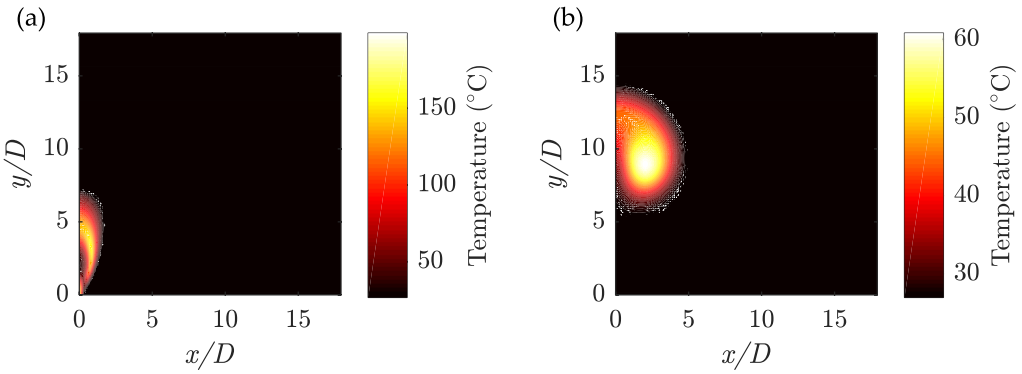

Figure 9: Temperature contour plots along the X-Y plane at (a) $z = 0.5D$ and (b) $z = 8D$, where $T_j = 500\,^{\circ}\mathrm{C}$ and $R = 5$.

which is consistent with the observations seen in the previous literature [61, 66]. The change in jet trajectory will also change the position of the thermal and velocity gradient shear layer.

A mesh grid independence study has been completed for flow associated with a non-isothermal JICF, where $R = 5$ and $T_j = 500\,^{\circ}\mathrm{C}$ and presented in Leav [16]. The results show that there is minimal mesh grid dependence, with the maximum variation in jet trajectory varying by 0.25% between the cases with 9.1 million and 36.1 million nodes. The slight dependency with the mesh density is noted, but it is concluded that for the purpose of reproducing the necessary flow features, a mesh of 9.1 million nodes is appropriate.

The fluid dynamic structures generated using CFD simulations are very similar in all cases investigated, however the plume's centreline trajectory changes with varying R. Fig. 10 shows the centreline trajectory of the plume with R. The centreline trajectory for the plume was calculated using ANSYS Fluent by tracking a particle that originates from the duct inlet. For a converged solution the tracked particle travelled along the plane of symmetry in the domain, which implies the plume is plane-symmetric, which is to be expected for a steady-state simulation for a JICF. An increase in R causes an increase in the height of the plume above the ground-level. The change in plume trajectory is also due

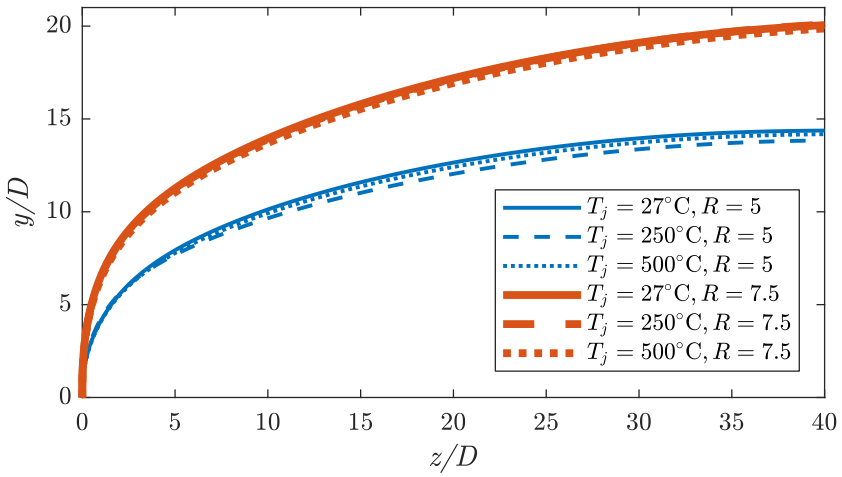

Figure 10: The plume's centreline trajectory for JICF where $R = 5$ and 7.5, and $T_j = 27\,°C$, 250 °C, and 500 °C.

to the reduction in cross-flow momentum with the rise in R. Also, shown in Fig. 10 are centreline trajectories for the same R, but with varying jet temperatures, and these show the centreline trajectories are effectively independent of jet temperature.

Since the fluid dynamic results were computed using steady-state simulations and the turbulence was modelled using RANS, the transient turbulent scales were not modelled, as indicated in Section 2.1. Consequently, the transient features of a JICF, such as vortical structures in the wake, were not modelled. Not taking into consideration the wake's vortical structures, leads to a reduction in the entrainment of the cooler cross-flow into the plume [71–74]. The decrease in cross-flow entrainment may lead to a slight overestimation of the plume's temperature.

3.2. Sound propagation

This section presents results from acoustic simulations for two significantly different conditions; the first is for a homogeneous field with no jet, the other is for the heated jet in cross-flow. As shown in Fig. 3, first a CFD simulation

is conducted to evaluate the nodal temperatures and mean bulk fluid velocities, due to selected conditions. The results from the CFD simulations are then applied to the nodes in the acoustic FE model. Note, this is a one-way coupling, so there is no backwards influence of the sound field on the fluid motion or temperature. The conditions in the acoustic FE model that were simulated three temperatures, $T_j = 27\,^{\circ}\mathrm{C}$, $250\,^{\circ}\mathrm{C}$, and $500\,^{\circ}\mathrm{C}$, two cross-flow ratios, $R = 5$ and 7.5, and six Helmholtz numbers ($0.3 \leq ka \leq 0.8$) were considered.

3.2.1. Sound propagation through an isothermal stationary field

Initially the sound propagation through an isothermal stationary field with constant ambient temperature and in the absence of fluid flow was solved. Two acoustic sources were used; (i) a harmonic velocity source at the outlet which is equivalent to a baffled piston and facilitates comparison against analytical modes [92], (ii) a harmonic velocity source at the opposite end of the duct, which represents what happens in practice. The inclusion of the duct with the sound source at the base of the duct changes the acoustic directivity slightly, which will be discussed in this section. A grid independence study was also conducted, which demonstrated that the results change as the mesh is altered. It should be noted that re results presented in this section were from solving the acoustic field using Eq. (8), with the acoustic FEM formulation described with Eq. (22a).

Fig. 11 present the sound radiation along the Y-Z plane (of symmetry). Fig. 11(a) show the contour plots of the sound pressure level (SPL) along the Y-Z plane, at $ka = 0.8$, where it can be seen that the sound radiation pattern is axisymmetric and spreading hemispherically. The directivity index (DI) is an alternative way to display the acoustic field, and is given by Eq. (26). Fig. 11(b) shows the contour plot of the directivity index (DI) along the Y-Z plane of symmetry, with a small variation with angle in DI ($-1.5\,\mathrm{dB} \leq \mathrm{DI} \leq 1.5\,\mathrm{dB}$) showing approximately spherical sound radiation.

In Fig. 12, the DI are plotted as polar line graphs and compared with the theoretical solution for the DI of a baffled piston in an infinite plane. Fig. 12

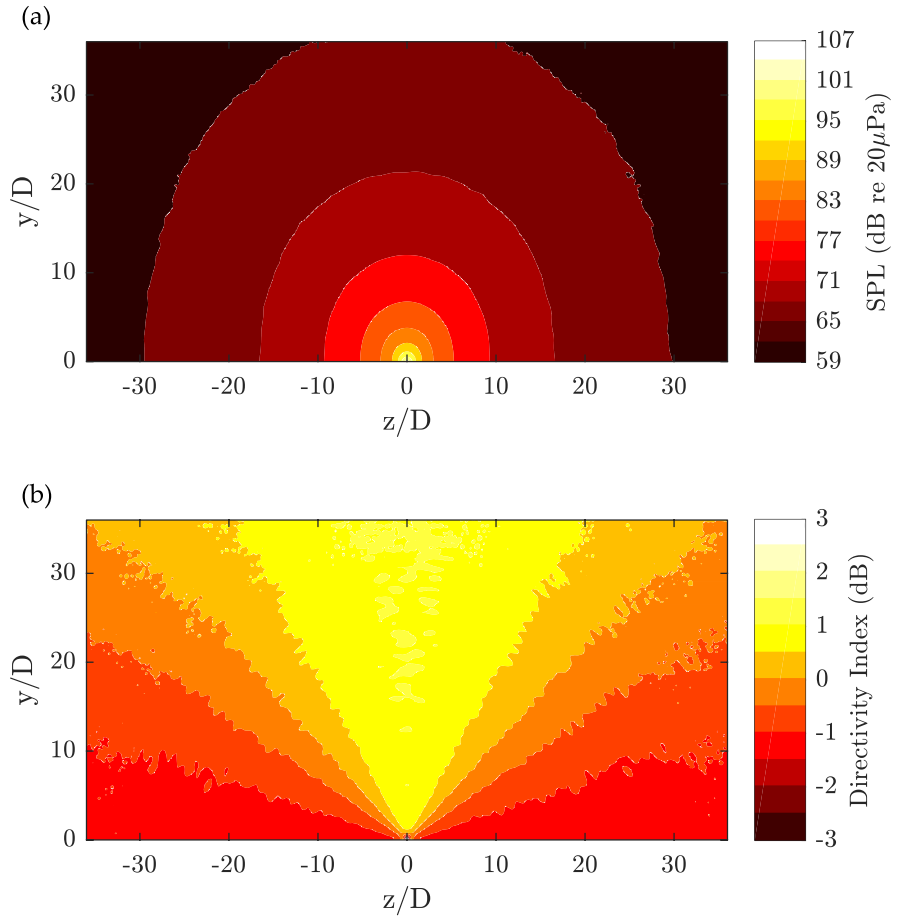

Figure 11: Contour plots of (a) the sound pressure level and (b) DI along the Y-Z plane (of symmetry) for sound propagation through the domain in the absence of flow at $ka = 0.8$.

shows the DI polar plots at two different Helmholtz numbers ($ka = 0.7$ and 0.8). Both polar plots in Fig. 12 show similar key features in which the sound is radiated hemispherically and is axisymmetric. Fig. 12 shows a good agreement with the DI polar plot results for the theoretical and numerical sound radiation from a baffled piston. However, in Fig. 12, the inclusion of the duct produces DI polar results that closely resembles the DI of a baffled piston but with a more concentrated lobe on-axis, along the duct centreline. Additionally, the

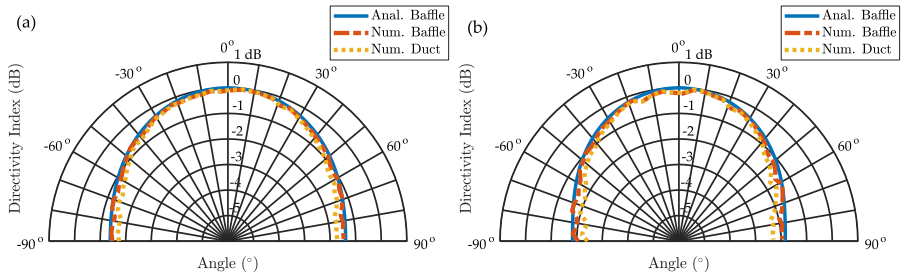

Figure 12: The DI along the Y-Z plane (of symmetry) for sound propagation through the domain in the absence of flow at $r = 32D$, where the results are for (a) $ka = 0.7$ and (b) 0.8. The results presented are for an analytical expression for a baffled piston, numerical results for a baffled piston, and numerical results for a baffled duct.

increase in Helmholtz number, ka, from Fig. 12(a) to (b) shows the accuracy in the solution reducing slightly.

A grid independence study for a directivity plot along the Y-Z plane was conducted to achieve a converged solution and determine the model's limitations with the total number of mesh nodes. The study was conducted for total node count of 3, 4.5, 6, 9, and 12 million nodes. The study showed that the results are node count dependent, with the largest case (12 million nodes) indicating that the solution had converged. However, the acoustic simulations in this section used Eq. (22a) with the single degree of freedom pressure formulation, whereby the limitation with the computational hardware and numerical code, the upper limit of the number of acoustic nodes that could be used in the FE model was 12 million. However, Eq. (22b) with the three degree of freedom velocity potential formulation will be used in Section 3.2.2, and with the limitation with computational hardware and numerical code, the upper limit was 6 million nodes. The acoustic results presented in the remainder of this study used a model with a node count of 6 million nodes for comparison.

3.2.2. Combining mean convective and thermal effects on sound propagation

Section 3.2.1 presented benchmark results that do not account for the refraction of sound local to the stack outlet and reflect current models and standards.

When accounting for sound refraction in the hot jet, the resulting sound field is very different. The acoustic results in this section will focus on the cases with R = 5-7.5, T_j = 27 °C-500 °C, for various ka. It should be noted that results in this section were from Eq. (21) and the acoustic FEM formulation described with Eq. (22a).

The superposition of the convective and thermal effects on the sound propagation leads to a distinctive sound radiation pattern along the Y-Z plane (of symmetry). Figs. 13(a) and (b) show contour plots of the SPL and DI along the Y-Z plane (of symmetry), respectively. The results in Fig. 13(a) indicate that in the near-field surrounding the duct outlet, the sound spreads spherically. As the sound propagates and the plume develops, a lobe in the sound field forms (Fig. 13(a)). Near the duct centreline axis, a 'cusp' forms as a result of the shear layer of the deflected plume. In Fig. 13(b), the DI contour plot shows similar features to Fig. 13(a), with the 'cusp' forming along a line slightly offset from the duct centreline and a significant increase in sound downwind of the duct outlet.

Fig. 14 shows the DI results as a polar plot along the Y-Z plane (of symmetry) at five different radial distances from the duct outlet ($r = [2D, 4D, 8D, 16D, 32D]$) and $ka = 0.8$. As discussed previously, at a radial distance of $r = 2D$ from the duct outlet, the sound has travelled an insufficient distance for fluid-acoustic interaction and a jet dominated plume leads to an approximately axisymmetric sound directivity pattern, which is approximately hemispherical, with the exception of a slight 'cusp' developing. Fig. 14 shows at $r = 4D$, that the sound has propagated a sufficient distance to interact with the plume and shows that the acoustic directivity has become asymmetric, with a more pronounced 'cusp' at approximately 10°. As the radial distance from the stack outlet increases, the depth of the cusp grows and this acoustic energy is redirected towards the horizontal, and predominantly downstream. The directivity at $r = 32D$ shows the largest increase in DI of up to 9 dB.

The increase in DI downwind observed in Fig. 14 is a result of the plume refracting sound downwards. As previously stated, the effective speed of sound,

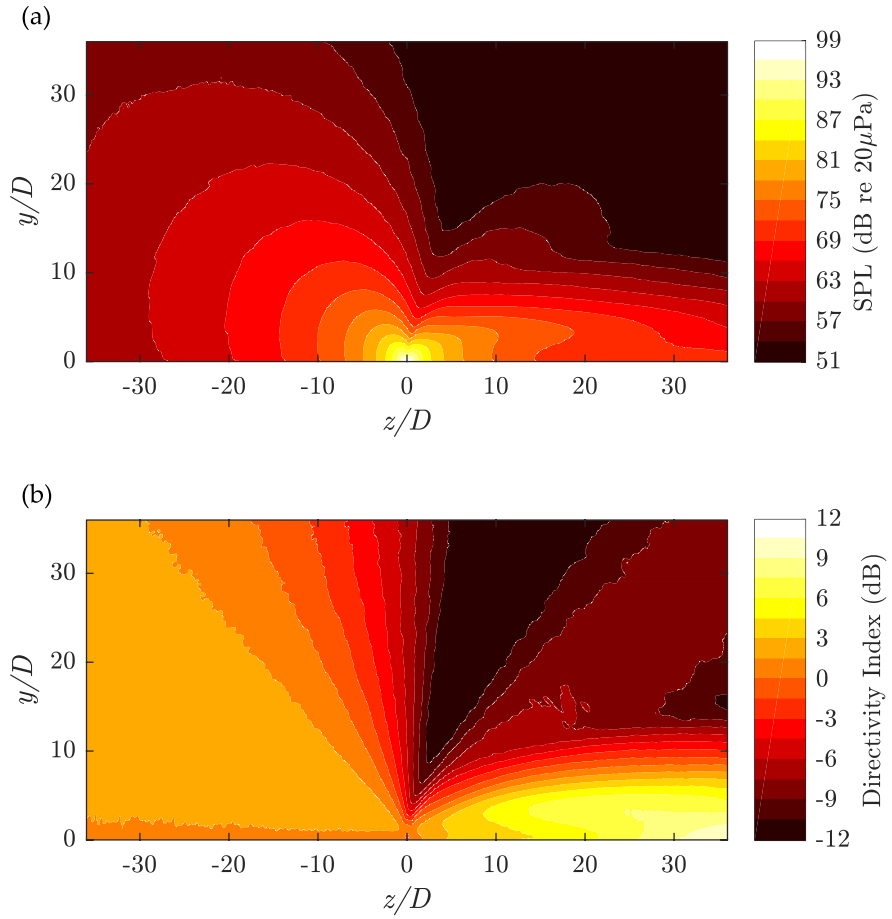

Figure 13: Contour plots of (a) the sound pressure level and (b) the DI along the Y-Z plane (of symmetry) for sound propagation through the convective and thermal gradients from a JICF with $R = 5$, $T_j = 500\,^{\circ}\mathrm{C}$, and $ka = 0.8$. The cross-flow is from left to right. Values less than -12 dB are saturated black.

which governs sound propagation, is mainly influenced by the gas temperature, rather than the steady-state fluid flow, however the superposition of the two terms has led to a significant increase in downwind DI. Upwind of the duct outlet ($\theta < 0^{\circ}$) the DI polar plots are approximately elliptical, with the incoming velocity gradient in the boundary layer causing acoustic refraction upwards

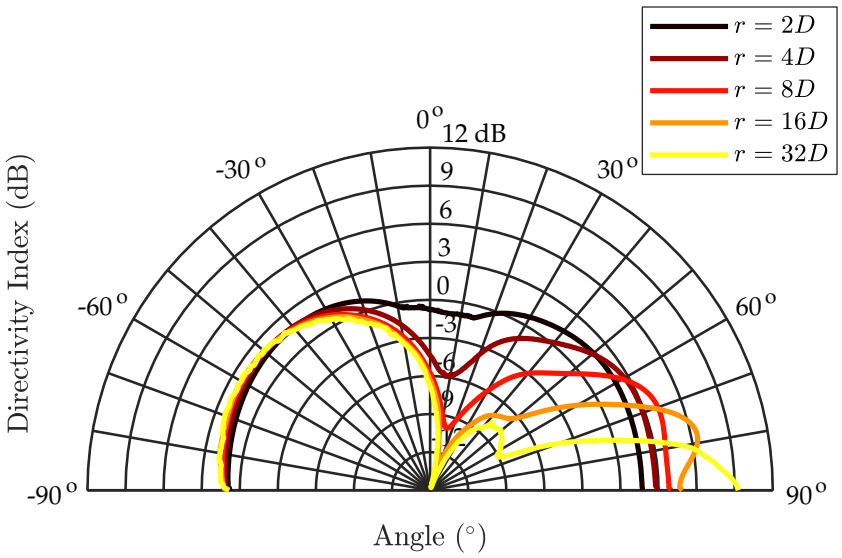

Figure 14: The DI at various distance from the duct outlet ($r = 2D, 4D, 8D, 16D$, and $32D$) along the Y-Z plane for sound propagation through the velocity and thermal gradients from a JICF with $R = 5$, $T_j = 500\,^{\circ}\text{C}$, and $ka = 0.8$.

upwind of the duct outlet, which reduces the DI at ground-level.

The sound propagation is also dependent on wavenumber, ka. Fig. 15 shows the DI results as a polar plot at six Helmholtz numbers (ka = [0.3, 0.4, 0.5, 0.6, 0.7, 0.8]) and at four different radial distances (r = [$2D$, $8D$, $16D$, $32D$]) along the Y-Z plane (of symmetry). In Fig. 15(a), the radiation pattern is approximately spherical, where the sound has not propagated a sufficient distance to interact with the plume. The directivity plots in Figs. 15(b), (c), and (d) all exhibit the following similar features that are ka dependent: the increase in downwind SPLs, a sound pressure level 'cusp', and upwind elliptical spreading with upwards acoustic refraction at ground-level. The increase in downwind DI is dependent on the Helmholtz number, where the results for $ka = 0.8$ had greatest increase in DI observed in Figs. 15(b), (c), and (d). The depth of the cusp in the directivity plots at $8D, 16D$ and $32D$ is influenced by ka, with a $ka = 0.8$ producing the deepest cusp.

Fig. 16 contains contour plots of the SPL and DI along the ground-level

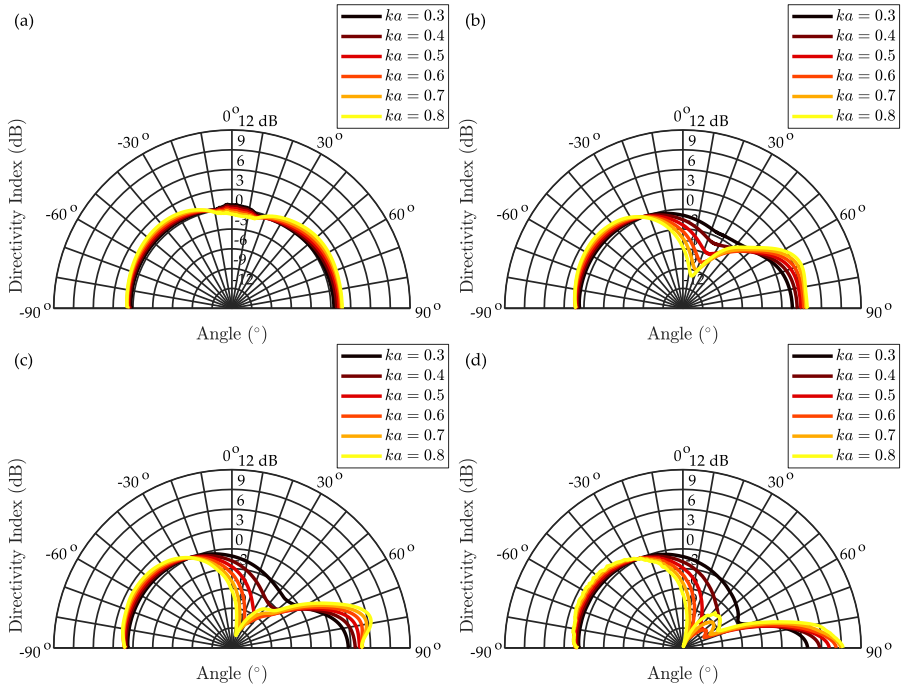

Figure 15: The DI at six different Helmholtz numbers ($ka = 0.3, 0.4, 0.5, 0.6, 0.7$, and 0.8) and at four different radial distances (a) $r = 2D$, (b) $r = 8D$, (c) $r = 16D$ and (d) $r = 32D$. The results are along the Y-Z plane (of symmetry) for sound propagation through the velocity and thermal gradients from a JICF with $R = 5$, and $T_j = 500\,^{\circ}\mathrm{C}$. Cross-flow is from left to right.

(X-Z plane). Fig. 16(a) shows an increase in the downwind SPL, and is clearly dominated by the refraction, where the greatest increase in sound level is observed downwind of the exhaust stack at the bottom left corner of Fig. 16(a). Fig. 16(b) presents the same data as a DI, and essentially represents the increase in SPL expected due to the refraction, with the maximum of 11 dB observed at the boundary of the simulation domain. This is a significant finding and means that an observer on the ground, downwind of an exhaust stack, would experience significantly louder sound levels.

Fig. 17 shows the DI contour plot across a spherical surface at a radial distance of $r = 32D$ and is used to illustrate the combined effects of the steady-state convective and thermal gradients. Fig. 17 shows that the DI has increased

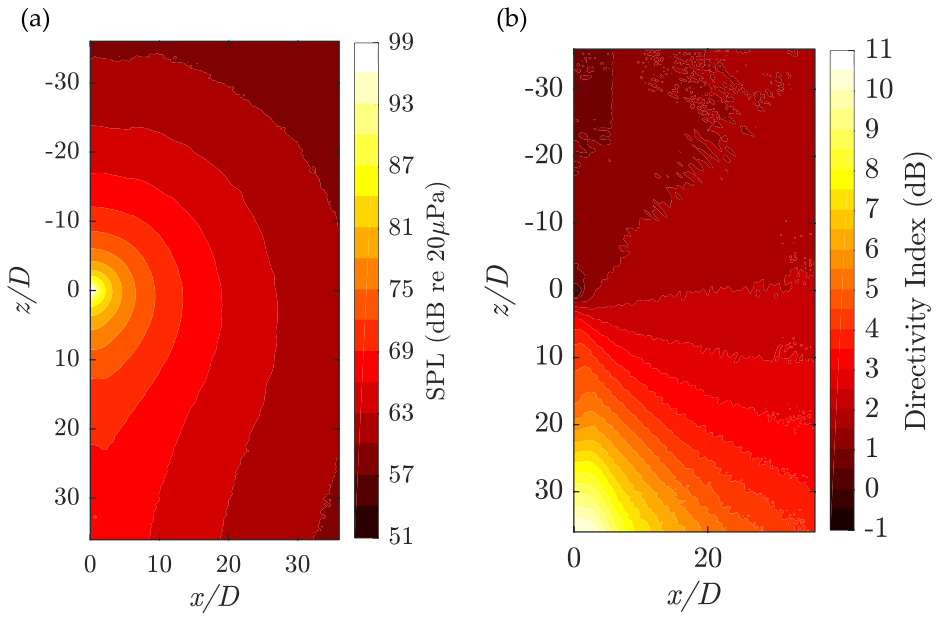

Figure 16: Contour plots of (a) the sound pressure level and (b) the DI along the X-Z plane (ground-level) for sound propagation through the velocity and thermal gradients from a JICF with $R = 5$, $T_j = 500\,^{\circ}\mathrm{C}$, and $ka = 0.8$. The cross-flow is from top to bottom in the Figure.

at ground-level downwind of the duct, and the region where the greatest increase in directivity occurs is along the Y-Z plane of symmetry. The increase in sound along the Y-Z plane of symmetry is due to the thermal and velocity gradients associated with the counter-rotating vortex pairs in the plume refracting sound downwards. Even though a single counter-rotating vortex is modelled in Figs. 8 and 9, with the symmetry condition, it is expected that there is a counter-rotating vortex pair, as seen in the literature and in Fig. 2. With the counter-rotating vortex pairs there is an increase of sound along the Y-Z plane (of symmetry), where the acoustic energy from the accompanying counter-rotating vortex would contribute. It can be seen in Fig. 17 that the sound pressure cusp is in the shape of a crescent that resembles the deflected jet and is caused by the velocity and thermal gradients within the shear layer of the jet.

To emphasise the effects of the steady velocity and thermal gradients from

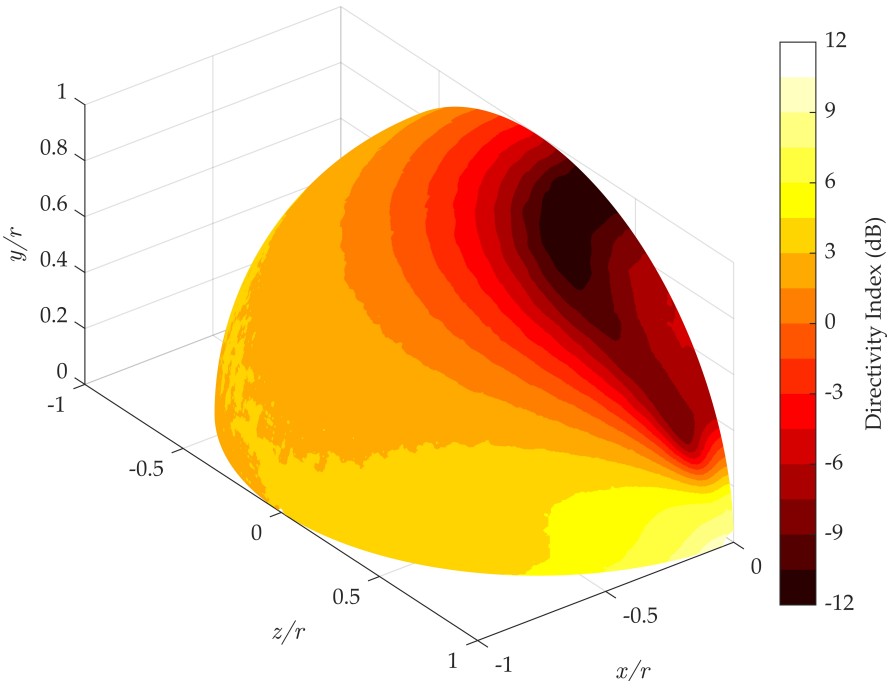

Figure 17: The DI contour plot across a spherical surface at a radial distance $r = 32D$ for sound propagation through non-isothermal JICF with $ka = 0.8$, $R = 5$ and $T_j = 500\,^{\circ}\mathrm{C}$. The cross-flow is flowing parallel to the Z-axis, towards the negative direction. Values less than -12 dB are saturated black.

non-isothermal ground-level JICF, 3-D directivity radiation plots are compared for four different conditions, which are:

- an isothermal stationary field,
- a steady-state temperature field associated with non-isothermal JICF,
- a steady-state convective flow associated with isothermal JICF, and
- a combined steady-state temperature and convective fluid flow associated with non-isothermal JICF.

The corresponding 3-D directivity radiation patterns are shown in Fig. 18. The acoustic results can be summarised as follows:

- Fig. 18(a) shows in the absence of the thermal and velocity gradients imposed from the CFD simulation, the acoustic radiation is axisymmetric, with a slight concentration of acoustic energy along the duct centreline as would be expected from previous published works.
- Fig. 18(b) shows the acoustic radiation is no longer axisymmetric. With the presence of the steady-state velocity from the ground-level JICF, the sound observed downwind of the exhaust stack has been refracted downwards, with an increase in sound observed at ground-level. Upwind of the exhaust stack, the steady-state velocity from incoming boundary layer shows upwards refraction in Fig. 18(b),
- Fig. 18(c) shows the effects of thermal gradients on the sound propagation. The sound radiation is now clearly asymmetric. A very distinct lobe has formed just above the horizontal downstream of the duct. The peak in this lobe grows with radial distance and is yet to converge.
- Fig. 18(d) shows the combination of both the thermal and convective effects and exhibits the greatest increase in DI downstream of the duct outlet. The convective effect shown in Fig. 18(b) have caused the elevated acoustic lobe in Fig. 18(c) to refract further downwards to be positioned at ground-level, as seen in Fig. 18(d).

The inclusion of both the convective and thermal gradients from non-isothermal ground-level JICF has shown the most drastic acoustic radiation plot when compared directly in Fig. 18(d), with the 'tongue' from the thermal effects observed in Fig. 18(c) pushed onto ground level by the convective effects (Fig. 18(b)).

The trajectory of the plume is affected by the cross-flow velocity. Fig. 19 shows the effects of increasing the plume height by increasing R (i.e. reducing the cross-flow velocity) at a radial distance of $32D$ from the duct outlet. The downstream lobe patterns are clearly visible for $T_j = 250\,^{\circ}\mathrm{C}$ and $500\,^{\circ}\mathrm{C}$, and are elevated ($\theta < 90^{\circ}$) with increasing values of R. For the case of $R = 5$, it can be seen that there is a significant increase in sound level downwind of the duct outlet, along the ground-level, but when R increases to 7.5, the acoustic lobe is elevated above ground-level at approximately 70°. It is clear that R has an impact on the angle of the acoustic lobe downwind. The angle of the 'cusp' is around 20° in Fig. 19 and is also dependent on R. For the two values of R investigated in Fig. 19, there is a strong relationship between R and the depth of the 'cusp' in the DI polar plot. The increase in jet temperature, T_j, and hence higher thermal gradients leads to an increase in sound refraction and a deepening in the 'cusp' in Fig. 19.

From the results in Figs. 18 and 19 it is clear that the jet temperature is a dominant factor in causing the increased downwind DI levels. Fig. 18 shows a drastic change in the sound directivity downwind from the refraction of sound from the plume between the homogeneous sound field (which most outdoor noise standards and models use) and the results obtained from these simulations. The change in sound radiation can be explained using the effective speed of sound,

$$c_{\mathrm{eff}} = c + v, \tag{29}$$

where c is the sound speed, and v is the bulk flow speed in the direction of sound propagation [23]. The speed of sound, c, can be calculated from the equation:

$$c = \sqrt{\gamma_d R_d T(1 + 0.511w)}, \tag{30}$$

where γ_d is the specific heat ratio for dry air, R_d is the gas constant for dry

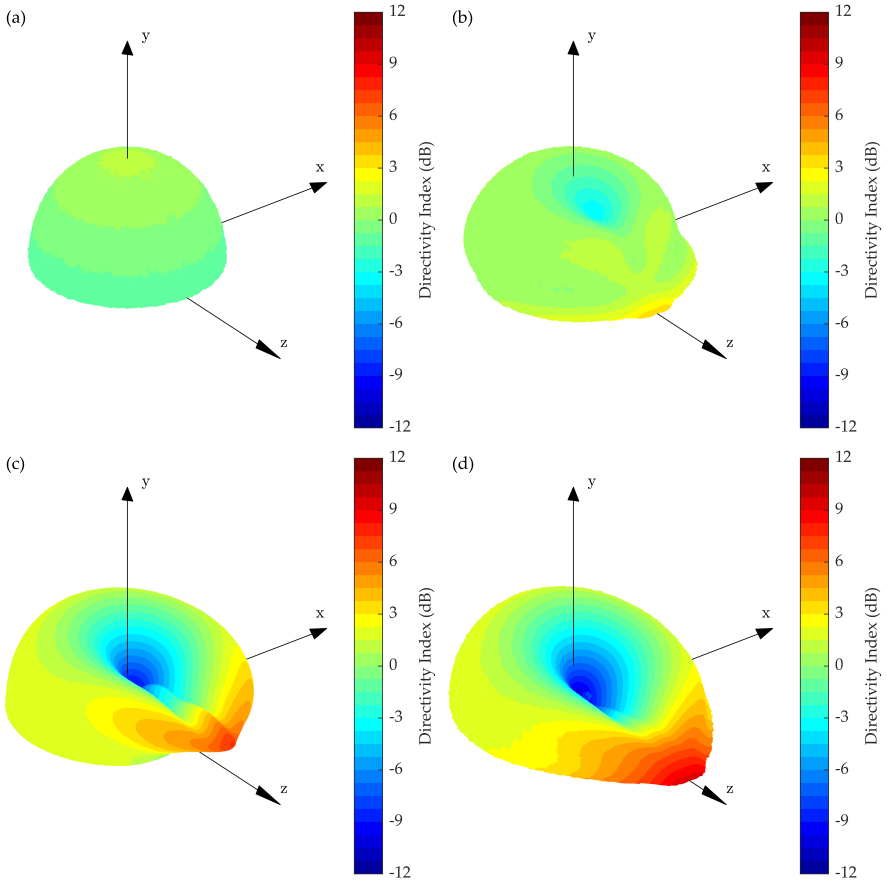

Figure 18: The 3-D directivity radiation pattern for sound propagation through four different cases: (a) homogeneous domain, (b) convective effects, (c) temperature effects, and (d) temperature and convective effects at a radius $r = 32D$ with $R = 5$, $T_j = 500\,^{\circ}\mathrm{C}$, $\vec{v_0} \neq 0$, and $ka = 0.8$. The cross-flow is flowing parallel to the Z-axis, going from left to right. Values of DI less than $-12\,\mathrm{dB}$ are saturated dark blue.

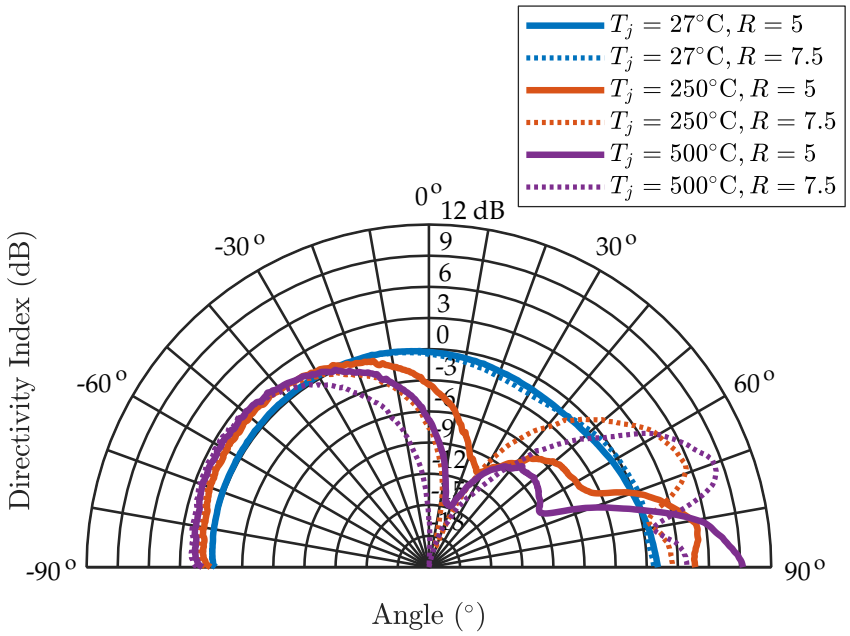

Figure 19: The DI at a radial distance of $32D$ along the Y-Z plane (of symmetry) for sound propagation through a non-isothermal JICF with $R = [5, 7.5]$, $T_j = [27\,°\text{C}, 250\,°\text{C}, 500\,°\text{C}]$, $\vec{v_0} \neq 0$, and $ka = 0.8$.

air, T is the absolute temperature, and w is the water vapour mixing ratio [23]. Eq. (30) shows that the speed of sound is proportional to the square root of absolute temperature. For an exhaust temperature of 500 °C and an ambient temperature of 27 °C, the ratio of the speeds of sound is 1.6. The effects of convective flow on sound propagation is $c_{\text{eff}} = c_0(1 + M)$. For a Mach number of 0.1, the effect of convection is approximately one-sixth of the thermal effect. This is reflected in Figs. 18 and 19, which show an important relationship with the increase of sound observed downwind with the jet temperature, T_j.

The acoustic results presented in this section incorporates the CFD results from Section 3.1 for sound propagation, with the assumptions outlined in Section 2.1. The results shown in Fig. 8 that there are flow gradients, but in particular the counter rotating vortex pairs contain rotational flow, which does not comply with the assumption of irrotational flow for the derivation in Section 2.1. However, for the velocity conditions described in Section 2.2, and the results generated from CFD and presented in Section 3.1, the highest Mach number observed is $M = 0.1$. Leav [16] has validated the linearised acoustic wave equation with mean flow using a scalar flow potentials, Eq. (21), and the acoustic FEM formulation described with Eq. (22a) against numerical cases in literature in the subsonic regime ($M < 0.5$). There is sufficient evidence in Leav [16] to suggest that the acoustic FE method in this paper with a scalar pressure and potential flow is adequate in quantitatively capturing the acoustic pressures, but it is not perfect when compared to a higher fidelity acoustic FE method, such as the linearised Euler equations, linearised Navier-Stokes, or Galbrun's equation. Hence, at the cost of minor differences in numerical accuracy, a less computationally demanding and time-efficient acoustic FE model can be utilised as a tool to investigate and understand the acoustic interaction with hot-exhaust jets with cooler cross-flow in the far-field ($r = 32D$).

4. Conclusion

The results from this study have shown that steady-state convective and thermal gradients found within the plumes of JICF significantly impact the propagation of sound from an exhaust stack. The sound radiation in the absence of steady-state thermal and velocity gradients resembles the directivity pattern for a baffled piston. However, when there is a JICF that has either a steady-state convective flow, or is hotter than the ambient gas temperature, or combination of both, the resulting sound propagation becomes asymmetric, due to the redistribution of acoustical energy, as sound is refracted by the thermal and velocity gradients in the shear layer.

The key results of this study are:

- In the presence of the plume and cross-flow, the sound radiation pattern is complicated and axisymmetric.
- The directivity of sound is dependent on the distance from the duct outlet, with the directivity near the duct outlet (at $r = 2D$) showing approximately spherical radiation, and at a radial distance of $r = 32D$ the directivity becomes very asymmetric.
- The change in sound propagation path depends significantly on the Helmholtz number, ka, with a higher value of ka more likely to cause the sound to interact with the plume, with an increase in the DI magnitude observed downwind of the stack in the acoustic lobe.
- Upwind of the jet, there is an upward refraction of sound caused by the velocity gradients in the incoming boundary layer.
- The plume causes a strong 'cusp' to initially form near the axis of the duct centreline. As the jet is deflected by the cross-flow, the position of the cusp rotates downstream with increasing distance from the stack.
- A dominant factor in sound refraction is the thermal gradient within the plume, which causes a strong 'lobe' of sound to form downstream.

- When both the steady-state fluid flow and temperature effects are present, a significant increase in DI of up to 11 dB is observed downwind at ground-level.
- The increase in the downwind SPL at ground-level is dependent on the cross-flow ratio, R, where an increase in the cross-flow ratio (decrease in the cross-flow velocity) causes the sound to strike the ground further downwind.

Future work can be done to investigate the influence of steady-state convective and thermal effects from non-isothermal JICF on the far-field sound propagation ($r > 32D$). In investigating the far-field sound propagation, the current numerical domain size would need to be substantially increased. Additional work can be undertaken for the sound propagation for $ka > 0.8$, which can be achieved by increasing the FEM mesh density in the current domain. Whilst this study investigated two cross-flow ratios, R, a more in-depth study involving a wider range of R should be conducted.

The numerical study has shown that significant sound refraction occurs downwind, as a result of the sound interacting with the hot exhaust plume being deflected by the cooler cross-flow. The refraction of sound downwind leads to the redirection of DI to form an acoustic lobe of increased sound level. Hence, practitioners and engineers should account for this when predicting community noise from hot exhaust stacks, such as these found in OCGTs. It is possible that popular models, such as CONCAWE or ISO 9613-2:1996 [93], will significantly under predict noise level from hot exhaust stacks under certain conditions.

5. Acknowledgements

Leav was sponsored by an Australian Government Research Training Program Scholarship from 2015 to 2018. This work was supported with supercomputing resources provided by the Phoenix HPC service at the University of Adelaide. This work would not have been possible without the technical expertise from LEAP Australia.

References

[1] E. Björk, Experimental study of measures to reduce noise radiated from power-station exhaust stacks, Noise Control Engineering Journal 42 (5) (1994) 171–178. doi:10.3397/1.2828354.
URL https://doi.org/10.3397/1.2828354

[2] N. Broner, A simple criterion for low frequency noise emission assessment, Journal of Low Frequency Noise, Vibration and Active Control 29 (1) (2010) 1–13. doi:10.1260/0263-0923.29.1.1.
URL https://doi.org/10.1260/0263-0923.29.1.1

[3] N. Broner, A simple outdoor criterion for assessment of low frequency noise emission, Acoustics Australia 39 (1) (2011) 7–14.

[4] N. Broner, Power to the people, in: V. Low Frequency Noise, A. Control (Eds.), 15th International Meeting on Low Frequency Noise and Vibration and its Control, Low Frequency Noise, Vibration and Active Control, Low Frequency Noise, Vibration and Active Control, Stratford upon Avon, United Kingdom, 2012, pp. 1–10.

[5] G. Hessler Jr, Proposed criteria in residential communities for low-frequency noise emissions from industrial sources, Noise Control Engineering Journal 52 (4) (2004) 179–185. doi:10.3397/1.2839748.
URL https://doi.org/10.3397/1.2839748

[6] G. Hessler Jr, Proposed criteria for low frequency industrial noise in residential communities, Low Frequency Noise, Vibration and Active Control 24 (2) (2005) 97–106. doi:10.1260/0263092054530957.
URL https://doi.org/10.1260/0263092054530957

[7] R. Hetzel, R. Putnam, Sources and rating criteria of low frequency gas turbine exhaust noise - via case study, in: I. of Noise Control Engineering (Ed.), INTER-NOISE and NOISE-CON Congress and Conference Proceedings, 2009, Ontario, Canada, 2009, pp. 1600–1607.

[8] G. Kudernatsch, Combustion turbine exhaust systems-low frequency noise reduction, in: I. of Noise Control Engineering (Ed.), INTER-NOISE 2000, The 29th International Congress and Exhibition on Noise Control Engineering, Nice, France, 2000, pp. 1–6.

[9] J. Newman, K. McEwan, Low frequency gas turbine noise, in: ASME 1979 International Gas Turbine Conference and Exhibit and Solar Energy Conference, American Society of Mechanical Engineers, 1979, pp. 1–12.

[10] J. R. Newman, K. I. McEwan, Low frequency gas turbine noise, Journal of Engineering for Power 108 (2) (1980) 476–481. doi:10.1115/1.3230280.
URL http://dx.doi.org/10.1115/1.3230280

[11] N. Broner, The effects of low frequency noise on people - A review, Journal of Sound and Vibration 58 (4) (1978) 483–500. doi:10.1016/0022-460X(78)90354-1.
URL http://dx.doi.org/10.1016/0022-460X(78)90354-1

[12] O. Leav, B. Cazzolato, C. Howard, Directivity analysis of sound in turbulent exhaust jets with laminar cross-flow: A numerical study, in: Acoustics 2015, Australian Acoustical Society, Australian Acoustical Society, Hunter Valley, New South Wales, 2015, pp. 1–10.

[13] O. Leav, B. Cazzolato, C. Howard, A computational analysis of sound directivity from sound propagation through non-isothermal, turbulent exhaust jets in cross-flow, in: 24th International Congress on Sound and Vibration, International Institute of Acoustics and Vibrations, International Institute of Acoustics and Vibrations, London, United Kingdom, 2017, pp. 1–8.

[14] O. Leav, B. Cazzolato, C. Howard, Experimental analysis of sound directivity from sound propagation through non-isothermal, turbulent exhaust jets in cross-flow, in: Acoustics 2018, Australian Acoustical Society, Australian Acoustical Society, Adelaide, South Australia, 2018, pp. 1–10.

[15] O. Leav, B. Cazzolato, C. Howard, Sound propagation through elevated, heated jets in cooler cross-flow: An experimental study, manuscript submitted for publication (2020).

[16] O. Y. Leav, An investigation into the mechanics of sound propagation through turbulent non-isothermal exhaust jets in cross-flow, PhD Thesis, University of Adelaide, Adelaide (Apr. 2020).

[17] Siemens, We power the world with innovative gas turbines - Siemens gas turbine portfolio, Data sheet (2019).

[18] F. Delaroche, Sur l'influence que le vent exerce dans la propagation du son, sous le rapport de son intensité, Annales de Chimie 1 (1816) 76.

[19] D. Arago, Resultats des experiences faites en 1822, par ordre du bureau des longitudes, por la determination de la vitesse du son dans l'atmosphere, Annales de Chimie et de Physique 20 (1822) 210.

[20] J. Piercy, T. Embleton, L. Sutherland, Review of noise propagation in the atmosphere, The Journal of the Acoustical Society of America 61 (6) (1977) 1403–1418. doi:http://dx.doi.org/10.1121/1.381455.
URL http://scitation.aip.org/content/asa/journal/jasa/61/6/10.1121/1.381455

[21] T. Embleton, Tutorial on sound propagation outdoors, The Journal of the Acoustical Society of America 100 (1) (1996) 31–48. doi:http://dx.doi.org/10.1121/1.415879.
URL http://scitation.aip.org/content/asa/journal/jasa/100/1/10.1121/1.415879

[22] K. Attenborough, Sound propagation close to the ground, Annual Review of Fluid Mechanics 34 (1) (2002) 51–82. arXiv:https://doi.org/10.1146/annurev.fluid.34.081701.143541, doi:10.1146/annurev.fluid.34.081701.143541.
URL https://doi.org/10.1146/annurev.fluid.34.081701.143541

[23] V. Ostashev, D. Wilson, Acoustics in moving inhomogeneous media, CRC Press, 2015.

[24] K. Attenborough, S. Taherzadeh, H. Bass, X. Di, R. Raspet, G. Becker, A. Güdesen, A. Chrestman, G. Daigle, A. L'Espérance, Benchmark cases for outdoor sound propagation models, The Journal of the Acoustical Society of America 97 (1) (1995) 173–191. doi:10.1121/1.412302.
URL http://dx.doi.org/10.1121/1.412302

[25] R. Blumrich, D. Heimann, A linearized Eulerian sound propagation model for studies of complex meteorological effects, The Journal of the Acoustical Society of America 112 (2) (2002) 446–455. doi:10.1121/1.1485971.
URL http://dx.doi.org/10.1121/1.1485971

[26] V. Ostashev, D. Wilson, L. Liu, D. Aldridge, N. Symons, D. Marlin, Equations for finite-difference, time-domain simulation of sound propagation in moving inhomogeneous media and numerical implementation, The Journal of the Acoustical Society of America 117 (2) (2005) 503–517. doi:10.1121/1.1841531.
URL https://doi.org/10.1121/1.1841531

[27] K. Rasmussen, Outdoor sound propagation under the influence of wind and temperature gradients, Journal of Sound and Vibration 104 (2) (1986) 321–335. doi:10.1016/0022-460x(86)90271-3.
URL http://www.sciencedirect.com/science/article/pii/0022460X86902713

[28] D. Wilson, Use of wave-number-domain windows in fast field programs, The Journal of the Acoustical Society of America 89 (1) (1991) 448–450. doi:10.1121/1.400480.
URL https://doi.org/10.1121/1.400480

[29] D. Wilson, Wind gusts or scattering by turbulence: Which is more important for near-ground propagation?, The Journal of the Acoustical Society

of America 108 (5) (2000) 2650–2650. doi:http://dx.doi.org/10.1121/1.4743881.
URL http://scitation.aip.org/content/asa/journal/jasa/108/5/10.1121/1.4743881

[30] D. Wilson, J. Noble, C. M.A., Sound propagation in the nocturnal boundary layer, Journal of Atmospheric Sciences 60 (20) (2003) 2473–2486. doi:10.1175/1520-0469(2003)060<2473:SPITNB>2.0.CO;2.
URL https://doi.org/10.1175/1520-0469(2003)060<2473:SPITNB>2.0.CO;2

[31] D. Wilson, E. Andreas, J. Weatherly, C. Pettit, E. Patton, P. Sullivan, Characterization of uncertainty in outdoor sound propagation predictions, The Journal of the Acoustical Society of America 121 (5) (2007) EL177–EL183. doi:10.1121/1.2716159.
URL http://dx.doi.org/10.1121/1.2716159

[32] D. Wilson, M. Lewis, J. Weatherly, E. Andreas, Dependence of predictive skill for outdoor narrowband and broadband sound levels on the atmospheric representation, Noise Control Engineering Journal 56 (6) (2008) 465–477. doi:10.3397/1.3010733.
URL https://doi.org/10.3397/1.3010733

[33] D. Wilson, C. Pettit, V. Ostashev, S. Vecherin, Description and quantification of uncertainty in outdoor sound propagation calculations, The Journal of the Acoustical Society of America 136 (3) (2014) 1013–1028. doi:http://dx.doi.org/10.1121/1.4890644.
URL http://asa.scitation.org/doi/full/10.1121/1.4890644

[34] J. Atvars, L. Schubert, H. Ribner, Refraction of sound from a point source placed in an air jet, The Journal of the Acoustical Society of America 37 (1) (1965) 168–170. doi:10.1121/1.1909297.
URL http://dx.doi.org/10.1121/1.1909297

[35] J. Atvars, L. Schubert, E. Grande, H. Ribner, Refraction of sound by jet flow or jet temperature, Book, Institute for Aerospace Studies, University of Toronto (1965).

[36] E. Grande, Refraction of injected sound by a very cold nitrogen jet, The Journal of the Acoustical Society of America 38 (6) (1965) 1063–1064. doi:10.1121/1.1909848.
URL http://dx.doi.org/10.1121/1.1909848

[37] E. Grande, Refraction of sound by jet flow and jet temperature II, Report, University of Toronto (1966).

[38] G. MacGregor, H. Ribner, H. Lam, "Basic" jet noise patterns after deletion of convection and refraction effects: Experiments vs. theory, Journal of Sound and Vibration 27 (4) (1973) 437–454. doi:10.1016/s0022-460x(73)80356-6.
URL http://dx.doi.org/10.1016/S0022-460X(73)80356-6

[39] L. Schubert, Numerical study of sound refraction by a jet flow. I. Ray acoustics, The Journal of the Acoustical Society of America 51 (2A) (1972) 439–446. doi:10.1121/1.1912861.
URL http://dx.doi.org/10.1121/1.1912861

[40] L. Schubert, Numerical study of sound refraction by a jet flow. II. Wave acoustics, The Journal of the Acoustical Society of America 51 (2A) (1972) 447–463. doi:10.1121/1.1912862.
URL http://dx.doi.org/10.1121/1.1912862

[41] P. Mungur, H. Plumblee, P. Doak, Analysis of acoustic radiation in a jet flow enviroment, Journal of Sound and Vibration 36 (1) (1974) 21–52. doi:10.1016/S0022-460X(74)80341-X.
URL http://dx.doi.org/10.1016/S0022-460X(74)80341-X

[42] R. J. Astley, W. Eversman, Wave envelope elements for acoustical radiation in inhomogeneous media, Computers and structures 30 (4)

(1988) 801–810, special Issue: Computational Engineering Mechanics. doi:https://doi.org/10.1016/0045-7949(88)90108-3.
URL http://www.sciencedirect.com/science/article/pii/0045794988901083

[43] A. Cummings, High temperature effects on the radiation impedance of an unflanged duct exit, Journal of Sound and Vibration 52 (2) (1977) 299–304. doi:10.1016/0022-460X(77)90648-4.
URL http://dx.doi.org/10.1016/0022-460X(77)90648-4

[44] C. Morfey, P. Joseph, Shear layer refraction corrections for off-axis sources in a jet flow, Journal of Sound and Vibration 239 (4) (2001) 819–848. doi:10.1006/jsvi.2000.3218.
URL http://dx.doi.org/10.1006/jsvi.2000.3218

[45] C. Tam, L. Auriault, Mean flow refraction effects on sound radiated from localized sources in a jet, Journal of Fluid Mechanics 370 (1998) 149–174. doi:10.1017/s0022112098001852.
URL https://doi.org/10.1017/S0022112098001852

[46] A. da Silva, G. Scavone, A. Lefebvre, Sound reflection at the open end of axisymmetric ducts issuing a subsonic mean flow: A numerical study, Journal of Sound and Vibration 327 (3) (2009) 507–528. doi:10.1016/j.jsv.2009.06.027.
URL https://doi.org/10.1016/j.jsv.2009.06.027

[47] A. Hirschberg, M. Hoeijmakers, Comments on the low frequency radiation impedance of a duct exhausting a hot gas, The Journal of the Acoustical Society of America 136 (2) (2014) 84–89. arXiv:https://doi.org/10.1121/1.4885540, doi:10.1121/1.4885540.
URL https://doi.org/10.1121/1.4885540

[48] H. Levine, J. Schwinger, On the radiation of sound from an unflanged circular pipe, Physical review 73 (4) (1948) 383. doi:10.1103/physrev.73.383.

URL https://journals.aps.org/pr/abstract/10.1103/PhysRev.73.383

[49] J. Andreopoulos, Wind tunnel experiments on cooling tower plumes: Part 1—in uniform crossflow, Journal of Heat Transfer 111 (4) (1989) 941–948. doi:10.1115/1.3250809.
URL http://dx.doi.org/10.1115/1.3250809

[50] J. Andreopoulos, Wind tunnel experiments on cooling tower plumes: Part 2—in a nonuniform crossflow of boundary layer type, Journal of Heat Transfer 111 (4) (1989) 949–955, 10.1115/1.3250810. doi:10.1115/1.3250810.
URL http://dx.doi.org/10.1115/1.3250810

[51] R. Huang, J. Lan, Characteristic modes and evolution processes of shear-layer vortices in an elevated transverse jet, Physics of Fluids 17 (3) (2005) 034103. doi:10.1063/1.1852575.
URL http://dx.doi.org/10.1063/1.1852575

[52] R. Huang, C. Hsu, Turbulent flows of an acoustically excited elevated transverse jet, American Institute of Aeronautics and Astronautics Journal 50 (9) (2012) 1964–1978. doi:10.2514/1.j051595.
URL https://doi.org/10.2514/1.J051595

[53] N. Saïd, H. Mhiri, G. Le Palec, P. Bournot, Experimental and numerical analysis of pollutant dispersion from a chimney, Atmospheric Environment 39 (9) (2005) 1727–1738. doi:10.1016/j.atmosenv.2004.11.040.
URL https://doi.org/10.1016/j.atmosenv.2004.11.040

[54] N. Said, S. Habli, H. Mhiri, H. Bournot, G. Le Palec, Flow field measurement in a crossflowing elevated jet, Journal of Fluids Engineering 129 (5) (2007) 551–562. doi:10.1115/1.2717614.
URL http://dx.doi.org/10.1115/1.2717614

[55] M. Adaramola, D. Sumner, D. Bergstrom, Effect of velocity ratio on the streamwise vortex structures in the wake of a stack, Journal of Fluids and

Structures 26 (1) (2010) 1–18. doi:10.1016/j.jfluidstructs.2009.07.007.
URL http://dx.doi.org/10.1016/j.jfluidstructs.2009.07.007

[56] O. Eiff, J. Kawall, J. Keffer, Lock-in of vortices in the wake of an elevated round turbulent jet in a crossflow, Experiments in Fluids 19 (3) (1995) 203–213. doi:10.1007/bf00189709.
URL https://doi.org/10.1007/BF00189709

[57] O. Eiff, J. Keffer, On the structures in the near-wake region of an elevated turbulent jet in a crossflow, Journal of Fluid Mechanics 333 (1997) 161–195. doi:10.1017/s0022112096004314.
URL http://dx.doi.org/10.1017/s0022112096004314

[58] J. Andreopoulos, W. Rodi, Experimental investigation of jets in a crossflow, Journal of Fluid Mechanics 138 (-1) (1984) 93–127. doi:10.1017/s0022112084000057.
URL http://dx.doi.org/10.1017/s0022112084000057

[59] J. Andreopoulos, On the structure of jets in a crossflow, Journal of Fluid Mechanics 157 (1985) 163–197. doi:10.1017/S0022112085002348.
URL http://dx.doi.org/10.1017/S0022112085002348

[60] T. Fric, A. Roshko, Vortical structure in the wake of a transverse jet, Journal of Fluid Mechanics 279 (1994) 1–47. doi:10.1017/s0022112094003800.
URL http://dx.doi.org/10.1017/s0022112094003800

[61] Y. Kamotani, I. Greber, Experiments on a turbulent jet in a cross flow, American Institute of Aeronautics and Astronautics Journal 10 (11) (1972) 1425–1429. doi:10.2514/3.50386.
URL http://dx.doi.org/10.2514/3.50386

[62] R. Kelso, T. Lim, A. Perry, A. Lim, An experimental study of round jets in cross-flow, Journal of Fluid Mechanics 306 (1) (1996) 111–144. doi:

10.1017/s0022112096001255.
URL http://dx.doi.org/10.1017/s0022112096001255

[63] R. Kelso, T. Lim, A. Perry, New experimental observations of vortical motions in transverse jets, Physics of Fluids 10 (9) (1998) 2427–2429. doi:10.1063/1.869761.
URL http://dx.doi.org/10.1063/1.869761

[64] S. Sherif, R. Pletcher, Measurements of the thermal characteristics of heated turbulent jets in crossflow, Journal of Heat Transfer 111 (4) (1989) 897. doi:10.1115/1.3250803.
URL http://dx.doi.org/10.1115/1.3250803

[65] S. Sherif, R. Pletcher, Jet-wake thermal characteristics of heated turbulent jets in crossflow, Journal of Thermophysics and Heat Transfer 5 (2) (1991) 181–191. doi:10.2514/3.246.
URL http://dx.doi.org/10.2514/3.246

[66] L. Su, M. Mungal, Simultaneous measurements of scalar and velocity field evolution in turbulent crossflowing jets, Journal of Fluid Mechanics 513 (2004) 1–45. doi:10.1017/s0022112004009401.
URL https://doi.org/10.1017/S0022112004009401

[67] M. Esmaeili, A. Afshari, F. Jaberi, Turbulent mixing in non-isothermal jet in crossflow, International Journal of Heat and Mass Transfer 89 (2015) 1239–1257. doi:10.1016/j.ijheatmasstransfer.2015.05.055.
URL http://dx.doi.org/10.1016/j.ijheatmasstransfer.2015.05.055

[68] F. Galeazzo, G. Donnert, P. Habisreuther, N. Zarzalis, R. Valdes, W. Krebs, Measurement and simulation of turbulent mixing in a jet in crossflow, Journal of Engineering for Gas Turbines and Power 133 (6) (2011) 061504. doi:10.1115/1.4002319.
URL https://doi.org/10.1115/1.4002319

[69] F. Galeazzo, G. Donnert, C. Cárdenas, J. Sedlmaier, P. Habisreuther, N. Zarzalis, C. Beck, W. Krebs, Computational modeling of turbulent mixing in a jet in crossflow, International Journal of Heat and Fluid Flow 41 (2013) 55–65. doi:10.1016/j.ijheatfluidflow.2013.03.012.
URL https://doi.org/10.1016/j.ijheatfluidflow.2013.03.012

[70] A. Hoda, S. Acharya, Predictions of a film coolant jet in crossflow with different turbulence models, Journal of Turbomachinery-Trans. ASME 122 (3) (2000) 558–569. doi:10.1115/1.1302322.
URL https://doi.org/10.1115/1.1302322

[71] S. Muppidi, K. Mahesh, Study of trajectories of jets in crossflow using direct numerical simulations, Journal of Fluid Mechanics 530 (2005) 81–100. doi:10.1017/S0022112005003514.
URL http://dx.doi.org/10.1017/S0022112005003514

[72] S. Muppidi, K. Mahesh, Two-dimensional model problem to explain counter-rotating vortex pair formation in a transverse jet, Physics of Fluids (1994-present) 18 (8) (2006) 085103. doi:10.1063/1.2236304.
URL http://dx.doi.org/10.1063/1.2236304

[73] S. Muppidi, K. Mahesh, Direct numerical simulation of round turbulent jets in crossflow, Journal of Fluid Mechanics 574 (2007) 59–84. doi:10.1017/S0022112006004034.
URL http://dx.doi.org/10.1017/S0022112006004034

[74] D. Rusch, L. Blum, A. Moser, T. Roesgen, Turbulence model validation for fire simulation by CFD and experimental investigation of a hot jet in crossflow, Fire Safety Journal 43 (6) (2008) 429–441. doi:10.1016/j.firesaf.2007.11.005.
URL http://dx.doi.org/10.1016/j.firesaf.2007.11.005

[75] P. Schlatter, S. Bagheri, D. Henningson, Self-sustained global oscillations in a jet in crossflow, Theoretical Computational Fluid Dynamics 25 (1-4)

(2010) 129–146. doi:10.1007/s00162-010-0199-1.
URL http://dx.doi.org/10.1007/s00162-010-0199-1

[76] ANSYS, ANSYS Mechanical APDL Theory Reference, ANSYS, Inc, 2600 ANSYS Drive, Canonsburg, PA 15317, 18th Edition (01 2017).

[77] ANSYS, ANSYS Mechanical APDL Acoustic Analysis Guide, ANSYS, Inc, 2600 ANSYS Drive, Canonsburg, PA 15317, 18th Edition (01 2017).

[78] A. Pierce, Wave equation for sound in fluids with unsteady inhomogeneous flow, The Journal of the Acoustical Society of America 87 (6) (1990) 2292–2299. arXiv:https://doi.org/10.1121/1.399073, doi:10.1121/1.399073.
URL https://doi.org/10.1121/1.399073

[79] P. Bergmann, The wave equation in a medium with a variable index of refraction, The Journal of the Acoustical Society of America 17 (4) (1946) 329–333. arXiv:https://doi.org/10.1121/1.1916333, doi:10.1121/1.1916333.
URL https://doi.org/10.1121/1.1916333

[80] G. Ross, R. C. Chivers, A note on the helmholtz equations for acoustic waves in inhomogeneous media, The Journal of the Acoustical Society of America 80 (5) (1986) 1536–1539. arXiv:https://doi.org/10.1121/1.394362, doi:10.1121/1.394362.
URL https://doi.org/10.1121/1.394362

[81] K.-J. Bathe, Finite element procedures, Klaus-Jurgen Bathe, 2006.

[82] C. Bailly, D. Juve, Numerical solution of acoustic propagation problems using linearized euler equations, American Institute of Aeronautics and Astronautics Journal 38 (1) (2000) 22–29. doi:https://doi.org/10.2514/2.949.
URL https://doi.org/10.2514/2.949

[83] R. Ewert, W. Schröder, Acoustic perturbation equations based on flow decomposition via source filtering, Journal of Computational Physics 188 (2) (2003) 365–398. doi:10.1016/S0021-9991(03)00168-2.
URL http://www.sciencedirect.com/science/article/pii/S0021999103001682

[84] F. Treysséde, G. Gabard, M. Ben Tahar, A mixed finite element method for acoustic wave propagation in moving fluids based on an Eulerian-Lagrangian description, The Journal of the Acoustical Society of America 113 (2) (2003) 705–716. arXiv:https://doi.org/10.1121/1.1534837, doi:10.1121/1.1534837.
URL https://doi.org/10.1121/1.1534837

[85] F. Treysséde, M. Ben Tahar, Comparison of a finite element model with a multiple-scales solution for sound propagation in varying ducts with swirling flows, The Journal of the Acoustical Society of America 115 (6) (2004) 2716–2730. arXiv:https://doi.org/10.1121/1.1707084, doi:10.1121/1.1707084.
URL https://doi.org/10.1121/1.1707084

[86] A. Holmberg, A. Kierkegaard, C. Weng, A frequency domain linearized Navier–Stokes method including acoustic damping by eddy viscosity using RANS, Journal of Sound and Vibration 346 (2015) 229–247. doi:https://doi.org/10.1016/j.jsv.2015.02.030.
URL http://www.sciencedirect.com/science/article/pii/S0022460X15001649

[87] A. Kierkegaard, S. Boij, G. Efraimsson, A frequency domain linearized Navier–Stokes equations approach to acoustic propagation in flow ducts with sharp edges, The Journal of the Acoustical Society of America 127 (2) (2010) 710–719. arXiv:https://doi.org/10.1121/1.3273899, doi:10.1121/1.3273899.
URL https://doi.org/10.1121/1.3273899

[88] C. Howard, B. Cazzolato, Acoustic analyses using MATLAB® and Ansys®, CRC Press, 2014.

[89] F. Menter, Two-equation eddy-viscosity turbulence models for engineering applications, American Institute of Aeronautics and Astronautics Journal 32 (8) (1994) 1598–1605. doi:10.2514/3.12149.
URL http://dx.doi.org/10.2514/3.12149

[90] W. Sutherland, LII. the viscosity of gases and molecular force, The London, Edinburgh, and Dublin Philosophical Magazine and Journal of Science 36 (223) (1893) 507–531. doi:10.1080/14786449308620508.
URL http://dx.doi.org/10.1080/14786449308620508

[91] S. Smith, M. Mungal, Mixing, structure and scaling of the jet in cross-flow, Journal of Fluid Mechanics 357 (1998) 83–122. doi:10.1017/s0022112097007891.
URL http://dx.doi.org/10.1017/s0022112097007891

[92] D. Bies, C. Hansen, C. Howard, Engineering Noise Control: Theory and Practice, 5th Edition, CRC Press, 2017.

[93] International Organization for Standardization, ISO 9613-2:1996 Acoustics - Attenuation of sound during propagation outdoors – Part 2: General method of calculation (1996).

Appendix I

Sound propagation through elevated, heated jets in cooler cross-flow: An experimental study

Statement of Authorship

Title of Paper	Sound proapagation through elevated, heated jets in cooler cross-flow: An experimental study
Publication Status	☐ Published ☐ Accepted for Publication ☐ Submitted for Publication ☑ Unpublished and Unsubmitted w ork w ritten in manuscript style
Publication Details	Leav, O. Y., Cazzolato, B. S., and Howard, C. Q. (2020) "Sound propagation through elevated, heated jets in cooler cross-flow: An experimental study", The Journal of the Acoustical Society of America.

Principal Author

Name of Principal Author (Candidate)	Orddom Leav		
Contribution to the Paper	Conducted the literature review, design and build of the experiments, performed the experimental tests, and completed the signal processing and data analysis. The manuscript was written by the principle author.		
Overall percentage (%)	80%		
Certification:	This paper reports on original research I conducted during the period of my Higher Degree by Research candidature and is not subject to any obligations or contractual agreements with a third party that would constrain its inclusion in this thesis. I am the primary author of this paper.		
Signature		Date	21/04/20

Co-Author Contributions

By signing the Statement of Authorship, each author certifies that:

i. the candidate's stated contribution to the publication is accurate (as detailed above);

ii. permission is granted for the candidate in include the publication in the thesis; and

iii. the sum of all co-author contributions is equal to 100% less the candidate's stated contribution.

Name of Co-Author	Benjamin Seth Cazzolato		
Contribution to the Paper	Supervised the development of work, helped in data interpreting, provided comments and edited manuscript.		
Signature		Date	22/4/2020

Name of Co-Author	Carl Quentin Howard		
Contribution to the Paper	Supervised the development of work, helped in data interpreting, provided comments and edited manuscript.		
Signature		Date	22/4/2020

Please cut and paste additional co-author panels here as required.

Sound Propagation Through Elevated, Heated Jets in Cooler Cross-Flow: An Experimental Study

O. Leav,[1] B. Cazzolato,[1] and C. Howard[1]

School of Mechanical Engineering, University of Adelaide, Adelaide, Australia[a)]

(Dated: 21 April 2020)

Sound propagation through hot exhaust plumes with cooler cross-winds is present in many real world systems. One particular example is the sound propagation from exhaust stacks attached to thermal power stations in particular open cycle gas turbines. The research presented in this paper investigates the sound propagation from a reduced-scale elevated exhaust stack with a cross-flow in a wind tunnel. Flow and temperature measurements of the reduced scale experiments provide insight into the complex flow and temperature field. Results from the acoustic measurements show the change in the sound directivity arising from the inclusion of the hot exhaust plume, leading to non-axisymmetric sound directivity. With the use of acoustic directivity plots, the hot jet in cooler cross-flow shows a concentration of sound downwind of the exhaust stack outlet. In certain cross-flow conditions, the hot exhaust plume can increase the sound observed downwind by up to 11 dB when compared to the scenario of sound propagation from an exhaust stack in the absence of a heated jet or cooler cross-flow. The paper investigates the acoustic directivity for different radial distances from the exhaust stack, acoustic frequencies, jet temperatures, and cross-flow free-stream velocity. The results from this paper emphasise the importance of taking into consideration the hot exhaust plume with cooler cross-flow when estimating sound levels downwind of the stack.

[a)]Electronic mail: orddom.leav@adelaide.edu.au

I. BACKGROUND

Outdoor sound propagation models commonly use monopole radiators and depends on the atmospheric conditions, the acoustic properties of the ground, the terrain, and geometry between source and receiver. An example of such a case is sound radiation from open-cycle gas turbines (OCGT), which has been shown in the literature to produce higher than expected low frequency noise levels in communities[1–9]. Typical low frequency noise for OCGT is within the range of 16 Hz to 63 Hz and has been reported in literature[1–10]. It has been reported that the low frequency noise levels from OCGT have caused the following impact on communities: perceived 'annoyance' or throbbing[4], 'beating' sensation in the chest[5,6,9], nausea[4], and acoustic excitation in structures with low resonance frequencies[4,9]. These high community noise levels observed from OCGT are not typically seen in combined cycle gas turbines, which use both Brayton and Rankin cycles and thus exhaust is at lower temperatures, which improves the efficiency of absorptive silencers[1,7].

Sound levels in neighbourhoods near exhaust stacks are commonly predicted using multiple ISO standards[11–13]. ISO 10494:2018 is used to estimate the sound power and sound pressure levels from exhaust stacks[13]. The sound propagation is modelled using ISO 9613-1:1993[11] and ISO 9613-2:1996[12]. For simple sound predictions ISO 9613-2:1996[12] states that a simple monopole source can be used, but for more complex sound sources, a directivity correction factor can be applied. If a single monopole source cannot be used, then multiple monopole sources can be used to represent a discretised line source or discretised area sound source. A single value correction factor based on the meteorological conditions obtained from the 'local authorities' can be applied to the sound propagation model. These sound prediction models can also be extended using numerical software to include the atmospheric boundary layer (thermal and velocity gradients) and complex terrains. There are also multiple literature reviews[14–19] on the topic of quantifying atmospheric sound propagation, which involves more sophisticated numerical modelling techniques for predicting sound in the far-field. However, these atmospheric sound propagation models do not take into consideration the complex sound field from the exhaust stack and the acoustic interaction with the exhaust plume.

Hot stacks are essentially an elevated jet in cross-flow (JICF), which is shown schematically in Fig. 1. The elevated JICF is a cylindrical duct protruding from a ground-plane, with a jet flow exiting the duct. The flow structures associated with isothermal elevated JICF have been studied experimentally by various researchers[20–26] and to a lesser extent non-isothermal elevated JICF

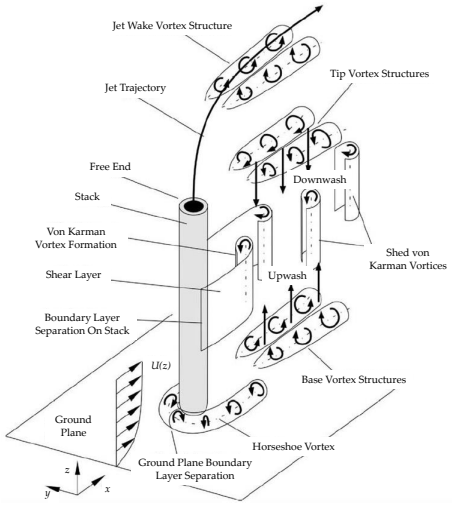

FIG. 1: Schematic of the dominant fluid dynamic structures associated with an elevated JICF for a value of R that is in the jet dominated regime[20].

have also been investigated[27–29]. The fluid structures are governed by the JICF momentum flux ratio, defined as the following:

$$R = \sqrt{\frac{\rho_j u_j^2}{\rho_{cf} u_{cf}^2}} \quad , \tag{1}$$

where ρ_j is the jet air density, ρ_{cf} is the cross-flow free stream air density, u_j is the average jet exit velocity, and u_{cf} is the cross-flow free stream velocity. The values for R in OCGTs are typically in a 'jet-dominated' regime[20,24,25,29]. The unique flow structures that form in this regime are the following: deflected jet, jet shear layer, counter rotating vortex pairs, and stack shear layer[20].

Research has shown that the sound radiation from exhaust ducts may be quite complex. One of the earliest studies for sound radiation from gas turbine exhaust stacks was conducted by Wells and Crocker[30], where they investigated the sound radiation from an exhaust duct in the absence of flow and temperature. This was an analytical and experimental study that has shown with directivity results an axisymmetric sound radiation with an acoustic lobe forming on-axis at 0°. A similar experimental studies have been conducted[31–33], with sound radiation from exhaust ducts in the absence of flow in an anechoic environment and show a similar outcome with a lobe forming on-axis as the acoustic frequency increases.

When the exhaust from a stack enters the atmosphere, a jet shear layer forms. It is known that in the presence of a shear layer sound refraction occurs[34,35]. The sound refraction due to the shear

layer can be extended to non-isothermal jet shear layers, showing significant sound refraction[36–38]. The change in sound directivity from sound refraction becomes more pronounced with an increase in jet Mach number M_j, jet temperature T_j, and acoustic frequency. Mungur, Plumblee, and Doak[39] showed that for isothermal jets, the location at which the sound directivity measurements are taken is also critical, with the developing jet shear layer downstream causing continual refraction at increasing duct diameters ($2D - 4$‘$0D$, where D is the duct diameter) from the exhaust outlet. Cummings[40] has conducted an experimental study for a reduced-scale boiler flue-gas stack, where he investigated the radiation impedance and transmission loss for an unflanged exhaust duct with a heated exhaust jet ($T_j = 300\,°\mathrm{C}$). Further numerical work was undertaken by Astley and Eversman[41] using similar test parameters as Cummings[40] and the transmission loss at the duct opening as validation. Using an acoustic FE solver with the Helmholtz equation, Astley and Eversman[41] has shown with sound directivity results the refraction of sound from a heated jet at varying directivity radii ($1D < r < 40D$) and a Helmholtz number, ($ka = 2.0$, where k is the wavenumber and a is the duct radius). Such work on jet shear layer refraction was also extended to OCGT exhaust flow with near-field measurements by Björk[1], which showed that sound is refracted by the jet shear layer and this was measured in both a real OCGT exhaust stack and in a scaled model[1].

It is hypothesised that sound radiating from OCGT exhaust stacks forms strong lobes, that under certain meteorological conditions, leads to the amplification of sound downstream as it interacts with the bent-over hot exhaust plume. Earlier work by Björk[1], stated that a bent-over hot exhaust plume with the thermal gradients and varying wind conditions would cause variations in sound levels downstream of up to $\pm 5\,\mathrm{dB}$ in the neighbourhood. However, Björk[1] only measured the sound in the near field; from the real exhaust stack at approximately $1.5D$ and approximately $3D$ with the small scale model. In the near-field the onset of refraction begins and cross-flow effects are yet to occur. Work previously done by Leav, Cazzolato, and Howard[42,43] has shown numerically that the propagation path of sound is affected by the temperature of the plume for both a 2-D non-isothermal ground-level JICF and for a 3-D elevated JICF. They have also shown that the propagation path of sound is dependent on the acoustic frequency and the distance from the exhaust outlet. Upstream of the exhaust stack the sound remains relatively unaffected by the cross-wind, with elliptical acoustic spreading observed[43]. However, downstream of the exhaust stack the sound field forms a highly directed lobe of sound. The numerical simulations were conducted using steady-state simulations with isotropic Reynolds-averaged Navier-Stokes equations (RANS)

models, which leads to limitations, namely, highly unsteady transient small-scale structures are not reproduced using RANS in Computational Fluid Dynamics (CFD). However, the steady state CFD model does reproduce coherent vortex structures downstream (counter rotating vortex pairs) that in reality would dissipate with the presence of the turbulence structures from the incoming cross-flow. The counter rotating vortex pairs provide a strong thermal gradient downstream that continues to refract as the sound as it propagates downstream. For the 3-D elevated JICF, an acoustically reflective duct and hard reflective ground produces complex sound diffraction patterns[43].

This paper experimentally investigates the sound directivity of an elevated hot exhaust jet in cooler cross-flow. A reduced scale (1:125) experimental rig is used to emulate the flow and acoustic conditions of a 190 MW OCGT. This was tested at the University of Adelaide's Wind Tunnel under three different flow conditions described in Fig. 2. The experimental findings from the reduced scale experiments are used to analyse the effects of the plume on the propagation of sound. The layout of the paper is as follows. A description of the experimental set up and the signal processing techniques used for the acoustic and flow measurements are discussed in Section II. The flow and temperature measurements are presented and discussed in Section III. In Section IV the acoustic directivity measurements are detailed. A discussion of the experimental findings in relation to real OCGT is presented in Section V. The main conclusions of the paper are summarised in Section VI.

II. EXPERIMENTAL APPARATUS AND METHODOLOGY

Experiments on real OCGT are difficult due to the practicality of controlling flow and speed, as well as taking measurements to characterise flow temperature, flow speed, and sound pressure. The aim of this research is to simulate the flow, temperature and acoustic parameters of a full-scale 190 MW OCGT (SGT5-2000E from Siemens[44]) with a small-scale exhaust rig where the relevant parameters can be controlled. This section will discuss the experimental apparatus representing the OCGT, the commissioning of the experimental apparatus at the University of Adelaide Wind Tunnel, shown in Fig. 3a, instrumentation, and the signal processing techniques used to process the acoustic data.

The experimental apparatus for simulating the exhaust flow and sound is shown in Fig. 3b. Table I shows the non-dimensional parameters relevant to full-scale OCGTs used for the exhaust rig. The values used in Table I are based on a 190 MW OCGT from Siemens (SGT5-2000E)[44], and

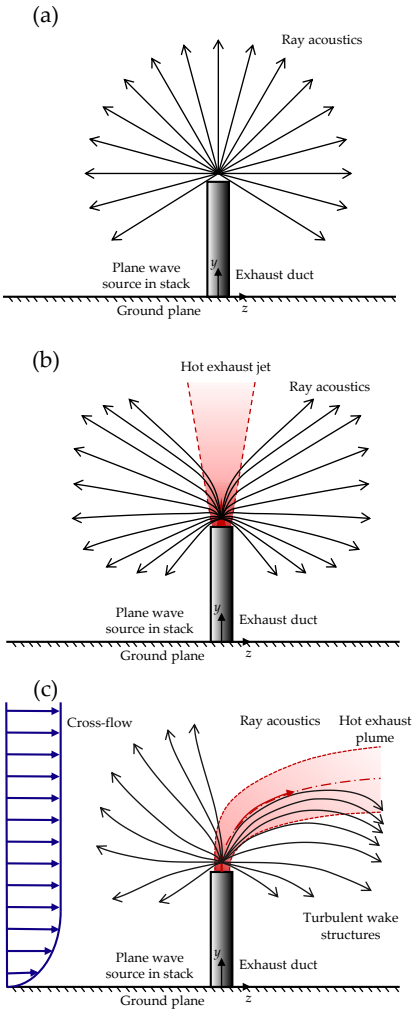

FIG. 2: Schematics of the experimental acoustic testing in the Adelaide Wind Tunnel of three different systems; (a) sound propagation through the exhaust stack in a stationary field, (b) sound propagation through a heated jet with no cross-flow, and (c) sound propagation through a non-isothermal heated JICF.

the experimental setup is approximately 1 : 125 scale. A centrifugal blower (Leister Airpack) was used to generate the flow in the duct network. The inlet and outlet of the blower were connected to an acoustic silencer on each end to minimise the sound from the blower affecting acoustic measurements. The flow travelled through a stainless-steel duct network with an outer diameter of 50.8 mm and an inner diameter of 47.6 mm ($D = 2a$). The flow from the outlet silencer to the Airpack blower was split into a Y-junction and was passed through two 16 kW Leister 61L System Air Heaters capable of variable temperature control, and then joined again with a 45° Y-

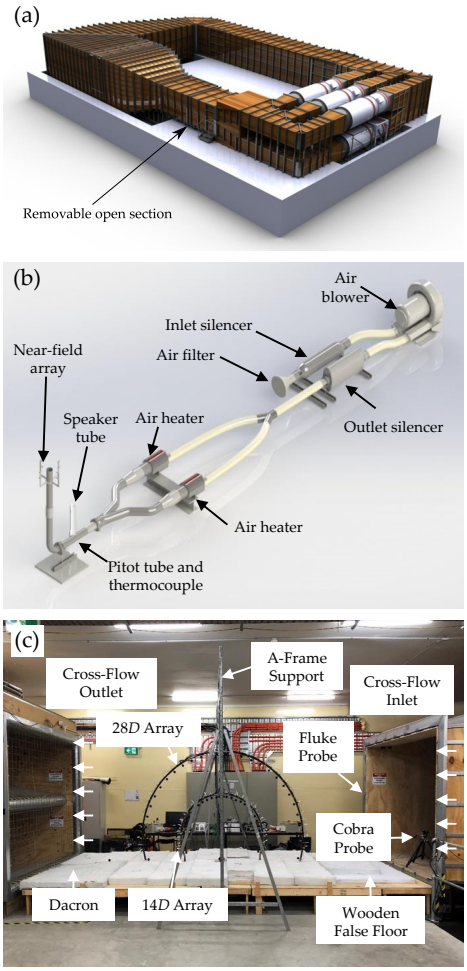

FIG. 3: Images showing (a) the closed-loop four-sided University of Adelaide Wind and the removable test section, (b) an illustration of the reduced-scale exhaust network experimental setup, and (c) a photo of the experimental set up at the University of Adelaide's Wind Tunnel showing the full span of the commissioned test set up.

junction into a single flow. Two heaters were used in lieu of a single unit due to the lower cost and practicality of delivering the required electricity. The flow in the duct network was measured with a pitot tube coupled to a differential pressure transducer (ManyYear Technology MPT-721). The temperature in the duct network was measured using k-type thermocouples. The flow then passed through a 90° bend to change the direction of flow to vertical before entering an automotive catalytic converter, which comprises of Corning Celcor with square pores, that acted to straighten the flow. The flow beyond the catalytic converter passed through a straight vertical section of pipe before exiting as a jet. The exhaust network was clad with Rockwool sectional pipe insulation to

TABLE I: Physical parameters for the experimental tests.

Parameters	Equation/Expression	Value	Units
Duct diameter	D	47.6	mm
Duct length	$L = 10D$	476	mm
Jet temperature	T_j	300-773	K
Momentum flux ratio	$R = \sqrt{\frac{\rho_j u_j^2}{\rho_{cf} u_{cf}^2}}$	$5 - 12.5$	
Helmholtz number	$ka = \frac{\pi f D}{c_j}$	$0.85 - 1.70$	-
Mach number	$M = \frac{u_j}{c_j}$	0.1	-

reduce the heat loss in the pipe network and attenuate structural acoustic radiation.

Fig. 3c shows a photograph of the experimental setup in the University of Adelaide's Wind Tunnel. A wooden decking, acting as a ground-plane, was placed over the exhaust rig. Acoustic foam (50 mm thick Dacron) was placed on the wooden decking to reduce acoustic reflections from the ground plant and to provide an anechoic surface above 500 Hz, thereby reducing the complexity of the sound field so that the effect of the plume, cross-flow and sound interaction could be examined. The wooden decking is used so that only the exhaust stack interacts with the flow, with the rest of the apparatus shielded from the flow. The cross-sectional area of the wind tunnel cross-flow is 2.75 m $\times$ 2 m and the available test section ground area covers a span of 3.5 m $\times$ 5.5 m. The cross-flow wind velocity was measured with a Cobra Probe 209 and a Fluke 922 airflow meter at discrete points in the cross-flow free-stream velocity.

The sound pressure was measured with 62 1/4" G.R.A.S. 40PH Free-Field Microphones along two circular arrays with radii $14D$ and $28D$ from the exhaust stack outlet. The microphones, according to the manufacturer, have a flat frequency response ($\pm$1 dB) within a frequency range of 20 Hz to 10 kHz. Microphone wind screens (G.R.A.S. AM0071 Windscreen) designed for the 1/4" G.R.A.S. 40PH Free-Field Microphones were used to minimise the flow induced noise. It should also be noted that further signal processing of the acoustic measurements was undertaken to minimise the effects of flow induced noise from measuring the acoustic pressure in the wind tunnel with the jet flow and cross-flow present. The microphones in Fig. 3c were placed along a circular arc spanning $\pm 105°$, with each microphone spaced 7.5°, except for the centre microphone at 0° being replaced by two microphones at $\pm 2.5°$ for the $14D$ array arc and for the $28D$

arc the centre microphone at 0° was removed to accommodate the vertical support. The microphone arrays were positioned parallel to the cross-flow free stream. The microphone arrays were supported by a frame, designed to have minimal flow and acoustic impact. The microphone signals were recorded by a NI (National Instruments) PXIe-4499 Sound and Vibration Module in a NI PXIe 1082 Chassis. The sound source used was uniform Gaussian white noise, generated from NI LABVIEW and the electrical signal was generated using a NI PXI-6221 Multifunction I/O Module. The sampling frequency was 25.6 kHz. The uniform white noise was passed through a dual channel analogue 4-pole Butterworth filter (Krohn-Hite Model 3362 Dual Channel Filter) designed with low-pass and high-pass filter to generate one-third octave bands over several frequencies ($f = [3150\,\text{Hz}, 4000\,\text{Hz}, 5000\,\text{Hz}, 6300\,\text{Hz}]$ or $ka = [0.85, 1.08, 1.35, 1.70]$). The sound was generated using two compression drivers, a 50.8 mm (2 inch) DS18 PRO-DKH1 1000 W compression driver and the 50.8 mm (2 inch) TIMPANO TPT-DH2000 400 W compression driver to deliver relatively uniform power over the desired bandwidth.

The acoustic data was post-processed in the frequency domain using MATLAB. The spectral analysis used a Hanning window with an FFT length of 4096 and 1500 averages. The degree of linearity between the acoustic-electrical signal generated by the DAQ (x) and the acoustic pressures measured at the microphones (y) may be quantified using the coherence function:

$$\gamma_{xy}{}^2(f) = \frac{|G_{xy}(f)|^2}{G_{xx}(f)G_{yy}(f)} \tag{2}$$

where f is the frequency of interest, G_{xy} is the cross power spectra of the acoustic-electrical signal into the speaker and the microphone acoustic pressures, G_{xx} is the power spectra of the acoustic-electrical signal into speaker and G_{yy} are the power spectra of the microphone acoustic pressures[45]. The results in this paper are presented as the coherent output power at each microphone given by the following formula:

$$COP(f) = G_{yy} \times \gamma_{xy}{}^2 \tag{3}$$

The acoustic coherent output power was used, rather than the raw sound pressure levels, so that only sound correlated with the loudspeaker is analysed, and thus noise from the blowers, wind tunnel fan and flow induced noise is removed. The acoustic results for directivity presented in Section IV are calculated as:

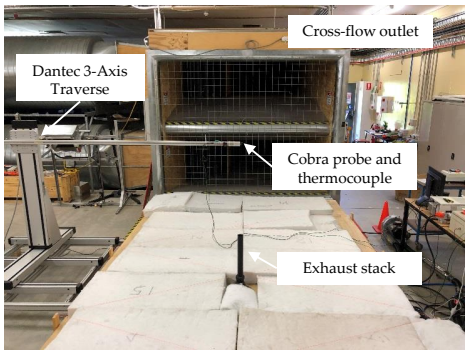

FIG. 4: Photo of the exhaust rig, the Dantec 3-Axis traverse for flow and temperature measurements at the University of Adelaide Wind Tunnel.

$$DI(f,\theta) = \frac{COP(f,\theta)}{COP_{av}} \tag{4}$$

where DI is the directivity index based on the acoustic coherent output power and not the standard formulation involving sound intensity[31], θ is the angular position from the centreline of the duct, and COP_{av} is the average acoustic coherent output power along the directivity arc. This method of presenting the coherent results was chosen to ensure that the sound field presented was coherent with the loudspeaker only and the incoherent sound from external sources are 'screened out' and not considered.

The flow and temperature measurements were conducted for the reduced-scale exhaust rig in the Adelaide Wind Tunnel. Fig. 4 shows the experimental setup for measuring flow and temperature. A Dantec three-axis transverse was used to accurately position the flow and temperature instrumentation. The flow velocity was measured with a Cobra Probe 209 at various positions in the flow and a Fluke 922 airflow meter was placed at a fixed position upwind of the exhaust stack as a reference velocity for the cross-flow. The Cobra Probe 209 is a dynamic multi-hole pressure probe that can measure all three Cartesian velocity components, and the corresponding pressures. The air velocity measurements from the Cobra Probe 209 were used to calculate the cross-flow free-stream velocity (w) and the turbulence intensities (TI) using:

$$I_{ww} = \frac{\sqrt{\overline{w'^2}}}{\overline{V}} = \frac{\sigma_w}{\overline{V}} \tag{5}$$

where w' is the fluctuating cross-flow free-stream velocity, and σ_w is the standard deviation of the cross-flow free-stream velocity.

It should be noted that there are limitations in measuring the velocities using a Cobra Probe 209. Due to the orientation of the Cobra Probe, only positive velocities can be measured for w, the cross-flow free-stream direction. This is due to the position of the holes at the head of the Cobra Probe for pressure measurements. Therefore, reverse flow measured for w saturates the signal and returns $0\,\mathrm{m\,s^{-1}}$ for those measurements. Note that the traverse arm is situated behind the Cobra Probe, and any reverse flow measurement would be compromised by the traverse. Additionally, the velocity limit of the sensor was $35\,\mathrm{m\,s^{-1}}$, and this velocity limit is near the maximum velocity of the isothermal jet, with Mach number 0.1. It should be noted that velocity measurements near the duct outlet may exceed the velocity limits.

Temperatures outside the duct and in the domain were measured using three k-type thermocouples. The three unique positions of the thermocouples are upwind of the exhaust stack at the Fluke 922 airflow meter, at the end of the Dantec three-axis traverse with the Cobra Probe 209, and downwind of the exhaust stack at the cross-flow outlet of the Adelaide Wind Tunnel. Due to the limitations of the wind tunnel, the ambient cross-flow temperature could not be held constant throughout the testing campaign. Testing was conducted on days with large temperature variations, with cross-flow temperatures varying from 26 °C to 36 °C. The large changes in temperature were not evident for small durations of measurements but were evident over multiple hours. Hence, to account for changes in the ambient temperature, a dimensionless temperature parameter based on an equation from Kamotani and Greber[46] was used:

$$\Theta = \frac{T - T_{cf}}{T_j - T_{cf}}, \tag{6}$$

where T is the measured temperature from the thermocouple at a point, T_j is the jet temperature from a thermocouple in the duct, and T_{cf} is the measured cross-flow temperature. The main difference in Eq. (6) and the equation in Kamotani and Greber[46] is that T_j is replaced with T_{max}, which is the maximum temperature measured in that particular temperature profile or temperature contour plane.

III. FLOW AND TEMPERATURE RESULTS

The experimental flow and temperature measurements for the reduced-scale elevated exhaust JICF are presented in this section for two different cases: isothermal (jet and cross-flow at identical ambient temperatures) and non-isothermal (heated jet in cooler cross-flow) JICF. The first set of

results presented in this section are the flow measurements for the isothermal JICF. The second set of results discussed are the temperature measurements for the heated JICF. Flow measurements were not taken for the heated JICF to prevent the Cobra Probe 209 from being damaged by the hot plume.

The flow measurements are presented as vertical (varying y) profiles at various positions upwind and downwind of the exhaust stack, along the Y-Z plane intercepting the centre of the duct ($x = 0$). Additional span-wise flow measurements were undertaken with varying heights ($y/D = [17, 18, 21]$) at $z/D = 8$ downwind of the exhaust stack. The span-wise measurements were limited to only three span-wise profiles due to the limited time available for measuring the flow at the wind tunnel. The experimental flow results for this section are presented with two different flow statistics: time-averaged velocity components and turbulence intensities.

The time-averaged velocity components (Cartesian) were measured to understand the isothermal JICF bulk fluid dynamics. Fig. 5a shows the cross-flow free-stream velocity, w, and corresponding turbulence intensities, I_{ww}, at various distance upwind and downwind of the duct outlet ($z/D = [-8, -4, 4, 8, 16]$), with the measurement along the Y-Z plane intercepting the centre of the duct ($x = 0$). For the upwind ($z/D = [-8, -4]$) velocity profiles, the velocity components are all relatively uniform, with small variations in the boundary layer. As the plume propagates downwind from the exhaust stack, from $z/D = 4$ to $z/D = 16$ the w component shows the following trends:

- a decrease in the maximum w velocity from $w \approx 18.4\,\mathrm{m\,s^{-1}}$ to $w \approx 7.2\,\mathrm{m\,s^{-1}}$, and
- an increase in the vertical (y) size of the plume.

All three trends listed are consistent with previous studies[20,27–29]. The following phenomena can explain these trends; as the plume propagates downwind, the plume spatially spreads and dissipates, with the entrainment of the cross-flow. The dissipation of the plume leads to the flow resembling the cross-flow free-stream profiles in Fig. 5a at $z = [-8D, -4D]$.

The incoming turbulence intensity was measured upwind of the exhaust stack to quantify the fluctuation in measured velocity. Fig. 5a shows that upwind of the stack ($z/D = [-8, -4]$) the turbulence intensity is relatively uniform in the cross-flow free-stream and shows an increase in turbulence intensity along the boundary layer. The increase in the TI in the boundary layer is due to the vorticity present in the boundary layer. It should be noted that the cross-flow free-stream turbulence intensity upwind of the exhaust stack in the reduced-scale model is relatively low (0.5%

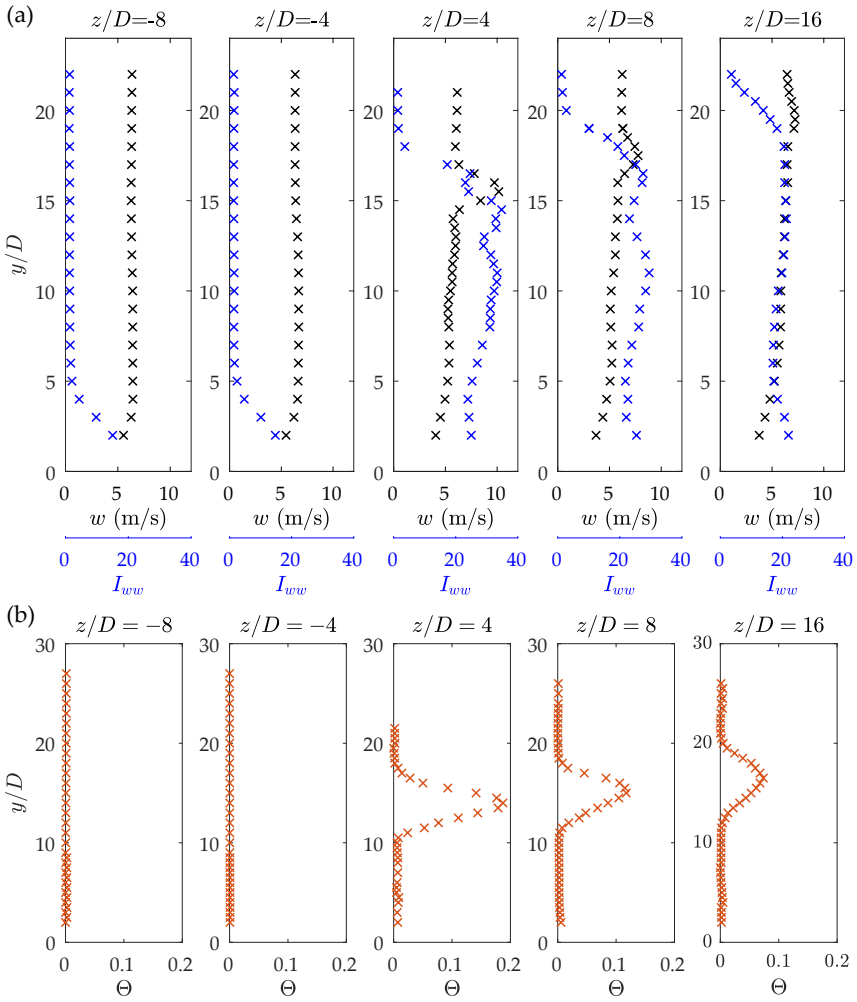

FIG. 5: The vertical profiles for (a) w, cross-flow free-stream velocity, and I_{ww}, turbulence intensity are shown with a jet ($T_j = 27\,^{\circ}\mathrm{C}$) in cross-flow. The vertical profiles for (b) Θ temperature are shown with a heated jet ($T_j = 500\,^{\circ}\mathrm{C}$) in cooler cross-flow. The vertical profiles are at varying distance downwind and upwind ($z/D = [-8, -4, 4, 8, 16]$), and measured along a plane with $x = 0$ (along the duct centreline).

to 1.5%) in comparison to the incoming turbulence intensity from atmospheric boundary layers (ABL) in nature. Hence in real OCGTs, the diffusion of the is expected to be faster than the diffusion of the plume observed in this experimental study. This can be supported by previous studies completed[27,28].

The cross-flow interacting with the elevated exhaust jet gives rise to complex features downwind of the exhaust stack due to the different flow structures that can be observed with TI measurements. Fig. 5a shows the TI has significantly increased downwind of the duct ($z/D = [4, 8, 16]$), in

comparison to upwind of the duct outlet ($z/D = [-8, -4]$). This is due to the incoming cross-flow interacting with the stack and jet to produce commonly observed fluid dynamic features, namely the plume, jet-wake, and stack-wake. There is also a distinguishing difference in TI for the plume and cross-flow free-stream, where the cross-flow free-stream TI is approximately 1%. From this, it can be ascertained that as the plume propagates the core of the plume increases in height downwind. The overall TI at $z/D = [4, 8, 16]$ reduces as the plume propagates and dissipates into the cross-flow. The TI measurements in Fig. 5a also show that the plume continues for the entire experimental domain and has yet to dissipate into the cross-flow. It would be ideal in the future to measure flow profiles further downwind of the exhaust stack ($z/D > 16$) to investigate distance before the plume dissipates into the cross-flow, however this requires a larger tunnel.

An issue with measuring the flow in the absence of a heated jet is that the effects of buoyancy are neglected. It is expected that the fluid dynamics of the plume, but in particular the position of the plume, would change slightly with the inclusion of the heated jet. However, for the the purpose of this study, the flow measurements were used to show that the reduced-scale experiments reproduced salient flow features observed in the literature[20,27,28]. Moreover, the complex velocity gradients measured downwind of the exhaust stack would effect the sound radiation.

The temperature gradients downwind of the exhaust stack are complex due to the heated plume, as will be shown in the temperature measurements presented. In Fig. 5b the vertical (y) temperature profiles at different distances upwind and downwind of the exhaust stack are presented, with all the measurements made along Y-Z plane that intercepts the centre of the duct ($x = 0$). A second set of temperature results are shown in Fig. 6 as contour plots along the X-Y planes at various distances downwind of the exhaust stack ($z/D = [8, 16]$).

Fig. 5b shows that upwind of the duct outlet, the temperature is approximately uniform, with $\Theta = 0$. However, downwind of the exhaust stack the temperature of the plume is not uniform and exhibits the following trends:

- a decrease in maximum normalised temperature from $\Theta \approx 0.19$ to $\Theta \approx 0.075$,
- increase in the vertical position of the maximum temperature from $y/D = 14$ to $y/D = 16.5$, and
- increase in the spatial size of the plume.

The results of the temperature measurements in Fig. 5b show a similar trend with the flow measurements in Fig. 5a. The temperature results observed here reflect previous work[27–29], which

show there is a decrease in temperature and increase in height of the plume, as plume propagates downwind of the exhaust stack.

Downwind of the exhaust stack the plume has a finite width in the span-wise direction, which was observed in the temperature measurements. Fig. 6 shows the temperature contour plot along the X-Y plane at two different positions downwind ($z/D = [8, 16]$). Fig. 6a and 6b show similar features with the increase in distance from the exhaust stack downwind: a decrease in the maximum temperature of the plume, an increase in the height of the plume, and an increase in the spatial size of the plume. From measuring the temperature, the shape of the counter rotating vortex pairs in Fig. 6 are similar to the counter-rotating vortex pairs observed in literature[29]. However, Fig. 6 shows that the maximum temperature was not in the middle of the counter-rotating vortex, as observed in the literature[29]. There are a number of possible reasons for the unexpected position for the maximum temperature. One of the reasons could be simply random experimental error in measuring the plume. Additionally, due to the discretised measurement, there could be a quantisation error in measuring the temperature at $1D$ intervals. Moreover, the duration for each temperature measurement (30 s) may be insufficient. Furthermore, the asymmetry bias in the counter-rotating vortex pairs could be related to asymmetry in the cross-flow or the jet.

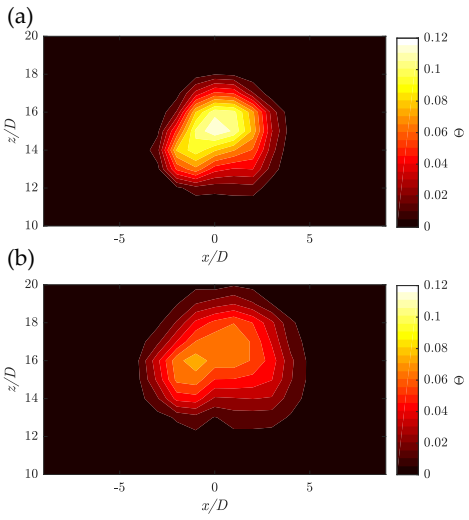

FIG. 6: Experimental temperature contour plot from the non-isothermal JICF at various distance downwind from the exhaust stack (a) $z/D = 8$, and (b) $z/D = 16$, with $R = 5$, and $T_j = 500\,°\text{C}$.

In summary, the temperature measurements downwind of the exhaust stack exhibits the expected jet spreading and entrainment of the cooler cross-flow, and a reduction in the temperature gradients with distance. The results were only measured up to $16D$ due to time constraints with

utilising the wind tunnel. All the measurements show the presence of a thermal gradient, and if measurements were taken further downwind of the exhaust, the plume would dissipate further, where eventually the temperature downwind would be the same as the cross-flow free-stream temperature.

IV. ACOUSTIC RESULTS

The sound propagation through the heated exhaust jet with cooler cross-flow is presented in this section for the following scenarios:

- sound propagation through an isothermal stationary field,
- sound propagation through a heated exhaust jet without cross-flow, and
- sound propagation through a heated elevated JICF.

Fig. 7a shows the experimental results for the sound directivity at distances of $14D$ and $28D$ in the absence of the heated jet and cross-flow. As expected for the 4 kHz one-third octave band ($ka \approx 1.08$), the sound directivity is axisymmetric and elliptical, with a lobe forming along the centreline of the duct axis at 0°. The results in Fig. 7a show a very similar radiation pattern to published duct directivity in free-field environments[31–33]. This differs from the commonly used monopole assumption in ISO 9613-2:1996[12]. In Fig. 7a, the elliptical lobe shows a reduction in sound levels of up to 4.5 dB at ±90° when compared to a monopole source with spherical spreading. Hence, for predictions of ground-level SPLs, the monopole assumption is likely to be conservative when designing noise control measures.

Fig. 7b shows the experimental results for the sound directivity at $28D$ with a heated jet of Mach number 0.1 and $T_j = 350\,°\text{C}$. The directivity plot shows that the sound is axisymmetric about the vertical axis, with a shadow zone or 'cusp' forming along the centreline of the duct axis (0°). The acoustic cusp has a DI of approximately −12 dB. The acoustic energy that was originally on-axis has been refracted by the jet shear layer to form acoustic lobes off-axis at approximately symmetrical locations of ±50°. The SPL of the lobes off-axis has increased by approximately 3 dB, compared with Fig. 7a. These results are qualitatively consistent from the results by Atvars, Schubert, and Ribner[36] and Björk[1]. It should be noted that the experimental results in this study were measured at a lower jet temperature ($T_j = 350\,°\text{C}$) than commonly seen in OCGT exhaust

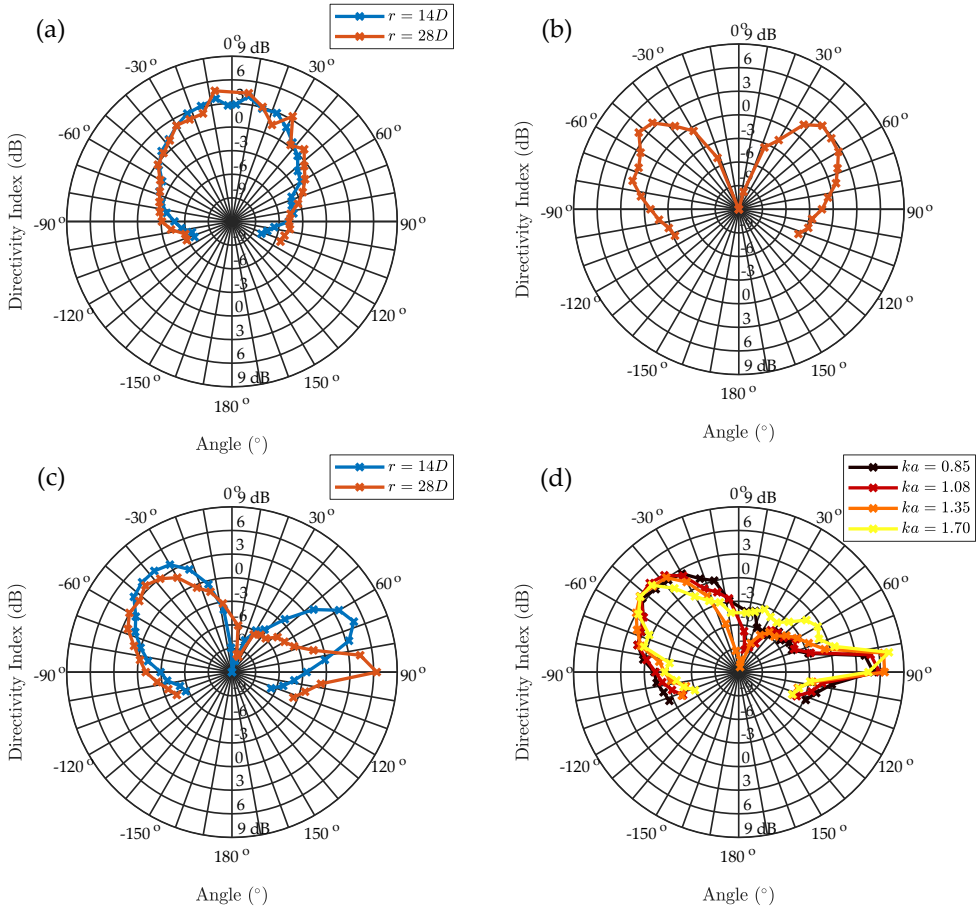

FIG. 7: The DI for sound propagation in (a) an isothermal stationary field ($T_j = 27\,°\text{C}$), (b) a heated jet ($T_j = 350\,°\text{C}$) with no cross-flow, (c) a heated jet ()$T_j = 500\,°\text{C}$) with cooler cross-flow at $ka = 0.85$, and (d) a heated jet ($T_j = 500\,°\text{C}$) with cooler cross-flow with $ka = [0.85, 1.08, 1.35, 1.70]$. The directivity results in (a), and (c) are for two different radii ($r = 14D$ and $28D$), where as the directivity results in (b) and (d) are for a single radius ($r = 28D$).

stacks and is a limitation of the experimental setup, where the air temperature at the $28D$ arc were not to exceed the 60 °C temperature rating of the microphones. Whilst, it was desirable to measure the directivity at $14D$ to observe the effects of distance on the sound propagation, in particular the refraction of sound as a result of the jet shear layer, unfortunately the microphone temperature limits were exceeded necessitating their removal during this test.

Fig. 7c shows the experimental result for the sound directivity at $14D$ and $28D$ of a heated JICF with $M = 0.1$, $T_j = 500\,°\text{C}$ and $R = 5$. Note that the cross-flow permitted higher stack exhaust temperatures than Fig. 7b whilst remaining under the 60 °C temperature limit at the microphone locations. By comparing Figs. 7a to 7c, it can be observed that with the heated plume and cross-

flow, the sound directivity is no longer elliptical or axisymmetric about 0°. The directivity of sound becomes biased towards the leeward side (or downstream) of the exhaust duct. The cross-wind shifts the peak observed in the downstream lobe from an angle of 65° to 90° for the 14D and 28D array, respectively. It can also be observed that as the sound propagates downstream the width of the lobe decreases from 40° to 25° for the 14D and 28D arcs, respectively. Comparing the results from Figs. 7a and 7c, as the downstream lobe bends over and becomes narrower, the energy becomes more concentrated, increasing in amplitude at the horizontal from -4.5 dB in Fig. 7a to 4.5 dB at 14D and 6.5 dB at 28D in Fig. 7c. However, upstream of the exhaust duct, the sound directivity patterns remain similar for the 14D and 28D arcs. The position of the acoustic 'cusp' or shadow zone shifted from 0° in Fig. 7b with no cross-flow to 10° at 14D and 20° at 28D with cross-flow present. It must be noted that the angular resolution of the directivity measurements is 7.5° increments and this may be insufficient in capturing fine detail in the directivity pattern. As sound propagates downstream, it can be observed that the plume continues to influence the propagation path and is strongly governed by the temperature gradients in the plume, which causes the sound to continually refract as it propagates downstream.

Fig. 7d shows the directivity with varying band-averaged one-third octave bands ($f = [3.15\,\text{kHz}$, 4 kHz, 5 kHz, 6.3 kHz] or $ka = [0.85, 1.08, 1.35, 1.70]$) at radius of 28$D$. All four curves show qualitative similarity in the acoustic results with: a cusp forming approximately at 10°, upwind of the exhaust stack a broad elliptical lobe resembling the off-axis lobe in Fig. 7b, and downwind a narrow acoustic lobe at approximately 90°. The key difference in directivity plots with the increase in acoustic frequency is the position of the acoustic lobe downwind, which shifts from 90° to approximately 80°. These results suggests that acoustic lobe downwind may not be fully resolved with the current angular spacing of the microphones. The results in Fig. 7d suggest that the directivity is dependant on the acoustic frequency.

Jet temperature is an important parameter that governs the sound radiation downwind of the jet outlet and this parameter was also investigated. Fig. 8a shows the directivity for the non-isothermal JICF, with $T_j = [27\,°\text{C}, 100\,°\text{C}, 300\,°\text{C}, 500\,°\text{C}]$. There are key features that remains the same in the directivity plots for all jet temperatures: a presence of a cusp on-axis (0°), a broad acoustic lobe upwind of the exhaust stack, and a concentration of sound downwind of the exhaust stack with narrow acoustic lobe. The increase in jet temperature shows unique temperature dependant features in the directivity plots, such as the following:

- the acoustic lobe position downwind of the exhaust stack shifts from approximately 50° to

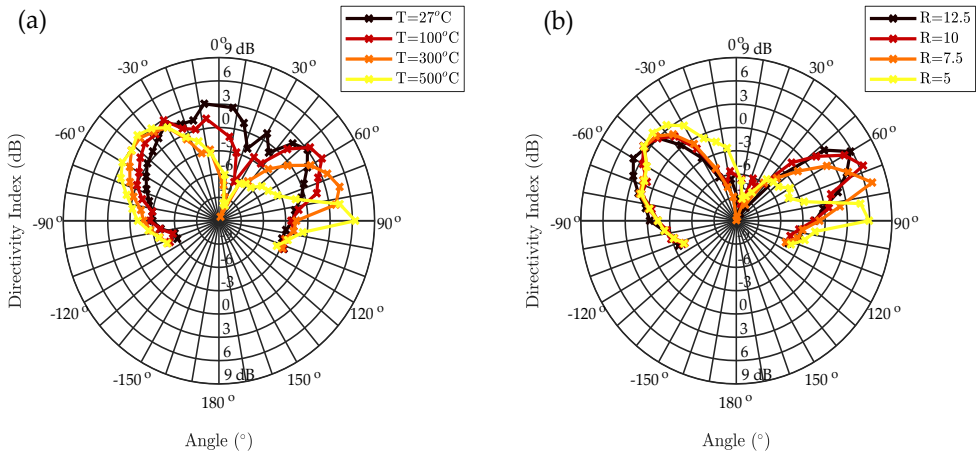

FIG. 8: The DI along the Y-Z plane (of symmetry) for sound propagation through a non-isothermal JICF for band-averaged one-third octave bands for (a) varying jet temperature, T_j, for $R = 5$ and (b) varying cross-flow ratios, R, for $T_j = 500\,°\text{C}$. The following parameters were consistent and for all tests; centre frequency, $ka = 1.08$, and $r = 28D$. The cross-flow is going from left to right.

90° with increasing temperature,

- the magnitude of the acoustic lobe downwind of the exhaust stack increases with temperature and can increase by up to approximately 4 dB from $T_j = 27\,°\text{C}$ to $500\,°\text{C}$,
- the depth of the cusp at approximately 7.5° to 22.5° increases with jet temperature, and
- upwind of the exhaust stack the magnitude of the lobe slightly increases with jet temperature.

Therefore, the jet temperature governs the directivity of sound, especially the refraction of sound downwind of the exhaust stack, with the hottest jet temperature ($T_j = 500\,°\text{C}$) showing the most significant increase in sound pressure levels downwind by up to 9 dB.

Fig. 8b shows the directivity for sound propagating through a non-isothermal jet in cross-flow with $R = [5, 7.5, 10, 12.5]$ and for a band-averaged one-third octave band ($f = 4\,\text{kHz}$ or $ka = 1.08$). The jet conditions remained consistent at $M = 0.1$ and $T_j = 500\,°\text{C}$, while the cross-flow free-stream velocity (u_{cf}) was varied to give the different values of R. The directivity plot shows that with a decrease in R from 12.5 to 5, the position of the acoustic lobe downwind shifts from 60° to 90°. While the increase in R towards 12.5 in Fig. 8b shows that the position of the acoustic lobe

downwind becomes more axisymmetric with the upwind acoustic lobe about the jet centreline axis at 0°. The acoustic directivity for $R = 12.5$ almost resembles the sound directivity to Fig. 7b, for $r = 28D$. The reason for similar directivity arcs is that with the reduction in cross-flow speed or increase in R, the plume downwind becomes more 'jet dominant'. Hence, since the plume is still in the 'jet dominant' regime for the directivity at $28D$, the directivity arc for Fig. 8b at $R = 12.5$ closely resembles the directivity in Fig. 7b. In the relative near-field the sound radiation at lower values of R or higher cross-flow free-stream velocities (u_{cf}) lead to the increase in SPL at ground-level ($28D$). In order to quantify the effects of the plume at these higher values of R then it is critical to increase the experimental domain spatially, but with the current facilities, this is not possible.

Fig. 8b shows that the cross-flow momentum flux ratio, $R = 7.5$, produces the highest magnitude acoustic lobe downwind of the exhaust stack. However, given that the spatial resolution of the microphones was only 7.5° the full resolution of the acoustic lobe may not be resolved. Hence, the full SPL magnitude of the acoustic lobe, as well as other acoustic features may not have been captured with the current array configuration.

V. DISCUSSION

In this experimental study it has been shown that the bent-over heated plume has changed the sound propagation path, with intermediate near-field refraction being the dominant mechanism for asymmetric sound radiation. The acoustic refraction downwind is due to the temperature and velocity gradients in the plume that alter the speed of sound (c) of the air. Fig. 8a shows that the majority of the refraction arises from the temperature gradients, causing a change in the speed of sound ($\Delta c \propto \sqrt{\Delta T}$), as opposed to the convective effects of the flow ($\Delta c = c + \Delta u_{\text{flow}}$)[18]. Work previously conducted by Leav, Cazzolato, and Howard[43] showed that the counter rotating vortex pairs produce thermal and velocity gradients. In their numerical work, the refraction continued for the entire computational domain ($40D$ downstream). Fig. 7c shows the relationship with the plume development, and acoustic refraction is consistent with the experimental directivity measurements in this paper at $14D$ and $28D$. Further experimental investigations will need to examine the directivity at radii greater than $28D$ to quantify far-field magnitude of the directivity index. The flow and temperature field associated with the experimental small-scale model will need to be measured to gain a better understanding on the fluid dynamics and temperature effects that govern

the propagation path of sound.

In Fig. 7c, the experimental results have shown the formation of a downstream lobe, which causes an increase in sound pressure level downwind. The results in Fig. 7c can be directly compared to the case without flow, seen in Fig. 7a, which results in an elliptical sound radiation pattern. Comparing Figs. 7a and 7c, the sound downstream at $-90°$ is approximately $-4.5\,\mathrm{dB}$ in Fig. 7a, whereas Fig. 7c shows the sound level is $6.5\,\mathrm{dB}$ at $-90°$, as a result of the sound interacting with the bent-over non-isothermal plume. Hence, in Fig. 7c, the plume has caused an $11\,\mathrm{dB}$ increase in the sound level parallel to the ground-plane when compared to the sound radiation in the absence of flow, as seen in Fig. 7a.

The cross-flow sensitivity study provides insight in to how the plume affects the sound. There are other factors that also change the position of the plume downwind, which includes the terrain downstream and the turbulence intensity of the incoming flow. It was observed in previous research[27,28] for elevated jets in cross-flow that the incoming turbulence intensity highly governs the diffusion of the plume, as well as span-wise and vertical flapping motion of the plume in the incoming flow. Hence, with the vertically flapping plume, it will cause the sound trajectory also to change, and subsequently, the downwind lobe position would also vary. The work presented in this paper analysed the time-average response of the sound, temperature and flow for the elevated jet in cross-flow. Hence, the transient effects of the sound interacting with the flapping plume was not quantified for this research.

The geometry of the reduced scale mode exhaust stack is a simple straight duct section that protrudes $10D$ into the flow. In real OCGTs, the geometry of the plant is considerably more complex, thereby affecting the cross-flow and consequently the sound refraction. This simplification of the model is appropriate for scientific investigation, as it resembles elevated jets in cross-flow seen in literature and reduces the acoustic and fluid dynamic complexity in the model. The main purpose of the research is to investigate the sound interaction with the plume and observe non-axisymmetry of the acoustic directivity, as well as broadly quantify the increase in sound level downstream.

In the experimental worked conducted here, measurements were taken with an anechoic ground to simulate an absorptive surface surrounding the stack. This is generally not the case for OCGTs, as the exhaust stacks are typically surrounded by complex structures and hard reflective surfaces. These reflective surfaces would change the sound directivity pattern and hence the experimental setup used here may not be an accurate representation of real installations. Work completed by Leav, Cazzolato, and Howard[43] suggests that a much more complex acoustic pattern occurs when

a reflective ground is included. As a result, Figs. 7 and 8 show 'smooth' directivity patterns in the absence of diffraction and reflections from other surfaces. Additionally, the sound directivity results in this paper are presented over four different one-third octave band averages to reduce the complexity of the results. Further tests over more than four different one-third octave bands should be undertaken to examine the relationship of the plume and the downstream sound levels.

VI. SUMMARY OF FINDINGS

The results presented in this paper has experimentally shown that under certain conditions, a heated jet in cooler cross-flow changes the propagation path of sound and can lead to increased sound levels observed downwind of the exhaust stack. The flow and temperature associated with the heated elevated JICF was measured and showed reproducible trends with the literature. Different operational conditions were investigated: the sound radiation through an isothermal stationary field, sound radiation in the presence of a heated jet without cross-flow, sound radiation in the presence of a heated JICF at $R = 5$, and sound radiation with $T_j = [27\,°\text{C}, 100\,°\text{C}, 300\,°\text{C}, 500\,°\text{C}]$, and sound radiation cross-flow sensitivity study for a heated jet with cooler cross-flow, with $R = [5, 7.5, 10, 12.5]$. The key findings for the acoustic results will be outlined in this section.

The sound directivity results for the duct network in the absence of the jet and cross-flow exhibits axisymmetric acoustic radiation. The directivity plot shows an approximately elliptical acoustic radiation pattern with a lobe forming on-axis (0°). The experimental sound directivity plot shows similar qualitative and quantitative trends the work published in literature[31–33]. For the case with the heated jet, the sound radiation is axisymmetric, but no longer spherical or elliptical, with a cusp forming on-axis and strong lobes forming off-axis. The results are due to the refraction of the propagating sound through the jet shear layer and the features in the directivity are qualitatively and quantitatively similar from work by others[36–38,41].

In the presence of the cross-flow, the sound radiation propagates through a heated elevated JICF and produces an asymmetrical directivity plot. It can be observed that the sound radiation lobe upwind is approximately elliptical and resembles the jet only directivity upwind of the exhaust stack. Downwind of the exhaust stack, the thermal and velocity gradients strongly refract the sound leading to the concentration of acoustic energy forming a narrow 'lobe'. The cusp previously seen on-axis for axisymmetric jets has rotated downwind by approximately 5°. Downwind of the exhaust stack, the non-isothermal JICF can increase the observed DI by up to 11 dB when

compared to the cases with the isothermal stationary field, and the heated jet without cross-flow.

The jet temperature has been shown to impact the sound directivity, whereby the hottest jet temperature ($T_j = 500\,°\mathrm{C}$) shows the greatest asymmetry in the directivity plot. The change in the directivity arises from the large change in temperature leading to the significant difference in the speed of sound ($\Delta c \propto \sqrt{\Delta T}$). Downwind of the exhaust stack the acoustic results show that increasing in T_j leads to: an increase in the DI magnitude for the acoustic lobe downwind of the exhaust stack, downwind of the exhaust stack there is a shift in the position of the acoustic lobe towards the ground-plane, and upwind of the exhaust stack the directivity lobe remains relatively unchanged with the change in jet temperature.

The sound radiation downwind of the exhaust stack is affected by the trajectory of the plume, which for this paper investigated altering the cross-flow frees-stream velocity. The DI plots in Fig. 8b has shown with the increase in R there is an decrease in the angular position of the acoustic lobe downwind of the exhaust stack. This indicates that if the cross-flow varies, then the acoustic lobe downwind will also vary, leading to fluctuating ground-level SPLs. The decrease in R causes the acoustic lobe in the directivity plot to reduce spatially. Furthermore, in the experimental domain of up to $28D$ the sound radiation converges at $R = 10 - 12.5$ and the sound radiation closely resembles acoustic directivity for a jet in the absence of cross-flow, as seen in Fig. 7b. Hence, for higher R the plume is in the 'jet dominant' regime causes almost axisymmetric spreading and to quantify the effects of the cross-flow speeds then a larger experimental domain would need to be considered for future testing.

The findings from the paper has alluded the importance of accounting for the heated plume in cooler cross-flow when predicting the sound downwind of a hot exhaust stack. The complex, asymmetric sound radiation observed in the experimental results are from a reduced-scale experimental rig with design of the experiment based on a 190 MW OCGT exhaust stack, but under various operating conditions outlined previously. However, additional research can be done to better understand the complex interaction between the acoustic field and a heated jet in cooler cross-flow in the far-field. This paper provides a fundamental investigation on the topic to assist acousticians in the field of environmental acoustics in understanding the increase in downwind sound levels for sound propagation from hot exhaust jets in cooler-cross-flow.

ACKNOWLEDGMENTS

Leav was sponsored by an Australian Government Research Training Program Scholarship from 2015 to 2018.

REFERENCES

[1]E. Björk, "Experimental study of measures to reduce noise radiated from power-station exhaust stacks," Noise Control Engineering Journal **42**, 171–178 (1994).

[2]N. Broner, "A simple criterion for low frequency noise emission assessment," Journal of Low Frequency Noise, Vibration and Active Control **29**, 1–13 (2010).

[3]N. Broner, "A simple outdoor criterion for assessment of low frequency noise emission," Acoustics Australia **39**, 7–14 (2011).

[4]N. Broner, "Power to the people," in *15th International Meeting on Low Frequency Noise and Vibration and its Control*, Low Frequency Noise, Vibration and Active Control (Low Frequency Noise, Vibration and Active Control, Stratford upon Avon, United Kingdom, 2012) pp. 1–10.

[5]G. Hessler Jr, "Proposed criteria in residential communities for low-frequency noise emissions from industrial sources," Noise Control Engineering Journal **52**, 179–185 (2004).

[6]G. Hessler Jr, "Proposed criteria for low frequency industrial noise in residential communities," Low Frequency Noise, Vibration and Active Control **24**, 97–106 (2005).

[7]R. Hetzel and R. Putnam, "Sources and rating criteria of low frequency gas turbine exhaust noise - via case study," in *INTER-NOISE and NOISE-CON Congress and Conference Proceedings, 2009* (Ontario, Canada, 2009) pp. 1600–1607.

[8]G. Kudernatsch, "Combustion turbine exhaust systems-low frequency noise reduction," in *INTER-NOISE 2000, The 29th International Congress and Exhibition on Noise Control Engineering* (Nice, France, 2000) pp. 1–6.

[9]J. R. Newman and K. I. McEwan, "Low frequency gas turbine noise," Journal of Engineering for Power **108**, 476–481 (1980).

[10]W. C. Lucas and G. F. Hessler Jr, "The reduction of low frequency gas turbine exhaust noise: A case study," in *ASME 1996 International Gas Turbine and Aeroengine Congress and Exhibition*, Turbo Expo: Power for Land, Sea, and Air, Vol. Volume 4: Heat Transfer Electric Power Industrial and Cogeneration (Birmingham, UK., 1996).

[11]International Organization for Standardization, "ISO 9613-1:1993 Acoustics - Attenuation of sound during propagation outdoors – Part 1: Calculation of the absorption by the atmosphere," (1993).

[12]International Organization for Standardization, "ISO 9613-2:1996 Acoustics - Attenuation of sound during propagation outdoors – Part 2: General method of calculation," (1996).

[13]International Organization for Standardization, "ISO 10494:2018 Gas turbines and turbine sets-Measurement of emitted airborne noise – Engineering/ survey method," (2018).

[14]K. Attenborough, S. Taherzadeh, H. Bass, X. Di, R. Raspet, G. Becker, A. Güdesen, A. Chrestman, G. Daigle, and A. L'Espérance, "Benchmark cases for outdoor sound propagation models," The Journal of the Acoustical Society of America **97**, 173–191 (1995).

[15]K. Attenborough, "Sound propagation close to the ground," Annual Review of Fluid Mechanics **34**, 51–82 (2002).

[16]T. Embleton, "Tutorial on sound propagation outdoors," The Journal of the Acoustical Society of America **100**, 31–48 (1996).

[17]U. Ingård, "A review of the influence of meteorological conditions on sound propagation," The Journal of the Acoustical Society of America **25**, 405–411 (1953).

[18]V. Ostashev and D. Wilson, *Acoustics in moving inhomogeneous media* (CRC Press, 2015).

[19]J. Piercy, T. Embleton, and L. Sutherland, "Review of noise propagation in the atmosphere," The Journal of the Acoustical Society of America **61**, 1403–1418 (1977).

[20]M. Adaramola, D. Sumner, and D. Bergstrom, "Effect of velocity ratio on the streamwise vortex structures in the wake of a stack," Journal of Fluids and Structures **26**, 1–18 (2010).

[21]O. Eiff, J. Kawall, and J. Keffer, "Lock-in of vortices in the wake of an elevated round turbulent jet in a crossflow," Experiments in Fluids **19**, 203–213 (1995).

[22]O. Eiff and J. Keffer, "On the structures in the near-wake region of an elevated turbulent jet in a crossflow," Journal of Fluid Mechanics **333**, 161–195 (1997).

[23]O. Eiff and J. Keffer, "Parametric investigation of the wake-vortex lock-in for the turbulent jet discharging from a stack," Experimental Thermal and Fluid Science **19**, 57 – 66 (1999).

[24]R. Huang and R. Hsieh, "An experimental study of elevated round jets deflected in a crosswind," Experimental Thermal and Fluid Science **27**, 77–86 (2002).

[25]R. Huang and R. Hsieh, "Sectional flow structures in near wake of elevated jets in a crossflow," American Institute of Aeronautics and Astronautics Journal **41**, 1490–1499 (2003).

[26]R. Huang and C. Hsu, "Turbulent flows of an acoustically excited elevated transverse jet," Amer-

ican Institute of Aeronautics and Astronautics Journal **50**, 1964–1978 (2012).

[27]J. Andreopoulos, "Wind tunnel experiments on cooling tower plumes: Part 1—in uniform crossflow," Journal of Heat Transfer **111**, 941–948 (1989).

[28]J. Andreopoulos, "Wind tunnel experiments on cooling tower plumes: Part 2—in a nonuniform crossflow of boundary layer type," Journal of Heat Transfer **111**, 949–955 (1989), 10.1115/1.3250810.

[29]B. Johnson, G. Elliott, and K. Christensen, "Structural characteristics of a heated jet in crossflow emanating from a raised, circular stack," Experiments in Fluids **54**, 1543 (2013).

[30]R. J. Wells and C. B. E., "Sound radiation patterns of gas turbine exhaust stacks," The Journal of the Acoustical Society of America **25**, 433–437 (1953).

[31]D. Bies, C. Hansen, and C. Howard, *Engineering Noise Control: Theory and Practice*, 5th ed., edited by C. Press (CRC Press, 2017).

[32]A. Day and B. Bennett, "Directivity of sound from an open ended duct," in *Acoustics 2008*, Australian Acoustical Society (Australian Acoustical Society, 2008).

[33]A. Day, C. Hansen, and B. Bennett, "Duct directivity index applications," Acoustics Australia **37**, 93–97 (2009).

[34]R. Amiet, "Refraction of sound by a shear layer," Journal of Sound and Vibration **58**, 467–482 (1978).

[35]S. Candel, "Acoustic transmission and reflection by a shear discontinuity separating hot and cold regions," Journal of Sound and Vibration **24**, 87–91 (1972).

[36]J. Atvars, L. Schubert, and H. Ribner, "Refraction of sound from a point source placed in an air jet," The Journal of the Acoustical Society of America **37**, 168–170 (1965).

[37]J. Atvars, L. Schubert, E. Grande, and H. Ribner, "Refraction of sound by jet flow or jet temperature," Book (Institute for Aerospace Studies, University of Toronto, 1965).

[38]E. Grande, "Refraction of injected sound by a very cold nitrogen jet," The Journal of the Acoustical Society of America **38**, 1063–1064 (1965).

[39]P. Mungur, H. Plumblee, and P. Doak, "Analysis of acoustic radiation in a jet flow enviroment," Journal of Sound and Vibration **36**, 21–52 (1974).

[40]A. Cummings, "High temperature effects on the radiation impedance of an unflanged duct exit," Journal of Sound and Vibration **52**, 299–304 (1977).

[41]R. J. Astley and W. Eversman, "Wave envelope elements for acoustical radiation in inhomogeneous media," Computers and structures **30**, 801–810 (1988), special Issue: Computational

Engineering Mechanics.

[42]O. Leav, B. Cazzolato, and C. Howard, "Directivity analysis of sound in turbulent exhaust jets with laminar cross-flow: A numerical study," in *Acoustics 2015*, Australian Acoustical Society (Australian Acoustical Society, Hunter Valley, New South Wales, 2015) pp. 1–10.

[43]O. Leav, B. Cazzolato, and C. Howard, "A computational analysis of sound directivity from sound propagation through non-isothermal, turbulent exhaust jets in cross-flow," in *24th International Congress on Sound and Vibration*, International Institute of Acoustics and Vibrations (International Institute of Acoustics and Vibrations, London, United Kingdom, 2017) pp. 1–8.

[44]Siemens, "We power the world with innovative gas turbines - Siemens gas turbine portfolio," Data sheet (2019).

[45]J. Bendat and A. Piersol, *Engineering applications of correlation and spectral analysis*, 2nd ed., edited by J. W. . Sons (John Wiley & Sons, 1993).

[46]Y. Kamotani and I. Greber, "Experiments on a turbulent jet in a cross flow," American Institute of Aeronautics and Astronautics Journal **10**, 1425–1429 (1972).